transactions of the ASME

journal of heat transfer

Published Quarterly by
The American Society of
Mechanical Engineers
Volume 98 • Series C • Number 3
AUGUST 1976

(Contents continued on page 352)

EDITED and PUBLISHED quarterly at the offices of The American Society of Mechanical Engineers, United Engineering Center, 345 E. 47th St., New York, N. Y. 10017. Cable address, "Mechaneer," New York, Second-class postage paid at New York, N. Y., and at additional mailing offices.
CHANGES OF ADDRESS must be received at Society headquarters seven weeks before they are to be effective. Please send old label and new address.
PRICES: To members, $25.00, annually; to nonmembers, $50.00. Single copies, $15.00 each. Add $1.50 for postage to countries outside the United States and Canada.
STATEMENT from By-Laws. The Society shall not be responsible for statements or opinions advanced in papers or . . . printed in its publications (B 13, Par. 4).

INDEXED by the Engineering Index, Inc.

CONTENTS (CONTINUED)

TECHNICAL NOTES

ERRATA

F. K. Moore
Professor.

C. C. Ndubizu
Research Assistant.

School of Mechanical and Aerospace Engineering,
Cornell University,
Ithaca, N. Y.

Analysis of Large Dry Cooling Towers With Power-Law Heat Exchanger Performance

An analysis is presented for heat exchanger area, tower exit area, and exchanger tube length and number, for heat exchangers in large dry cooling towers, having performance parameters given by powers of Reynolds number, but otherwise under very general cooling-cycle constraints. The calculation method is illustrated for a "spine-fin" heat exchanger which, in a tube size of about 3/8 in., seems capable of achieving low tower size in a practical device.

Calculations, over ranges of water pumping power, approach, ITD, number of passes, tube size, tower shape (natural draft) or fan power (mechanical draft), and ambient pressure altitude are shown to be well represented by a chain of powers of these variables, and certain functions of the ratio of real to ideal tower exit area. This ratio is shown to have a best value, depending on the cost coefficients of heat exchange and exit areas, and it is pointed out that typical cost proportions lead to a fluid-mechanical "packaging" problem for the shallow heat exchangers which would be preferred.

Introduction

The future realization of the benefits of dry cooling for large power plants will depend on the reductions of size and cost that can be made, on the basis of technical improvement. In [1],[1] of which this paper is a continuation, it was suggested that the key to such improvement is the use of a shallow and hence "fine" heat exchanger. In that paper, an idealized plate-fin exchanger was used to illustrate the analysis.

Here we illustrate the analysis of [1] by adopting a specific heat-exchanger type, namely the "spine-fin" device familiar through its use in General Electric home air conditioners. Essentially, a 3/8-in. tube (carrying water in our case) is helically wrapped with a thin sheet slit into a series of narrow fins, so that when assembled, these fins stand out from the tube as spines. Visually, the device looks like a bottle brush of about 1 in. dia. We choose the spine-fin heat exchanger for study because it is a quite fine configuration which has proven satisfactory in long continuous service and which is claimed to have an attractively slow and gradual loss of performance due to fouling, and to be easily cleaned when necessary [2]. A particular tube and fin geometry will be specified for study in a later paragraph. The essential results probably apply for any reasonably fine finned surface.

After fully describing the heat exchanger type, the number of important parameters requiring specification remain very numerous; initial temperature difference, approach, and water pumping power are a few examples. Therefore, we make calculations over as wide a range of relevant parameters as possible, keeping the process as analytic as possible and, especially, looking for algebraic correlations of the results, so as to facilitate subsequent cost optimization studies. In fact, we shall find our results[2] to be well represented by certain simple chain formulas which bring out the importance of the ratio (called ξ in [1]) of tower exit area to its ideal minimum.

General Analysis

We begin by recording the draft equation and certain definitions from [1]:[3]

$$A_c = \sqrt{\frac{KE}{(\alpha_I I')^2 Y}\frac{{\alpha_I}^2\psi}{FI'}}\frac{\xi}{\sqrt{\xi^2-1}}\ell^{5/2} \tag{1}$$

$$A_E = \xi\frac{\ell^{5/2}}{(\alpha_I I')^{3/2}Y^{1/2}} \tag{2}$$

We regard ξ, I', P_I (involved in ψ), and ℓ to be parameters. The quantity multiplying ξ in equation (2) is the minimum A_E, which

[1] Numbers in brackets designate References at end of paper.

Contributed by Heat Transfer Division of THE AMERICAN SOCIETY OF MECHANICAL ENGINEERS, and presented at the Winter Annual Meeting, Houston, Texas, November 5, 1975. Revised manuscript received by the Heat Transfer Division June 21, 1976. Paper No. 75-WA/HT-46.

[2] Numerical details are provided in a Cornell Report [3].

[3] Symbols are defined in the Nomenclature.

would result if the only head loss were at the tower exit; that is, if the heat-exchanger exerted no drag on the rising air. Thus, ξ is the ratio of A_E to its ideal minimum value [1]. α_I, the air temperature rise, is a variable requiring solution. Y is constant for mechanical draft, but is proportional to $\sqrt{A_E}$ for natural draft towers of constant shape. This will be our basic distinction between the two tower types.

To continue, we introduce certain definitions concerning the heat exchanger. By definition of hydraulic radius r_{h_a},

$$A_a = g_3 A_c; \quad \text{where } g_3 \equiv L_a/r_{h_a} \tag{3}$$

and the hydraulic radius also enters into air-side Reynolds number (divided by 1000 for convenience) with the result

$$\underline{R} = g_4/(\alpha_I A_c); \quad g_4 \equiv W\ell r_{h_a}/(1000\, I') \tag{4}$$

We expect that power laws may satisfactorily describe the Reynolds-number dependences of heat exchanger behavior:

$$\mathrm{St}_a \equiv \mathrm{St}_0 \underline{R}^{-t}; \quad K \equiv \frac{f}{\mathrm{St}} \equiv K_0 \underline{R}^{-k}; \quad \eta_0 \equiv \eta_{00} \underline{R}^{-u} \tag{5}$$

Hence, equation (6) of [1], which gives E, takes the form

$$\lambda \equiv 1 - \frac{1}{\eta_0 E} \simeq 1 - \frac{1}{L_a/r_{h_a}} \frac{1}{\mathrm{St}_0 \eta_{00} F} \underline{R}^{t+u} \alpha_I{}^3 \psi \tag{6}$$

In effect, equations (1), (4), and (6) provide an equation connecting $\underline{R}$ and α_I.

Turning to the water side, we may combine equations (10) and (11) of [1] to give the water pumping-power ratio

$$p_w \equiv \frac{\text{power}}{Q} = \frac{1}{2} v_{c_w}{}^2 \frac{n L_w f_w}{d_i C_{p_w} I' T_0 (1 - P_I)} \tag{7}$$

Adopting the Colburn formula for f_w (equation (9) of [1]) gives

$$p_w = \frac{v_{c_w}{}^2 n L_w (0.184) \mathrm{Re}_w{}^{-1/5}}{2 d_i C_{p_w} I' T_0 (1 - P_I)} \tag{8}$$

where

$$v_{c_w} \equiv v^*/[(1 - P_I)N] \tag{9}$$

Thus, p_w is related to N and L_w, both unknowns.

Fig. 1 shows that

$$L_w = g_8 A_c/N; \quad g_8 \equiv (r A_c/A_f)^{-1} \tag{10}$$

or, eliminating L_w between equations (8) and (10),

$$N = \left(\frac{g_7 A_c}{p_w}\right)^{5/14} \frac{1}{1 - P_I}; \quad g_7 \equiv p^* n \tag{11}$$

We contemplate specifying p_w, so N and L_w are known if A_c is found. It should be emphasized that p_w refers only to pumping loss in the tubes, not including header and header connection losses.

From equation (3) of [1], and appropriate definitions, we know

$$A_w h_w = \frac{Q}{F I' T_0} \frac{\alpha_I{}^2 \psi}{\lambda} \tag{12}$$

Inasmuch as $A_w = n N L_w \pi d_i$, and the Colburn formula for St_w may be used to express h_w, we learn that

$$0.023\pi\, \mathrm{Re}_w{}^{4/5} \mathrm{Pr}_w{}^{1/3} k_w n N L_w = \frac{Q}{F I' T_0} \frac{\alpha_I{}^2 \psi}{\lambda} \tag{13}$$

Equation (13) can be evolved into an equation connecting $\underline{R}$ and α_I by first introducing equations (10) and (11) to eliminate NL_w in favor

Nomenclature

A_a, A_w = heat-exchange areas on air and water sides
A_c, A_f = free-flow area and frontal areas of heat exchanger
A_E = exit area of tower
a_0 = ambient sound speed
C_a, C_E = cost coefficients of exchanger and exit areas (equation (31))
C_p = specific heat at constant pressure

$$c \equiv \left[\frac{0.092\pi C_{p_w} \mu_a n^{5/7} I'}{C_{p_a} \mu_a \mathrm{Pr}_w{}^{2/3} W \ell p^{*2/7} r} \left(\frac{A_f}{A_c}\right) \left(\frac{v^* d_i \rho_w}{\mu_w}\right)^{4/5}\right]^{7/5}$$

d_i = inside diameter of tubes
E = effectiveness factor
F = counterflow equivalence factor
f = friction factor
G = defined in equation (20)
g_0, g_1, g_2, g_6 = defined in equation (21)
g_3, g_4, g_7, g_8 = defined in equations (3), (4), (10), and (11)
g^* = defined in equation (25)
h_w = water-side heat-transfer coefficient
I' = ratio of initial temperature difference (ITD) to ambient air temperature
K = Reynolds-analogy factor f/St
k, t, u = exponents in equation (5)
L_a = heat-exchanger depth (Fig. 1)
L_w = length of water passages (Fig. 1)
$\ell \equiv [Q/(\sqrt{2g}\rho_0 C_{p_0} T_0)]^{2/5}$
N = number of water passages (Fig. 1)
n = number of water passes
P_I = ratio of approach to initial temperature difference (Fig. 1)
p_f = ratio of fan power to Q
p_w = ratio of frictional pumping power in tubes to Q

$$p^* \equiv 0.092 v^{*2} \left[d_i C_{p_w} I' T_0 r \frac{A_c}{A_f} \left(\frac{v^* d_i \rho_w}{\mu_w}\right)^{1/5}\right]^{-1}$$

Q = heat rejected from tower
r = transverse tube spacing (Fig. 1)
r_{h_a} = hydraulic radius, air side
Pr, Re, St = Prandtl, Reynolds, and Stanton numbers
$\underline{R} \equiv \mathrm{R}_{e_a}/1000$
St_0, K_0, η_{00} = coefficients in equation (5)
s = shape factor, $Y A_E{}^{-1/2}$
T_0 = ambient air temperature
v_{c_w} = bulk velocity in water tubes

$$v^* \equiv Q \Big/ \left[\rho_w C_{p_w} I' T_0 \frac{\pi}{4} d_i{}^2\right]$$

$W \equiv 4Q/(C_{p_0} T_0 \mu_0 \ell)$
Y = generalized draft height ($a_0{}^2 p_f/(\gamma - 1)g$ for mechanical draft, $s\, A_E{}^{1/2}$ for natural draft)
$z_0 \equiv 2/(2 - k - t)$

$$z_{N1} \equiv \frac{z_0}{14}[40 - 19(k + t)]; \quad z_{M1} \equiv \frac{z_0}{14}[43 - 19(k + t)]$$

$$z_{N2} \equiv \frac{10}{z_0}[30 - 15k - 13t + 2u]^{-1}; \quad z_{M2} \equiv \frac{2}{z_0}(6 - 3k - 2t + u)^{-1}$$

α_I = ratio of air temperature rise to ITD
η_0 = air-side overall fin effectiveness
κ = defined in equation (25)
λ = deviation of E from unity (equation (6))
μ, ρ = viscosity and density
ξ = ratio of actual A_E to its minimum (equation (2))

$$\left.\begin{matrix}\tau_N \\ \tau_M\end{matrix}\right\} \equiv \frac{g_4}{\sqrt{\dfrac{L_a K_0 \mathrm{St}_0}{r_{h_a}}}} \begin{cases} \ell^{-2} I'^{6/5} s^{2/5} \\ \ell^{-5/2} I'^{3/2} \left[\dfrac{a_0{}^2 p_f}{(\gamma - 1)g}\right]^{1/2} \end{cases}$$

$\psi \equiv \alpha_I{}^{-2}(1 - P_I - \alpha_I)^{-1} \ln|(1 - \alpha_I)/P_I|$

Subscript $_0$ represents ambient conditions, a and w represent air and water sides of the heat exchanger. Subscripts $_N$ and $_M$ represent natural and mechanical draft, and $_A$ represents evaluation for Case A with $P_I = 0.6$ and $p_w = 0.001$.

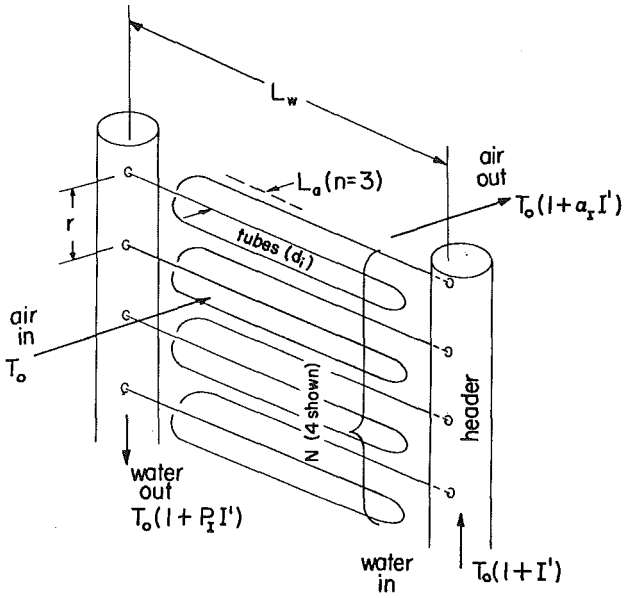

Fig. 1 Sketch of heat-exchanger arrangement. Only bare tubes are indicated. Fin geometry appears in Fig. 2

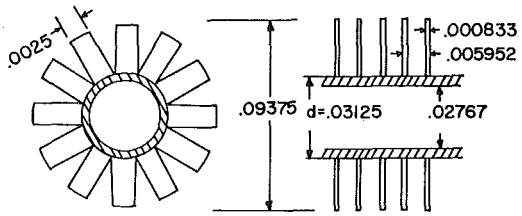

Fig. 2 Sketch of assumed dimensions (in ft) of heat exchange element

of A_c and then recalling equations (4) and (6). The result is

$$\underline{R} = g_4 c p_w^{2/3} \left(\frac{F}{\psi}\right)^{7/5} \alpha_I^{-19/5} \left[1 - \frac{\alpha_I^3 \psi \underline{R}^{t+u}}{(L_a/r_{h_a}) \mathrm{St}_0 \eta_{00} F}\right]^{7/5} \quad (14)$$

Then, recalling that the draft equation (1), in combination with equations (4) and (6) also gives an equation relating $\underline{R}$ and α_I, we may derive a single equation for α_I. After considerable algebra, one finds this transcendental equation for α_I:

$$\alpha_I = \left(g_0 G^{t+u} \frac{F}{\psi} - \frac{g_1}{p_w^{2/7} G^{5/7-t-u}}\right)^{z_2} \quad (15)$$

The various constants are tabulated below, and in the Nomenclature. One may easily solve equation (15) for α by iteration, and then calculate other quantities directly, by the equations which follow. In writing them, one must generally distinguish between mechanical draft (fixed Y) and natural draft ($Y \propto A_E^{1/2}$); in the latter case, Y depends on α_I, according to equation (2).

$$A_{c_N} = g_{N2} G_N \alpha_I^{-(1+\frac{1}{2}z_0)}; \; A_{c_M} = g_{M2} G_M \alpha_I^{-(1+\frac{1}{2}z_0)} \quad (16)$$

$$\underline{R} = g_4 (\alpha_I A_c)^{-1} \quad (17)$$

$$\lambda = 1 - g_5 \underline{R}^{t+u} \alpha_I^3 \psi / F; \; g_5 \equiv [(L_a/r_{h_a}) \mathrm{St}_0 \eta_{00}]^{-1} \quad (18)$$

$$A_{E_N} = g_{N6} \xi^{4/5} \alpha_I^{-6/5}; \quad A_{E_M} = g_{M6} \xi \alpha_I^{-3/2} \quad (19)$$

A_a, N, and L_w follow from equations (3), (10), and (11).

The various quantities not already defined are

$$G_N \equiv (\xi^{4/5}/\sqrt{\xi^2 - 1})^{z_0}; \quad G_M \equiv (\xi/\sqrt{\xi^2 - 1})^{z_0} \quad (20)$$

$$g_{N,M0} \equiv (L_a/r_{h_a}) \mathrm{St}_0 \eta_{00} \tau_{N,M}^{-z_0(t+u)} \quad (21a)$$

$$g_{N,M1} \equiv g_{N,M0} [\tau_{N,M}^{z_0}/(c g_4)]^{5/7} \quad (21b)$$

$$g_{N,M2} \equiv g_4 \tau_{N,M}^{-z_0} \quad (21c)$$

$$g_{N6} \equiv \ell^2 I'^{-6/5} s^{-2/5}; \; g_{M6} \equiv \ell^{5/2} I'^{-3/2} [(\gamma - .1) g/(a_0^2 p_f)]^{1/2} \quad (21d)$$

where the τ's and z's are defined in the Nomenclature.

The counter-flow equivalence factor F requires determination, and it depends on α_I, P_I and heat-exchanger type. If we assume a succession of water passes ($n = 3$ in Fig. 1) in cross-counter arrangement, with passes of equal effectiveness, and with each pass characterized by full mixing on the air side and no mixing on the water side, use of a standard chart [4] gives a Table of $F(\alpha_I, P_I)$ which is well represented by the following formula over the parameter ranges of interest:

$$F = 1 - A(1 - \alpha_I)^{-B}$$

where

n	A	B
1	$0.179 - 0.382\mathrm{P_I} + 0.212 P_I^2$	$2.21 + 0.10\mathrm{P_I} - 0.80 P_I^2$
2	$0.0365 - 0.0425\mathrm{P_I}$	$2.65 - 2.25\mathrm{P_I}$
3	$0.0101 - 0.0055\mathrm{P_I}$	$3.22 - 3.70\mathrm{P_I}$

(22)

This completes the general analysis. The foregoing formulas are applicable to any tower for which either shape (s) or draft height (p_f) are constant, so long as the heat exchanger performance depends on Reynolds number according to power laws of the sort defined in equation (5).

Heat Exchanger Performance

Fig. 2 shows a suitable idealization of the spine-fin heat exchanger, with a realistic set of dimensions; ⅜ in. is typical of the practical tube diameter used in air conditioners. The first four entries in Table 1 correspond to these dimensions. We assume a longitudinal pitch of 0.07715 ft, and a staggered array for $n = 2$ or 3. Calculations were made using a General Electric Company compilation [5] of heat-exchanger data for various general types, including the spine fin. The results appear in Fig. 3.

Clearly, straight-line approximations are reasonable in this case, and we infer the parameters shown in Table 1 for use in equation (5). We will be interested in the effect of making d_i much smaller than ⅜ in. On the basis of Reynolds-number similarity, we may still use the Table 1 parameters provided all dimensions are reduced in proportion.

Parameter Selection

The heat exchanger is now fully described, and it remains only to specify cases for calculation, according to some scheme which would provide a broad picture of performance possibilities upon which subsequent optimizations could be based.

The left column of Table 1 gives what we shall consider the basic case (A). The shape $s = 1.703$ is that of the Rugeley tower [6], and is probably reasonable for natural-draft towers. For mechanical draft, a fan power of 1 percent of heat rejected (about 2 percent of electric power generation) is reasonable; often 3 percent of output is mentioned in describing such installations. Sea-level atmospheric pressure is assumed, and the design ambient temperature is taken to be 87°F, which is 95 percent maximum at Philadelphia, for example. ITD is taken to be 40°F; thus, entering water temperature is 127°F, and if the terminal temperature difference of the condenser is 7°F, condensation would occur at 5.0 in Hg. [1]. We take Q to be $1.6 \cdot 10^5$ Btu/s, which is about that of the Rugeley tower. This heat-rejection rate would be needed for about 90 MWe of nuclear power generation. Thus, about 14 of our towers would be needed for a 1200 MWe nuclear plant. From these parameters, the last column of Table 1 and a set of the various g's may be calculated.

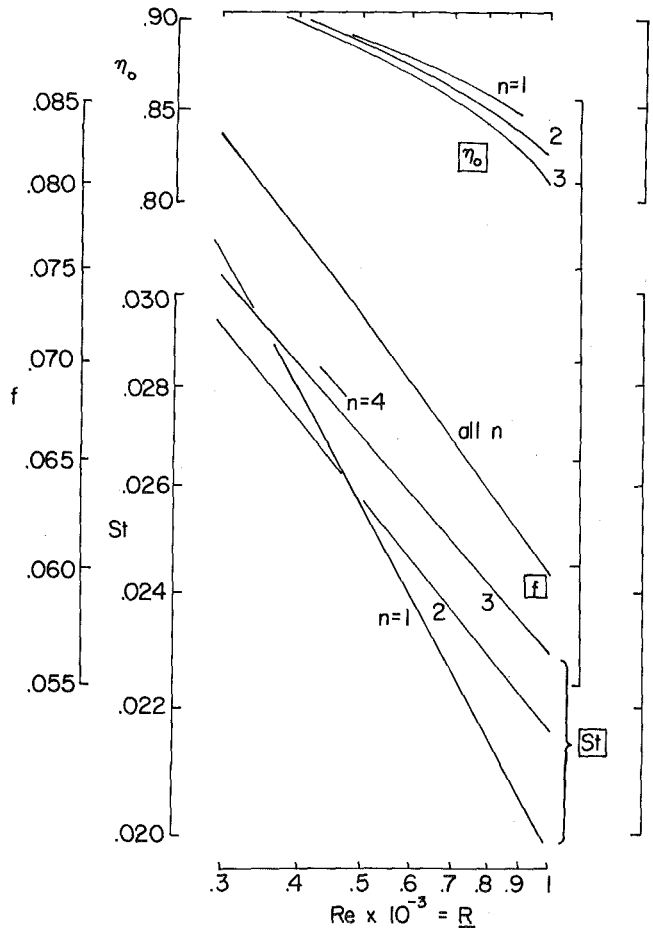

Fig. 3 Friction factor, Stanton number, and fin effectiveness, versus Reynolds number for spine-fin heat exchanger, for *n* passes

Water pumping power (frictional loss in tubes, only) is typically very small and $p_w = 0.0001$ or 0.02 percent of electric power would be not unreasonable. In contrast, $p_w = 0.01$ would mean 2 percent of electric power for frictional loss—surely too high to be acceptable. $p_w = 0.001$, or 0.2 percent would be higher than ordinary, but perhaps economically desirable if the resulting tower cost is low.

Approach P_I is typically 0.4 or 0.5; however, larger values result in a smaller tower. In fact, the limit $P_I = 1$ proves to be thinkable for the tower (but not, of course, for the condenser!). We choose $P_I = 0.6$ and $p_w = 0.001$ as basic values.

We envision calculating tower performance, with both natural and mechanical draft, for the foregoing basic case over a range of the remaining parameter ξ between 1.1 and 2.5. In the limit $\xi = 1$, A_E would have its minimum value, and A_a would presumably be infinite, while if $\xi > 2.5$, the tower would be too large, as we shall see.

Next, we consider repeating our calculations for various modifications of our basic case. P_I and p_w must be varied, and other changes are listed in Table 2, labeled by letter for convenience. For example, Case *C* is unchanged from Case *A* except that the heat exchanger has 3 passes instead of 2. We explore other changes, taken one at a time: They are mostly of self-evident interest; it might be remarked that in Case *I*, we change ambient pressure altitude from sea level to 5000 ft, and in Cases *N* through R, we run through cases of constant *Y* down to 150 ft—these results would be convenient for assessing changes of *Q* for natural draft towers of fixed height.

Owing to the simple algebraic character of the equations, each of the *g*'s vary as powers of the parameters of Table 2, except n.

Results and Discussion

For each case, for various ξ, p_w, and P_I, we solve equation (15) for α_I. Then, using equations (16), (3), (19), (10), and (11), we find the four basic design requirements: A_a, A_E, N, and L_w. This procedure was carried out, and the results in tabular form appear in [3]. Here we will present certain graphical and analytical interpretations of those tables, emphasizing natural draft for the sake of brevity.

Calculated Results. Fig. 4 shows results for A_a and A_E for Case *A* (natural draft), under variations of P_I and p_w. For a given p_w, P_I,

Table 1 Primary quantities for tower calculations (dimensions are ft, lb, Btu, s, and °R

	Assumed parameters		Derived quantities				
d_i	0.02767	n	1	2	3	ℓ	21.28
$4r_{ha}$	0.009080	L_a	0.0776	0.1543	0.2319	W	$1.741 \cdot 10^7$
A_c/A_f	0.5200	St_o	0.01971	0.02163	0.02292	p^*	16530
r	0.08333	K_o	3.031	2.762	2.607	z_0	1.1594
s	1.703	η_{oo}	0.8465	0.8312	0.8247	v^*	107,850
p_f	0.01	t	0.375	0.251	0.233	c	0.019464
p_a	2116	k	−0.100	0.024	0.042	τ_N	0.6759
Q	$1.6 \cdot 10^5$	u	0.066	0.089	0.092	τ_M	1.7258
T_o	547						
I	40; $P_I = 0.6$; $p_w = 0.001$						

Table 2 Definition of calculated cases—blanks are left where entries would be unchanged from Case A

Symbol	$Q \cdot 10^{-5}$	I	s	p_f	d_i	n	T_o	p_a
A	1.6 Btu sc^{-1}	40°F	1.703	0.01	3/8 in.	2	87°F	1 atm
B						1		
C						3		
D					1/8			
E		50						
F		60						
G							60	
H							95	
I								0.832
J	3.2							
K	0.8							
L			2.4	0.015				
M			1.0	0.005				
N				0.004				
R				0.0015				

and A_E (or tower height), A_a and ξ are fixed. Evidently, a small tower size requires a large heat-transfer area, especially for small approach or low pumping power. It seems clear that no particular benefit results from using the very large p_w of 0.01, as compared with 0.001. The apparent benefits of high approach would have to be balanced against the increased size and cost of the condenser and water headers.

Presumably owing mostly to the greater depth (6 in.) of the Rugeley heat exchanger [1, 6], that tower would appear at the point $A_a = 7.5 \cdot 10^6$, $A_E = 3.5 \cdot 10^4$ in Fig. 4. A finer heat exchanger, such as the spine-fin, seems to provide a clear advantage as regards both tower size and exchanger weight.

To each point in Fig. 4 corresponds a point on Fig. 5, which then gives the particular combination of N and I_w implied by A_a and A_E. In effect, Fig. 5 describes how a given parallel-circuit flow resistance (p_w) may be achieved for a certain total line length NL_w proportional to A_a; obviously, if one wished to hold A_a constant, and reduce p_w (for example), one would simply use more, shorter tubes. Fig. 5 shows such a tendency when results for $p_w = 0.001$ and 0.0001 are compared. For $P_I = 0.6$, tube lengths are about 18 ft in the former case and about 9 ft in the latter.

In this study, we are ignoring questions of header arrangement and associated losses. For example, if L_w is very small and N is very large, the question of exit and entrance losses arises. Also, if P_I is near 1, frictional losses in the headers themselves could become important. These corrections would not be important in our parameter ranges, apparently. For a study of these "arrangement losses," see [7].

Fig. 6 shows the same sort of information as Fig. 4, but for the various (natural draft) cases defined in Table 2. Here, to reduce clutter, we give curves only for $p_w = 0.001$ and $P_I = 0.6$. However, ξ varies along each curve, typically from 1.1 at the left to 2.5 at the right. The curve labeled A repeats the (0.6, 0.001) curve of Fig. 4. Referring now to Table 1, it would seem that over our range of interest, the 2-pass arrangement would be preferred over either 1 or 3 (or more) passes, at least for the spine-fin surface assumed in this study.

A_a would apparently improve by about 15 percent if all exchange-element dimensions were reduced by a factor of 3. It turns out that tube lengths would also be reduced by about the same factor (but number would be larger, of course). It would seem doubtful that the A_a savings would warrant the development of a heat-exchanger surface based on ⅛ in. tubing.

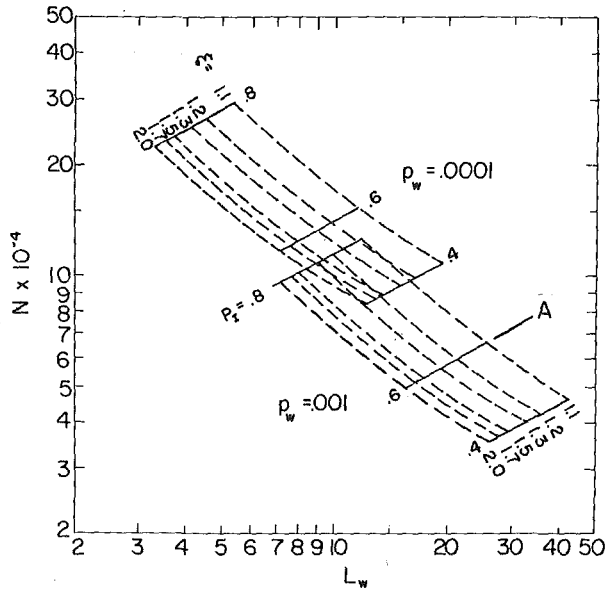

Fig. 5 Number versus length of tubes, corresponding to Fig. 4

Curves E and F show the expected powerful effect of ITD on A_a and A_E; a 20°F increase of ITD could reduce both areas by about ⅓. For the same ITD, changes of temperature level (Cases G and H) have negligible effect, and are not shown. An area penalty of about 15 percent results from a change of altitude from sea level to 5000 ft, owing to the reduced density of the air coolant.

From [1], we would expect areas to scale roughly with $Q^{4/5}$, and Case K would thus give areas about 60 percent of those in Case A, as curve

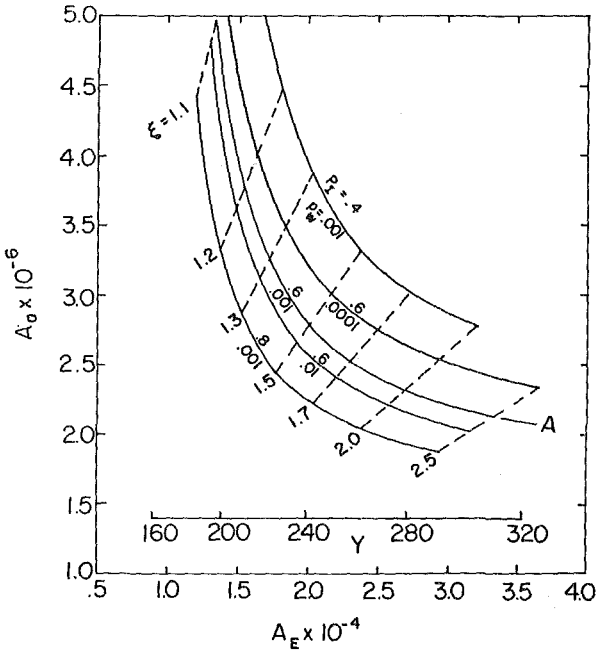

Fig. 4 Heat-exchanger area versus tower exit area for Case *A*, natural draft, with various approaches and water pumping powers, and otherwise the same parameters as Case *A*. Dimensions in ft

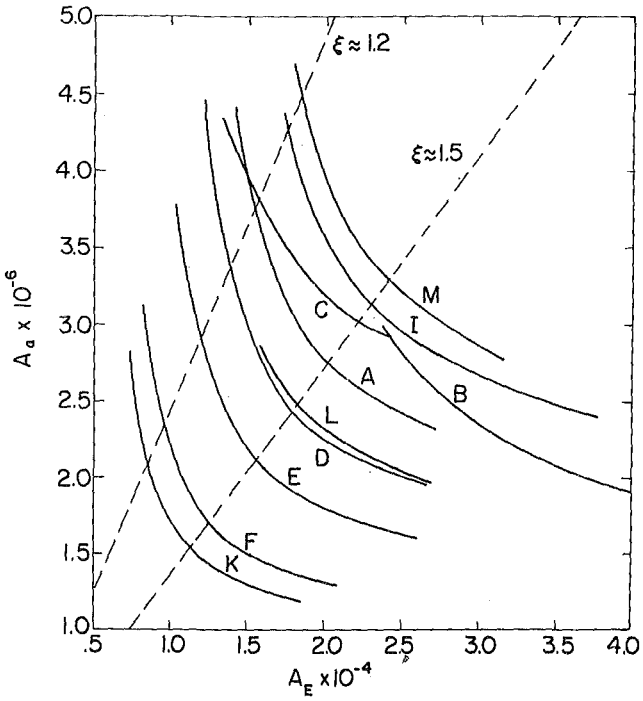

Fig. 6 Heat-exchanger area versus natural-draft exit area for various cases defined in Table 2. Case *A* is the "basic" one. Except for *B*, *C*, and *D*, ξ is nearly constant on rays from origin. $p_w = 0.001$ and $P_I = 0.6$ in all cases

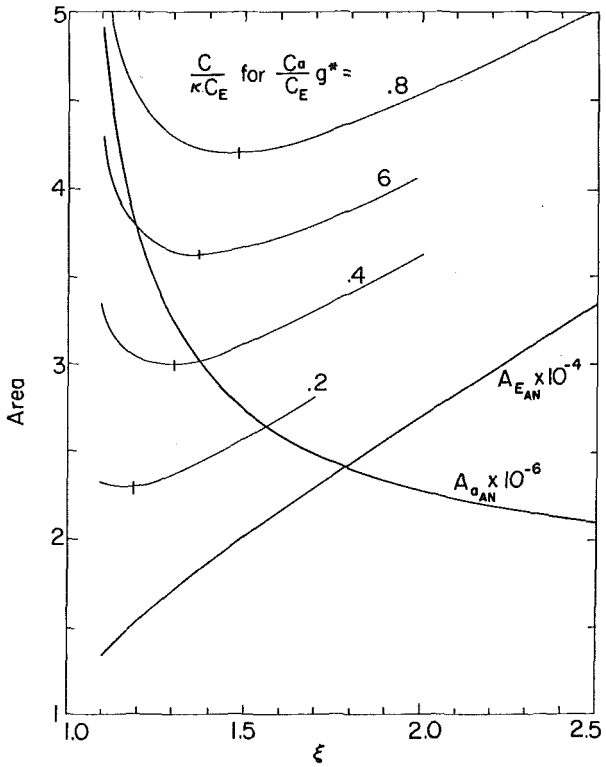

Fig. 7 Area and cost functions for natural draft

K in Fig. 6 in fact shows.

Results for mechanical draft are generally similar to those just described, except that 3 passes is a more attractive, and 1 pass is a less attractive option. This result is presumable due to the effectiveness of large equivalent draft height in overcoming the drag associated with multiple passes.

So far, the only tower losses we have considered are those due to the heat exchanger and the tower exit loss. Other losses occur, of course, and Rossie, et al. [8] have estimated these extra losses as 37 percent of exit head loss, for natural draft. The present analysis can easily accommodate such a correction, because ξ is also directly related to exit head loss. In effect, we may imagine that exit head loss is increased by a factor β (= 1.37, if Rossie's suggestion is adopted). Then, since the factor multiplying ξ in equation (2) is proportional to the square-root of the exit loss, equation (2) may be modified by inserting the factor $\sqrt{\beta}$ on the right side. The rest of the analysis is unaffected (equation (1) stands without change), and β enters only in the final calculation of A_E, if Y is fixed (as for mechanical draft). For natural draft (e.g., Fig. 6), it is quite accurate to interpret the abscissa A_E as the actual A_E divided by $\beta^{2/5}$; i.e., the scale is contracted by 13 percent if $\beta = 1.37$.

Analytical Correlations. Figs. 4 and 6 show properties suggesting two possibilities for correlation:

(1) Constant values of ξ tend to lie along rays from the origin; that is, A_a/A_E tends to be a function of ξ alone. In fact, equations (3), (16), and (19) give

$$\frac{A_a}{A_E} = \left(\frac{g_3 g_{N2}}{g_{N6}}\right) \frac{G_N(\xi)}{\xi^{4/5}} \alpha_I^{0.2(1-z_0)} \tag{23}$$

for natural draft, and a similar equation for mechanical draft. Since $0.2(1-z_0) = -0.032$ and α_I is in the range 0.6–0.7, the last factor of equation (23) is always very nearly 1. Similarly, it may be shown that the first factor, while depending strongly on n, and slightly on d_i, is nearly independent of other parameters. Using the values for Case A, namely 145.8 (natural) and 125.5 (mechanical) as references, we record in Table 3 the values of

$$g^* \equiv \left(\frac{g_3 g_{N2}}{g_{N6}}\right) \Big/ 145.8 \quad \text{or} \quad \left(\frac{g_3 g_{M2}}{g_{M6}}\right) \Big/ 125.5 \tag{24}$$

(2) The shapes of the various curves in Figs. 5 and 7 tend to be similar, though they are not hyperbolas, as one might first guess. Instead, they follow closely a rule that $A_a A_E$ is a function of ξ. There is no easily-seen theoretical reason for this result. In any event, if it is true, then the additional fact that A_a/A_E is a function of ξ (nearly) means that A_E and A_a separately must be functions of ξ.

In other words, we propose the correlations

$$A_E = \kappa A_{E_A}(\xi); \quad A_a = g^* \kappa A_{a_A}(\xi) \tag{25}$$

at least for $P_I = 0.6$, $p_w = 0.001$. Fig. 7 shows the reference functions based on Case A. For each case, over a range of ξ, the ratio A_E/A_{E_A} was found to vary only slightly (except when number of passes was changed) as shown in the column $\Delta\kappa$ of Table 3. The representative value of κ was chosen at $\xi = 1.5$ for natural and 1.3 for mechanical draft. For Cases E through L, omitted from Table 3, the variation of κ is less than 1 percent, and g^* is within 2 percent of unity. Clearly, the correlations of equation (25) are successful within the expected accuracy of heat-exchanger analysis.

As to variations with P_I and P_w, numerical results show that A_E varies independently with P_I, and (less accurately) with p_w. Other data at $P_I = 0.8$ and $p_w = 0.01$ support the idea that a power-law-variation may be assumed. For example, $A_E \sim P_I^{-0.43}$ for natural draft. Applying the same reasoning for the other variations described in Table 2, we develop the final grand correlation formulas for all 2-pass cases considered.

Natural.

$$\frac{A_E}{A_{E_A}(\xi)} = \frac{1}{g^*}\frac{A_a}{A_{a_A}(\xi)} = \left(\frac{P_I}{0.6}\right)^{-0.43} \left(\frac{p_w}{0.001}\right)^{-0.033} \left(\frac{d_i}{3/8}\right)^{0.20} \times \left(\frac{I}{40}\right)^{-1.18} \left(\frac{s}{1.70}\right)^{-0.28} \left(\frac{Q}{1.6 \cdot 10^5}\right)^{0.85} \tag{26}$$

Mechanical.

$$= \left(\frac{P_I}{0.6}\right)^{-0.49} \left(\frac{p_w}{0.001}\right)^{-0.045} \left(\frac{d_i}{3/8}\right)^{0.27} \times \left(\frac{I}{40}\right)^{-1.35} \left(\frac{p_f}{0.01}\right)^{-0.32} \frac{Q}{1.6 \cdot 10^5} \tag{27}$$

Both Natural and Mechanical.

Table 3 Summary of results as to variation with ξ —unless otherwise noted, $P_I = 0.6$ and $p_w = 0.001$

	Natural			Mechanical		
Case	κ at $\xi = 1.5$	$\Delta\kappa$	g^*	κ at $\xi = 1.5$	$\Delta\kappa$	g^*
A (0.6, 0.001)	1	0	1	1	0	1
(0.6, 0.0001)	1.08	0.04	1	1.13	0.05	1
(0.4, 0.001)	1.19	0.01	1	1.23	0	1
(0.4, 0.0001)	1.29	0.07	1	1.39	0.07	1
D	0.80	−0.07	1.191	0.74	−0.04	1.191
M	1.17	−0.02	1.035	1.24	−0.02	1.057
N	—			1.35	−0.05	1.076
R	—			1.88	−0.13	1.163

$$N = 9.11 \left(\frac{d_i}{3/8}\right)^{-2.07} \left(\frac{I}{40}\right)^{-1} \left(\frac{T}{547}\right)^{-1} \times \left(\frac{Q}{1.6 \cdot 10^5}\right)^{0.64} \frac{A_a{}^{5/14}}{(1 - P_I)p_w{}^{5/14}} \quad (28)$$

$$L_w = 0.340 \left(\frac{d_i}{3/8}\right)^{-1} \frac{A_a}{N} \quad (29)$$

These correlations show the important role of ξ, the ratio of A_E to its theoretical minimum, which appears to be analogous to the "effectiveness" (ϵ) of heat-exchanger analysis.

Cost Optimization. The chain character of the correlations just described implies that each parameter may be separately optimized against its external counterpart (e.g., approach P_I versus condenser size), and that a relative cost minimum exists for variations of A_a and A_E. In other words, there is a best ξ which is nearly independent of other variables.

Specifically, suppose a general cost expression includes these two linear terms

$$C = C_E A_E \cdot 10^{-4} + C_a A_a \cdot 10^{-6} + \ldots \quad (30)$$

with constant coefficients C_E and C_a. Such a linear formula cannot always be assumed, of course; however, it will suffice for present purposes of illustration. Equation (25) permits equation (30) to take the form

$$\frac{C}{\kappa C_E} = A_{E_A}(\xi) \cdot 10^{-4} + \left(\frac{C_a}{C_E} g^*\right) A_{a_A}(\xi) \cdot 10^{-6} + \ldots \quad (31)$$

If so, Fig. 7 shows that the right side of equation (31) would be minimum at a value of ξ below about 1.5 (about 1.3 applies for mechanical draft). In any event, knowledge of C_a and C_E would fix a best ξ, regardless of other parameters. Further, the special importance of reducing heat-exchanger cost is demonstrated; it is associated with the more strongly varying quantity when ξ is small.

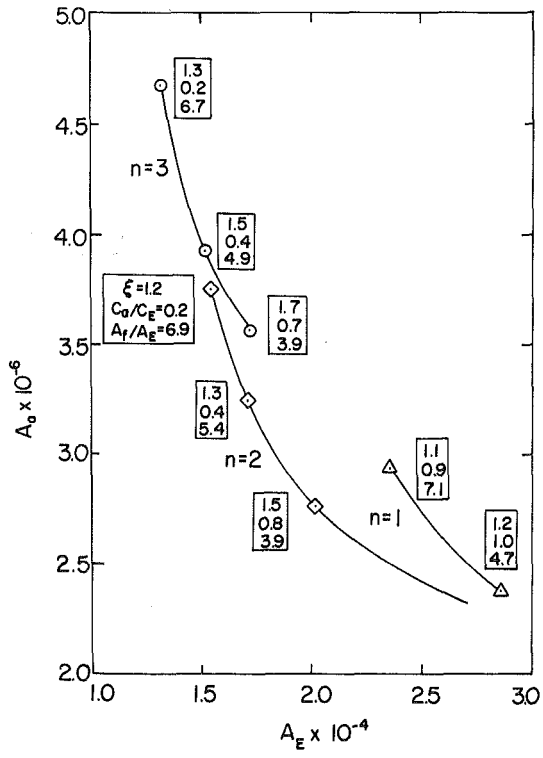

Fig. 8 Heat-exchanger versus exit area, for natural draft and 1, 2, and 3 passes (Cases *B*, *A*, and *C*) with $p_w = 0.001$ and $P = 0.6$, showing values of ξ, C_a/C_E, and A_f/A_E at various points

Finally, we return to Fig. 6 and observe that a best ξ in the range of 1.5 would imply a firm choice of two passes for natural draft, but results [3] are ambiguous as to a choice between two and three passes for mechanical draft, if ξ should be less than 1.3. This point requires further study, for a variety of fine surface types.

Heat-Exchanger "Packaging" in the Tower. Finally, we must recall that tower geometry must be arranged to provide the frontal area called for by the solutions we have presented. This requirement can be expressed as the ratio A_f/A_E. In the natural-draft Rugeley Tower [6], an A_f/A_E of 2.18 is achieved by arranging heat-exchanger panels in a folded oblique pattern. The obliquity is nearly 60 deg, which seems to be a conventional limit for heat exchangers. If the heat exchanger panels are in a horizontal array, as at Grootvlei [9], a maximum A_f/A_E of about 4 would seem feasible, for a 60 deg folding of the panels.

Equations (20) and (23) yield the following approximate but general equation for natural draft, and a similar one for mechanical draft:

$$\frac{A_f}{A_E} = \frac{A_f}{A_c} \frac{r_{h_a}}{L_a} \frac{A_a}{A_E} = \frac{1}{A_c/A_f} \frac{g_{N2}}{g_{N6}} \frac{\xi^{0.8(z_0-1)}}{(\xi^2 - 1)^{0.5z_0}} \quad (32)$$

Clearly, the nearer A_E is to its minimum, the greater the A_f/A_E requirement. This relationship is shown for natural draft in Fig. 8 for one, two, or three passes. Also shown are the cost-coefficient ratios for which each particular value of ξ would be optimum, according to Fig. 7. Thus, for two passes, if C_a/C_E were 0.2, the optimum ξ would be 1.2 and a "packaging ratio" of 6.9 would be needed to achieve that optimum. The figure shows that there is little advantage in choosing three passes instead of two. In that case, A_f/A_E would be 6.7, and the total cost (from equation (30)) would be nearly the same. A single pass would not be of advantage for reasonable values of C_a/C_E.

It should be remarked that values of C_a/C_E ranging between 0.2 and 0.8 are reasonable; equation (30) shows the corresponding ratios of heat-exchanger to tower costs to be 0.5 and 1.1. The cost breakdowns given in the Appendices of [8] suggest that "bundle" costs and costs attributable to tower size are about equal. A decrease of heat-exchanger cost or a continuation of the trend to relatively higher field construction costs could certainly lead to values of the ratio in the neighborhood of 0.5.

If, as we suggest, the best C_a/C_E ranges between 0.2 and 0.8, then horizontal arrays would probably be favored, to make large values of A_f/A_E more feasible. Even so, one would need much more than the customary 60-deg obliquity in order to achieve the optimum A_f/A_E. It is therefore clear that innovative tower shapes and heat-exchanger configurations will be needed to exploit the potential savings associated with shallow heat exchangers.

Concluding Remarks

The present study has shown that shallow arrays of rather fine heat exchangers have excellent prospects for achieving important reductions of heat-exchange area and draft requirement for large dry cooling towers. The spine-fin surface exemplifies this approach, but other finned surfaces of comparable fineness would no doubt do as well. It seems from Fig. 6 that there is no great advantage in air-side hydraulic diameters much less than the value of 0.01 ft emphasized herein.

Rather extensive calculations covering changes of all important performance parameters were shown to correlate strongly with a ratio (ξ) of exit area to the ideal exit area for no heat-exchanger drag. A chain formula was shown to represent the correlation quite well, permitting step-by-step cost optimization. In particular, if the cost coefficients for A_a and A_E are known, a relative cost minimum exists for some ξ, regardless of other parameters.

Research will be needed to discover how an optimally shallow heat exchanger of large frontal area may be "packaged" in a cooling tower of the corresponding minimum size.

Acknowledgment

This research was supported by the National Science Foundation, Division of Advanced Technology Applications (RANN).

References

1 Moore, F. K., and Hsieh, T., "Concurrent Reduction of Draft Height and Heat-Exchange Area for Large Dry Cooling Towers," JOURNAL OF HEAT TRANSFER, TRANS. ASME, Series C, Vol. 96, No. 3, Aug. 1974, pp. 279–285.

2 "Fouling and Cleaning of Condenser Surfaces," *Specifier's Guide*, General Electric Co., Air Conditioning Division, Louisville, Kentucky, Publ. No. 20-2023-05.

3 Moore, F. K., and Ndubizu, C., "Analysis of Large Dry Cooling Towers With Spine-Fin Heat-Exchange Elements," Cornell Energy Program Report No. EPR-75-2, June 1975.

4 Krieth, F., "Principles of Heat Transfer," International, Scranton, Pa., 1958.

5 "Heat Exchanger Design," User's Guide 905218A, Mark II, General Electric Co., Information Systems, Bethesda, Md.

6 Christopher, P. J., and Forster, V. T., "Rugeley Dry Cooling Tower System," *Proc. Inst. Mech. Eng.*, Vol. 184, PF 1, No. 11, 1969–1970, pp. 197–222.

7 Pimputkar, S. M., "Configuration of Module Heat Exchangers for Dry Cooling Towers of Large Power Plants," MS thesis, Cornell University, Jan. 1974.

8 Rossie, J. P., Cecil, E. A., and Young, R. O., "Cost Comparison of Dry-Type and Conventional Cooling Systems for Representative Nuclear Generating Plants," TID-26007, prepared for the U.S. Atomic Energy Commission, Mar. 1972.

9 van der Walt, N. T., West, L. A., Sheer, T. J., And Kuball, D., "The Design and Operation of a Dry Cooling System for a 200 MW Turbo-Generator at Grootvlei Power Station, South Africa," Presented at 9th World Energy Conference, Detroit, Sept. 22–27, 1974.

W. L. Oberkampf
Assistant Professor,
Mechanical Engineering,
The University of Texas at Austin,
Austin, Texas
Assoc. Mem., ASME

L. I. Crow
Staff Engineer,
Texas Water Rights Commission,
Austin, Texas

Numerical Study of the Velocity and Temperature Fields in a Flow-Through Reservoir[1]

The fluid dynamic and temperature fields in a reservoir are numerically simulated by means of a finite difference procedure. The flow in the rectangular reservoir is assumed to be two-dimensional in a vertical plane. Inflow is allowed at the surface on one end of the reservoir and outflow occurs at any depth on the opposite end. The reservoir inflow is set at a given temperature and velocity so as to simulate the thermal discharge from a power generating facility. At the surface of the reservoir wind shear, short wave and long wave radiation, evaporation, and convective heat transfer are taken into account. The effects of inflow/outflow, wind shear, and heat transfer on the reservoir are discussed.

Introduction

In the United States today there is a growing concern for the preservation and improvement of the quality of the nation's environment. Recently emerging as a special environmental issue is the problem of the thermal pollution of the nation's water resources. Thermal pollution refers to the degradation of the aquatic environment by heat. The discharge of heated water into ambient water causes a temperature rise which leaves very few physical, chemical, or biological processes unaffected [1].[2] In order to understand the natural fluid motion in lakes and rivers, and to predict the effects of thermal discharges from power plants, mathematical modeling of the phenomena must be employed.

Water Resources Engineers (WRE) [2, 3] developed a mathematical model to describe the thermal behavior of a deep reservoir subject to various hydrologic, meteorologic, and climatic conditions. While the model is capable of simulating prototype thermal behavior, it has the disadvantage of being one-dimensional. That is, even though all mass and energy in the reservoir is accounted for, transfer of mass and energy occurs only along the vertical axis; horizontal flows are disregarded. Park and Schmidt [4] extended the WRE model to include mass and energy transfer in the horizontal direction. The extended model is two-dimensional, but it does not treat the mechanics of the flow. Clay and Fruh [5] developed a model similar to the WRE model to investigate selective withdrawal. Except for the outflow profile, reservoir hydrodynamics and currents are ignored in the reservoir simulation. Liggett [6] presented a finite difference method for computing the flow in shallow lakes. The MAC method was used to solve the Navier-Stokes equations in horizontal layers of the lake. The continuity equation was used to calculate the motion in the vertical plane. Although Liggett did not consider heat transfer effects, he presented one of the first solutions to lake circulation using the full nonlinear equations.

Stratified flows were modeled numerically by Terry, Mercier, and Slotta [7] using the MAC method. The model deals with the hydrodynamics of stratified flows, but the thermal behavior of the water is ignored. Dake and Harleman [8] presented an analytical and laboratory study of thermal stratification in lakes. A theory was developed for the time dependent vertical temperature distribution in a deep lake during the yearly cycle of solar heating and cooling. The analytical model was based upon the one-dimensional energy equation in the vertical direction, neglecting the hydrodynamics of the lake. A numerical model was developed by D'Arezzo and Masch [9] to investigate near-surface hydrodynamic and transport phenomena in water impoundments. Considering two-dimensional transport in the fully mixed surface layer of a water impoundment, it was concluded that wind induced surface currents were the most important transport mechanism. The effect of surface wind was also studied in laboratory experiments by Urban [10]. He investigated the thermal behavior as well as the flow fields in a small stratified laboratory reservoir. With a heated surface discharge, the development of temperature fields was studied for various withdrawal depths and surface wind conditions. Wind velocity and direction were found to strongly affect the temperature field development. Huber, Harleman, and Ryan [11] presented a method for the prediction of the vertical temperature distribution in stratified reservoirs. The mathematical model presented was similar to that of Dake and Harleman [8], but they added energy transport by means of convection in the vertical direction. An

[1] This work was funded by the Lower Colorado River Authority, State of Texas.

[2] Numbers in brackets designate References at end of paper.

Contributed by the Heat Transfer Division and presented at the Winter Annual Meeting, Houston, Texas, November 27–December 5, 1975, of THE AMERICAN SOCIETY OF MECHANICAL ENGINEERS. Revised manuscript received by the Heat Transfer Division June 7, 1976. Paper No. 75-WA/HT-60.

explicit finite difference method was used to solve one-dimensional unsteady energy transport equation.

The present study is concerned with the simulation of the velocity and temperature fields in a reservoir under various natural and artificial conditions. The motion of a viscous heat conducting fluid is considered in the vertical plane of an idealized two-dimensional reservoir. The reservoir is of rectangular cross section in the vertical plane with inflow at one end and outflow at the other. The Navier-Stokes and energy equations are solved on a digital computer using finite difference approximations. In order to show the fundamental fluid motion, the effects of wind shear and inflow/outflow without temperature effects are presented first. These driving phenomena are then combined with heat transfer effects and heated inflow so as to treat the thermal discharge problem.

Mathematical Analysis

Governing Equations. Consider the two-dimensional motion of a viscous, heat conducting, Newtonian liquid. Equations describing this motion are the vorticity transport equation, stream function equation, and energy equation.

$$\frac{\partial \zeta}{\partial t} = -\frac{\partial (u\zeta)}{\partial x} - \frac{\partial (v\zeta)}{\partial y} + \frac{1}{R_e}\left(\frac{\partial^2 \zeta}{\partial x^2} + \frac{\partial^2 \zeta}{\partial y^2}\right) - \frac{1}{F_r}\frac{\partial \rho}{\partial x} \tag{1}$$

$$\frac{\partial^2 \Psi}{\partial x^2} + \frac{\partial^2 \Psi}{\partial y^2} = \zeta \tag{2}$$

$$\frac{\partial T}{\partial t} = -\frac{\partial (uT)}{\partial x} - \frac{\partial (vT)}{\partial y} + \frac{1}{P_e}\left(\frac{\partial^2 T}{\partial x^2} + \frac{\partial^2 T}{\partial y^2}\right) \tag{3}$$

and $u = \partial\Psi/\partial y$, $v = -\partial\Psi/\partial x$, R_e = Reynolds number, F_r = Froude number, and P_e = Peclet number. These equations have been nondimensionalized by defining

$$x = x'/L_0', \qquad y = y'/L_0', \qquad u = u'/u_0',$$
$$v = v'/u_0', \qquad \zeta = \zeta'/(u_0'/L_0'), \qquad T = T'/T_0',$$
$$\rho = \rho'/\rho_0', \qquad t = t'/(L_0'/u_0'), \qquad \Psi = \Psi'/u_0'L_0',$$

where L_0' = lake depth, u_0' = characteristic velocity, T_0' = inflow temperature, and ρ_0' = density at inflow.

Concerning the assumptions applied to equations (1)–(3), the flow is assumed to be laminar. Most investigators in the past have made the same assumption, although it is typically stated as "The eddy viscosity coefficient for momentum and energy transfer is assumed constant." The Peclet number is assumed constant for a given flow field. The density is considered to be a function of temperature only and is calculated from a second degree polynomial curve fit of experimental data for water.[3]

The vorticity equation and the energy equation are both parabolic in time, second order, nonlinear, partial differential equations. They are coupled through the temperature dependent buoyancy term in the vorticity equation. The stream function equation poses a boundary value problem given by the linear elliptic Poisson equation with vorticity acting as the driving function.

Finite Difference Method. The geometry of the assumed rectangular reservoir and the finite difference nomenclature are shown in Fig. 1. The mesh spacing in the x-direction is Δx and the y-direction is Δy. Subscripts (i, j) are associated with each mesh point, so that the space variables may be expressed as $x_i = (i-1)\Delta x$, for $i = 1, 2, \ldots, I$ and $y_j = (j-1)\Delta y$, for $j = 1, 2, \ldots, J$. Time is segmented into equal intervals Δt so that the nondimensional time t is $t = n\Delta t$, for $n = 0, 1, 2, \ldots$. The notation $\phi_{ij}{}^n$ denotes the value of a variable ϕ at the mesh point (i, j) at time level n.

In a large scale reservoir, advection is the principal transport mechanism because relatively high Reynolds numbers are being considered. For high Reynolds numbers it was found that particular care had to be taken in choosing a differencing scheme for the advection terms in the vorticity equation. After several numerical experiments it was decided to use a scheme reported by Gentry, Martin, and Daly [13] termed the second upwind differencing method. The second upwind differencing method possesses both the conservative and transportive properties and, for certain advection fields, is a second order differencing scheme [14, p. 73].

The second upwind differencing method applied to the advection term $\partial(u\zeta)/\partial x$ is

$$\left.\frac{\delta(u\zeta)}{\delta x}\right|_{ij} = \frac{u_R\zeta_R - u_L\zeta_L}{\Delta x}$$

where

$$u_R = (u_{ij} + u_{i+1,j})/2, \qquad u_L = (u_{i-1,j} + u_{ij})/2$$

$$\zeta_R = \begin{cases} \zeta_{ij} & \text{for } u_R > 0 \\ \zeta_{i+1,j} & \text{for } u_R < 0 \end{cases}$$

$$\zeta_L = \begin{cases} \zeta_{i-1,j} & \text{for } u_L > 0 \\ \zeta_{ij} & \text{for } u_L < 0 \end{cases}$$

The finite difference representation of the y-derivative advection term is

$$\left.\frac{\delta(v\zeta)}{\delta y}\right|_{ij} = \frac{v_T\zeta_T - v_B\zeta_B}{\Delta y}$$

where

$$v_T = (v_{ij} + v_{i,j+1})/2, \qquad v_B = (v_{i,j-1} + v_{ij})/2$$

$$\zeta_T = \begin{cases} \zeta_{ij} & \text{for } v_T > 0 \\ \zeta_{i,j+1} & \text{for } v_T < 0 \end{cases}$$

$$\zeta_B = \begin{cases} \zeta_{i,j-1} & \text{for } v_B > 0 \\ \zeta_{ij} & \text{for } v_B < 0 \end{cases}$$

The advection terms in the energy equation are treated analogously.

[3] For more details of the present investigation, see reference [12].

Nomenclature

c_p = specific heat at constant pressure
g' = gravitational constant
F_r = Froude number, $[u_0'^2/(g'L_0')]$
k = thermal conductivity
L_0 = reservoir depth
P_e = Peclet number, (R_eP_r)
P_r = Prandtl number, $(c_p'\mu'/k')$
q_a = long wave atmospheric radiation to the surface
q_b = back radiation from the surface
q_c = convective heat transfer to the surface
q_e = heat transfer from the surface by evaporation
q_s = short wave radiation to the surface
q_T = total heat transfer to the surface
R_e = Reynolds number, $(u_0'L_0'/\nu')$
t = time
T = temperature
T_0 = inflow temperature
u, v = velocities in the x-, y-directions, respectively
u_0 = characteristic velocity
x, y = coordinate system (Fig. 1)
ζ = vorticity, $(\partial u/\partial y - \partial v/\partial x)$
μ = absolute viscosity
ν = kinematic viscosity, (μ/ρ_0)
ρ = mass density
τ_s = shear stress of the air on the water surface
Ψ = stream function

Superscripts

( )′ = dimensional quantity
( )^n = time level n of numerical integration

Subscripts

( )$_a$ = air
( )$_{i,j}$ = mesh point (i, j)
( )$_w$ = water
( )$_s$ = surface

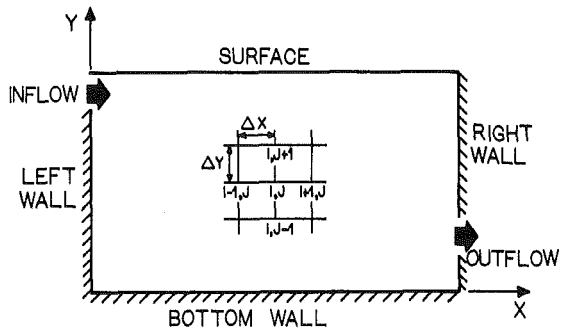

Fig. 1 Reservoir and finite difference mesh

The buoyancy term in the vorticity equation is differenced using the first upwind differencing method [14, p. 64–67]. This is a first order, one-sided, differencing scheme with the choice of differencing side dependent on the direction of the local flow. The finite difference form of the buoyancy term is

$$\left.\frac{\delta\rho}{\delta x}\right|_{ij} = \frac{\rho_R - \rho_L}{\Delta x}$$

where

$$\rho_R - \rho_L = \begin{cases} \rho_{ij} - \rho_{i-1,j} & \text{for } u_{ij} \geq 0 \\ \rho_{i+1,j} - \rho_{ij} & \text{for } u_{ij} < 0 \end{cases}$$

The parabolic vorticity and energy equations are solved using the alternating direction implicit (ADI) method of Peaceman and Rachford [15]. The method is second order in time and, because of its numerical stability properties, permits a larger time step than most explicit methods. The ADI method advances the solution from time level n to time level $n + 1$ in two steps. The first step advances the solution in the x-direction to an intermediate level, usually termed $n + \frac{1}{2}$. The second step advances the solution in the y-direction to time level $n + 1$. For details of the ADI procedure applied to the vorticity and energy equations, see reference [12].

The stream function equation, equation (2), is approximated by using second order centered space differences.

$$\zeta_{ij} = \frac{\Psi_{i+1,j} - 2\Psi_{ij} + \Psi_{i-1,j}}{\Delta x^2} + \frac{\Psi_{i,j+1} - 2\Psi_{ij} + \Psi_{i,j-1}}{\Delta y^2}$$

This equation is solved using successive overrelaxation [16].

Initial and Boundary Conditions for Vorticity and Velocity. The computational problem is initialized with the fluid at rest. Consequently, at all interior points the u and v velocity components and the vorticity are set to zero, while the stream function is constant.

The left, right, and bottom boundaries of the reservoir (see Fig. 1) are considered impermeable; requiring that the normal component of velocity be zero at the walls. Imposition of the no-slip condition at solid boundaries makes the tangential velocity component zero. A first order difference approximation is used for vorticity along the solid walls.

The fluid surface is considered a rigid, slip wall. That is, the vertical velocity component is zero at the surface, while the horizontal velocity is free to develop.

The influence of wind on the water surface is treated in the following manner. Assume that the local shearing stress τ_s due to wind action at the air-water interface is known. Then at any point on the surface $\tau_s = \mu_w(\partial u/\partial y)_s$ where μ_w is the viscosity of water. Using the definition of vorticity and the fact that $v = 0$ at the surface, one has $\zeta_s = \tau_s/\mu_w$.

An expression was sought for shearing stress at the water surface which would reflect the turbulent boundary layer of the wind. The following empirical expression by Schultz-Grunow [17] for estimating the local shear of a turbulent boundary layer at a distance x from the leading edge of a flat plate was chosen for τ_s.

$$\tau_s = 0.185\ \rho_a'(u_a')^2\ (\log R_{e_x})^{-2.584}$$

where R_{e_x} = local Reynolds number for air. This expression compares very well with experimental data for turbulent boundary layers on flat plates. In order to simulate the build up of the boundary layer over land, the lake edge was taken to be two-dimensional units from a hypothetical "leading edge." After nondimensionalizing, the expression for vorticity at the surface due to wind shear becomes

$$\zeta_s = \frac{0.185\ \rho_a'(u_a')^2 L_0'}{u_0'\mu_w'}\ (\log R_{e_x})^{-2.584}$$

Because vorticity is generated by a temperature gradient in the x-direction, the vorticity at the surface must be calculated at each time step when temperature is being considered in the problem. Advancing the value of vorticity at the surface is accomplished by using an appropriate finite difference analog of the continuum vorticity equation represented by

$$\frac{\delta\zeta}{\delta t} = -u\frac{\delta\zeta}{\delta x} - v\frac{\delta\zeta}{\delta y} + \frac{1}{R_e}\left(\frac{\delta^2\zeta}{\delta x^2} + \frac{\delta^2\zeta}{\delta y^2}\right) - \frac{1}{F_r}\frac{\delta\rho}{\delta x}$$

The y-advection term makes no contribution, because the v-velocity is zero at the surface. The y-diffusion term is evaluated by defining an image point $(J + 1)$ a distance Δy above the surface. By letting $\zeta_{J+1} = \zeta_J$, the y-diffusion term at the surface is differenced as

$$\left.\frac{\delta^2\zeta}{\delta y^2}\right|_J = \frac{\zeta_{J+1} - 2\zeta_J + \zeta_{J-1}}{\Delta y^2} = -\frac{\zeta_J - \zeta_{J-1}}{\Delta y^2}$$

The inflow is restricted to the left boundary near the surface while outflow is at the right boundary at any depth. It is assumed that the rates of inflow and outflow are equal, and there is no accumulation of fluid in the reservoir. For computational convenience, inflow and outflow take place over four boundary nodes. A parabolic velocity profile is assumed at inflow, while a slug flow is used at the outflow. Using these velocity profiles one can easily calculate the values of stream function and vorticity at the inflow and outflow.

Initial and Boundary Conditions for Temperature. The temperature is initially considered constant everywhere unless the reservoir is to be initially stratified. In this case, the temperature distribution is represented as horizontal isotherms.

At inflow, the temperature is an input parameter and is specified as a constant. At outflow, the temperature gradient in the x-direction is taken to be zero. The walls are assumed to be perfectly insulated, implying a zero normal temperature gradient at the walls. This is expressed using a first order difference approximation.

Like vorticity, the surface temperature must be updated at each time step. Let the finite difference form of the energy equation at the surface be represented by

$$\frac{\delta T}{\delta t} = -u\frac{\delta T}{\delta x} + \frac{1}{P_e}\left(\frac{\delta^2 T}{\delta x^2} + \frac{\delta^2 T}{\delta y^2}\right) + q_T$$

The y-advection term is omitted because the v-velocity at the surface is zero. The y-diffusion term at the surface is evaluated as

$$\left.\frac{\delta^2 T}{\delta y^2}\right|_J = -\frac{T_J - T_{J-1}}{\Delta y^2}$$

by setting the temperature at the image point $(J + 1)$ equal to the surface temperature and using centered differencing.

The source term, q_T, represents the net energy flux to the surface. This can be expressed as the algebraic sum of five separate fluxes as follows [2, 3]:

$$q_T = q_s + q_a - q_b - q_e + q_c$$

where

q_s = net short wave radiation flux absorbed at the surface,
q_a = net long wave atmospheric radiation flux absorbed at the surface,
q_b = back radiation flux from the water surface to the atmosphere,
q_e = energy loss by evaporation, and

q_c = convective energy flux between the water surface and the overlying air mass.

Short wave solar radiation and long wave atmospheric radiation represent energy gains which are independent of the temperature of the water. Heat exchange dependent on the surface water temperature occurs through back radiation, evaporation, and convection. Back radiation and evaporation represent heat losses, while the contribution by convection may be positive or negative depending on the water and air surface temperatures.

The net short wave solar radiation crossing the air-water interface may be calculated as described by WRE [2, 3] as a complicated function of latitude of the site, time of day, season, cloud cover, reflectivity of the water, etc. Rather than admit parameters such as season and time of day into the problem, a daily average reported by Park and Schmidt [4] was used for the value of the heat flux due to solar radiation.

$$q_s' = 9.237\ W/m^2$$

The net long wave atmospheric radiation is calculated as described by WRE as

$$q_a' = C'\sigma'(T_a')^6 c_L(1 - R)$$

where

C' = empirical constant = $9.36 \times 10^{-6}/K^2$
c_L = correction factor for cloudiness given by $c_L = 1.0 + 0.17\,c^2$
c = fraction of sky occupied by clouds = 0.1
R = reflectivity of water surface for atmospheric radiation = 0.03.

Loss of energy from the surface by long-wave back radiation is expressed by WRE as a function of the absolute water surface temperature as

$$q_b' = 0.97\,\sigma'(T_w')^4$$

WRE proposed that the evaporative energy flux be represented by

$$q_e' = \rho_w' L_w' E'$$

where

L_w' = latent heat of vaporization, J/kg
E' = evaporation rate, m/s

The rate of evaporation is given by WRE as

$$E' = N' u_a'(e_s' - e_a')$$

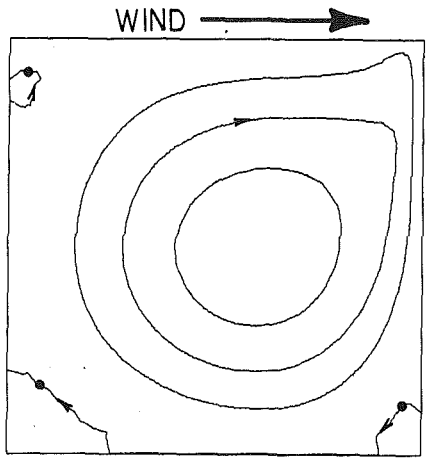

Fig. 2 Streamlines for a 3.05 m/s surface wind ($\Delta\Psi = 0.005$, $R_e = 7.5 \times 10^5$)

where

N' = an empirical constant = 1.56×10^{-9} millibars^{-1},
e_s' = saturation vapor pressure of air at the temperature of the water surface, millibars,
e_a' = water vapor pressure, millibars.

Convective heat transfer at the surface is considered to be a function of wind velocity, pressure, and the temperature gradient in the air mass immediately above the water surface. WRE represents these factors in the equation

$$q_c' = \frac{P'}{2.586}\rho_w' c_p' N' u_a'(T_{ad}' - T_w')$$

where

P' = barometric pressure = 995.6 millibars
T_{ad}' = dry bulb air temperature, °C

The previous expressions for surface heat flux when summed give the net heat flux at the surface as a dimensional quantity which must be properly nondimensionalized to be consistent with the rest of the problem.

Discussion of Results

Computational results are obtained using a 21×21 finite difference mesh for a square reservoir geometry and a 31×21 mesh for a rectangular geometry. The Reynolds numbers, based on reservoir depth, inflow velocity (or average surface velocity if no inflow occurred), and absolute viscosity, are in the range 1.3×10^3–7.5×10^5. The depth of the reservoir is 6.10 m for the wind alone case and 0.61 m for all other cases computed. The computer time on a CDC 6600 is typically 250 s on the 21×21 mesh, 400 s on the 31×21 mesh without the energy equation, and 700 s on the 31×21 mesh with the energy equation.

The results will be presented in three phases. First, the water is driven only by the wind shear acting at the surface. Next, inflow and outflow are introduced to the problem with wind being retained as an optional parameter. Finally, the effect of heat transfer is incorporated into the problem.

Wind Effects. Consider the case of a 3.05 m/s surface wind blowing from left to right over a square reservoir. A streamline plot of the steady state computer solution is shown in Fig. 2. An arrow on certain streamlines denotes the direction of flow and a dot indicates a dividing streamline, i.e., a streamline which divides different circulation regions. The surface vorticity, which is proportional to the shearing stress of the wind, decreases slightly from left to right reflecting the growth of the boundary layer of the wind on the water. The water at the surface is accelerated by the wind from roughly 1.5×10^{-4} m/s near the left corner to about 0.27 m/s near the right corner. As can be seen from the spacing between streamlines ($\Delta\Psi = 0.005$) the motion in the reservoir is very slow except near the corner of the surface and leeward boundary.

The streamlines near the surface are seen to rise as they approach the right wall. This is a phenomenon characteristic of stagnation flows in which streamlines divide as they approach a solid barrier. As a consequence of the fluid's being constrained at the surface, the water is forced to move back down the right edge of the cavity.

After the present investigation was completed, it was brought to the authors' attention that experimental correlations for wind shear stress on water surfaces are available. Typical correlations for various size bodies of water are presented by Wu [18]. A comparison was made between the average shear stress calculated by the present method and that obtained from the correlations of Wu. It was found that they compared very well for the reservoir size and wind speed used in the present simulation. For larger reservoirs, however, experimental correlations, such as that of Wu, should be used.

Inflow-Outflow Effects. Fig. 3 shows streamline plots of the steady-state solutions obtained with the outflow positioned at the surface, at middepth, and at the bottom of the reservoir. Regardless of the outflow position, the flow is segregated into two distinct regions by the dividing streamline. Below the dividing streamline, the fluid

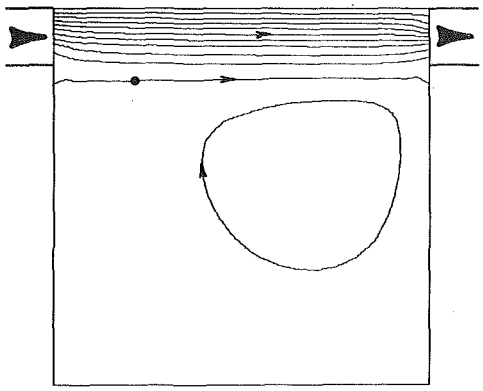

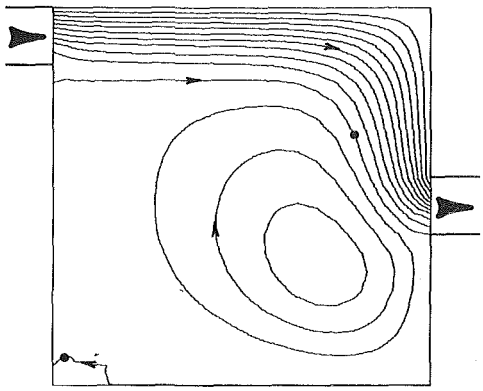

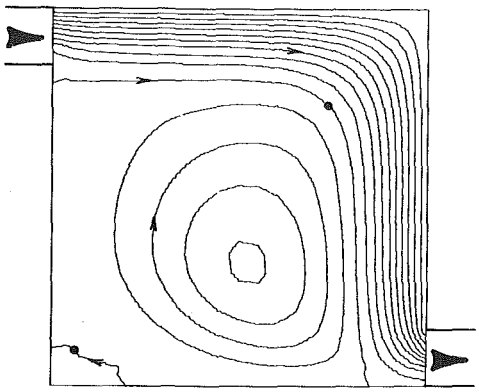

Fig. 3 Streamlines for outflow at various depths ($\Delta\Psi = 0.01$, $R_e = 1.3 \times 10^3$): (*a*) outflow at surface; (*b*) outflow at middepth; (*c*) outflow at bottom

is slow moving and is trapped within a region bounded by the dividing streamline and the walls. Providing impetus for the circulation is the relatively fast moving fluid above which enters at inflow, passes through the cavity, and exits at the outflow. Fig. 3(*a*) shows the trapped flow below the dividing streamline is moving extremely slowly with respect to the through-flow. Lowering the outflow position (Figs. 3(*b*) and 3(*c*)) increases the speed of the trapped fluid in two ways. First, the amount of circulating fluid is reduced because the through-flow occupies a greater portion of the cavity. Second, the length of the interface between the two flows is increased, which tends to increase the total shear acting on the circulating fluid along the interface.

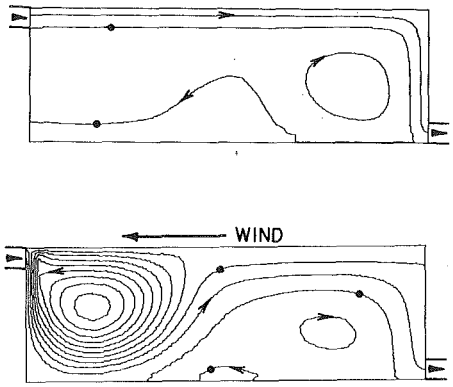

Fig. 4 Streamlines for inflow/outflow and wind ($\Delta\Psi = 0.05$, $R_e = 1.1 \times 10^4$): (*a*) inflow/outflow; (*b*) inflow/outflow with 1.52 m/s opposing wind

Fig. 4 shows the streamline plots of the steady flow in a reservoir with a length to depth ratio of 3. The flow produced with inflow/outflow and no wind is shown in Fig. 4(*a*). The flow is naturally divided into three regimes by the two dividing streamlines indicated in the figure. Comprising the first regime is the relatively fast moving flow near the surface which merely passes through the reservoir. This flow drives the adjacent slower moving fluid in the second regime which is circulating in the clockwise direction within the reservoir. This flow in turn drives the fluid in the third regime which circulates more slowly yet and in the counterclockwise direction on the bottom of the lake.

The complex flow shown in Fig. 4(*b*) was produced by imposing a light opposing wind (1.52 m/s) to the inflow-outflow problem shown in Fig. 4(*a*). The flow velocities in the lake have dramatically increased as compared to the previous case. Even though the wind is very light, the incoming water is immediately driven down by the wind and the motion at the surface is from right to left. The inflow is entrained in the strong vortex at the left end of the reservoir and then rises toward the surface before being drawn down to the outflow.

Heat Transfer Effects. In the previous discussion, only steady-state flows were presented. With temperature in the problem, attention will be focused on the time developing flow and temperature fields. Because of the extremely large thermal capacity of the reservoir, the temperature solution develops very slowly. Additionally, the flow in actual reservoirs and cooling ponds is not steady, because the parameters affecting the flow are transient. Of greater interest then, is the effect of various parameters on the developing flow.

The developing flow and temperature fields are illustrated with plots of the streamlines and isotherms presented after every 200 computational time steps up to 1000 time steps. Water at a temperature of 32.2°C (90°F) is discharged into a reservoir with a length to depth ratio of 3. The air temperature is taken to be 28.1°C (82.5°F). The flow fields shown in Figs. 5 and 6 are produced by discharging the heated water into a reservoir initially at rest and at a uniform temperature of 26.7°C (80°F). The flow is then allowed to develop under different wind conditions.

Fig. 5 shows the developing flow and temperature fields with no wind included in the problem. After 200 time steps, the thermal plume is clearly seen spreading across the surface of the reservoir. Below the bottom isotherm the water is of uniform temperature, and buoyancy will not affect the flow. After 400 time steps, the warmer surface water is beginning to reverse at the end of the reservoir and flow back toward the inflow. This trend continues until after 1000 time steps the flow traverses the length of the reservoir at the surface, reverses and travels all the way back just beneath the surface. This is caused by the buoyance force tending to keep the warm water near the surface and the colder water near the bottom. This is a radical departure from the flows that developed under the same circumstances before buoyancy effects were considered (e.g., see Fig. 4(*a*)).

Although no experimental data are available for quantitative

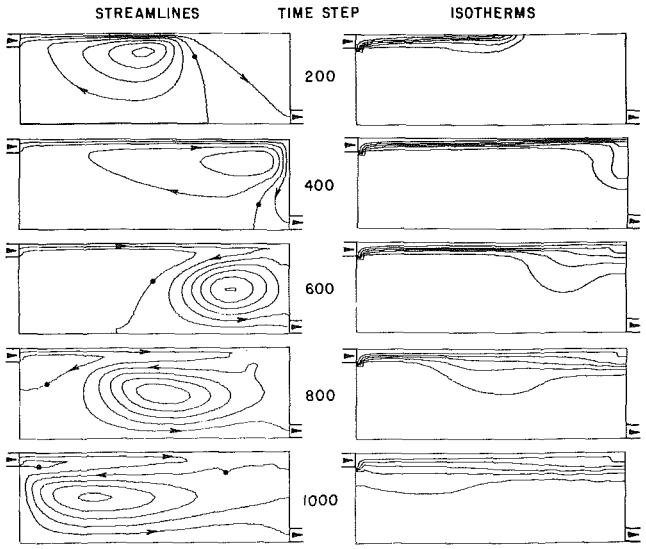

Fig. 5 Streamlines and isotherms for inflow/outflow ($\Delta\Psi = 0.05$, $\Delta T = 0.02$, $R_e = 1.1 \times 10^4$, $\Delta t = 0.005$)

comparisons, present results compare qualitatively with experimental data of Urban [10]. Urban detected current reversals with depth that were closely associated with the degree of stratification and the depth of withdrawal. Multiple current reversals have also been observed in field reservoirs. Velocity data presented by the Tennessee Valley Authority [19] indicate as many as seven distinct current reversals in their Ocoee No. 1 Reservoir.

Fig. 6 shows the development of the flow and temperature fields for a 1.52 m/s opposing wind. It is seen that the opposing wind drives the warm water discharge beneath the surface and generates a counterclockwise rotating cell of denser water at the surface. The thermal structure near the surface is very interesting. The maximum temperature is found beneath the surface in the discharge water with temperatures decreasing outward both above and below.

Because the maximum temperatures occur beneath the surface, less heat is transferred from the water across the air-water interface. Consequently, an opposing wind tends to increase the heat content of the reservoir. There is a net heat loss, however, at the surface due to evaporation and convective cooling. This causes the surface temperature actually to decrease by about 0.17°C (0.3°F) after 1000 time steps. The surface temperature rises nearly 5.5°C (10°F) in the same time without an opposing wind.

The previous two cases simulate the flow in a well mixed reservoir under conditions of thermal loading and selective withdrawal. The flow patterns depart radically from those produced under the same conditions but without thermal loading or surface heat transfer. In each case, the flow reversal near the surface is easily related to the temperature distribution in the reservoir.

For the short time the simulation was allowed to proceed, the heat load discharged into the reservoir remained fairly near the surface with little downward mixing. With no temperature gradients below about middepth to inhibit vertical flow, large circulation vortices are present similar to those witnessed in the flows considered earlier. In a reservoir stratified from top to bottom, circulation vortices would be expected to be greatly diminished or absent altogether.

To determine the flow in a stratified reservoir suddenly subjected to thermal loading, a simulation was made with the desired temperature distribution input as an initial condition. Fig. 7 shows the streamlines and isotherms calculated for an initially stratified reservoir with the flow starting from rest. The initial temperature distribution was chosen so that the reservoir was stratified from top to bottom with the thermocline located just above middepth. It can be seen from the figure that as the simulation proceeds the thermocline moves downward and the temperature gradient becomes less steep.

The initial thermal structure of the reservoir tends to inhibit vertical flow, and the circulation vortices discussed earlier do not appear. It can also be seen that the overall speed of the fluid has significantly decreased. The relationship between the locations of the thermocline and the flow reversal is apparent from the figure.

Conclusions

The flows that occur in a stratified reservoir are quite different from those found in a well mixed reservoir. The numerical simulation employed in the present investigation reveals the water in a well mixed reservoir being freely circulated from top to bottom by large vortices. By contrast, buoyancy forces in a stratified reservoir tend to inhibit vertical motion and flows are largely horizontal with currents reversing direction with depth.

The flows are shown to be strongly influenced by wind speed and

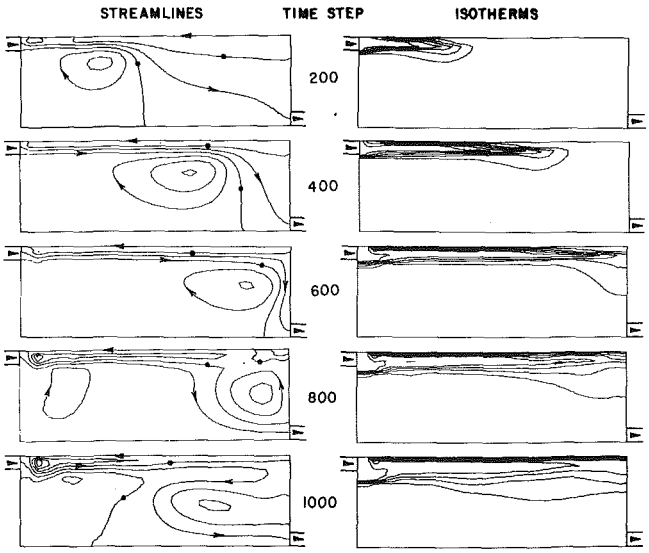

Fig. 6 Streamlines and isotherms for inflow/outflow and a 1.52 m/s opposing wind ($\Delta\Psi = 0.05$, $\Delta T = 0.02$, $R_e = 1.1 \times 10^4$, $\Delta t = 0.005$)

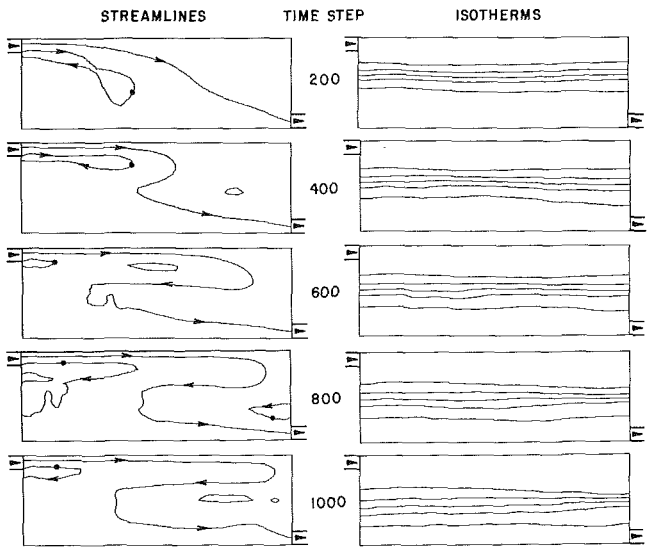

Fig. 7 Streamlines and isotherms for an initially stratified reservoir ($\Delta\Psi = 0.05$, $\Delta T = 0.02$, $R_e = 1.3 \times 10^4$, $\Delta t = 0.005$)

direction. An assisting wind is seen to increase the speed of the flow but without basically altering existing flow patterns. At the same time, an assisting wind dissipates a greater amount of heat from the thermal discharge by convective and evaporative cooling. An opposing wind tends to drive the heated discharge beneath the surface. While the heat from the discharge remains in the reservoir, the surface water actually experiences a temperature drop.

Although the present results are for laminar flow, they should qualitatively agree with full scale reservoir measurements. The present numerical procedure can be easily extended to calculate turbulent flow in reservoirs. The difficulty, however, is that existing two-dimensional models for turbulent transport of momentum and energy are lacking.

The computer simulation, while very flexible and presumably accurate, consumes a large amount of computer time. Even so, weighted against the time and expense incurred in field and experimental work, its use in future parametric studies should represent a considerable savings.

References

1 Parker, F. L., and Krenkel, P. A., ed., *Engineering Aspects of Thermal Pollution, Proceedings of the National Symposium on Thermal Pollution,* Nashville, Tenn., Aug. 14–16, 1968, Vanderbilt, University Press, 1969.

2 "Prediction of Thermal Energy Distribution in Streams and Reservoirs," Water Resources Engineers, Inc., final report to the California Department of Fish and Game, Walnut Creek, Calif., 1967.

3 Orlob, G. T., and Selna, L. G., "Temperature Variations in Deep Reservoirs," *Journal of the Hydraulics Division,* ASCE, Vol. 96, No. HY2, 1970, pp. 391–410.

4 Park, G. G., and Schmidt, P. S., "Before and After Studies of the Effects of a Power Plant Installation on Lake LBJ," *A Numerical Temperature Model for Lake LBJ,* Interim Report No. 1 to the Lower Colorado River Authority, 1971.

5 Clay, H. M., Jr., and Fruh, E. G., "Selective Withdrawal at Lake Livingston—An Impoundment Water Quality Model Emphasizing Selective Withdrawal," CRWR Report No. 66, The University of Texas at Austin, 1970.

6 Liggett, J. A., "Cell Method for Computing Lake Circulation," *Journal of the Hydraulics Division,* ASCE, Vol. 96, No. HY3, 1970, pp. 725–743.

7 Terry, M. D., Mercier, H. T., and Slotta, L. S., "The Numac Method for Nonhomogeneous Unconfined Marker-and-Cell Calculations," *Stratified Reservoir Currents,* Bulletin No. 44, Oregon State University, 1969.

8 Dake, J. M. K., and Harleman, D. R. F., "Thermal Stratification in Lakes: Analytical and Laboratory Studies," *Water Resources Research,* Vol. 5, No. 2, 1969, pp. 484–495.

9 D'Arezzo, A. J., and Masch, F. D., "Analysis and Prediction of Conservative Mass Transport in Impoundments," CRWR Report No. 73, The University of Texas at Austin, 1970.

10 Urban, L. V., "A Laboratory Investigation of Temperature and Velocity Fields in a Stratified Cooling Reservoir," Ph.D. Dissertation, The University of Texas at Austin, 1971.

11 Huber, W. C., Harleman, D. R. F., and Ryan, P. J., "Temperature Prediction in Stratified Reservoirs," *Journal of the Hydraulics Division,* ASCE, Vol. 98, No. HY4, 1972, pp. 645–666.

12 Crow, L. I., "A Numerical Study of the Velocity and Temperature Fields in a Stratified Reservoir," MS thesis, The University of Texas at Austin, May 1974.

13 Gentry, R. A., Martin, R. E., and Daly, B. J., "An Eulerian Differencing Method for Unsteady Compressible Flow Problems," *Journal of Comp. Physics,* Vol. 1, 1966, pp. 87–118.

14 Roache, P. J., *Computational Fluid Dynamics,* Hermosa Publishers, Albuquerque, 1972.

15 Peaceman, D. W., and Rachford, H. H., "The Numerical Solution of Parabolic and Elliptic Differential Equations," *Journal of Soc. Indus. Appl. Math.,* Vol. 3, 1955, p. 28.

16 Young, D., "Iterative Methods for Solving Partial Differential Equations of Elliptic Type," *Transactions of the American Mathematical Society,* Vol. 76, 1954, pp. 92–111.

17 Schlicting, H., *Boundary Layer Theory,* 6th Edition, McGraw-Hill, New York, 1968, p. 604.

18 Wu, Jin, "An Estimation of Wind Effects on the Dispersion in Wide Channels," *Water Resources Research,* Vol. 5, No. 5, 1969, pp. 1097–1104.

19 Tennessee Valley Authority, "Ocoee No. 1 Reservoir Selective Withdrawal (1970)," Water Resources Research Laboratory Report No. 26, Norris, Tenn., 1970.

S. C. Johnston
Combustion Research Division,
Sandia Laboratories,
Livermore, Calif.

H. A. Dwyer
Mechanical Engineering Department,
University of California,
Davis, Calif.

Thermal Instabilities in Discharging Gas Reservoirs

The flow structure in a discharging gas reservoir has been studied using schlieren cinematography. Effects due to discharge orientation, gas species, and vessel wall vibration have been observed. Initially, the internal flow structure has been found to be controlled by the mass sink, with streamlines going in approximate straight lines from the vessel wall to the exit orifice. At later time, free convection dominates and recirculation patterns are established. Discharge orientation can have a dramatic effect on the free convection flow field as well as on the growth and stability of the wall thermal diffusion layer. A jet-like structure (initiated at very early time and believed to be caused by wave effects) was observed to extend from the vessel wall diametrically opposite the exit orifice. When the discharge was parallel to but in the opposite direction of the gravitational vector, this jet-like structure was found to cause an instability in the lower wall diffusion layer. Vessel wall vibration resulted in a standing cellular acoustic wave pattern in the gas which, depending on discharge orientation, caused a violent instability. A model for temperature variation in the thermal diffusion layer is discussed and a numerical solution is given. Results of the predicted thermal diffusion layer histories are compared to data. A discussion of vessel orientation effects on critical Rayleigh number is given.

1 Introduction

The thermal instability of a layer of fluid heated from below has been studied for many years. Although the phenomenon of thermal convection was first recognized by Count Rumford in 1797 and later by James Thomson in 1882, the first experiments to demonstrate in a definitive manner the onset of thermal instability in fluids were those of Bénard in 1900. So impressed was Lord Rayleigh with the results of Bénard's experiments that in 1916 he published the first mathematical treatise on the subject [1].[1] In it he set forth the conditions which govern the onset of the instability.

Heating of the fluid can be accomplished in a variety of ways. One way that occurs naturally is the rapid discharge of gas from an enclosing container. As the gas expands, it cools, but the container walls remain essentially at the initial temperature. Heat transferred from the wall to the gas provides the temperature (and hence density) stratification in the fluid required for the instability.

As heat is transferred to the cool gas, the gas near the wall becomes warm and, since the pressure is approximately uniform spatially (for quasi-steady discharge), this warm region expands, causing a low gas density adjacent to the wall. This low density region is called a thermal diffusion layer. Thus a potentially unstable situation develops in which a heavier gas resides adjacent to a lighter gas. Whether this arrangement is stable or unstable depends among other things on the direction of the gravitational vector, $\hat{g}$ (Fig. 1). The Rayleigh number, R_a, which may be thought of as a ratio of (buoyant forces x inertia forces)/(viscous forces)^2, is a measure of the influences which tend to enhance gas motion and set up conditions where instabilities occur. These conditions are usually represented by some critical value of the Rayleigh number.

The study reported in this paper was motivated by a desire to contribute to the understanding of a class of unsteady, internal flow problems generically referred to as gas transfer problems. The term gas transfer is meant to describe the unsteady movement of gas from one reservoir (initially at an elevated pressure) through a valve and connecting tube to another reservoir (initially at some lower pressure). Gas transfer is initiated in such a system by suddenly opening the valve between the reservoirs.

There are two important characteristic times (measured from the initiation of transfer) associated with gas transfer problems: (1) the time required for pressure equilibrium and (2) the time required for thermal equilibrium. Two limiting cases describing the heat transfer which occurs during gas transfer can immediately be identified—adiabatic or isothermal transfer. Chenoweth [2] has shown that large differences between the mass transferred under isothermal and adiabatic conditions can exist at pressure equilibrium, depending on the value of the volume ratio of the two reservoirs, the initial pressure ratio between the two reservoirs, and the specific heat ratio of the transfer gas. Of course, in most applications, the transfer is neither adiabatic nor isothermal, but somewhere in-between. This means that the

[1] Numbers in brackets designate References at end of paper.

Contributed by the Heat Transfer Division for publication in the JOURNAL OF HEAT TRANSFER. Manuscript received by the Heat Transfer Division January 27, 1976. Paper No. 76-HT-GGG.

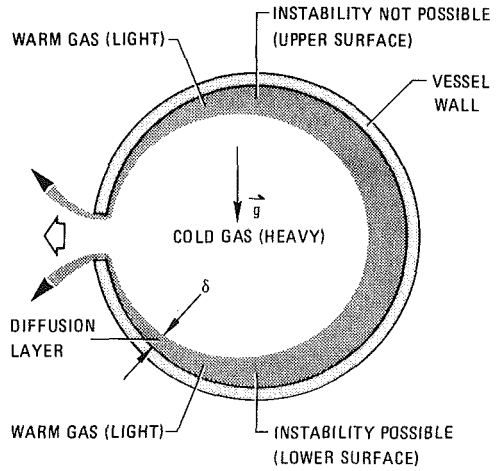

Fig. 1 Instability prone and inherently stable regions in a discharging vessel

amount of mass transferred at pressure equilibrium depends strongly on how much heat has been transferred to the gas up to this point.

In addition, the nature of the upstream vessel heat transfer (as well as the nature of the downstream vessel and connecting tube heat transfer) strongly affects the time required for thermal equilibrium of the transfer gas. Any factors which increase the upstream vessel heat transfer rate increase the amount of mass transferred at pressure equilibrium and decrease the time required to achieve thermal equilibrium. When an accurate estimate of temporal mass transfer and gas temperature are required for a gas transfer system, it is crucial to identify those factors which can affect system heat transfer rates.

One objective of this study was to identify in a qualitative sense the most important factors which affect the nature of the discharge vessel heat transfer. In addition, a simplified model of the diffusion layer growth was developed, and the numerical results generated were compared to data. Several investigators [3, 4] have previously studied this topic experimentally but in each of these studies, internal flow structure was inferred from local temperature measurements. This has resulted in much speculation and confusion over the internal flow field during discharge. Hopefully the results reported here will elucidate these phenomena.

2 Experimental Apparatus and Procedure

To obtain a phenomenological understanding of the internal gas dynamics, a flow visualization experiment utilizing schlieren cinematography was devised, the details of which are given in [5]. A cylindrical test vessel whose ends were transparent to light was used; the vessel volume was 2.6 l and it had a 15.24-cm dia. Gas was discharged normal to the axis of symmetry at vessel mid-plane through a 0.64-cm dia orifice.

Two types of valves were used to initiate gas discharge. One incorporated a blowout-cup and the other was an explosively actuated valve. The explosive valve was used to provide a large mechanical shock to the vessel at the beginning of discharge to study the effects of vessel wall vibration on thermal diffusion layer stability. The characteristics of impulsively excited vessel wall vibrations are similar for a particular geometry vessel, so that it does not matter how the impulse is delivered. In contrast to the explosively-actuated valve, the blowout-cup valve does not cause vessel wall vibration when it functions.

Internal flow diagnostics consisted of three chromel-constantan thermocouples and a flush-mounted pressure transducer. Thermocouple junctions were formed from two 0.008-mm dia wires. Location of the thermal probes in the vessel is shown in Fig. 2. The thermocouples were used to obtain a quantitative assessment of the differences in temperature between the bright and dark regions in the photographs.

Prior to each experiment, the cylindrical test vessel was purged of air and filled with dry gas to a pressure of either 4.4, 7.8, or 21.4 atm and a temperature of 293 K. Initial temperature was not varied, since in most applications it is the initial pressure which is varied. Gas discharge was initiated by functioning either the blowout-cup or the explosively-actuated valve.

Each experiment was performed twice to ensure repeatability of results. Several experiments were performed without thermocouple probes to ensure that their presence did not affect the results. Parameters varied in the experiments were discharge orientation, gas species, initial pressure, wall vibration state and discharge rate. In total, more than 80 separate experiments were performed. Only the results of the 7.8 atm initial pressure experiments have been reported here, because the results were qualitatively the same as initial pressure level was varied.

3 Experimental Results

Vessel Orientation Effects on Discharge.

Nitrogen. The discharge of nitrogen from a cylindrical vessel for three orientations is shown in Fig. 2. Real time has been nondimensionalized by the adiabatic reference time, $t_{ref}^{-1} = A_e/V\sqrt{\gamma RT(0)}\,[(\gamma-1)/2][2/(\gamma+1)]^{(\gamma+1)/2(\gamma-1)}$. At $\tau = 0$, a small dark spot (about one orifice diameter in extent) occurs at the exit orifice location in both the downward and horizontal discharges. This is caused by the acceleration of the gas to sonic velocity at the exit orifice, causing a large density gradient. The general dark area at the top of the upward discharge orientation (caused by slight misalignment of the schlieren system) prevents observation of this region. In the $\tau = 0.13$ frames, a small jet-like structure is visible in the upward and horizontal discharges on the vessel wall diametrically opposite from the exit orifice. The reason for the structure is not known for certain, but because of the time scale on which it first occurs ($\tau \approx 0.009$), it is believed to be caused by an interaction between the initial expansion waves that enter the vessel and the growing thermal diffusion layer. The small jet visible at the exit orifice of each orientation emanates from the hole through which the vessel was initially pressurized.

At $\tau = 0.18$, convective waves leaving the three thermocouples are clearly visible. The mass sink prevents formation of these waves in the downward discharge orientation. Notice that during this early part of discharge, particle path lines (which one distinguishes by following the path of the lower density gas leaving the thermocouple) appear

Nomenclature

A_e = exit orifice cross-sectional area
α = thermal diffusivity
β = coefficient of thermal expansion
C_p = specific heat at constant pressure
C_v = specific heat at constant volume
δ = thermal diffusion layer thickness
g = gravitational acceleration
γ = specific heat ratio
k = thermal conductivity
P = gas pressure
r_0 = vessel radius
R = gas constant per mass
R_a = Rayleigh number, $R_a = g\beta\Delta T\delta^3/\alpha\nu$
ρ = gas density
T = gas temperature
ΔT = temperature difference between wall and gas
t = time
t_{ref} = adiabatic reference time
$\tau = t/t_{ref}$
V = vessel volume
ν = kinematic viscosity

Superscripts

— = referenced to initial conditions

to go in a direct trajectory from the interior of the vessel to the exit orifice. Later these particle path lines change as free convection patterns are established.

As time progresses, the thermal diffusion layer grows inward from the vessel wall. At $\tau = 0.30$, the diffusion layer on the lower wall in the upward discharge orientation becomes unstable, while the diffusion layer at the same location in the other two configurations remains stable throughout discharge. In a separate experiment, the upward discharge diffusion layer exhibited the same instability when the thermocouples were removed. It is believed that the jet-like structure provides the perturbation for this instability. The instability is referred to here as a "natural" instability, since it occurs from perturbations generated in a natural way during discharge. Contrast will later be made to "forced" instabilities, which result from vessel wall vibration.

The flow pattern exhibits three distinct regimes separated in time:

1 An early time regime in which particle path lines, due to the mass sink effect, proceed from the interior of the vessel in a direct trajectory to the exit orifice; $0 \leq \tau \leq 0.23$.

2 An intermediate time regime in which free convection begins to establish recirculation patterns which compete with the direct particle path lines established by the mass sink; $0.23 \leq \tau < 0.45$.

3 A late time pattern in which free convection dominates and the particle path lines result from recirculation patterns, $0.45 \leq \tau \leq \tau_{Teq}$, where τ_{Teq} is the dimensionless thermal equilibrium time.

There is also a distinct discharge orientation effect on the recirculation pattern beginning at about $\tau = 0.30$ and extending to at least $\tau = 0.63$ (not shown). At pressure equilibrium ($\tau = 0.45$), note the difference in diffusion layer thickness on the lower vessel wall. It has become unstable in the upward discharge orientation, has been virtually "sucked away" in the downward discharge orientation, and appears to be stable and lifting off the lower wall in the horizontal discharge orientation. The black regions shown in the photographs indicate large density gradients or, since the pressure in the vessel is approximately uniform, large temperature gradients. At some instants in time, temperature differences as much as 40°C were measured between adjacent dark (warm) and bright (cold) regions.

Helium. Space limitations prevent the inclusion of the helium photographs. This information is contained in [5]. Because helium has a larger thermal diffusivity than nitrogen, diffusion layer growth is more rapid and penetration is deeper in the helium discharges than in the nitrogen discharges. Starting at $\tau = 0.46$ the diffusion layer on the upper wall of the vessel begins to disappear for all discharge orientations. This is believed to occur through the combined effects of the mass sink and the convection patterns that are set up. Recirculation patterns similar to those observed for nitrogen form for helium also, but it is not possible from the information available to distinguish this development or separate it into distinct time regimes as it was possible to do for nitrogen.

Vessel Wall Vibration Effects on Thermal Diffusion Layer Stability.

Nitrogen. Horizontal Discharge. The effects of vessel wall vibration on the stability of the diffusion layer for nitrogen discharge are shown in Fig. 3. Frames from Fig. 2 have been repeated in the left-hand column (No Wall Vibration) to help contrast the instability that develops in the photos of the right-hand column (Wall Vibration). The experiments associated with the pictures shown in the two columns

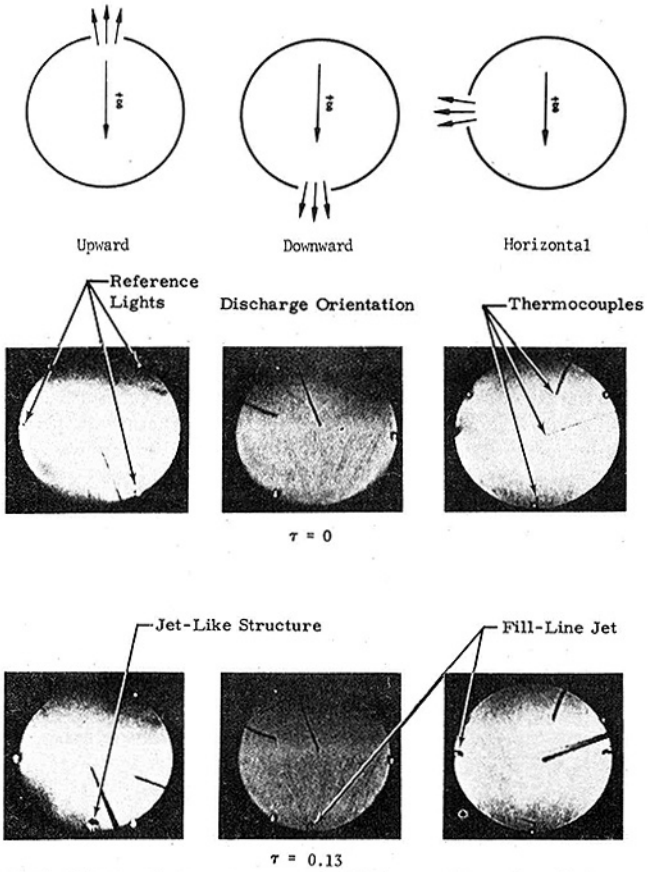

Fig. 2 Nitrogen discharge from a cylindrical vessel for various discharge orientations relative to the gravitational vector—t_{ref} = 1.994s

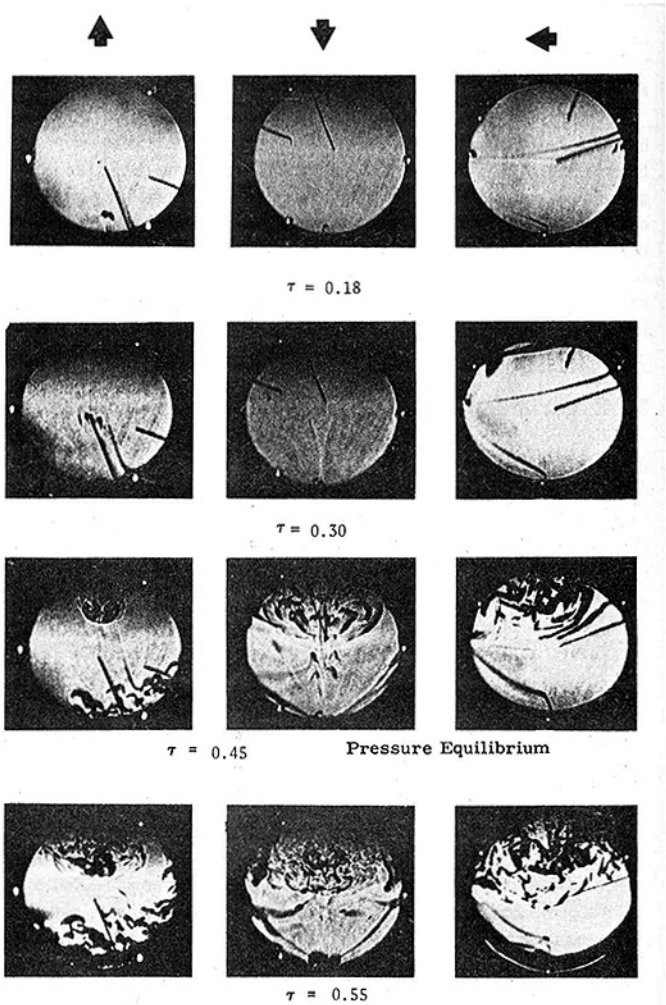

Fig. 2 (Cont'd.)

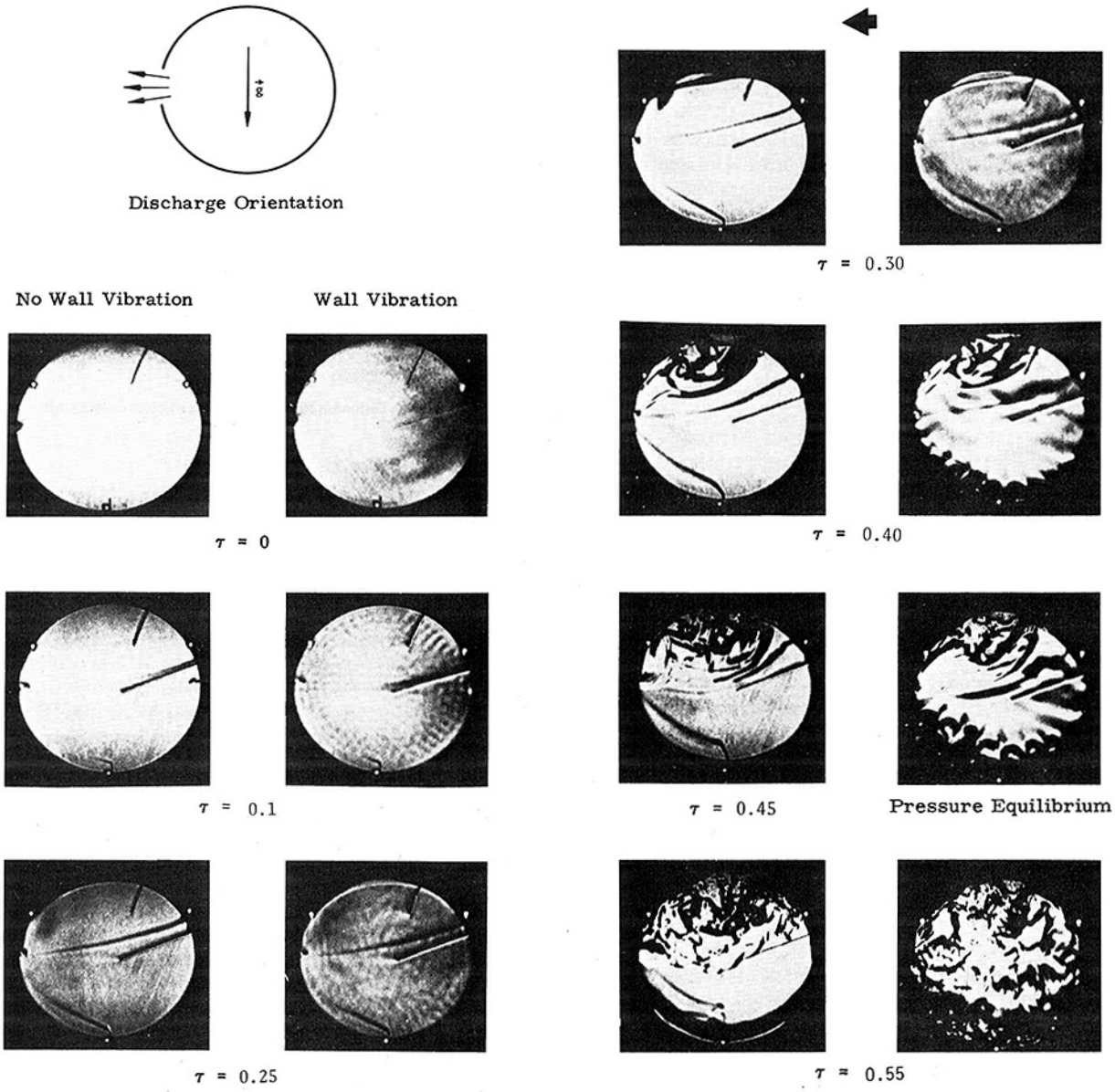

Fig. 3 Horizontal discharge of nitrogen from a cylindrical vessel with and without vessel wall vibration—t_{ref} = 1.994s

Fig. 3 (Cont'd.)

were identical in every detail except that an explosively-actuated valve was used to initiate discharge in the right-hand column photos and blowout-cup valve was used in the left-hand column photos. With the explosively-actuated valve, vessel ringing results after the valve is functioned. No such ringing occurs with the blowout-cup valve.

After a period of time during which vessel ringing occurs, a standing acoustic wave pattern with a regular cell structure is formed in the gas, as seen in the $\tau = 0.10$ and $\tau = 0.25$ frames. Viscous dissipation has damped out the acoustic waves in the $\tau = 0.30$ frame. Up until this time, the diffusion layers for each configuration grow at approximately the same rate. At $\tau = 0.30$, however, an instability begins to form in the diffusion layer on the lower vessel wall in the right-hand column. Subsequently, the instability spreads rapidly toward the center of the vessel.

Upward Discharge. Because of space limitations, photographs of both the upward and downward discharge have been omitted. Instability formation occurred sooner and its extent was much greater at pressure equilibrium for the explosively-actuated valve discharge.

Downward Discharge. In this discharge orientation, an instability never formed because the mass sink located in the lower vessel wall sucked away the diffusion layer before it was able to develop. Late time movie frames showed little difference between the nonvibrating and the vibrating wall discharge configurations.

Helium. When the same experiments discussed above were repeated using helium, no instabilities were observed. The reason for this is that the maximum transient Rayleigh number is lower than the critical Rayleigh number necessary for instability formation. As a result, even with acoustic disturbances, the diffusion layer Rayleigh number is far enough away from being critical that it remains stable.

4 Analysis

The expanding gas within the vessel can be considered to consist of two regions—a region far from the vessel wall in which gas temperature is unaffected by heat transfer and follows an adiabatic drop, and a region adjacent to the vessel wall in which gas temperature is affected by conduction heat transfer from the vessel wall.

Following the treatment given by Landram [4], gas temperature history in the outer region is determined from a zero-dimensional adiabatic gas discharge solution and is thus a function of time alone.

Gas temperature history in the region adjacent to the vessel wall is determined from the solution of the one-dimensional, unsteady heat conduction equation with a sink term (which accounts for the adiabatic discharge of the bulk gas in the vessel). The effects of convection and vessel orientation are neglected in this model.

Region Far From the Wall. If the assumptions of no vena contracta, a thermodynamically reversible ideal gas process, an isentropic acceleration region from stagnant reservoir conditions to the exit orifice and quasi-steady flow choked at the exit orifice are made, the time dependence of the thermodynamic properties of the gas are given by [6].

$$\overline{P} = (1 + \tau)^{2\gamma/(1-\gamma)} \text{ and } \overline{T} = (1 + \tau)^{-2} \quad (1)$$

Region Near the Wall. If one-dimensional thermal diffusion layer growth only is considered and convection is neglected, the governing equations for the region near the wall may be combined to yield

$$\rho C_P \frac{\partial T}{\partial t} - \frac{\partial}{\partial y}\left(k \frac{\partial T}{\partial y}\right) = \frac{\partial P}{\partial t}$$

where the right-hand side arises from the mass sink. With the assumptions that the gas in the outer region experiences an isentropic expansion and the isentropic pressure is constant through the diffusion layer, this equation becomes

$$\rho_1 C_P \frac{\partial T_1}{\partial t} - \frac{\partial}{\partial y}\left(k \frac{\partial T_1}{\partial y}\right) = \rho_2 C_P \frac{dT_2}{dt} \quad (2)$$

where the subscript 1 denotes the inner region and the subscript 2 denotes the outer region. In this form, the diffusion layer formulation is analogous to the formulation of a velocity boundary layer over a body with a pressure gradient. The sink term ($\rho_2 C_P dT_2/dt$), which arises as a consequence of the outer gas cooling during the isentropic expansion, is analogous to the boundary layer pressure gradient term which arises from the external potential flow solution.

If the Prandtl number is assumed to be constant, the temperature dependence of the thermal conductivity can be expressed using the Sutherland approximation

$$\frac{k_1}{k(0)} = \left(\frac{T_1}{T(0)}\right)^N \quad (3)$$

The functional form of the sink term appearing in (2) can be approximated using the isentropic choked discharge solution (1). This term couples the inner and outer regions.

Substitution of (1) and (3) into (2) and nondimensionalizing with respect to initial conditions yields

$$\overline{T}^{-1}\frac{\partial \overline{T}}{\partial \tau} - \alpha(0) t_{ref}(1 + \tau)^{2\gamma/(\gamma-1)}\left[N\overline{T}^{N-1}\left(\frac{\partial \overline{T}}{\partial y}\right)^2 + \overline{T}^N \frac{\partial^2 \overline{T}}{\partial y^2}\right] = -2(1 + \tau)^{-1} \quad (4)$$

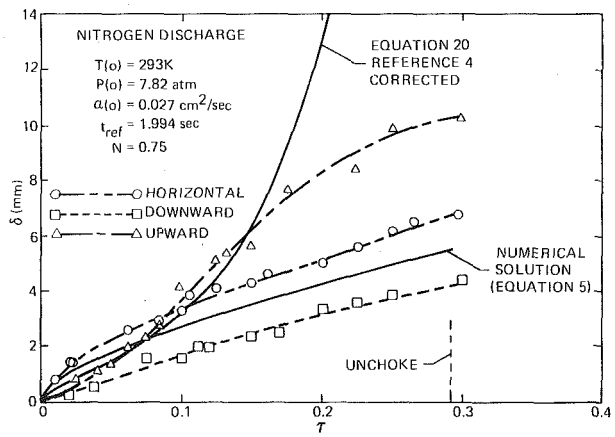

Fig. 4 Diffusion layer histories for nitrogen discharge

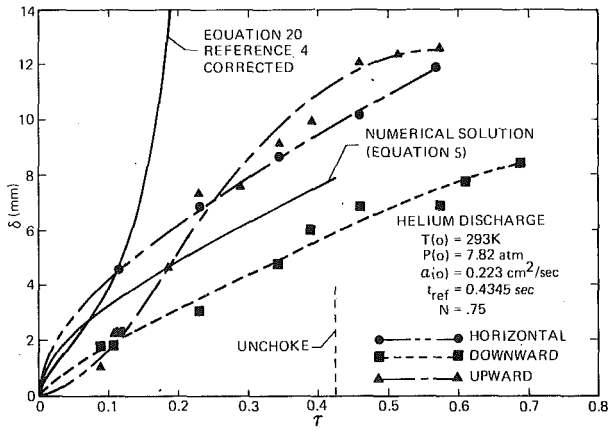

Fig. 5 Diffusion layer histories for helium discharge

where the subscript notation 1 has been dropped and T is the temperature in the diffusion layer. $\alpha(0)$ is the initial value of the thermal diffusivity, $k(0)/\rho(0)C_P$. The initial and boundary conditions are

$$\overline{T}(y, 0) = 1, \quad \overline{T}(0, \tau) = 1, \overline{T}(\infty, \tau) = (1 + \tau)^{-2}$$

The finite difference form of (4) is

$$\overline{T}_{i,n+1} = \overline{T}_{i,n}\{1 - 2(\Delta\tau)(1 + \tau_n)^{-1} + \lambda(1 + \tau_n)^{2\gamma/(\gamma-1)} \times [N\overline{T}_{i,n}{}^{N-1}(\overline{T}_{i+1,n}{}^2 - 2\overline{T}_{i,n}\overline{T}_{i+1,n} + \overline{T}_{i,n}{}^2) + \overline{T}_{i,n}{}^N(\overline{T}_{i-1,n} - 2\overline{T}_{i,n} + \overline{T}_{i+1,n})]\} \quad (5)$$

where i denotes space and n denotes time, $\Delta\tau$ is the time step, $\lambda = \alpha(0)t_{ref}\Delta\tau/(\Delta x)^2$ and Δx is the space step.

Since the temperature in the diffusion layer asymptotically approaches the adiabatic temperature far from the vessel wall, diffusion layer thickness at any instant in time can be found from the solution of (5) at that instant in time by locating the distance from the wall at which $\overline{T}$ is 99.5 percent of the adiabatic temperature. This is analogous to numerical determination of a velocity boundary layer thickness at different spatial locations over a body.

5 Theoretical Results and Discussion

Diffusion layer histories obtained as described above are shown in Figs. 4 and 5 for nitrogen and helium discharges, respectively. These histories were found to be a weak function of the parameter N. Also shown is an approximate solution given in [4], in which the diffusion layer history was obtained analytically using a heat-balance integral method similar to the Karman-Pohlhausen momentum integral technique used in boundary layer theory. It should be noted [7] that C_v should be replaced by C_P and there is a missing $1/\omega$ in the next to last term of equation 20 in [4].

The data shown in Figs. 4 and 5 were obtained from the schlieren photographs. Since diffusion layer thickness can be measured at an infinite number of positions along the vessel wall, a single measurement location with respect to the gravitational vector was chosen for all three discharge orientations. This location was at the 7 o'clock position in the discharge orientations shown in Fig. 2. Although this location may not be the optimum for comparison of data with theory, it is consistent and in each case is along the lower vessel wall, where instability formation is possible. Because of the uncertainty in measuring δ from the photographs, values of δ given in Figs. 4 and 5 possess considerable scatter. Lines have been drawn through the data in both of these figures to help the reader discern trends in the data.

After an initial growth period during which the thermal sink effect is relatively small, the data for the horizontal and downward discharge orientations appear to confirm the linear diffusion layer growth predicted by the finite difference solution of equation (5). One would expect the horizontal discharge data to be greater than the numerical

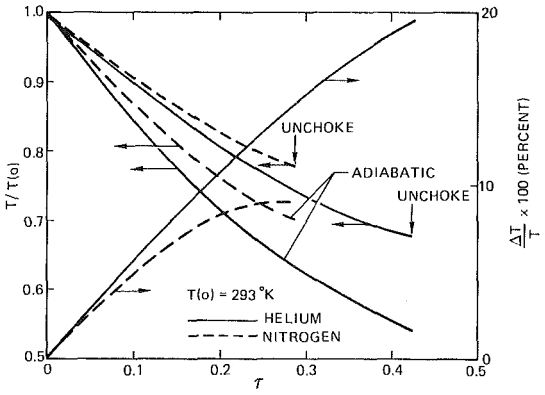

Fig. 6 Temperature histories

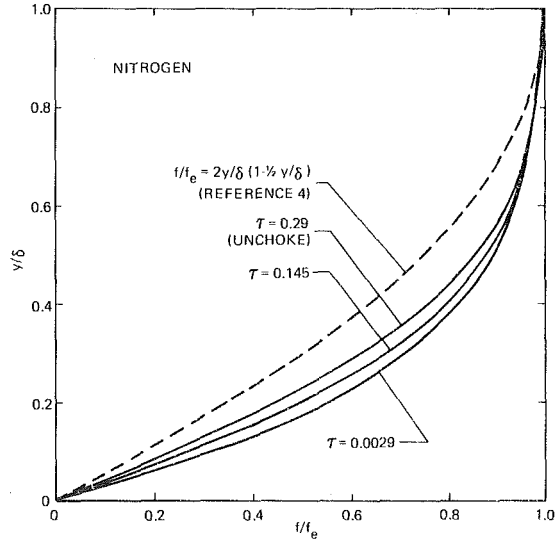

Fig. 7 Reduced temperature profiles through diffusion layer

solution because this data contains the effects of convection, which were omitted from the analytical formulation of the problem. In the downward discharge, however, the numerical solution over-predicts the diffusion layer thickness. This occurs because the mass sink tends to suck away the diffusion layer even though the increased convection tends to cause increased heat transfer, which promotes more rapid diffusion layer growth. For the upward discharge, there are several possible factors which could act together to cause the large diffusion layer growth. These include the orientation (such that gas particles proceeding to the exit orifice act to thicken the layer), the amplification of small disturbances to form an instability in the diffusion layer, an adverse pressure gradient, and possibly other factors. It is difficult to ascertain for certain which factors are the most important in leading to the rapid diffusion layer growth shown in Figs. 4 and 5. These figures also indicate that a maximum value of δ/r_0 of 0.1 results at the unchoke point, meaning that the assumption of one-dimensionality is justified.

In deriving (4), the isentropic discharge solution was used to approximate the functional form of the sink term of (2). Fig. 6 gives an indication of how good that approximation is during discharge up to unchoke time. Plotted in this figure are the measured gas temperature at the vessel center and the adiabatic temperature calculated using the measured pressure history and the isentropic relationship. Also given is the percentage difference between the adiabatic and measured temperatures for nitrogen and helium. With nitrogen, about a 9 percent error occurs at unchoke time and about a 19 percent error for helium.

In Figs. 4 and 5 the approximate solution of [4] is given along with the numerical solution (5). Since the value of δ obtained with the numerical method is based on a definition of a certain percentage of the attainment of the bulk gas temperature far from the wall (i.e., 99.5 percent) and δ obtained from the integral method is based on a particular approximating polynomial, it is not possible to directly compare numerical values of these two quantities. This is an inherent difficulty due to the arbitrarily defined thermal diffusion layer thickness. It is possible, however, to base a comparison of the two methods on a physical quantity such as wall heat flux.

The unsteady wall heat flux can be written

$$\dot{q}(\tau) = kT(0, \tau)\left(\frac{\partial f}{\partial y}\right)_{y=0} \tag{6}$$

For the numerical method described herein,

$$\dot{q}_N = kT(0, \tau)\left(\frac{\partial f}{\partial y}\right)_{y=0} \tag{7}$$

For the integral method described in [4],

$$\dot{q}_I = \frac{2kT(0,\tau)f_e}{\delta_I} \tag{8}$$

where

$$f/f_e = 2y/\delta_I(1 - y/2\delta_I) \tag{9}$$

is the dimensionless temperature distribution used in [4] and

$$f_e = (2 + \tau)\tau/(1 + \tau)^2$$

We can combine (7) and (8) to give

$$\dot{q}_N/\dot{q}_I = \frac{\delta_I\left(\frac{\partial f}{\partial y}\right)_{y=0}}{2f_e}$$

which is the ratio of the magnitude of the wall heat flux calculated by the numerical method and the wall heat flux calculated by the integral method. Note that the thermal diffusion layer thickness calculated by the integral method, δ_I, enters this equation, but the thermal diffusion layer thickness calculated by the numerical method does not. Values of this ratio at different dimensionless times and different gases are given in the following table.

Gas	τ	$\dot{q}_N/\dot{q}_I$
Nitrogen	0.0029	1.23
	0.29 (unchoke)	12.5
Helium	0.006	1.18
	0.43 (unchoke)	250

The integral and numerical methods are in approximate agreement at early time. At unchoke time, however, over two orders of magnitude difference in this ratio can exist. The only parameter which could be responsible for this disagreement is the value of δ_I, and there are two possible reasons to account for this.

In [4], it was tacitly assumed that similar solutions to (2) exist when the sink term was evaluated for an isentropic discharge. Dimensionless distance from the vessel wall through the diffusion layer as a function of the ratio of reduced temperature ($f = 1 - T/T(0)$) and reduced temperature at the edge of the thermal diffusion layer f_e are plotted in Figs. 7 and 8. Also plotted in these figures is the quadratic relationship (9) used in [4] to approximate the reduced temperature profile in the heat-balance integral. Note that this function implies similarity (in the boundary layer sense) of reduced temperature profiles during discharge. As can be seen in this figure, similar solutions do *not* exist for (2) using the isentropic discharge sink term. Also, the quadratic expression used in [4] does not adequately represent the temperature variation through the diffusion layer. The combined effects of the assumption of similarity and the inability of a quadratic profile to approximate the real reduced temperature profiles contribute to the overestimation of δ_I at late times.

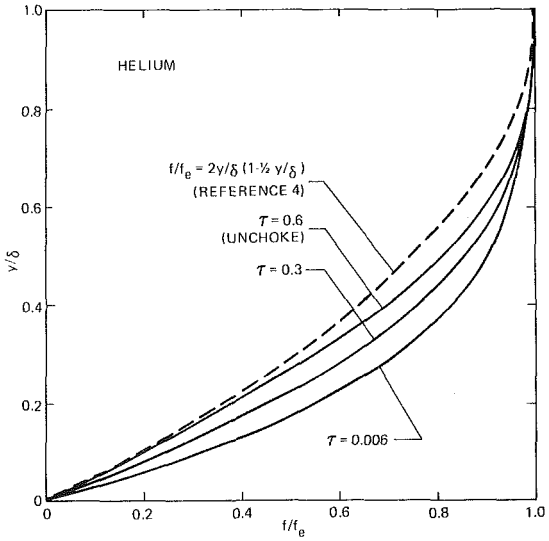

Fig. 8 Reduced temperature profiles through diffusion layer

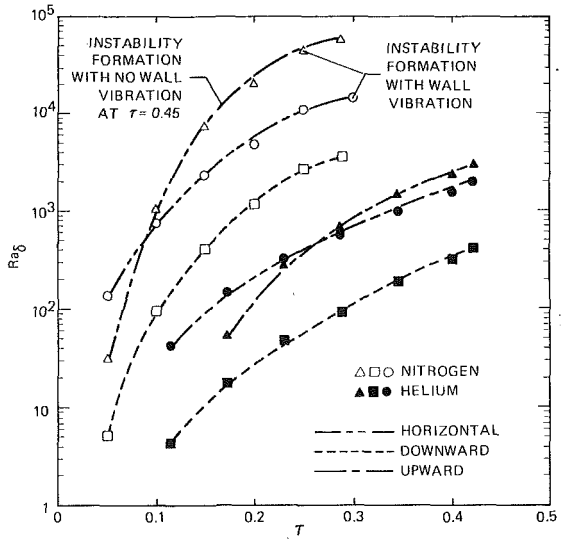

Fig. 9 Rayleigh number histories

In Fig. 9 the Rayleigh number based on δ as a function of dimensionless time is given. Both the thermal diffusivity and viscosity used in calculating the Rayleigh number have been temperature-corrected using the measured gas temperature in the center of the vessel. For the upward nitrogen discharge, the critical Rayleigh number appears to be $\sim 10^5$. With no wall vibration, instability formation at the location where the measurements were taken appears to occur at $\tau \approx 0.45$. With wall vibration, and thus larger amplitude disturbances, instability formation appears to occur sooner at $\tau \approx 0.25$. These results are analogous to those obtained for laminar boundary layers as the intensity of free stream turbulence is increased. Apparently, the smaller amplitude disturbances resulting from the jet-like structure in the upward discharge require longer time to grow into an instability than do the larger amplitude disturbances generated acoustically by wall vibration.

For the horizontal discharge, a critical Rayleigh number was never attained for the nonvibrating wall case, but with wall vibration, instability formation occurred at $\tau \approx 0.3$. The horizontal discharge differs from the upward discharge in that the jet-like structure which forms is not along the lower vessel wall where instability formation first begins. Thus the disturbances which grow to eventually form an instability along the lower vessel wall must be smaller in the horizontal than in the upward discharge. Wall vibration introduces additional disturbances in the horizontal discharge and the diffusion layer subsequently becomes unstable.

For the downward discharge, no instability formation was observed. This is due to the combined effects of the thinning of the diffusion layer by the loss of mass to the mass sink and by the favorable pressure gradient along the lower hemisphere. These results indicate that a different critical Rayleigh number exists for each discharge orientation.

For the helium discharges, a critical Rayleigh number was never achieved, even with wall vibration. In addition, there appears to be a γ-effect in the Ra_δ versus τ plot.

6 Conclusions

During discharge, an asymmetric thermal diffusion layer forms on the interior vessel wall due to wall-to-gas heat transfer. Factors affecting the character of the diffusion layer include a strong dependence on both gas species and vessel discharge orientation. Instabilities may develop in the lower wall diffusion layer as a result of natural or forced perturbations, depending on the value of the characteristic Rayleigh number. Natural perturbations arise by what is thought to be an early time expansion wave-diffusion layer interaction, which results in a jet-like structure emanating from the vessel wall diametrically opposite the exit orifice. Forced perturbations arising from vessel wall vibration can cause a standing acoustic wave pattern in the gas which in turn can act to trigger diffusion layer instability. With instabilities there is greater mixing of cold (interior to the vessel) and hot (near the wall) gas and most likely, greater wall-to-gas heat transfer. Instability development is also highly sensitive to discharge orientation.

The thermal diffusion layer history can be estimated using a finite difference solution to the transient heat conduction equation with a thermal sink term. The neglected effects of convection limit the accuracy of this model. An approximate method using the heat-balance integral technique appears to give a poor estimation of wall heat flux at late time.

References

1 Rayleigh, Lord, "On Convection Currents in a Horizontal Layer of Fluid, When the Higher Temperature is on the Under Side," *Philosophical Magazine*, Series 6, Vol. 32, 1916.

2 Chenoweth, D. R., "Gas Transfer Analysis—SECTION A—An Introduction to Gas-Transfer Fundamentals," Sandia Laboratories, Livermore, SAND74-8211, Sept. 1974.

3 Deckker, B. E. L., and Chang, Y. F., "Transient Effects in Discharge of Compressed Air from a Cylinder through an Orifice," *Journal of Basic Engineering*, TRANS ASME, Vol. 90, Sept. 1968, pp. 333–42.

4 Landram, C. S., "Heat Transfer During Vessel Discharge: Mean and Fluctuating Gas Temperature," JOURNAL OF HEAT TRANSFER, TRANS., ASME. Series C, Feb. 1973, pp. 101–106.

5 Johnston, S. C., "A Characterization of Unsteady Gas Discharge From a Vessel," PhD dissertation, University of California, Davis, Dec. 1974.

6 Chenoweth, D. R., "Gas Transfer Analysis—SECTION B—Pseudo-Polytropic Expansion of a Perfect Gas," Sandia Laboratories, Livermore, SAND74-8212, Sept. 1974.

7 Landram, C. S., Personal communication.

M. A. Shirazi
Chief of Ecosystems Modeling,
Corvallis Environmental Research Laboratory,
U.S. Environmental Protection Agency,
Corvallis, Oreg.
Mem. ASME

L. R. Davis
Professor,
Oregon State University,
Corvallis, Oreg.
Mem. ASME

Analysis of Buoyant Surface Jets

To obtain improved prediction of heated plume characteristics from a surface jet, an integral analysis computer model was modified and a comprehensive set of field and laboratory data available from the literature was gathered, analyzed, and correlated for estimating the magnitude of certain coefficients that are normally introduced in these analyses to achieve closure. The parameters so estimated include the coefficients for entrainment, turbulent exchange, drag, and shear. Since there appeared considerable scatter in the data, even after appropriate subgrouping to narrow the influence of various flow conditions on the data, only statistical procedures could be applied to find the best fit. This and other analyses of its type have been widely used in industry and government for the prediction of thermal plumes from steam power plants. Although the present model has many shortcomings, a recent independent and exhaustive assessment of such predictions revealed that in comparison with other analyses of its type the present analysis predicts the field situations more successfully.

Introduction

Various mathematical models of heated surface jets are available to predict two- and three-dimensional plume configurations. Two widely accepted methods are used for solving the equations in these models, the integral analysis approach and the differential numerical analysis methods. The latter approach, while capable of greater generality, is considerably more costly and due to limited funds and resources was excluded from further consideration for this work. However, a certain degree of generality of results is retained by considering only three-dimensional plume models herein.

Comprehensive reviews of thermal plume models are presented in references [4 , 9].[1] Among the three-dimensional surface jet models seriously considered is one by Stolzenbach and Harleman (MIT Model) [3, 5], another by Prych [1] and the third model by Stefan, et al. [10]. It is outside the scope of this paper to discuss in detail results of all experiments on the three models during our attempt to provide a working program. The MIT model, despite its many fine features, runs into considerable computational difficulties. Prych's model is the result of a reasonably successful attempt to remove some of these difficulties from MIT's model. Stefan's model was written for the developed zone alone and thus can't be compared with others directly. Even though it includes wind effects absent in the other two, it ignores the hydrostatic pressure in the longitudinal direction.

In general, the MIT and Prych models yield comparable predictions [1]. The greatest deviation between the predictions of both models and data is in plume width. Both models overestimate the plume width except near the source or at high Froude numbers. The magnitude of the over predictions can best be assessed from reading references [3, 9].

Modifications are introduced in Prych's model to make it better agree with existing data. These are discussed in the following.

Theoretical Analysis

The analysis due to Prych [1] is given here in an abbreviated form. All lengths have been normalized by H_0, velocities by U_0, excess temperatures by ΔT_0, and densities by ρ_0. All terms have been defined in the Nomenclature. The temperature and velocity profiles are assumed to be Gaussian such that

$$T_r = T \exp(-n^2/B^2) \cdot \exp(-Z^2/H^2) \tag{1}$$

$$U_r = U \exp(-n^2/B^2) \cdot \exp(-Z^2/H^2) + V \cos\theta \tag{2}$$

where n and Z are distances perpendicular to the plume center line in the lateral and vertical directions, respectively. T and U are the center-line excess temperature and velocity, respectively. Fig. 1 shows the coordinate system used.

The energy, volume, and momentum fluxes across the plume at an arbitrary cross section are calculated in terms of center-line velocity, center-line temperature, plume characteristic width, B, and plume characteristic depth, H. Accordingly, the volume flux is

$$Q = \int\int U_r dn dZ \simeq \pi BH \left(\frac{U}{2} + V\cos\theta\right) \tag{3}$$

where the limits of integration for $V \cos\theta$ are taken as the bottom half of the region

$$\left(\frac{n}{\sqrt{2}B}\right)^2 + \left(\frac{Z}{\sqrt{2}H}\right)^2 \leqslant 1 \tag{4}$$

Solving (3) for U yields

[1] Numbers in brackets designate References at end of paper.

Contributed by the Heat Transfer Division for publication in the JOURNAL OF HEAT TRANSFER. Manuscript received by the Heat Transfer Division. Paper No. 76-HT-FFF.

$$U = 2\left(\frac{Q}{\pi BH} - V\cos\theta\right) \tag{5}$$

The heat flux, J, is

$$J = \int\int U_r T_r \, dndZ \simeq \frac{\pi}{2} TBH\left(\frac{U}{2} + V\cos\theta\right) = \frac{QT}{2} \tag{6}$$

The momentum flux, M, is

$$M = \int\int U_r^2 \, dndZ \simeq \pi BH\left(\frac{U}{2} + V\cos\theta\right)^2 \tag{7}$$

$$M = \frac{Q^2}{\pi BH} \tag{8}$$

The quantities dQ/ds, dT/ds, and dM/ds are calculated from the conservation equations. dQ/ds is assumed to be the sum of contributions of jet entrainment and ambient turbulent mixing in the horizontal and vertical directions.

The horizontal jet entrained fluid is

$$\left.\frac{dQ}{ds}\right|_{j,h} = \sqrt{\pi}\, HE_0(U^2 + V^2\sin^2\theta)^{1/2} \tag{9}$$

where E_0 is an entrainment coefficient.

The vertical jet entrainment fluid is

$$\left.\frac{dQ}{ds}\right|_{j,v} = 2\int_0^{\sqrt{2}B} E_0 f(\mathrm{R}_i)\,[U^2\exp(-2n^2/B^2) + V^2\sin^2\theta]^{1/2}\,dn \tag{10}$$

The function $f(\mathrm{R}_i) = [\exp(-5\,\mathrm{R}_i) - 0.0183]/0.982$ is a curve fit to the experimental data of Ellison and Turner [7] with respect to the local Richardson number R_i.

The effective entrainment due to ambient turbulent mixing, according to Prych, is

$$\left.\frac{dQ}{ds}\right|_{a,h} = 11.0\frac{H}{B}\frac{\epsilon_h}{U_0 H_0} \tag{11}$$

$$\left.\frac{dQ}{ds}\right|_{a,v} = 11.0\frac{B}{H}\frac{\epsilon_v}{U_0 H_0} f(\mathrm{R}_i') \tag{12}$$

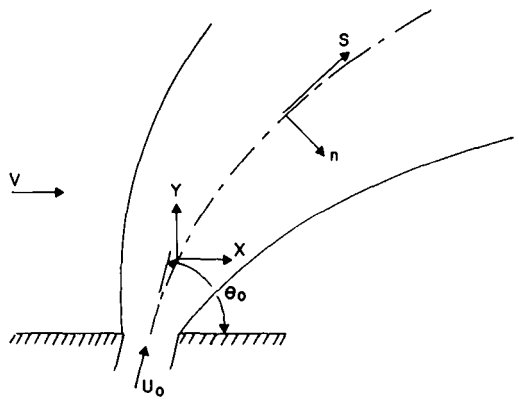

Fig. 1 Plan view of surface plume showing coordinate system

and ϵ_h and ϵ_v are the horizontal and vertical turbulent diffusion coefficients, respectively.

The change in heat flux along the plume is

$$\frac{dJ}{ds} = -2\int_0^\infty KT_r\,dn = \sqrt{\pi}KTB \tag{13}$$

where K is the dimensionless surface heat exchange coefficient. Substituting (6) into (13) yields

$$\frac{dT}{ds} = \frac{-T}{Q}\left(2\sqrt{\pi}KB + \frac{dQ}{ds}\right) \tag{14}$$

The net forces on the plume are balanced by the change in momentum flux. The forces considered important are: (*a*) internal pressure forces due to buoyancy, (*b*) form drag due to ambient current, and (*c*) interfacial shear forces.

The pressure forces are found by determining the excess pressure due to buoyancy as a function of depth and then integrating the pressure over the vertical cross section of the plume. Thus, the normalized pressure force is

Nomenclature

A = aspect ratio $2B_0/H_0$
B = local characteristic width of jet = $\sqrt{2}\sigma_n$
B_0 = half width of outlet
$B_{1/2}$ = plume half width = 1.177 σ_n
C_D = form drag coefficient
C_F = interfacial shear drag coefficient
c = celerity of a density front
C_s = spreading coefficient
E_h = dimensionless horizontal eddy diffusion coefficient ϵ_h/U_0H_0
E_0 = entrainment coefficient
E_v = dimensionless vertical eddy diffusion coefficient ϵ_v/U_0H_0
F_0 = densimetric Froude number at outlet, $U_0/\sqrt{g'H_0}$
g = acceleration due to gravity
g' = reduced gravitational acceleration, $g\Delta\rho/\rho_a$
H = local characteristic thickness of jet $\sqrt{2}\sigma_z$
H_0 = depth of outlet
J = heat flux
K = dimensionless surface heat transfer coefficient
M = momentum flux
n = curvilinear coordinate horizontal and normal to jet center line
P = normalized hydrostatic pressure force
Q = mass flux
R = velocity ratio V/U_0
R_i = local Richardson number defined by $R_i = \sqrt{2}HT_r(n, 0)/\{\mathrm{F}_0^2[U^2\exp(-2n^2/B^2) - V^2\sin^2\theta]\}$
R_i' = bulk Richardson number defined by $\mathrm{R}_i' = \sqrt{2}HT'/[F_0^2(U + V\cos\theta)]$
s = curvilinear coordinate along jet center line
S_i = distance from outlet to end of initial zone
T = dimensionless center line excess temperature $\Delta T_c/\Delta T_0$
ΔT_c = excess water surface temperature on jet center line
ΔT_0 = discharge excess water temperature
T_r = local excess temperature in plume cross section defined in equation (1)
U = excess jet velocity on jet center line
U_0 = discharge velocity from outlet
U_r = local velocity in plume cross section defined in equation (2)
V = ambient current velocity
X = rectilinear coordinate parallel to ambient current
Y = rectilinear coordinate, horizontal and perpendicular to X
Z = coordinate in vertical direction
$\Delta\rho$ = difference between outlet and ambient water densities
ϵ = turbulent diffusion coefficient
ϵ_h, ϵ_v = ambient turbulent diffusion coefficient for horizontal and vertical directions
θ = angle between X axis and plume center line
ρ = fluid density
σ_n, σ_z = standard deviation of Gaussian profile in n- and z-directions

Subscripts

a = ambient conditions
c = center-line value at surface
h = horizontal
i = refers to variables at end of development zone
0 = discharge conditions
r = perpendicular to s in n- and Z-directions
v = vertical

$$P = \frac{1}{F_0^2} \int\int \left\{ \int_{-\infty}^{Z} T_r dZ \right\} dn dZ = \sqrt{\pi}\, TH^2 B / 2F_0^2 \qquad (15)$$

The form drag acting normal to the plume center line is assumed similar to the drag on a solid body. The interfacial shear forces are assumed to be similar to turbulent flow over a flat surface with a boundary layer thickness of $\sqrt{2}H$.

The change in momentum flux includes the effects of the momentum of the entrained ambient fluid, VdQ/ds, which acts in the X-direction. Equating the forces to the change in momentum flux in the X- and Y-direction yields

$$\frac{d}{ds}(M + P)\cos\theta = SF_X + F_D \sin\theta + V\frac{dQ}{ds} \qquad (16)$$

$$\frac{d}{ds}(M + P)\sin\theta = SF_Y - F_D \cos\theta \qquad (17)$$

where F_D is the drag force and SF_X and SF_Y are the X and Y components of the interfacial shear force. Using equations (8) and (15) for M and P, multiplying (16) by $-\sin\theta$, (17) by $\cos\theta$, and combining, yields an expression for the change in flow direction

$$\frac{d\theta}{ds} = \frac{SF_Y \cos\theta - SF_X \sin\theta - F_D - V\sin\theta\,(dQ/ds)}{\dfrac{Q^2}{\pi BH} + \dfrac{\sqrt{\pi}}{2F_0^2} TH^2 B} \qquad (18)$$

Differentiating M and P, multiplying (16) by $\cos\theta$ and (17) by $\sin\theta$, and combining yields

$$\frac{dH}{ds} = [SF_Y \sin\theta + SF_X \cos\theta + (V\cos\theta - 2Q/\pi BH)(dQ/ds) - (\sqrt{\pi}\, BH/2F_0^2)(dT/ds) + (Q^2/\pi B^2H^2 - \sqrt{\pi}\, H^2T/2F_0^2)(dB/ds)] \times [\sqrt{\pi}\, THB/2F_0^2 - Q^2/\pi BH^2]^{-1} \qquad (19)$$

It should be noted that this expression for change in depth is undefined when the denominator becomes zero.

Momentum in the lateral direction is included only indirectly through lateral spreading. It is assumed that the contributions to spreading by nonbuoyant horizontal jet mixing and buoyancy are independent of one another.

The nonbuoyant spreading is found by writing equation (19) without the buoyancy terms (any terms containing F_0) and by assuming that

$$\left(\frac{dB/ds}{dH/ds}\right)_{nb} = (B/H)(dQ/ds)_h/(dQ/ds)_v$$

where $(dQ/ds)_h$ and $(dQ/ds)_v$ are the horizontal and vertical entrainment rates. Accordingly,

$$\left(\frac{dB}{ds}\right)_{nb} = \frac{SF_Y \sin\theta + SF_X \cos\theta + \left(V\cos\theta - \dfrac{2Q}{\pi BH}\right)\dfrac{dQ}{ds}}{-(Q^2/\pi B^2 H)[(dQ/ds)_v/(dQ/ds)_h + 1]} \qquad (20)$$

The buoyant spreading function used by Prych was based on the analysis of an immiscible film, such as oil spreading without friction over water. This ignores the shear interaction between the fluid systems as well as the variation in fluid densities at the interface. Furthermore, the fluid particles were assumed to move with a velocity equal to the velocity caused by an abrupt density front. When applied to a heated plume, these assumptions lead to an overprediction of plume width compared with the actual spreading.

In a separate analysis of a buoyant spreading of a pool of warm water, Koh and Fan [6] accounted for the interfacial shear but ignored the actual entrainment of the cool water. They found that near the source the spreading velocity and the fluid velocity used by Prych are the same, i.e.,

$$V_n^2 = c^2 \sim g'h$$

where H is the local depth of the buoyant pool. However, far away from the source where the shear forces become very important, the fluid front velocity is

$$V_n^2 \sim \frac{g'H}{(\epsilon/H\rho)}(H/B)$$

where $g'H$ is proportional to c^2, $(\epsilon/H\rho)$ is proportional to the shear velocity and H/B is the ratio of the local pool depth to its width. If interpreted in terms of plume spread, this finding implies that spreading velocity is inversely proportional to the local aspect ratio of the plume.

The appearance of the local aspect ratio in the expression for the plume velocity offers an intuitively appealing ground for assuming

$$V_n^2 \sim (g'H)(H/B)$$

This can also be explained as follows. The lower density of the plume causes it to rise slightly about the free surface of the surrounding water. The height of rise at any point is proportional to the local vertical density difference between the plume and the ambient and the depth of the plume at this point. Since both the density difference and depth of the plume decrease from the center to the edge, this height varies from a maximum at the center to zero at the edge, causing the plume to spread in that direction. The spreading rate due to buoyancy is related to the slope of this free surface. Since the height of rise at the center is proportional to $g\Delta\rho_c H/\rho$, the slope of the free surface and thus the spreading rate is a function of $g\Delta\rho_c H/\rho B$.

As a result of the foregoing discussion the buoyant spreading developed in this study is

$$\left(\frac{dB}{ds}\right)_b = \frac{C_s}{\left(\dfrac{B}{H}F^2 - 1\right)^{1/2}} \qquad (21)$$

where C_s is an imperical spreading coefficient and F is the local Froude number defined by $F = F_0 Q/(TH^3B^2\pi^{3/2})^{1/2}$.

The preceding equations are sufficient to perform a step-wise integration along the plume. From the local conditions of the plume, dQ/ds and then dT/ds, $d\theta/ds$, dB/ds, and finally dH/ds can be calculated in that order. These derivatives are integrated step-wise along the plume trajectory to give local values of X, Y, T, H, B, θ, and Q.

To start the integration within the developed zone where the foregoing analysis is valid, starting conditions must be calculated. These are determined by a simplified analysis of the development zone.

The length of the development zone is based on experiments made in a still tank at the Corvallis Environmental Research Laboratory [11]. It was found to be approximately:

$$S_i = 5.4\left(\frac{A^2}{F_0}\right)^{1/3} \qquad (22)$$

For details of the development zone calculation, the reader is referred to reference [11]. The work by Stefan, et al. [15] provides more up-to-date information necessary for improved predictions in the development zone.

Fitting the Model with Data

Reference [2] provides a comprehensive set of data that is a good representation of available experiments both in the field and laboratory. The data provide a wide range of plume conditions with which one can test and accordingly adjust numerous analytical functions of the plume model. The plume model contains a number of free variables such as entrainment coefficient E_0, turbulent exchange coefficients E_h, E_v, drag coefficient C_D, and shear coefficient C_F. The magnitudes of these coefficients must be prespecified so that the model produces the best fit with the measured plume characteristics.

To accomplish this task, the following procedure is adopted: (a) Data for plume characteristics are subgrouped with a narrow range of the experimental scaling parameters. These parameters are the current ratio, R, the discharge densimetric Froude number, F_0, the jet aspect ratio, A, and the angle of discharge, θ_0. Each subgroup contains data from several sources, thus providing considerable realism with respect to possible experimental scatter and variations in

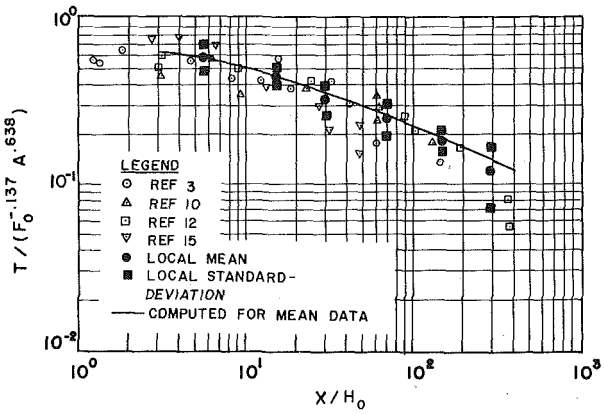

Fig. 2 Correlation of selected field and laboratory surface plume temperature data at negligible ambient current as compared to calculated values

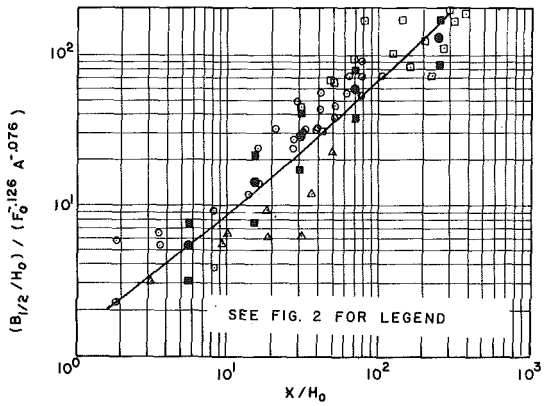

Fig. 3 Correlation of selected field and laboratory width data at negligible ambient current as compared to calculated values

experimental parameter scales. The choice of a narrow range in certain experimental parameters was dictated by the desire to obtain as strong a correlation of the data within a given subgroup as possible. (*b*) For each subgroup, the range and mean of all experimental parameters are determined. (*c*) The data are correlated using dimensional analysis with the scaling parameters as variables and multiple regression methods separately for each subgroup following the procedure outlined in [2]. (*d*) The measured plume characteristics are plotted against dimensionless axial distance using the correlation results. (*e*) Finally, the analytical program is used to calculate the plume characteristics in each subgroup for the mean of the experimental parameters R, F, A, and θ_0. Agreement between the calculated characteristics and the data mean is sought by adjusting one or more of the model coefficients E_0, E_h, E_v, C_D, C_F, and C_S. This process is repeated for several subgroups, adjusting in each trial one or more coefficients until best fits are obtained to plume characteristics for all subgroups.

The correlations obtained by this method have been used in ordinates in the figures of this paper. It should be pointed out that these correlations of each data subgroup are useful mainly for the mean data in that subgroup. They are not universal correlations and cannot be used outside the data range they represent.

Turbulent Exchange Coefficients, E_h, E_v. It should be understood that the turbulent exchange coefficients, E_h and E_v, will vary from case to case since ϵ_h and ϵ_v are not necessarily constant and in the analysis they have been nondimensionalized using U_0 and H_0, which depend on discharge conditions. When accurate values for these coefficients can be determined, they should be used. In this work they were back calculated based on a best fit with data. The values so determined were assumed to be representative of the mean and taken as constant.

The data used to determine the effects of ambient turbulence on plume behavior is provided by Weil [2, 8]. In his experiments, Weil injected heated water at the surface in a turbulent channel from a semicircular jet at a relatively large densimetric jet Froude number. The discharge was in the direction of the channel current ($\theta_0 = 0$). The jet velocity in all his experiments was held equal to the local channel flow velocity. Since the relative velocity between the plume and ambient water is zero and since buoyancy effects are small due to a high Froude number, dilution is largely due to turbulence effects.

For the conditions of this experiment, the following simplifications can be introduced in the mathematical model: (*a*) Terms containing entrainment coefficient E_0 can be set equal to zero because there is no relative velocity between the jet and the ambient water. (*b*) For the same reason, the terms containing the shear coefficient, C_F, also can be set equal to zero. (*c*) The drag coefficient, C_D, is zero because the jet is parallel to the ambient current and the pressure distributions on the left- and right-hand sides of the plume are identical. (*d*) Because the heat loss in the experiments was small, one can choose a typical value of $K = 10^{-5}$ without greatly affecting the calculated plume characteristics. (*e*) Since the jet densimetric Froude number is high, the influence of the buoyant forces on the plume spread is not substantial. The plume width grows predominantly due to turbulent entrainment of the ambient water, a mechanism which the analysis accounts for through E_h and E_v. It was found that the best computer fit was obtained when $E_h = 0.02$, $E_v/E_h = 0.2$, and $C_s = 1.4$.

Entrainment Coefficient, E_0. The next group of data consists of information from several sets of laboratory and some field experiments for a surface discharge in zero or negligibly small cross current.

For the conditions of this group, one can assume that the drag coefficient is zero. As a first approximation we also assume that the contribution of the ambient turbulence is accounted for by the previously assigned values of E_h and E_v.

The best fit of the computer model with the data for this case was obtained with $E_0 = 0.05$. Since the shear coefficient had negligible effect on the result, it was set equal to zero.

Fig. 2 is a plot of the reduced temperature data from several sources where the ambient velocity was zero or negligible. Also shown are the mean and standard deviation of the data along with a computer prediction using input variables comparable to the mean experimental values. Fig. 3 is the same for plume width. It is seen that the computer prediction agrees very well with the mean of the data.

Drag Coefficient, C_D. For given values of discharge angle, Froude number, aspect ratio, and ambient current, the plume trajectory is mainly influenced by the entrainment of ambient fluid with a minor influence due to pressure drag. Since the entrainment coefficient is prespecified from the above, only the drag coefficient can be used to further adjust the trajectory. Consequently, trajectory data were regrouped for a reasonably wide range of all plume parameters mentioned above.

The best value of C_D was found to be 1.0. Fig. 4 gives reduced trajectory data from a large number of sources. Also shown are the mean and standard deviation of the data along with a computer prediction of trajectory for the mean input variables of the data.

In order to complete the adjustment of the model to fit the data, we need to check the model against measured plume width and temperature for a wide range of parameters. If agreement is obtained with such data without the need to readjust the previously specified coefficients E_0, E_h, E_v, C_F and C_D, then the fitting of the model with data is considered complete.

The raw data and calculated values based on previous coefficients are compared in Fig. 5 for plume width and in Fig. 6 for plume temperature. The agreement obtained from the comparison of calculated and measured plume width is excellent, and the agreement for plume temperature is reasonably good.

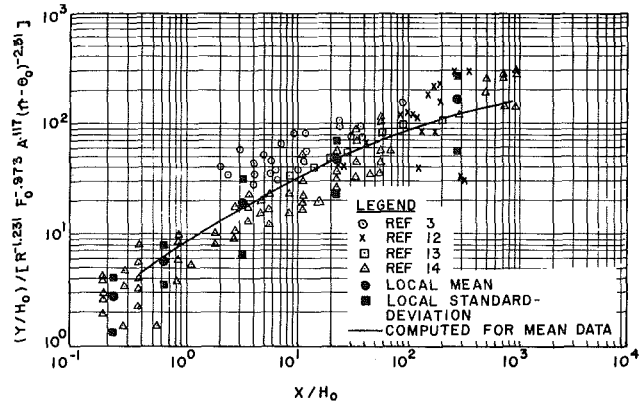

Fig. 4 Correlation of selected field and laboratory plume trajectory data as compared to calculated values

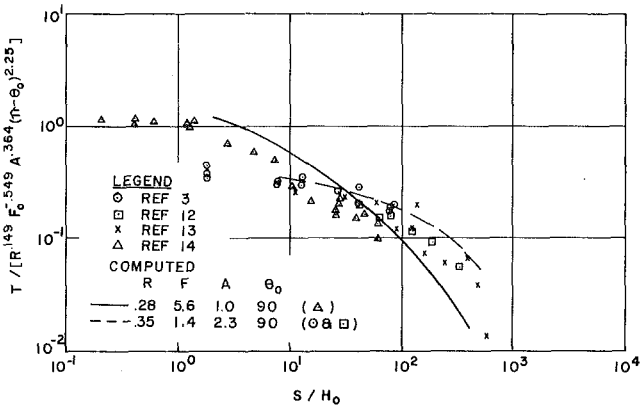

Fig. 6 Correlation of selected field and laboratory surface plume temperature as compared to calculated values

Discussion

A notable degree of data scatter could not be avoided when attempting to correlate information on plume characteristics from several sources. Physical factors not included in the data analysis but which are believed to have contributed to the data scatter are: (*a*) the lack of a universal simple exponential correlation such as used in this report; (*b*) the influence of diverse turbulence scales; (*c*) the influence of surface heat transfer; (*d*) time-dependency and boundary effects, and (*e*) instrumentation and experimental errors.

The exponential correlations employed are intended for data presentation in a compact form within each data grouping. They are not used to explain the physics of the problem exclusive of the mathematical model. They do, however, provide a statistical presentation of the level of data scatter one can expect when dealing with data from numerous sources.

There are at least two reasons why data from more than one source should be used. These are: (1) there exists no single set of data that covers a sufficiently wide range of parameters relating to initial jet conditions and ambient current; (2) data obtained for a wide range of ambient turbulence levels are reported in the literature. While the ambient turbulence level and turbulence scale affect the plume characteristics, information on these parameters is lacking in nearly all the data reported. It is felt, therefore, that a plume analysis based on several sources carries a greater degree of realism than one based on a single source.

It should be noted that the turbulence exchange coefficients in the model were back-calculated based on the best fit with the data. The coefficients are entered in a form of a turbulent Reynolds number ϵ/U_0H_0. In this manner, even though diffusivities are not directly measured in each experiment, the use of the model does provide an indirectly calculated value for the correlation parameters that best represent the available data. If in a given application, one has a better knowledge of these or any other coefficients entering the model, then of course, those should be used in the model instead.

The final conclusion is that the model can be tuned to satisfactorily predict buoyant surface jet characteristics including trajectory, width, and temperature. A set of nomograms obtained from the final tuned model for a wide range of discharge and environmental conditions is found in [11].

Reference [9], which was published after the foregoing model became available and widely used, presents an exhaustive state of the art review, critique, and assessment of the available surface jet models. As a common criterion for such assessment, the authors utilized one of the most comprehensive but recently obtained large scale field data from conventional power plant thermal outfalls. Among the analyses using the integral approach, the present model was shown to be superior in comparison with others. It was also shown, however, that much work needs to be done to obtain a truly accurate surface plume model that includes the effects of topography, wind, ambient stratification, etc.

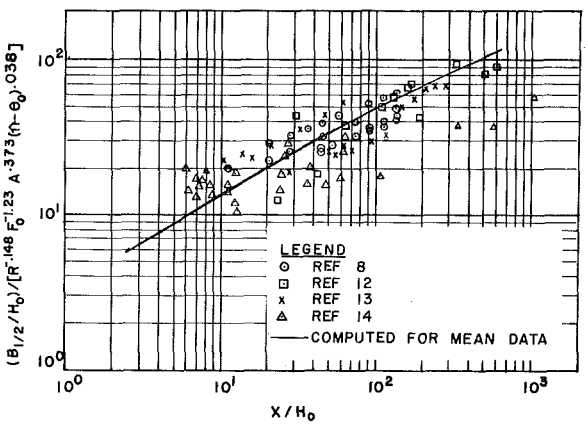

Fig. 5 Correlation of selected field and laboratory width data as compared to calculated values

References

1 Prych, E. A., "A Warm Water Effluent Analysis as a Buoyant Surface Jet," Swedish Meteorological and Hydrological Institute, Series Hydroli, No. 21, 1972.

2 Shirazi, M. A., "Some Results From Experimental Data on Surface Jet Discharge of Heated Water," *Proceeding of the International Water Resources Association*, Chicago, 1973.

3 Stolzenbach, K. D., and Harleman, D. R. F., "An Analytical and Experimental Investigation of Surface Discharges of Heated Water," Water Pollution Control Series 16130 DJV 02/71, Feb. 1971.

4 Policastro, A. J., and Tokar, J. V., "Heated Effluent Dispension in Large Lakes: State-of-the-Art of Analytical Modeling Part I, Critique of Model Formulations," Argonne National Laboratory ANL/ES-11, Jan. 1972.

5 Stolzenbach, K. D., Adams, E. E., and Harleman, D. R. F., "A User's Manual for Three-Dimensional Heated Surface Discharge Computations," Environmental Protection Technology Series EPA-R2-73-133, Jan. 1973.

6 Koh, R. C. Y., and Fan, L. N., "Mathematical Models for the Prediction of Temperature Distributions Resulting From the Discharge of Heated Water into Large Bodies of Water," Water Pollution Control Series 16130 DWO 10/70, Oct. 1970.

7 Ellison, T. H., and Turner, J. S., "Turbulent Entrainment in Stratified Flows," *Journal of Fluid Mechanics*, Vol. 6, Part 3, Oct. 1959, pp. 423–448.

8 Weil, J., "Mixing of a Heated Surface Jet in Turbulent Channel Flow," Report No. WHM-1, Department of Civil Engineering, University of California, Berkeley, June 1972.

9 Dunn, W., Policastro, A. J., and Paddock, R., "Surface Thermal Plumes: Evaluation of Mathematical Models for the Near and Complete Field," Argonne National Laboratory ANL/WR-75-3, Part 1, May 1975, Part 2, Aug. 1975.

10 Stefan, H., Hayakawa, N., and Schiebe, F. R., "Surface Discharge of

Heated Water," Water Pollution Control Research Series 16130 FSU 12171, Dec. 1971.

11 Shirazi, M. A., and Davis, L. R., "Workbook of Thermal Plume Prediction Vol. 2, Surface Discharge," Environmental Protection Technology Series, EPA-R2-72-005b, May 1974.

12 Wiegel, R. L., Mobarek, I., and Jen, Y., "Discharge of Warm Water Jet Over Sloping Bottom," Hydraulic Engineering Laboratory, University of California, Berkeley, Calif., Report No. HEL 3-4, 1964.

13 Simmons, L. L., Kueser, P. E., Wright, J. H., and Jouris, G. M., "Near Field Thermal-Plume Parameters for Electric-Power Plants Discharging Into Rivers or Transverse Currents," Westinghouse Electric Corp., Pittsburgh, Pa., presented in the AECHE, N. Y., 1972.

14 Motz, H., and Benedict, B. A., "Heated Surface Jet Discharging Into a Flow Ambient Stream," Vanderbilt University, EPA Project Report No. 16130 FDQ 03/71, Mar. 1971.

15 Stefan, H., Bergstedt, L., and Mrosla, E., "Flow Establishment and Initial Entrainment of Heated Water Surface Jets," EPA-660/3-75-015, U.S. Environmental Protection Agency Ecological Research Series, May 1975.

G. Bergeles
A. D. Gosman
B. E. Launder

Mechanical Engineering Department,
Imperial College,
London SW7 2BX, England

The Near-Field Character of a Jet Discharged Normal to a Main Stream

The paper reports an experimental study of the flow created by the injection of a circular jet of air at 90 deg through a plane wall past which an external stream is flowing. Particular attention has been given to obtaining details of the flow in the vicinity of the injection hole and upstream from the hole. These regions have been omitted, or received only slight attention in earlier studies of discrete-hole cooling processes. Four ratios of average injectant velocity: external velocity were chosen in the range 0.046- 0.50. Even at the lowest injection rate there is still a clearly identifiable reverse flow region springing from the downstream side of the hole which extends approximately 0.3 dia downstream. The velocity distribution in the jet at discharge was found to be greatly affected by the presence of the external stream, more than 75 percent of the flow leaving from the downstream half of the discharge hole with a peak velocity in the jet approximately three times the average. Contour mappings of the surface isobars, show the upstream and lateral effects on the static pressure caused by the injection. In addition a number of flow visualization experiments help to reinforce the inferred character of the flow. Detailed film-cooling effectiveness data are reported which help delineate the near-wall flow structure.

1 Introduction

Discrete-hole cooling perhaps offers the most promising technique for protecting the first stages of gas-turbine stators and rotors from the ever-increasing temperature of the combustion products. Already blades are in use that employ one or a few rows of holes located usually over the leading half of the chord. Complete coverage systems, whereby myriads of smaller holes extend over nearly all the blade surface are also under development. Despite the successes achieved already with this cooling technique, it is well known that the performance of discrete-hole cooling depends rather crucially on adopting the correct spacing between holes and the right velocity of ejection relative to that of the external stream. At the moment, therefore, each new application of discrete-hole cooling requires an extensive—and very expensive—program of tests in an attempt to approach an optimum arrangement of holes. To limit expense several of the potentially influential parameters (such as free stream turbulence or streamwise pressure gradients) may be omitted altogether from study or examined only scantily.

Recent advances in the development of three-dimensional numerical procedures for fluid-flow problems make it feasible to develop computer-based prediction schemes for simulating the flow structure associated with discrete-hole cooling. The authors are currently engaged in developing such a code [1].[1] It has emerged during this work that the satisfactory prediction of the flow and cooling effectiveness behind a row of holes depends crucially on predicting correctly the detailed structure of the flow in the immediate vicinity of the holes, and indeed, upstream therefrom. Now, although there have been several experimental studies of discrete-hole cooling both for single row of holes [2, 3] and multirow coverage [4, 5] there has been no serious study of the character of the flow in the all important region right in the neighborhood of the jet discharge. It was to provide information in this area that the measurements reported in the following were undertaken.

The region around and upstream of the injection hole is not an ideal region for data acquisition. There is always the suspicion that one's probe may itself be affecting the flow pattern. For this reason, a number of different approaches have been used for documenting the flow, including flow visualization. Taken together these results provide a consistent and fairly comprehensive picture of 90 deg discrete-hole injection for injectant:free stream velocities in the range 0.046:1- 0.5:1.

Contributed by the Heat Transfer Division and presented at the Winter Annual Meeting, New York, N.Y., November 30 -December 5, 1975, of THE AMERICAN SOCIETY OF MECHANICAL ENGINEERS. Revised manuscript received by the Heat Transfer Division May 11, 1976. Paper No. 75-HT-WA/108.

[1] Numbers in brackets designate References at end of paper.

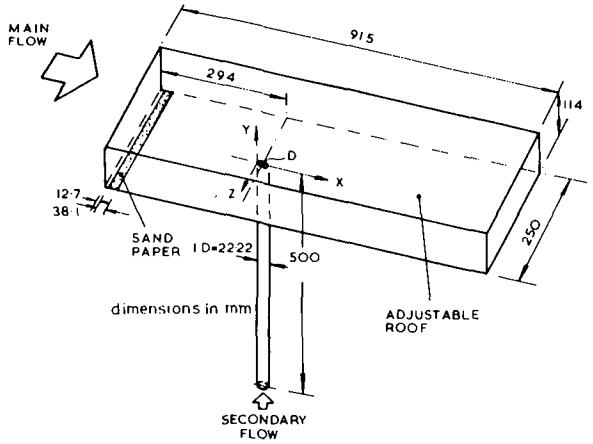

Fig. 1 Diagram of test section

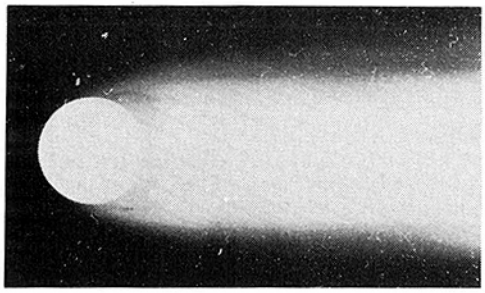

Fig. 2(*a*) Lateral spread of the jet ($M = 0.24$)

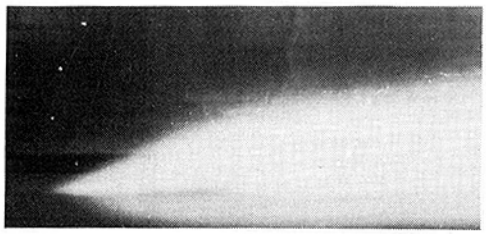

Fig. 2(*b*) Vertical spread of the jet ($M = 0.24$)

2 Apparatus and Measurement Techniques

(*a*) **Apparatus.** The experiments were performed in the rectangular test section depicted in Fig. 1, which was supplied with a uniform-velocity stream of air at entry by means of a blower, feeding through a contraction section equipped with screens, and with slots to bleed off the boundary layers. A sandpaper strip was attached to the upstream surface of the bottom plate of the section to promote turbulent flow, and the top plate was adjusted so as to give zero mean streamwise pressure gradient in the absence of secondary injection. The sides and bottom were constructed of perspex, to facilitate flow visualization.

The secondary jet was introduced via a circular hole in the lower plate, located on the center line some distance downstream of the entry (the exact location, together with other important dimensions, are shown in Fig. 1). Air was supplied to the hole via a circular tube of the same diameter, and the flow rate was monitored by means of an orifice.

The area in the immediate vicinity of the injection hole was drilled with an array of static pressure tappings of diameter 0.79 mm: the precise locations of these are shown in Fig. 4.

(*b*) **Measurement Techniques.** Measurements of the distribution of static and dynamic pressure within the flow, excluding the region immediately above the injection hole, were obtained with the aid of pitot-static probes manufactured to NPL recommendations; the diameter of the total pressure tubes ranged from 0.50 to 0.64 mm with corresponding scaling of the other pertinent dimensions. In regions where appreciable variations in static pressure occurred the dynamic and static heads were measured separately, at corresponding locations. The pressure registered by the probes, and by the wall tappings, was determined to an accuracy of 0.2 percent by use of an electronic micromanometer. The accuracy of the streamwise velocities deduced from the pitot measurements was estimated, with due allowance for the errors associated with yaw and turbulence, to be of the order of 2 percent in all regions apart from the zone immediately downstream of the injection hole, where the disturbances provoked by injection give rise to indeterminate errors. The measured values of C_p were influenced by small departures from the zero pressure gradient condition induced by injection and boundary-layer growth on the tunnel walls giving rise to variation in C_p ranging from zero at the upstream row of tappings to about 10 percent of the recorded values at the downstream row.

A hot-wire anemometer coupled to an ancillary on-line signal processing equipment, [6], was used to investigate the flow at the exit of the injection hole. In the absence of a transverse stream, the measurements with the foregoing system using a single-wire probe would, according to the analysis of [7], be expected to yield injection velocities and turbulence intensities accurate to within 1 percent and 8 percent, respectively. However, the presence of transverse flow, with the attendant distortion of the streamlines and generation of high turbulence levels, introduces problems of signal interpretation that make it difficult to estimate the accuracy attained. Certainly, at an injection rate of 0.24 the profiles shown in Fig. 7(*b*) at different depths inside the hole show consistent behavior.

Film-cooling effectiveness was measured by adding a tracer of helium (approximately 1 percent by volume) to the secondary stream upstream of the metering section. The concentration of helium on the surface of the test plate was obtained by withdrawing samples of the air:helium mixture through the static pressure taps and metering using an on-line kathometer (see [8] for further details). The small sampling rate, 100 m l/min, was found to have no effect on the flow field in the slow-moving wake region behind the hole. The adiabatic

Nomenclature

C_p = pressure coefficient ($C_p = (P - P_{ref})/(\rho_j U_\infty V_j/2)$)
C = concentration of tracer gas
D = hole diameter
M = injection ratio ($M = \rho_j V_j/\rho_\infty U_\infty$)
P = static pressure
U = local x-direction velocity
U_∞ = free stream velocity of the main flow
v = root mean square fluctuating velocity in y-direction
V = local y-direction velocity
V_j = mean injection velocity
x = downstream direction
y = vertical direction
z = lateral direction
ρ_∞ = density of free stream
ρ_j = density of coolant

Subscripts

$\mathfrak{C}$ = center line
off $\mathfrak{C}$ = line parallel to the $\mathfrak{C}$ at a distance $z/D = 0.64$
ref = reference point, located at $x/D = -1.2$, $z/D = 0.64$
w = wall
inj = injection

film-cooling effectiveness is then obtained from $\eta \equiv C_w/C_{inj}$.

(c) **Conditions of the Experiments.** The experiments were carried out for a free-stream velocity of 26 m/s, density ratio ρ_j/ρ_∞ of unity and values of the injection: free-stream velocity ratio, between 0.046 and 0.5. In the absence of injection and at a plane located at $x/D = -1.17$ the boundary layer thickness was determined to be 0.36 hole dia (displacement thickness = $0.05D$) with less than 1.5 percent spanwise variation and the shape factor and momentum thickness Reynolds number were 1.23 and 1350, respectively.

3 Presentation and Discussion of Results

Let us start with the visual observations of the flow for they provide a clear, albeit qualitative, view of the flow structure. Fig. 2 shows a plan and side view of the jet for an injection ratio of 0.24. The jet is made visible by introducing into the secondary jet a mixture of carbon dioxide and vaporized oil. From the side view it is evident that the jet is very rapidly bent over. On the downstream side of the hole, however, there is a region where the jet lifts a little away from the surface, evidenced by the greyish patch behind the hole. The width of the jet increases rapidly at first, then rather more gradually. At a distance of 3 dia behind the hole the total width of the jet is approximately 2.5 hole dia. It should be borne in mind that when viewing the jet in plan view, the perceived width is the maximum width of the jet and not necessarily the width at the surface.

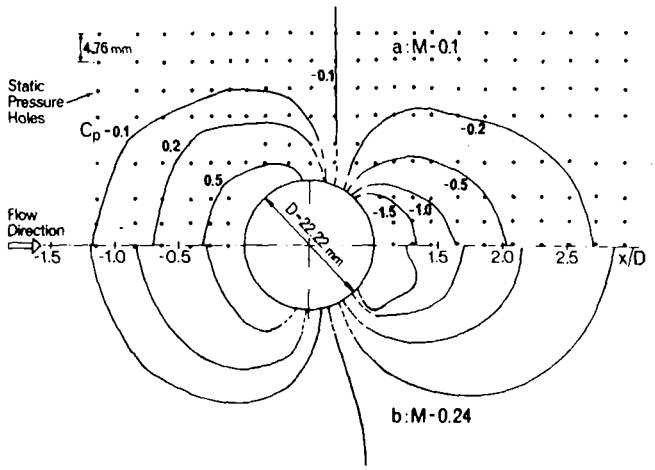

Fig. 4 Surface isobaric contours

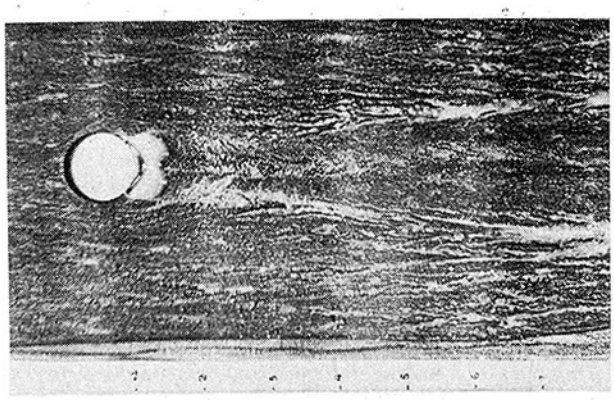

Fig. 3(*a*) Surface flow pattern ($M = 0.10$)

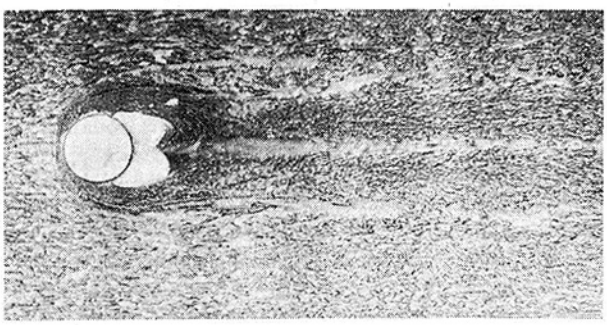

Fig. 3(*b*) Surface flow pattern ($M = 0.24$)

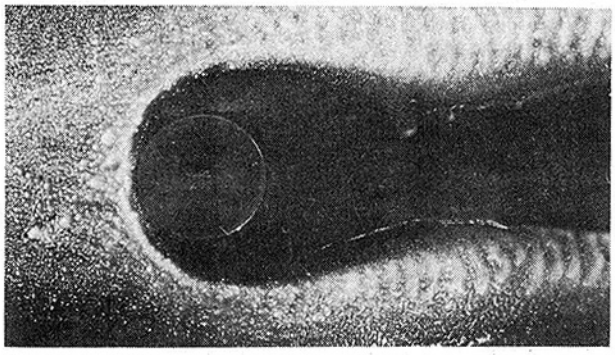

Fig. 3(*c*) Surface flow pattern ($M = 0.24$)

Fig. 3(*a*) shows the flow pattern obtained when the jet velocity is 10 percent of the mainstream. Clearly visible is the development of a wake downstream from the hole. The two lobes adjacent to the downstream side of the injection hole mark a region of separated flow extending approximately half a diameter downstream. A similar pattern is displayed for $M = 0.046$ (not shown) though the two lobes then extend only $0.3D$ behind the hole. The corresponding distribution for a dimensionless blowing rate of 0.24 is shown in Fig. 3(*b*). Several features are the same as before: the spread of the wake downstream of the hole and the two separated flow lobes abutting the downstream side of the hole. The region of separated flow has, not unexpectedly, lengthened. To some extent the injectant fluid affects the main flow rather as a blister attached to the surface.[2] The greater the normalized injection rate the blunter the "equivalent" blister and, hence, the more extensive the recirculation zone.

The recirculating flow region in fact extends further downstream than the limits of the lobes suggest. At $M = 0.24$, successive tests in which the mixture was painted only downstream of the hole established that the recirculation zone extended approximately 2 dia downstream; further details appear in [9]. A feature of Fig. 3(*b*) that could hardly be seen at the lower injection rate is the deflection of the flow upstream of the hole and the associated bending of the vortex lines around the hole. It is entirely expected that this vortex should become more pronounced as the blowing rate is increased since then, as explained previously, the injectant stream acts as a progressively blunter obstacle in the path of the external stream. There is just

[2] The analogy is not complete however for it allows no recognition of the streamwise vorticity added to the flow by injection.

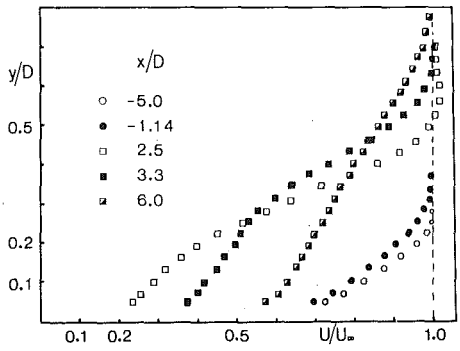

Fig. 5(*a*) Profiles of streamwise velocity along center line; $z/D = 0.0$, $M = 0.10$

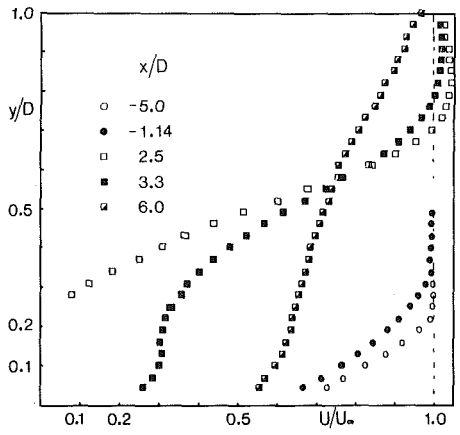

Fig. 5(*b*) Profiles of streamwise velocity along center line $z/D = 0.0$, $M = 0.24$

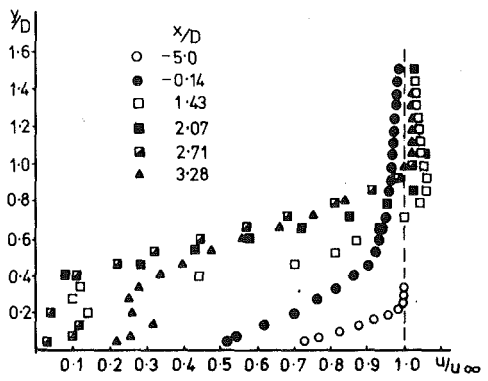

Fig. 5(*c*) Profiles of streamwise velocity $z/D = 0.0$, 0.50

perceptible in Fig. 3(*b*) a "pinching" in of the vortex downstream of the hole. The behavior can be seen more clearly in Fig. 3(*c*). Here the injection rate was the same as in Fig. 3(*b*) but the white spirit/kerosene mixture was coated only in a patch upstream of the injection hole. The character of the near surface flow structure indicated by these photographs is quite different from that found by similar surface-visualization techniques when M is well in excess of unity [10, 11]. In that case, the jet does not reattach, there is strong entrainment of the primary flow into the jet on all sides and the boundaries of the wake region behind the jet are much sharper than in the present study.

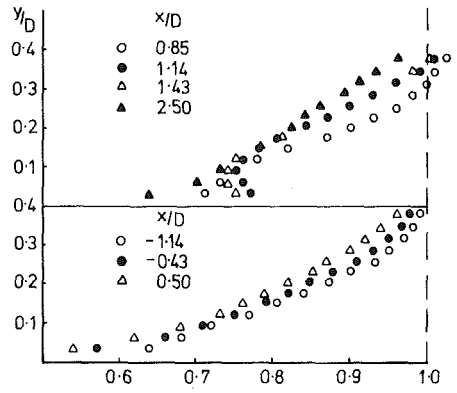

Fig. 6 Profiles of steamwise velocity off center line; $z/D = 0.64$, $M = 0.24$

Let us examine now some features of the flow documented quantitatively. Contours of static pressure on the plate surface for two injection rates are shown in Fig. 4. The contours give the local pressure (above the undisturbed value at the reference location) normalized by a dynamic head based on the product of the primary and secondary stream velocities. The reason for this choice was that it brings the contours for the two blowing rates into close agreement—certainly much closer than if the jet velocity or the freestream velocity alone had been used. The shapes of the contours have a similar qualitative appearance to those presented by Vogler [12] for blowing rates in the range 1.0–3.3. Taking the smallest significant value of the pressure coefficient as 0.1 it may be concluded from the present results that

(i) the effects of injection extend approximately 1½ dia upstream;

(ii) the maximum value of the pressure coefficient is approximately 1.0 in each case;

(iii) negative values of pressure coefficient as low as −2 occur around the downstream edge of the hole;

(iv) the rate of pressure recovery downstream is substantially more gradual than the rise upstream;[3]

(v) lateral effects on the pressure field are more substantial on the downstream side of the hole, the contour for $C_p = -0.1$ extending approximately 2½ dia off the center line.

At $M = 0.5$ only a small proportion of the static pressures were sampled. These point values, however, were in line with the behavior noted above for lower rates of injection.[4]

The distribution of mean velocity in the turbulent boundary layer on the plate is shown in Figs. 5 and 6. Fig. 5 shows the different kinds of boundary layer measured at five positions along a line parallel with the main flow passing through the hole center. At $M = 0.1$, Fig. 5(*a*) there is a large wake-like region behind the hole that gradually fills in with distance downstream. At the higher injection rates shown in Figs. 5(*b*) and 5(*c*) the behavior is similar except that reverse flow is present at $x/D = 2.50$ (i.e., 1.50 dia behind the downstream side of the hole). This behavior bears out the earlier comment that the reverse flow region extends somewhat further downstream than is indicated by the two lobe-shaped patched in Fig. 3(*b*). Measurements for $M = 0.1$ and 0.24 have also been taken along a line again parallel with the main flow but 0.64 dia displaced from the hole center. Fig. 6 shows the near-wall profiles for $M = 0.24$ (complete profiles for $M = 0.1$ and $M = 0.24$ appear in [9]). The flow close to the wall is progressively

[3] The pinching in of the main stream fluid behind the hole noted in Fig. 3(*c*) may be interpreted as a gradual filling-in of the low pressure region behind the hole; or, (equivalently) as a necessary consequence of the diffusion of the intense patch of streamwise vorticity associated with the injection itself.

[4] In the limit, as M becomes very large the surface pressure field may be expected to become independent of V; the isobars normalized by ρU_∞^2 should then be independent of M.

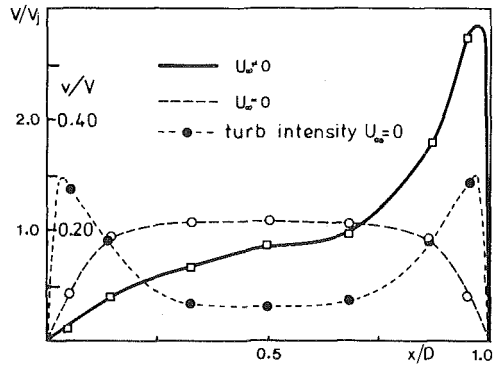

Fig. 7(*a*) Exit velocity of secondary jet, $M = 0.10$

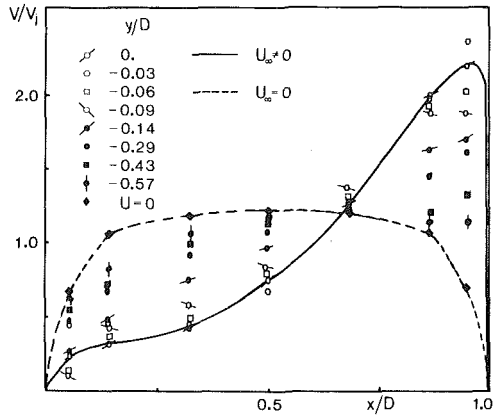

Fig. 7(*b*) Velocity of secondary jet at and near exit plane, $M = 0.24$

decelerated from far upstream to about the midhole position; from $0.5 < x/D < 1.4$ however the near-wall flow is accelerated. This behavior is consistent with the contours of surface static pressure in Fig. 4(*b*): along the line $z/D = 0.64$ the pressure rises from zero far upstream to a maximum at $x/D = 0.4$; there is then a sharp fall in pressure to $x/D = 1.4$ and, thereafter, a gentle rise back to atmospheric pressure. The same qualitative behavior is exhibited in the profiles of mean velocity for $M = 0.1$ though the effects are less pronounced than for $M = 0.24$.

The final flow-field data refer to the velocity of efflux from the injection hole. Our presumption at the start of the study had been that the mean velocity profile from the injection tube would resemble nearly fully developed axisymmetric turbulent pipe flow. The very severe pressure gradients around the hole however had suggested that this conjecture might be some way from the truth. Accordingly a hot-wire traverse was made of the flow leaving the injection hole. For $M = 0.10$ and 0.24 the profiles, shown in Fig. 7, displayed great nonuniformity. For the lower injection ratio the average velocity over the upstream half of the hole was barely one half that over the downstream half; for the higher injection rate the ratio had fallen to one quarter. It should perhaps be said that the values of velocity plotted in Fig. 7 refer to the total value; this comprises both horizontal and vertical components which we did not attempt to separate. However, for $M = 0.24$, profile traverses were made at various depths in the hole and these are also shown in Fig. 7. Evidently most of the adjustment in the velocity profile in the tube takes place in the last half diameter prior to discharge. The discovery of the great nonuniformity in the discharge velocity has implications for when one attempts to calculate the flow behavior. The authors' numerical predictions for laminar flow [1] have assumed a uniform injection velocity. While this suffices for displaying the feasibility of a numerical treatment one should of course use the actual inlet profiles (where these are known) in order to achieve accurate predictions of discrete-hole cooling—at any rate, in the vicinity of discharge.

Turbulence intensity profiles were also measured in the hole for $M = 0.1$ and 0.24, with relative turbulence intensities in excess of 50 percent recorded over the leading half. At such high turbulence levels the accuracy of the measurements is quite uncertain, however, and for this reason they are not reproduced here. A turbulence intensity profile with the primary air turned off is included in Fig. 7(*a*); the pipe flow Reynolds number is about 3500. The profile is typical of those found in developing turbulent pipe flows. It thus appears reasonable to draw direct comparison with measurements by other workers at higher Reynolds numbers since, provided transition has taken place, the flow structure will be only weakly Reynolds number dependent.

The distribution of wall film-cooling effectiveness, η is shown in Fig. 8 for all the different injection rates studied at four values of z/D. At the smallest injection rate ($M = 0.046$) the wall concentrations fall monotonically with increasing x/D and z/D. For $M = 0.1$ the general concentration levels are higher and just behind the discharge hole higher values of η are recorded off the center line than at $z/D = 0$. This behavior becomes more pronounced at the two higher blowing rates shown in Figs. 8(*c*) and 8(*d*). In these cases, even for $z/D = 0$ there is an increase in η with x for the first 0.5–1.0 dia behind the hole. The

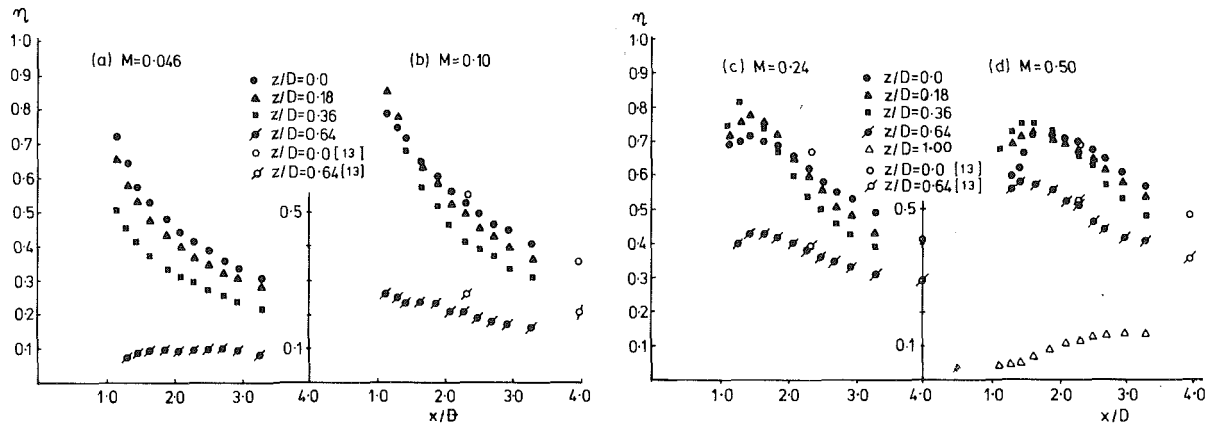

Fig. 8 Wall film cooling effectiveness

peak values of effectiveness measured in the immediate neighborhood of the hole occurred along the line 0.36 dia displaced from the hole center. This general behavior is consistent with the distortion of the jet to a kidney shape by the streamwise vortices induced by injection (see, for example, the sketch in [13]); the center of the jet is lifted away from the surface but the sides are drawn down in two lobes by the vortex action. Comparison may be made with measurements obtained in the Heat Transfer laboratory of the University of Minnesota—investigations that were mainly concerned with the far-field region. Agreement with the present results is close for $M = 0.5$ and also at other blowing rates for positions along $z/D = 0$. However, for $M = 0.1$ the present data along $z/D = 0.64$ lie 20–30 percent below those of Ramsey and Goldstein [13] and for $M = 0.24$ about 10 percent below (making allowance for the fact that the Minnesota test was for $M = 0.20$). The fact that differences become larger as M diminishes suggests that the effect may be partly due to different effective diffusion coefficients in the external streams in the two experiments (as M increases this factor becomes of diminishing importance near the discharge, becoming progressively swamped by the strong jet/mainstream mixing). The momentum thickness Reynolds numbers in the boundary layer upstream of injection were approximately twice as large in [13] as in the present study (which would produce twice as large effective diffusivities) but the effect should be very nearly balanced by the higher convection velocities in the former experiments. The ratio of boundary layer thickness to hole diameter—which references [14, 1] have shown to be an influential parameter—were also nearly the same. Moreover, although the hole Reynolds numbers in the present study are only one half of those of [13] we have seen in Fig. 7(*a*) that the flow in the supply pipe was nevertheless turbulent; we should thus not expect there to be a significant Reynolds number effect. One possibly important difference between the experiments was that Ramsey and Goldstein [13] studied heat transfer, not mass transfer. Thus, heat conduction in the wall could lead to too high levels of η off the center line contributing to some extent to the disagreement with the present results.

4 Conclusions

The near-field flow due to a jet injected at right angles through a wall to a main stream flow has been studied experimentally. The main findings were:

- Even at injection rates of only 5 percent of that of the free stream the jet induces a reverse flow region on the downstream side of the hole extending to about 0.3 dia beyond the downstream end of the hole.
- Surface static pressure measurements show the pressure fields to be distorted by the injection approximately 1½ dia upstream of the hole and 2½ dia downstream.
- The static pressure disturbance created by the jet is almost independent of injection rate when normalised by $\rho_j V_j U_\infty$, at least for the conditions of the present study.
- The acceleration and deceleration of the mainstream flow caused by the secondary jet appear to be consistent with the surface static pressure contours.
- The velocity of ejection is substantially nonuniform due to the rapid variation of static pressure around the hole. For $M = 0.24$ only about 25 percent of the injectant leaves from the leading half of the hole.
- For injection ratios 0.24 or above the peak effectiveness immediately downstream of discharge occurs off the center line and increases for a time with x. This pattern is consistent with the jet taking on a kidney shape as it is bent over by the external stream.
- Where the two studies overlap, very close agreement is obtained with the Ramsey and Goldstein data for $M = 0.5$. Certain differences emerge, however, in the off-center line values at lower injection rates, particularly for $M = 0.1$.

Acknowledgments

We gratefully acknowledge the support of this work by Ministry of Defence, Procurement Executive. Our thanks are due to Mr. M. Ribeiro for loaning the hot wire equipment and for assisting in these measurements.

References

1 Bergeles, G., Gosman, A. D., and Launder, B. E., "The Prediction of Three-Dimensional Discrete-Hole Cooling Processes: 1. Laminar Flow," ASME Winter Annual Meeting, ASME paper 75-WA/HT-109, 1975.

2 Goldstein, R. J., Eckert, E. R. G., and Ramsey, J. W., "Film Cooling Following Injection Through Holes," *Journal of Engineering for Power*, TRANS., ASME, Series A, Vol. 90 Oct. 1968, p. 385.

3 Eriksen, V. L., and Goldstein, R. J., "Heat Transfer and Film Cooling Following Injection Through Inclined Circular Tubes," JOURNAL OF HEAT TRANSFER, TRANS., ASME, Series E, Vol. 96, May 1974.

4 Launder, B. E., and York, J., "Discrete-Hole Cooling in the Presence of Free Stream Turbulence and Strong Favourable Pressure Gradient," *International Journal of Heat and Mass Transfer*, Vol. 17, No. 11, 1974.

5 le Brocq, P. V., Launder, B. E., and Priddin, C. H., "Discrete Hole Injection as a Means of Transpiration Cooling; an Experimental Study," *The Institution of Mechanical Engineers, Proceedings 1973*, Vol. 187, 17, 1973.

6 Ribeiro, M. M., and Whitelaw, J. H., "Statistical Characteristics of Turbulent Jet," HTS/74/19, 1974, Imperial College, Mechanical Engineering Department Report.

7 Ribeiro, M. M., and Whitelaw, J. H., "Verification of Turbulence Models with Hot Wire Anemometry," HTS/72/20, 1972, Imperial College, Mechanical Engineering Department Report.

8 Baker, R. J., and Launder, B. E., "The Turbulent Boundary Layer With Foreign Gas Injection I. Measurements in Zero Pressure Gradient," *International Journal Heat Mass Transfer*, Vol. 17, Feb. 1974, p. 275.

9 Bergeles, G., Gosman, A. D., and Launder, B. E., "The Near Field Character of a Jet Discharged Through a Wall at 90 deg to a Mainstream," ASME Winter Annual Meeting, ASME Paper No. 75-WA/HT-108, 1975.

10 Margason, R. J., and Fearn, R., "Jet-Wake Characteristics and Their Induced Aerodynamic Effects on V/STOL Aircraft in Transition Flight," NASA SP-128, 1969, p. 1.

11 McMahon, H. M., and Mosher, D. K., "Experimental Investigation of Pressures Induced on a Flat Plate by a Jet Issuing into a Subsonic Stream," NASA SP-218, 1969, p. 49.

12 Vogler, R. D., "Surface Pressure Distributions Induced on a Flat Plate by a Cold Air Jet Issuing Perpendicularly from the Plate and Normal to a Low-Speed Flow," NASA TN D-1629.

13 Ramsey, J. W., and Goldstein, R. J., "Interaction of a Heated Jet With a Deflecting Stream," NASA CR-72613, April 1970.

14 Kadotani, K., "Effect of Mainstream Variables on Heated and Unheated Jets Issuing from a Row of Inclined Round Holes," University of Minnesota, PhD thesis, Dec. 1975.

G. Bergeles
A. D. Gosman
B. E. Launder

Mechanical Engineering Department,
Imperial College,
London, England

The Prediction of Three-Dimensional Discrete-Hole Cooling Processes

Part 1: Laminar Flow

The paper describes the application of a three-dimensional finite-difference procedure to the problem of predicting the flow and thermal fields arising from the injection of fluid in discrete jets through a wall past which an external stream is flowing. The numerical scheme is of the "partially parabolic" type originated by D. B. Spalding. Predictions of mean velocity and temperature for laminar flow are provided for the cases of a single row of holes inclined at 90, 45, and 35 deg to the plate surface and for a surface with multiple rows of holes in a staggered array. These specifications are for a uniform density flow and a uniform velocity external stream. A final example is presented, simulating typical operating conditions for a gas turbine blade cooled with a single row of holes aligned at 30 deg to the blade surface. Strong streamwise accelerations and density gradients are present. The results show, as has been observed experimentally, that due to the strong acceleration the lateral rate of spread is diminished. Moreover a counter-rotating vortex pair is created downstream from the hole which shifts the minimum effectiveness away from the mid-plane between the holes.

1 Introduction

In recent years there has been growing interest in the behavior of jets of fluid discharged obliquely into a mainstream flow. The basic flow configuration is to be found in such practical problems as the dispersion of effluents from chimney stacks, the discharge of sewage (or hot water from power stations) into lakes or rivers, the injection of secondary air into combustion chambers and the cooling of leading stages of gas turbine rotors and stators. In the first two examples, the desired outcome is the dispersion of the jet fluid as rapidly, and completely as possible into the main stream. The last example—that of turbine blade cooling—is the one that has motivated the present study, however. Here the intention is to arrange for jets, which emerge through holes in the blade surface, to form a "blanket" of cool fluid between the hot outer stream and the blade. These considerations make it desirable that the jet velocity should be but a small fraction of the mainstream velocity and that, where technically possible, the jet axis should be pointed downstream at an acute angle with the surface. In a large proportion of well-designed discrete-hole cooling systems the jet will, therefore, be strongly deflected immediately on discharge and either remain in contact with the surface or reattach so quickly that there will be negligible streamwise recirculation.

The flow field generated by discrete-hole injection is a three-dimensional one but, because of the special character of the flow noted previously, numerical prediction schemes can make some simplification of the complete, three-dimensional elliptic equations of motion. Perhaps the obvious approach is to invoke the boundary-layer assumptions, in which the streamwise diffusion terms are discarded and the streamwise pressure gradient in any plane normal to the main flow is taken as uniform and known. When this is done, the equations become parabolic in respect of the main flow direction, and velocities and pressures on any cross-stream plane become formally uninfluenced by those on parallel planes downstream. Thus, to obtain numerical solutions of this type of three-dimensional flow it is possible to use a forward-marching procedure, in which velocities are calculated and stored at each plane in two-dimensional arrays which are then successively overwritten as the computations proceed downstream. There now exist several finite-difference procedures of this

Contributed by the Heat Transfer Division and presented at the Winter Annual Meeting, Houston, Texas, November, 1975, of THE AMERICAN SOCIETY OF MECHANICAL ENGINEERS. Revised manuscript received by the Heat Transfer Division March 16, 1976. Paper No. 75-WA/HT-109.

kind, the most general of which is the scheme of Patankar and Spalding [1].[1]

Earlier work by the present authors [2] using the procedure of [1] has, however, shown that the flow in the vicinity of the discharge holes could not be correctly resolved by a conventional boundary-layer treatment. The problem lies mainly in the behavior of the pressure field, and to a lesser extent in the velocity field in the wake of the hole. Thus, for normal injection, even where the injection velocity is only 10 percent of the external-stream velocity, the jet nevertheless causes important modifications to the static pressure *upstream* of the hole, and provokes streamwise recirculation immediately downstream. The upstream pressure effects, introduce an element of ellipticity which precludes the use of a forward-marching procedure, and necessitates the storage of the complete (three-dimensional) pressure field.

Fortunately Pratap and Spalding [3] have recently devised an algorithm capable of solving problems of this kind—which they term "partially parabolic"—and have applied it to flows in strongly curved ducts [4]. The new procedure, though obviously requiring more computer time and storage than a conventional boundary-layer treatment, achieves significant savings both in computing time and in the amount of core storage required over that of a discretization of the complete three-dimensional equations of motion.

The present contribution reports our work in obtaining numerical predictions of various discrete-hole-cooling configurations employing the partially parabolic procedure. The present computations relate entirely to laminar flow. Besides being both computationally and physically simpler than turbulent flow, laminar flow predictions have at least some practical relevance for flow over turbine blades because the very strong accelerations which occur over the blade prevent or delay the boundary layer becoming turbulent. The configurations studied in the present work are a single row of holes, where the hole axis makes angles of 90, 45, 35, and 30 deg with the surface and a multiple-row arrangement for 90 deg injection. Most of the computations relate to a flow of uniform density with a uniform-velocity external stream. For illustration, however, one run is presented where a strongly favorable pressure gradient exists and density variation included representative of engine conditions.

2 Method of Analysis

2.1 Description of the Problem. The class of problems considered in the present investigation is depicted in Fig. 2.1. The geometry is that of a flat plate, drilled with holes of diameter D whose axes make an angle α of between 0 and 90 deg with the surface and are arranged in a single row or a staggered array, as shown in the diagram. The flow is laminar, and the pressure far from the surface is prescribed. Fluid is injected through the holes with uniform velocity V_j and temperature T_j. To be calculated are the distributions of velocity, pressure, and temperature within the fields of influence of injection. The wall is assumed adiabatic and frictional heating neglected: of particular interest therefore is the distribution of film-cooling effectiveness, η, downstream from the holes.

2.2 Mathematical Description. The Cartesian directions x, y, and z are identified (Fig. 2.1) with the streamwise, vertical, and spanwise directions, respectively, and the corresponding velocity components are designated u, v and w; the equations of motion and enthalpy within the framework of partially parabolic flows, take the form:

Direction—x-momentum

$$\frac{\partial}{\partial x}(\rho uu) + \frac{\partial}{\partial y}(\rho vu) + \frac{\partial}{\partial z}(\rho wu) = -\frac{\partial p}{\partial x} + \frac{\partial}{\partial y}\left(\mu\frac{\partial u}{\partial y}\right) + \frac{\partial}{\partial z}\left(\mu\frac{\partial u}{\partial z}\right) \quad (2.1)$$

Direction—y-momentum

$$\frac{\partial}{\partial x}(\rho uv) + \frac{\partial}{\partial y}(\rho vv) + \frac{\partial}{\partial z}(\rho wv) = -\frac{\partial p}{\partial y} + \frac{\partial \tau_{yy}}{\partial y} + \frac{\partial \tau_{yz}}{\partial z} \quad (2.2)$$

Direction—z-momentum

$$\frac{\partial}{\partial x}(\rho uw) + \frac{\partial}{\partial y}(\rho vw) + \frac{\partial}{\partial z}(\rho ww) = -\frac{\partial p}{\partial z} + \frac{\partial \tau_{zy}}{\partial y} + \frac{\partial \tau_{zz}}{\partial z} \quad (2.3)$$

Continuity

$$\frac{\partial}{\partial x}(\rho u) + \frac{\partial}{\partial y}(\rho v) + \frac{\partial}{\partial z}(\rho w) = 0 \quad (2.4)$$

Enthalpy

$$\frac{\partial}{\partial x}(\rho uc_pT) + \frac{\partial}{\partial y}(\rho vc_pT) + \frac{\partial}{\partial z}(\rho wc_pT) = -\frac{\partial}{\partial y}(J_y) - \frac{\partial}{\partial z}(J_z) \quad (2.5)$$

where in tensor notation

$$\tau_{ij} = \mu\left(\frac{\partial u_i}{\partial x_j} + \frac{\partial u_j}{\partial x_i}\right) \quad (2.6)$$

$$J_i \equiv -\lambda\,\partial T/\partial x_i \quad (2.7)$$

and ρ, μ, and λ are the density, viscosity, and thermal conductivity, respectively. Note the absence of streamwise diffusion terms and the requirement that (strictly) u must be everywhere positive.

Solutions of the foregoing equations would typically be sought over

[1] Numbers in brackets designate References at end of paper.

Nomenclature

C_p = pressure coefficient, $(p - p_0)/{}^1/_2\rho_j v_e u_\infty$
c_p = specific heat at constant pressure
D = hole diameter
J = diffusion flux of heat
M = injection ratio $(\rho_j V_j/\rho_\infty u_\infty)$
p = static pressure
p_0 = reference static pressure far upstream of injection
P_x = streamwise pitch
P_z = lateral pitch
T = temperature
$\bar{T}$ = normalised temperature, $(T - T_\infty)/(T_j - T_\infty)$
u = streamwise velocity
u_e = streamwise velocity at exit of the hole
u_∞ = free stream velocity
v = vertical velocity
v_e = vertical velocity at exit of the hole
V_j = resultant coolant velocity at exit of the hole
w = lateral velocity
x = streamwise direction
y = vertical direction
z = lateral direction
α = angle of injection
δ = boundary layer thickness
$\bar{\eta}$ = span-wise averaged $\eta = \frac{1}{P_z}\int_0^{P_z}\eta dz$
η = film-cooling effectiveness, $(T_w - T_\infty)/(T_j - T_\infty)$
λ = thermal diffusivity of coolant
μ = dynamic viscosity of the mixed stream
ν = kinematic viscosity of the mixed stream
ρ = density of the mixed stream
τ_{ij} = shear stress

Subscripts

w = wall value
j = conditions at hole exit
∞ = undisturbed free-stream value

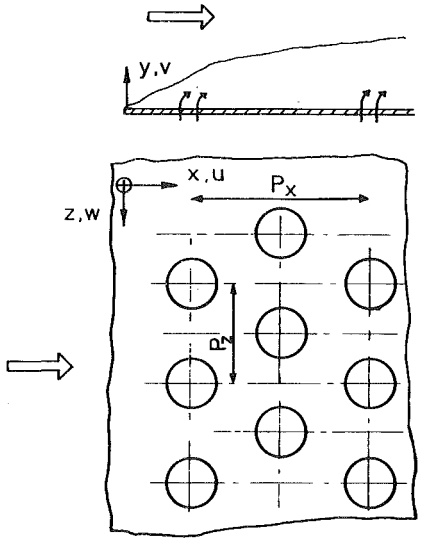

Fig. 2.1(*a*) The geometry

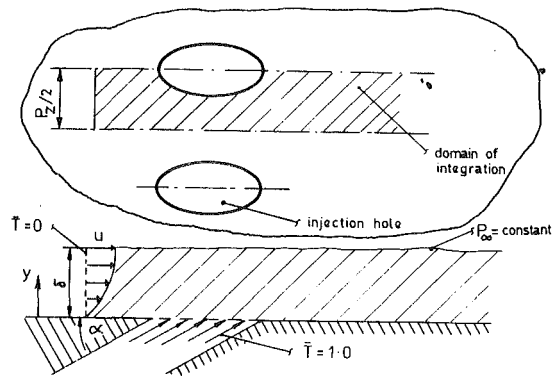

Fig. 2.1(*b*) Boundary conditions and domain of integration

the region shown cross-hatched in Fig. 2.1(*b*) which depicts a row of inclined holes. The lateral boundaries are located at planes of symmetry, and the upstream and outer-edge boundaries are located in regions of undisturbed flow. In the present examples, the upstream boundary is located 1.5 dia upstream of injection, the flow being prescribed as two-dimensional. The boundary-layer velocity profile is given by:

$$\frac{u}{u_\infty} = \frac{3}{2}\left(\frac{y}{\delta}\right) - \frac{1}{2}\left(\frac{y}{\delta}\right)^3 \tag{2.8}$$

where u_∞ and δ are the free-stream velocity and boundary-layer thickness, respectively. Equation (2.8) is known to fit closely the exact solution to the laminar boundary in zero pressure gradient. The velocity components u_e and v_e of the fluid exiting from the hole are calculated from:

$$\left.\begin{aligned} u_e &= V_j \cos\alpha \\ v_e &= V_j \sin\alpha \end{aligned}\right\} \tag{2.9}$$

where V_j is the injection velocity. The dimensionless temperature $\bar{T}$ is set equal to unity in the injected fluid and zero in the free stream.

2.3 Numerical Solution Procedure. The main elements of the partially parabolic finite-difference procedure (of which full details are given in [3]) may be summarized as follows:

1 The dependent variables u, v, w, p, and T are computed on grids superimposed on the domain of solution, and arranged such that, while pressure and temperature share the same locations, the velocity components lie midway between the pressures which drive them. The grid is nominally Cartesian, but may expand or contract in the vertical direction to conform with the boundary-layer profile.

2 Finite-difference equations (fde's) are derived for u, v, w, and T: these relate each variable at a point to its nearest neighbors in the same cross-stream plane and to the adjacent upstream (but *not* downstream) neighbor. In the case of the velocity equations, the neighboring pressures in the direction of the component in question appear as well.

3 Pressure is obtained from its own equation, derived by combining the fde's for momentum and continuity. Unlike the other members of the set, this equation relates to the nearest grid neighbors in *all* directions, including downstream.

4 Starting from initial guesses for the velocity, pressure, and temperature fields, the procedure operates by scanning the cross-stream planes one by one, beginning from the upstream end and solving at each plane for all variables, on the assumption that the values on neighboring planes are known. In the case of the velocities, which do not depend on values at downstream planes, the latter supposition is a reasonable one (likewise for temperature). Thus, provided that the pressures were correctly specified, one scan of the field would secure the solution to the problem (this of course is precisely the way conventional boundary-layer methods operate). In practice, the effects of injection will necessitate that adjustments be made to the pressures and hence the velocities: thus, the scanning procedure is repeated in an iterative fashion using the pressure field of the previous iteration until a satisfactory solution is achieved.

5 The procedure therefore preserves as far as possible the limited-storage requirements of boundary-layer methods, requiring only that the static pressure, whose influence is transmitted in all directions, be stored three-dimensionally.

A summary of the boundary conditions applied is provided in Table 2.1. The results which are presented in the next section were obtained, after grid-refinement tests, with grids which typically comprised 70, 18, and 17 planes in the x, y, and z directions, respectively, spaced so as to be concentrated in regions of steep gradients. Approximately 70 iterations are needed to achieve a converged pressure field. Computing times per run and storage requirements on a CDC 6600 machine were about 14 min and 50 K, respectively.

3 Results

3.1 Single Row of Holes, 90 deg Injection. For this series of calculations normal injection was simulated through a single row of holes with pitch P_Z equal to $2D$. The upstream boundary was located 1.5 D from the leading edge of the hole, and the initial conditions were specified as $\delta = 5.5\ D$ and $R_\delta\ (\equiv u_\infty\ \delta/\nu) = 690$. Results will be presented for values of the injection ratio $M\ (\equiv \rho_j V_j/\rho_\infty u_\infty)$ of 0.1 and 0.2. For these and subsequent examples the Prandtl number was 0.70.

An immediate impression of the importance of elliptic pressure effects may be gained from Fig. 3.1(*a*), which shows for $M = 0.2$ surface contours of the pressure coefficient C_p the reference pressure is that in the undisturbed flow far away from the holes. (It may be remarked that the choice of $\rho_j v_e u_\infty$ as the normalizing quantity was made on the basis of experiments in turbulent flow [5] where this practice was found nearly to collapse the data for the two injection ratios onto identical curves.) Evidently there is an appreciable upstream effect even for the smaller of the injection ratios: the 10 percent contour extends to about one diameter. Also evident are appreciable lateral and downstream variations, with the latter persisting for longer distances than upstream, and revealing the presence of adverse pressure gradients in the region immediately downstream of the hole. Over the hole itself there exist strong favorable pressure gradients.

The predicted flow pattern for $M = 0.2$ is conveyed by Figs. 3.1 (*b*), (*c*), and (*d*). The first of these shows the velocity vectors in the symmetry plane which bisects the hole: the action of the pressure field in deflecting upward the oncoming stream can be clearly seen (it is worth recalling that a conventional boundary-layer procedure is incapable of simulating this effect), as can the further deflection over the hole provoked by the injected fluid. Immediately downstream is a small

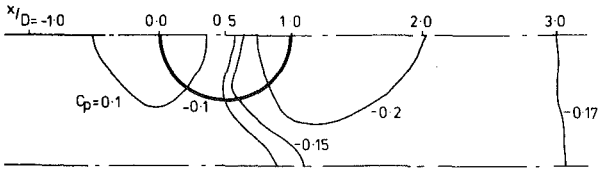

Fig. 3.1(*a*) Isobars for $M = 0.2$

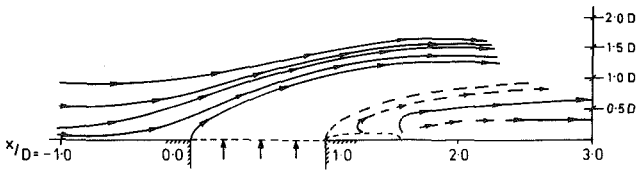

Fig. 3.1(*b*) Velocity directions in the symmetry plane

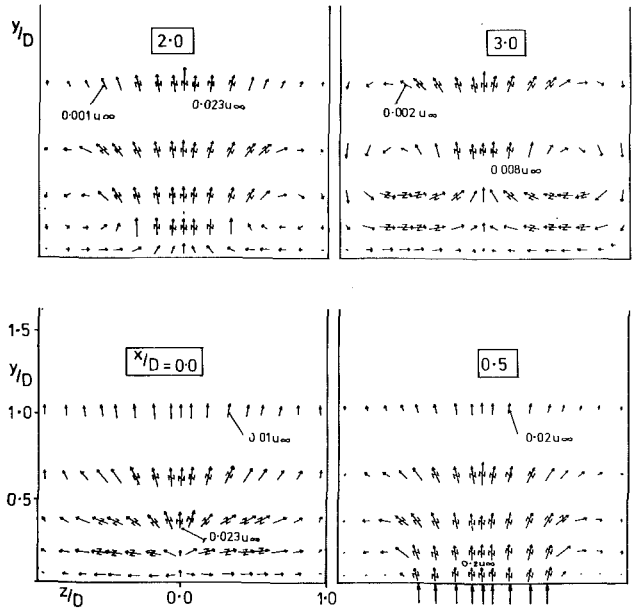

Fig. 3.1(*c*) Velocity vector field in cross-stream plane

zone of backward flow which, although strictly not allowed by the procedure, can be patched over by replacing the calculated small negative values by zero; this practice does not appreciably affect the results elsewhere. Fig. 3.1(*c*) shows projections of the velocity vectors into cross-stream planes at various locations, starting from the upstream edge of the hole ($x/D = 0.0$) and proceeding downstream. The symbol z marked across a vector line denotes that it has been drawn at less than full scale to avoid cross-over of the lines. The first two plots merely serve to confirm the statements made earlier about the initial upward deflection of the flow: the remaining ones, however, reveal a new, but expected, feature; namely, the formation of the familiar streamwise vortex pair in the wake of the hole, which is a manifestation of the vorticity added to the flow by the fluid injection. The remaining set of velocity plots in Fig. 3.1(*d*) show contours of the streamwise component at various cross-stream planes, in which the dashed lines represent the contours which would prevail in the absence of injection. The contours confirm the expected retardation of the flow at the leading edge, the acceleration over the hole itself, and the deceleration in the downstream wake. Also shown is the tendency for the lateral variations to diminish with distance from the holes. The general hydrodynamic behavior for $M = 0.1$, although not shown, is qualitatively similar, but the disturbances produced by the jet are, of course, less pronounced.

Fig. 3.1(*e*) displays contours of $\bar{T}$ in cross-stream planes for $M = 0.2$ (which is the highest blowing rate for which solutions could be obtained with normal injection). These show how the thermal field spreads initially in an almost radially symmetrical fashion and is subsequently distorted by the velocity field and the interaction with neighboring holes. Of particular interest are the center panels, which illustrate the action of the streamwise vortices in bringing fluid of low normalized temperature in from the sides, thereby causing "pinching" of the contours near the plate, and the displacement of the maximum value of $\bar{T}$ from the surface.

Fig. 3.2 shows the wall film-cooling effectiveness for $M = 0.1$ and 0.2. Here we note the rather rapid lateral spread around the hole which seems to be a consequence of the strong lateral motions induced by the jet, and the comparatively low velocity of the fluid layers fed by these motions. The effect of increasing M is to raise the effectiveness. This behavior is to be expected at the low values of M considered in the present study where the jet fluid reattaches to the surface a short distance behind the hole.

3.2 Single Row of Holes, Various Injection Angles, $M = 0.2$. Fig. 3.3 shows the effect on the temperature field of varying the angle of injection, with all other conditions held constant and $M = 0.2$. The upper sequence of panels contains results for $\alpha = 35$ deg, and the lower set for $\alpha = 45$ deg. Comparisons of these predictions, and those for $\alpha = 90$ deg in Fig. 3.1(*e*) show that as the angle is reduced, the rate of vertical spread is diminished.

An impression of the effect of injection angle on surface effectiveness may be seen in Fig. 3.4, which displays the variation along lines

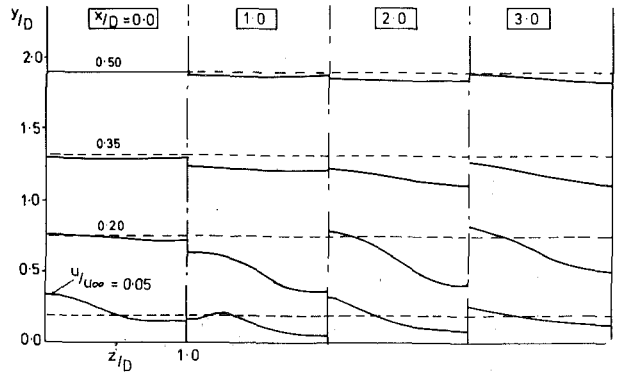

Fig. 3.1(*d*) Contours of *u* velocity in cross-stream planes

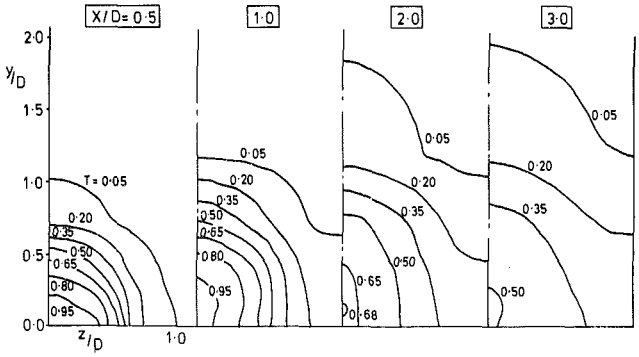

Fig. 3.1(*e*) Normalized isotherms in cross-stream planes

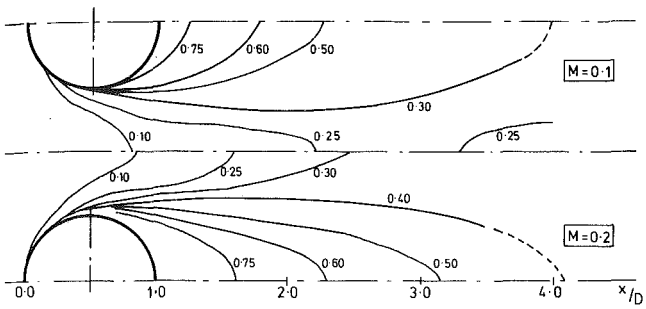

Fig. 3.2 Wall-film cooling effectiveness for $M = 0.1$ and $M = 0.2$

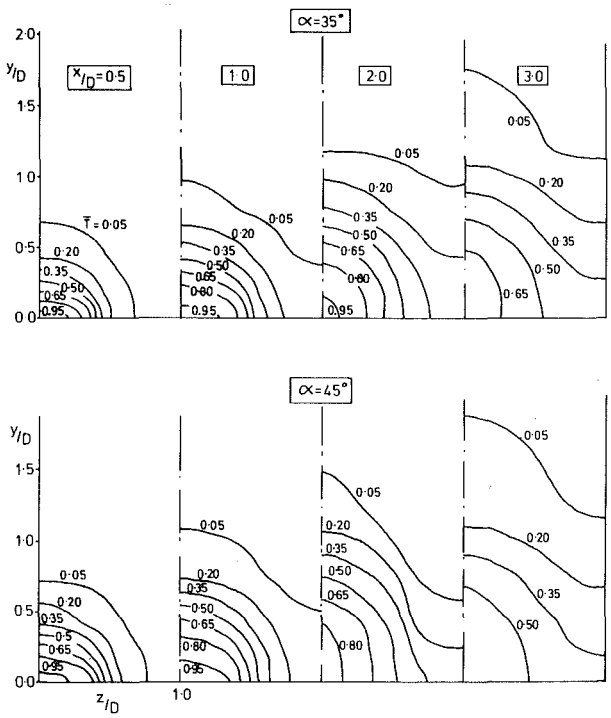

Fig. 3.3 Normalized isotherms in cross-stream planes $\alpha = 35$ deg, $\alpha = 45$ deg

passing through the hole axis and midway between adjacent holes, for $\alpha = 35$, 45, and 90 deg. It is seen that reducing the angle of injection from 90 to 45 deg reduces the streamwise rate of decay of η (qualitatively in agreement with experimental data of turbulent flow [6]) but that reducing the angle further to 35 deg has relatively little effect. (The broken lines show the rate of decay along the $z = 0$ line; there has been a shift of origin of the x axis to make the downstream end of the hole occur at the same position for all three angles of injection.) It is seen that immediately behind the hole, the effectiveness along $z/D = 1.0$ decreases as injection angle is reduced. This is attributable to changes in the flow field: the smaller the injection angle the less the disturbance created by the jet; in particular the static pressure variation around the hole is reduced. As a result, w velocities are weaker and the displacement thickness of the wake is considerably less. Further downstream, however, effectiveness levels become significantly higher along $z/D = 1$ the smaller the injection angle implying a faster lateral spreading rate. This behavior is qualitatively different from that observed in turbulent flow experiments. There is not necessarily any conflict in these results, however. In turbulent flow the effective transport coefficients are large wherever the mean rates of strain are large (as indicated, for example, by the mixing-length hypothesis). It is thus quite possible that in a turbulent flow the reduction in strain rates that occurs as the angle of injection is progressively decreased reduces the transport coefficients sufficiently for the lateral rate of spread to fall. It is noted that the present results all show a tendency to approach two-dimensional behavior at about the same rate.

3.3 Multirow Injection: 90 deg Holes. When only a single row of cooling holes is used most blade-cooling applications will require higher injection rates than are considered in the present paper. Raising the level of M, however, tends to make the jet lift away from the surface promoting increased mixing (and, hence, hastening the rate of dilution of the coolant) and adversely affecting the aerodynamic characteristics of the blade. For this reason attention is being given to cooling systems employing more than one row of holes: by this means sufficient coolant can be introduced to the blade surface while keeping injection velocities at acceptably low levels. Figs. 3.5 and 3.6 provide illustrations of the calculated behavior of a multirow injection system for $M = 0.1$. As before, the boundary-layer thickness is taken as 5.5 D but now the lateral pitch between holes is 4.0 with successive rows being staggered and repeated rows occurring every three diameters downstream. The results shown in these figures have been obtained by making a number of computations in which the finite-difference grid covered only a portion of the total flow domain, the grid being successively moved downstream until the region shown in Fig. 3.5 had been covered.

Surface effectiveness contours are shown in plain view in Fig. 3.5(a) while the variation of effectiveness along the two lateral edges of the flow domain and along the line midway between the edges is shown in Fig. 3.5(b). In addition, an impression of the temperature field in the boundary layer is provided by the normalized isotherms at various y-z planes shown in Fig. 3.6. It may be seen that immediately behind the leading hole the normalized temperature falls off more rapidly than for the single row test displayed in Fig. 3.2. This seems to be mainly due to the greater lateral spacing between holes in the same row. Overall, however, the multihole arrangement is superior to the single-row configuration. For example, after the second row, the amount of injected fluid is the same as for the single row test with $M = 0.1$; the minimum effectiveness level at $x/D = 2.9$ (i.e., just upstream of the third row) is 0.29 in Fig. 3.5 compared with 0.26 in Fig. 3.2. Correspondingly, after the fourth row of holes the amount of coolant is the same as for the single row test with $M = 0.2$. Now, in the latter case, computations extended only three diameters behind the injection holes ($x/D = 4$). From Fig. 3.4 it is seen that at that station the minimum effectiveness level of 31 percent is considerably less than the 44 percent at $(x/D) = 5.9$ for the multihole injection. There will also be aerodynamic advantages to the multihole geometry that we do not attempt to quantify in the present paper. An interesting subject for further investigation would be the discovery of whether improved

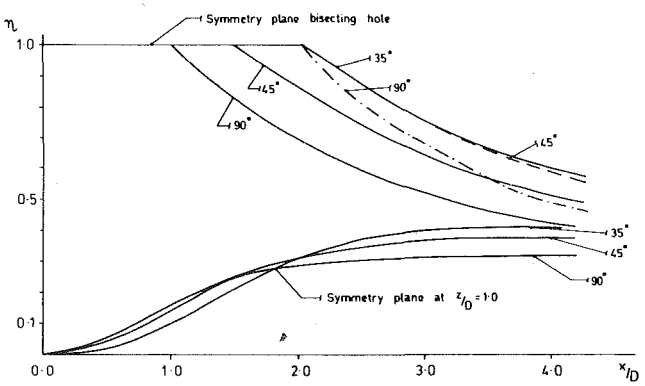

Fig. 3.4 Effect of injection angle on surface effectiveness along symmetry lines—single row, $P_z = 2.0$, $M = 0.2$

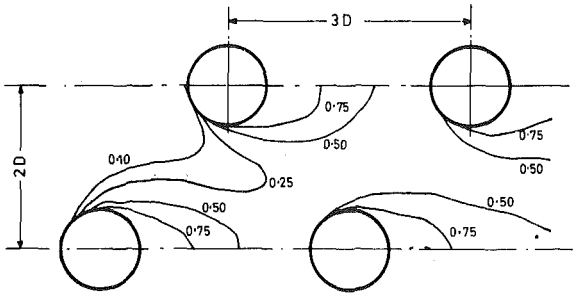

Fig. 3.5(*a*) Film cooling effectiveness for multirow geometry

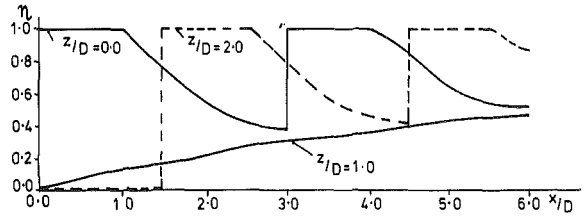

Fig. 3.5(*b*) Film-cooling effectiveness along and midway between symmetry planes

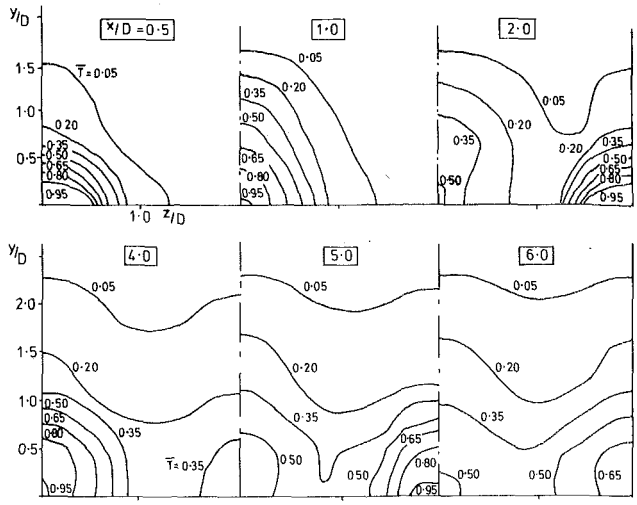

Fig. 3.6 Contours of normalized isotherms in cross-stream planes for multirow geometry

cooling effectiveness resulted from directing the jets at an angle to the x-y plane.

3.4 Single-Row Injection With Density Gradient and Free-Stream Acceleration. The final example relates to conditions approximating more closely than the earlier examples the kind of situations met under actual operating conditions. It simulates a test from a series performed on a single blade by Rolls Royce (1971) Ltd. The coolant is injected through a single row of 30 deg holes, the mass velocity ratio M being 0.31 and the ratio of lateral pitch to hole diameter being 2.5. The ratio of injectant to mainstream densities is 1.4:1 and the streamwise mean velocity gradient, du_∞/dx is taken as constant, the initial value of $(\nu/u_\infty{}^2)du_\infty/dx$ being 0.8×10^{-6}. The density was obtained from the ideal gas equation of state. The viscosity was treated as uniform, though this simplification would have had only a very secondary effect on the results. The computations with the partially parabolic procedure extended from two diameters upstream of the hole to 5.0 dia downstream. At the point of injection the boundary layer on the blade was reported to be laminar, with a boundary layer thickness a little greater than the diameter of the injection holes. Our own estimate of boundary thickness (obtained from a Polhausen-type integral solution from stagnation to the injection point) gave a value of only 0.2 D, however. We therefore decided to make computations of the flow development for *both* the indicated values of boundary layer thickness at the upstream end of the computational domain; the Pohlhausen fourth-order polynomial was used to describe the velocity distribution in the layer. The variation of free-stream velocity implied by the acceleration parameter was applied at the free-stream edge of the domain. In practical computations, the finite-difference calculations would need to extend tens of hole diameters downstream rather than just a few. This would be unnecessarily expensive, however, since the cross-stream pressure variations become very small a few hole diameters downstream. Instead we have employed the orthodox three-dimensional parabolic treatment of Patankar and Spalding [1] beginning the computation five diameters downstream from the leading edge of the injection holes using, as initial profiles, the values given at that section by the partially parabolic method. The computation proceeds downstream in a noniterative marching fashion with the streamwise pressure gradient being treated as uniform at any section in the x-momentum equation.

The development of the streamwise velocity profile along a plane through the "hole center" is shown in Fig. 3.7 for the case where the initial $\delta/D = 0.2$. For reference, the mean velocity profile at the upstream station ($x/D = -0.2$) is shown by a broken line. The curves are normalized by the local free-stream velocity. There is only a small displacement of the boundary layer upstream of the hole but a substantial displacement of the profile over the hole itself.[2] Note that the profile at $x/D = 1.0$ displays a slip velocity at $y/D = 0$ due to the streamwise component of velocity of the injected stream. Behind the hole a large wake in the boundary layer is evident. The jet itself lifts away from the surface but has reattached by $x/D = 4.50$ as evidenced by the small peak in velocity close to the wall. As the shear flow develops downstream the velocity maximum disappears leaving a patch

[2] The hole extends from $x/D = 0$ to $x/D = 2.0$ since the holes are aligned at 30 deg with the surface.

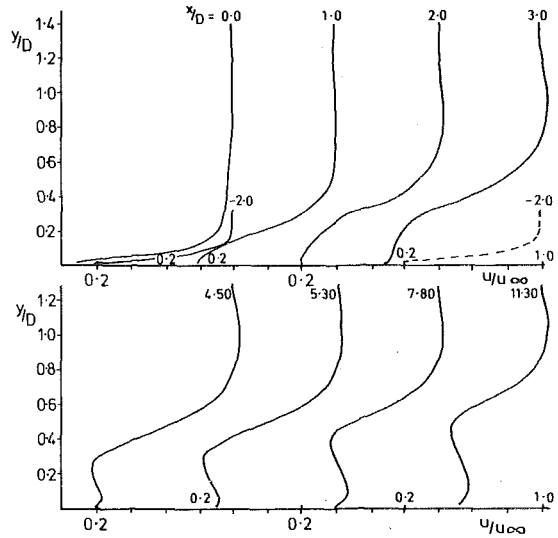

Fig. 3.7 Streamwise velocity profiles in the symmetry plane through a hole. Single row, α = 30 deg, nonuniform density, free-stream acceleration

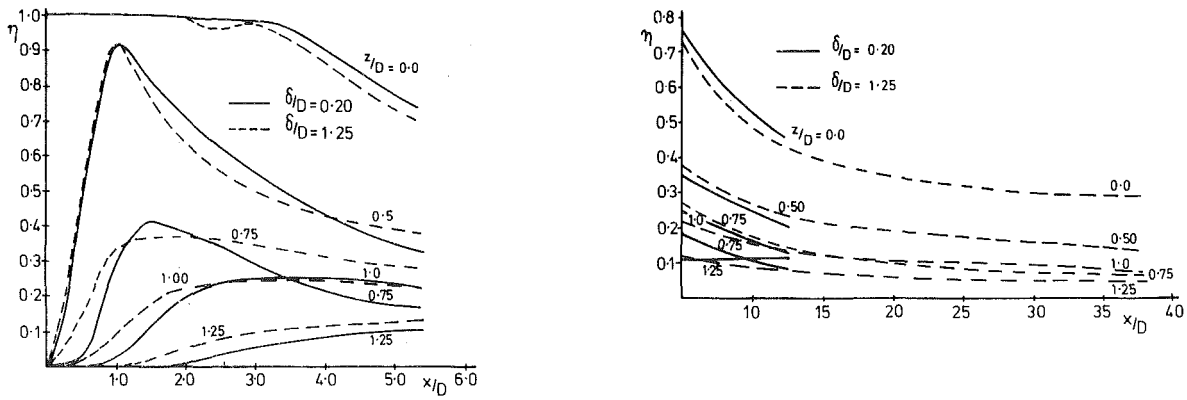

Fig. 3.8 Wall film-cooling effectiveness: (*a*) the near-field partially parabolic region; (*b*) the far-field parabolic region

of slow moving, virtually uniform-velocity fluid close to the wall. With further development downstream this patch accelerates more rapidly than the free stream fluid (as required by Bernoulli's equation) and a "new" boundary layer may be seen developing beneath it.

The variation of film-cooling effectiveness along a number of constant z/d lines is shown in Figs. 3.8(a) and (b), which relate to the partially parabolic and parabolic regions of computation, respectively. In the former we note that the computations with $\delta/D = 1.25$ indicate a faster lateral spread of the jet and that for $\delta/D = 0.2$ the effectiveness along $z/D = 0.75$ is *less* than along $z/D = 1.0$ for x/D greater than about 3.5. This pattern of development continues into the parabolic region; from Fig. 3.8(b) for $x/D > 9$ the minimum effectiveness at any station occurs along $z/D = 0.75$. Computations were halted at $x/D = 14$ in the case of the thin initial boundary layer. For $\delta/D = 1.25$, however, computations were continued to $x/D = 40.00$. It may be seen that the "cross-over" effect noted for $\delta/D = 0.2$ is much less pronounced in this case: the minimum concentration always lies on $z/D = 1.25$ and only for $x/D > 17$ is the value of η at $z/D = 0.75$ less than that at $z/D = 1.0$.

The cause of this contrasting behavior may be inferred from Fig. 3.9, which shows for the case of $\delta/D = 0.2$ computer drawn velocity vectors in the y-z plane at $x/D = 4.5$. Injecting fluid through the holes creates two eddies rotating in the y-z plane (i.e., with axes in the x-direction). One of these, induced directly by the injection, rotates clockwise (viewed from the upstream side) and is located in the left-hand half of the section shown in Fig. 3.9. The second vortex may be thought of as being an indirect consequence of the jet; it is the so-called horseshoe vortex in which the vortex lines in the boundary layer upstream of the hole bend around the jet giving an extra component to the streamwise vorticity. This vortex rotates counterclockwise and is located in the right-hand half of Fig. 3.9. It is evident from this figure that the right-hand member of this counter-rotating vortex pair is very much weaker than the left-hand one. Nevertheless, together their action is to bring high temperature fluid down toward the surface, displacing the cooler fluid to each side. This pattern of development may clearly be seen in Fig. 3.10, which shows normalized temperature contours in the y-z plane at different stations. A further item to be noted from this figure is that the peak normalized temperature at any section occurs at some distance away from the wall. This is due at first to the fact that the jet lifts away from the surface immediately behind the hole; further downstream the phenomenon may be attributed to the counter-rotating vortices discussed previously.

In the case where $\delta/D = 1.25$ the secondary horseshoe vortex is much weaker because most of vorticity present in the upstream boundary layer passes over the top of the injection hole without the vortex lines being significantly bent. This explains why, in this case, there is less tendency for the effectiveness lines to cross over; it also

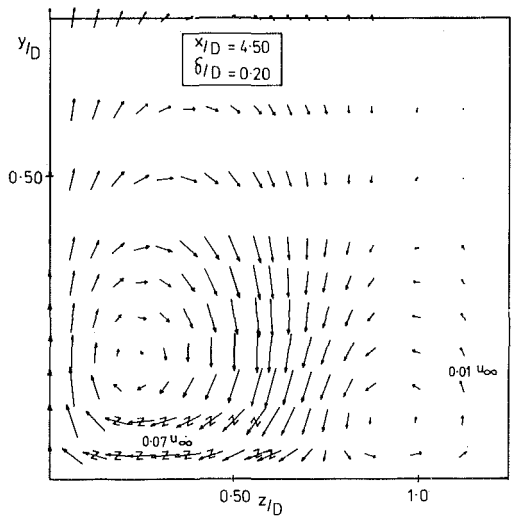

Fig. 3.9 Velocity direction lines in *y*-*z* plane

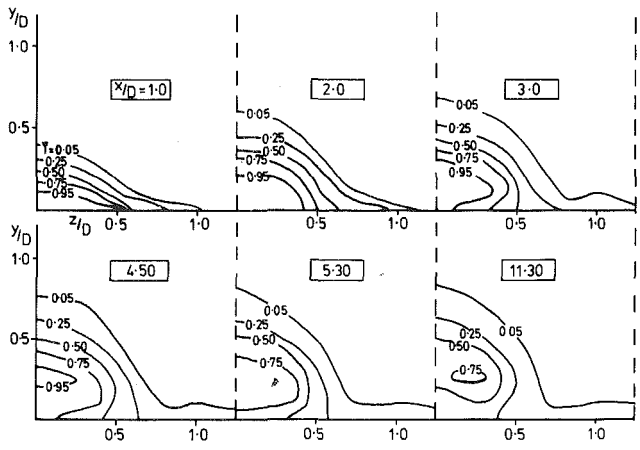

Fig. 3.10 Normalized isotherms in cross-stream planes

Table 2.1 Summary of boundary conditions

Boundary	u	v	w	p	T
bottom (plate) face	0	0	0	—	$\frac{\partial T}{\partial y} = 0$
at hole exit	u_e	v_e	0	—	T_f
top (free steam face	$u = u_\infty(x)$		0	—	T_∞
upstream face	$u = u(y/\delta)$	$v = v(y/\delta)$	0		T_∞
downstream face	—	—	—	extrapolation	
edges	$\frac{\partial u}{\partial z} = 0$	$\frac{\partial v}{\partial z} = 0$	0	$\frac{\partial p}{\partial z} = 0$	$\frac{\partial T}{\partial z} = 0$

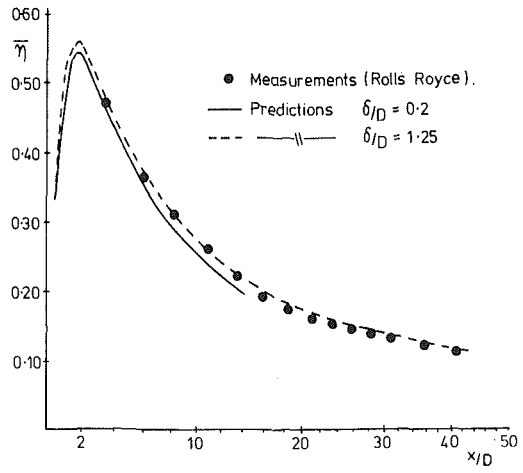

Fig. 3.11 Span-wise averaged cooling effectiveness: comparison with experiment

explains the faster lateral spread indicated in Fig. 3.8(*a*) since the horseshoe vortex acts to inhibit the lateral spread of the jet.

The measurements obtained in the Rolls Royce tests gave span-wise-averaged values of effectiveness. In Fig. 3.11 comparison is made between the experimental data and our two predicted lines. The maximum difference between the two sets of predictions is only 8 percent, which is probably well within the experimental uncertainty. Agreement between the experimental and calculated values is thus entirely satisfactory. Two further points need emphasizing. First, the relative insensitivity of these predictions to boundary layer thickness occurs only because the injection rates are low and the flow is laminar. Second, Fig. 3.8(*a*) brings out how steep are the local variations in adiabatic wall temperature around the hole. Although conduction within the blade would in practice reduce these gradients, it appears that there would still be substantial thermal stresses induced. To predict these effects satisfactorily will always require a very detailed finite-difference treatment such as reported here in the vicinity of the holes even if simpler schemes can be devised to serve adequately further downstream.

Acknowledgments

We gratefully acknowledge the support of this work by the Ministry of Defence Procurement Executive and the Ministry's permission to publish the results. The computer program used in the calculations has been developed from the three-dimensional parabolic code STABL loaned to us by Combustion, Heat and Mass Transfer Ltd. We also wish to express our thanks to Rolls Royce (1971) Ltd. for allowing us to make comparisons with their as yet unpublished measurements of flow over a blade cooled by discrete hole injection.

Several helpful discussions and exchanges with Mr. V. S. Pratap and Professor D. B. Spalding are acknowledged with thanks.

References

1 Patankar, S. V., and Spalding, D. B., "A Calculation Procedure for Heat, Mass and Momentum Transfer in Three-Dimensional Parabolic Flows," *International Journal of Heat and Mass Transfer*, Vol. 15, 1972, pp. 1787–1806.

2 Bergeles, G., Gosman, A. D., and Launder, B. E., "The Prediction of Discrete Hole Cooling: A Progress Report on Experience With Parabolic and Partially-Parabolic Versions of STABL," Imperial College, Mechanical Engineering Department Report, Aug. 1974.

3 Pratap, V. S., and Spalding, D. B., "A Calculation Procedure for Partially-Parabolic Flow Situations," HTS/74/35, Dec. 1974, Imperial College, Mechanical Engineering Department Report.

4 Pratap, V. S., and Spalding, D. B., "Numerical Computations of the Flow in Curved Ducts," HTS/75/3, Imperial College, Mechanical Engineering Department Report, Feb. 1975.

5 Bergeles, G., Gosman, A. D., and Launder, B. E., "The Near-Field Character of a Jet Discharged Through a Wall at 90 deg to a Main Stream," ASME Paper No. 75-WA/HT-108.

6 Ramsey, J. W., and Goldstein, R. J., "Interaction of a Heated Jet With a Deflecting Stream," NASA CR-72613, Apr. 1970.

E. M. Sparrow
Leonardo Goldstein, Jr.

Department of Mechanical Engineering,
University of Minnesota,
Minneapolis, Minn.

Effect of Rotation and Coolant Throughflow on the Heat Transfer and Temperature Field in an Enclosure

Measurements were performed to determine the local heat transfer coefficients along the heated shroud of a shrouded parallel disk system. The temperature field within the enclosure formed by the shroud and the disks was also measured. One of the disks was rotating, whereas the other disk and the shroud were stationary. Coolant air was introduced into the enclosure through an aperture at the center of the stationary disk and exited through a slot at the rim of the rotating disk. The coolant entrance-exit arrangement differed from that of previous studies, with the additional difference that the incoming coolant stream was free of rotation. The coolant flow rate, the disk rotational speed, and the aspect ratio of the enclosure were varied during the experiments. The heat transfer coefficients were found to be increasingly insensitive to the absence or presence of rotation as the coolant flow rate increased. There was a general increase of the transfer coefficients with increasing coolant flow rate, especially for low rotational speeds. The temperature field in the enclosure differed markedly depending on the relative importance of rotation and of coolant throughflow. When the latter dominates, the temperature in the core is relatively uniform, but in the presence of strong rotation there are significant nonuniformities. A comparison was made between the present Nusselt number results and those of prior experiments characterized by different coolant entrance—exit arrangements. The positioning of the coolant exit slot relative to the direction of the boundary layer flow on the shroud emerged as an important factor in the comparison.

Introduction

This paper describes an experimental study of the heat transfer characteristics and fluid temperature distributions for a rotating, recirculating, forced convection flow in an enclosure. Fluid passing through the enclosure plays the role of a coolant. These experiments are intended to provide basic information about a complex convective heat transfer situation. They are also a terminal phase of a long-term research effort undertaken to model the heat transfer processes in cavities and enclosures situated adjacent to the rotating shaft in devices such as turbines and compressors. In such enclosures, one or more of the walls may be rotating. For high temperature turbines, the enclosure walls have to be cooled, and bleed air is used for this purpose.

Contributed by the Heat Transfer Division for publication in the JOURNAL OF HEAT TRANSFER. Manuscript received by the Heat Transfer Division October 3, 1975. Paper No. 76-HT-DDD.

The enclosure employed in the experiments is pictured schematically in Fig. 1. It consists of a stationary cylindrical shroud and a pair of disks, one of which is stationary and the other of which rotates. The shroud is electrically heated, whereas the disks are not heated. Air is introduced into the enclosure through a circular aperture at the center of the stationary disk and leaves through an annular gap situated at the rim of the rotating disk.

The apparatus is designed so that the separation distance S between the rotating and stationary disks can be varied. For the present experiments, dimensionless separation distances S/R of 4/9, 8/9, and 2 were employed. Also varied throughout the course of the experiments were the pipe inlet Reynolds number Re_i (from nominal values of 15,000 to 50,000) and the disk rotational speed ω (0 to 3000 rpm). The rotational Reynolds numbers Re_{rot}, based on the disk tip velocity and the disk radius, ranged from 0 to 10^6.

Local heat transfer coefficients were determined as a function of position along the shroud and are presented in terms of local Nusselt numbers. The temperature field in the air in the enclosure was measured by a thermocouple rake. This information is presented in terms

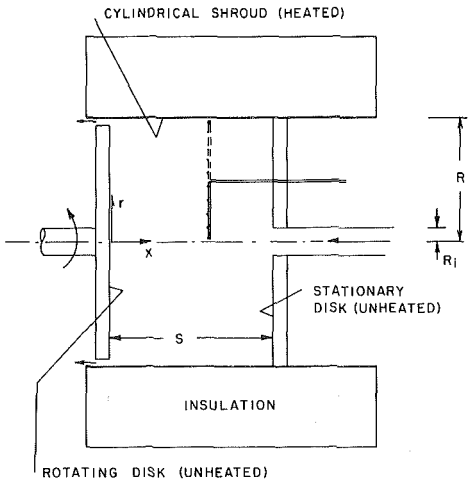

Fig. 1 Schematic diagram of the investigated enclosure

of isotherms, the shapes of which are suggestive of certain features of the flow field.

A major departure of the present experiments from those conducted earlier in this research program [1, 2][1] is that the air flow entering the enclosure is free of rotation. When the entering air flow is rotating, a radial pressure distribution is induced across the inlet aperture, with the minimum pressure at the center line. The relatively low pressure at the center line tends to draw air from the enclosure toward the aperture, and this backflow tendency affects the spreading of the coolant jet as it enters the cavity.

Another important difference brought about by the repositioning of the fluid inlet aperture is the direction of fluid flow along the shroud. For the configuration shown in Fig. 1, the shroud flow is expected to be in the positive x-direction. There are two factors which contribute to this. First, there is the coolant jet, which impinges on the rotating disk and then forms a wall jet that flows radially outward along the disk surface. Second, the pumping action of the rotating disk induces an additional radial outflow. A portion of the radial outflow exits from the enclosure at the rim of the rotating disk, and the other portion turns and becomes an axial flow along the shroud in the positive x-direction. Therefore, in the present configuration, the coolant jet and the disk rotation are mutually assisting with respect to the flow direction along the shroud.

Suppose, instead, that the coolant jet enters the enclosure via a central aperture in the rotating disk, with the exit maintained at the rim of the rotating disk and the stationary disk is solid (i.e., no aperture). This is the configuration employed in the experiments of [2]. In that case, as in the present, the pumping action of the rotating disk tends to set up an axial flow in the positive x-direction along the shroud. On the other hand, the coolant jet, after deflection from the stationary disk, would tend to induce a shroud flow in the negative x-direction. Thus, the coolant jet and the disk rotation cause oppositely directed shroud flows. The dominance of one flow over the other depends on the relative values of the coolant inlet Reynolds number and the disk rotational Reynolds number. The configuration of [1] also is such that oppositely directed shroud flows can be set up by the coolant jet and the disk rotation.

In view of the aforementioned differences between the present experiments and those performed earlier in this research program, it is relevant to compare the available Nusselt number results. Such comparisons are made here with a view toward relating differences among the results to differences in flow configuration.

Aside from the references already cited, there appears to be very little published literature dealing with heat transfer in enclosures with rotation, recirculation, and throughflow. Haynes and Owen [3] employed an enclosure with relatively closely spaced disks ($S/R \leq 0.18$) and with a different throughflow pattern from that of the present experiments.

Experimental Apparatus

The general features of the apparatus have already been introduced in the previous section of the paper with the aid of Fig. 1. Additional information relevant to the further understanding of the experiment and the results will now be presented.

The coolant air was supplied by a building-wide distribution system. It passed successively through a pressure regulator, control valve, heat exchanger, and metering orifice before being ducted to a length of straight pipeline whose downstream end mated with an aperture in the stationary disk. Both the aperture and the air delivery pipeline were 5.08 cm (2 in.) in diameter. The length of the delivery pipeline (~42 dia) was selected to provide fully developed turbulent flow at the inlet to the enclosure.

For the determination of the bulk temperature of the inlet air, the pipeline was fitted with six thermocouples and was also well insulated with fiberglass. Three of the thermocouples were distributed across a section situated about 2.5 cm (1 in.) upstream of the enclosure inlet. The other three were positioned at the pipe centerline at stations that were 30, 60, and 210 cm upstream of the inlet. The three thermocouples in the cross section nearest the inlet gave fairly uniform readings (to within 0.3°C) at the highest coolant flow rate. However, with progressive decreases in flow rate, greater nonuniformities were in evidence, suggesting an interaction with the recirculating flow in the enclosure. On the other hand, the readings of the thermocouples in the three upstream cross sections were always uniform to within 0.15°C. The average of the readings of these three thermocouples was employed as the inlet bulk temperature.

Both the rotating and stationary disks were made of 2.54 cm (1 in.) thick Benelex 401, a pressed wood product. The shroud was a 22.9 cm (9 in.) radius cylinder that had been formed from 0.064 cm (0.025 in.) stainless steel sheet. The overall length of the cylinder was 53.3 cm (21 in.). Thirty thermocouples were affixed to the back side (convex side) of the cylinder along an axial line, at positions that will be apparent from the presentation of results. Electrical resistance ribbon wrapped around the cylinder provided the desired heating. The ribbon was wired so that for each preselected separation distance between

[1] Numbers in brackets designate References at end of paper.

Nomenclature

h = local heat transfer coefficient, $q/(T_w - T_{bi})$
k = thermal conductivity
$\dot{m}$ = coolant flow rate
Nu = local Nusselt number, hR/k
q = local wall heat flux
R = radius of cylindrical shroud
R_i = radius of coolant delivery pipe
R_d = radius of rotating disk
Re_i = coolant inlet Reynolds number, equation (3)
$\mathrm{Re}_{\mathrm{rot}}$ = disk rotational Reynolds number, equation (3)
r = radial coordinate
S = spacing between disks
T = temperature
T_{bi} = coolant inlet temperature
T_w = local wall temperature
x = axial coordinate, Figs. 1 and 5
x' = axial coordinate, Fig. 5
V_d = tip speed of rotating disk
$\bar{V}$ = mean velocity of entering coolant
μ = viscosity
ν = kinematic viscosity
ω = disk rotational speed

the disks, a main heater section was flanked by a pair of guard heaters. The cylinder was embedded in a 15 cm (6 in.) thick layer of polyurethane insulation.

The radius of the stationary disk was the same as that of the shroud. The rotating disk had a radius of 21.6 cm (8.5 in.), which left a 1.27 cm (0.5 in.) annular gap between the rim of the disk and the shroud through which the coolant air left the enclosure.

The thermocouple probe employed to measure the temperature distribution within the enclosure, shown schematically in Fig. 1, was a rebuilt version of one that had been used in [2]. The probe was situated in the enclosure only during data runs specifically earmarked for fluid temperature measurements (i.e., not during the heat transfer data runs). The body of the probe was an L-shaped stainless steel tube (0.48 cm (3/16 in.) OD) through which the thermocouple wires were drawn. The junctions emerged through holes in the vertical leg of the L. The tips of the junctions protruded about 0.5 cm (0.2 in.) beyond the surface of the tube.

The probe was fitted with five thermocouples. By successively orienting the probe in the two positions shown in Fig. 1 (solid and dashed lines), temperatures at 10 radial stations could be measured in each cross section. These radial stations were nominally at 0.635, 5.08, . . . , 20.3, and 22.2 cm from the axis. Axial traversing of the probe enabled the temperature field to be mapped out. Typically, about twelve axial stations were employed.

All thermocouples were from calibrated rolls of wire. The thermocouple emf's were recorded by a digital voltmeter capable of resolving one microvolt. Heating power measurements were made with the aid of a laboratory grade wattmeter, and a cathetometer with a resolving power of 0.005 cm (0.002 in.) was employed for reading the manometer tubes associated with the flow metering orifice. The rpm of the rotating disk was detected by both a mechanical counter and a strobe.

Data Reduction

The procedure for evaluating local heat transfer coefficients will now be discussed. The ingredients needed for the evaluation are the local wall heat flux q, the local wall temperature T_w, and a fluid reference temperature. In the selection of the latter, cognizance has to be taken of the fact (to be demonstrated later) that the temperature field in the enclosure is not well represented as consisting of wall boundary layers and an isothermal core. Whereas regions of relatively high temperature gradient do exist near the walls, there are also substantial temperature variations throughout the entire enclosure. Therefore, the usual approach of employing a free stream temperature (for boundary layers) or a local bulk temperature (for duct flows) is not applicable here. In view of these considerations, the inlet bulk temperature T_{bi}, which is a directly measurable quantity in these experiments, appeared to be the most reasonable fluid reference temperature. It has the particular advantage that its value would also be known in practice.

The local coefficients were, therefore, evaluated from the expression

$$h = q/(T_w - T_{bi}) \tag{1}$$

The local wall heat flux q was determined from the electrical power input, modified by corrections for axial conduction in the stainless steel sheet which formed the shroud and for radial conduction in the polyurethane foam. The axial conduction correction involved the numerical evaluation of $\partial^2 T/\partial x^2$. This was accomplished by means of central differences subsequent to smoothing of the wall temperature data. Whereas, in the main, this correction was not large, there were a number of such corrections on the order of 10–15 percent. In view of the high sensitivity of the second derivative to an uncertainty of a few tenths of a degree in the temperature data, these corrections introduced some scatter into the surface distributions of the heat transfer coefficient. The radial conduction corrections were always small, ranging from ½ to 2 percent depending on the temperature difference between the shroud and ambient.

With the measured values of T_w and T_{bi}, and with q determined as described in the foregoing, the local transfer coefficients were calculated from equation (1). A dimensionless representation was then obtained via the local Nusselt number

$$\mathrm{Nu} = hR/k \tag{2}$$

in which R is the radius of the enclosure and k is the mean bulk conductivity of the air.

The distributions of the Nusselt number along the shroud depend on three parameters. These are the coolant inlet Reynolds number Re_i, the disk rotational speed ω, and the cavity aspect ratio S/R. Alternatively, the disk rotational Reynolds number $\mathrm{Re}_{\mathrm{rot}}$ may be employed instead of ω. Re_i and $\mathrm{Re}_{\mathrm{rot}}$ are defined as

$$\mathrm{Re}_i = 2\dot{m}/\mu\pi\mathrm{R}_i, \quad \mathrm{Re}_{\mathrm{rot}} = R_d(R_d\omega)/\nu \tag{3}$$

where R_i and R_d are, respectively, the radii of the coolant delivery pipe and the rim of the rotating disk, and $\dot{m}$ is the mass flow rate of the coolant air. The viscosity appearing in Re_i corresponds to the coolant inlet temperature, while the kinematic viscosity in $\mathrm{Re}_{\mathrm{rot}}$ corresponds to the mean bulk temperature.

Property variations were not a major factor in the experiments. The coolant air typically entered the enclosure at about 22°C and experienced a bulk temperature rise in the range from 8 to 19°C. The Prandtl number was about 0.7 for all cases.

The relationship between ω and $\mathrm{Re}_{\mathrm{rot}}$ for the conditions of the experiment are listed in Table 1. The table also contains information on the tip speed V_d of the rotating disk and on the mean velocity $\bar{V}$ of the entering coolant flow.

Results and Discussion

Local Nusselt Numbers. Distributions of the local Nusselt number along the shroud are presented in Figs. 2–4, respectively, for enclosure aspect ratios S/R of 2, 8/9, and 4/9. Each figure is subdivided into three graphs which, from left to right, correspond to Reynolds numbers of approximately 15,000, 24,000, and 47,000. Within each graph, data for the various disk rotational speeds from 0 to 3000 rpm are plotted using different symbols (see Table 1 for the corresponding values of $\mathrm{Re}_{\mathrm{rot}}$). In Figs. 2 and 3, the data points are sufficiently dense so that there is no need for faired curves to provide continuity. On the other hand, faired curves are included in Fig. 4 because of the lesser density of the data points.

Attention may first be turned to Fig. 2. It is seen that in all cases, the heat transfer coefficients decrease with increasing distance from the rotating disk. This behavior is in accord with the pattern of fluid flow discussed in the Introduction. As described there, the radial outflow on the disk becomes, after deflection, an axial flow along the shroud in the positive x-direction. As the fluid passes along the shroud, the thermal boundary layer thickens and, consequently, there is an increase in the thermal resistance of the flow.

From a comparison of the successive graphs, the interactive effects of the coolant flow and the disk rotational speed on the heat transfer coefficients may be observed. At the lowest coolant inlet Reynolds number ($\mathrm{Re}_i \sim 15{,}000$), the transfer coefficients are insensitive to the magnitude of the rotational speed up to $\omega = 500$ rpm, but are ordered according to increasing ω for $\omega = 1500$ and 3000 rpm. When Re_i is increased to 23,500, the insensitivity to rotational speed extends from 0 to 1500 rpm. For $\mathrm{Re}_i \sim 47{,}000$, the effect of rotational speed is small over the entire range of ω values investigated here. It is seen, therefore, that the extent to which rotation influences the results depends on the coolant Reynolds number and that the presence or absence of rotation becomes progressively less relevant with increasing Reynolds number.

Table 1 Velocity and Reynolds number relationships

ω(rpm)	$\mathrm{Re}_{\mathrm{rot}}$	$V_d(m/s)$	Re_i	$\bar{V}(m/s)$
0	0	0	15,000	4.4
500	156,000	11.3	24,000	7.1
1500	465,000	33.9	47,000	13.9
3000	920,000	67.8		

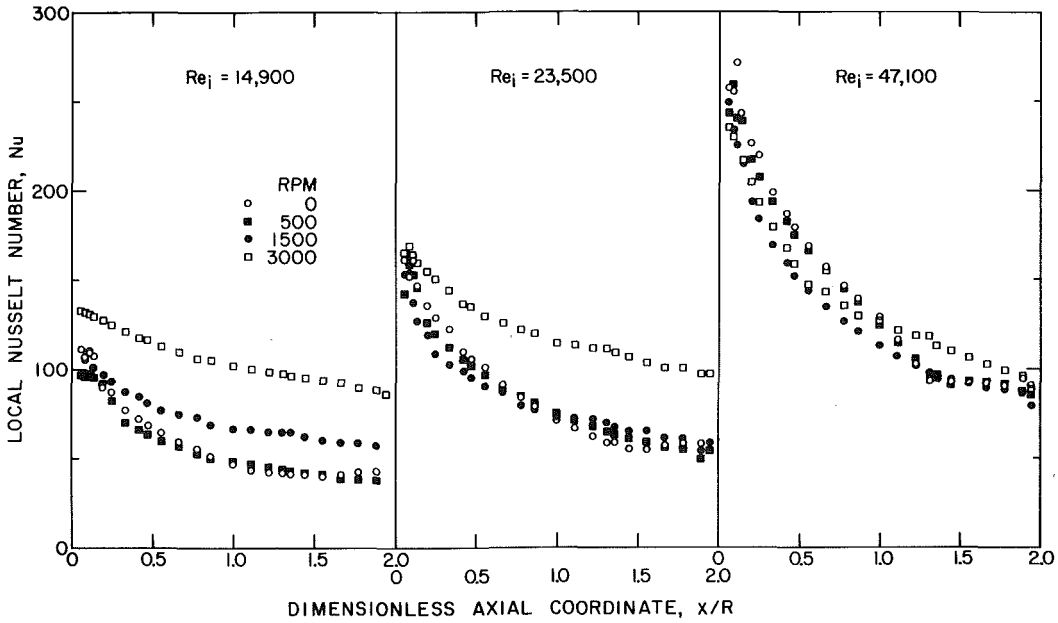

Fig. 2 Distributions of the local Nusselt number along the shroud, $S/R = 2$

A more detailed examination of Fig. 2 shows that there are conditions where the transfer coefficients for the no rotation case are actually higher than those for certain magnitudes of rotation. This is in evidence along a section of the shroud surface adjacent to the rotating disk, the length of which increases as the Reynolds number increases. Furthermore, in that section of the shroud and with increasing Reynolds number, the no-rotation results tend to rise toward the top of the assemblage of data points, followed closely by the results for 500 rpm.

The fact that the rotation can produce degradation as well as aug-

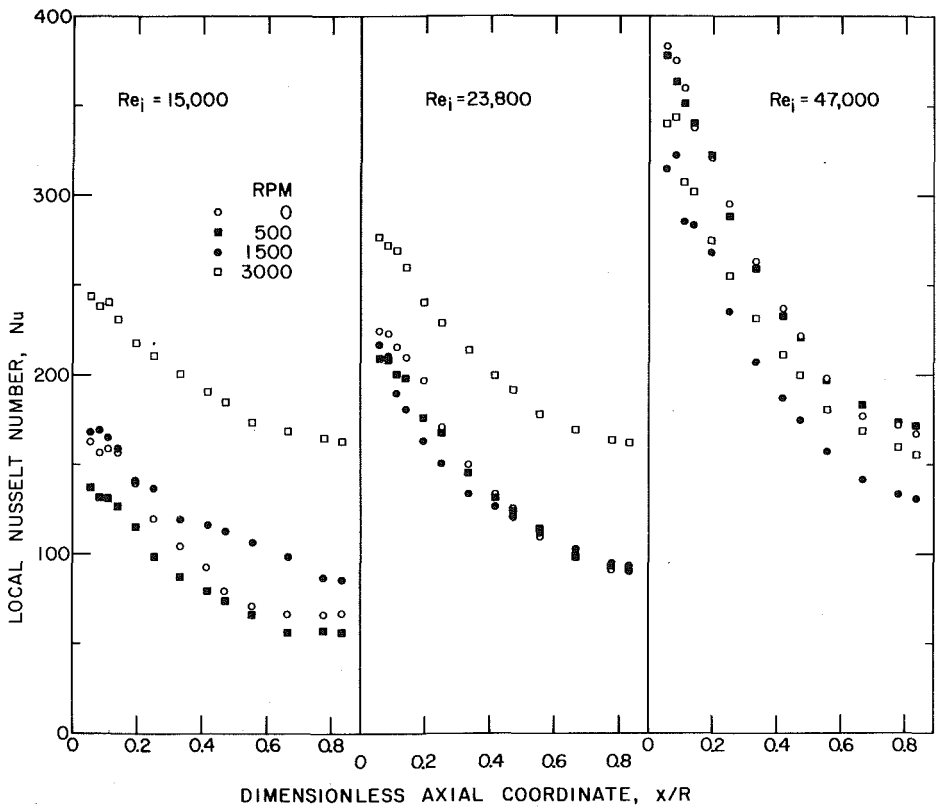

Fig. 3 Distributions of the local Nusselt number along the shroud, $S/R = 8/9$

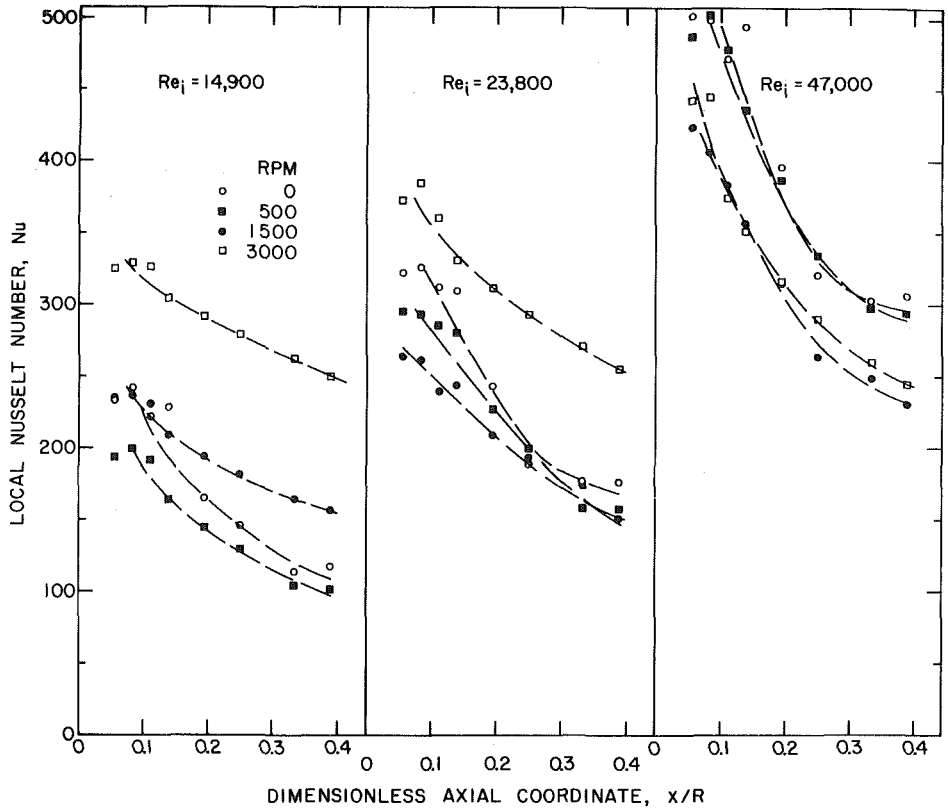

Fig. 4 Distributions of the local Nusselt number along the shroud, S/R = 4/9

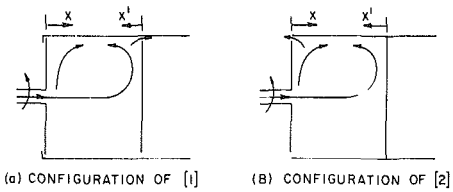

Fig. 5 Schematic diagrams of the enclosure configurations of [1, 2]

mentation of the transfer coefficients can be made plausible by taking note of its various effects on the velocity field. As discussed in the Introduction, the pumping action of the rotating disk induces a radial outflow on the disk surface which is superposed on the radial outflow caused by the coolant jet. It is not unreasonable to expect that the resulting higher velocities would carry over to the axial flow along the shroud and thereby enhance the heat transfer coefficients.

On the other hand, the rotation tends to break up a well-ordered, energy-transporting recirculating flow that is established in the enclosure in the absence of rotation. The deleterious effect of such a breakup on the heat transfer coefficients has been demonstrated by analysis for laminar flow [4]. In addition, in the presence of strong rotation, the deflection of the radial outflow on the disk into an axial flow on the shroud may be accompanied by separation effects which degrade the transfer coefficients.

The effect of the coolant Reynolds number on the magnitude of the transfer coefficients will now be examined. If Fig. 2 is scanned from left to right, it is clear that there is a general increase of the transfer coefficients with increasing Reynolds number. This increase is especially marked when the disk rotational speed is low. In addition, the distribution curves tend to become steeper at larger Reynolds numbers. That is, the transfer coefficients at small values of x are more sensitive to Reynolds number than are those at large x. This behavior is, presumably, related to the greater sensitivity of thinner boundary layers to changes in velocity.

The trends that have just been described for Fig. 2 (S/R = 2) are also in evidence for the results for the smaller aspect ratios, S/R = 8/9 and 4/9, Figs. 3 and 4, respectively. The major effect of decreasing aspect ratio is to bring about a general increase in the magnitude of the heat transfer coefficients. Thus, for example, for Re_i = 15,000 and ω = 3000 rpm, the level of the Nusselt number increases from 100 to 200 to 300 as S/R changes from 2 to 8/9 to 4/9. The increase in the Nusselt number is due to the higher fluid velocities in the boundary layers along the enclosure surfaces as well as to more intense recirculation in the core of the enclosure.

Nusselt Number Comparisons. It is relevant to compare the results of the present experiments with those of [1, 2], where similar experiments were performed, but with different flow patterns owing to differences in the positioning of the coolet inlet and exit. Schematic diagrams of the enclosure configurations of [1, 2] are shown in Fig. 5. These diagrams also contain an indication of some possible flow patterns (sketched in the upper half of the enclosure), the existence and relative strength of which depend on aspect ratio, disk rotational speed, and coolant Reynolds number. For example, in either of Figs. 5(a) or 5(b), the forward (positive x) flow along the shroud should dominate over the back flow (negative x) when the rotational speed is high and the coolant Reynolds number is low.

The shroud heating conditions for the experiments of [1, 2] were similar to those of the present experiments. However, in [1], the rotating disk was also electrically heated, the heat flux level being the same as that for the shroud.[2] Depending on the flow pattern, the effect

[2] The heated rotating disk of [1] became inoperative shortly after the completion of those experiments.

of heating at the disk could result in preheating of the fluid which washes the surface of the shroud, thereby reducing the heat transfer coefficients. This factor should be kept in mind when comparisons are made.

The Nusselt number comparisons are presented in Figs. 6–8, respectively, for aspect ratios S/R = 2, 8/9, and 4/9. Each figure contains two graphs, one for 500 rpm and the second for 3000 rpm. The abscissa variable for the 500 rpm results is either x/R or x'/R, respectively, for the present experiments and for those of [1, 2]. The use of x' for the latter was motivated by the expected dominance of the back flow along the shroud. The 3000 rpm results are plotted as a function of x/R for all cases. Comparisons are made at nominal values of coolant Reynolds number of 15,000, 25,000, and 50,000 for ω = 500 rpm. Inasmuch as results for Re_i = 15,000 were not obtained in [1] for ω = 3000 rpm, comparisons are made only for Re_i = 25,000 and 50,000 at that rotational speed.

Attention may first be turned to the results for 3000 rpm (right-hand graphs of Figs. 6–8). It is seen that for all cases, the Nusselt number decreases with increasing x, indicating that the flow is in the positive x direction along the shroud. Thus, for the experiments of [1, 2], the back flows pictured in Fig. 5 did not materialize to an extent sufficient to affect the heat transfer results.

It is relevant to observe that for the experiments of [1] as contrasted to the present experiments and those of [2], the fluid exit slot is differently positioned with respect to the positive x flow (see Figs. 1 and 5). In particular, for the former experiments, the exit slot is at the downstream end of the shroud flow path, whereas for the latter it is at the upstream end. With the exit slot at the upstream end, it might be expected that there would be less flow along the shroud than when the exit slot is at the downstream end. On the basis of this reasoning, the transfer coefficients of [1] should be higher than those of the present experiments and those of [2].

The comparisons shown in the right-hand graphs of Figs. 6–8 indicate that the foregoing expectations are, for the most part, fulfilled. At the smallest aspect ratio, S/R = 4/9 (Fig. 8), the expected ordering of the results is only partially realized. This may be due, in part, to the previously mentioned preheating effect in the experiments of [1]. The importance of this effect should be greater when the heated surface area of the shroud becomes smaller (relative to the fixed surface area of the heated rotating disk). In addition, the validity of the simple flow patterns that were postulated in the discussion may be in some jeopardy at smaller aspect ratios.

From further examination of the right-hand graphs, it is seen that the results of [2] for $Re_i \sim 50{,}000$ are somewhat higher than the present results (25 percent, at the very most), whereas there is very close agreement at $Re_i \sim 24{,}000$.

Consideration may now be given to the results for 500 rpm. Whereas the distribution curves representing the present experiments vary monotonically along the shroud, those of [1, 2] tend to tip up near the end. This tipping up is due to the conflict between the forward and backward flows along the shroud as illustrated in Fig. 5. By reasoning along lines similar to those used in the foregoing, it may be concluded that the results of [2] should lie highest. This expectation is fairly well realized for the larger aspect ratios, but only partially for S/R = 4/9. For the most part, the results of [1] fall somewhat below the others.

If a broad view is taken of Figs. 6–8, it appears that for a given set of operating parameters (S/R, Re_i, and ω), a curve could be sketched which represents the results of the three experiments with fair accuracy. That such a conclusion can be drawn is noteworthy in view of the complex flow phenomena that are involved.

Temperature Field in the Enclosure. The measured temperature profiles were employed in the construction of isotherm maps which are presented in Figs. 9 and 10. These results are for the intermediate aspect ratio, S/R = 8/9. Fig. 9 illustrates the response of the temperature field to changes in disk rotational speed from ω = 0 to 3000 rpm, with the coolant Reynolds number held constant at a value of about 24,000. In Fig. 10, the coolant Reynolds number is varied from 15,000 to 47,000, while the rotational speed is fixed at 1500 rpm.

The plotted isotherms represent the locus of constant values of $T - T_{bi}$, expressed in °F. The temperature interval between successive isotherms is 4°F. Occasional additional isotherms are indicated by dashed lines. Representative values of $T_w - T_{bi}$ are noted along the upper margin of the graphs.

If attention is first given to Fig. 9, it is seen that the temperature field is of a different character depending on the absence or presence of rotation. In the no-rotation case, the temperature in the core is relatively uniform, and there is a sharp temperature change in the boundary layer adjacent to the shroud. In the presence of rotation, the temperature in the core becomes more nonuniform, and the nonuniformity is accentuated with increasing rotational speed.

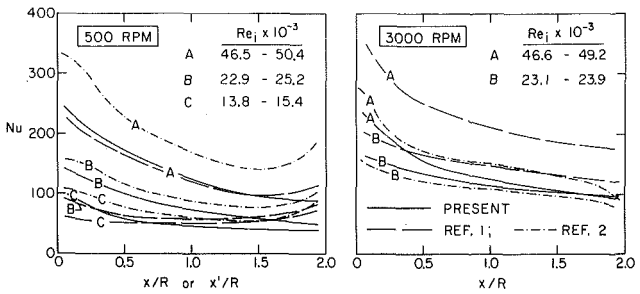

Fig. 6 Comparisons of local Nusselt numbers, S/R = 2

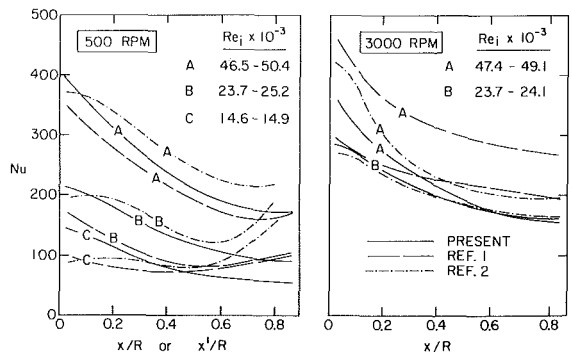

Fig. 7 Comparisons of local Nusselt numbers, S/R = 8/9

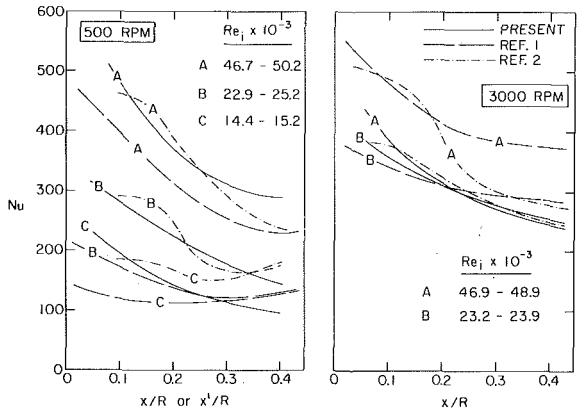

Fig. 8 Comparisons of local Nusselt numbers, S/R = 4/9

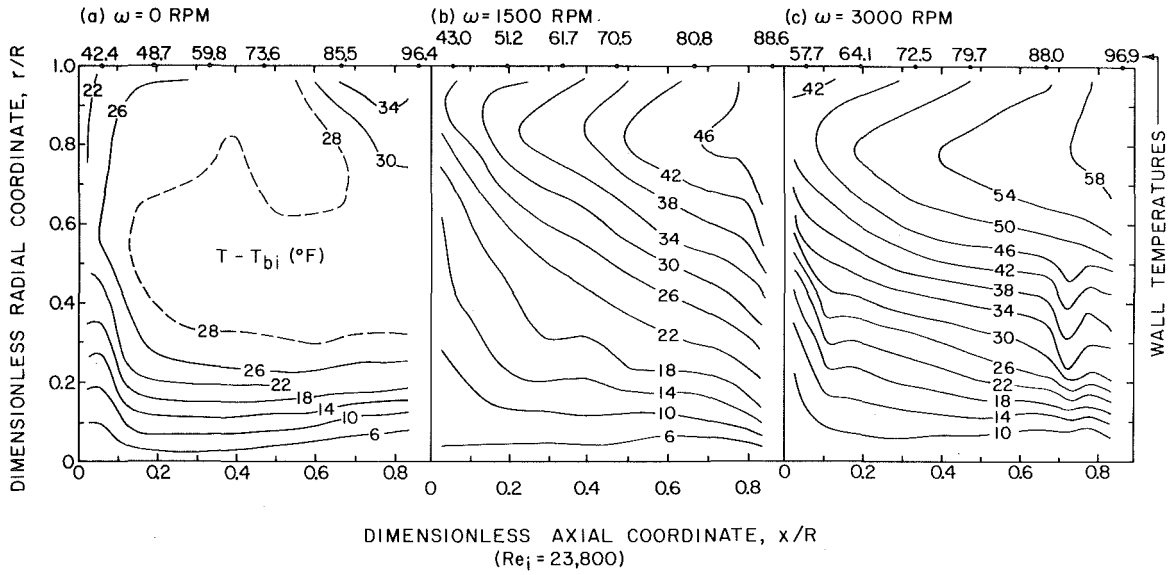

Fig. 9 Isotherm maps for various disk rotational speeds at a fixed coolant inlet Reynolds number, $S/R = 8/9$

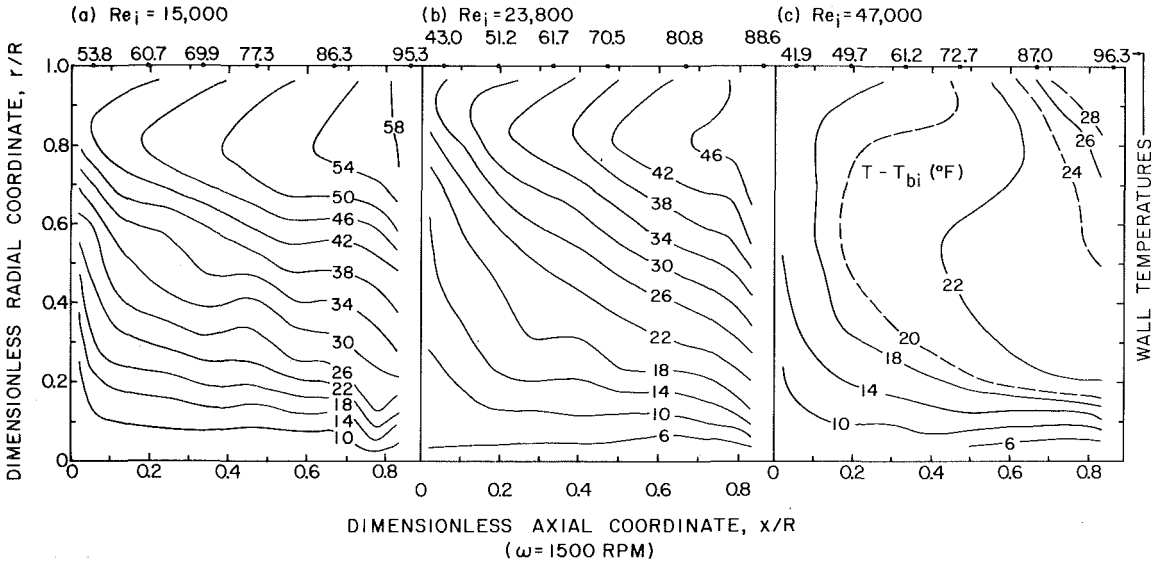

Fig. 10 Isotherm maps for various coolant inlet Reynolds numbers at a fixed rotational speed, $S/R = 8/9$

Concurrently, the temperature change across the shroud boundary layer diminishes.

Examination of the results of Fig. 10 reveals remarkable similarities to those of Fig. 9, except that the graphs are in reverse order. That is, the (a) part of Fig. 10 is comparable to the (c) part of Fig. 9, as is 10(c) to 9(a). In this light, the isotherm pattern of 10(c) can be regarded as dominated by the coolant jet, whereas 10(a) appears to represent a case where rotational effects are very strong.

In order to classify the relative importance of the coolant jet and disk rotation in shaping the temperature field, a ratio such as ω/Re_i (or, $\mathrm{Re}_{rot}/\mathrm{Re}_i$) may be employed. The values of this parameter are very similar for Figs. 10(a) and 9(c). Also, the similarities between Figs. 10(c) and 9(a) suggest that the ω/Re_i value for the former is small enough to signal the dominance of the coolant jet.

Study of the isotherm shapes provides insights into the pattern of fluid flow in the enclosure. Especially interesting in this connection are the bulges in evidence near the top of Figs. 9(b), 9(c) and 10(a), 10(b) and near the middle of 9(a) and 10(c). These bulges are suggestive of a pattern whereby the boundary layer flow along the shroud is turned and deflected by the stationary disk, and subsequently streams back toward the rotating disk. The presence of the bulges is also indicative of a nonmonotonic temperature distribution. If one proceeds radially inward from the shroud, the temperature drops sharply at first and reaches a minimum, then increases moderately and attains a maximum, and then decreases monotonically. The existence of such a temperature distribution and, in particular, of the maximum, is due to the relatively high temperatures possessed by the aforementioned back flowing stream.

It may also be noted that with increasing rotation, the isotherms, aside from those that are bulged, tend to become flatter. This suggests

a transfer mechanism similar to radial conduction, perhaps turbulent diffusion.

Concluding Remarks

In the present experiments, where the shroud flows induced by the coolant jet and disk rotation both have the same direction, the Nusselt numbers are relatively insensitive to rotation at high coolant flow rates. On the other hand, in [1, 2], where the aforementioned induced flows tend to be opposed, the results are more sensitive to rotation.

For conditions where the direction of the flow along the shroud is relatively unidirectional, it was found that for a given set of operating parameters, the results of the three experiments can be represented to fair accuracy by a single curve.

The isotherm maps showed that at higher disk rotational speeds, the temperature distribution in the core of the enclosure is quite nonuniform. This suggests that in an analytical approach to the problem, the turbulence modeling for the core will have to be performed with greater care than would have been necessary had the core been isothermal.

Acknowledgment

The research reported in this paper was supported by the Power Branch of the Office of Naval Research.

References

1 Yu, J. P., Sparrow, E. M., and Eckert, E. R. G., "Experiments on a Shrouded, Parallel-Disk System With Rotation and Coolant Throughflow," *International Journal of Heat and Mass Transfer*, Vol. 16, 1973, pp. 311–328.

2 Sparrow, E. M., Buszkiewicz, T. C., and Eckert, E. R. G., "Heat Transfer and Temperature Field Experiments in a Cavity With Rotation, Recirculation, and Coolant Throughflow," JOURNAL OF HEAT TRANSFER, TRANS. ASME, Series C, Vol. 97, 1975, pp. 22–28.

3 Haynes, C. M., and Owen, J. M., "Heat Transfer From a Shrouded Disk System With a Radial Outflow of Coolant," *Journal of Engineering for Power*, TRANS. ASME, Series A, Vol.97, 1975, pp. 28–36.

4 Hennecke, D. K., Sparrow, E. M., and Eckert, E. R. G., "Flow and Heat Transfer in a Rotating Enclosure With Axial Throughflow," *Wärme- und Stoffübertragung*, Vol. 4, 1971, pp. 222–235.

R. M. Fand
K. K. Keswani
M. M. Jotwani
R. C. C. Ho

Department of Mechanical Engineering,
University of Hawaii,
Honolulu, Hawaii

Simultaneous Boiling and Forced Convection Heat Transfer From a Horizontal Cylinder to Water

This paper presents the results of experiments involving simultaneous boiling and forced convection heat transfer from horizontal cylinders to water in crossflow. In these experiments all of the following primary variables were varied: heat flux, crossflow velocity, pressure, subcooling, and surface material. Based on these data an empirical correlation equation is developed which permits one to predict the performance of a cylindrical heater in the presence of crossflow and boiling, *provided only that its performance* in the absence of crossflow (pool boiling) *is known. This correlation equation eliminates the need to perform experiments in the presence of crossflow to ascertain the performance of a "crossflow-plus-boiling" cylindrical heater.*

Introduction

Two methods have been suggested in the literature for correlating heat transfer in the presence of simultaneous boiling and forced convection. The first of these methods, proposed by Rohsenow [1],[1] consists of the simple superposition of effects as expressed by the following formula:

$$\bar{q} = \bar{q}_f + \bar{q}_b \tag{1}$$

where $\bar{q}$ is the total heat flux, and $\bar{q}_f$ and $\bar{q}_b$ represent forced convection and boiling heat fluxes, respectively. The second approach to this problem, formulated by Kutatedeladze [2], is embodied in the following equation:

$$\frac{h}{h_f} = \left[1 + \left(\frac{h_b}{h_f}\right)^n\right]^{1/n} \tag{2}$$

Kutatedeladze found that, with $n = 2$, equation (2) correlates the results of several experimental studies of boiling water flowing inside tubes. The objective of the present investigation was to obtain experimental heat transfer data for simultaneous boiling and forced convection (crossflow) on the outside of a horizontal cylinder immersed in water and to develop a correlation equation for this data. This geometry has practical utility, as exemplified by the use of cylindrical immersion heaters.

[1] Numbers in brackets designate References at end of paper.

Contributed by the Heat Transfer Division for publication in the Journal of Heat Transfer. Manuscript received by the Heat Transfer Division October 29, 1974. Paper No. 76-HT-UU.

Experimental Procedure

The experimental portion of the present investigation was conducted by placing cylindrical, electrically heated test specimens horizontally into a water tunnel, such that the flow of water was vertically upward and normal to the axes of the test specimens (crossflow). The test specimens (diameters approximately 0.012 m) and the water tunnel (diameter 0.08661 m) used here are described in detail in references [3, and 4]. Specimens having polished stainless steel and titanium heat transfer surfaces were tested. Distilled water was used. The water tunnel contained a circular glass window through which the test specimens could be observed and photographed from the viewing angle shown in Fig. 1. All of the photographs exhibited herein were taken with a camera shutter speed of 0.001 s. The apparatus permitted simultaneous measurements of pressure, velocity, power input to the test specimens, and surface and bulk water temperatures,

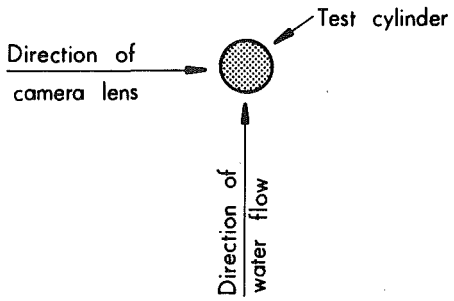

Fig. 1 Sketch of test geometry

from which the heat transfer coefficient and all other relevant parameters could be calculated. The ranges of the experimental variables were:

$\bar{q}$ = 166,000–335,000 W/m^2
V = 0.024–0.122 m/s
p = 2–4 atm
t_b = 71–102°C
t_s = 122–165°C
Δt = 42–83°C
Δt_{sup} = −5–32°C

The electric power fed into the test section of the heated cylinder was measured with an error of less than 0.1 percent by means of a carefully calibrated wattmeter. A precision potentiometer was used to read the output of all thermocouples with an accuracy better than 0.03°C. The water tunnel was calibrated with respect to velocity by means of the "hydrogen bubble technique" correct to within 1 percent, as described in reference [4]. Pressure was measured with a high precision gage correct to within 0.01 atm.

The water in the tunnel was degassed by repeatedly heating it to 104°C at approximately 3 atm pressure and then suddenly venting the system to the atmosphere. The venting caused violent flash boiling throughout the body of water, which drove off dissolved gases. Although the final gas content of the water was not measured, it is believed that this procedure removed most of the dissolved gases. The small amount of dissolved gases remaining in the water did not interfere with the collection of consistent data relevant to the objectives of this investigation, as is explained subsequently.

Boiling heat transfer depends upon a relatively large number of parameters, some of which, especially those relating to the condition of the heat transfer surface and the chemical purity of both the surface and the boiling liquid, are extremely difficult to control experimentally. One such problematic parameter is the time-in-use or so-called aging of a surface on which boiling occurs. However, the rates of change associated with aging generally diminish as a function of time, and this fact provides a basis for eliminating the effects of this sometimes troublesome parameter; because this fact implies that, after a sufficiently long time has elapsed, a surface will have reached a quasistatic condition relative to experiments of sufficiently short duration. The progressively diminishing effect of aging is demonstrated by the series of photographs and data in Fig. 2. These photographs and data show that the number of nucleation sites on a cylinder diminish with time (probably due to the degassing of the surface), and that the rate of change of Δt decreases continuously with time.

In order to eliminate the effect of surface aging and the effect of possible variations in the quantity of dissolved air upon the boiling data presented herein, an experimental procedure was adopted whereby a quasistatic condition relative to these two variables was

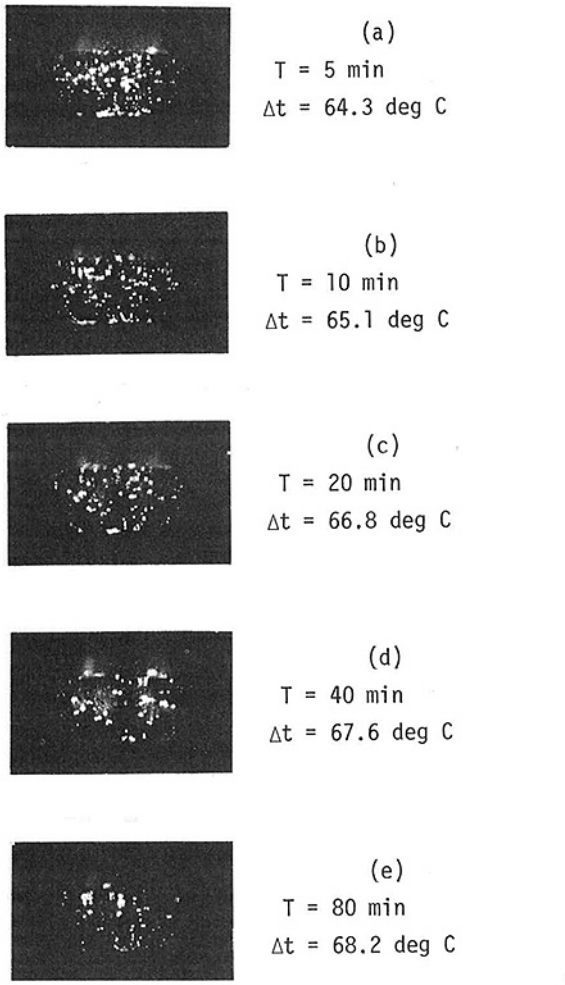

Fig. 2 Effect of aging on bubble formation: titanium cylinder, $D = 1.191 \times 10^{-2}$ m; $p = 3.00$ atm; $V = 0.1219$ m/s; $\bar{q} = 322100$ W/m^2; $t_b = 102.3 \pm 0.1$°C

Nomenclature

D = cylinder diameter
h = heat transfer coefficient in the presence of simultaneous boiling and forced convection; $h = \bar{q}(\Delta t)^{-1}$
h_b = boiling heat transfer coefficient in the absence of forced convection (see equation (4))
h_f = forced convection heat transfer coefficient in the absence of boiling (calculated by equation (5))
k = thermal conductivity
n = numerical constant (see equation (2))
N = Nusselt number: N = hDk^{-1}
p = pressure
P = Prandtl number: P = $c\mu k^{-1}$
$\bar{q}$ = heat flux (rate of heat transfer per unit area)
q = boiling heat flux
q_f = forced convection heat flux
R = Reynolds number: R = $DV\rho\mu^{-1}$
t_b = bulk temperature of liquid
t_f = mean film temperature; $t_f = \frac{1}{2}(t_s + t_b)$
t_s = surface temperature in the presence of forced convection
t_{sat} = saturation temperature
t_{s0} = surface temperature in the absence of forced convection
Δt = temperature difference: $\Delta t = (t_s - t_b)$
Δt_0 = temperature difference = $(t_{s0} - t_b)$
Δt_{sub} = subcooling: $\Delta t_{sub} = (t_{sat} - t_b)$
Δt_{sup} = superheat: $\Delta t_{sup} = (t_s - t_{sat})$
Δt_x = superheat: $t_x = (t_{s0} - t_{sat})$
T = time
V = velocity

created, as described in what follows. First, an appropriate operating pressure and a bulk temperature were selected. Then, with a given test cylinder in place, a series of tests were made as in Test Series A recorded in Table 1. The series began and ended with identical runs. If the values of Δt for the initial and final runs of a series differed by less than 2 percent, it was assumed that the condition of the surface and the quantity of dissolved air had not changed significantly during the series and that, in fact, a quasistatic condition relative to these variables had been achieved during the time in which the data for the series had been collected.[2] Typically, a series had to be repeated three or four times before a quasistatic condition was reached and "final data" like those recorded in Table 1 were obtained. Five such quasistatic series, designated A, B, C, D, and E, were completed in this investigation, under the conditions listed in Table 1. In addition, certain other quasistatic test sequences were performed in order to demonstrate the effects of pressure, velocity, heat flux, and subcooling on bubble formation, as shown photographically in Figs. 3–5. To gather all these data, the apparatus was operated continuously 24 hr per day for approximately 12 days.

Correlation of Results and Discussion

An effort was made to correlate the experimental data obtained here for simultaneous boiling and forced convection heat transfer by means of equation (1), but without success. However, equation (2) was found to provide an acceptable correlation, provided that the heat transfer coefficients contained therein are defined and calculated as follows:

$$h = \bar{q}(\Delta t)^{-1} \tag{3}$$

$$h_b = \bar{q}(\Delta t_0)^{-1} \tag{4}$$

$$h_f = N_f k_f D^{-1} \tag{5}$$

where N_f is calculated from the forced convection formula presented in reference [4], namely,

$$N_f = (0.255 + 0.699\, R_f^{0.50}) P_f^{0.29} \tag{6}$$

In equation (6) the subscript f implies that fluid properties are to be evaluated at the mean film temperature t_f. The defining equation for h_b, equation (4), contains the quantity Δt_0, which is the steady-state temperature difference that occurs at zero velocity corresponding to the heat flux $\bar{q}$. This temperature difference could not be accurately determined by direct measurement in the water tunnel employed here, because for zero velocity (no flow in the tunnel) steady-state conditions could not be achieved in the tunnel's relatively small test section. Therefore, in order to obtain the required values of Δt_0, the measured steady-state values of Δt at progressively lower velocities were plotted as shown, by way of example, in Figs. 6 and 7 for test series A and B, and these data were extrapolated to zero velocity as per the curves indicated in the figures. Similar plots (not shown here) were made for test series C, D, and E. The values of Δt_0 versus $\bar{q}$ for test series A, B, C, D, and E are listed in Table 2. It is believed that these extrapolations are valid, since it is apparent from the data that the influence of the crossflow velocity upon t_s at velocities less than the lowest velocity at which measurements at Δt were actually made is small.

All data points in Table 1, except those for which the superheat, Δt_{sup}, is less than 5.5°C (10°F), are plotted in Fig. 8 together with equation (2) with $n = 5.5$; this value for n was found to be the optimum value for correlation. The reason why data points for which $\Delta t_{sup} < 5.5$°C (10°F) were not plotted is that, for such low degrees of superheat, bubble formation is somewhat erratic and hence the associated heat transfer measurements are also somewhat erratic; however, this behavior does not seriously affect the validity of the correlation equation represented by the curve in Fig. 8 since none of the experimental data points for which $\Delta t_{sup} < 5.5$°C (10°F) deviates from the curve by more than 7 percent. The maximum and mean deviation between the data points and equation (2) in Fig. 8, where

[2] Since the final run of each series was a repetition of the initial run, the final runs were not included in subsequent correlation calculations.

Table 1 Experimental data for stainless steel cylinder (Test Series A): $D = 1.143 \times 10^{-2}$ m; $p = 3.00$ atm; $t_{sat} = 134.0$°C; $t_b = 102.4 \pm 0.2$°C

Run No.	$\bar{q}$ (W/m²)	V (m/s)	t_s (°C)	t_b (°C)
1	335600	0.1213	160.9	102.5
2	243600	0.1213	156.9	102.6
3	165900	0.1213	144.8	102.5
4	335600	0.0942	162.2	102.4
5	243600	0.0942	157.5	102.5
6	165900	0.0942	149.9	102.3
7	335600	0.0610	162.3	102.4
8	243600	0.0613	160.0	102.4
9	165900	0.0610	154.6	102.4
10	335600	0.0299	162.8	102.2
11	243600	0.0299	160.0	102.2
12	165900	0.0299	155.2	102.2
13	335600	0.1213	161.4	101.9

Table 1 (cont'd) Experimental data for titanium cylinder: $D = 1.188 \times 10^{-2}$ m

			Test Series B $p = 4.00$ atm $t_{sat} = 144.1$°C $t_b = 93.2 \pm 1.0$°C		Test Series C $p = 3.00$ atm $t_{sat} = 134.0$°C $t_b = 82.1 \pm 0.4$°C		Test Series D $p = 2.00$ atm $t_{sat} = 120.7$°C $t_b = 82.1 \pm 1.0$°C		Test Series E $p = 2.00$ atm $t_{sat} = 120.7$°C $t_b = 71.0 \pm 0.9$°C	
Run No.	$\bar{q}$ (W/m²)	V (m/s)	t_s (°C)	t_b (°C)	t_s (°C)	t_b (°C)	t_s (°C)	t_b (°C)	t_s (°C)	t_b (°C)
1	322700	0.1219	160.7	93.6	152.2	81.9	146.8	82.2	145.8	70.7
2	234300	0.1219	152.2	93.3	143.4	81.9	139.2	81.9	136.6	70.8
3	159500	0.1219	138.9[a]	93.8	130.9[a]	81.7	128.2	81.9	122.3[a]	70.2
4	322700	0.0976	162.0	93.2	153.9	82.5	148.3	82.7	148.3	70.8
5	234300	0.0976	154.0	93.3	146.4	82.4	142.0	82.6	139.9	70.6
6	159500	0.0976	142.2[a]	93.2	134.3[a]	81.9	132.3	82.2	126.1[a]	70.6
7	322700	0.0732	163.2	93.6	155.8	82.3	150.1	82.1	150.4	71.7
8	234300	0.0732	156.9	93.2	148.5	82.1	143.8	82.0	142.3	71.9
9	159500	0.0732	146.0[a]	93.4	136.5[a]	81.9	134.7	82.1	130.9	71.3
10	322700	0.0488	164.1	92.4	157.8	82.4	150.6	82.8	152.4	71.8
11	234300	0.0488	157.9	92.9	151.7	82.0	144.9	82.8	145.3	71.8
12	159500	0.0488	149.2[a]	93.8	141.2	81.9	137.2	82.8	135.3	71.6
13	322700	0.0244	164.8	92.2	158.2	82.2	151.9	81.2	153.0	70.3
14	234300	0.0244	158.1	92.4	152.3	82.3	146.6	81.1	147.2	70.4
15	159500	0.0244	150.4	93.6	143.3	82.3	138.9	81.2	139.1	70.5
16	322700	0.1219	160.8	94.7	152.7	82.1	146.9	82.3	146.8	71.2

[a] $\Delta t_{sup} < 5.5$° C (10° F)—tests not plotted in Fig. 8.

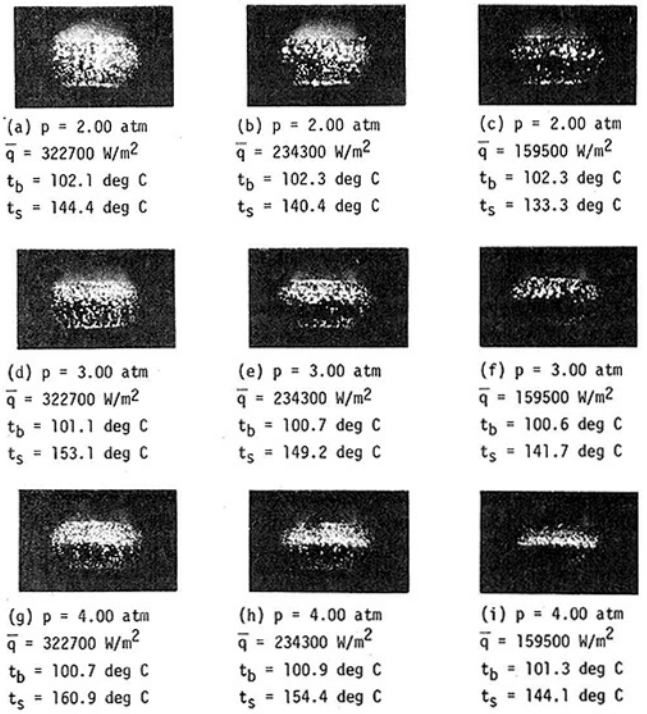

Fig. 3 Effect of pressure and heat flux on bubble information: titanium cylinder, $D = 1.189 \times 10^{-2}$ m; $V = 0.1219$ m/s; $t_b = 101.5 \pm 0.8$°C

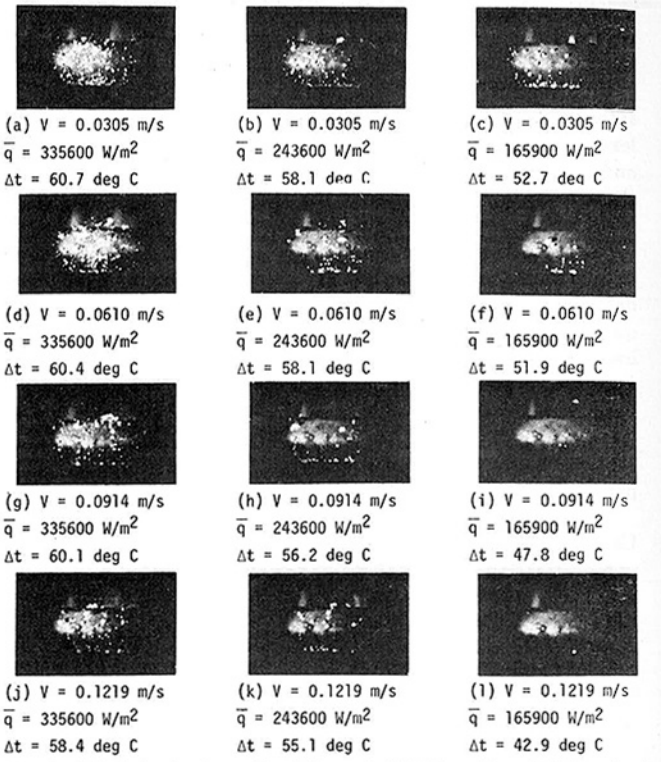

Fig. 4 Effect of velocity and heat flux on bubble formation: stainless steel cylinder, $D = 1.143 \times 10^{-2}$ m; $p = 3.00$ atm; $t_{sat} = 134.0$°C; $t_b = 102.4 \pm 0.2$°C

the deviation is expressed as a percentage of the experimentally measured value, are 4.7 and 1.3 percent, respectively. This level of agreement between the data and the equation is considered to be sufficient to warrant the contention that the said correlation equation is acceptable.

The photographs in Figs. 3–5 demonstrate that the number of nucleation sites on a heated cylinder in the presence of simultaneous boiling and forced crossflow decreases with an increase in pressure, crossflow velocity, and degree of subcooling. The photographs also show that the distribution of nucleation sites is not, in general, uniform: the forward stagnation line and the rear half of the cylinder are regions where the density of nucleation sites are highest. A comparison of Fig. 3(d) and Fig. 4(j) reveals an important aspect of the physical processes involved in this study. The values of p, V, t_b, and $\bar{q}$ are substantially the same for both these photographs, and yet the number of nucleation sites and the size of the bubbles generated at the sites are very different in the two cases. The reason for this difference is, of course, that the cylinders shown in these two photographs are made of different materials (titanium versus stainless steel), and also that the aging and roughness of the cylinder surfaces are different. Titanium is extremely resistant to corrosion, whereas stainless steel (type 304) is less so; as a consequence, the titanium surface in Fig. 3 remained unaffected throughout the boiling tests, whereas the stainless steel surface in Fig. 4 developed microscopic pits. Side lighting was used in making the photographs exhibited here. Such lighting is capable of revealing minute flaws in a polished surface, and in the present instance it reveals the pits in the stainless steel surface in Fig. 4 in the form of a gray haze on the rear portion of the cylinder. These pits are so small as to be hardly visible to the naked eye, for when the cylinder was removed from the apparatus at the conclusion of the testing program its surface polish, under normal lighting conditions, appeared to be substantially the same as in the pristine condition (mirror finish). These observations substantiate the statement made earlier that boiling depends to a large extent upon the kind and condition of a heat transfer surface.

The correlation procedure described previously utilizes a pool boiling heat transfer coefficient h_b whose definition, per equation (4),

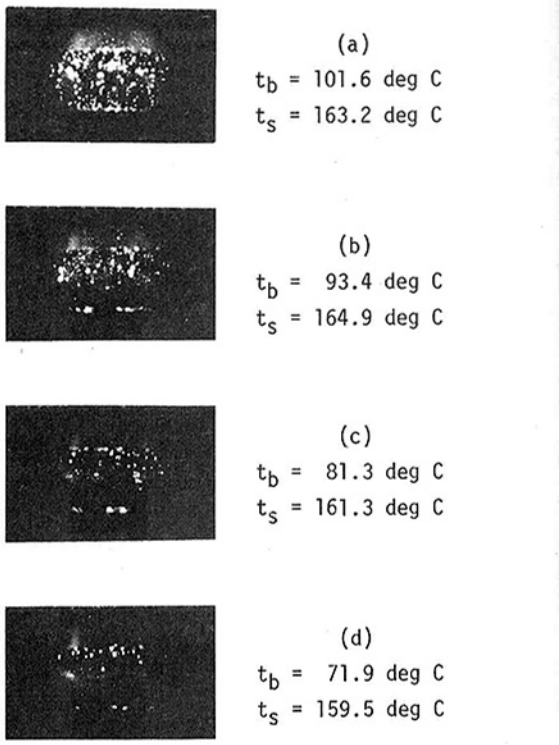

Fig. 5 Effect of subcooling on bubble formation: titanium cylinder, $D = 1.189 \times 10^{-2}$ m; $p = 3.00$ atm; $t_{sat} = 134.0$°C; $V = 0.1219$ m/s; $\bar{q} = 322700$ W/m^2

Table 2 Δt_0 versus $\bar{q}$ for Test Series A, B, C, D, and E

Test series	$\bar{q}$ (W/m^2)	Δt_0 (°C)
A	335600	60.6
	243600	57.8
	165900	53.0
B	322700	71.8
	234300	65.3
	159500	57.8
C	322700	76.4
	234260	70.3
	159500	61.9
D	322700	70.1
	234260	64.7
	159500	57.2
E	322700	82.1
	234260	76.4
	159500	69.7

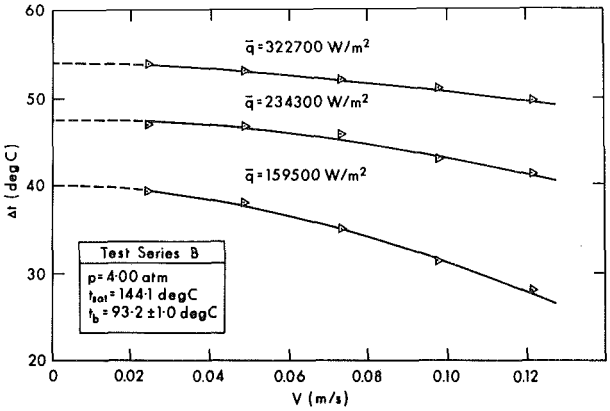

Fig. 7 Plot of experimental data for Test Series B

is based upon Δt_0 rather than upon Δt_x, as is more frequently encountered in the boiling literature. The justification for this deviation from usual practice is as follows: It is usually assumed that the rate of heat transfer from a surface to a liquid in the presence of nucleate pool boiling depends upon the degree of superheat Δt_x, but does not depend appreciably upon the degree of subcooling Δt_{sub}. But this conclusion is not generally correct, as has been demonstrated by Fand and Keswani [5], who performed a series of pool boiling experiments with various degrees of subcooling. These experiments were performed with a stainless steel heated cylinder (dia = 1.157×10^{-2} m) submerged in a tank of water open to the atmosphere, so that the saturation temperature was constant for all tests. The curves in Fig. 9 show the influence of subcooling on $\bar{q}$ at constant Δt_x as determined in [5]: the variation in $\bar{q}$ at constant Δt_x is as much as 100 percent. It was decided that variations of this magnitude would not be disregarded in the correlation of the data acquired in the present investigation. Accordingly, a definition for h_b based on Δt_0 was adopted, per equation (4), which is dependent on both Δt_x and Δt_{sub}, since $\Delta t_0 = \Delta t_x + \Delta t_{sub}$. The relatively high level of agreement between equation (2) with $n = 5.5$ and the experimental data gathered under the diverse condition of the present investigation, particularly for various degrees of subcooling, justifies the definition of h_b adopted here for correlation purposes.

An effort was made to correlate the pool boiling (zero velocity) data gathered in this investigation, but this effort was not successful. Therefore, the present authors conclude, in agreement with Gebhart [6] and Bennett and Myers [7], that pool boiling is not sufficiently well understood at the present time to be predictable with reasonable accuracy. Hence, in order to design a "crossflow-plus-boiling" cylindrical heater of the kind studied here, one would first need to perform a series of experimental zero-velocity (pool boiling) tests; then, based on these zero-velocity experimental data, equation (2) with $n = 5.5$ could be used to predict the performance of the heater in crossflow.

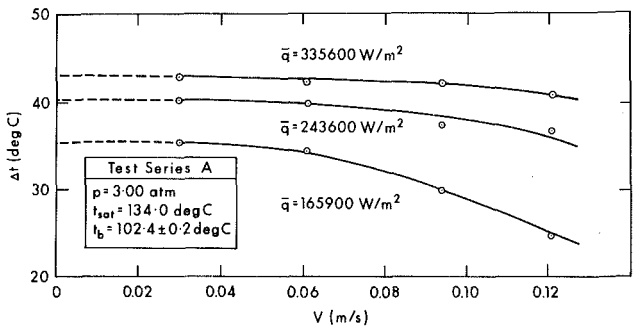

Fig. 6 Plot of experimental data for Test Series A

Conclusion

The experiments described herein on simultaneous boiling and force convection heat transfer from a horizontal cylinder to water were performed under conditions wherein all of the following primary quantities were varied: heat flux, crossflow velocity, pressure, subcooling, and surface material. It was found that equation (2) with $n = 5.5$ correlates all the data satisfactorily, provided that the heat transfer coefficients contained therein are defined as per equations (3)–(5). This is a useful result, because equation (2) permits one to predict the performance of a cylindrical heater *in the presence of*

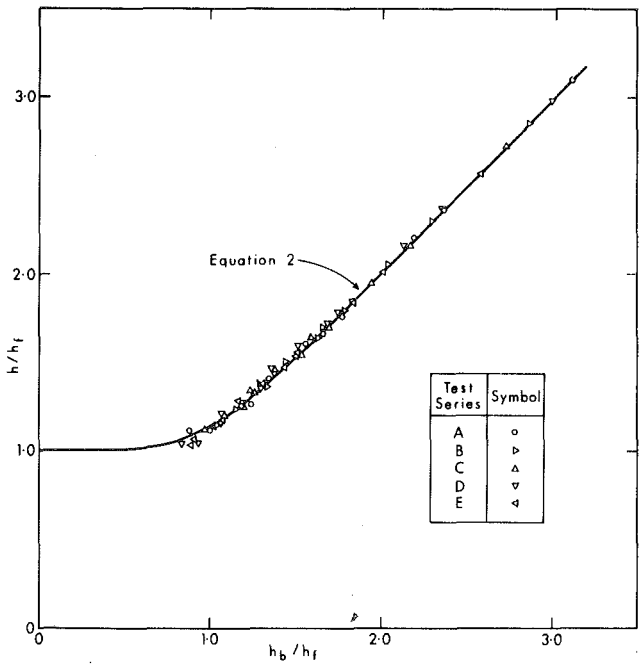

Fig. 8 Graphical comparison of equation (2) ($n = 5.5$) with experimental data

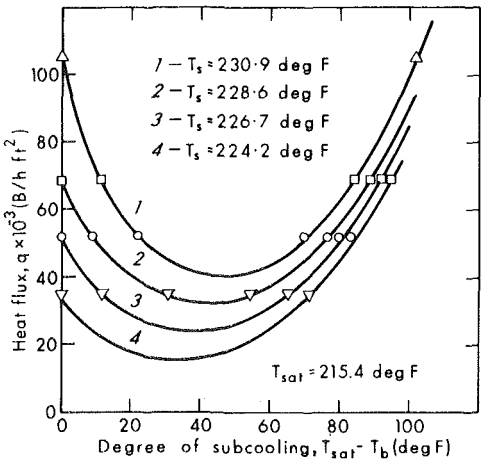

Fig. 9 Heat flux versus degree of subcooling for constant surface temperature [5]

crossflow and boiling, provided only that its performance *in the absence of crossflow* (*pool boiling*) is known. It is relevant to mention here that Bergles and Rohsenow [8] have proposed an approximate forced-convection surface-boiling correlation equation for pipe flow in which the quantity $\bar{q}$ is a function of $\bar{q}_f$ and two other quantities called, respectively, the "fully developed boiling heat flux" and the "fully developed boiling heat flux at incipient boiling." The Bergles-Rohsenow approach was not employed in the present study because the two fully developed fluxes contained therein are difficult to determine with precision and because these difficulties are entirely avoided by using the correlation technique adopted herein, per equation (2).

The maximum crossflow velocity employed in these experiments is a modest 0.122 m/s. At first glance it might appear that this constitutes a serious limitation on the applicability of the correlation presented herein. However, such is not the case, because the range of applicability of the correlation is more properly defined by the range of the ratio h_b/h_f than by the velocity. In this study the experimental value of h_b/h_f varied from 1 to 3. The correlation is expected to hold for $h_b/h_f > 3$ because equation (2) predicts that h approaches h_b with increasing h_b/h_f, and this behavior conforms with observed fact. The correlation is also expected to hold for $h_b/h_f < 1$ because equation (2) predicts that h approaches h_f with decreasing h_b/h_f and, again, this behavior conforms with observed fact.

Efforts were made to reconcile the zero-velocity boiling data obtained here with the predictions of standard, published pool-boiling correlation equations, but without success. For this and related reasons the present authors have concluded that Gebhart's [6] and Bennett and Myers' [7] evaluations of these pool-boiling correlation equations are justified, namely, that they are not reliable. Therefore, in order to design a "crossflow-plus-boiling" cylindrical heater of the kind studied here, one would first need to perform a series of zero-velocity (pool boiling) tests; then, based on this zero-velocity experimental data, equation (2) with $n = 5.5$ could be used to predict the performance of the heater in the presence of crossflow. In effect, equation (2) eliminates the need to perform experiments in the presence of crossflow to ascertain the performance of a "crossflow-plus-boiling" cylindrical heater—this represents a major saving of time and effort with respect to the design and selection of such heaters.

Acknowledgment

This work was supported by a grant from the National Science Foundation.

References

1 Rohsenow, W. M., "Heat Transfer with Evaporation," *Heat Transfer,* University of Michigan Press, 1953.

2 Kutateladze, S. S., "Boiling Heat Transfer," *International Journal of Heat and Mass Transfer,* Vol. 4, 1961, pp. 31–45.

3 Fand, R. M., "Acoustic Water Tunnel," *Journal Acoust. Soc. Am.,* Vol. 38, 1965, pp. 561–569.

4 Fand, R. M., and Keswani, K. K., "The Influence of Property Variation on Forced Convection Heat Transfer to Liquids," *International Journal of Heat and Mass Transfer,* Vol. 15, 1972, pp. 1515–1536.

5 Fand, R. M., and Keswani, K. K., "The Influence of Subcooling on Pool Boiling Heat Transfer from a Horizontal Cylinder to Water," *Proceedings, Fifth International Heat Transfer Conference,* Tokyo, Japan, Vol. 3, 1974, p. 11.

6 Gebhart, B., *Heat Transfer,* second ed., McGraw-Hill, New York, 1971, p. 418. See also first ed., 1961, p. 294.

7 Bennett, C. O., and Myers, J. E., *Momentum, Heat, and Mass Transfer,* second ed., McGraw-Hill, New York, 1974, p. 405.

8 Bergles, A. E. and Rohsenow, W. M., "The Determination of Forced-Convection-Surface-Boiling Heat Transfer," JOURNAL OF HEAT TRANSFER, TRANS. ASME, Vol. 8, 1964, p. 365.

A. Singh
B. B. Mikic
W. M. Rohsenow

Massachusetts Institute of Technology, Cambridge, Mass.

Active Sites in Boiling

Effects of cavity size, shape, and their population on nucleation characteristics of a surface were investigated. A theoretical model has been developed for the stability of a cylindrical cavity in boiling considering the wetting characteristics of the fluid and the transient inertial, viscous, and heat transfer effects. For cavities having small depth/diameter ratio and boiling with organics (low contact angle) the model predicts higher superheats than those predicted by the static equilibrium criterion, and as depth/diameter ratio becomes large, the static criterion successfully predicts the required superheat. The predictions of the model are consistent with the experimental observations made on the natural and artificial cavities made by laser. A qualitative theoretical approach has been presented to predict the population of active sites at different superheats for a given fluid and surface.

Introduction

Attempts have been made in the past to relate the active site density in boiling on a given surface to the cavity size distribution of the surface. The present study considers the effect of different fluids on the population of active sites in boiling. A successful prediction of the number of active sites in boiling requires an understanding of the nucleation phenomenon. Theoretical models for the prediction of initiation of boiling and the size range of active sites have been made [1, 2, 3, 4].[1] None of these theories has successfully predicted the experimental data for artificial cavities boiling with different fluids like water and organics, as observed in reference [4, 5]. Griffith and Wallis [1], in their analysis based on the static equilibrium of a hemispherical vapor nucleus (without any noncondensibles present), proposed the following criteria for nucleation,

$$R_0 = \frac{2\sigma T_{\text{sat}} v_{fg}}{H_{fg}\Delta T} \tag{1}$$

The analysis of bubble incipience criteria by Hsu [2] and Han and Griffith [3] considered the effect of temperature gradient in liquid near the surface and for a saturated liquid boiling over a surface with a constant superheat ΔT, they obtained the following relations between the active cavity size and fluid properties, Hsu [2]:

$$(R_0)_{\text{max, min}} = \frac{\delta}{2c_1}\left[1 \pm \left(1 - \frac{8C_2\sigma T_{\text{sat}}}{H_{fg}P_v\Delta T}\right)^{1/2}\right] \tag{2}$$

Han and Griffith [3]:

$$(R_0)_{\text{max, min}} = \frac{\delta}{3}\left[1 \pm \left(1 - \frac{12\sigma T_{\text{sat}}}{H_{fg}P_v\delta\Delta T}\right)^{1/2}\right] \tag{3}$$

Bankoff [6] first considered the effect of liquid motion into the cavity and the transient heat transfer effects for predicting the superheat required for ebullition. Neglecting the radical heat flux from cavity walls and inertial effects, Bankoff modeled the problem as viscous controlled capillary penetration due to vapor condensation. Later Marto and Rohsenow [7] and Shai and Rohsenow [8] considered the problem of cavity stability in boiling with liquid metals, and in their study they realized the significance of cavity depth in determining the superheat of nucleation. J. J. Lorenz [9] modeled the boiling sites as conical cavities and concluded that dynamic effects are not important in determining the nucleation superheat for a conical configuration. In the present study, the stability of a single isolated cavity in boiling with different fluids (water and organics like ethanol, methanol) has been studied both theoretically and experimentally to determine the effective parameters involved. A qualitative theoretical approach has been presented to predict the population of active sites for known values of these parameters.

Theoretical Model

The theoretical model to predict the superheat required for stable boiling from an isolated cylindrical cavity in boiling has been described in the following.

Entrapment of Vapor in the Cavity. During the growth of a bubble at superheated surface, heat is transferred to the liquid layer adjacent to the surface primarily through conduction which superheats the liquid layer and causes evaporation. Due to evaporation, a thermodynamic equilibrium is expected to exist between the vapor and liquid in the immediate vicinity of the cavity. As the bubble grows and detaches, liquid in the immediate vicinity of cavity moves toward the cavity mouth due to inertial effects caused by the detaching bubble. Due to the thermodynamic equilibrium between liquid and vapor condensation effects are expected to be small during the entrapment process. At the end of entrapment, vapor is compressed due to inertia effects of the liquid resulting in condensation at the interface. The vapor entrapment model used in the present analysis is

[1] Numbers in brackets designate References at end of paper.

Contributed by the Heat Transfer Division for publication in the JOURNAL OF HEAT TRANSFER. Manuscript received by the Heat Transfer Division February 4, 1976. Paper No. 76-HT-JJJ.

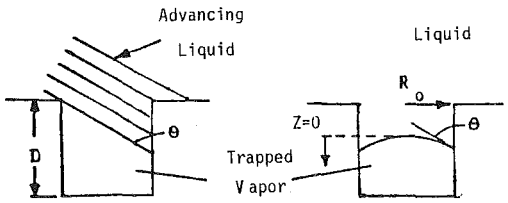

a. Postulated vapor trapping mechanism for a cylindrical cavity.

b. Formation of spherical meniscus from the trapped vapor inside the cylindrical cavity.

Fig. 1 Sketch of the postulated vapor trapping mechanism for a cylindrical cavity

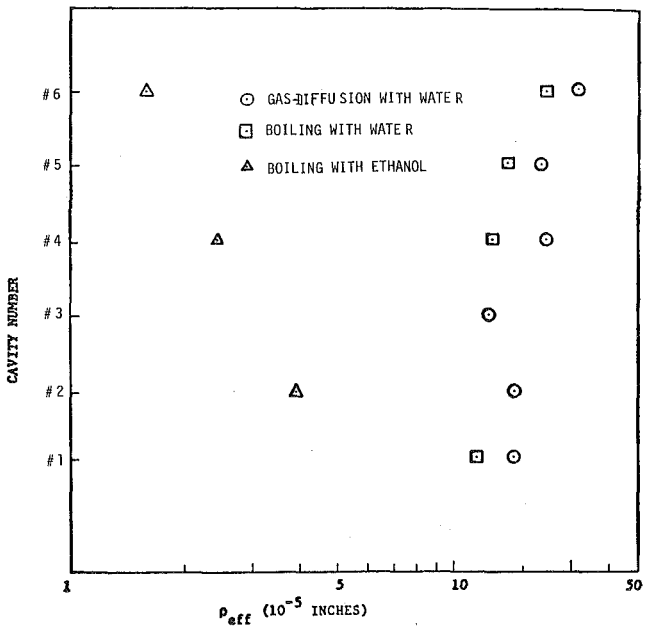

Fig. 2 Results of gas diffusion and boiling experiments for single artificial cavities

based on Bankoff's model [10], as shown in Fig. 1. Clearly, the volume of the trapped vapor depends upon the cavity radius R_0, depth D, and advancing contact angle θ. From the available data, references [9–11], values of θ in the range of 40–50 deg (on copper surface) have been considered for water and 8–15 deg for ethanol and methanol. It is apparent that, because of the smaller θ, organics penetrate deeper into the cavity and thus entrap less volume of vapor as compared to water.

At the completion of the entrapment process, the liquid vapor interface is assumed to take a hemispherical shape, the initial radius of curvature being given by:

$$\rho_0 = \frac{R_0}{\cos\theta} \tag{4}$$

Analysis for the Motion of Liquid-Vapor Interface. A stationary one-dimensional coordinate system, with origin at the initial position of the interface has been selected. Z represents the position of the interface at time t, as shown in Fig. 1(b). The system forces acting on the control volume include shear at cavity walls, pressure force at the vapor-liquid interface, and the inertia force due to the liquid motion inside the cavity. The pressure inside the cavity is determined by the net effect of condensation or evaporation and compression or expansion of the vapor due to interface motion (ideal gas law has been assumed for vapor). The amount of condensation or evaporation depends upon the net heat flux in the axial direction at the liquid-vapor interface. A one-dimensional analysis has been performed to evaluate the axial heat flux. The effect of heat transfer to the liquid from cavity walls is estimated to be small and has been approximated by a uniformly distributed heat source within the liquid. Convection effects have been neglected. Governing equations for motion have been derived in reference [14]. In the following section the experimental results are described and compared with the predictions of the theoretical model.

In order to study the relative behavior of water and organics, two kinds of experiments were carried out—boiling experiments and gas diffusion experiments. Details of these experiments have been presented in reference [12]. Six artificial cavities of arbitrary shape and size were made on the surface of a copper test section hitting the surface with a sharp-pointed object. The fluids were boiled at high heat flux for about 1 hr to remove the dissolved gas before the data were taken. For individual cavities, the surface superheat, ΔT_w, at which the bubble production ceased, was recored with each of fluids. The equilibrium radius of nucleation for the individual cavity was obtained using equation (1), e.g.,

$$\rho_{\text{eff}} = \frac{2\sigma T_{\text{sat}} v_{fg}}{H_{fg}\Delta T_w} \tag{5}$$

In the gas diffusion experiments, the test surface is immersed in a supersaturated solution of air in the test fluid. As the dissolved gas diffuses out of the liquid it nucleates at the cavities on the test surface. Due to slower rates of gas diffusion through the liquid, the nucleation process is slow and hence, the dynamic effects in the gas diffusion system can be assumed to be negligible as compared to that in boiling. The equilibrium radius of nucleation is obtained by:

$$\rho_{\text{eff}} = \frac{2\sigma}{P_v + P_g - P_\ell} \tag{6}$$

Experimental results have been plotted in Fig. 2 for the six artificial cavities. All cavities were found to be active in gas diffusion, but some of the cavities were not seen to be active in the isolated bubble region in boiling at low heat fluxes, where each of the active cavities could be identified easily without interference from the neighborhood sites. As seen in Fig. 2, the observed ρ_{eff} is 40 percent smaller in boiling than gas diffusion, possibly due to the dynamic effects. ρ_{eff} in boiling with

Nomenclature

D = cavity depth
H_{fg} = latent heat of evaporation
N/A = number of active sites per unit area
P = pressure
R_0 = cavity radius, critical radius of nucleation for a cylindrical cavity
T = temperature
ΔT = superheat
V_0 = penetration velocity of liquid
v = volume of vapor
v_{fg} = specific volume change of evaporation
W_g = mass of vapor
z = distance coordinate for penetration
δ = thermal layer thickness
ρ = radius of curvature of liquid vapor interface
ρ_ℓ = density of liquid
σ = surface tension
μ = viscosity of liquid
θ = contact angle

Subscripts

g = gas
i = interface
ℓ = liquid
0 = initial condition
s, sat = saturated condition
v, vap = vapor

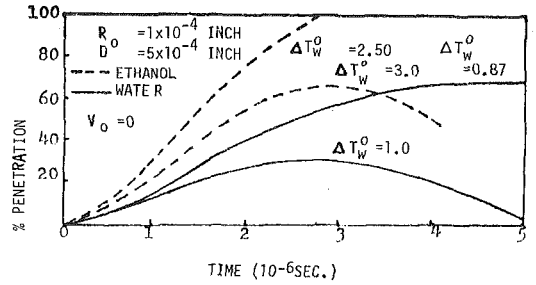

Fig. 3 Effect of fluid on cavity stability—relative behavior of water and ethanol with a cylindrical cavity in boiling

ethanol is seen to be much smaller (2–10 times) than ρ_{eff} with water. The observed relative behavior of water and ethanol can be explained qualitatively by the theoretical model described earlier, as discussed in the following.

Results of Theoretical Model

In the following, results of the theoretical model are presented for a cylindrical cavity of a typical size, and the effects of varying R_0 and D are discussed separately.

It is to be noted (Fig. 1 in reference [5]) that predictions of equations (1)–(3) merge together as cavity radius decreases. Therefore for a cavity radius as small as 1×10^{-4} in., the superheat predicted by the equations (1)–(3) will approximately be equal and is referred to as $(\Delta T)_{2\sigma/R_0}$ in the present work, e.g.,

$$(\Delta T)_{2\sigma/R_0} = \frac{2\sigma T_{sat} v_{fg}}{H_{fg} R_0} \tag{7}$$

$\Delta T_w{}^0$ has been defined as the ratio of the actual value of ΔT_w that is imposed on cavity walls during activation, to the static equilibrium superheat $(\Delta T)_{2\sigma/R_0}$. Since P_{eff} is inversely proportional to ΔT_w, equation (5), $\Delta T_w{}^0$ also represents the ratio of the static equilibrium radius of nucleation, R_0 and P_{eff}, e.g.,

$$\Delta T_w{}^0 = \frac{\Delta T_w}{(\Delta T)_{2\sigma/R_0}} = \frac{R_0}{\rho_{eff}} \tag{8}$$

Fig. 3 shows the relative behavior of water and ethanol in boiling form a cylindrical cavity, as obtained from the numerical solution of the *theoretical model*. The ordinate in Fig. 3 represents penetration of the liquid into the cavity. Initially at $t = 0, z$ is zero and as the liquid interface moves into the cavity, percent penetration increases and becomes complete (100 percent) when the interface reaches the cavity bottom; at this instant the cavity is assumed to be deactivated from boiling. This happens with ethanol, Fig. 3, when $\Delta T_w{}^0 = 2.5$. As $\Delta T_w{}^0$ is increased to 3, evaporation starts and the liquid interface recedes back before penetration is 100 percent. For water the required superheat ratio $\Delta T_w{}^0$ is slightly less than 1. In other words, using equation (8), it could be concluded that the predicted ρ_{eff} for ethanol is more than 2.5–3 times smaller than that for water, a trend similar to that observed in the boiling experiments, Fig. 2. For the above calculation, θ for water and ethanol was taken to be 45 and 10 deg, respectively, and V_0, initial penetration velocity, was taken equal to zero.

Parametric Effects in the Theoretical Model

The effects of varying different parameters on the required superheat for stable boiling and the sensitivity of theoretical results to their magnitudes are discussed in the following in order of their importance.

Effect of Contact Angle. For a smaller contact angle, liquid penetrates deeper into the cavity and the amount of trapped vapor is small. The heat transferred to the liquid due to complete condensation of this small amount of vapor may not be enough to raise the liquid temperature to a level so that evaporation could start and the cavity may thus be deactivated. Fig. 4 shows the effect of contact angle on the required superheat for stable boiling for methanol. When θ is large ($\theta \geq 12$ deg), a wall superheat ΔT_w equal to $(\Delta T)_{2\sigma/R_0}$ is enough for cavity stability. As θ is decreased, higher ΔT_w is required, the liquid penetration being complete when θ is reduced to 4 deg and sufficiently large superheats may be required for nucleation. Activation of completely flooded cavities has not been considered in this paper. The cavity stability is not much affected when θ for water is changed by small amounts ($\Delta\theta \sim \pm 5$ deg) from its base value, $\theta \sim 45$ deg.

Effect of Initial Liquid Velocity. An increase in the initial liquid penetration velocity decreases cavity stability because of greater penetration caused not only by enhanced inertial effects but also due to the additional condensation caused by internal compression which tends to increase the vapor pressure and the corresponding interface temperature. Thus, higher superheats are required for greater initial liquid velocities, the effect being more pronounced for methanol than water, as demonstrated in Fig. 5. Initial liquid penetration velocities of about 5–20 in./s were measured for water boiling on glass cavities in reference [13]. No data for liquid velocity is available for ethanol and methanol. As is evident, liquid velocity is a dependent parameter and it would be difficult to verify its effects experimentally.

Effect of Cavity Size, Mouth Radius R_0 and Depth D. For a given mouth radius R_0, as depth decreases, comparatively less amount of vapor is trapped and the stability of the cavity also decreases, resulting

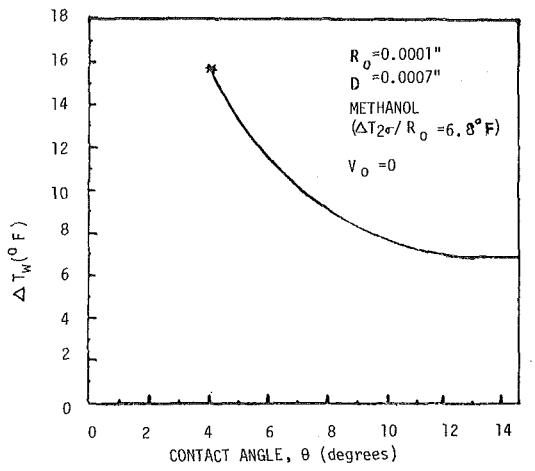

Fig. 4 Effect of contact angle on the superheat required for stability

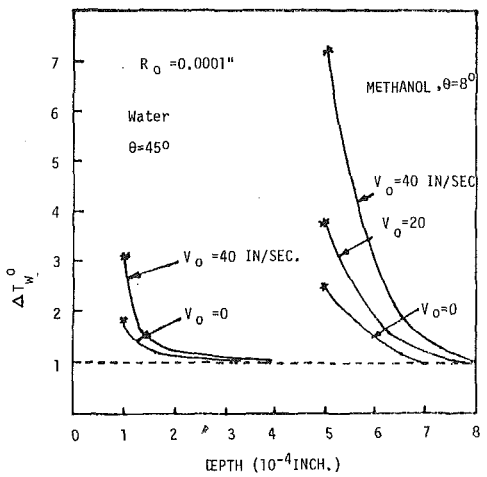

Fig. 5 Effect of cavity depth and velocity on superheat required for stable boiling

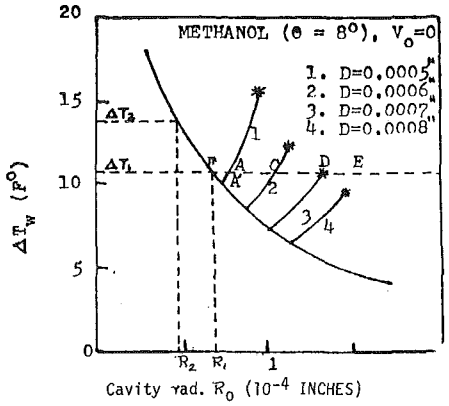

Fig. 6 Effect of cavity size on superheat for stable boiling

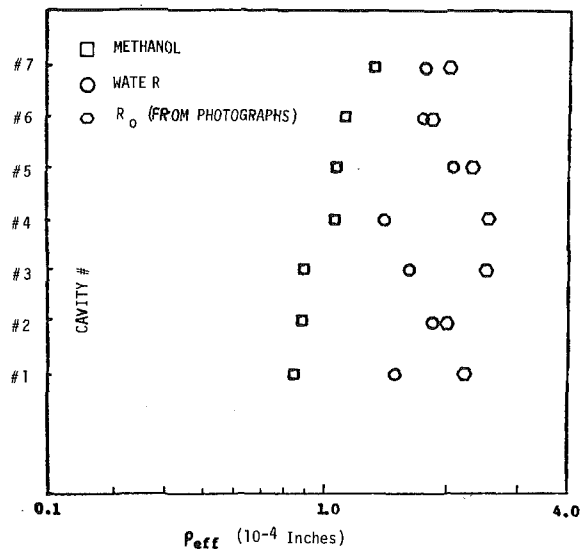

Fig. 7 Boiling data for the individual laser cavities with methanol and water

in higher values of required superheats. The effect of varying cavity depth for fixed R_0 and different values of V_0 is plotted in Fig. 5. For large depths, the required superheat ratio $\Delta T_w{}^0$ is approximately 1, both for water and methanol, i.e., the required superheat is equal to that predicted by the static equilibrium criteria. As depth decreases, the required superheat increases almost exponentially, the rate of increase being much more severe at higher initial velocities. For a given R_0 and θ, the penetration is complete when depth attains a certain minimum value, as denoted by (*) in Fig. 5, and substantially higher superheats may be required for stable nucleation to occur. The effect of varying the cavity size (R_0 and D) on the required nucleation superheat for methanol is shown in Fig. 6. The curve $(\Delta T)2\sigma/R_0$ versus R_0 in Fig. 6 is based on equation (7), which represents the criterion of nucleation outside the cavity. The branched curves 1–4 shown in Fig. 6 are obtained from computer solution of the transient theoretical model for the motion of the meniscus within the cavity, reference [14]. For water, the required superheat is closely predicted by equation (7) when depth/diameter ratio is of the order of unity or greater, as seen in Fig. 5.

Boiling Data With Laser Cavities and Comparison With Analytical Results

In order to investigate the effect of cavity size R_0 and D, boiling experiments were carried out on deep artificial cavities made by laser drilling technique.

Boiling data for some individual laser cavities have been plotted in Fig. 7. The observed (ρ_{eff}) water to (ρ_{eff}) methanol ratio varies from 1.3 to 2.1 for these cavities and is much smaller than the same observed for natural cavities, reference [9], where it varied from 2 to 6. Most of the natural cavities existing on the ordinary surface have their depth/diameter ratio of about 1 and thus are not good vapor traps for wetting fluids like methanol requiring $\Delta T_w{}^0 > 1$. For the same reason, smaller ρ_{eff} is observed for such cavities on ordinary surfaces during boiling with organics. The artificial laser cavities, on the other hand, have larger depth/diameter ratio; hence require lower superheats for methanol. The mouth radius R_0 of the laser cavities was observed with a microscope and its minimum value, plotted in Fig. 7, agrees well with the observed ρ_{eff} for water for most cavities, suggesting that static criteria predict the critical nucleation size for water.

Fig. 8 shows the observed effect of laser cavities on the total population of active sites in boiling with methanol and water on the same surface. N/A versus ρ_{eff} characteristics, indicated by dashed lines and obtained from similar boiling experiments on an ordinary 0.3μ(rms) polished surface have been included in Fig. 8 for comparison. It could be seen that for the same active site population of methanol, higher ρ_{eff} (as high as six times), e.g., lower superheat, is required with laser drilled surface than the ordinary surface without laser cavities. It is apparent that nucleation characteristics could be greatly enhanced by drilling deep laser cavities on the surface for boiling organic fluids.

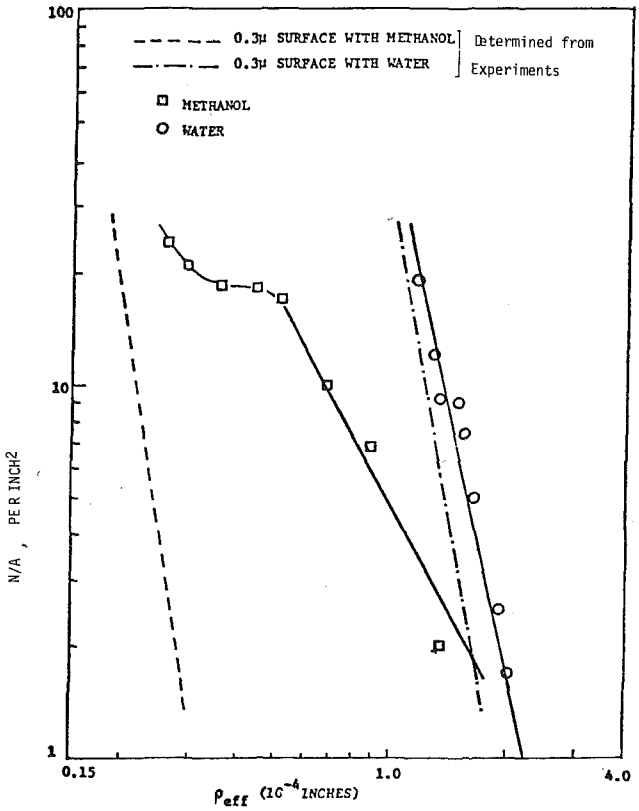

Fig. 8 N/A versus ρ_{eff} characteristics of the boiling surface having laser drilled cavities

Theoretical Approach to Determine Size Range of Active Sites

A qualitative conceptual approach, based on the theoretical model, to predict the size range of active sites has been discussed in the following.

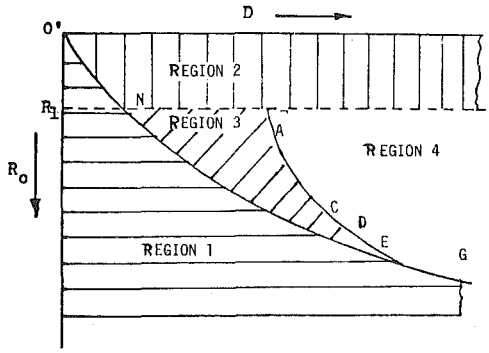

Fig. 9 Regions of inactive and active sites, governed by three different criteria, at superheat ΔT_1 and given contact angle

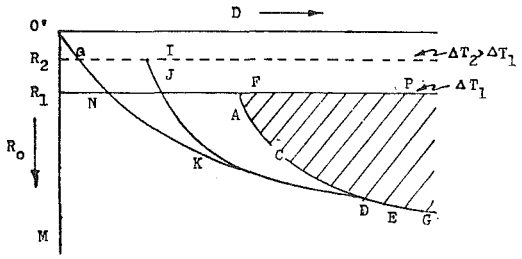

Fig. 10 Size range of active sites at a given superheat ΔT_1 and contact angle θ

Let us assume that a surface contains cavities with a continuous size distribution of R_0 and D, the minimum values being zero. For a certain boiling fluid (contact angle θ), there is a relationship between R_0 and D for which the initial penetration of liquid is complete, i.e., just after the completion of the entrapment process, the interface touches the cavity bottom. This could be defined as the limiting vapor entrapment criterion and represented as the curve 0'G on the $R_0 - D$ plot shown in Fig. 9. All cavities having sizes corresponding to the Region below the curve 0'G do not entrap sufficient amount of vapor to be potential nucleation sites and consequently, are inactive. The limiting vapor entrapment criterion, represented by curve 0'G, depends only upon the value of θ. For smaller values of θ, curve 0'G moves up and Region 1 expands.

For a given superheat ΔT_1, there is a critical radius of nucleation, R_1, as determined by the static equilibrium criterion (equation (1), for example), such that all cavities having $R_0 < R_1$ will be inactive as depicted by the Region 2 in Fig. 9. As superheat is increased, R_1 gets smaller and Region 2 contracts.

Region 3 represents those cavities which satisfy the limiting vapor entrapment criterion and the static equilibrium criterion but are inactive due to dynamic effects. The boundary FACDE of Region 3 could be derived implicitly from the theoretical model or from Fig. 6. Points F, A, C, D, and E in Fig. 9 correspond qualitatively to the same in Fig. 6. The effect of increasing the superheat to ΔT_2 has been shown in Fig. 10, the Region 4 of active sites increasing in size at higher superheats. The effect of superheat on the size range of active cavities for a given surface fluid combination has been summarized in the three-dimensional plot of Fig. 11. The vertical surface 01230 represents the limiting vapor entrapment criterion; cavities belonging to the region between the vertical plane $R_0 = 0$ and the surface 01230 will be good vapor traps and potential nucleation sites. Surface 45674 represents the $(\Delta T)2\sigma/R_0$ surface and all cavities in the region above this surface satisfy the static equilibrium criterion, i.e., $\Delta T_w > (\Delta T)_{2\sigma/R_0}$. Surface 45674 intersects the surface 01230 along the curve iQN6. Thus, all cavities in the region enclosed by these two surfaces and to the right of curve iQN6 entrap sufficient vapor and satisfy the static equilibrium criterion. However, some of these cavities will not be active due to dynamic effects. Regions of active nucleation sites at superheats ΔT_1 and ΔT_2, shown in Fig. 10, have been shown as shaded areas in planes ΔT_1 and ΔT_2 in Fig. 11. The region of dynamic effects is enclosed by surfaces iQn6 2i; iQn6 P5i, and a twisted curved surface whose intersecting curves with planes ΔT_1 and ΔT_2 are FACD and IJK, respectively. Thus, regions FACDNF and IJKQI represent those cavities which are inactive due to dynamic effects, as described earlier in Figs. 9 and 10. The region of dynamic effects becomes narrower as ΔT_w is increased in Fig. 11, and the region of active sites grows in size, entrapping cavities of smaller sizes.

Summary and Conclusions

A theoretical model to determine the required superheat for stable boiling from a cavity has been developed considering the liquid penetration, the effects of transient heat flux and the inertial and viscous effects of liquid moving inside the cavity. Cavity radius and depth, contact angle of the fluid, and the initial penetration velocity of the fluid are important parameters determining the stability of cavity in boiling.

The observed relative behavior of water and organics (ethanol and methanol) has been explained qualitatively by the theoretical model. Boiling data taken on deep laser drilled cavities verifies the predictions of the model that for such cavities, the required superheat is determined by the static equilibrium criterion, both for water and organics. A qualitative conceptual approach, based on the theoretical model, has been presented to predict the size range of active sites at different values of superheat.

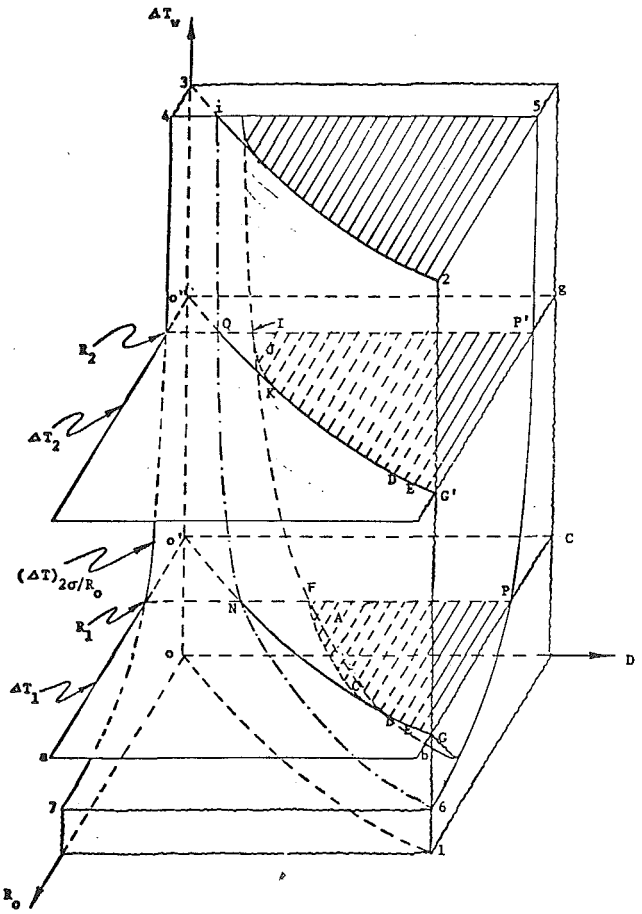

Fig. 11 Size range of active sites versus superheat, a three-dimensional presentation

Acknowledgment

The authors wish to express gratitude to the U.S. Army research office for the financial support of this work. Special thanks are due to Prof. Peter Griffith of M.I.T. for his helpful comments.

References

1 Griffith, P., and Wallis, J. D., "The Role of Surface Conditions in Nucleate Boiling," *Chemical Engineering Progress Symposium Series*, Vol. 56, No. 30, 1960, pp. 49–63.

2 Hsu, Y. Y., "On the Size Range of Active Nucleation Cavities on a Heating Surface," JOURNAL OF HEAT TRANSFER, TRANS. ASME, Series C, Vol. 84, No. 3, Aug. 1962, pp. 207–216.

3 Han, C. Y., and Griffith, P., "The Mechanisms of Heat Transfer in Nucleate Pool Boiling," *International Journal of Heat and Mass Transfer*, Vol. 8, No. 6, June 1965, pp. 887–904.

4 Howell, J. R., and Siegel, R., "Incipience, Growth and Detachment of Boiling Bubbles in Saturated Water from Artificial Sites of Known Geometry," Third International Heat Transfer Conference, Chicago, Vol. 4, 1966, p. 12.

5 Hatton, A. P., James, D. D., and Liew, T. L., "Measurements of Bubble Characteristics for Pool Boiling From Single Cylindrical Cavities," *Heat Transfer 1970*, Elsevier Publishing Co., Amsterdam, Vol. V, P. B1.2.

6 Bankoff, S. G., "The Prediction of Surface Temperatures at Incipient Boiling," *Chemical Engineering Progress Symposium Series*, Vol. 55, No. 29, May 1966, pp. 87–92.

7 Marto, P. J., and Rohsenow, W. M., "The Effects of Surface Conditions on Nucleate Pool Boiling Heat Transfer to Sodium," JOURNAL OF HEAT TRANSFER, TRANS. ASME, May 1966, pp. 183–195.

8 Shai, I., and Rohsenow, W. M., "The Mechanisms of Nucleate Pool Boiling," M.I.T. Engineering Projects Laboratory Report No.—DRS 76303-45, 1967.

9 Lorenz, J. J., "The Effects of Surface Conditions on Boiling Characteristics," PhD thesis, Department of Mechanical Engineering, M.I.T., Dec. 1971.

10 Bankoff, S. G., "Entrapment of Gas in the Spreading of a Liquid over a Rough Surface," *A. I. Chemical Engineering Journal*, Vol. 4, 1958, pp. 24–26.

11 Simon, F. F., and Hsu, Y. Y., "Effect of Contact Angle Hysteresis on Moving Liquid Film Integrity," Technical Paper proposed for presentation at Seventy Third National Meeting of the A.I.Ch.E., Minneapolis, Minn., Aug. 27–30, 1972.

12 Singh, A., "Effect of Surface Conditions on Boiling Characteristics," S.M. thesis, Mechanical Engineering Department, M.I.T., Jan. 1972.

13 Anton, I., and Ve'kas', I., "A Study on the Cavitation Bubble Formation Process," *Rev. Roum. Sci., Tech.-Mec' Appl.*, Vol. 18, No. 6, Bucarest, 1973, pp. 113–129.

14 Singh, A., "Effects of Surface Conditions on Nucleation and Boiling Characteristics," Sc.D. thesis, Department of Mechanical Engineering, M.I.T., Sept. 1974.

15 Lorenz, J. J., Mikic, B. B., and Rohsenow, W. M., "The Effects of Boiling Characteristics," Fifth International Heat Transfer Conference, Tokyo, Japan, Sept. 1974.

S. S. Dua
Graduate Research Assistant.

C. L. Tien
Professor.
Fellow ASME

Department of Mechanical Engineering,
University of California,
Berkeley, Calif.

Two-Dimensional Analysis of Conduction-Controlled Rewetting With Precursory Cooling

This paper presents a two-dimensional analysis of the effect of precursory cooling on conduction-controlled rewetting of a vertical surface, whose initial temperature is higher than the sputtering temperature. Precursory cooling refers to the cooling caused by the droplet-vapor mixture in the region immediately ahead of the wet front, and is described mathematically by two dimensionless constants which characterize its magnitude and the region of influence. The physical model developed to account for precursory cooling consists of an infinitely extended vertical surface with the dry region ahead of the wet front characterized by an exponentially decaying heat flux and the wet region behind the moving film-front associated with a constant heat transfer coefficient. Apart from the two dimensionless constants describing the extent of precursory cooling, the physical problem is characterized by three dimensionless groups: the Peclet number or the dimensionless wetting velocity, the Biot number and a dimensionless temperature. Limiting solutions for large and small Peclet numbers have been obtained utilizing the Wiener-Hopf technique coupled with appropriate kernel substitutions. A semiempirical matching relation is then devised for the entire range of Peclet numbers. Existing experimental data with variable flow rates at atmospheric pressure are very closely correlated by the present model. Finally a comparison is drawn between the one-dimensional limit of the present analysis and the corresponding one-dimensional solution obtained by treating the dry region ahead of the wet front characterized by an exponentially decaying heat transfer coefficient.

Introduction

Surface rewetting refers to the establishing of liquid contact with a solid surface whose initial temperature is higher than the sputtering temperature, the temperature up to which the surface may wet. Due to its application to the emergency core cooling of water reactors in the event of postulated loss-of-coolant accidents, the problem of surface rewetting has gained much attention in recent years. For conduction-controlled rewetting, the one-dimensional conduction model has been quite successful in correlating the experimental data at low coolant flow rates [1–3].[1] In an attempt to correlate the experimental data at high coolant flow rates, several two-dimensional analyses and numerical calculations have appeared recently in the literature [4–8]. These studies show only partial success in correlating the experimental data at high flow rates. This is due to the fact that the effect of the mass flow rate has not been explicitly accounted for and the commonly employed assumption of treating the dry region as adiabatic no longer holds at high coolant flow rates because of the strong influence of the droplet-vapor mixture in the vicinity of the wet front.

Existing studies on the effect of precursory cooling include the one-dimensional work of Sun, Dix and Tien [9] and Chun and Chon [10], and a two-dimensional analysis by Edwards and Mather [11]. The former is not applicable to situations where both the Biot number and the Peclet number are large and two-dimensional effects can not be ignored. The latter study considers exponentially decaying heat fluxes on both upstream and downstream of the wet-front and, thereby, completely decouples the heat transfer inside the solid from outside. Although the study by Edwards and Mather does demonstrate an increase in the wet front velocity due to precursory cooling, it does not depict a clear picture of the role of mass flow rate in the rewetting phenomenon as no quantitative relationship is drawn here between the mass flow rate and the extent of precursory cooling it causes. No attempts were made in their work to correlate the experimental data at varying flow rates. The mathematical solution obtained in this work is implicit and in the form of an infinite series, and

[1] Numbers in brackets designate References at end of paper.

Contributed by the Heat Transfer Division for publication in the JOURNAL OF HEAT TRANSFER. Manuscript received by the Heat Transfer Division December 15, 1975. Paper No. 76-HT-WW.

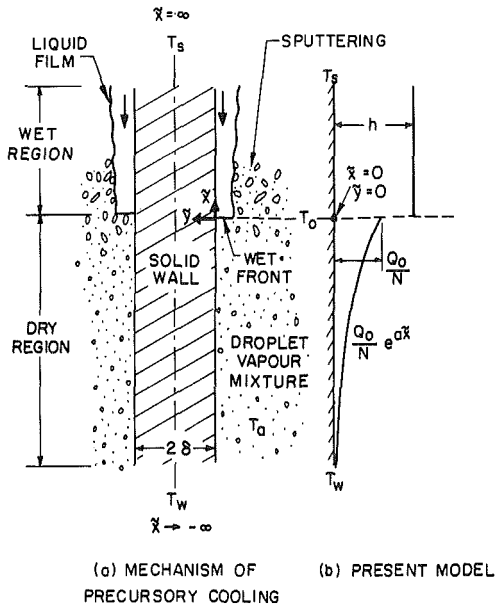

Fig. 1 Falling-film rewetting of a slab and the present model with precursory cooling ahead of the wet front

such a solution, besides being inconvenient in application, characteristically masks the functional dependence of rewetting rate on different parameters.

It is the purpose of the present study to quantitate the effect of mass flow rate in determining the extent of precursory cooling which, in turn, governs the wet front velocity. Asymptotic solutions for small and large Peclet numbers, obtained by applying the Wiener-Hopf technique coupled with the kernel-substitution method [4, 12], are simple in functional form, readily calculable and in close agreement with the available experimental data. A semiempirical matching relation has been established to cover the entire range of Peclet numbers.

Analysis

Physical Model. The physical model under consideration is an infinitely extended vertical slab with the liquid coolant supplied from above as shown in Fig. 1. When the liquid film progresses downward on a vertical hot surface, the surface is first cooled down from its initial wall temperature, T_w, to rewetting temperature, T_0, at which the surface begins to wet. Behind the wet front, the surface temperature drops sharply to the saturation temperature, T_s. To simplify the heat transfer characteristics outside the slab, it is a common practice to assume the region behind the wet front ($\tilde{x} > 0$) associated with a constant heat transfer coefficient, h [1, 2, 4, 6–8]. This assumption is retained in the present model.

The mechanism of precursory cooling in the region ahead of the wet front ($\tilde{x} < 0$) is rather complex. At large flow rates, part of the coolant is sputtered away as droplets which bounce between surfaces, causing precooling of the dry surface ahead of the wet front. Apart from the precooling caused by the direct impingement of small water-droplets on the hot surface ahead of the wet front, the precursory cooling also occurs as a result of convection and radiation from the wall to the surrounding droplet-vapor mixture. The net effect of this complex mechanism of heat transfer in the region ahead of the wet front can be conveniently characterized by an exponentially decaying heat transfer coefficient [9] or by an exponentially decaying heat flux [11]. If the precursory cooling is characterized by an exponentially decaying heat transfer coefficient, it would, then, be necessary to know the variation of the ambient temperature of the droplet-vapor mixture, T_a, with increasing distance from the wet front in order to calculate the wall heat flux. As such information is not easily obtainable in a real situation, the present model characterizes the precursory cooling ahead of the wet front by an exponentially decaying heat flux. Similar to the model advanced previously [9], the magnitude of the precursory cooling is measured by a dimensionless constant, N, which represents as shown in Fig. 1 a fractional drop in the heat flux within an infinitesimally small distance ahead of the wet front. The value of N depends on the coolant mass flow rate. For increasing flow rates, the precursory cooling is enhanced resulting in a smaller N.

In their one-dimensional analysis of precursory cooling, Sun, Dix, and Tien [9] characterized the region ahead of the wet front by an exponentially decaying heat transfer coefficient, assuming, however, the ambient temperature of the droplet-vapor mixture, T_a, to be constant and equal to the saturation temperature, T_s. For large values of θ_1 (high initial dry wall temperatures), their analysis predicted higher values of the Peclet numbers compared to the experimental data of Yamanouchi [2] and Duffey and Porthouse [13]. In Fig. 2 is shown the comparison between their one-dimensional solution and the corresponding one-dimensional solution obtained by considering an exponentially decaying heat flux in the region ahead of the wet front. The comparison is drawn for different values of the Biot number, B, and for different magnitudes of precursory cooling as measured by N, the function representing the exponential decay being exp ($0.05\tilde{x}$) in either case [9, 13]. As seen from Fig. 2, the model with an exponentially varying heat flux in the region ahead of the wet front significantly lowers down the prediction curves in the range of large θ_1, indicating a trend in closer agreement with the experimental data [2, 9, 13]. The detailed comparison of the present model with the

Nomenclature

a = exponential power, Fig. 1
A = constant, equation (11)
A_1 = dimensionless quantity, 3B/(B + 3)
b = dimensionless exponent, $a\delta$
b_1 = dimensionless exponent, $2a\delta$/P
B = Biot number, $h\delta/k$
c = specific heat of solid
D = constant, B/P
h = heat transfer coefficient
$i = (-1)^{1/2}$
k = thermal conductivity of solid
n = arbitrary constant in matching function
N = constant
P = Peclet number, $\rho cu\delta/k$
Q_0 = heat flux at the wet-front, $h(T_0 - T_s)$
Q_0' = constant, equation (36)
t = time
T = temperature
T_a = ambient temperature of droplet-vapor mixture
T_0 = rewetting or sputtering temperature
T_s = saturation temperature
T_w = initial dry wall temperature
u = wetting front velocity
$\tilde{x}$ = axial coordinate, Fig. 1
x = dimensionless axial coordinate, $\tilde{x}/\delta$
$\tilde{y}$ = transverse coordinate, Fig. 1
y = dimensionless transverse coordinate, $\tilde{y}/\delta$
Y = constant, equation (26)
Z = constant, equation (43)
α = transformation variable, equation (12) or (13)
τ = imaginary part of α
δ = one-half slab thickness, Fig. 1
θ = dimensionless temperature, equation (3)
θ_0 = dimensionless rewetting temperature, $(T_w - T_0)/(T_w - T_s)$
θ_1 = dimensionless temperature, $(T_w - T_0)/(T_0 - T_s)$
$\Theta = \Theta_+ + \Theta_-$
Θ_+ = Fourier transform of θ for $x \geq 0$, equation (12) or (37)
Θ_- = Fourier transform of θ for $x < 0$, equation (13) or (38)
λ = constant, equation (20)
ρ = density of solid
ψ = mass flow rate per unit perimeter

Subscripts

x, y = derivatives with respect to x and y, respectively

available experimental data is made later with the two-dimensional results derived here. As expected, the difference between the two models shown in Fig. 2, decreases with increasing N as in the limit of $N \to \infty$, both the models have to reduce to a common result of one-dimensional rewetting with no precursory cooling [2].

Mathematical Formulation. The transient two-dimensional conduction equation in a coordinate system moving with the wet front at a constant velocity u can be written as [4–8]

$$k\left[\frac{\partial^2 T}{\partial \tilde{x}^2}+\frac{\partial^2 T}{\partial \tilde{y}^2}\right]=\rho c u\frac{\partial T}{\partial \tilde{x}} \tag{1}$$

Equation (1) can be expressed in the following dimensionless form:

$$\theta_x-\frac{1}{P}(\theta_{xx}+\theta_{yy})=0 \tag{2}$$

where

$$\theta\equiv\frac{T_w-T}{T_w-T_s},\quad x\equiv\frac{\tilde{x}}{\delta},\quad y\equiv\frac{\tilde{y}}{\delta} \tag{3}$$

$$\mathrm{P}\equiv\frac{\rho c u\delta}{k}\ (\text{Peclet number}) \tag{4}$$

and subscripts x and y in equation (2) denote partial derivatives with respect to x and y, respectively. The boundary conditions associated with equation (2) are:

$$x\to-\infty \qquad \theta=0 \tag{5}$$

$$x\to+\infty \qquad \theta=1 \tag{6}$$

$$y=0,\ x\geq 0 \qquad \theta_y=\mathrm{B}(\theta-1) \tag{7}$$

$$y=0,\ x<0 \qquad \theta_y=Ae^{bx} \tag{8}$$

$$y=1,\ \text{all } x \qquad \theta_y=0 \tag{9}$$

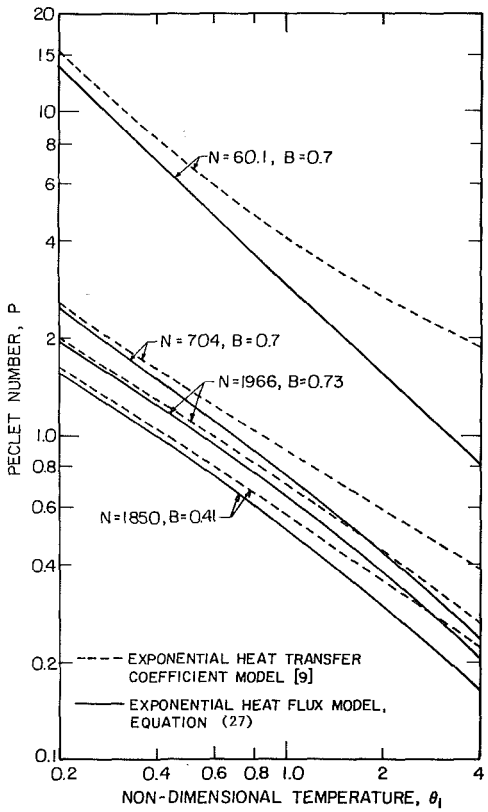

Fig. 2 Comparison of the one-dimensional solutions obtained with the exponential heat flux model and the exponential heat transfer coefficient model

$$x=0,\ y=0 \qquad \theta=\theta_0 \tag{10}$$

where

$$A\equiv\frac{Q_0\delta}{Nk(T_s-T_w)}=\left(\frac{\mathrm{B}}{N}\right)\left(\frac{T_0-T_s}{T_s-T_w}\right),$$

$$\mathrm{B}\equiv\frac{h\delta}{k}\ (\text{Biot number}) \tag{11}$$

and

$$b\equiv a\delta$$

It does not seem possible to get a general analytical solution to equation (2) with its associated boundary conditions as given by equations (5)–(10). A numerical solution, though possible, would not reveal any functional relationship among various system parameters. At the present state of knowledge on surface rewetting with precursory cooling, it seems logical to seek approximate analytical solutions in search for simple functional forms that would reveal the effect of various system parameters on the rewetting rate. This is achieved by first obtaining the asymptotic solutions, applying the Wiener-Hopf method coupled with appropriate kernel substitutions, for the two cases of very small and very large Peclet numbers, and then matching these limiting solutions in a semiempirical manner for the entire range of Peclet numbers.

Solution for the Limiting Case of Small Peclet Numbers ($\mathrm{P}\ll 1$). Following the Wiener-Hopf technique, equation (2) is reduced to an ordinary differential equation by use of the Fourier transform defined as:

$$\Theta_+(\alpha,y)=\int_0^\infty e^{i\alpha x}\theta(x,y)dx \tag{12}$$

$$\Theta_-(\alpha,y)=\int_{-\infty}^0 e^{i\alpha x}\theta(x,y)dx \tag{13}$$

The inverse transform to equations (12) and (13) is

$$\theta(x,y)=\frac{1}{2\pi}\int_{-\infty+i\tau}^{\infty+i\tau}\Theta(\alpha,y)e^{-i\alpha x}d\alpha$$

(τ = real, positive) (14)

where

$$\Theta(\alpha,y)=\Theta_+(\alpha,y)+\Theta_-(\alpha,y)$$

Applying the previously defined Fourier transform, equation (2) and its associated boundary conditions given by equations (5)–(9) become:

$$\frac{d^2\Theta}{dy^2}-\alpha(\alpha-i\mathrm{P})\Theta=0 \tag{15}$$

$$\frac{d\Theta_+}{dy}(\alpha,0)=\mathrm{B}\left[\Theta_+(\alpha,0)+\frac{1}{i\alpha}\right] \tag{16}$$

$$\frac{d\Theta_-}{dy}(\alpha,0)=A/(b+i\alpha) \tag{17}$$

$$\frac{d\Theta}{dy}(\alpha,1)=0 \tag{18}$$

Solving equations (15)–(18) gives

$$\Theta_+(\alpha,0)+\Theta_-(\alpha,0)$$

$$=\left(\frac{-\mathrm{B}\coth\lambda}{\lambda}\right)\left[\Theta_+(\alpha,0)+\frac{1}{i\alpha}\right]-\frac{A\coth\lambda}{\lambda(b+i\alpha)} \tag{19}$$

where

$$\lambda=(\alpha(\alpha-i\mathrm{P}))^{1/2} \tag{20}$$

Equation (19) is equivalent to an integral equation and the term $(\coth\lambda/\lambda)$ is the kernel function whose transform must be decomposed in accordance with the Wiener-Hopf method. Exact decomposition of this kernel in terms of simple functions is unlikely to exist [4]. However, in view of the major contribution of the kernel being in the neighborhood of the singular points corresponding to $\lambda=0$, it should

be a good approximation to represent coth λ by the first two terms in the asymptotic series expansion near $\lambda = 0$:

$$\coth \lambda = \frac{1}{\lambda} + \frac{\lambda}{3} + 0(\lambda^3) \tag{21}$$

Substitution of equation (21) into equation (19), along with the standard application of the Wiener-Hopf method, enables explicit determination of $\Theta_+(\alpha, 0)$ and $\Theta_-(\alpha, 0)$ whose inverse Fourier transform gives the surface temperature distribution as

For $x \geq 0$;

$$\theta(x, 0) = 1 + \left[\frac{A_1 + A_1 P[(P/2) + \sqrt{(P/2)^2 + A_1}]/3}{[(P/2) + \sqrt{(P/2)^2 + A_1}]^2} - 1\right] \times \exp\{(P/2) - \sqrt{(P/2)^2 + A_1}\}x - \left(\frac{3A}{B+3}\right)\left[\frac{1}{b[(P/2) + \sqrt{(P/2)^2 + A_1}]}\right] \times \exp\{(P/2) - \sqrt{(P/2)^2 + A_1}\}x \tag{22}$$

For $x \leq 0$;

$$\theta(x, 0) = \frac{A_1}{[(P/2) + \sqrt{(P/2)^2 + A_1}]^2} \exp(Px) - \frac{(b^2 - bP - 3)(A/3)}{b(b - P)} \times \exp(bx) - \left[\frac{(A/3)(b^2 - bP - 3)\{(P/2) - \sqrt{(P/2)^2 + A_1}\}}{(P - b)b\{b - [(P/2) + \sqrt{(P/2)^2 + A_1}]\}} + \frac{(A_1 - 3)(A/3)}{\{(P/2) + \sqrt{(P/2)^2 + A_1}\}\{(P/2) + \sqrt{(P/2)^2 + A_1} - b\}}\right] \times \exp(Px) \tag{23}$$

where

$$A_1 = 3B/(B + 3) \tag{24}$$

At the wet front, the temperature is

$$\theta_0 = \theta(0, 0) = \frac{A_1}{[(P/2) + \sqrt{(P/2)^2 + A_1}]^2} - \frac{3A}{b(B+3)[(P/2) + \sqrt{(P/2)^2 + A_1}]} + 0(P, B/N) \tag{25}$$

The discrepancy in $\lim_{x \to +0} \theta(x, 0)$ and $\lim_{x \to -0} \theta(x, 0)$ results from the asymptotic approximation of the kernel and is represented by the term $O(P,B/N)$ in equation (25), signifying that the difference is of the order of the Peclet number and the quantity B/N. However, the said discrepancy becomes neglegibly small in the limiting cases of either very small Biot numbers ($B \ll 1$) or very small Peclet numbers ($P \ll 1$), and the equation (25) then yields the following asymptotic solution for the dimensionless wet-front velocity:

$$P = [Y - (A_1/Y)] \tag{26}$$

where

$$Y = \frac{1}{2}\left[\frac{A_1}{Nb}\left(\frac{1 - \theta_0}{\theta_0}\right) + \sqrt{\frac{A_1^2}{N^2 b^2}\left(\frac{1 - \theta_0}{\theta_0}\right)^2 + \frac{4A_1}{\theta_0}}\right]$$

Equation (26) is an explicit result for the wet-front velocity in terms of the Biot number B and the system parameters N, b, and θ_0. In the limit of $N \to \infty$ (no precursory cooling), $Y \to (A_1/\theta_0)^{1/2}$ and equation (26) yields

$$\frac{\sqrt{A_1}}{P} = \theta_0^{1/2}(1 - \theta_0)^{-1}$$

which is the same result as derived by Tien and Yao [4] for the case without precursory cooling. It is also interesting to consider the limiting case of $B \ll 1$. In this limit, $A_1 = 3B/(B + 3) \to B$ and equation (26) then yields:

$$P = [Y - (B/Y)] \tag{27}$$

where

$$Y = \frac{1}{2}\left[\frac{B}{Nb}\left(\frac{1 - \theta_0}{\theta_0}\right) + \sqrt{\frac{B^2}{N^2 b^2}\left(\frac{1 - \theta_0}{\theta_0}\right)^2 + \frac{4B}{\theta_0}}\right]$$

Equation (27) can be derived independently by the one-dimensional analysis of precursory cooling with the physical model proposed here. This indicates, as anticipated, that one-dimensional solution is valid only in the limit of very small Biot numbers. As expected, the limit of equation (27) for $N \to \infty$ gives the well known one-dimensional solution [1–3] for the case without precursory cooling.

Solution for the Limiting Case of Large Peclet Numbers ($P \gg 1$). For the case of large Peclet numbers, the thermal region of interest lies in the immediate vicinity of the wet front [4]. Due to the smallness of this region, the parameter δ does not play any role in the problem and the independent nondimensional variables x and y are defined as

$$x = \frac{\tilde{x}}{(2\delta/P)} = \frac{\tilde{x}}{(2k/\rho c u)}; \quad y = \frac{\tilde{y}}{(2\delta/P)} = \frac{\tilde{y}}{(2k/\rho c u)} \tag{28}$$

Equation (1) becomes

$$2\theta_x - (\theta_{xx} + \theta_{yy}) = 0 \tag{29}$$

The boundary conditions associated with equation (29) are

$$x \to -\infty \qquad \theta = 0 \tag{30}$$

$$x \to +\infty \qquad \theta \text{ is bounded} \tag{31}$$

$$y = 0, x \geq 0 \qquad \theta_y = 2D(\theta - 1) \tag{32}$$

$$y = 0, x \leq 0 \qquad \theta_y = Q_0' e^{b_1 x} \tag{33}$$

$$y \to \infty \qquad \theta = 0 \tag{34}$$

$$x = 0, y = 0 \qquad \theta = \theta_0 \tag{35}$$

where

$$D = \frac{B}{P} = \frac{h}{\rho c u}; \quad b_1 = \frac{2a\delta}{P}, \quad Q_0' = \frac{2\delta Q_0}{NPk(T_s - T_w)} \tag{36}$$

For subsequent algebraic convenience, the Fourier transform employed here is slightly different from the one used earlier for the case of $P \ll 1$. The modified Fourier transform is

$$\Theta_+(\alpha, y) = \int_0^\infty e^{(i\alpha - 1)x}\theta(x, y)dx \tag{37}$$

$$\Theta_-(\alpha, y) = \int_{-\infty}^0 e^{(i\alpha - 1)x}\theta(x, y)dx \tag{38}$$

The inverse transform of equations (37) and (38) is

$$\theta(x, y) = \frac{1}{2\pi}\int_{-\infty}^{\infty} e^{-(i\alpha - 1)x}\Theta(\alpha, y)d\alpha \tag{39}$$

Following a similar procedure as in the case of $P \ll 1$, the solution of equations (29)–(34) gives

$$\Theta_+(\alpha, 0) + \Theta_-(\alpha, 0) = \frac{-2D}{\sqrt{\alpha^2 + 1}}\left[\Theta_+(\alpha, 0) - \left(\frac{i}{\alpha + i}\right)\right] + \frac{Q_0'}{\sqrt{\alpha^2 + 1}}\left[\frac{i}{\alpha - i(b_1 - 1)}\right] \tag{40}$$

Using the standard approximate method of kernel substitution [12], the kernel $[1/(\alpha^2 + 1)^{1/2}]$ in equation (40) is replaced by $[2/(\alpha^2 + 2)]$, the Fourier transforms of which have the identical area and the first moment. This substitution of the approximate kernel in equation (40), along with the standard application of the Wiener-Hopf technique, enables explicit determination of $\Theta_+(\alpha, 0)$ and $\Theta_-(\alpha, 0)$ whose inverse Fourier transforms give the surface temperature distributions for the regions $x \geq 0$ and $x \leq 0$, respectively,

$$\theta(x, 0) = \left(\frac{4D}{4D + 1}\right) - \left[\frac{2(2 + \sqrt{2})D}{(4D + 1)(1 + \sqrt{2D + 1})} + \frac{\sqrt{2}\,Q_0'}{\{(b_1 - 1) + \sqrt{2}\}(1 + \sqrt{2D + 1})}\right] \times \exp[-(\sqrt{4D + 2} - 1)x] \qquad (x \geq 0) \tag{41}$$

$$\theta(x,0) = \left[\frac{2\sqrt{2}\,D}{(1+\sqrt{4D+2})(1+\sqrt{2D+1})} + \frac{2\sqrt{2}\,Q_0'(1-\sqrt{2D+1})}{\{2-(b_1-1)^2\}\{(b_1-1)-\sqrt{4D+2}\}} + \frac{\sqrt{2}\,Q_0'}{(\sqrt{2D+1}+1)\{\sqrt{4D+2}-(b_1-1)\}}\right] \times \exp\left(\sqrt{2}+1\right)x - \frac{2Q_0'}{[2-(b_1-1)^2]}\exp(bx)\ (x \le 0) \quad (42)$$

It is easy to visualize at this point that in the limit $N \to \infty$, Q_0' tends to zero and equations (41) and (42) reduce to the corresponding results of Tien and Yao [4] for the case without precursory cooling. Finally, applying the condition $\theta = \theta_0$ at $x = 0$ to either equation (41) or (42) gives the following explicit solution for the dimensionless wet-front velocity.

$$\mathrm{P} = 2\mathrm{B}/(Z^2-1) \quad (43)$$

where Z is the real and positive root of the cubic equation given in the following

$$Z^3 + \left[\frac{\sqrt{2}\,\mathrm{B}}{Nb} - \frac{(\sqrt{2}+\theta_0)}{\sqrt{2}\,(1-\theta_0)}\right]Z^2 + \left[\left(\frac{N-1}{N}\right)(\sqrt{2}-1)\frac{\mathrm{B}}{b} - 1\right]Z + \left[\left(\frac{N-1}{N}\right)\frac{\mathrm{B}}{b} + \left(\frac{1}{1-\theta_0}\right)\left\{\frac{\theta_0}{\sqrt{2}} + 1 - \frac{(2-\theta_0)\mathrm{B}}{\sqrt{2}\,b}\right\}\right] = 0$$

The solution of the foregoing equation is available in any standard mathematical handbook [14, 15].

Semiempirical Matching. Equations (26) and (43) contain the limiting relations for either very small or very large values of the Peclet number. In practice, however, the Peclet number encountered often falls in the intermediate range [13, 16]. Therefore, it is desirable to establish a continuous expression for the entire range of the Peclet number. The semiempirical matching

$$\frac{nP}{(1-nP^2)} = \frac{n\left(\dfrac{Z^2-1}{2\mathrm{B}}\right)[Y-(A_1/Y)]}{\left(\dfrac{Z^2-1}{2\mathrm{B}}\right) - n[Y-(A_1/Y)]} \qquad (n<1)$$

provides a family of curves corresponding to different values of n, which satisfy both the limits in equations (26) and (43) and allows a smooth continuous relation for all the values of the Peclet number. In particular, the relation with $n = 0.01$

$$\frac{0.01\mathrm{P}}{1-0.01\mathrm{P}^2} = \frac{0.01\left(\dfrac{Z^2-1}{2\mathrm{B}}\right)[Y-(A_1/Y)]}{\left(\dfrac{Z^2-1}{2\mathrm{B}}\right) - 0.01\,[Y-(A_1/Y)]} \quad (44)$$

agrees well with the available experimental data of Yamanouchi [2], and Duffey and Porthouse [13]. In Fig. 3, equation (44) is shown along with the asymptotic two-dimensional solutions contained in equations (26) and (43). Also shown in Fig. 3 is the corresponding one-dimensional solution, equation (27). All the curves in Fig. 3 are drawn for a fixed values of $B = 0.5$ and $b = 0.005$, with varying magnitudes of precursory cooling represented by $N = 1$, 10 and 100. The purpose of Fig. 3 is to reveal the nature of the matching relation, equation (44), and to demonstrate the inadequacy of the one-dimensional solution for large Peclet numbers. It shows that one-dimensional solution differs significantly from a two-dimensional solution in the range of large Peclet numbers.

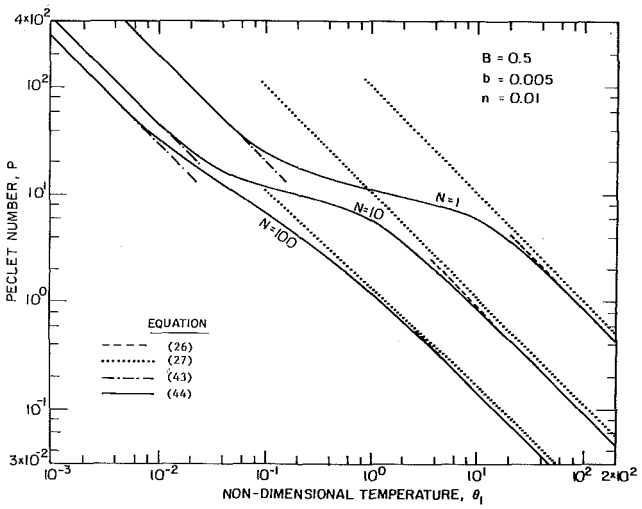

Fig. 3 Variation of the Peclet number in falling film rewetting for different magnitudes of precursory cooling

Results and Discussion

The approximate analytical results presented in equations (26), (43), and (44) indicate that in the present analysis, there exist two independent dimensionless parameters θ_0 and B, and two dimensionless constants N and b. The latter two constants characterize the effect of precursory cooling, N signifying its magnitude and b representing its region of influence. To visualize the significance of the nondimensional temperature, a slightly modified definition $\theta_1 = \theta_0/(1-\theta_0) = (T_w - T_0)/(T_0 - T_s)$ reveals θ_1 to characterize the dry wall temperature far downstream relative to the temperature at the wet front. The Biot number, B, represents the resistance to heat transfer inside the solid wall relative to that on the outside.

The effect of precursory cooling on the wet-front velocity is very well depicted in Fig. 3, from which it is seen that precursory cooling can substantially increase the film rewetting rate. The number of droplets generated in the sputtering region increases with increasing mass flow rate, resulting in stronger precursory cooling and a decrease in the value of N. Therefore, in Fig. 3 the curve with $n = 1$ is much higher than the curve with $N = 100$, the former conveying stronger precursory cooling. The detailed information about the magnitudes of N and b has to emerge from the experimental results.

While the present analysis is generally applicable to all coolants, the experimental data compared here refers to experiments with water as coolant in atmospheric steam environments [2, 13]. To compare the present model with the experimental data, the values of sputtering temperature, T_0, heat transfer coefficient, h, and the exponent in the decay of precursory cooling, a, are kept constant, a priori with an adjustable N. In the absence of any definitive information available on the variation of heat flux ahead of the wet front, the constant a in the exponential decay function is taken as 0.05 cm^{-1}, similar to that suggested in an earlier work [9]. Specification of the wet-front temperature, T_0, is more difficult because of the ambiguity that exists in literature regarding the precise knowledge of boiling phenomena at the wet front [2, 9, 13, 17]. However, for the comparison drawn here between the present prediction, equations (26), (43), and (44), and the experimental data of Yamanouchi [2] and Duffey and Porthouse [13], the value of T_0 is taken as 260°C which corresponds to the temperature at the minimum film boiling heat flux [3, 9]. The value of heat transfer coefficient h is chosen as 3.0×10^3 Btu/hr-ft^2-F°, this value being comparable to the average boiling heat transfer coefficient based on the maximum and the minimum heat fluxes of pool boiling [9].

Figs. 4, 5, and 6 show very good agreement between the prediction and the experimental results of Yamanouchi [2] and Duffey and Porthouse [13]. Not enough experimental data are available at high enough Peclet numbers for the asymptotic solution in the limiting case of large Peclet numbers, equation (43), to be directly applicable. In Figs. 4–6, the experimental data for $\mathrm{P} \ll 1$ are correlated by the corresponding asymptotic solution in that limit, equation (26), while the rest of the experimental data in the intermediate range of Peclet numbers are correlated by the semiempirical matching relation,

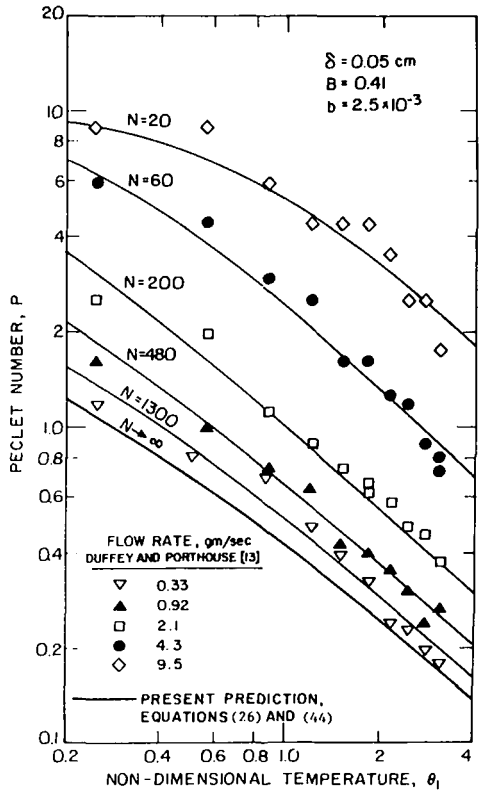

Fig. 4 Comparison of the predicted dimensionless wet front velocity with the experimental results (δ = 0.05 cm) of Duffey and Porthouse [13]

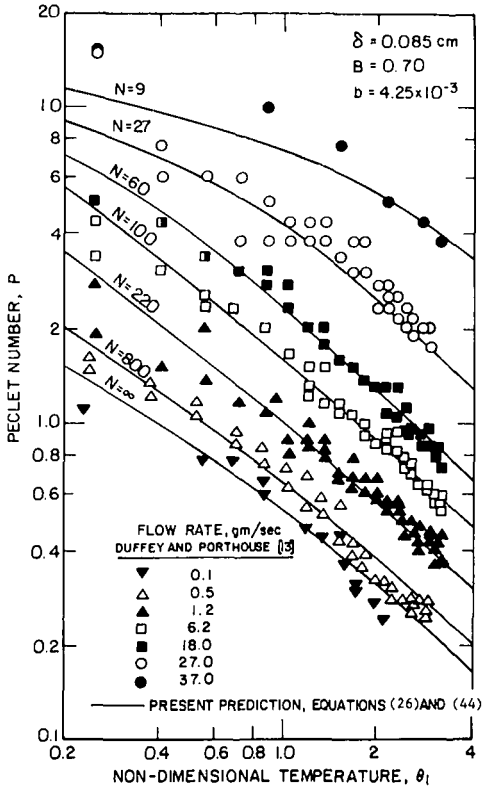

Fig. 5 Comparison of the predicted dimensionless wet front velocity with the experimental results (δ = 0.085 cm) of Duffey and Porthouse [13]

equation (44), which implicitly makes use of the analytic results derived for the two asymptotic limits.

Besides the scatter of the data, typical of experimental measurements on rewetting, it is inferred from the comparison shown in Figs. 4–6, that the present two-dimensional model is very accurate in describing the effect of the mass flow rate on falling film rewetting. The fact, as demonstrated here, that the effect of the coolant flow rate on rewetting is manifested in precursory cooling rather than in the sputtering heat transfer coefficient is further substantiated by Thompson's analysis [18] of the Harwell and Winfrith experimental results [19–21]. The experimental data shown in Figs. 4–6 are for the Biot numbers of 0.41, 0.7, and 0.73 with the Peclet number ranging from 0.1 to 15. In accordance with the findings of the present work, the one-dimensional analysis of precursory cooling is not adequate in correlating the presented experimental data as the Biot number and the Peclet number are not small enough to justify the neglect of two-dimensional effects.

It is of interest to correlate N with the mass flow rate for the data presented in Figs. 4–6. In accordance with the physical model proposed here, N should tend to 1.0 for the limiting case of very high mass flow rate ($\psi \to \infty$). As shown in Fig. 7, the N values for three test sections with different diameters can be approximately correlated by the following relation:

$$N = \left(\frac{160}{\psi} + 1\right) \tag{45}$$

where ψ in gm/cm-s is the spray flow rate per unit perimeter. The scatter of data at high flow rates is due to the uncertainty in the measurement of rather fast wet-front velocities at such operating conditions. This uncertainty, in turn, affects the accuracy with which N can be determined corresponding to a given mass flow rate. Also it is worth mentioning, at this point, that the rewetting temperature and the sputtering heat transfer coefficient are indeed very difficult to measure accurately. The values of these parameters, along with that of the exponent a in the description of precursory cooling, are only the best possible representative estimates based on rather limited experimental evidence presently available on precursory cooling.

The foregoing concludes the discussion of the experimental data at atmospheric conditions. We have not included the Elliott-Rose

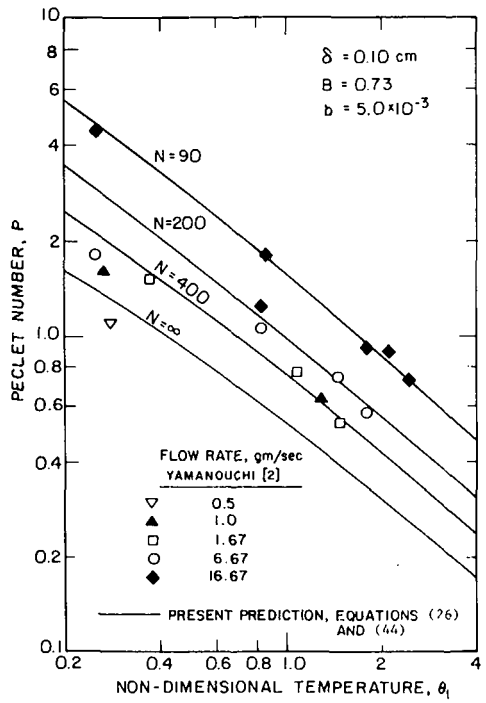

Fig. 6 Comparison of the predicted dimensionless wet front velocity with the experimental data (δ = 0.10 cm) of Yamanouchi [2]

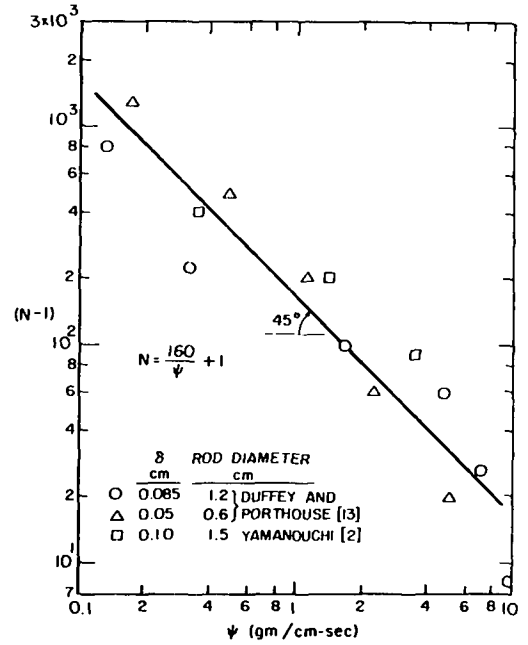

Fig. 7 Variation of *N* with the spray flow rate per unit perimeter

experimental data [20, 21] at high system pressures because the effect of mass flow rate at such operating conditions is so small that it is usually masked by the scatter in the data, as is indicated in their study. Indeed, the Duffey-Porthouse data, compared in the present study, cover a much wider range of flow rates (with a factor of 300) than that in the Elliott-Rose data (with a factor of 4). For high system pressures, the effect of mass flow rate on wet-front velocities is much less significant than the effect of increased sputtering temperatures. This is demonstrated in Thompson's study [18] wherein he correlated the experimental data of Elliott and Rose [20, 21] and Bennett [19] by incorporating the effect of increased sputtering temperatures at high pressures and ignoring the effect of mass flow rate. The findings of Elliott and Rose as well as those of S. K. W. Yu have been discussed in further details in a recent report [16].

Conclusions

1 When a liquid film progresses downward on a very hot vertical surface, the droplets generated at the sputtering front cause precooling of the dry surface ahead of the wet front. The extent of this precursory cooling increases with increasing mass flow rates. The heat transfer mechanism from the dry wall ahead of the wet front to the surrounding droplet-vapor mixture is rather complex but can successfully be modelled with an exponentially decaying heat flux.

2 Precursory cooling increases the wet-front velocity substantially. At large mass flow rates, the wet front velocity, indeed, is so high that the one-dimensional analysis of precursory cooling is inadequate. The two-dimensional analysis of rewetting with precursory cooling becomes essential in the prediction of wet-front velocities at such flow rates.

3 Assuming the average boiling heat transfer coefficient in the sputtering region to be invariant with the mass flow rate, the available experimental data on rewetting obtained under the atmospheric steam environment with variable flow rates are very closely correlated with the two-dimensional analysis of precursory cooling presented here.

References

1 Semeria, R., and Martinet, B., "Calefaction Spots on a Heating Wall; Temperature Distribution and Resorption," Symposium on Boiling Heat Transfer in Steam-Generating Units and Heat Exchangers, Manchester, England, Sept. 1965.

2 Yamanouchi, A., "Effect of Core Spray Cooling in Transient State After Loss-of-Coolant Accident," *Journal of Nuclear Science and Technology*, Vol. 5, 1968, pp. 547–558.

3 Sun, K. H., Dix, G. E., and Tien, C. L., "Cooling of a Very Hot Vertical Surface by a Falling Liquid Film," JOURNAL OF HEAT TRANSFER, TRANS. ASME, Series C, Vol. 96, 1974, pp. 126–131.

4 Tien, C. L., and Yao, L. S., "Analysis of Conduction-Controlled Rewetting of a Vertical Surface," JOURNAL OF HEAT TRANSFER, TRANS. ASME, Series C, Vol. 97, 1975, pp. 161–165.

5 Thompson, T. S., "An Analysis of the Wet-Side Heat Transfer Coefficient During Rewetting of a Hot Dry Patch," *Nuclear Engineering and Design*, Vol. 22, 1972, pp. 212–224.

6 Duffey, R. B., and Porthouse, D. T. C., "The Physics of Rewetting in Water Reactor Emergency Core Cooling," *Nuclear Engineering and Design*, Vol. 25, 1973, pp. 379–394.

7 Dua, S. S., and Tien, C. L., "A Generalized Two-Parameter Relation for Conduction-Controlled Rewetting of A Hot Vertical Surface" to appear in the *International Journal of Heat and Mass Transfer*.

8 Coney, M. W. E., "The Calculation of the Rate of Rewetting of Hot Fuel Rods by Emergency Cooling Systems in Water Reactors," *Nuclear Engineering and Design*, Vol. 31, No. 2, 1974, pp. 246–257.

9 Sun, K. H., Dix, G. E., and Tien, C. L., "Effect of Precursory Cooling on Falling-Film Rewetting," JOURNAL OF HEAT TRANSFER, TRANS. ASME, Series C, Vol. 97, 1975, pp. 360–365.

10 Chun, M. H., and Chon, W. Y., "Analyses of Rewetting in Water Reactor Emergency Core Cooling Inclusive of Heat Transfer in the Unwetted Region," ASME Paper No. 75-WA/HT-32, presented at Winter ASME Annual Meeting, Houston, Texas, Nov. 30–Dec. 4, 1975.

11 Edwards, A. R., and Mather, D. J., "Some U.K. Studies Related to the Loss-of-Coolant Accident," *Proceedings of the Tropical Meeting on Water Reactor Safety*, Salt Lake City, Mar. 26–28, 1973, pp. 720–739.

12 Carrier, G. F., Krook, M., and Pearson, C. E., *Functions of a Complex Variable*, McGraw-Hill, New York, 1966.

13 Duffey, R. B., and Porthouse, D. T. C., "Experiments on the Cooling of High Temperature Surfaces by Water Jets and Drops," Report No. RD/B/N2386, Berkeley Nuclear Laboratories, England, Aug. 1972.

14 Spiegel, M. R., *Mathematical Handbook of Formulas and Tables*, McGraw-Hill, New York, 1968.

15 Selby, S. M., *CRC Standard Mathematical Tables*, The Chemical Rubber Co., Ohio, 1973.

16 Butterworth, D., and Owen, R. G., "The Quenching of Hot Surfaces by Top and Bottom Flooding—A Review," Report No. AERE-R7992, AERE Harwell, Oxfordshire, England, Mar. 1975.

17 Howard, P. A., Linehan, J. H., and Grolmes, M. A., "Experimental Study of the Stationary Boiling Front in Liquid Film Cooling of a Vertical Heated Rod," CSChE/ME Paper No. 75-HT-14, presented at the *Fifteenth National Heat Transfer Conference*, San Francisco, Aug. 10–13, 1975.

18 Thompson, T. S., "Rewetting of a Hot Surface," presented at the 5th International Heat Transfer Conference, Tokyo, Sept. 1974.

19 Bennett, A. W., Hewitt, G. F., Kearsey, H. A., and Keeys, R. K. F., "The Wetting of Hot Surfaces by Water in a Steam Environment at High Pressure," U.K.A.E.A. Report No. AERE-R5146, 1966.

20 Elliott, D. F., and Rose, P. W., "The Quenching of a Heated Surface by a Film of Water in a Steam Environment at Pressures up to 53 bar," U.K.A.E.A. Report No. AEEW-M976, 1970.

21 Elliott, D. F., and Rose, P. W., "The Quenching of a Heated Zircaloy Surface by a Film of Water in a Steam Environment at Pressures up to 53 bar," U.K.A.E.A. Report No. AEEW-M-1027, 1971.

K. H. Sun
Mem. ASME

J. M. Gonzalez-Santalo[1]
Nuclear Energy Systems Division
General Electric Co.,
San Jose, Calif.

C. L. Tien,
Department of Mechanical Engineering,
University of California, Berkeley, Calif.
Fellow ASME

Calculations of Combined Radiation and Convection Heat Transfer in Rod Bundles Under Emergency Cooling Conditions

A model has been developed to calculate the heat transfer coefficients from the fuel rods to the steam-droplet mixture typical of Boiling Water Reactors under Emergency Core Cooling System (ECCS) operation conditions during a postulated loss-of-coolant accident. The model includes the heat transfer by convection to the vapor, the radiation from the surfaces to both the water droplets and the vapor, and the effects of droplet evaporation. The combined convection and radiation heat transfer coefficient can be evaluated with respect to the characteristic droplet size. Calculations of the heat transfer coefficient based on the droplet sizes obtained from the existing literature are consistent with those determined empirically from the Full-Length-Emergency-Cooling-Heat-Transfer (FLECHT) program. The present model can also be used to assess the effects of geometrical distortions (or deviations from nominal dimensions) on the heat transfer to the cooling medium in a rod bundle.

Introduction

Spray cooling is one of the important emergency core cooling systems (ECCS) for Boiling Water Reactors (BWR) during the hypothetical loss-of-coolant accident (LOCA). Extensive experiments have been conducted to demonstrate its effectiveness under simulated LOCA conditions [1 3].[2] At the same time continuing efforts have been made, both experimentally and theoretically [4–7], to enhance the fundamental understanding of the thermal-hydraulic phenomena occurring during spray cooling.

In the early stage of the emergency spray cooling process, part of the injected water droplets fall through the fuel bundle while others are deposited on the upper portion of the channel wall and rod surfaces forming liquid films that advance downward to quench the hot surfaces [4]. In the region immediately downstream of the sputtering quench front, the droplets ejected from the sputtering region bounce around the surfaces, precooling the surfaces ahead of the quenching front [5]. Farther downstream of the front, typically the middle and lower part of the bundle, the droplets fall straight downward. An upward vapor flow is generated as the result of vaporization of the water droplets. In this region, the vapor and droplets serve as a heat sink for cooling the surfaces and removing the decay heat. The vapor-droplet heat transfer in the middle and lower part of the bundle is of our primary interest since it governs the peak fuel cladding temperature in the emergency spray cooling transient. Typically, the heat transfer coefficient in the region is an order of magnitude less than that in the precursory cooling region which in turn is an order of magnitude less than that in the sputtering region.

A typical model [2, 3] for predicting the fuel cladding temperature during the core spray cooling transient consists of a channel wetting correlation, a surface-to-surface radiation model for the rod bundle, and convection heat transfer coefficients that were empirically determined for different regions of the bundle. This approach is empirical and does not account separately for the individual heat transfer mechanisms associated with the cooling process, such as vapor convection, radiation to vapor and droplets, and evaporation of droplets. The purpose of the present study is to investigate these individual heat transfer mechanisms. A model which accounts for radiation and convection to the vapor-droplet medium has been developed to evaluate analytically the heat transfer coefficient during core spray cooling.

[1] Presently chairman of Departamento de Energia, Universidad Autonoma Metropolitana-Azcapotzalco, Mexico 16, D.F.

[2] Numbers in brackets designate References at end of paper.

Contributed by The Heat Transfer Division of THE AMERICAN SOCIETY OF MECHANICAL ENGINEERS at the AIChE-ASME National Heat Transfer Conference, San Francisco, Calif., August 10–13, 1975. Revised manuscript received by the Heat Transfer Conference, November 18, 1975. Paper No. 75-HT-64.

Physical Model

The thermal-hydraulic phenomena in a rod bundle during spray cooling are inherently complex. To simplify the problem, the rod bundle will be treated as a system of parallel subchannels, with each subchannel representing a unit cell. For a Boiling Water Reactor (BWR) bundle, a unit cell is defined as the open space among four adjacent rods. The physical system under consideration is the unit cell which is characterized by a circular tube of hydraulic diameter D_h. The hydraulic diameter approach is a convenient approximation to characterize flow and heat transfer in a channel of noncircular cross section [8]. The possible interactions among the adjacent unit cells are not treated here.

During the core spray cooling process, the updrafting steam velocities through the bundle are typically of the order of 9 ft/s (2.74 M/s),[3] a value which justifies the assumption of laminar flow.

With these considerations, the relevant heat transfer mechanisms to the spray cooling process can be listed as follows:

1 Convection to the vapor.
2 Radiation from the walls to the vapor.
3 Radiation from the walls to the droplets.
4 Vapor-droplet heat transfer.

The energy equation for this system can be derived for a control volume as shown in Fig. 1. An energy balance for this vapor-phase control volume under steady-state conditions yields

$$E_1 + E_3 + E_4 = E_2 + E_5 \tag{1}$$

The energy terms, E_1 and E_2, correspond to conduction through the vapor, and can be expressed as:

$$E_1 = -\alpha k(\partial T/\partial r)2\pi r\Delta z \tag{2}$$

$$E_2 = -\alpha k(\partial T/\partial r)2\pi r\Delta z - \partial/\partial r(2\pi rk\partial T/\partial r)\alpha\Delta r\Delta z \tag{3}$$

The heat transferred by radiation from the walls and the droplets to the vapor is denoted by E_3. It can be defined in terms of ϕ_{wv} and $\phi_{\ell v}$, the equivalent quantities of heat absorption per unit volume, which are discussed in detail in Appendix A. Thus,

$$E_3 = (\phi_{wv} + \phi_{\ell v})2\pi r\Delta r\Delta z \tag{4}$$

The quantities, E_4 and E_5, represent the energy transported by the vapor flow across the control volume and can be expressed as

$$E_4 = W_v h_v \tag{5}$$

$$E_5 = W_v h_v + \partial/\partial z(W_v h_v)\Delta z \tag{6}$$

Substituting equations (2)–(6) in equation (1) results in the following expression:

$$(\alpha k/r)\partial/\partial r(r\partial T/\partial r) + \phi_{wv} + \phi_{\ell v} = \partial/\partial z(W_v h_v)/2\pi r\Delta r \tag{7}$$

where k is assumed to be independent of temperature.

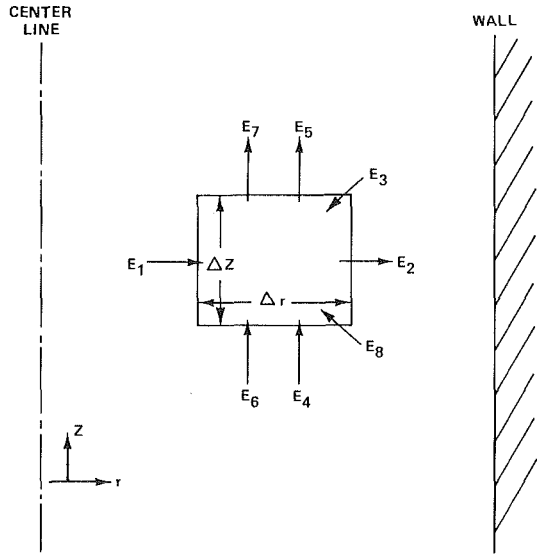

Fig. 1 Energy balance for control volume

[3] In BWR Core Spray Distribution test, the design basis for updraft is 8 ft/s of air [14] which is equivalent to approximately 10 ft/s (based on channel cross-sectional area of 0.193 ft^2) of steam at the bundle exit. Since the steam updraft is zero at the bottom of the bundle during the ECCS test, it is reasonable to assume a typical value of 9 ft/s (based on bundle cross-sectional area of 0.108 ft^2) for middle and lower half regions of the bundle.

Nomenclature

A_c = open cross-sectional area of the bundle
a = absorption coefficient
B = radiosity
C_p = thermal capacitance
D, D_h = rod diameter and hydraulic diameter of a unit cell, respectively
d = droplet diameter
E_{1-8} = symbols represent the energy flux in and out of the control volume W
$\mathcal{F}_{w\ell,wv,v\ell}$ = gray body factors between the wall and droplets, the wall and vapor, and the vapor and droplets, respectively
g = gravitational acceleration
h_d = heat transfer coefficient between the vapor and the liquid droplet
h_{fg} = latent heat of vaporization
h_{sat} = combined radiation and convection heat transfer coefficient, defined in equation (23)
$h_{v,f}$ = enthalpy of vapor and liquid, respectively
k = thermal conductivity of steam
L_m = mean beam length
M = spray flow rate
n = droplet number density
q'' = heat flux
$R_{v,\ell,w}$ = parameters defined in equation (A3)
r = coordinate originated from and perpendicular to the center line
s = scattering coefficient
T = temperature
U = velocity in z-direction
u_d = downward droplet velocity
U_∞ = relative velocity between the droplet and the updrafting vapor
W = mass flow rate
X = efficiency, given in equation (25)
z = longitudinal coordinate
α = void fraction
β = droplet-vapor heat transfer constant, defined in equation (27)
ϵ = emissivity
κ = extinction coefficient
λ = characteristic wavelength
ν = kinematic viscosity of vapor
$\phi_{wv}, \phi_{w\ell}, \phi_{v\ell}$ = volumetric radiation heat flux from the wall to vapor and liquid droplets, and between the vapor and droplets, respectively
$\rho_{d,v}$ = density of the liquid droplets and vapor, respectively
τ_0 = optical thickness or opacity, defined in equation (24)
Θ = temperature parameter, defined as $T - T_{\text{sat}}$
η = droplet concentration factor
ξ = parameter defined in equation (34)
ψ = parameter defined in equation (35)

Subscripts

c = designates convection
ℓ = designates liquid droplet
m = designates mean
r = designates radiation
t = designates extinction
v = designates vapor
w = designates wall surface
sat = designates saturation
a = designates absorption
s = designates scattering

Similarly, an energy balance for the liquid-phase control volume yields

$$E_6 + E_8 = E_7 \tag{8}$$

The quantities E_6 and E_7 are the energy terms due to the droplet flow:

$$E_6 = W_\ell h_f \tag{9}$$

$$E_7 = W_\ell h_f + \partial/\partial z(W_\ell h_f)\Delta z \tag{10}$$

Finally, E_8 which represents radiation from the walls and the vapor to the droplet is given as:

$$E_8 = (\phi_{w\ell} + \phi_{v\ell})2\pi r\Delta r\Delta z \tag{11}$$

Substituting equations (9)–(11) into equation (8) leads to the following expression:

$$\phi_{w\ell} + \phi_{v\ell} = h_f(\partial W_\ell/\partial z)/2\pi r\Delta r \tag{12}$$

where h_f, corresponding to liquid at saturation, is a constant.

For steady-state operation, the continuity equation applied to the control volume yields

$$\partial W_\ell/\partial z + \partial W_v/\partial z = 0 \tag{13}$$

Also the vapor flow can be expressed as

$$W_v = \rho_v U(2\pi r\Delta r)\alpha \tag{14}$$

and

$$\partial h_v/\partial z = C_p\partial T/\partial z \tag{15}$$

Combining equation (7) with equations (12)–(15), and noting that $\phi_{v\ell} = -\phi_{\ell v}$, there follows

$$\rho_v UC_p\alpha\partial T/\partial z = (k\alpha/r)\partial/\partial r(r\partial T/\partial r) + \phi_{wv} + \phi_{w\ell} - (h_v - h_f)(\partial W_v/\partial z)/2\pi r\Delta r \tag{16}$$

The last term in equation (16) needs further consideration. The gradient $\partial W_v/\partial z$ is the amount of liquid evaporated within the control volume. Since it was assumed that the liquid would always be at saturation, it can be expressed as

$$(\partial W_v/\partial z)\Delta z = \dot{q}_d/h_{fg} \tag{17}$$

where $\dot{q}_d$ is the total energy transferred to the liquid in the control volume per unit time. The energy transferred to the liquid will be the sum of the radiation energy from the walls and the vapor to the droplets and a convective heat transfer between the superheated vapor and the droplets. The driving force for the vapor-droplet heat transfer is the temperature difference between the vapor and the droplet. The convective heat transfer to the droplets can be expressed as a constant, β, times the driving force, where β is a droplet-vapor heat transfer constant dependent on the droplet characteristics defined in the next section. With these concepts, equation (17) can be written as:

$$(\partial W_v/\partial z)\Delta z = [\phi_{w\ell} + \phi_{v\ell} + \beta(T - T_{\text{sat}})]2\pi r\Delta r\Delta z/h_{fg} \tag{18}$$

The term $(h_v - h_f)$ can be written as $C_p(T - T_{\text{sat}}) + h_{fg}$. The void fraction α varies from 0.981 to 1.000 for practical range of interest. Hence, it is treated as one throughout the present analysis. Furthermore, for a typical reactor bundle, the ratio of bundle length to hydraulic diameter is about 220. It is, therefore, a reasonable approximation to neglect the temperature variation in the z-direction. With these simplifications, the substitution of equation (18) for the last term in equation (16) leads to

$$(k/r)d(r\,dT/dr)/dr + \phi_{wv} - \phi_{v\ell} - \beta(T - T_{\text{sat}}) - C_p(T - T_{\text{sat}})[\phi_{w\ell} + \phi_{v\ell} + \beta(T - T_{\text{sat}})]/h_{fg} = 0 \tag{19}$$

The boundary conditions associated with equation (19) are:

$$\partial T/\partial r = 0 \text{ at } r = 0 \quad \text{and} \quad T = T_w \text{ at } r = D_h/2 \tag{20}$$

The solution of equation (19) with its boundary conditions (20) provides the temperature distribution through the medium and allows the surface heat flux due to convection to be calculated from:

$$q_c'' = (k\,dT/dr)_{r=D_h/2} \tag{21}$$

The heat fluxes due to radiation to the vapor and the droplets are evaluated as

$$q_{w\ell}'' = \phi_{w\ell}D_h/4 \quad \text{and} \quad q_{wv}'' = \phi_{wv}D_h/4 \tag{22}$$

With the results of equations (21) and (22), an effective overall heat transfer coefficient based on the saturation temperature, h_{sat}, can be defined as:

$$h_{\text{sat}} = h_{\text{sat},c} + h_{\text{sat},r} = (q_c'' + q_{w\ell}'' + q_{wv}'')/(T_w - T_{\text{sat}}) \tag{23}$$

In the present case of uniform wall temperature, only the heat transfer to the medium has been considered, without accounting for the surface to surface radiation. Hence, the heat transfer coefficient defined by equation (23) is equivalent to the experimental values obtained in the Full-Length-Emergency-Cooling-Heat-Transfer (FLECHT) program [2, 3] in which the surface to surface radiation heat transfer was calculated and the remainder was lumped into a set of heat transfer coefficients for different regions of the bundle.

Radiation From the Wall to the Vapor-Droplet Mixture

For the case of rod bundles under emergency cooling conditions where vapor and droplets are present, the optical thickness [9, 10] can be expressed as

$$\tau_0 = \kappa D_h = (\kappa_v + \kappa_\ell)D_h = [a_v + (a_\ell + S_\ell)]D_h \tag{24}$$

where κ, a, and S are the extinction, absorption and scattering coefficients, respectively. For calculation purposes, a_ℓ and κ_ℓ are often expressed in terms of the geometric cross section and the number density of the droplet medium:

$$a_\ell = X_a\,\pi d^2n/4,\ S_\ell = X_s\pi d^2n/4$$

and

$$\kappa_\ell = a_\ell + S_\ell = (X_a + X_s)\pi d^2n/4 = X_t\pi d^2n/4 \tag{25}$$

where d is the droplet diameter, n the droplet number density, and X_t, X_a, and X_s are, respectively, the extinction, absorption and scattering efficiencies. These dimensionless quantities, X's, constitute the basic parameters for droplet radiation, and are often expressed in analytical forms or computed numerically in the literature [9].

The appropriate mean vapor absorption coefficients are the Planck mean for the optically thin medium and the Rosseland mean for the optically thick medium [11]. It will be shown that in the typical case of emergency core spray cooling, τ_0 evaluated from equation (24) is much smaller than one (i.e., the medium is in the optically thin regime).

In the system under consideration, the optically thin assumption implies that the vapor and the liquid droplets are optically thin individually, and each can be characterized by a single node representing the whole individual medium. Each node (vapor, droplets or wall) will then exchange energy among one another. Assuming that the system is gray and diffuse, the absorption and emission of the mixture can be incorporated into the network analysis by treating the system as an enclosure filled by a radiating gas and a cloud of liquid droplets [9]. With these simplifications the radiative transfer between the wall and the vapor-droplet mixture can be formulated (Appendix A). Substituting equation (A1), the radiation terms in equations (19) and (22) can be expressed as

$$\phi_{ij} = 4\sigma\mathcal{F}_{ij}(T_i^4 - T_j^4)/D_h \tag{26}$$

where $ij = w\ell$, wv and $v\ell$, $T_\ell = T_{\text{sat}}$, $T_v = T_m$. σ is the Stefan-Boltzmann constant, T_m is a mean temperature of the vapor, and $\mathcal{F}_{v\ell}$, $\mathcal{F}_{wv}$ and $\mathcal{F}_{w\ell}$ are gray-body factors which are functions of vapor and droplet properties.

Droplet-Vapor Heat Transfer

The droplet-vapor heat transfer constant, β, physically represents the heat transfer between the surface of droplets and its superheated vapor surroundings per unit degree of temperature in a unit volume space. In algebraic form, it can be expressed as

$$\beta = \pi d^2 n h_d \tag{27}$$

where h_d is the convective heat transfer coefficient between the surface of a droplet and its vapor environment.

Assuming that the droplets are spherical, and the effect of vaporization and internal circulation on the convective heat transfer are not appreciable, the equation recommended by McAdams for flow past a sphere [12],

$$\mathrm{Nu} = h_d d/k = 0.37(\mathrm{Re})^{0.60} \tag{28}$$

for $17 < \mathrm{Re} < 70{,}000$, is applicable since the Prandtl number for steam is close to unity.

With equations (27) and (28), β can be calculated as

$$\beta = 0.37\pi k n d (U_\infty d/\nu)^{0.60} \tag{29}$$

Where U_∞ is the relative velocity between the droplet and the vapor stream.

Governing Equation

By incorporating the radiation terms specified in equation (26) and the constant, β, given in equation (29), a solution to the governing equation can be presented with the assumptions required for the mathematical process.

To provide a physical description of the governing equation, equation (19) can be rearranged as follows:

$$(k/r)d(r\,dT/dr)/dr + \phi_{wv} - C_p(T - T_{\mathrm{sat}})[\phi_{w\ell} + \phi_{v\ell} + \beta(T - T_{\mathrm{sat}})]/h_{fg} - \phi_{v\ell} - \beta(T - T_{\mathrm{sat}}) = 0 \tag{30}$$

Equation (30) relates the temperature distribution of the vapor to the heat transfer mechanisms. The first two terms represent the net heat input to the vapor at a given location by both conduction through the medium and direct radiation from the wall to the vapor. The last three terms represent an effective "heat sink" to the vapor caused by the evaporation of the droplets. The last term, $\beta(T - T_{\mathrm{sat}})$, accounts for the energy transferred to the droplets from the surrounding vapor by convection. From equation (30), the bracketed term $[\phi_{w\ell} + \phi_{v\ell} + \beta(T - T_{\mathrm{sat}})]/h_{fg}$ is the amount of droplet evaporation due to both radiation to the droplets and vapor-droplet heat transfer. This vapor is generated at saturation temperature on the surface of the droplets and subsequently mixes with the surrounding medium. In the mixing process, the newly formed vapor increases its temperature to reach equilibrium with the rest of the steam. This amount of sensible heat effectively represents an additional sink to the surrounding vapor. Hence, the third term in equation (30) is effectively an additional form of heat sink.

Since the vapor that forms around the droplet redistributes throughout the flow passage, it is appropriate to characterize the vapor superheat by a mean temperature rather than the local vapor temperature.

Defining the mean temperature as

$$T_m = (8/D_h{}^2)\int_0^{D_h/2} rT\,dr \tag{31}$$

and incorporating these considerations into equation (30), there results

$$d(rd\Theta/dr)/rdr = \xi\Theta + \psi \tag{32}$$

where

$$\Theta \equiv T - T_{\mathrm{sat}} \tag{33}$$

$$\xi \equiv \beta[1 + C_p(T_m - T_{\mathrm{sat}})/h_{fg}]/k \tag{34}$$

$$\psi \equiv [C_p(T_m - T_{\mathrm{sat}})(\phi_{w\ell} + \phi_{v\ell})/h_{fg} + \phi_{v\ell} - \phi_{wv}]/k \tag{35}$$

The solution of equation (32) subjecting to the boundary conditions given in equation (20) is

$$\Theta(r) = (\Theta_w + \psi/\xi)I_0(\sqrt{\xi}\,r)/I_0(\sqrt{\xi}D_h/2) - \psi/\xi \tag{36}$$

where I_0 is the modified Bessel function of the first kind, of order zero, and

$$\Theta_w \equiv T_w - T_{\mathrm{sat}} \tag{37}$$

The mean temperature T_m from equation (31) can be evaluated as

$$\Theta_m \equiv T_m - T_{\mathrm{sat}} = -\psi/\xi + 2(\Theta_w + \psi/\xi) \times I_1(\sqrt{\xi}D_h/2)/[(\sqrt{\xi}D_h/2)I_0(\sqrt{\xi}D_h/2)] \tag{38}$$

It should be pointed out that the mean temperature T_m was required to calculate the terms ξ and ψ in equations (34) and (35). The solution has to be achieved by an iterative procedure: assuming T_m for the first calculation, then re-evaluating T_m with equation (38) until convergence is achieved.

From equations (21), (23), (36), the heat transfer coefficients based on T_m and T_{sat} can be evaluated as

$$h_{m,c} \equiv q_c''/(T_w - T_m) = [k\sqrt{\xi}I_1(\sqrt{\xi}D_h/2)/I_0(\sqrt{\xi}D_h/2)]/\{1 - 2I_1(\sqrt{\xi}D_h/2)/[\sqrt{\xi}D_h/2)I_0(\sqrt{\xi}D_h/2)]\} \tag{39}$$

and

$$h_{\mathrm{sat},c} = k\sqrt{\xi}(1 + \psi/\Theta_w\xi)I_1(\sqrt{\xi}D_h/2)/I_0(\sqrt{\xi}D_h/2) \tag{40}$$

From equations (22) and (23), the heat transfer coefficient due to radiation can be calculated by

$$h_{\mathrm{sat},r} = (\phi_{wv} + \phi_{w\ell})D_h/4(T_w - T_{\mathrm{sat}}) \tag{41}$$

and, the effective overall heat transfer coefficient, defined in equation (23) can thus be calculated.

Application to a Rod Bundle

To evaluate the heat transfer coefficient h_{sat} for a typical bundle under core spray cooling conditions, the basic information required are the hydraulic diameter, D_h, the droplet size, d, their number density, n, the velocity of droplet, u_d, and the radiation parameters, X_a, X_s and X_t. To obtain the values and relations for these parameters, information from the existing literature and the BWR ECCS experiments is used.

Hydraulic Diameter. The hydraulic diameter for a unit cell in a BWR bundle, can be calculated from the rod diameter and the pitch which is the distance between the center lines of two adjacent rods. For typical BWR's, $D_h = 0.673$ in. (1.709 cm) for 7×7 bundles, and $D_h = 0.565$ in. (1.435 cm) for 8×8 bundles.

Terminal Velocity of a Droplet Falling Through Vapor. The relative movement between a droplet and the surrounding vapor can be characterized by the terminal velocity U_∞ which is calculated by equating its weight to the drag force [13]. The drag coefficient for flow over a sphere [13] is used in the present calculation. Since the drag coefficient is not known prior to the calculation of U_∞, the terminal velocity can be obtained through iteration based on a known droplet size.

Droplet Number Density. The droplet number density can be calculated by knowing the liquid flow rate through the rod bundle and the droplet velocity. During core spray cooling, the droplet number density, n, can be calculated by the following equation

$$n = \frac{M\eta}{\frac{1}{6}\pi d^3 \rho_d A_c u_d} \tag{42}$$

where η is a droplet concentration factor that can vary with different regions of the bundle. It is defined as the ratio of the local droplet number density to the bundle average number density. In a rod bundle, the relation $\Sigma\eta_i A_i/A = 1.0$ where A is the area and the subscript i designates the local bundle region, is satisfied. The droplet velocity, u_d, is the difference between the terminal velocity and the

updrafting steam velocity. With the spray rate known, the droplet number density is dependent on the droplet size and concentration only.

Absorption and Extinction Coefficient for Water Droplets. With the characteristic droplet size, d, and the number density, n, evaluated, the droplet absorption coefficient, a_ℓ, and the droplet extinction coefficient, κ_ℓ, can be determined.

It has been shown in equation (25) that to determine a_ℓ and κ_ℓ requires the knowledge of the absorption and extinction efficiencies which depend on the regime of scattering as well as the optical constants of the droplets. The regime of scattering is defined by the ratio of the droplet size to the characteristic length of radiation. For the case of spray cooling with a typical wall temperature of 1800°F (2260°R), Wien's displacement law gives the characteristic wavelength, $\lambda = 2.31\ \mu$ (7.57×10^{-6} ft). With a typical range of droplet size from 0.01 to 0.2 cm, it can be shown that $\pi d/\lambda \gg 1$. Thus, during spray cooling, the droplets are in the geometric scattering regime. In this case, irrespective of the optical constants of the droplets reference [9, p. 381], the extinction efficiency is $X_t = 2.0$.

Noting that $X_t = X_a + X_s$, and that $X_s \approx 1.7\ X_a$ from the Mie equation for scattering reference [9, p. 406]. X_s and X_a can be obtained as

$$X_s = 1.26 \qquad \text{and } X_a = 0.74 \tag{43}$$

Inserting equation (43) into equation (25) leads to the relations for the absorption and extinction coefficients for water droplets

$$a_\ell = 0.74\pi d^2 n/4 \tag{44}$$

$$\kappa_\ell = a_\ell + S_\ell = 2.0\pi d^2 n/4 \tag{45}$$

With a_ℓ and κ_ℓ obtained from equations (44) and (45) and a_v obtained from reference [10] based on T_m, the optical thickness can be determined from equation (24) and the gray-body factors $\mathcal{F}_{wv}$, $\mathcal{F}_{w\ell}$, and $\mathcal{F}_{v\ell}$ from equation (A2). Thus, the optical thin assumption can be justified and the radiation heat flux can be calculated.

Results and Discussion

Calculation of the Heat Transfer Coefficients for Rod Bundles. The present analysis accounts for the radiation and convection from the wall to the vapor-droplet mixture during core spray cooling. Solutions are obtained for the radiation heat flux, the temperature profile and the heat transfer coefficient. The fundamental independent variables in the present spray system are the droplet diameter, and the spray concentration factor. The other parameters required for the present calculation are the wall temperature, the emissivity of wall, and the updrafting vapor velocity. These parameters are obtained from typical full-scale core spray cooling experiments [1, 2]. Throughout the present calculations, representative values of u_v = 9 ft/s (2.74 M/s) and $\epsilon_w = 0.7$ and the nominal spray rate of $M = 1500$ lb/hr (0.189 Kg/s) are used. The properties k and ν are evaluated at saturation temperature for the calculation of the droplet vaporization constant, and the Reynolds number for droplet. Otherwise, k is evaluated at the mean steam temperature.

To calculate the heat transfer coefficients for different regions of the bundle requires the information of droplet size and spray concentration which are generally not known. Typical droplet sizes in simple-geometry spray cooling systems were reported by Duffey and Porthouse [6]. They observed relatively large drops of the order of 0.2 cm that fell through the bundle under the action of gravity while smaller droplets of 0.01–0.1 cm were generated in the sputtering region at the wetting front. The smaller droplets are likely to be carried away by the steam updraft due to their low terminal velocity. Hence, from their observations the droplet size which should be considered for the radiation and convection sinks in the lower part of the bundle is on the order of 0.1 and 0.2 cm. The spray distribution is difficult to determine experimentally in a rod bundle. However, it has been shown from the FLECHT emergency spray cooling experiments for BWR 7×7 bundles [2, 3] that the heat transfer coefficient, h_{sat}, varies from 1.5 Btu/ft²hr°F for rods at the interior region to 3.0 Btu/ft²hr°F for rods at the corner region and 3.5 Btu/ft²hr°F for rods at the peripheral region adjacent to channel walls. It is evident from the difference of h_{sat} that the droplet concentration factor varies in different regions of the bundle.

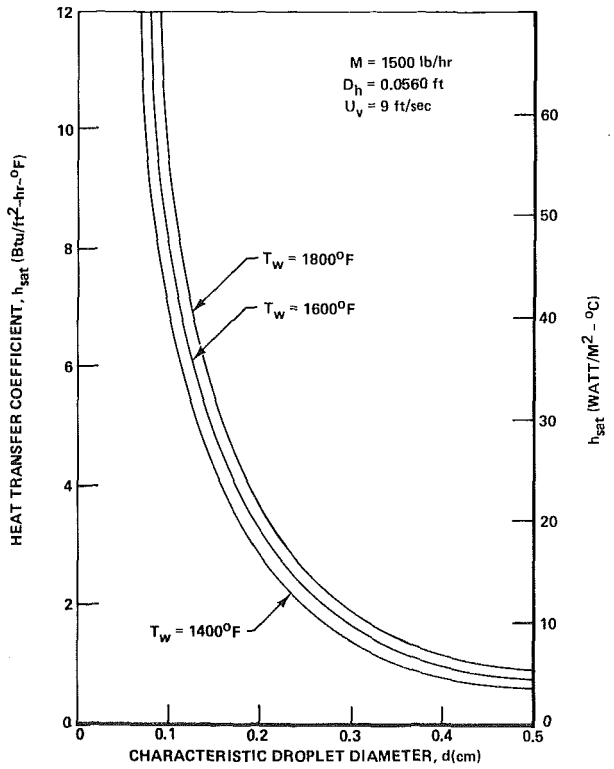

Fig. 2 The variation of h_{sat} with d for parametric T_w

By treating the droplet size as an independent parameter and assuming uniform concentration in the calculations, Fig. 2 depicts the effect of droplet size on the heat transfer coefficient for a typical case of BWR core spray cooling. A comparison of the calculated h_{sat} given in Fig. 2 and the h_{sat} determined empirically from experiments indicates that the typical droplet sizes in a BWR rod-bundle are between 0.15 and 0.30 cm. Choosing a mean heat transfer coefficient of 2.5 Btu/ft²hr°F and a mean surface temperature of 1600°F for the fuel rods from Fig. 2, the characteristic average droplet diameter is 0.228 cm which agrees well with the observations by Duffey and Porthouse [6]. It is of interest to note that for this case $h_{sat,r} \approx 1.35$ Btu/ft²hr°F, $h_{sat,c} \approx 1.15$ Btu/ft²hr°F and the ratio of $q_{wv}'' : q_{w\ell}'' : q_{v\ell}''$ is 1.000: 0.531:0.047. The number density n is calculated to be 1.12×10^4 (ft)$^{-3}$. Assuming the droplets are cubically packed in this case, the distance between the centers of two adjacent droplets is about six times the droplet diameter. Therefore, in the present range of interest, it is a reasonably good approximation to neglect the effect of adjacent droplet on the drag coefficient.

In Fig. 2, the steep increase of heat transfer coefficient for droplet size smaller than about 0.15 cm is due to a large increase of droplet number densities. In this region, the present analysis which is based on individual drop vaporization heat transfer and the radiation optical thin assumption will tend to overpredict the heat transfer coefficient. Fig. 3 presents the variation of heat transfer coefficient with the droplet concentration factor using the characteristic droplet diameter. The result indicates that, for the rods in the interior region of the bundle, the droplet concentration is about 54.5 percent of the average. Correspondingly, for the peripheral and corner regions, the associated droplet concentrations are 155 percent and 126 percent of the average.

Effect of Rod Spacing on the Heat Transfer Coefficient. The present analysis can be used to assess the effects of geometric distortions in the rod bundles on the heat transfer coefficients.

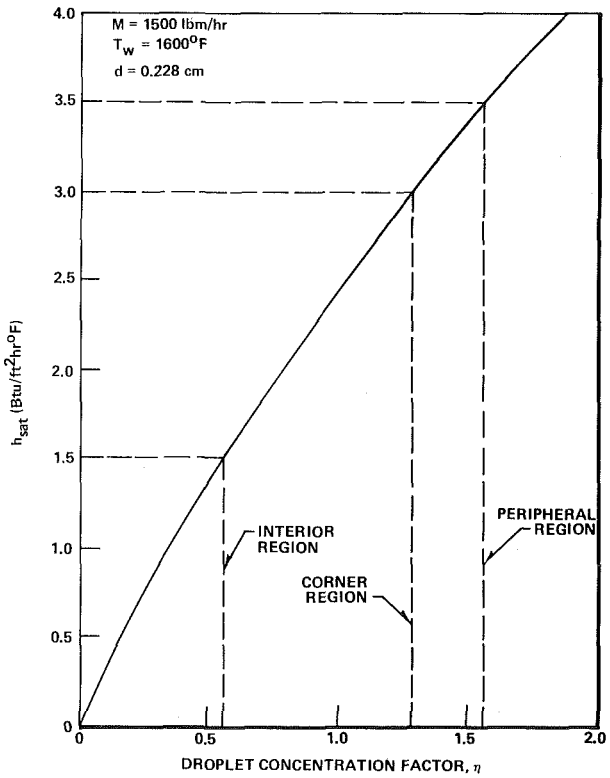

Fig. 3 The determination of droplet concentration factor for the interior, corner, and peripheral regions in a 7 × 7 BWR bundle

Fig. 4 depicts the variation of heat transfer coefficient with respect to rod spacing for the three regions in a 7 × 7 bundle with M = 1500 lb/hr, T_w = 1600°F, U_v = 9 ft/s and d = 0.228 cm. The result can be applied to the case of a 7 × 7 bundle with bowed rods. It is noticed that the heat transfer coefficient is higher for sections with larger rod spacings which are characterized by larger hydraulic diameters. The monotonic increase of the heat transfer coefficient with larger rod spacing is due to the existence of larger number of droplets.

Justification of the Optical Thin Assumption. The present analysis is based on the assumption that the vapor-droplet mixture is in the optically thin regime. This allows the independent evaluation of radiation from the wall to the mixture, and its incorporation into the overall energy balance as volumetric heat sinks. With the radiation parameters calculated, the optical thickness, given in equation (24), can be evaluated. Fig. 5 shows the variation of optical thickness with rod spacing corresponding to Fig. 4. It is evident that in the present range of interest the optical thickness is much less than one, thus verifying the justification of the optical thin assumption.

Conclusions

1 During the emergency core spray cooling process in a rod bundle after the hypothetical Loss-of-Coolant Accident, the vapor-droplet mixture serves as a heat sink for both radiation and convection heat transfer. The radiation cooling includes heat loss from the surface directly to the steam-droplet mixture. The convection cooling is due to vaporization from the droplets. The driving forces for droplet vaporization are the temperature difference between the superheated steam and the droplets at saturation temperature, and the radiation to the droplets.

2 The combined convection and radiation heat transfer coefficient can be calculated once the characteristic droplet size is known. The comparison of present calculations with the empirical heat transfer coefficients determined from the FLECHT program shows that the average droplet size in the rod bundle is 0.228 cm. This value agrees

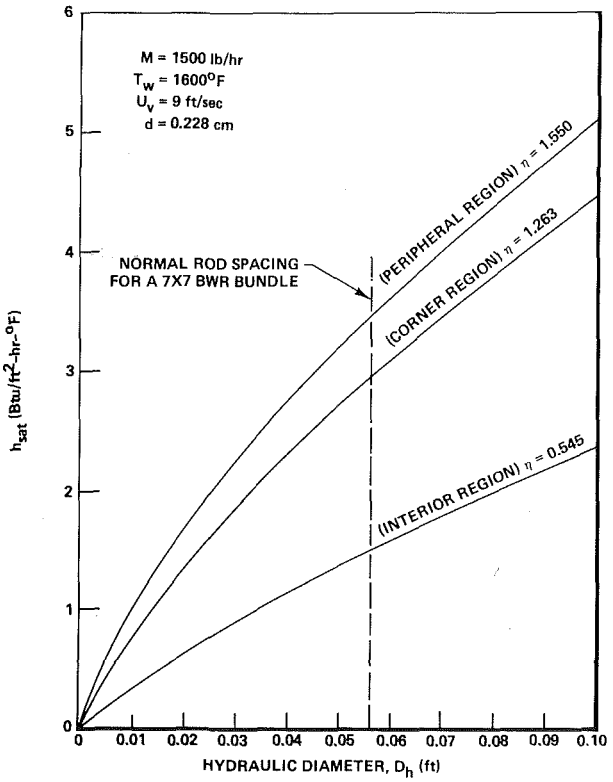

Fig. 4 The variation of h_{sat} with rod spacing for the interior, corner, and peripheral regions of a 7 × 7 bundle

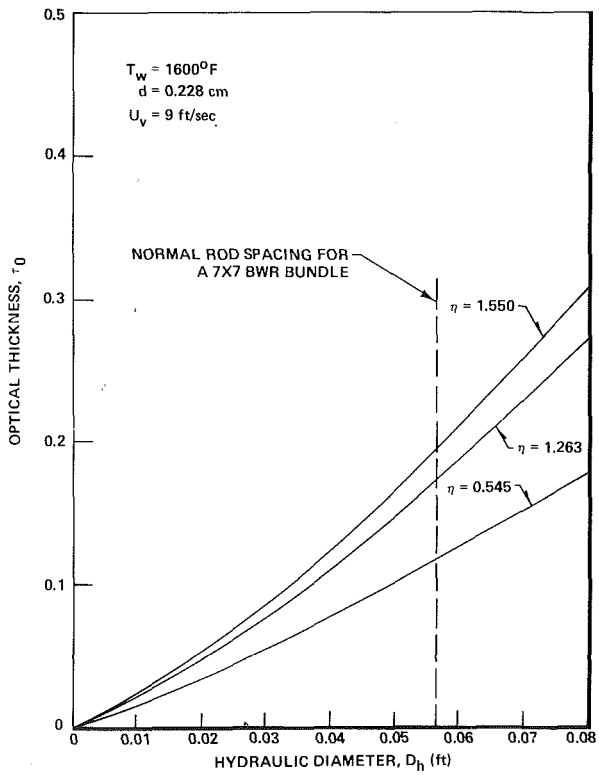

Fig. 5 The variation of optical thickness with rod spacing for the interior, corner, and peripheral regions of a 7 × 7 bundle

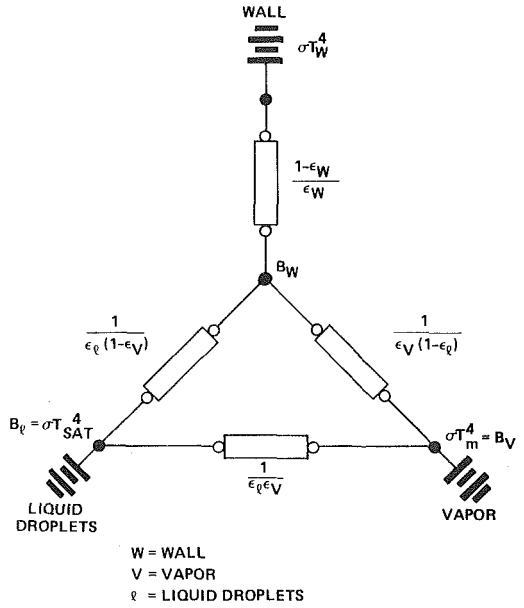

Fig. A1 Electrical analog of the vapor and droplet medium enclosed by gray wall

well with the observations from the existing literature.

3 The heat transfer coefficient in the rod bundle increases monotonically with rod spacing. This means that for the regions of the bundle where rod spacing is reduced the heat transfer decreases. Conversely, the heat transfer is enhanced by an increase of rod spacing.

4 For the typical case of emergency spray cooling of BWR rod bundles, the vapor and droplets mixture inside the bundle is optically thin. That is, the fluid element exchanges radiation directly with the boundary surfaces. This justifies the present analysis in which the radiation heat fluxes are evaluated independently and incorporated into the overall heat transfer as uniformly distributed volumetric heat fluxes.

Acknowledgments

The authors would like to record their acknowledgment to Dr. J. Andersen of the Research Establishment Riso of Danish Atomic Energy Commission and Drs. R. T. Lahey and G. E. Dix of General Electric Company, Nuclear Energy Division, for their helpful suggestions and comments.

References

1 Schraub, F. A., and Leonard, J. E., "Core Spray and Core Flooding Heat Transfer Effectiveness in a Full-Scale Boiling Water Reactor Bundle," APED-5529, Nuclear Energy Division, General Electric Co., June 1968.

2 Duncan, J. D., and Leonard, J. E., "Emergency Cooling in BWR's Under Simulated Loss-of-Coolant Conditions (BWR-FLECHT Final Report)," GEAP-13197, Nuclear Energy Division, General Electric Co., June 1971.

3 Rogers, A. E., and Leonard, J. E., "An Analytical Model of the Transient Reactor Core Spray Cooling Process," *Chemical Engineering Progress Symposium*, Series 119, Vol. 67, 1971.

4 Sun, K. H., Dix, G. E., and Tien, C. L., "Cooling of a Very Hot Vertical Surface By A Falling Liquid Film," JOURNAL OF HEAT TRANSFER, TRANS. ASME, Series C, Vol. 96, May 1974, pp. 126–131.

5 Sun, K. H., Dix, G. E., and Tien, C. L., "Effect of Precursory Cooling On Falling Film Rewetting," JOURNAL OF HEAT TRANSFER, TRANS. ASME, Series C, Vol. 97, Aug. 1975, pp. 360–365.

6 Duffey, R. B., and Porthouse, D. T. C., "Experiments on the Cooling of High-Temperature Surfaces by Water Jets and Drops," RD/B/N 2386, Berkeley Nuclear Lab., England, Aug. 1972.

7 Anderson, J. G. M., "REMI/HEAT COOL, A Model for Evaluation of Core Heat-up and Emergency Core Spray Cooling System Performance for Light-Water-Cooled Nuclear Power Reactors," Riso Report No. 296, Reactor Physics Department, Research Establishment Riso, Danish Atomic Energy Commission, Denmark, Sept. 1973.

8 Kays, W. M., *Convective Heat and Mass Transfer*, McGraw-Hill, New York, 1966, p. 116 and 182.

9 Hottel, H. C., and Sarofim, A. F., *Radiative Transfer*, McGraw-Hill, N. Y., 1967.

10 Sparrow, E. M., and Cess, R. D., *Radiation Heat Transfer*, Brooks/Cole, Belmont, Calif., 1970.

11 Tien, C. L., "Thermal Radiation Properties of Gases," *Advances in Heat Transfer* T. F. Irvine, Jr., and J. P. Hartnett, eds., Vol. 5, 253–324, Academic Press Inc., N. Y. 1968.

12 McAdams, W. H., *Heat Transmission*, 3rd. edition, McGraw-Hill, N. Y., 1954, p. 265.

13 Wallis, G. B., *One-Dimensional Two-Phase Flow*, McGraw-Hill, N. Y., 1969.

14 Simon, T. W., and Shields, C. M., "BWR Core Spray Distribution," NEDO-10846, Nuclear Energy Division, General Electric Co., Apr. 1973.

APPENDIX A

Radiation Interchange Among the Wall, the Vapor and the Droplets

Based on the assumption that the vapor-droplet mixture is in the optically thin regime, the radiation interchange among the wall, the vapor, and the droplet can be characterized by an electrical network with three nodes, each node representing one medium. Fig. A1 illustrates the electrical-network analog for the present system by assuming the wall gray. The symbol B designates radiosity, while ϵ and $(1-\epsilon)$ represent the absorptance and transmittance. In the present case all the geometric view factors are equal to unity.

Through simple algebraic manipulations, the radiation heat flux among the nodes can be expressed as

$$q_{ij}'' = \mathcal{F}_{ij}\sigma(T_i^4 - T_j^4) \tag{A1}$$

where $\mathcal{F}$ is the gray-body factor. The subscripts ij represent $w\ell$, wv and $v\ell$, respectively, and $T_\ell = T_{\text{sat}}$, $T_v = T_m$.

The gray-body factors $\mathcal{F}_{w\ell}$, $\mathcal{F}_{wv}$ and $\mathcal{F}_{v\ell}$ are defined as

$$\mathcal{F}_{ij} = 1/(R_i + R_j + R_iR_j/R_k) \tag{A2}$$

where the subscript k represents v, ℓ, and w, respectively, corresponding to $ij = w\ell$, wv, and $v\ell$, and

$$\begin{aligned} R_v &= (1-\epsilon_v)/[\epsilon_v(1-\epsilon_v\epsilon_\ell)] \\ R_\ell &= (1-\epsilon_\ell)/[\epsilon_\ell(1-\epsilon_v\epsilon_\ell)] \\ R_w &= 1/(1-\epsilon_v\epsilon_\ell) + (1-\epsilon_w)/\epsilon_w \end{aligned} \tag{A3}$$

In the present analysis which treats the vapor and droplet medium as optical thin, the second order term $\epsilon_v\epsilon_\ell$ is an approximation. They can be separately expressed by

$$\epsilon_v = 1 - \exp(-a_vL_m) \text{ and } \epsilon_\ell = 1 - \exp(-a_\ell L_m) \tag{A4}$$

where L_m is the mean beam length [11], and for the present system, L_m is equal to the hydraulic diameter D_h.

The effect of radiation contributions which are given in equation (A1) on the overall heat transfer between the wall and the vapor-droplet medium can be accounted for by treating the radiation heat transfer as uniformly distributed heat sink or source in each individual medium. This is, to define volumetric heat fluxes, $\phi_{w\ell}$, ϕ_{wv}, and $\phi_{v\ell}$ which are related to the heat fluxes of equation (A1) by a multiplier $4/D_h$, and are expressed in equation (26).

I. S. Habib

Professor,
The University of Michigan-Dearborn,
Dearborn, Mich.
Mem. ASME

The Interaction of a Hot Gas Flow and a Cold Liquid Spray in Channels

The coupled interaction of cold liquid sprays and a hot gas stream is analyzed. The effect of liquid droplets introduced into a hot gas stream flowing in channels of constant and of varying areas is investigated as a rapid cooling process for a hot gas discharge. The effects of spray distribution, duct geometry, and wall friction are examined. Variations of gas and liquid spray properties such as gas temperature and velocity, droplets velocity, temperature, and distribution are presented as a function of distance along the duct in the direction of flow. The effectiveness of this rapid cooling process for a hot gas flow is assessed.

Introduction

In the present work we study the interacting effects of sprays of cold liquid droplets introduced into a high temperature gas stream moving in an adiabatic duct. The effects of spray distribution, duct geometry, and wall friction are included in the analysis. Changes with time in gas temperature, velocity, and pressure are evaluated along with the history of the droplets at various locations in the duct. The analysis and results presented in [1][1] excluded these effects and therefore, the present work is considered a more representative model in studying the coupled changes in the properties of the flowing gas and the liquid droplets in the duct. Applications of such a problem exist in the need for a rapid cooling process of a hot gas discharge into or from ducts or nozzles and in the prediction of the reacting mixture temperature in flowing chemically reacting systems.

Inasmuch as the problem considered here involves a hot gas flow and cold liquid sprays, the analysis is applicable as well to the interaction of a cold gas and cold sprays. Such a problem arises in the induction system of the internal combustion engine.

Analysis

In the analysis which follows, the droplets are assumed to be spherical and the flow involves a one-dimensional quasi-steady transport of heat and mass with no shattering of the droplets, no liquid deposition by migration or settling on the duct walls, and nonreacting system. Because the analysis invokes adiabatic ducts in which the gas temperature and velocity are uniform across each section of the duct, the effects of viscous dissipation and gaseous radiation on the mixed mean gas temperature are not important, and, hence, they are ignored along with thermal diffusion. The effect of direct radiation interchange between the duct walls and the liquid droplets on the gas and spray properties was evaluated and was also found to be insignificant relative to the convective processes.

It is known [2] that shattering of droplets does occur for values of Weber number $(2r_d\rho_g U^2/\sigma) \approx 20$ and that spherical droplets will remain spherical if they seldom collide with each other, so that collision-induced oscillations are viscously damped to a negligible amplitude for most drops. However, the uncertainties associated with the various assumptions that could be invoked on the formation of new droplets and on coalescence such as droplet shape, degree of oscillations and damping, manner of droplets shattering, etc., overwhelm any accuracy one might attempt to obtain. Therefore, the assumptions of spherical droplets with no coalescence (and, hence, thin sprays) are invoked in the present analysis.

Gas Stream Conditions. The gas stream conditions namely temperature, velocity, pressure, and density are evaluated locally from the conservation equations which follow, and they are written for the control volume shown in Fig. 1.

[1] Numbers in brackets designate References at end of paper.

Contributed by the Heat Transfer Division of THE AMERICAN SOCIETY OF MECHANICAL ENGINEERS and presented at the AIChE-ASME National Heat Transfer Conference, San Francisco, Calif., August 10–13, 1975. Revised manuscript received by the Heat Transfer Division January 12, 1976. Paper No. 75-HT-37.

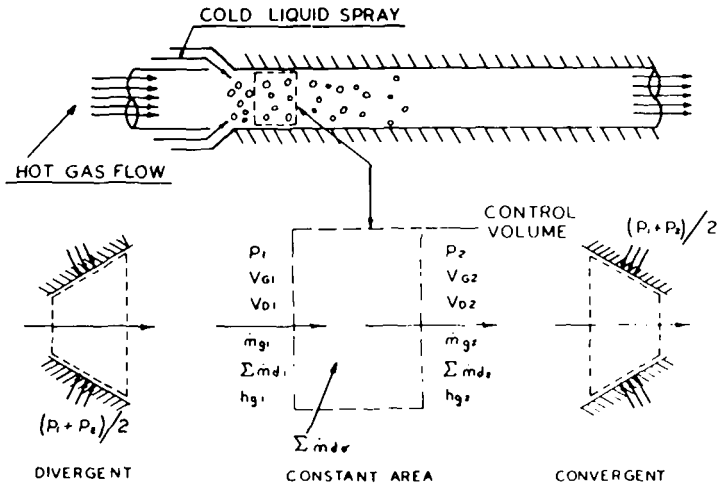

Fig. 1 The model used in the study

Energy Equation.

$$\dot{m}_{g1}\left(h_{g1}+\frac{V^2_{g1}}{2}\right)+\Sigma\,\dot{m}_{d1}\left(h_{d1}+\frac{V^2_{d1}}{2}\right)$$
$$=\dot{m}_{g2}\left(h_{g2}+\frac{V^2_{g2}}{2}\right)+\Sigma\,\dot{m}_{d2}\left(h_{d2}+\frac{V^2_{d2}}{2}\right)$$
$$+\frac{d}{dt}\left[\Sigma\, m_d\left(h_d+\frac{V^2_d}{2}\right)\right]_\sigma \quad (1)$$

In equation (1), the last term represents changes in the sensible heat and in the kinetic energy of the sprays within the control volume.

Momentum Equation. The momentum equation when applied to the gas mixture including the droplets can be written in the following form

$$P_1A_1+\frac{(P_1+P_2)}{2}(A_2-A_1)+\dot{m}_{g1}V_{g1}$$
$$=P_2A_2+\dot{m}_{g2}V_{g2}+\Sigma\,\text{Drag}+\mathcal{F} \quad (2)$$

In Σ Drag, we lump the total drag forces exerted by the gas on the total number of the droplets. Such forces which are evaluated and discussed later on in the analysis may be represented by

$$\Sigma\,\text{Drag}=\sum_i\left(C_dA_{cs}\rho_{fm}\frac{U^2}{2}\right)_i \quad (3)$$

$\mathcal{F}$ is the frictional force between the gas and the duct wall expressed as

$$\mathcal{F}=\frac{F\rho_{fm}V^2A_w}{2}=\tau_wA_w \quad (4)$$

Continuity Equation. From the law of conservation of mass we can write

$$\dot{m}_{g1}+\Sigma\,\dot{m}_{d1}=\dot{m}_{g2}+\Sigma\,\dot{m}_{d2}+\frac{d}{dt}\Sigma\,m_{d\sigma} \quad (5a)$$

$$\dot{m}_{g2}-\dot{m}_{g1}=w \quad (5b)$$

$$\frac{d}{dt}\Sigma\,m_{d\sigma}=\Sigma\,\dot{m}_{d1}-\Sigma\,\dot{m}_{d2}-w \quad (5c)$$

Equation of State. When a mixture of gases is treated as a perfect gas mixture the equation of state can be stated in the form

$$\rho_{fm}=\left[\frac{P_s\mathcal{M}}{RT}\right]_{fm} \quad (6)$$

The local enthalpies of the gas mixture h_{g1} and h_{g2} are taken equal to $\bar{c}_{p1}T_{g1}$ and $\bar{c}_{p2}T_{g2}$ respectively where $\bar{c}_p$ is a mass weighted mean specific heat between the hot gas and the evaporated liquid. The properties of the diffusing vapor were evaluated at the arithmetic

Nomenclature

A = area; A_d = droplet surface area; A_w = wall area
C_d = drag coefficient; c_p = specific heat at constant pressure
D = mass diffusivity of the vaporizing liquid
F = friction factor = $\tau_w/(\rho_{fm}V^2/2)$
G/L = gas to liquid ratio on a mass basis
h = heat transfer coefficient; h_g = enthalpy of gas; h_d = enthalpy of droplet
k = thermal conductivity; k_m = mass transfer coefficient
M = mass of droplet; $\dot{m}_g$ = mass flow rate of gas; $\dot{m}_d$ = mass flow rate of droplets of one size; $\Sigma\,\dot{m}_d$ = total mass flow rate of droplets summed over all sizes
$\mathcal{M}$ = molecular weight
Nu = Nusselt number defined in equation (14)
P = pressure; P_s = static pressure
Pr = Prandtl number = $(c_p\mu/k)_{fm}$
Q_d = heat received at droplet surface
R = universal gas constant; R_M, r_m = mass mean droplets radius, r_d = drop radius, $r_{d,o}$ = initial droplet radius
Re = Reynolds number = $2r_dU\,\rho_{fm}/\mu_{fm}$
Sc = Schmidt number = $\mu_{fm}/D\,\rho_{fm}$
Sh = Sherwood number defined in equation (9)
T = temperature; T_g, T_G = gas temperature; $\bar{T}=(T_g+T_1)/2$; t = time
U = velocity difference between gas and the droplet
V_g, V_G = gas velocity; V_d, V_D = droplet velocity
w = vaporization rate
λ = latent heat of vaporization
$\gamma = D\mathcal{M}_f\,\text{Sh}\,P_{1d}\,\alpha/2R\bar{T}$
δ = vapor film thickness
μ = viscosity; droplet size in microns
ρ = density
σ = surface tension; σ_G = Geometric standard deviation
τ_w = wall shear stress

Subscripts

d, D = pertaining to droplet; droplet surface
f = vaporizing liquid vapor
fm = pertaining to the gas and vapor mixture
ld = liquid at surface of droplet
l = liquid
s, S = gas static conditions
σ = pertaining to the mass of droplets within the control volume
g, G = gas
cs = cross sectional

mean temperature of the gas and the particular category of the droplets. Relations to compute the weighted mixture properties are presented in reference [3].

History of Liquid Droplets. Relations pertaining to the evaluation of the vaporization rate, temperature, velocity, Nusselt number, and the new size of the droplets as they move in a gas have been derived and presented before [1–11]. As the model used in the present analysis for the liquid droplets is that discussed in references [1, 3], we, therefore, present here only certain appropriate relations required in the present analysis.

Mass Transfer. The mass transfer rate from the droplet is expressed by the following expressions [1, 3, 4] in which the driving potential is the concentration gradient

$$dM/dt = (4/3)\pi d(\rho_d r^3{}_d)/dt \equiv w = \frac{2\pi D \mathcal{M}_f r_d}{R\bar{T}} \alpha \text{ Sh } P_{1d} \tag{7}$$

$$\alpha = \frac{P_s}{P_{1d}} \ln\left(\frac{P_s}{P_s - P_{1d}}\right)$$

and Sh is given by the known Ranz-Marshall relation (6)

$$\text{Sh} = \frac{2r_d R\bar{T} K_m}{D\mathcal{M}_f} = 2 + 0.6\,(\text{Sc})^{1/3}(\text{Re})^{1/2} \tag{8}$$

The approximate relation

$$r^2{}_d = r^2{}_{d,0} - 2\gamma t \tag{9}$$

has been used in the literature [11] to represent the variation of the droplet radius with time. Such a relation can be obtained from equation (7) by allowing the liquid density and the quantity $D\mathcal{M}_f\alpha$ Sh $P_{1d}/2R\bar{T}$ to be constant and then integrating the equation. Fig. 8 compares the droplet radius as obtained from equation (7) and from the approximate relation given by equation (9).

Heat Transfer. In the absence of radiation, the heat transfer rate Q_d reaching the droplet is equal to the total heat transfer rate toward the droplet reduced by the amount needed to superheat the diffusing vapor. It has been shown to be given in the following form [1, 3, 4]

$$Q_d = hA_d(T_g - T_1)Z \tag{10}$$

where

$$Z = z/(e^z - 1) \tag{11}$$

Z represents the ratio of the heat that would be conducted to the surface with pure convection heat transfer and no mass transfer, to the heat transfer with convection and mass transfer. The expression for z is

$$z = \frac{wc_{p,f}\delta}{4\pi r_d(r_d + \delta)k_{fm}} \tag{12}$$

with

$$\delta = 2r_d/(\text{Nu} - 2) \tag{13}$$

In equation (10) the average heat transfer coefficient, h, is expressed by

$$\text{Nu} = \frac{2r_d h}{k_{fm}} = 2 + 0.6(\text{Pr})^{1/3}(\text{Re})^{1/2} \tag{14}$$

The total heat transfer from the gas will then be equal to that expressed by equation (10) summed over the total number of the droplets.

An energy balance on the liquid droplet yields the following expression for the change in the droplet temperature.

$$\frac{dT_1}{dt} = \frac{1}{Mc_{p,1}}(Q_d - w\lambda) \tag{15}$$

From equation (15) we conclude that the droplet temperature decreases or increases with time depending on whether Q_d is less or greater than $w\lambda$ (the heat transfer carried by the vapor). When $w\lambda$ is equal to Q_d, the droplet experiences no change in temperature. This equilibrium temperature represents the wet bulb temperature.

Momentum Transfer. The aerodynamic drag force acting on the droplet will force the velocity of the droplet to approach that of the flowing gas. For a spherical droplet we have

$$\text{Drag force} = -M\frac{dV_d}{dt} = C_d A_{cs}\rho_{fm}\frac{U^2}{2} \tag{16}$$

or

$$\frac{dV_d}{dt} = -\frac{3}{8}C_d\frac{\rho_{fm}}{\rho_1}\frac{U^2}{r_d} \tag{17}$$

where C_d is the drag coefficient and taken for evaporating droplets as [7, 12]

$$C_d = 27(\text{Re})^{-0.84} \tag{18}$$

which gives excellent results for the Reynolds number below 400, and U is the velocity difference between the gas and the droplet.

Droplet Size Distribution. For convenience, as was done in [1] a logarithmic normal distribution function was used to describe the droplet sizes and mass distribution. Five sizes were arbitrarily chosen from the log-normal scale such that the percent of drops smaller than a given radius is equal to 10, 30, 50, 70, and 90 percent. Taking these sizes, the number of drops were chosen such that each size constitutes 20 percent of the total liquid mass.

Results and Conclusions

The method of solution used in the present study follows the one described in [1] and is outlined as follows. The gas path was broken into small increments of length. The size of the increment varied from 2.54×10^{-6} cm near the entrance of the duct to 0.127 cm away from the entrance. At each increment, the droplets velocity, size, vaporization rate, temperature, and Nusselt number were calculated using equations (7)–(18). At the same location the gas mixture properties were calculated using equations (1)–(6). Numerical evaluation of these properties was achieved by iteration from these equations.

Representative results are shown in Table 1 and in Figs. 2–8 for a mixture of a product of combustion from a gas turbine and liquid water sprays. The mixture is considered flowing in a channel of 34.54 cm in entrance diameter, and for the case of the diverging channel the diameter increased at the rate of 0.76 cm/cm in length while for the converging channel the diameter decreased at the rate of 0.36 cm/cm in length.

In Table 1, the droplets size, distribution, and percent of total liquid mass in each category are shown for various locations along the duct.[2] It can be seen that as the whole liquid gas mixture moves in the channel, the percent of mass of droplets having radii below the mean radius decreases while droplets having radii larger than the mean occupy a greater percentage of the liquid mass. The table shows such a behavior for one spray distribution with a mean radius r_m of 25 microns and a geometric standard deviation of 2.3. Other spray distributions behaved in a similar way. The numbers shown under droplets distribution represent the manner in which the liquid sprays are injected into the gas to give the initial liquid to gas mass ratio. The table shows also that at the initial stages of evaporation (at a time while the droplets are still warming up at a fast rate near the entrance of the duct), the droplets undergo a thermal expansion, and hence, their radii slightly increase although their mass is decreased due to the loss of mass by vaporization.

Figs. 2–4 show the behavior of the gas and droplets velocities along the duct for the three geometries considered. In the constant area and in the divergent channel cases, the finer droplets, after accelerating to a velocity equal to that of the gas, they decelerate at a slower rate, and hence, they maintain for sometime a velocity greater than that of the gas. This behavior is more pronounced in the divergent channel. The initial decrease in gas velocity in the convergent channel (Fig. 4) is attributed to the dominating total drag force on the droplets being greater than the contribution to the increase in gas velocity from

[2] The duct is divergent and the conditions are stated at the end of Table 1.

Table 1 Droplets size, distribution and total mass in each category along the duct

$r_m = 25\ \mu$

$\sigma_G = 2.3$

Drop Size (Microns)	Drops Distributions	Percent of Total Mass	Distance cm
8.59	26401551	20.000	
16.16	3972471	20.000	0
25.00	1072568	20.000	
38.68	289593	20.000	
72.72	43573	20.000	
8.70	26401551	19.994	
16.29	3972471	20.000	
25.15	1072568	20.001	
38.86	289593	20.002	
72.95	43573	20.003	1.66×10^{-3}
5.93	26401551	9.466	
13.45	3972471	16.580	
22.46	1072568	20.850	
36.66	289593	24.476	
72.63	43573	28.628	1.23
4.04	26401551	4.411	
11.37	3972471	14.750	
19.62	1072568	20.467	
33.03	289593	26.351	
67.64	43573	34.021	5.04
1.81	26401551	0.483	
10.36	3972471	13.504	
18.68	1072568	21.363	
31.48	289593	27.610	
65.30	43573	37.040	8.85
0.0	0	0.0	
8.42	3972471	8.701	
17.42	1072568	20.817	
30.50	289593	30.096	
63.25	43573	40.386	14.56
0.0	0	0.0	
0.0	0	0.0	
11.36	1072568	9.829	
25.88	289593	31.341	
60.06	43573	58.829	35.51
0.0	0	0.0	
0.0	0	0.0	
4.83	1072568	1.133	
20.97	289593	25.037	
56.57	43573	73.830	54.56

Gas to Liquid Ratio, G/L = 1.76 lb_m of gas/lb_m of liquid

V_g = 222.5 m/s

T_g = 1821 °K

$P_s = 19 \times 10^5$ N/m^2

F = 0.04

Duct inlet diameter = 34.54 cm

Duct divergence rate. = 0.76 cm increase in diameter/cm in length

droplets vaporization and from area change. For the length and convergence of the duct considered in this study, the droplets were always at a lower velocity than that of the gas.

Fig. 5 compares the gas temperature in the direction of flow for constant area, diverging, and converging channels. The results reveal that the convergent channel cools the hot gas faster than the other two cases considered; a result which can be expected in view of the additional cooling provided by the expansion of the gas in the channel.

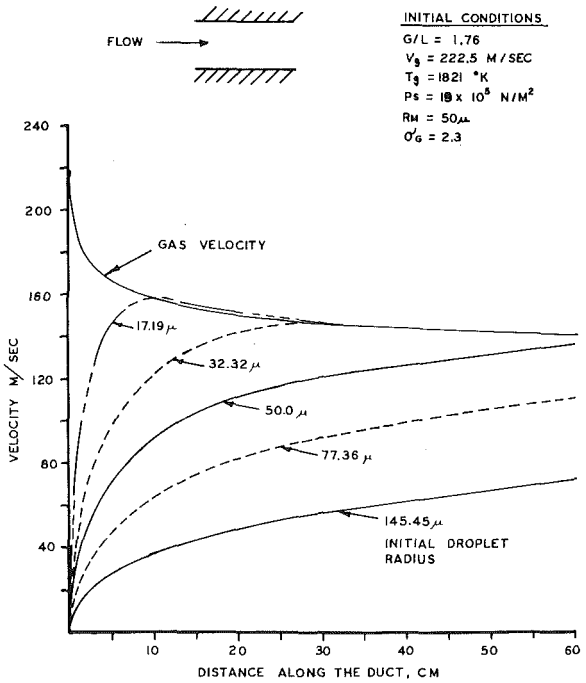

Fig. 2 Droplets and gas velocity along the duct (constant area duct)

Also shown in Fig. 5 is a curve representing the gas temperature when the initial droplets mean radius is 25 μm while the initial liquid to gas ratio is maintained the same. The curve verifies that a spray distribution of finer droplets is more effective in cooling a hot gas discharge.

In Fig. 6, the droplets temperature along the direction of flow is shown. It is interesting to note that the droplets experience a peak in their temperature within the first 5 cm in the duct. As the hot gas

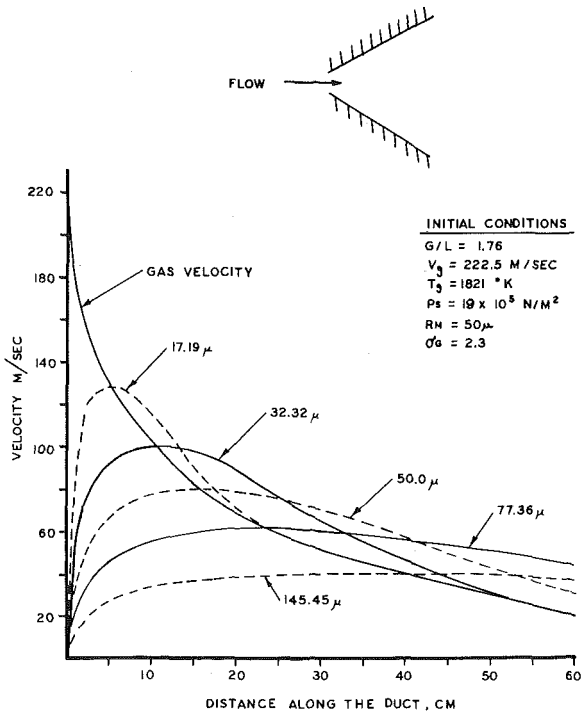

Fig. 3 Droplets and gas velocity along the duct (divergent duct)

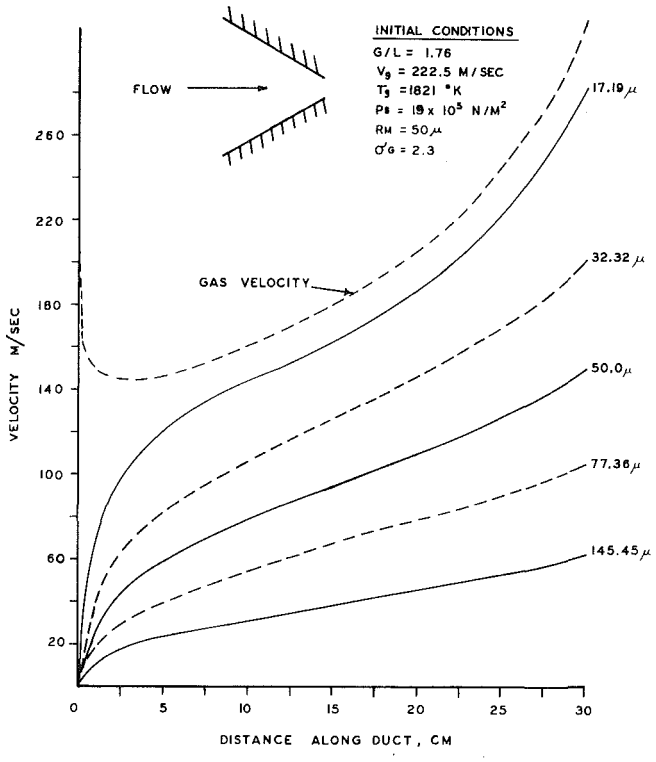

Fig. 4 Droplets and gas velocity along the duct (convergent duct)

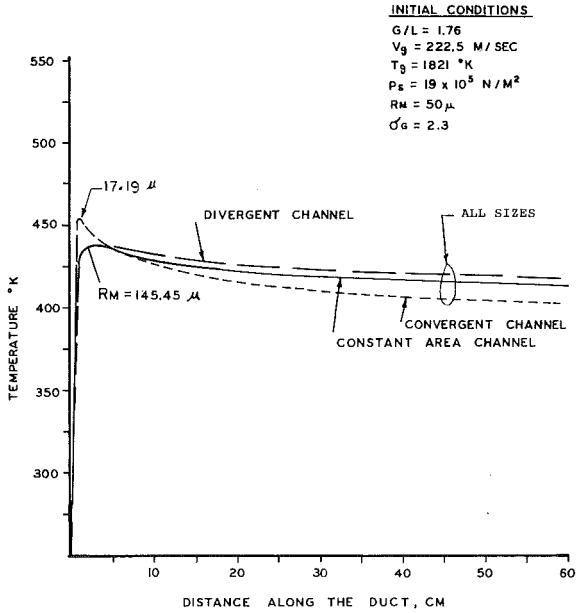

Fig. 6 Droplets temperature along the duct

draws cold liquid droplets within it, the droplets heat up experiencing a sharp change in temperature. During that period, the quantity Q_d is larger than the product of $w\lambda$. As the gas continues to cool down, the droplets experience a lower heat input from the gas such that $Q_d < w\lambda$. In this case the droplets temperature starts decreasing and hence exhibits the peaks shown. Following that the temperature continues to decrease approaching the wet bulb temperature of the droplets. Information of this sort, as was stated before, is considered very significant in the analysis and calculation of the chemical reactions in flowing chemically reacting systems.

It is important to note that the effect of including wall friction through a friction coefficient of 0.04 did not have a significant effect on the behavior of the cooling spray and on the gas and droplets velocity and temperature. The gas velocity for the case with friction ($F = 0.04$) was found at 60 cm from the entrance to be 1.4 percent higher than that with no friction for the constant area channel. This might seem to be unusual, however, we like to indicate that, although the

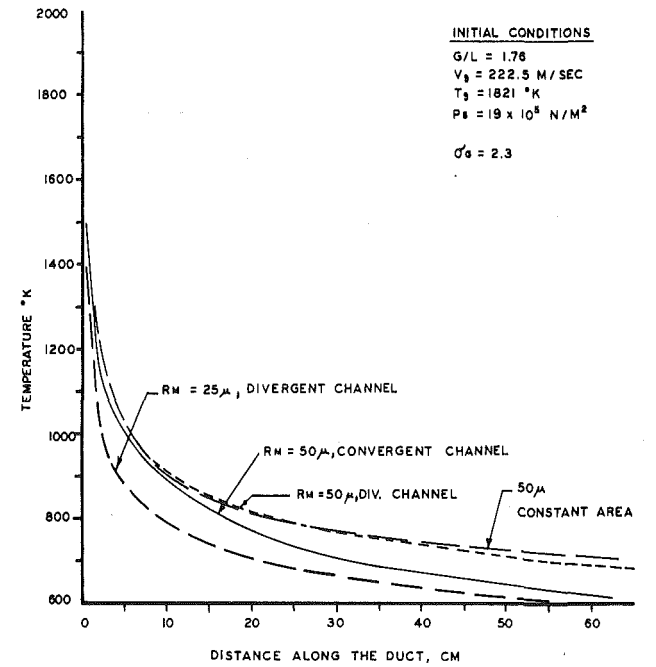

Fig. 5 Gas temperature along the duct

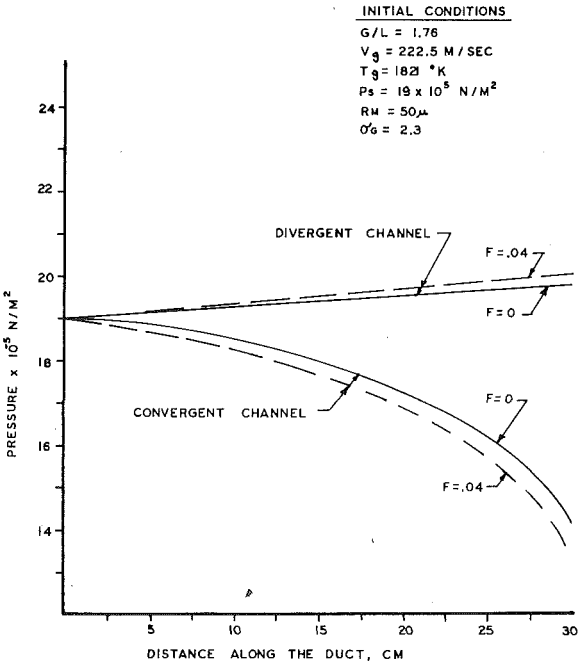

Fig. 7 Static pressure along the duct

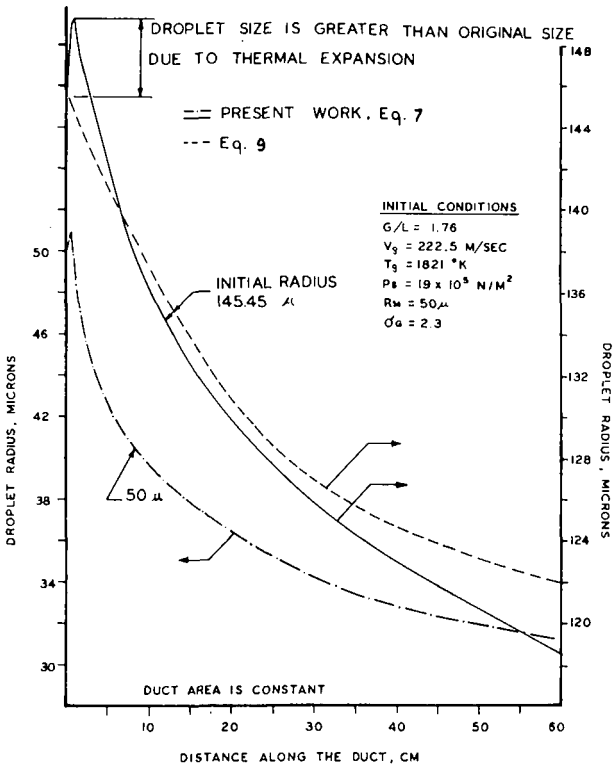

Fig. 8 Droplets radius along the duct

flow cannot be considered totally Fanno flow, in Fanno flow an increase in friction is accompanied by an increase in velocity when the flow is subsonic.

Fig. 8 shows that the approximate relation $r^2_d = r^2_{d,0} - 2\gamma t$ can reasonably predict the droplet radius away from the duct inlet. Near the duct inlet, there exists a steep rise in droplets temperature with time (or distance). Because of that, and because the liquid and gas properties were considered temperature and pressure dependent, the rapid thermal expansion of the droplets led to droplets radii larger than the initial values; see Table 1. As evident, equation (9) cannot predict this thermal expansion and the overshoot in the radii of the droplets.

Finally, it can be stated that the present analysis further shows that the spray cooling process investigated here is an effective method for the rapid cooling of a hot gas discharge.

References

1 Habib, I. S., "The Rapid Cooling of a Hot Gas Discharge by Liquid Sprays," *Applied Scientific Research*, Vol. 28, July 1973.

2 Williams, F. A., *Combustion Theory*, Addison-Wesley Publishing Co., Inc., 1965.

3 Priem, R. J., and Heidmann, M. F., "Propellent Vaporization as a Design Criterion for Rocket-Engine Combustion Chambers," NASA TR R-67, 1960.

4 Habib, I. S., "Fuel Droplets Evaporation in a Moving Gaseous Medium," *International Journal of Heat and Mass Transfer*, Vol. 13, 1970, pp. 1378-1383.

5 Sherwood, T. K., and Pigford, R. L., *Absorption and Extraction*, Second ed., McGraw-Hill, New York, 1952.

6 Ranz, W. E., and Marshall, W. R., Jr., "Evaporation From Drops," *Eng. Prog.*, Vol. 48, 1952, pp. 141--146, 173--180.

7 Ingebo, R. D., "Vaporization Rates and Drag Coefficients for Isooctane Sprays in Turbulent Air Streams," NASA TN 3265, 1954.

8 Cumo, M., et al., "On Two-Phase Highly Dispersed Flows," ASME Paper No. 73-HT-18, 1973.

9 Bracco, F. V., "Unsteady Combustion of a Confined Spray," AIChE Preprint 23, 1973.

10 Hougen, O. A., and Watson, K. M., *Chemical Process Principles*, Wiley, New York, 1943.

11 Mohinder, B. S., and Savery, C. W., "Augmentation of Heat Transfer in a Laminar External Gas Boundary Layer by the Vaporization of Suspended Droplets," AIAA Paper No. 74-708, ASME Paper No. 74-HT-28, Thermophysics and Heat Transfer Conference, Boston, Mass., July 1974.

12 Fuchs, N. A., *The Mechanics of Aerosols*, Macmillan, New York, 1964.

A. S. El-Ariny
Assoc. Professor.

A. Aziz
Assoc. Professor.

Department of Mechanical Engineering,
College of Engineering,
University of Riyadh,
Riyadh, Saudi Arabia

A Numerical Solution of Entrance Region Heat Transfer in Plane Couette Flow

A numerical procedure has been developed to solve the problem of entrance region heat transfer in steady, plane Couette flow of an incompressible viscous fluid. The formulation includes the effects of additional pressure gradient and viscous dissipation. The analysis leads to an eigenvalue problem which is solved numerically by an adaptation of Rutishauser technique. Numerical results are presented for two sets of boundary conditions: (i) fixed but different temperatures at the lower and upper plates and (ii) fixed temperature at the lower plate and zero flux at the upper plate. The effects of additional pressure gradient and viscous dissipation on the spatial development of temperature profile and Nusselt number are shown. For (i), Bruin neglected viscous dissipation and obtained an analytical solution of the energy equation. However, due to the difficulty in computing higher eigenvalues, the solution was truncated to a few terms. Besides avoiding this difficulty, the present approach offers computational simplicity and yields highly accurate results. A comparison of present results with those of Bruin shows that the latter are significantly in error. To confirm the accuracy of the numerical procedure, the method is tested for slug flow model which admits simple analytical solution. Excellent agreement is exhibited between numerical and analytical results throughout the entrance region.

Introduction

Entrance region heat transfer in fluid flow systems with moving boundaries is of interest in many industrial applications e.g., heat transfer in bearings, thermal pasteurization of liquid foods, etc. Recent representative studies of entrance region plane Couette flow are [1–5].[1] In [1] consideration is given to the case of zero pressure gradient, and developing velocity profiles are predicted using finite difference analysis. The numerical solution of Hatton [2] is concerned with the prediction of Nusselt number for turbulent flow conditions and zero pressure gradient. These results cover two sets of boundary conditions; first, plates with unequal temperatures and second, plates with unequal heat fluxes. Recently, Sestak and Rieger [3] considered laminar Couette flow in the absence of pressure gradient and obtained analytical solutions for developing temperature and Nusselt number profiles for four combinations of uniform temperature and zero heat flux boundary conditions.

The effect of additional pressure gradient was introduced in the analysis of Hudson and Bankoff [4] who treated the case of plates at equal temperatures different from that of entering fluid. The solution of the resulting Sturm-Liouville problem was obtained by computing the first five eigenvalues and eigenfunctions using numerical integration. The same problem for unequal plate temperatures was studied recently by Bruin [5]. The flow situation was the same as depicted as an insert in Fig. 1. For $P = 0$, he employed Laplace transformation, and obtained the solution in terms of Airy functions; while for $P \neq 0$, the solution was expressed in terms of confluent hypergeometric functions. However, in solving the subsequent Sturm-Liouville problem, computational difficulties were encountered in obtaining higher eigenvalues and expansion coefficients, and the solution had to be truncated to a few terms. As demonstrated later in the paper, this truncation introduces significant errors in the results. Furthermore, his results cover only the case of specified temperatures at the plates.

In all the aforementioned studies the effect of viscous dissipation was omitted. The present paper deals with a numerical approach to entrance region heat transfer in plane Couette flow and has three distinct merits. First, the formulation includes the effects of both pressure gradient and viscous dissipation. To the authors' knowledge this has not been attempted so far. In certain applications, information about the simultaneous effect of pressure gradient and viscous dissipation on heat transfer could be more useful. Second, the eigenvalues and eigenfunctions of the Sturm-Liouville problem arising in the analysis are obtained numerically by an adaptation of Rutishauser technique [6, 7]. This overcomes the shortcoming of the Bruin solution [5] and gives highly accurate results even for a mod-

[1] Numbers in brackets designate References at end of paper.

Contributed by the Heat Transfer Division for publication in the JOURNAL OF HEAT TRANSFER. Manuscript received by the Heat Transfer Division January 26, 1976. Paper No. 76-HT-CCC.

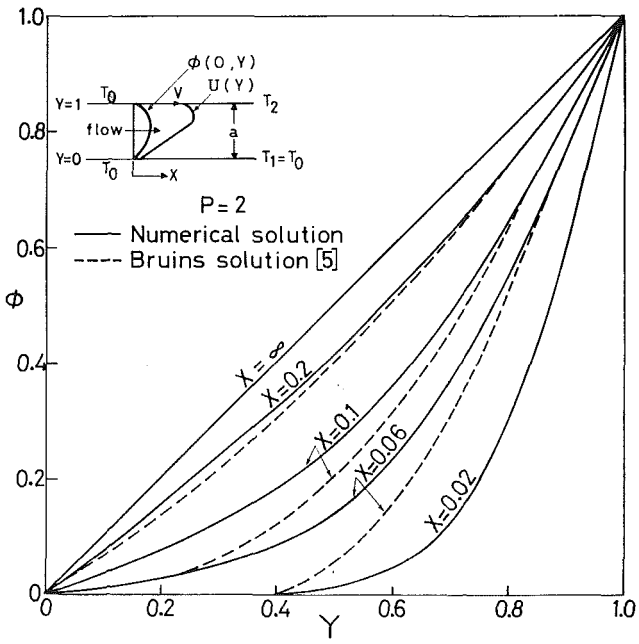

Fig. 1 Developing temperature profiles in Couette flow for boundary conditions *A* and $P = 2$ (Ec Pr = 0, ϕ (0, *Y*) = 0)

erate size grid. The accuracy of the numerical procedure is confirmed by applying it to slug flow model which admits simple analytical solution and by comparing the numerical and analytical results. Third, the method can handle other boundary conditions and is potentially suitable for many thermal entrance problems. To demonstrate the capability of the method, results are presented for two sets of boundary conditions: (i) specified temperatures at the upper and lower plates, and (ii) specified temperature at the lower plate and zero flux at the upper plate.

Analysis

Problem Description. The typical physical situations analyzed are shown as inserts in Figs. 1 and 2. In Fig. 1 the plate temperatures are T_1 and T_2 while in Fig. 2 the lower plate is at temperature T_1 and the upper plate has zero flux. These boundary conditions are hereafter referred to as boundary conditions *A* and boundary conditions *B*, respectively. In both cases the lower plate is stationary but the upper plate moves with a uniform velocity, V. The fully developed velocity profile in dimensionless form can be written as [8]

$$U = Y[1 + P(1 - Y)] \tag{1}$$

where the dimensionless parameters are as defined in the Nomenclature.

Neglecting streamwise conduction compared with streamwise convection, the simplified energy equation for steady flow of constant property fluid becomes

$$u\frac{\partial T}{\partial x} = \alpha\frac{\partial^2 T}{\partial y^2} + \frac{\mu}{\rho c}\left(\frac{du}{dy}\right)^2 \tag{2}$$

which is the same as in [5] except for the additional viscous dissipation term. To solve equation (2) we define

$$\phi = \frac{T - T_0}{\Delta T} \tag{3}$$

and further

$$\theta = \phi - \psi \tag{4}$$

where ψ is a function of y alone and $\Delta T = T_2 - T_0$ for boundary conditions *A* and $\Delta T = T_1 - T_0$ for boundary conditions *B*. Introducing equations (1), (3), and (4) into equation (2) and using dimensionless parameters (See Nomenclature) there results

$$U\frac{\partial\theta}{\partial X} = \frac{\partial^2\theta}{\partial Y^2} + \frac{d^2\psi}{dY^2} + \text{Ec Pr}[1 + P(1 - 2Y)]^2 \tag{5}$$

If ψ is chosen such that

$$\frac{d^2\psi}{dY^2} + \text{Ec Pr}\,[1 + P(1 - 2Y)]^2 = 0 \tag{6}$$

then equation (5) reduces to

$$U\frac{\partial\theta}{\partial X} = \frac{\partial^2\theta}{\partial Y^2} \tag{7}$$

The solutions of equations (6) and (7) are to be obtained subject to

$$Y = 0, X > 0, \theta = 0, \psi = 0 \tag{8a}$$

$$Y = 1, X > 0, \theta = 0, \chi = 1 \tag{8b}$$

$$X = 0, 0 \leqslant Y \leqslant 1, \theta = \phi(0, Y) - \psi(Y) \tag{8c}$$

for boundary conditions *A* and

$$Y = 0, X > 0, \theta = 0, \psi = 1 \tag{9a}$$

$$Y = 1, X > 0, \frac{\partial\theta}{\partial Y} = 0, \frac{d\psi}{dY} = 0 \tag{9b}$$

$$X = 0, 0 \leqslant Y \leqslant 1, \theta = \phi(0, Y) - \psi(Y) \tag{9c}$$

for boundary conditions *B*.

Nomenclature

a = distance between the plates
c = specific heat
C_j = jth expansion coefficient, equation (16)
$\mathbf{D}$ = coefficient matrix, equation (14)
$\mathbf{D}^t$ = transpose of $\mathbf{D}$
Ec = Eckert number, $V^2/c\ \Delta T$
f = function of X, equation (10)
g = function of Y, equation (10)
$\mathbf{g}$ = eigenvectors associated with $\mathbf{D}$
g_{ij} = ith element of jth eigenvector
h = heat transfer coefficient
k = thermal conductivity
Nu = Nusselt number, ha/k
p = pressure
P = dimensionless pressure gradient, $-a^2\ dp/dx/2\ \mu V$
Pe = Peclet number, Va/α
Pr = Prandtl number, $\mu c/k$
$\mathbf{s}$ = eigenvectors associated with $\mathbf{D}^t$
s_{ij} = ith element of jth eigenvector
T = temperature
u = fluid velocity in x-direction
U = dimensionless velocity, u/V
V = velocity of upper plate
x = streamwise coordinate
X = dimensionless x coordinate, x/a Pe
y = transverse coordinate
Y = dimensionless y coordinate, y/a
α = thermal diffusivity, $k/\rho c$
θ, ψ = dimensionless temperature, equation (4)
ϕ = dimensionless temperature, $(T - T_0)/\Delta T$
λ_j = jth eigenvalue
μ = dynamic viscosity
ρ = density

Subscripts

0 = entrance, $x = 0$
1 = lower plate
2 = upper plate
i = general grid point
m = cup-mixing
X = local
∞ = limiting

Solution Method. The solution of equation (6) is straightforward. The function $\phi(0, Y)$ represents the fully developed temperature profile resulting from viscous dissipation in the preceding hydrodynamic entrance region ($X < 0$). This is obtained by setting $\partial T/\partial x = 0$ in equation (2) and solving it subject to, for example, constant temperature T_0 at the plates. Equation (7) is analogous to that of Bruin [5] who solved it analytically for boundary conditions A. As mentioned earlier, the solution was truncated to a few terms owing to difficulties in computing higher eigenvalues. As demonstrated later, the truncated solution is significantly in error particularly at low values of X. To overcome this shortcoming and to obtain highly accurate results, a numerical procedure was adopted to solve equation (7).

Utilizing the method of separation of variables by writing $\theta = f(X)\, g(Y)$, equation (7) separates into

$$\frac{g''}{gU} = \frac{f'}{f} = -\lambda \tag{10}$$

where primes denote differentiation. The solution is

$$\theta = \sum_j C_j\, g_j(Y) \exp(-\lambda_j X) \tag{11}$$

where λ_j, $g_j(Y)$, and C_j are to be determined. Writing the equation for g in finite difference form using central differences with grid size ΔY, one obtains for point i

$$-D_i\, g_{i-1} + 2D_i\, g_i - D_i\, g_{i+1} = \lambda g_i \qquad i = 1, 2, \ldots n \tag{12}$$

with

$$D_i = \frac{1}{(\Delta Y)^2 U_i} \tag{13}$$

Applying equation (12) at n points, a set of algebraic equations in matrix form is obtained as

$$\mathbf{D}\,\mathbf{g} = \lambda\,\mathbf{g} \tag{14}$$

where $\mathbf{D}$ and $\mathbf{g}$ denote respectively the coefficient matrix and the eigenvectors. At any point i,

$$\theta_i = \sum_j C_j\, g_{ij} \exp(-\lambda_j X) \tag{15}$$

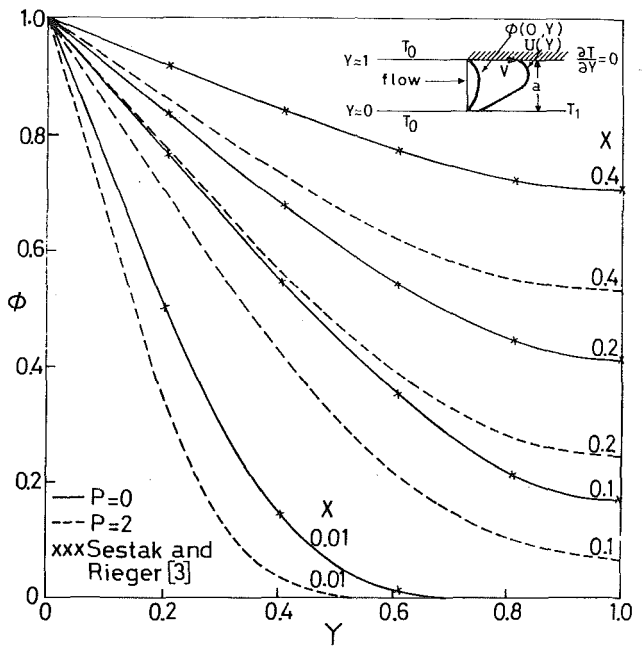

Fig. 2 Effect of pressure gradient on developing temperature profiles in Couette flow with boundary conditions *B* (Ec Pr = 0, ϕ (0, *Y*) = 0)

In equation (15), g_{ij} is the ith element of the jth eigenvector. Since $\mathbf{D}$ is unsymmetric, its eigenvectors are not orthogonal. The eigenvalues of $\mathbf{D}$ are obtained by successive application of LR transformation based on Rutishauser method [6]. Subsequently, the corresponding eigenvectors are determined by gaussian elimination. To determine C_j, the foregoing is applied to the transpose of $\mathbf{D}$ i.e., $\mathbf{D}^t$. The eigenvectors of $\mathbf{D}$ and $\mathbf{D}^t$ possess the orthogonal property and thus, applying the initial condition at point i, that is $X = 0, \theta_i = \phi_i - \psi_i$ (see equation (8c) or (9c)), the coefficients C_j can be obtained as [7]

$$C_j = -\left(\sum_{i=1}^{n} s_{ij}\,(\phi_i - \psi_i)\right) \Big/ \left(\sum_{i=1}^{n} s_{ij}\, g_{ij}\right) \tag{16}$$

where s_{ij} represents the ith element of jth eigenvector of $\mathbf{D}^t$.

The solution for ψ can be readily obtained from equation (6) and boundary conditions on ψ from equations (8a), (8b) or (9a), (9b) and added to θ just obtained to give the temperature ϕ in accordance with equation (4). The cup-mixing temperature ϕ_m is next calculated according to its usual definition

$$\phi_m = \frac{\int_0^1 U\,\phi\, dY}{\int_0^1 U\, dY} \tag{17}$$

In calculating ϕ_m the numerator in equation (17) was integrated using Simpson's rule. Finally, the Nusselt number is evaluated as [5]

$$\mathrm{Nu}_X = -\frac{1}{1-\phi_m}\frac{\partial \phi}{\partial Y}\bigg|_{Y=0 \text{ or } 1} \tag{18}$$

The derivative of ψ can be obtained from the closed form solution of ψ. The derivative of θ is obtained numerically by using a Gregory-Newton interpolating polynomial fitted to previously computed θ_i values.

Full details of the numerical procedure together with program listing are available in [9]. All computations were performed on HP 2100S digital computer.

Results and Discussion

First, the results of the application of numerical procedure to slug flow model are presented. Since, in this case, the energy equation has an exact analytical solution, it serves to provide a check on the accuracy of the numerical results. The results for Couette flow appear next and here, to conserve space, only selected results are shown. For boundary conditions A, the results presented pertain to the case of zero viscous dissipation. These results comprise a typical set of temperature profiles for $P = 2$ followed by results for the Nusselt number at the upper moving plate for $P = 0$ and 1. The aforementioned results are compared with the corresponding results given by Bruin [5]. For boundary conditions B, two sets of temperature profiles are illustrated, one for $P = 0$ and the other for $P = 2$. For $P = 0$, a comparison with the results of Sestak and Rieger [3] is made. The final set of results shows the development of the Nusselt number at the lower plate for $P = 0$, 1, and 2, and here again, the case of $P = 0$ permits comparison with results from [3]. In addition, the effect of viscous dissipation with Ec Pr = 0.1 and 1 is shown for all three values of P.

Validation of the numerical solution. For the physical situation of Fig. 1 consider the slug flow model. The upper plate is taken stationary and $U = 1$, $\phi(0, Y) = 0$. The equations governing θ and ψ together with the appropriate boundary conditions are

$$\frac{\partial \theta}{\partial X} = \frac{\partial^2 \theta}{\partial Y^2} \tag{19}$$

$$Y = 0, \quad X > 0, \quad \theta = 0 \tag{20a}$$

$$Y = 1, \quad X > 0, \quad \theta = 0 \tag{20b}$$

$$X = 0, \quad 0 \le Y \le 1, \quad \theta = -\psi \tag{20c}$$

and

$$\frac{d^2 \psi}{d\, Y^2} = 0; \quad Y = 0, \quad \psi = 0, \quad Y = 1, \quad \psi = 1 \tag{21}$$

Table 1 Nu_X, slug flow

X	Numerical	Analytical
0.01	6.069	5.871
0.02	4.620	4.495
0.04	3.590	3.547
0.08	2.896	2.898
0.20	2.294	2.298
1.00	2.000	2.000

The solution for ψ is $\psi = Y$. The method of separation of variables gives the solution for θ. Thus,

$$\phi = Y + 2 \sum_{n=1}^{\infty} \frac{(-1)^n}{n\pi} \sin n\pi Y \exp(-n^2 \pi^2 X) \qquad (22)$$

To assess the accuracy of the procedure, the numerical solution for temperature distribution obtained with grid size of $\Delta Y = 1/12$ (eleven eigenvalues) was compared with the analytical solution, equation (22). Excellent agreement was obtained which indicated high accuracy of the present procedure. As a further check, calculations were repeated with grid size of $\Delta Y = 1/20$ (nineteen eigenvalues). The two sets of results were graphically indistinguishable. A comparison of results for the Nusselt number appears in Table 1. In Table 1, the numerical and analytical values agree very closely. The maximum discrepancy at $X = 0.01$ is about 3 percent. The discrepancy is mainly due to the error in numerical computation of the temperature gradient at the plate.

Temperature profiles. Typical sets of temperature profiles for Couette flow with boundary conditions A and B are shown in Figs. 1 and 2, respectively. The grid size used is $\Delta Y = 1/12$. The eigenvalues obtained for boundary conditions A and B appear in Table 2. The number of eigenvalues equals the number of unknown temperatures at grid points.

In Fig. 1 the dashed lines indicate the results of Bruin [5]. On basis of the discussion in the last section, it seems logical to conclude that Bruin's results are significantly in error particularly at low values of X. As the fully developed condition is approached the discrepancy between the results ultimately disappears. As mentioned earlier, the deficiency in Bruin's results is due to the limitation on the number of eigenvalues which could be obtained from the characteristic equation involving hypergeometric functions. At low values of X, the higher eigenvalues contribute significantly to the solution, and the truncation there introduces large errors. Further confirmation of the accuracy of the present solution is evidenced from numerical results for $X = 0$ which reproduce the sudden change suffered by the fluid at the upper plate with a deviation of 10^{-4}.

Temperature results are now presented for boundary conditions B. Fig. 2 shows two sets of profiles for $P = 0$ and 2. The case of $P = 0$ has been solved analytically by Sestak and Rieger [3] and this provides further opportunity for validation of the present method. In [3], the situation under consideration is referred to as Case C. It is shown in [3] that the eigenvalues in this case are the positive roots of $J_{-2/3}(\lambda_j)$

Table 2 Eigenvalues, λ_j

	Boundary conditions A		Boundary conditions B	
j	$P = 0$	$P = 2$	$P = 0$	$P = 2$
1	4126	1481	4126	1481
2	1883	747.8	1883	747.8
3	1219	549.6	1219	550.1
4	901.4	485.0	901.4	525.9
5	713.9	424.7	716.2	462.5
6	576.0	343.8	605.2	387.3
7	439.4	257.2	500.4	301.8
8	301.8	173.7	367.0	215.5
9	176.9	100.9	235.1	136.3
10	79.57	44.94	123.2	71.12
11	18.83	10.37	43.37	25.26
12	—	—	3.465	2.378

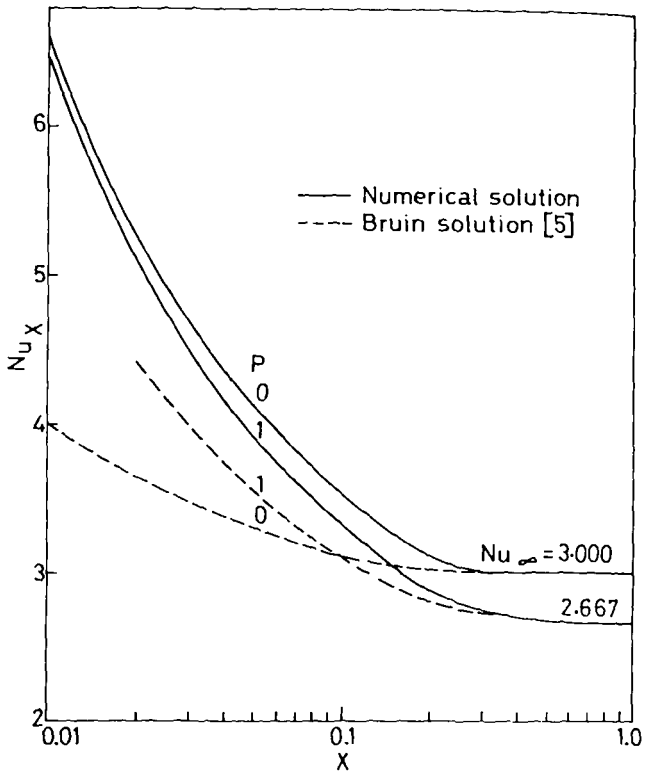

Fig. 3 Effect of pressure gradient on the Nusselt number at the upper plate for boundary conditions A (Ec Pr = 0, ϕ (0, Y) = 0)

= 0 which are tabulated in [10], and thus the analytical solution could be obtained to high accuracy. In Fig. 2 the solution [3] for $P = 0$ is indicated with crosses, and is seen to be in very good agreement with our results. The case of $P > 0$ has not been treated in the literature, and therefore no comparison is possible. However, the close agreement for $P = 0$ leads us to believe that the results for $P = 2$ are of similar high accuracy.

Nusselt number. For boundary conditions A, the variation of the upper plate Nusselt number with longitudinal distance is presented in Fig. 3 together with prediction in [5]. For both $P = 0$ and $P = 1$, the values from [5] are lower, compared to present results. For example, for $P = 0$ and $X = 0.01$, Bruin's solution underpredicts the Nusselt number by almost 40 percent. The error at $P = 1$ is smaller but still quite significant. As fully developed condition is approached, both results converge to the limiting values of 3.000 and 2.667 for $P = 0$ and $P = 1$, respectively.

The effect of viscous dissipation which has so far been deferred will now be discussed in connection with the results for boundary conditions B. The variation of the Nusselt number at the lower plate with longitudinal distance is shown in Fig. 4 for $P = 0$, 1 and 2. For each P, three curves are shown for Ec Pr = 0 (zero viscous dissipation), 0.1 and 1. For Ec Pr = 0, results taken from [3] are indicated with crosses and are in complete agreement with present results. The effect of viscous dissipation is to reduce the Nusselt number and it is most pronounced at $P = 2$. The value Ec Pr = 1 is typical of bearings and pasteurization systems and it would appear that the neglect of viscous dissipation could introduce substantial errors in the calculation of heat transfer.

Conclusions

A numerical approach has been adopted to analyze entrance region heat transfer in plane Couette flow with pressure gradient and viscous dissipation. The Sturm-Liouville problem arising in the analysis has been solved numerically by Rutishauser method. This overcomes the difficulties encountered previously by Bruin [5] and yields highly accurate results. The method is capable of handling different

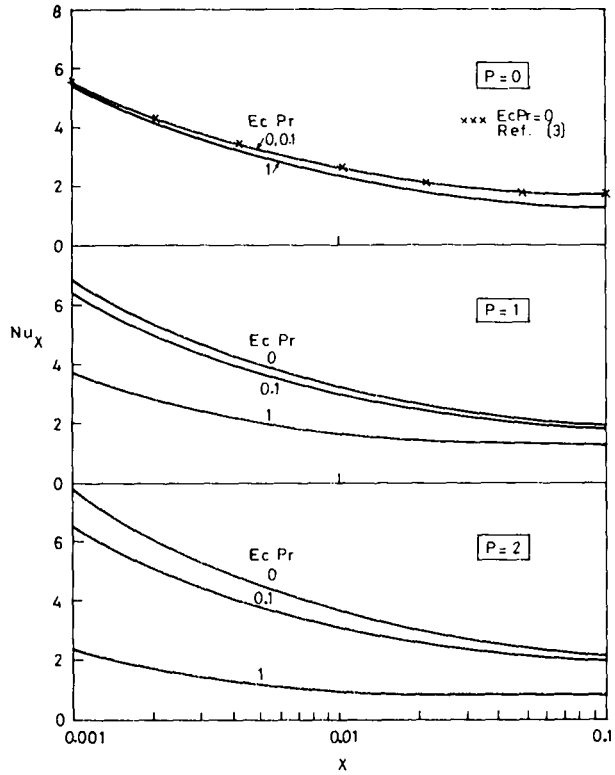

Fig. 4 Effect of pressure gradient and viscous dissipation on the Nusselt number at the lower plate for boundary conditions *B*

boundary conditions and appears to be potentially suitable for other thermal entrance problems.

Acknowledgment

The authors acknowledge the assistance of Mr. A. Sharaf Eldin Ahmed of the Computer Centre, College of Engineering, Riyadh, in programming the subroutine for Rutishauser technique for execution on HP 2100S digital computer.

References

1 Bodoia, J. R., and Osterle, J. F., "Finite Difference Analysis of Plane Poiseuille and Couette Flow Developments," *Applied Scientific Research*, Section A, Vol. 10, 1961, pp. 265–275.

2 Hatton, A. P., "Heat Transfer in the Thermal Entrance Region With Turbulent Flow Between Parallel Plates at Unequal Temperatures," *Applied Scientific Research*, Section A, Vol. 12, 1963, pp. 249–266.

3 Sestak, J., and Rieger, F., "Laminar Heat Transfer to Steady Couette Flow Between Parallel Plates," *International Journal of Heat and Mass Transfer*, Vol. 12, 1969, pp. 71–80.

4 Hudson, J. L., and Bankoff, S. G., "Heat Transfer to a Steady Couette Flow With Pressure Gradient," *Chemical Engineering Science*, Vol. 20, 1965, p. 415.

5 Bruin, S., "Temperature Distributions in Couette Flow With and Without Additional Pressure Gradient," *International Journal of Heat and Mass Transfer*, Vol. 15, 1972, pp. 341–349.

6 Rutishauser, H., "Solution of Eigenvalue Problems With LR Transformation," *National Bureau of Standards, Applied Mathematics Series*, 49, 1958, pp. 47–81.

7 Carnahan, B., Luther, H. A., and Wilkes, J. O., *Applied Numerical Methods*, Wiley, New York, 1969.

8 Schlichting, H., *Boundary Layer Theory*, Sixth ed., McGraw Hill, New York, 1968, p. 78.

9 El-Ariny, A. S., Aziz, A., and Ahmed, A. S. E., "A Numerical Solution of Entrance Region Heat Transfer in Plane Couette Flow," Research Report No. AM-3/96, College of Engineering, Riyadh, Saudi Arabia, Jan., 1976.

10 Abramowitz, M., Editor, Tables of Bessel Functions of Fractional Order, Vol. I, II, Columbia University Press, New York, 1948–49.

A. Hashemi[1]
T. C. Hsieh[2]
R. Greif

University of California, Berkeley,
Department of Mechanical Engineering,
Berkeley, Calif.

Theoretical Determination of Band Absorption With Specific Application to Carbon Monoxide and Nitric Oxide

Results are derived for infrared absorption in a fundamental manner directly from the basic spectroscopic variables. Comparison with the experimental data for carbon monoxide and nitric oxide shows very good agreement. Further work is suggested which includes the effect of variable line spacing.

Introduction

In the study of thermal radiation the fundamental quantity is the spectral absorption coefficient from which the total band absorptance, and thus the radiative transport, may be obtained. In the present work expressions for these quantities are derived directly from the basic spectroscopic variables for a vibration-rotation band.

In 1964, Edwards and Menard [1][3] used an exponential dependence for the mean line intensity to spacing ratio in conjunction with a statistical model for a band [2] to obtain results for the total band absorptance. Various limiting expressions were obtained in this work. In the intervening years several studies have utilized, altered, and expanded this proposal (e.g., [3–13, 25–27]). One remaining consideration, among others, is the determination of the absorption directly from the spectroscopic variables in a fundamental manner without recourse to arbitrary constants. It is this problem which is partially solved in the present work for a specified intensity distribution and molecular model. The results should be of special usefulness when absorption measurements are not available or are incomplete.

Analysis

We consider a vibration-rotation band composed of lines having the dispersion contour with the jth line described by an intensity S_J, a half-width b_J and a line center ω_J. The band is assumed to consist of two series of lines, called the R and P branches, which are equally spaced. The variation of the intensity of the lines in a vibration-rotation band as a function of J is given by [14, 15]:

$$S_J = S_{(n,J),(n+1,J\pm1)} = S_0 \begin{Bmatrix} J+1 \\ J \end{Bmatrix} \exp\left[-\eta_1 J(J+1)/kT\right] \quad (1)$$

where $\eta_1 = hc[B_e - \alpha_e(n + \frac{1}{2})]$ with the vibrational quantum number, n, and the specified constants B_e and α_e [14, pp. 106–108]. The quantity S_0 is determined from the relation for the integrated band intensity, $\alpha = \int S_J dJ$ which yields $S_0 = \alpha\eta_1/kT$. In a previous study a simpler approximate variation was used for the intensity S_J, and results were then obtained for the absorption coefficient and the total band absorptance [6]. In the present study the quantum mechanical representation of the intensity will be used, namely equation (1), in determining the absorption coefficient and the band absorption.[4] It should be noted that there are no arbitrary constants employed; all the quantities presented are evaluated a priori.

Determination of Absorption Coefficient and Band Absorptance. The formal expression for the absorption coefficient for the band is obtained by summing the contribution from each line [28]. The result, using the intensity distribution given by equation (1) for equally spaced lines is

$$k_\omega = \frac{\alpha b}{\pi} \cdot \frac{\eta_1}{kT} \sum_{J=0}^{\infty} J \left\{ \frac{e^{-\eta_1 J(J+1)/kT}}{(\eta_0 + \eta_3 J)^2 + b^2} + \frac{e^{-\eta_1 J(J-1)/kT}}{(\eta_0 - \eta_3 J)^2 + b^2} \right\} \quad (2)$$

where

[1] Present Address: Assistant Professor Arya-Mehr University of Technology, Tehran, Iran.

[2] Present address: Westinghouse Nuclear Center, Pittsburgh, Pa.

[3] Numbers in brackets designate References at end of paper.

Contributed by the Heat Transfer Division of THE AMERICAN SOCIETY OF MECHANICAL ENGINEERS and presented at the National Heat Transfer Conference, St. Louis, Missouri, August 8–11, 1976. Manuscript received by the Heat Transfer Division August 7, 1975. Paper No. 76-HT-1.

[4] We point out that the relation for S_0, obtained herein, differs from the relation previously obtained [6]. This is a consequence of the approximate representation of the intensity that was used in the earlier work. Note, however, that the result for the optical depth u will prove to be *identical* in both studies.

$$\eta_0 = \omega - \eta_2 \tag{3a}$$

$$\eta_2 = [1 - 2\chi_e(n+1)]\omega_e \tag{3b}$$

$$\eta_3 = [B_e + B_e' - \alpha_e(n + \tfrac{1}{2}) - \alpha_e'(n + \tfrac{1}{2})] \tag{3c}$$

The spectroscopic constants are defined in [14, pp. 92–96, 106–108] with b equal to the line half-width.

To evaluate the sums of these series the residue theorem is utilized [16] in conjunction with the following function of the complex variable z:

$$f(z) = \left(\frac{\alpha b \eta_1}{kT}\right) z \cot(\pi z) \left\{\frac{e^{-\eta_1 z(z+1)/kT}}{(\eta_0 + \eta_3 z)^2 + b^2} + \frac{e^{-\eta_1 z(z-1)/kT}}{(\eta_0 - \eta_3 z)^2 + b^2}\right\} \tag{4}$$

This function is integrated over the contour consisting of the curves $z = \rho e^{\pm i\pi/4}$, with ρ varying from ϵ to R, and the arcs $z = \epsilon e^{i\theta}$, $z = Re^{i\theta}$, with θ varying from $-\pi/4$ to $+\pi/4$. Taking the limits of the resulting integrals as R goes to infinity and ϵ goes to zero and using the residue theorem yields

$$k_\tau = \pm \frac{\alpha\eta_1}{\eta_3 kT} \frac{\exp\left\{\frac{-\eta_1}{kT}\left[\frac{\tau}{\pi}\left(\frac{\tau}{2\pi} - 1\right) - \left(\frac{\beta}{2\pi}\right)^2\right]\right\}}{\cosh\beta - \cos\tau}$$
$$\times \left\langle \frac{\sin\tau}{2\pi}\left\{\tau \sin\left[\frac{\eta_1\beta}{2\pi kT}\left(\frac{\tau}{\pi} - 1\right)\right] - \beta\cos\left[\frac{\eta_1\beta}{2\pi kT}\left(\frac{\tau}{\pi} - 1\right)\right]\right\}\right.$$
$$\left. + \frac{\sinh\beta}{2\pi}\left\{\tau\cos\left[\frac{\eta_1\beta}{2\pi kT}\left(\frac{\tau}{\pi} - 1\right)\right] + \beta\sin\left[\frac{\eta_1\beta}{2\pi kT}\left(\frac{\tau}{\pi} - 1\right)\right]\right\}\right\rangle \tag{5}$$

where the + sign refers to $\tau > 0$, the − sign to $\tau < 0$, and $\beta = 2\pi b/\eta_3$ and $\tau = 2\pi\eta_0/\eta_3 = 2\pi(\omega - \eta_2)/\eta_3$.[5] The contribution from the line integrals is small for most cases of interest and has been neglected. Furthermore, the parameter η_1/kT also proves to be small so that the absorption coefficient is given by

$$k_\tau = \pm \frac{\alpha\eta_1}{2\pi\eta_3 kT} \frac{\exp\left\{\frac{-\eta_1}{kT}\left[\frac{\tau}{2\pi}\left(\frac{\tau}{2\pi} - 1\right) - \left(\frac{\beta}{2\pi}\right)^2\right]\right\}}{\cosh\beta - \cos\tau}$$
$$\times [\tau\sinh\beta - \beta\sin\tau] \tag{6}$$

Using equation (6) it will be possible to obtain explicit results for the total band absorptance in terms of the basic spectroscopic variables.

The total band absorptance A defined by

$$A = \int_{-\infty}^{\infty} [1 - e^{-\kappa_\tau x}]\, d(\omega - \eta_2) \tag{7}$$

is the important parameter in the determination of the energy transport by thermal radiation. This quantity may also be written as follows:

$$A = \sum_{n=-\infty}^{\infty} \int_{(n-1/2)\eta_3}^{(n+1/2)\eta_3} (1 - e^{-\kappa_\tau x})\, d(\omega - \eta_2)$$
$$= \frac{\eta_3}{2\pi} \sum_{n=-\infty}^{\infty} \int_{(2n-1)\pi}^{(2n+1)\pi} (1 - e^{-\kappa_\tau x})\, d\tau$$
$$= \sum_{n=-\infty}^{\infty} A_n \tag{8}$$

This form is particularly suitable for the evaluation of the total band absorptance when β is small, that is, when the lines are effectively isolated.[6] For this condition the expression for A_n is approximated by

$$A_n \simeq \frac{\eta_3}{\pi}\int_0^\pi \left\{1 - \exp\left[\frac{-y_n\beta}{1 + \frac{\beta^2}{2} - \cos\tau'}\right]\right\} d\tau'$$
$$= \beta\eta_3 \int_0^{y_n/\beta} \exp\left[-\left(1 + \frac{\beta^2}{2}\right)\zeta\right] I_0(\zeta)\, d\zeta \tag{9}$$

with $\tau' = \tau - 2\pi n$, I_0 the modified Bessel function of order zero and

$$y_n = \frac{\alpha\eta_1 x}{\eta_3 kT}|n| \exp(-[n^2 + n]\eta_1/kT) \tag{10}$$

There are several limiting cases for which useful relations for A_n and A may be obtained. (Recall that this is for small β.) First, for $y_n\beta/2 \ll 1$, there results

$$A_n = y_n\eta_3 \exp(-y_n/\beta)\,[I_0(y_n/\beta) + I_1(y_n/\beta)] \tag{11}$$

This result was previously obtained for absorption by a single Lorentz line [29]. Using the series representations for the modified Bessel functions in conjunction with the Euler-MacLaurin summation formula, we obtain the following result for small values of u/β:

$$\frac{A}{2F} = u\left[1 - 0.157\left(\frac{u}{\beta}\right) + 0.028\left(\frac{u}{\beta}\right)^2\right] \tag{12}$$

[5] For $\eta_3 \approx B_e + B_e' = d$ (for diatomic gases) we have $\beta = 2\pi b/2B_e$. It should be noted that broadening parameters have sometimes been defined as $4b/d$ and $\pi b/d$.

[6] Note that for β very small, A_n corresponds to the line absorption. This is not true when β is not small and under this condition equations (8) simply serve to define A_n. (However, under this condition we prefer to utilize equation (18) for the total band absorption.)

Nomenclature

A = total band absorptance
b = half-width
B = self-broadening coefficient
B_e = rotational constant
c = speed of light
d = spacing between lines
E_1 = exponential integral
F = band parameter equal to $(kTB_e/hc)^{1/2}$
h = Planck's constant
I_0 = modified Bessel function of order zero
J = rotational quantum number
k = Boltzmann's constant
k_τ = spectral absorption coefficient
k_ω = spectral absorption coefficient
P_a = partial pressure of absorbing gas
P_T = total pressure of mixture
S = line intensity
T = temperature
u = optical depth
x = pressure path length
y_n = defined in equation (10)
z = complex variable
α = integrated band intensity
β = broadening parameter
γ = Euler's constant
η_0, η_2, η_3 = defined in equations (3a), (3b), and (3c)
η_1 = defined after equation (1)
σ = defined in equation (18)
τ = dimensionless wave number
ω = wave number
ω_J = center of spectral line

where the optical depth $u = (\alpha x/\eta_3)(\eta_1/kT)^{1/2}$ reduces to $u = (\alpha x/2)(hc/B_e kT)^{1/2}$. This is identical to our previous relation for the optical depth. The parameter $F = (\eta_3/2)(kT/\eta_1)^{1/2}$, which for $\alpha_e = \alpha_e' = 0$ (cf. equations (3)), reduces to $F = (kTB_e/hc)^{1/2}$. This is also identical to the expression that was previously obtained for F [6].[7] The linear dependence of the absorption for very small path lengths has been previously reported [1–6, 25].

We may obtain another important limiting case directly from equation (11). For $y_n/\beta \gg 1$ (and also $y_n\beta/2 \ll 1$ as required by equation (11)) we use the asymptotic expansions for large values of the arguments of the modified Bessel functions. Then, using the Euler-MacLaurin summation formula the following "square root dependence" is obtained for the total band absorptance:

$$\frac{A}{2F} = 2.06\left(\frac{2\beta u}{\pi}\right)^{1/2} \tag{13}$$

The square root dependence has been previously reported [1–4, 6, 25].

We now return to equation (9) and require that $y_n/\beta \gg 1$. This yields

$$A_n = \eta_3 \operatorname{erf}\left[(y_n\beta/2)^{1/2}\right] \tag{14}$$

The total band absorptance may now be obtained by numerically summing the values of A_n specified by equation (14) or by using the Euler-MacLaurin formula to obtain

$$\frac{A}{2F} = 2\int_1^\infty \operatorname{erf}\left[(u\beta Z e^{-Z^2}/2)^{1/2}\right] dZ \tag{15}$$

For small values of u, the series representation for the error function may be used which yields[8]

$$\frac{A}{2F} = 2.06\left(\frac{2\beta u}{\pi}\right)^{1/2} \tag{16}$$

This result may also be obtained from equation (14) (which requires that $y_n/\beta \gg 1$) by making the additional requirement that $y_n\beta/2 \ll 1$. Note that these requirements are identical to those used in deriving equation (13), although they have been applied in reverse order. Hence, the two results, equations (13) and (16), should be identical and indeed they are.

For very large values of $u\beta$ an asymptotic relation may be obtained for the absorption utilizing equation (15). The result is

$$\frac{A}{2F} \sim 2\sqrt{2\ln(u\beta)} \tag{17}$$

Recall that β is small so that equation (17) is limited to extremely large values of the optical depth u.

The limiting cases given here have been obtained for small values of the broadening parameter β. Another important condition corresponds to moderately large values of β. For this condition the appropriate expression for the absorption coefficient is given by

$$k_\tau = \frac{\alpha\eta_1|\tau|}{2\pi\eta_3 kT}\exp\left[\frac{-\eta_1}{kT}\left(\frac{\tau}{2\pi}\right)^2\right] \tag{18}$$

Substituting this result into the relation for the total band absorptance yields

$$\frac{A}{2F} = 2\int_0^\infty \{1 - \exp\left[-u\xi\exp(-\xi^2)\right]\} d\xi = 2\sigma \tag{19}$$

For small values of u the total band absorptance varies linearly with u while for large values of u there is a $(\ln u)^{1/2}$ dependence. The integral denoted by σ has been numerically integrated and the following approximate expression has been given ([15], pp. 279 and 330; [18]):

$$\sigma \simeq \{[\ln(u/2) + \gamma + E_1(u/2)][1 - \exp(-u/2)]\}^{1/2} \tag{20}$$

where γ is Euler's constant (0.577 . . .) and E_1 is the exponential integral [17]. Additional discussion of the evaluation of the integral, equation (19), is given by Edwards and Menard [1] and Cess and Tiwari [4].

Results and Discussion

The preceding theoretical results give explicit relations for the total band absorptance for the vibrating rotator. Thus, the band absorptance and its derivatives may be obtained directly from the basic spectroscopic variables. Note that a general expression for the total band absorptance is obtained by combining equations (6) and (7).

It is most convenient to have general results in the form of a dimensionless absorptance $A/2F$ as a function of the optical depth u and the broadening parameter β, and this is shown in Fig. 1. With this figure and the specified values for u, β, and F, the total band absorptance for infrared radiating gases is obtained.

To evaluate the absorptance for a particular gas the values for u, β, and F must first be determined. These have been defined in terms of basic spectroscopic variables and numerical values are presented in Table 1 for carbon monoxide and nitric oxide. The value of the integrated band intensity, α, for nitric oxide at 300 K is determined from the data at 273 K (cf. Table 1) by using an inverse temperature variation. Also, the value of $b_0/2B_e$ specified in Table 1 is multiplied by P_e (atm) to obtain the dimensionless value for $b/2B_e$. $P_e = P_T + (B - 1)P_a$, with the total pressure of the mixture equal to P_T, the partial pressure of the absorbing gas equal to P_a, and the self-broadening coefficient equal to B (cf. Table 1) [20, 23].

The total band absorptance may now be directly determined and the results for the 4.7 μm fundamental band of carbon monoxide are presented in Tables 2 and 3. The theoretical results are seen to be in very good agreement with the experimental data of Burch and Williams [21] and Abu-Romia and Tien [19]. In Table 4, a comparison is made between the theoretical results and the experimental data of Green and Tien [22] for the 5.35 μm fundamental band of nitric oxide and good agreement is obtained. For completeness we point out that there is a significant variation in the experimental values reported for the integrated band intensity of nitric oxide. These results have been tabulated in reference [26] and we have used the value of 132 $\text{atm}^{-1}\,\text{cm}^{-2}$ which is recommended [26, p. 170] (cf. Table 1).

Of special interest and importance is the square root logarithmic relation that was obtained for large optical depths and was in good agreement with the experimental data. This is noteworthy because a logarithmic dependence is widely used to correlate absorption data

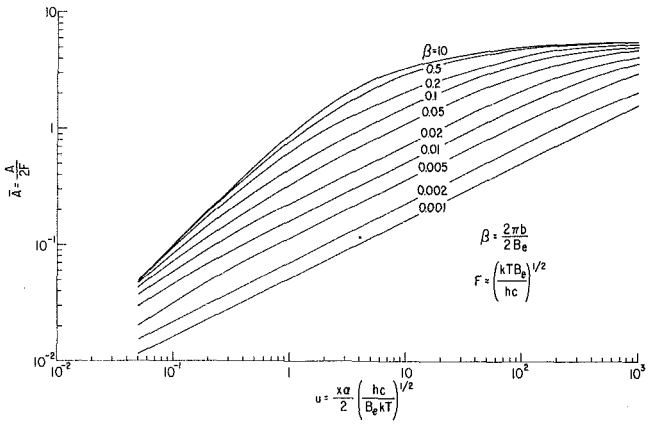

Fig. 1 Total band absorptance from present analysis in terms of generalized variables

[7] In our earlier study the approximate relation for the intensity resulted in an arbitrary constant, D_1, which was set equal to unity. This value proves to be consistent with the results of this study—which does not employ any arbitrary constants.

[8] The contribution to the integral over the range from $z = 0$ to $z = 1$ is small and has been included in this evaluation.

Table 1 Tabulation of parameters (numbers in brackets correspond to references)

	CO 4.7μ	NO 5.35μ
B_e (cm^{-1})	1.9313 [14, p.522] [15, p.307] [21, p.177]	1.0746 [14, p.558]
b_o ($atm^{-1}cm^{-1}$)	0.076 [15, p.305]	0.055 [26, p.172] [24, p.23]
α ($atm^{-1}cm^{-2}$)	237 [15, p.378] [21, p.142]	132* [26, p.170]
β	1.02 [20, p.361]	1.0 [22, p.49]

*Value corresponds to 273° K. Other values correspond to 300 K.

for large optical depths. Edwards and Menard [1] noted that the simple extrapolation of data with a logarithmic dependence may not always be appropriate and the present results are in accord with this warning. It should also be pointed out that this may be especially significant in the evaluation of the derivative of the total band absorptance which is important in nonisothermal transport calculations.

Edwards and Menard have also obtained a logarithmic dependence for the nonrigid rotator (using equation (1) in conjunction with variable line spacing) and state that a gas which appears as a rigid vibrating rotator at fairly large path lengths (square root logarithmic dependence) might well appear as a nonrigid rotator at much higher path lengths (logarithmic dependence). The study of a nonrigid rotator and in particular variable line spacing, within the framework of the present analysis, results in significant modifications since the inclusion of this effect yields a more complex expression for the absorption coefficient with attendant difficulties. This suggests that the goal of directly obtaining analytic relations in terms of the basic spectroscopic variables over the entire range of optical depths requires, at very large path lengths, the inclusion of the effects of nonrigid rotation.

Acknowledgment

The authors acknowledge with appreciation the support of this research by the National Science Foundation.

References

1 Edwards, D. K., and Menard, W. A., "Comparison of Models for Correlation of Total Band Absorptance," *Appl. Optics*, Vol. 3, 1964, pp.1621–625.

2 Goody, R. M., *Atmospheric Radiation: I. Theoretical Basis*, Oxford University Press, London, 1964.

3 Tien, C. L., "Thermal Radiation Properties of Gases," *Advances in Heat Transfer*, J. P. Hartnett and T. F. Irvine, eds., Vol. 5, Academic Press, New York, 1968, pp. 253–324.

4 Cess, R. D., and Tiwari, S. N., "Infrared Radiative Energy Transfer in Gases," *Advances in Heat Transfer*, J. P. Hartnett and T. F. Irvine, eds., Vol. 8, Academic Press, New York, 1972, pp. 229–283.

5 Tien, C. L., and Lowder, J. E., "A Correlation for Total Band Absorptance of Radiating Gases," *International Journal of Heat and Mass Transfer*, Vol. 9, 1966, pp. 698–701.

6 Hsieh, T. C., and Greif, R., "Theoretical Determination of the Absorption Coefficient and the Total Band Absorptance Including a Specific Application to Carbon Monoxide," *International Journal of Heat and Mass Transfer*, Vol. 15, 1972, pp. 1477–1487.

7 Edwards, D. K., and Balakrishnan, A., "Thermal Radiation by Combustion Gases," *International Journal of Heat and Mass Transfer*, Vol. 16, 1973, pp. 24–40.

8 Jones, M. C., "Computed Total Radiation Properties of Compressed Oxygen Between 100 and 1,000 K," *International Journal of Heat and Mass Transfer*, Vol. 15, 1972, pp. 2203–2217.

9 Khetan, S., and Cess, R. D., "Pressure-Induced Radiative Transfer in Hydrogen," *International Journal of Heat and Mass Transfer*, Vol. 17, 1974, pp. 365–366.

10 Novotny, J. L., Negrelli, D. E., and Vanden Driessche, T., "Total Band Absorption Models for Absorbing-Emitting Liquids: CCl_4," JOURNAL OF HEAT TRANSFER, TRANS. ASME, Series C, Vol. 96, 1974, pp. 27–31.

11 Felske, J. D., and Tien, C. L., "A Theoretical Closed Form Expression for the Total Band Absorptance of Infrared-Radiating Gases," *International Journal of Heat and Mass Transfer*, Vol. 17, 1974, pp. 155–158.

12 Chan, S. H., "Geometric Band Absorptance of a Nongray Gas With Arbitrary Configurations," *International Journal of Heat and Mass Transfer*, Vol. 17, 1974, pp. 381–383.

Table 2 Comparison of experimental and theoretical results for the 4.7 μm fundamental band of carbon monoxide (experimental data of Burch and Williams [21])

EFFECTIVE PRESSURE P_e (atm)	PRESSURE PATH LENGTH $P_a x$ (atm-cm)	OPTICAL DEPTH u	BROADENING PARAMETER β	EXPERIMENTAL DATA[21] $A_{(cm^{-1})}$	PRESENT RESULTS $A_{(cm^{-1})}$	CORRELATION[1,23] $A_{(cm^{-1})}$
0.0329	0.0048	0.028	0.0041	0.53	0.60	0.76
0.0329	0.012	0.069	0.0041	0.84	0.92	1.3
0.0355	0.080	0.474	0.0045	2.9	2.9	3.9
0.0345	1.45	8.57	0.0043	14.2	12.6	17.0
0.0334	5.30	31.28	0.0042	26.0	23.7	32.3
0.337	0.0029	0.017	0.042	0.64	0.64	0.68
0.334	0.0398	0.235	0.042	5.1	5.4	5.7
0.317	0.484	2.85	0.040	20.5	21.4	22.9
0.325	0.879	5.19	0.041	27.9	29.5	31.6
0.312	15.82	93.45	0.039	110.0	108.0	119.7
0.338	50.11	295.92	0.043	156.8	154.7	166.0
3.97	0.0029	0.017	0.499	0.69	0.68	0.68
3.97	0.0193	0.114	0.499	4.67	4.4	4.6
3.91	0.08	0.474	0.491	16.3	16.5	17.4
3.90	0.327	1.93	0.489	46.3	49.8	44.7
3.91	1.45	8.57	0.491	102.6	113.5	97.5
3.91	5.30	31.28	0.491	151	160.9	146.9
3.91	15.82	93.45	0.491	183.4	187.6	188.6
0.133	50.1	295.9	.0167	123.3	120.0	138.3
1.01	50.1	295.9	.127	184.6	183.4	197.7

Table 3 Comparison of experimental and theoretical results for the 4.7 μm fundamental band of carbon monoxide (experimental data Abu-Romia and Tien [19])

EFFECTIVE PRESSURE P_e (atm)	PRESSURE PATH LENGTH $P_a x$ (atm-cm)	OPTICAL DEPTH u	BROADENING PARAMETER β	EXPERIMENTAL DATA [19] $A_{(cm^{-1})}$	PRESENT RESULTS $A_{(cm^{-1})}$	CORRELATION [1,23] $A_{(cm^{-1})}$
.51	.5	2.95	.064	22.0	27.3	27.8
1.02	1.0	5.9	.128	48.5	54.6	52.2
2.04	2.0	11.81	.256	90.0	100.5	93.8
3.06	3.0	17.72	.385	127.2	132.8	119.5
.255	1.25	7.38	.032	30.2	31.5	34.5
.51	2.5	14.8	.064	58.5	61.1	64.5
1.02	5.0	29.5	.128	112.0	109.3	110.0
2.04	10.0	59.1	.256	159.2	160.5	155.1
3.06	15.0	88.6	.385	193.5	181.2	180.8
.255	2.5	14.8	.032	45.0	44.1	49.2
.51	5.0	29.5	.064	89.0	84.0	90.2
1.02	10.0	59.1	.128	148.0	136.8	136.4
2.04	20.0	118.1	.256	184.0	178.6	181.5
3.06	30.0	177.2	.385	205.0	195.2	207.2
.255	5.0	29.5	.032	66.0	61.1	70.1
.51	10.0	59.1	.064	122.0	109.3	116.6
1.02	20.0	118.1	.128	169.0	160.5	162.8
2.04	40.0	236.2	.256	210.0	193.0	208.0
3.06	60.0	354.3	.385	226.0	207.5	233.6

13 Lin, J. C., and Greif, R., "Theoretical Determination of Absorption With an Emphasis on High Temperatures and a Specific Application to Carbon Monoxide," JOURNAL OF HEAT TRANSFER, TRANS. ASME, Series C, Vol. 95, 1973, pp. 535–538.

14 Herzberg, G., *Spectra of Diatomic Molecules*, Van Nostrand, New York, 1961.

15 Penner, S. S., *Quantitative Molecular Spectroscopy and Gas Emissivities*, Addison-Wesley, Reading, Mass., 1959.

16 Copson, E. T., *An Introduction to the Theory of Functions of a Complex Variable*, Oxford University Press, 1955.

17 Abramowitz, M., and Stegun, I. A., *Handbook of Mathematical Functions*, U.S. Dept. of Commerce, N.B.S., A.M.S. 55, 1964.

18 Lapp, M., Gray, L. D., and Penner, S. S., *Equilibrium Emissivity Calculations for CO_2, International Heat Transfer Conference*, Part IV, ASME, 1961, p. 812.

9 Abu-Romia, M. M., and Tien, C. L., "Measurments and Correlations of Infrared Radiation of Carbon Monoxide at Elevated Temperatures," *Journal Quant. Spectrosc. and Radiat. Transfer*, Vol. 6, 1966, pp. 143-167.

20 Burch, D. E., Singleton, E. B., and Williams, D., "Absorption Line Broadening in the Infrared," *Applied Optics*, Vol. 1, No. 3, May 1962, pp. 359–363.

21 Burch, D. E., Gryvnak, D. A., Singleton, E. B., France, W. L., and Wil-

Table 4 Comparison of experimental and theoretical results for the 5.35 μm fundamental band of nitric oxide (experimental data of Green and Tien [22])

EFFECTIVE PRESSURE P_e (atm)	PRESSURE PATH LENGTH $P_a x$ (atm - cm)	OPTICAL DEPTH u	BROADENING PARAMETER β	EXPERIMENTAL DATA [22] $A_{(cm^{-1})}$	PRESENT RESULTS $A_{(cm^{-1})}$	CORRELATION [22] $A_{(cm^{-1})}$
1.0	.845	2.69	0.101	35.76	31.0	36.2
1.0	1.22	3.89	0.101	45.25	37.0	44.3
1.0	2.45	7.81	0.101	67.37	53.0	64.6
1.0	3.09	9.84	0.101	70.83	59.0	73.0
2.025	1.71	5.45	0.205	64.99	62.0	65.6
2.025	2.47	7.87	0.205	84.7	73.0	80.2
2.025	4.96	15.80	0.205	113.92	97.0	111.6
2.025	6.24	19.88	0.205	119.18	105.6	121.9
3.05	2.575	8.20	0.309	91.44	88.1	92.0
3.05	3.725	11.87	0.309	113.87	101.6	108.6
3.05	7.47	23.80	0.309	142.7	127.5	139.9
2.98	9.195	29.29	0.302	142.7	134.0	148.7
4.075	3.44	10.96	0.413	108.15	109.5	111.7
4.075	4.975	15.85	0.413	131.42	123.3	128.3
4.075	9.97	31.76	0.413	157.54	146.7	159.6
4.075	12.56	40.01	0.413	157.40	153.2	169.9

liams, D., "Infrared Absorption by Carbon Dioxide, Water Vapor, and Minor Atmospheric Constituents," Research Report AFCRL-62-698, July 1962.

22 Green, R. M., and Tien, C. L., "Infrared Radiation Properties of Nitric Oxide at Elevated Temperatures," *Journal Quant. Spectosc. and Radiat. Transfer*, Vol. 10, 1970, pp. 805–817; also Green, R. M., "The Infrared Radiation Properties of Nitric Oxide at Elevated Temperatures," PhD dissertation, U.C. Berkeley, 1969.

23 Siegel, R., and Howell, J. R., *Thermal Radiation Heat Transfer*, McGraw-Hill, New York, 1972.

24 Abels, L. L., and Shaw, J. W., "Widths and Strengths of Vibration-Rotation Lines in the Fundamental Band of Nitric Oxide," *Journal Molecular Spectroscopy*, Vol. 20, 1966, pp. 11–28.

25 Tiwari, S. N, "Band Models and Correlation for Infrared Radiation," AIAA 10th Thermophysics Conference, May, 1975, AIAA 75-699.

26 Ludwig, C. B., Malkmus, W., Reardon, J. E., and Thomson, J. A. L., *Handbook of Infrared Radiation from Combustion Gases*, R. Goulard and J. A. L. Thomson, eds., NASA SP-3080, Washington, D.C., 1973.

27 Lin, C. C., and Chan, S. H., "A General Slab Band Absorptance for Infrared Radiating Gases," JOURNAL OF HEAT TRANSFER, TRANS. ASME, Series C, Vol. 97, 1975, pp. 478 480.

28 Elsasser, W. M., *Heat Transfer by Infrared Radiation in the Atmosphere*, Harvard University, Blue Hill, Milton, Mass., 1972.

29 Ladenberg, R., and Reiche, F., "Uber Selektive Absorption," *Ann. Phys.*, Vol. 42, 1913, p. 181.

W. M. Toscano
CTi—Cryogenics,
Waltham, Mass.
Assoc. Mem. ASME

E. G. Cravalho
Department of Mechanical Engineering,
Massachusetts Institute of Technology,
Cambridge, Mass.
Mem. ASME

Thermal Radiative Properties of the Noble Metals at Cryogenic Temperatures

Experimental values of the monochromatic, near normal emittance, $\epsilon_{\lambda N}$, of gold at cryogenic temperatures are presented and compared with values predicted by existing theoretical models. From this comparison recommendations are made regarding the engineering suitability of these models.

Data obtained by the present authors for $\epsilon_{\lambda N}$ of gold in the wavelength range 1 to 30μ and at temperatures of 300, 79, and 6.0 K are compared with the Drude free electron model, the anomalous skin effect theory for both specular and diffuse electron reflections, and the Holstein quantum mechanical model. Results show that the anomalous skin effect model with diffuse electron reflections predicts $\epsilon_{\lambda N}$ most accurately. At room temperature and at liquid nitrogen temperature the agreement between this model and the data is within 5 percent. At liquid helium temperatures the agreement is somewhat poorer, i.e., within 30 percent.

Introduction

The rapidly expanding application of cryogenic technology, particularly in the areas of superconducting power generation systems, magnetic levitation systems, cryogenically cooled electrical transmission lines, helium refrigerators and liquifiers and cryogenic storage systems, have stressed the importance of thermally isolating the cryogenic systems from the environment. At the low temperatures characteristic of these systems (<150 K), thermal radiation is the dominant heat transfer mechanism, and much attention has been devoted to the study of thermal radiative heat transfer between surfaces at these temperatures [1–5].[1] However, the successful application of these studies depends heavily upon knowledge of the thermal radiative properties of solids at these temperatures, and this area has not received the attention it deserves.

The present paper summarizes and consolidates the several existing theoretical models for the thermal radiative properties of the noble metals and compares the results of these models with recent experimental measurements made in our laboratory [6] for the purpose of identifying the most satisfactory of these models. Suggestions for further work in this area are also presented.

[1] Numbers in brackets designate References at end of paper.

Contributed by the Heat Transfer Division of THE AMERICAN SOCIETY OF MECHANICAL ENGINEERS and presented at the AIChe-ASME National Heat Transfer Conference, August 9–11 1976. Manuscript received by the Heat Transfer Division January 7, 1976. Paper No. 76-HT-6.

Existing Theoretical Models

The thermal radiative properties of solid surfaces, i.e., emittance and absorptance, can be determined experimentally, but sometimes it is expedient to use values obtained from existing theoretical models when the models apply. There are three theoretical models which are currently being used to explain the thermal radiative properties of metals at low temperatures: the classical Drude free electron theory, the anomalous skin effect theory, and the Holstein quantum mechanical model which has been extended by Gurzhi and others.

Drude Free Electron Theory. In the classical Drude free electron theory [7], the metal atoms are considered to have two components: (*a*) the nucleus with the electrons of the inner shells (core electrons) tightly bound to it and (*b*) the electrons in the outer shells bound less strongly to the nucleus. The model assumes the nuclei and core electrons to be arranged in a stationary periodic lattice while the electrons of the outer shell are "free" to associate themselves with any atom in the lattice because of their weak binding forces. Thus, these latter electrons are the "free electrons" of the model and as such are free to move throughout the metal in response to any applied electric field.

The Drude approach is to write the Newtonian equation of motion that describes the response of these free electrons to the applied electromagnetic field. From the solution of this equation for the position vector of a free electron as a function of time, it is possible to obtain the current density. From the current density, the dc electrical conductivity can be determined and eventually the dc relaxation time, τ, via the Lorentz-Sommerfield relation [8].

With the aid of the dispersion equations relating the optical con-

stants, n and k, to the electrical properties, σ and ϵ, expressions for n and k can be written in terms of τ and ω.

$$n^2 - k^2 = \epsilon = 1 - \frac{4\pi Ne^2}{m}\frac{\tau^2}{1+\omega^2\tau^2} \tag{1}$$

$$\frac{\omega nk}{2\pi} = \sigma = \frac{Ne^2}{m}\frac{\tau}{1+\omega^2\tau^2} \tag{2}$$

The general solution of the monochromatic normal absorptance is obtained simply by substituting the derived expressions for n and k into the classical expression for $\alpha_{\lambda N}$, which can be derived from electromagnetic theory [9].

$$\alpha_{\lambda N} = 1 - \rho_{\lambda N} = 1 - \frac{(n-1)^2 + k^2}{(n+1)^2 + k^2} = \frac{4n}{(n+1)^2 + k^2} \tag{3}$$

For most metals and for wavelengths longer than 1μ ($\lambda > 1\mu$), $n \gg 1$. Then it is possible to simplify the expression for the monochromatic normal absorptance to the following [10]:

$$\alpha_{\lambda N} = \frac{4n}{n^2+k^2} \simeq 8^{1/2}\left(\frac{\lambda_1}{\lambda}\right)\left[\left(1+\frac{\lambda^2}{\lambda_2{}^2}\right)^{1/2} - 1\right]^{1/2} \tag{4}$$

where λ_1 is the characteristic wavelength corresponding to the plasma angular frequency, ω_p, and is known as the plasma wavelength.

$$\lambda_1 = \lambda_p = \left(\frac{\pi mc^2}{Ne^2}\right)^{1/2} \tag{5}$$

On the other hand, λ_2 is the characteristic wavelength corresponding to the angular frequency when $\omega = 1/\tau$ and is known as the relaxation wavelength

$$\lambda_2 = \lambda_\tau = 2\pi c\tau. \tag{6}$$

In the long-wavelength limit, equation (4) reduces to the well-known Hagen-Rubens relation [11].

As a test of the validity of the Drude model, measured values of the d-c electrical conductivity, σ_0, have been compared with values of σ_0 predicted by the Drude free electron theory, and the experimental values have been found to be somewhat larger than the theoretical values [12]. By inserting the electron effective mass, m*, and the effective number density, N_e, in place of the conventional quantities m and N in the expressions resulting from the Drude theory, one can include the periodicity of the lattice in the theory. For the noble metals for which the Fermi surface is spherical, the effective quantities m^* and N_e differ only slightly from their conventional counterparts m and N. Use of the effective mass and the number density permits very good correlation between the experimental and theoretical values of σ_0, n, and k though the Drude model is only qualitatively correct.

For the noble metals at wavelengths less than one micron, the Drude model is no longer valid since the photoelectric effect occurs below this wavelength (i.e., bound electrons contribute to the emittance through the photoelectric effect at $\lambda < 1\mu$). However, this effect is of little consequence for thermal radiation at cryogenic temperatures. At temperatures below 100 K, the results predicted from the Drude model begin to differ significantly from the experimental results. This divergence can be attributed to the fact that the reduction of temperature decreases with such effects as electron-electron interactions and electron-lattice interactions while quantum mechanical effects start to become significant. As a result, the Drude free electron theory is an inadequate description of the thermal radiation processes occurring in metals at low temperatures. Also, the Drude free electron theory incorrectly predicts a vanishing absorptance (or emittance) as the temperature of a pure metal approaches 0 K.

To summarize, the "modified effective" Drude free electron theory is an excellent approximate representation for the calculation of the thermal radiative properties of metals at room and moderately low temperatures ($T > 100$ K) in the infrared region of the electromagnetic spectrum.

Anomalous Skin Effect Theory. In an attempt to improve upon the Drude free electron theory, Rueter and Sondheimer [13] and Dingle [14] have formulated the anomalous skin effect theory which takes into consideration the fact that the electric field is space dependent as well as time dependent. This model is useful at very low temperatures since the electron mean free path becomes quite large compared to the spatial variation of the electric field. Therefore, during the time between collisions for a free electron in a metal, the electric field which the electron "sees" varies with distance. As a result, the current density as given by Ohm's law is incorrect since the field is no longer uniform in space.

At high temperatures, ($T \gg \Theta$, where Θ is the Debye temperature), Ohm's law is valid for all frequencies, but for low temperatures, ($T \ll \Theta$), it is necessary to consider the three frequency regions, low, intermediate, and high. For the low frequency region, the penetration depth (the depth at which the electric field amplitude is reduced by a factor of e^{-1}) is large compared with the electron mean free path and Ohm's law is valid at any point in the metal. For the high frequency region, the penetration depth is large compared with the distance traveled by an electron during one period of the electromagnetic wave so that again the classical theory may be applied. For intermediate frequencies, the electron mean free path is larger than the skin depth; as a result, the electric field is not constant over the mean free path of the electron.

In order to determine the thermal radiative properties of metals at low temperatures and intermediate frequencies, the electric field must be known at all points in the metal. The electric field, E, as a function of time and space is determined by solving the Boltzmann equation for the distribution function of the free electrons. The distribution function can then be used to evaluate the current density generated by the incident electromagnetic wave. Finally, the expression for current density is substituted into Maxwell's equations to obtain an integro-differential equation for E. The solution of this

Nomenclature

c = velocity of light
E = electric field
e = electric charge of an electron
h = Planck's constant divided by 2π
K = Boltzmann constant
k = attenuation coefficient
m = rest mass of an electron
m^* = effective mass of an electron
N = number density of free electrons
N_e = effective number density of free electrons
n = index of refraction
p = fraction of electrons reflected specularly
T = temperature
v = fermi velocity
Z = surface impedance
α = absorptance
α_H = total hemispherical absorptance
$\alpha_{\lambda N}$ = monochromatic normal absorptance
ϵ = dielectric constant
ϵ_H = total hemispherical emittance
$\epsilon_{\lambda N}$ = monochromatic normal emittance
Θ = Debye temperature
λ = wavelength
λ_{MB} = Wien's wavelength
λ_D = Debye wavelength
λ_p = plasma wavelength
λ_τ = relaxation wavelength
μ = magnetic permeability
ν = frequency
$\bar{\nu}$ = dimensionless frequency = $[2c(3\pi m/Ne^2\mu)^{1/2}/3v]\nu$
$\rho_{\lambda N}$ = monochromatic normal reflectance
σ = electrical conductivity
σ_0 = dc electrical conductivity
τ = relaxation time
τ_{cl} = classical d-c relaxation time
τ_{ep} = electron-phonon relaxation time
ω = angular frequency of the electromagnetic wave
ω_p = plasma angular frequency

equation yields E as a function of space and time.

The optical properties are related to the electric field in the metal by means of the surface impedance, Z, defined as the ratio of the electric field at the surface of the metal to the total current per unit area in the metal. The monochromatic normal reflectance can be expressed in terms of this surface impedance.

$$\rho_{\lambda N} = 1 - \alpha_{\lambda N} = \left| \frac{\frac{4\pi}{c} - Z}{\frac{4\pi}{c} + Z} \right|^2 \tag{7}$$

where $4\pi/c$ corresponds to the impedance of free space.

For purposes of comparison of the anomalous skin effect with the other theoretical models, we present here the simplified results of Dingle [14] for the visible and near infrared regions of the electromagnetic spectrum. These results are valid for metals in the region $(\nu/e)(m/N)^{1/2} \ll 1 \ll \bar{\nu}^2$ which corresponds to $0.1\mu < \lambda < 30\mu$. The displacement current, photoelectric current and atomic polarization are ignored in this wavelength region.

For the case of specular electron reflections at the surface:

$$\alpha_{\lambda N1} = \underline{\left(\frac{m}{\pi Ne^2}\right)^{1/2} \frac{1}{\tau}} + \underline{\underline{\frac{2\pi Ne^2}{m\omega^2} \frac{v^3}{c^3}}} + 2\left(\frac{\pi Ne^2}{m}\right)^{1/2} \frac{1}{\omega^2 \tau} \frac{v^2}{c^2} - \underline{\frac{1}{8} \frac{1}{\tau^3 \omega^2} \left(\frac{m}{\pi Ne^2}\right)^{1/2}} \tag{8}$$

For the case of diffuse electron reflections at the surface:

$$\alpha_{\lambda NO} = \underline{\underline{\frac{3}{4} \frac{v}{c}}} + \underline{\left(\frac{m}{\pi Ne^2}\right)^{1/2} \frac{1}{\tau}} - \frac{3\pi Ne^2}{m\omega^2} \frac{v^3}{c^3} \left(\frac{16 \ln 2}{106} + \frac{8723}{80646}\right) - \frac{83(3)}{192} \left(\frac{\pi Ne^2}{m}\right)^{1/2} \frac{1}{\omega^2 \tau} \frac{v^2}{c^2} - \frac{3}{4} \frac{1}{\omega^2 \tau^2} \frac{v}{c} - \underline{\frac{1}{8} \left(\frac{m}{\pi Ne^2}\right)^{1/2} \frac{1}{\tau^3 \omega^2}} \tag{9}$$

The singly underlined terms are identical to the expressions obtained from the classical Drude free electron theory for the optical and near infrared regions. The doubly underlined terms are identical to the expressions obtained by Holstein [15] who considered only diffuse or specular reflections of electrons from the surface of the metal and neglected interactions of the electrons with the lattice, the impurities or themselves. Thus, it appears that to the first approximation, the monochromatic normal absorptance at low temperatures is equal to the sum of the absorptance for either diffuse reflection or specular reflection of electrons from the metal surface and the absorptance due to the interaction of the free electrons with the lattice, impurities, and other free electrons in the skin region. The expressions for $\alpha_{\lambda N1}$ and $\alpha_{\lambda NO}$ can be written in the following form:

$$\alpha_{\lambda N1} = \left(\frac{2\pi Ne^2}{m\omega^2} \frac{v^3}{c^3}\right)_{S1} + \left[\left(\frac{m}{\pi Ne^2}\right)^{1/2} \frac{1}{\tau} - \frac{1}{8} \frac{1}{\tau^3 \omega^2} \left(\frac{m}{\pi Ne^2}\right)^{1/2}\right]_B + \text{correction and higher order terms} \tag{10}$$

$$\alpha_{\lambda NO} = \left(\frac{3}{4} \frac{v}{c}\right)_{SO} + \left[\left(\frac{m}{\pi Ne^2}\right)^{1/2} \frac{1}{\tau} - \frac{1}{8} \frac{1}{\tau^3 \omega^2} \left(\frac{m}{\pi Ne^2}\right)^{1/2}\right]_B + \text{correction and higher order terms} \tag{11}$$

The subscript $S1$ indicates specular reflection of the electrons at the metal surface, the subscript SO indicates diffuse reflection of the electrons at the metal surface, and the subscript B indicates the interaction of the electrons with the medium in the skin region of the metal. Note that the quantity with subscript B in equations (10) and (11) is identical with the monochromatic normal absorptance as predicted by the Drude free electron theory in the visible and near infrared regions of the electromagnetic spectrum.

The anomalous skin effect theory can be used to describe the physics of the thermal radiation processes in solids. The incident electromagnetic wave penetrates into the metal and interacts with the free electrons which are accelerated away from, or toward, the surface of the metal. During the trajectory in the skin region of the metal, the free electrons will interact with the lattice, impurity atoms, and other electrons. Thus, the free electrons relinquish to the surrounding medium some of the energy which they acquired from the incident electromagnetic wave. When the free electrons travelling toward the surface of the metal reach the surface, they will be reflected diffusely or specularly; in either case, they will absorb additional energy from the incident electromagnetic wave and then will travel into the interior of the skin region where they will eventually relinquish the energy to the surrounding medium.

There are differences between the anomalous skin effect theory and the Drude free electron theory at low temperatures, but at room temperatures the results predicted by both models are in good agreement. Thus, in spite of the fact that anomalous skin effect theory is an improvement over the Drude free electron theory, it still does not explain fully the absorption and emission processes in solids at cryogenic temperatures.

Holstein Quantum Mechanical Model. Holstein [16] has introduced a third theoretical model which is a combination of the anomalous skin effect and quantum mechanical effects. At very low temperatures, $T \ll \Theta$, it is necessary to take into consideration quantum mechanical effects ($\hbar\omega \gg KT$) since they become very significant. For example, at 4.2 K (the normal boiling point of helium) the wavelength region in which quantum effects play an important role is for $\lambda \ll 3400\mu$ as compared to $\lambda \ll 45\mu$ at room temperature. Holstein [17, 18] derived an expression for the bulk absorption of thermal radiation in the skin region of a metal for the visible and near infrared regions of the spectrum by employing a quantum mechanical model. He postulated that the bulk absorption mechanism is a two-stage process which involves the simultaneous absorption (or emission) of a photon and the emission (or absorption) of a phonon by an electron. The significance of this two-stage process is that instead of only the low frequency phonons being emitted, a larger portion of the phonon frequency spectrum is excited. Since $T \ll \Theta$ and and the energy available for the generation of an individual phonon is of the order of KT, the additional excitation energy is supplied by the electromagnetic wave for which $\hbar\omega \gg KT$. If $\hbar\omega \gg K\Theta \gg KT$ as Holstein assumed, then the entire phonon frequency spectrum is excited. The Debye temperature Θ is actually an indicator of the maximum frequency at which the phonons in a solid may be generated.

Like the classical Drude free electron model and the anomalous skin effect model, the quantum mechanical model is based on the equations of motion of the "free" electrons. In the quantum mechanical approach, the motion of the free electrons of the metal is described by the time dependent Schrodinger wave equation. Using second order perturbation theory, Holstein solves the Schrodinger wave equation for the free electrons. This results in an expression for an effective relaxation time or a relaxation time due to an electron-phonon interaction.

$$\frac{1}{\tau_{\text{eff}}} = \frac{1}{\tau_{ep}} = \frac{\Theta}{T_{\text{ref}}\, \tau_{cl}} \left[\frac{2}{5} + 4\left(\frac{T}{\Theta}\right)^5 \int_0^{\Theta/T} \frac{z^4}{e^z - 1} dz\right] \tag{12}$$

where τ_{dc} is the classical d-c relaxation time measured at a reference temperature, T_{ref}, much higher than the Debye temperature.

Holstein replaced $1/\tau$ in the classical expression for the monochromatic normal absorptance derived by Drude with the quantum mechanically derived $1/\tau_{ep}$. Then for the quantum mechanical model

$$(\alpha_{\lambda N})_B = \left(\frac{m^*}{\pi Ne^2}\right)^{1/2} \frac{\Theta}{T_{\text{ref}}\, \tau_{cl}} \left[\frac{2}{5} + 4\left(\frac{T}{\Theta}\right)^5 \int_0^{\Theta/T} \frac{z^4}{e^z - 1} dz\right] \tag{13}$$

For low temperatures, i.e., $T/\Theta < 0.15$, equation (13) reduces to

$$(\alpha_{\lambda N})_B = \frac{2}{5} \left(\frac{m^*}{\pi Ne^2}\right)^{1/2} \frac{\Theta}{T_{\text{ref}}\, \tau_{cl}} \tag{14}$$

In order to obtain the monochromatic normal absorptance, Holstein has added his expression for the skin effect absorptance, i.e., the absorptance occurring at the metal surface due to the diffuse or specular reflection of the electrons at the metal surface, to the foregoing expression for the bulk absorptance for the visible and near infrared

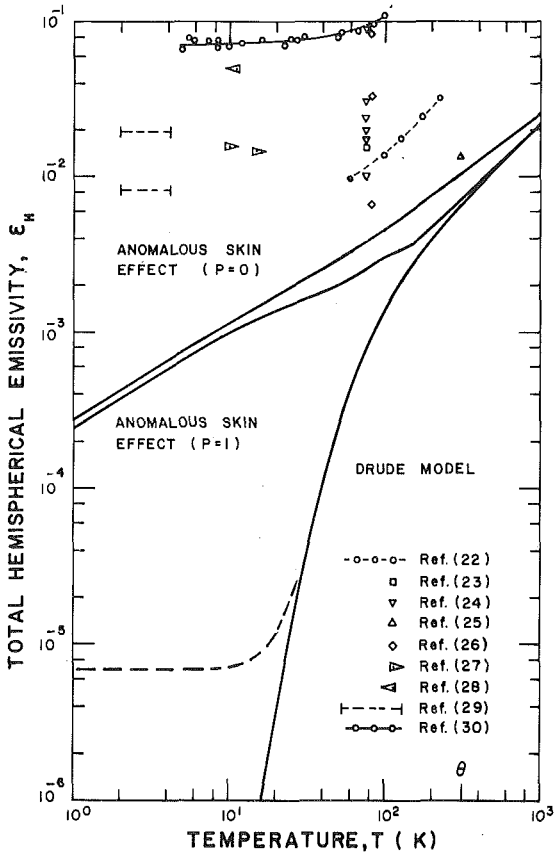

Fig. 1 Total hemispherical emittance of copper

Realizing some of the inadequacies of the Holstein model, Gurzhi [20, 21] improved the Holstein model by including the spatial variation of both the electromagnetic field and the electron distribution and the possibility of other interactions occurring such as electron-electron, electron-phonon and electron-impurity interactions. However, the calculated values of $\sigma_{\lambda NO}$ as predicted by Gurzhi for the noble metals in the optical and near infrared regions of the electromagnetic spectrum were equal to the calculated values of $\sigma_{\lambda NO}$ as predicted by Holstein; consequently at low temperatures, the Gurzhi result is identical to the Holstein result.

Experimental Data

An alternate and more direct method for determining the thermal radiative properties of metals at cryogenic temperatures is to measure them experimentally. Up to the present time, experimental values of the absorptance, emittance, or reflectance for the noble metals at low temperatures have been sparse. Variations exist in the available data which may be attributed to experimental technique and sample preparation. The various experimental techniques used to measure thermal radiative properties of solids at low temperatures are as follows: (*a*) calorimetric technique for the direct measurement of the absorptance, emittance, or reflectance (*b*) multiple reflection technique for the direct measurement of the near normal reflectance, (*c*) a technique utilizing the boil-off rate of a cryogen for the direct measurement of the absorptance or emittance, (*d*) blackbody comparison technique for the direct measurement of the emittance, and (*e*) optical constants technique for the indirect measurement of the absorptance, emittance, or reflectance.

The existing experimental data for the total hemispherical emittance of copper, gold, and silver are shown in Figs. 1–3, respectively. Also presented in these figures are the theoretical curves for the total hemispherical emittance as predicted by the Drude free electron

regions of the electromagnetic spectrum in the skin region of the metal.

$$\alpha_{\lambda N} = (\alpha_{\lambda N})_S + (\alpha_{\lambda N})_B = \left[p \frac{2\pi N e^2}{m\omega^2} \frac{v^3}{c^3} + (1-p) \frac{3}{4} \frac{v}{c} \right]_S + \left[\frac{2}{5} \left(\frac{m^*}{\pi N e^2} \right)^{1/2} \frac{\Theta}{T_{\text{ref}}\, \tau_{cl}} \right]_B \quad (15)$$

One way of justifying Holstein's decision to add skin effect absorptance to the bulk absorptance is that the results obtained from the anomalous skin effect model, equations (10) and (11), contain a bulk contribution term, a skin effect contribution term, and higher order terms. The bulk term that appears in the anomalous skin effect model is the Drude result. Since the quantum mechanical model reduces to the Drude result in the classical limit, it would appear reasonable to replace the Drude result in the anomalous skin effect model with Holstein's quantum mechanical model as Holstein has done. Thus, in the first approximation the bulk contribution and the skin effect contribution of the absorptance are uncoupled and additive. Of course, this argument breaks down if the two absorption mechanisms are coupled to each other. The limitations or errors that might exist in the Holstein quantum mechanical model have been discussed elsewhere [19].

The Holstein quantum mechanical model also can be used to describe the physics of the thermal radiation process in solids. The incident electromagnetic wave penetrates into the metal and interacts with the free electrons. This interaction, which may occur anywhere in the metal, is a two-stage process in which the electron simultaneously absorbs (or emits) a photon and emits (or absorbs) a phonon. Concurrently, those free electrons which reflect diffusely or specularly from the metal surface will absorb energy from the incident electromagnetic wave. These reflected electrons will travel in the skin region of the metal where they will eventually relinquish their energy to the lattice.

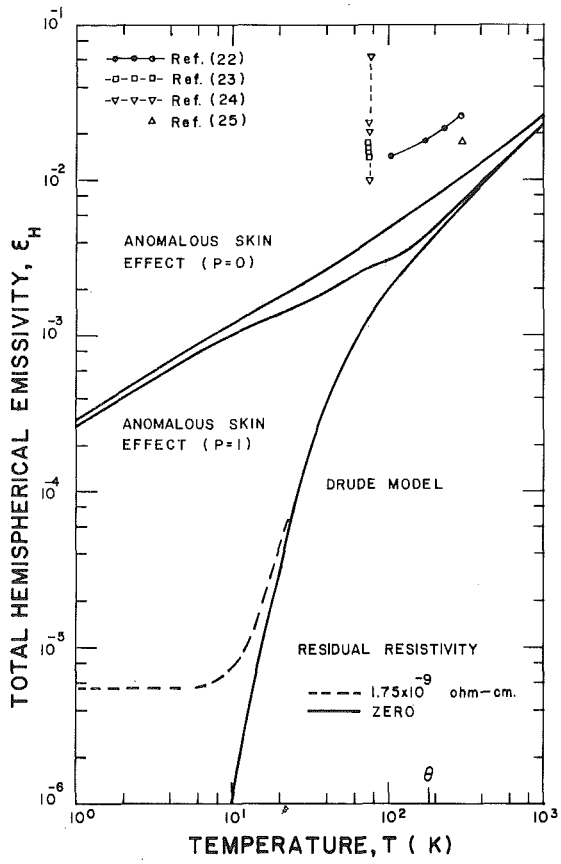

Fig. 2 Total hemispherical emittance of gold

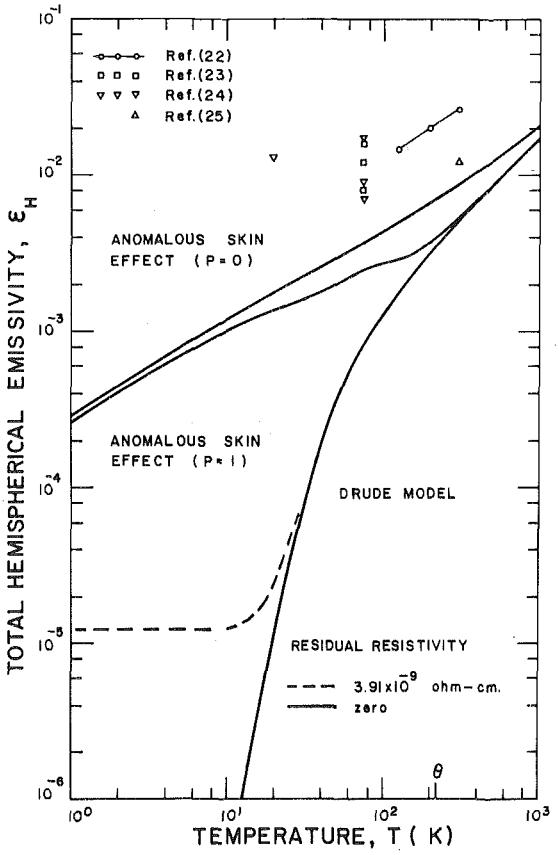

Fig. 3 Total hemispherical emittance of silver

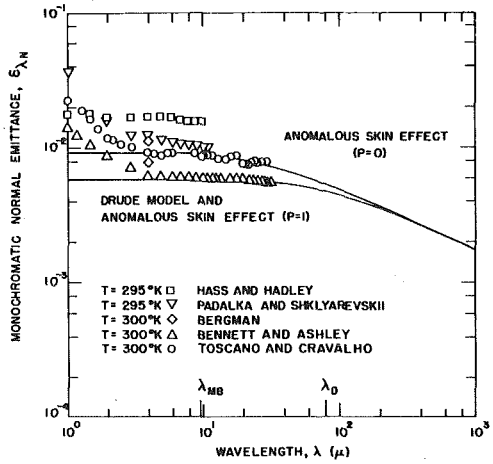

Fig. 4 Monochromatic normal emittance of gold at $T = 300$ K

theory and the anomalous skin effect theory (equation (4) and equations (8) and (9), respectively). The solid line for the Drude model represents a pure metal, i.e., a sample for which the residual resistivity is equal to zero, while the dashed line for the Drude model represents a sample with a residual resistivity of 1.84×10^{-9} ohm-cm, 1.75×10^{-9} ohm-cm and 3.91×10^{-9} ohm-cm for copper, gold, and silver, respectively. There was very little difference in the values of the total hemispherical emittance predicted by the anomalous skin effect theory for a clean metal and a "dirty" metal. Consequently, only pure metals were considered in the tabulation of ϵ_H predicted by the anomalous skin effect theory. Note that there is a lack of consistent experimental data to compare carefully with the theoretical curves. At temperatures below 76 K, there exist no experimental data of ϵ_H for gold and silver. For copper there exist a few experimental data points of ϵ_H between 2 K and 15 K but the range of values of ϵ_H varies from 0.0082 to 0.0765, a factor of nine. The discrepancy between the existing experimental data and the theoretical curves is quite large at cryogenic temperatures. For example, the difference between the existing experimental data and the theoretical data predicted by the anomalous skin effect theory for copper is one to two orders of magnitude in the temperature range of 2–20 K. In view of this large discrepancy, the wavelength dependence of the monochromatic emittance at various temperatures should be examined more carefully. The existing experimental data and the theoretical curves of the monochromatic normal emittance of gold at 300 K are presented in Fig. 4. The gold samples of Haas and Hadley [31] and Padalka and Shklyarevskii [32] were deposited in a vacuum of 10^{-5} Torr. Padalka and Shklyarevskii measured the monochromatic normal reflectance in an indirect manner by experimentally measuring the optical constants n and k and then calculating $\rho_{\lambda N}$ by means of Fresnel's formula. Bennett and Ashley [33] and Bergman [34] prepared their gold samples in a vacuum of 10^{-9} Torr. The technique of Bennett and Koehler [35] was an absolute double reflection technique, i.e., no standard or reference surface was required, in which the angle of incidence was 5 deg from the metal sample normal. Bergman used a single reflection technique but he required a calibrated reference surface. The lower data point at 4μ obtained by Bergman corresponds to a gold sample for which the reflection of electrons at the gold surface was specular while the upper data point corresponds to a gold sample for which the electron reflection was diffuse. Toscano and Cravalho [6] used a multiple reflection technique to measure the monochromatic near normal reflectance. The angle of incidence was 10 deg and their samples were prepared in a vacuum of 10^{-6} Torr.

Note that the experimental values of $\epsilon_{\lambda N}$ obtained by Toscano and Cravalho are less than those values obtained by Haas and Hadley, Padalka and Shklyarevskii, and Bergman ($p = 0$) but are greater than those values obtained by Bennett and Ashley and Bergman ($p = 1$). This is in agreement with the findings of Dickson and Jones [26] who have shown a direct relationship between deposition pressure and measured values of $\epsilon_{\lambda N}$. The experimental samples of Toscano and Cravalho were prepared at a pressure intermediate to the pressure levels used by the other investigators for sample preparation. Also, the gold samples prepared by Padalka and Shklyarevskii and Haas and Hadley were only 99.99 percent pure whereas the gold samples prepared by Bennett and Ashley, Toscano and Cravalho, and Bergman were 99.999+ percent pure. Notice that the experimental values of $\epsilon_{\lambda N}$ obtained by Bennett and Ashley for wavelengths equal to and larger than 4μ coincide with the results predicted by the anomalous skin effect theory for the case of the specular reflection of the electrons at the metal surface. (Note that at room temperature the anomalous skin effect theory for the electronically specular case ($p = 1$) is identical to the Drude model.) This result has been reported previously [37] and the investigators have shown that the surfaces of their gold samples were electronically specular (the surface roughness was less than 16Å rms). For wavelengths equal to and larger than 4μ the experimental values of $\epsilon_{\lambda N}$ obtained by Toscano and Cravalho very nearly coincide with the curve of $\epsilon_{\lambda N}$ predicted by the anomalous skin effect theory for the case of the diffuse reflection of the electrons at the metal surface. This is consistent with the criterion that metal surfaces with surface roughness larger than 30Å rms are electronically diffuse [38]. From the theoretical curves of Fig. 4, it is apparent that at the short wavelengths the difference between the Drude model and the anomalous skin effect theory for the electronically diffuse case is small, e.g., in the wavelength region between 4 and 10μ this difference is approximately 45.5 percent and at wavelengths larger than 100μ the difference is negligible; in fact, the two models reduce to the Hagen-Rubens relationship. Thus, in the visible and near infrared regions of the electromagnetic spectrum the surface condition for electron reflection is quite important for determining values of $\epsilon_{\lambda N}$. Note in Fig. 4 that the agreement between theory and experiment is

poorer at the short wavelengths for which the photoelectric effect begins to become significant. None of the theoretical models account for this phenomenon.

In Fig. 5 are presented the existing experimental data along with the theoretical curves of $\epsilon_{\lambda N}$ as predicted by the Drude free electron theory and the anomalous skin effect theory for gold at 78 K. Again the upper data point at 4μ obtained by Bergman corresponds to a gold sample for which the electron reflection at the gold surface was diffuse and the lower data point corresponds to a gold sample for which the reflection was specular. It is apparent that at 78 K in near infrared and infrared regions of the electromagnetic spectrum, the Drude model is beginning to differ from the anomalous skin effect theory for the case of specular reflection of electrons at the metal surface. The difference between the Drude model and the anomalous skin effect theory for the diffuse case at 78 K is a little bit larger than at room temperature, i.e., at 300 K.

The existing experimental data along with the theoretical curves of $\epsilon_{\lambda N}$ as predicted by the Drude free electron theory, and the anomalous skin effect theory, and the Holstein quantum mechanical model for gold at 4.2 K are presented in Fig. 6. It is apparent that the measurements by the present authors tend to favor the anomalous skin effect model rather than the Holstein model; however, short-wavelength measurements of $\epsilon_{\lambda N}$ for electronically specular surfaces are necessary before a conclusive judgement can be made. Again the upper data point at 4μ obtained by Bergman corresponds to a gold sample for which the reflection of electrons at the gold surface was diffuse ($p = 0$) and the lower data point corresponds to a gold sample for which the electron reflection was specular ($p = 1$). The large discrepancy between the results obtained by Bergman and results obtained by Toscano and Cravalho at liquid helium temperatures may be due to the differences in the experimental measurement technique. Notice that at 4.2 K the Drude model predicts a small value of $\epsilon_{\lambda N}$; in fact, if the residual resistivity were taken to be equal to zero, then the values of $\epsilon_{\lambda N}$ would reduce to zero. At wavelengths larger than 10^4 μm the Drude model and the anomalous skin effect theory reduce to the Hagen-Rubens relationship.

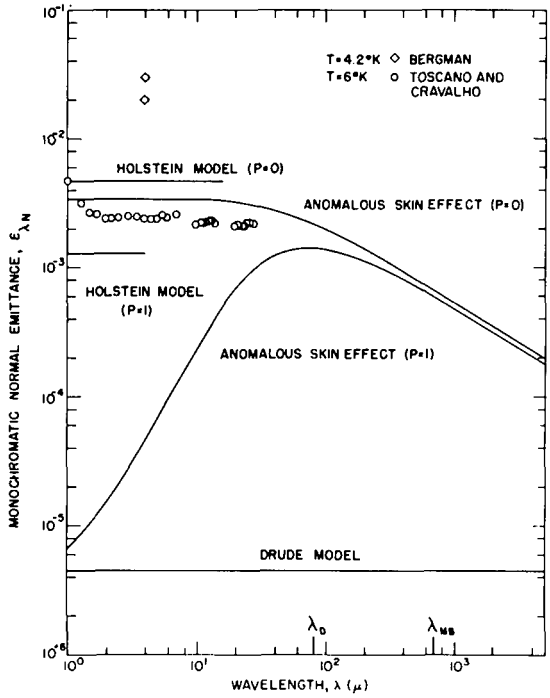

Fig. 6 Monochromatic normal emittance of gold at $T = 4.2$ K

Conclusions and Recommendations

Even though the room temperature experimental values of $\epsilon_{\lambda N}$ of gold are in close agreement with the theoretical values of $\epsilon_{\lambda N}$ predicted by the anomalous skin effect theory for the case of diffuse reflection of the electrons at the metal surface, it is recommended that the Drude free electron model be used to predict the values of $\epsilon_{\lambda N}$ in the wavelength region 4–30μ. The Drude model is easier to use than the anomalous skin effect theory and with the replacement of N and m with N_e and m^*, respectively, the model can be forced to fit the experimental curves exactly.

At liquid helium temperatures it is recommended that the anomalous skin effect theory for the case of diffuse reflection of electrons at the metal surface be used to predict values of $\epsilon_{\lambda N}$ of gold in the wavelength region to 2–30μ. Even though this model predicts values of $\epsilon_{\lambda N}$ 30 percent larger than the experimental values of $\epsilon_{\lambda N}$ of gold in the aforementioned wavelength region, it is the only reasonable existing model which may be applied to the entire electromagnetic spectrum. In this temperature range, the Drude model is totally inadequate since it predicts a vanishingly small value of $\epsilon_{\lambda N}$.

Unfortunately, the experimental values of $\epsilon_{\lambda N}$ for gold at cryogenic temperatures have been obtained only in the visible and near infrared regions of the electromagnetic spectrum. Since the Wien wavelength, λ_{MB}, which is the wavelength corresponding to the maximum energy emitted by a blackbody at a particular temperature is equal to 36μ at 77.4 K and 690μ at 4.2 K, the wavelength region of 1–30μ corresponds to only 16 percent and 0.01 percent of the blackbody radiation at temperatures of 77.4 and 4.2 K, respectively. As a result, there is not enough information available to predict thermal radiation heat fluxes from a gold surface at low temperatures. Therefore, it is suggested that the $\epsilon_{\lambda N}$ of gold be measured for the wavelength region of 1–1000μ at liquid helium temperatures. The dependence of $\epsilon_{\lambda N}$ on wavelength is strongest at wavelengths greater than the Debye wavelength. Thus, the proposed measurements of $\epsilon_{\lambda N}$ would also verify the validity of the anomalous skin effect theory at the longer wavelengths ($\lambda > \lambda_D$) and would establish the existence of a plateau at low temperatures and the location of the knee in the curve predicted by the anomalous skin effect theory for $\epsilon_{\lambda N}$ as a function of temperature [39].

Another area of interest is the value of the rms surface roughness for transition from specular to diffuse reflection of the electrons at the metal surface in the temperature range of 4.2–78 K. The difference

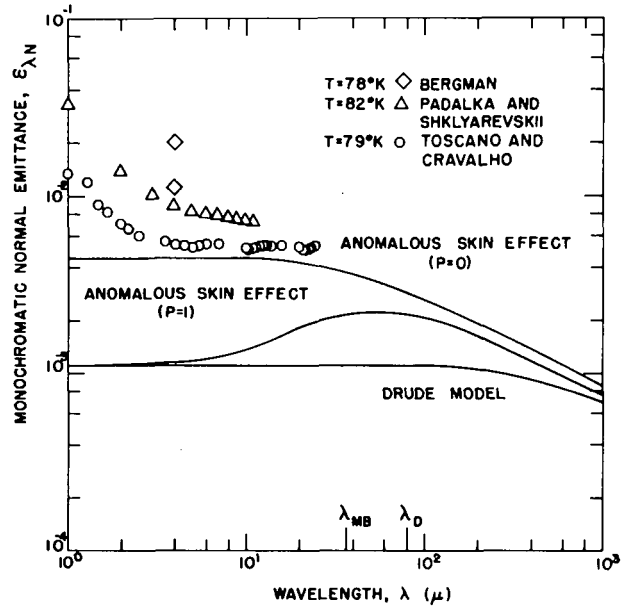

Fig. 5 Monochromatic normal emittance of gold at $T = 78$ K

Table 1 Physical properties of the noble metals

	Copper	Gold	Silver
N (electrons/cm^3)	8.5×10^{22}	5.8×10^{22}	5.9×10^{22}
θ (K)	310	180	220
σ_0 (T = 273 K) (ohm − cm)$^{-1}$	6.45×10^5	4.85×10^5	6.80×10^5
$T_{\text{ref}}\,\tau_{cl}$	7.96×10^{-12}	8.21×10^{12}	11.50×10^{-12}
λ_p (Å)	1147	1377	1377
λ_D (μ)	46.5	80.0	65.5
m*/m	1.38	1.0	1.0
v (cm/s)	1.58×10^8	1.39×10^8	1.38×10^8

in the values of $\epsilon_{\lambda N}$ as predicted by the anomalous skin effect theory becomes more significant at lower temperatures. Müser [40] concluded that specular reflection of the electrons at the metal surface will occur only for rms surface roughness on the order of the electron de Broglie wavelength (~ 5Å). More recently, Greene [41] concluded that it is possible for electrons to be reflected specularly from surfaces with values of rms surface roughness larger than the de Broglie wavelength. On the basis of experimental measurements, Bennett, et al. [42] and Bergman [43] have shown at room temperature the transition from specular to diffuse electron reflection occurs rather abruptly in the rms surface roughness range of 16–30Å. These experimental results appear to be in agreement with Green's conclusions. On the other hand, if the free electrons are treated as a gas, the mean kinetic energy of the free electrons is equal to πKT and and de Broglie wavelength is then 346Å at 4.2 K and 43Å at 300 K. It is then possible that p may have the same temperature dependence as the de Broglie wavelength for the free electron gas, i.e., $T^{-1/2}$. Therefore, it is suggested that the $\epsilon_{\lambda N}$ of metal samples with rms surface roughnesses of 16Å and larger be measured in wavelength regions of 1–1000μ at cryogenic temperatures. This information would be useful for the design and manufacture of thermal radiation shields.

Much work needs to be done on the theoretical models. The present work has shown that all of the existing models have some attractive features to them and that possibly these features could be combined in a more meaningful way. However, more experimental work also needs to be done in order to better define the attractive features and limitations of existing models.

Acknowledgment

The authors wish to acknowledge the support of the National Science Foundation (NSF Grant No. GK 16908).

References

1 Cravalho, E. G., Tien, C. L., and Caren, R. P., "Effect of Small Spacing on Radiative Transfer Between Two Dielectrics," JOURNAL OF HEAT TRANSFER, TRANS. ASME Series C, Vol. 89, 1967, pp. 351–358.

2 Rolling, R. E., and Tien, C. L., "Radiant Heat Transfer for Nongray Metallic Surfaces at Low Temperatures," *Thermophysics of Spacecraft and Planetary Bodies*, Vol. 20, Academic Press, New York, 1967, pp. 677–693.

3 Domoto, G. A., and Tien, C. L., "Thick Film Analysis of Radiative Transfer Between Parallel Metallic Surfaces," JOURNAL OF HEAT TRANSFER, TRANS ASME, Series C, Vol. 92, No. 3, 1970, pp. 399–404.

4 Boehm, R. F., and Tien, C. L., "Small Spacing Analysis of Radiative Transfer Between Metallic Surfaces," JOURNAL OF HEAT TRANSFER, TRANS. ASME, Series C, Vol. 92, No. 3, 1970, pp. 405–411.

5 Caren, R. P., "Radiation Heat Transfer Between Closely Spaced Metal Surfaces at Low Temperature: The Impact of Discrete Modes of the Radiation Field," JOURNAL OF HEAT TRANSFER, TRANS. ASME, Series C, Vol. 94, No. 3, 1972, pp. 295–299.

6 Toscano, W. M., and Cravalho, E. G., "Experimental Measurements of the Monochromatic Near Normal Reflectance of Gold at Cryogenic Temperatures," *Proceedings of the Fifth International Heat Transfer Conference*, Vol. 1, Tokyo, Japan, 1974, pp. 16–20.

7 Born, M., and Wolf, E., *Principles of Optics*, Third ed., Pergamon Press, New York, 1965, pp. 624–627.

8 Wilson, A. H., *The Theory of Metals*, Second ed., Cambridge, London, 1965, p. 2.

9 Siegel, R., and Howell, J. R., *Thermal Radiation Heat Transfer*, McGraw-Hill, New York, 1972, p. 100.

10 Parker, W. J., and Abbott, G. L., "Total Emittance of Metals," in *Symposium on Thermal Radiation of Solids*, NASA SP-55, 1965, pp. 11–28.

11 Mott, N. F., and Jones, H., *The Theory of the Properties of Metals and Alloys*, Dover Publications, New York, 1958, p. 108.

12 Sokolov, A. V., *Optical Properties of Metals*, American Elsavier Publishing Co., New York. 1967, p. 76.

13 Reuter, G. E. H., and Sondheimer, E. H., "The Anomalous Skin Effect in Metals," *Proceedings of the Royal Society*, London, Series A, Vol. 195, 1948, pp. 336–364.

14 Dingle, R. B., "The Anomalous Skin Effect and the Reflectivity of Metals. I," *Physica*, Vol. 19, 1953, pp. 311–347.

15 Holstein, T., "Optical and Infrared Reflectivity of Metals at Low Temperatures," *Physical Review*, Vol. 99, 1952, pp. 1427–1428.

16 Holstein, T., "Optical and Infrared Volume Absorptivity of Metals," *Physical Review*, Vol. 96, 1954, pp. 535–536.

17 Holstein, T., "Optical and Infra-Red Volume Absorption by Conduction Electrons," Westinghouse Research Laboratories Research Report 60-94698-3-R6, 1955.

18 Holstein, T., "Optical and Infra-Red Volume Absorption by Conduction Electrons III," Westinghouse Research Laboratories Research Report 60-94698-3-R6, 1955.

19 Toscano, W. M., "Thermal Radiative Properties of the Noble Metals at Cryogenic Temperatures," PhD thesis, Department of Mechanical Engineering, Massachusetts Institute of Technology, Nov. 1973.

20 Gurzhi, R. N., "On the Theory of the Infrared Absorptivity of Metals," *Soviet Physics JETP*, Vol 6, No. 6, 1958, pp. 506–512.

21 Gurzhi, R. N., "Mutual Electron Correlations in Metal Optics," *Soviet Physics JETP*, Vol. 35, No. 4, 1959, pp. 673–675.

22 Caren, R. P., "Low-Temperature Emittance Determinations," *Thermophysics and Temperature Control of Spacecraft and Entry Vehicles*, Vol. 18, Academic Press, New York, 1966, pp. 61–73.

23 Zimmerman, F. J., "Total Emissivities and Absorptivities of Some Commercial Surfaces at Room and Liquid-Nitrogen Temperatures," *Journal of Applied Physics*, Vol. 26, No. 12, 1955, pp. 1483–1488.

24 Fulk, M. M., and Reynolds, M. M., "Emissivities of Metallic Surfaces at 76°K," *Journal of Applied Physics*, Vol. 28, No. 12, 1957, pp. 1464–1467.

25 Armaly, B. F., and Tien, C. L., "Emissivities of Thin Metallic Films at Cryogenic Temperatures," *Heat Transfer 1970 Papers Presented at the Fourth International Heat Transfer Conference Paris-Versailles*, Vol. III, p. R1.1.

26 Betz, H. T., Olson, O. H., Schurin, B. D., and Morris, J. C., *Determination of Emissivity and Reflectivity Data on Aircraft Structure Materials, Part II*, ASTIA No. 202493, WADC TR 56-22, 1956.

27 Domoto, G. A., Boehm, R. F., and Tien, C. L., "Experimental Investigation of Radiative Transfer Between Metallic Surfaces at Cryogenic Temperatures," *Journal of Heat Transfer, Trans. ASME*, Series C, Vol. 92, No. 3, 1970, pp. 412–417.

28 Cravalho, E. G., Domoto, G. A., and Tien, C. L., "Measurements of Thermal Radiation of Solids at Liquid-Helium Temperatures," *Progress in Aeronautics and Astronautics*, Vol. 22, J. T. Bevans, ed., Academic Press, New York, 1968, pp. 531–542.

29 Ramanathan, R. G., "Infrared Absorption by Metals at Low Temperatures," *Proceedings of the Physical Society*, Series A., Vol. 65, 1952, pp. 532–540.

30 Hawks, K. H., and Cottingham, W. B., "Total Normal Emittances of Some Real Surfaces at Cryogenic Temperatures," in *Advances in Cryogenic Engineering*, Vol. 16, K. D. Timmerhaus, ed., Plenum Press, New York, 1971, pp. 467–474.

31 Haas, G., and Hadley, L., "Optical Properties of Metals," in *American Institute of Physics Handbook*, Second ed., McGraw-Hill, New York, D. E. Gray, ed., 1963, pp. 6–119.

32 Padalka, V. G., and Shklyarevskii, I. N., "Determination of the Microcharacteristics of Silver and Gold from the Infrared Optical Constants and the Conductivity at 82 and 295°K," *Optics and Spectroscopy*, Vol. 11, 1961, pp. 285–288.

33 Bennett, J. M., and Ashley, E. J., "Infrared Reflectance and Emittance of Silver and Gold Evaporated in Ultrahigh Vacuum," *Applied Optics*, Vol. 4, 1965, pp. 221–224.

34 Bergman, T. G., *Reflectivity of Silver and Gold as a Function of Temperature at Four Micron Wavelength*, NWC TP 5043, 1970.

35 Bennett, H. E., and Koehler, W. F., "Precision Measurement of Absolute Specular Reflectance With Minimized Systematic Errors," *Journal of the Optical Society of America*, Vol. 50, 1960, pp. 1–6.

36 Dickson, P. F., and Jones, M. C., *Infrared Reflectances of Metals at Cryogenic Temperatures --A Compilation from the Literature*, NBS Tech. Note 348, National Bureau of Standards, 1966.

37 Bennett, H. E., and Bennett, J. M., "Validity of the Drude Theory for Silver, Gold, and Aluminum in the Infrared," in *Optical Properties and Electronic Structure of Metals and Alloys*, F. Abeles, ed. North Holland Publishing Co., Amsterdam, 1966, pp. 175–188.
38 Bergman, T. C., *op. cit.*, p. 23.
39 Toscano, W. M., and Cravalho, E. G., *op. cit.*, p. 20.
40 Müser, H. A., "The Physical Nature of a Metal Surface in Conduction Theory," *Philosophical Magazine*, Vol. 45, 1954, pp. 1237–1246.
41 Greene, R. F., "Boundary Conditions for Electron Distributions for Crystal Surfaces," *Physical Review*, Vol. 141, No. 2, 1966, pp. 687–689.
42 Bennett, H. E., Bennett, J. M., Ashley, E. M., and Motyka, R. J., "Verification of the Anomalous Skin-Effect Theory for Silver in the Infrared," *Physical Review*, Vol. 165, No. 3, 1968, pp. 775–764.
43 Bergman, *op. cit.*

C. C. Chen
Graduate Research Assistant.

R. Eichhorn
Professor.
Mem. ASME

Department of Mechanical Engineering,
University of Kentucky,
Lexington, Ky.

Natural Convection From a Vertical Surface to a Thermally Stratified Fluid

Results are presented of a study of natural convection from an isothermal finite plate immersed in a stable thermally stratified fluid. An analytical solution to the problem is obtained by using the local nonsimilarity method. Theoretical local and overall heat transfer coefficients are given for Pr = 0.7 and 6.0. Velocity and temperature profiles are given for Pr = 6.0. The actual experimental configuration was a vertical copper cylinder enclosed in a cube with rigid walls. Heat transfer data are correlated with the measured ambient thermal gradient. Visual studies of the flow field are also discussed. Excellent agreement is achieved between analysis and experiment.

Introduction

The problem of natural convection heat transfer from bodies submerged in stratified fluids arises in many important applications. Only a few studies of the effect of stratification on the heat removal process have been published. Eichhorn's [1][1] series solution predicts the heat transfer from a vertical plate immersed in a linearly stratified fluid. Fujii, Takeuchi, and Morioka [2] give both analytical and experimental results for a temperature stratification in which the ambient temperature distribution varies with distance to the 0.7 power. Piau [3] carried out a study in which both the plate temperature and the ambient temperature varied with a power of the distance along the plate. His experimental temperature distributions compare well with his theory, but in order to make the comparison, he had to use a nonzero starting length. Eichhorn, Lienhard, and Chen [4] have given experimental heat transfer results for isothermal spheres and horizontal cylinders.

In this paper, a finite isothermal vertical plate in a stable, thermally stratified fluid is considered. Cheesewright's work [5] and the paper of Yang, Novotny, and Cheng [6], have shown that a similarity solution is not possible. This fact was recognized by Eichhorn and by Fujii, et al., who developed series solutions to account for the nonzero leading edge temperature difference. Eichhorn had calculated only three terms in the series solution. Fujii, et al., showed that the fourth term is also necessary. In reconsidering the problem in this paper, the local nonsimilarity method developed by Sparrow and coworkers [7, 8, 9], and recently applied by Chen and Mucoglu [10] as well, has been used.

The experimental portion of this paper presents information on heat transfer to a vertical cylinder in water for both the unstratified and the stratified cases. The Prandtl number ranged from 5.5 to 7.5 and the Rayleigh number from 1.5×10^6 to 2.2×10^8 for the unstratified case and from 1.7×10^6 to 3.2×10^7 for the stratified case. The stratification parameter (defined in equation (2)) ranged from 0.6 to 4.5.

Outline of the Problem

The coordinate system and boundary condition scheme are shown in Fig. 1. The wall temperature is uniform at T_w and the ambient temperature varies linearly with distance from the leading edge. The natural convection boundary layer equations for a vertical plate are the standard ones.

The boundary conditions appropriate to the problem are:

$$u(x, 0) = v(x, 0) = 0;\ T(x, 0) = T_w = \text{constant}$$

$$u(x, \infty) = 0;\ T(x, \infty) = T_{\infty 0} + ax \tag{1}$$

where $a \equiv dT_\infty/dx$ and $T_{\infty 0}$ is the ambient temperature at $x = 0$. Positive values of a imply a stably stratified ambient fluid, the only concern in this paper.

As shown in [4], heat transfer from bodies immersed in a stratified environment can be expressed in terms of the usual Grashof (or Rayleigh) and Prandtl numbers and a parameter, S, involving the dimensionless ambient temperature gradient:

$$\text{Nu} = \text{Nu}(\text{Gr}, \text{Pr}, S)$$

where

$$S \equiv \frac{L}{\Delta T}\frac{dT_\infty}{dx} \tag{2}$$

with L a characteristic body dimension, ΔT a characteristic temper-

[1] Numbers in brackets designate References at end of paper.

Contributed by the Heat Transfer Division and presented at the Winter Annual Meeting, Houston, Texas, November 30–December 5, 1975, of THE AMERICAN SOCIETY OF MECHANICAL ENGINEERS. Revised manuscript received by the Heat Transfer Division February 12, 1976. Paper No. 75-WA/HT-62.

ature difference and dT_∞/dx the slope of the ambient temperature profile with vertical distance. In this paper: L = length of the plate

$$\Delta T = \Delta T_m = \text{mean temperature difference}$$
$$dT_\infty/dx = a = \text{constant}$$

and $S \geq 0$ only. The condition $T_w > T_\infty$ implies $S < 2$ so long as $a > 0$. When $a = 0$, the ambient fluid is isothermal and $S = 0$. When $T_w = T_\infty$ at some point on the plate, $S > 2$ and for the condition $T_w \to T_\infty$ at $x = 0.5L$, $S \to \infty$. The numerical value of S has a significant effect on the heat transfer rate and the plume configuration. These will be discussed in a later section.

With a finite initial temperature difference, ΔT_0, the local temperature difference, ΔT, decreases linearly with x, the distance from the leading edge:

$$\Delta T = \Delta T_0 \left(1 - \frac{2S}{2+S}\frac{x}{L}\right) \tag{3}$$

When $x/L = (2 + S)/2S$, the buoyancy of the fluid near the wall is zero.

Analysis

The equations governing natural convection to a vertical surface in a thermally stratified environment have been presented by a number of authors. Eichhorn [1] considered the case of a linear thermal-stratification and presented solutions for three terms in the series expansion of the nonlinear partial differential equations. Fujii, et al. [2] solved four terms of a similar series, but their case (both experimental and theoretical) was for an environment with a nonlinear thermal-stratification so the results cannot be compared directly with either Eichhorn's earlier results or those of the present study.

Instead of extending the series to include a fourth, as Fujii, et al., did, and possibly a fifth term, we decided to try the local nonsimilar solution technique proposed recently by Sparrow and developed by him and a number of co-workers [7–9]. This method is not without its own set of problems, however, some of which will be alluded to in the following discussion. An elaborate discussion of the local nonsimilarity method, though, will not be given.

As a starting point, the dimensionless transformed partial differential equations are:

$$F''' + 3FF'' - 2F'F' + \theta = 4\xi[F'(\partial F'/\partial\xi) - F''(\partial F/\partial\xi)],$$
$$(1/\mathrm{Pr})\theta'' + 3F\theta' - 4\xi F' = 4\xi[F'(\partial\theta/\partial\xi) - \theta'(\partial F/\partial\xi)],$$
$$F(\xi, 0) = F'(\xi, 0) = \theta(\xi, 0) - 1 + \xi = 0,$$
$$F'(\xi, \infty) = \theta(\xi, \infty) = 0 \tag{4}$$

where the primes denote partial derivatives with respect to η.

The transformations used to develop the equations are:

$$\Psi = 4\nu[g\beta(T_w - T_{\infty 0})/4\nu^2]^{1/4}x^{3/4}F(\xi, \eta)$$
$$\theta = (T - T_\infty)/(T_w - T_{\infty 0})$$
$$\xi = ax/(T_w - T_{\infty 0})$$
$$\eta = [g\beta(T_w - T_{\infty 0})/4x\nu^2]^{1/4}y \tag{5}$$

so the physical variables can be recovered in the usual fashion.

In the local similarity technique (also called the first level of truncation in the parlance of the local nonsimilarity method), the right-hand sides in equation (4) are deleted. The equations that remain are treated as ordinary differential equations and solved with the variable ξ taking the role of a parameter.

In the second level of truncation, the terms on the right-hand sides are retained, but additional differential equations are developed to provide estimates for them. The additional equations are found simply by differentiating each of the foregoing equations with respect to the variable ξ and defining the new terms

$$G = \partial F/\partial\xi, \quad \phi = \partial\theta/\partial\xi$$

to allow the right-hand sides, deleted in the first level of truncation, to be retained in the second level.

The result is

$$F''' + 3FF'' - 2F'F' + \theta + 4\xi(GF'' - F'G') = 0,$$
$$(1/\mathrm{Pr})\theta'' + 3F\theta' - 4\xi F' + 4\xi(G\theta' - F'\phi) = 0,$$
$$G''' + 3FG'' - 8F'G' + 7F''G + \phi + \underline{4\xi(GG'' - G'G')} = 4\xi[F'(\partial G'/\partial\xi) - F''(\partial G/\partial\xi)],$$
$$(1/\mathrm{Pr})\phi'' + 3F\phi' - 4F'\phi + 7G\theta' - 4F' - 4\xi G' + \underline{4\xi(G\phi' - G'\phi)} = 4\xi[F'(\partial\phi/\partial\xi) - \theta'(\partial G/\partial\xi)],$$
$$F(\xi, 0) = F'(\xi, 0) = G(\xi, 0) = G'(\xi, 0) = \theta(\xi, 0) - 1 + \xi = \phi(\xi, 0) + 1 = 0,$$
$$F'(\xi, \infty) = G'(\xi, \infty) = \theta(\xi, \infty) = \phi(\xi, \infty) = 0 \tag{6}$$

To close the system of equations at the second level, terms involving $\partial G/\partial\xi$ and $\partial\phi/\partial\xi$ in equation (6) are deleted (being regarded as small) and the whole set is treated as a coupled system of ordinary differential equations, parameterized in ξ.

The equations resulting from the foregoing transformation and simplifications were programed for solution on the digital computer. A modified predictor-corrector integration routine was used with appropriate first guesses for the missing initial boundary conditions. Subsequent initial values were obtained using the Nachtsheim-Swigert [11] method. This technique finds modified initial values by seeking to minimize the error of the solution at infinity. Additional differential equations are solved along with the system equations to

Nomenclature

a = ambient temperature gradient, dT_∞/dx
F = dimensionless stream function, equation (5)
G = auxiliary function, $\partial F/\partial\xi$
Gr_x = Grashof number based on initial temperature difference, $g\beta\Delta T_0 x^3/\nu^2$
Gr = Grashof number based on mean temperature difference, $g\beta\Delta T_m x^3/\nu^2$
g = gravitational acceleration
$\bar{h}$ = average heat transfer coefficient
k = thermal conductivity
L = height of plate
L_1, L_2 = plume-related dimensions, Fig. 7
Nu = local Nusselt number based on initial temperature difference, $qx/k\Delta T_0$
$\overline{\mathrm{Nu}}$ = average Nusselt number based on mean temperature difference, $Q/k\Delta T_m$
Pr = Prandtl number
q = local heat transfer rate per unit surface area
Q = overall heat transfer rate per unit width
Ra = Rayleigh number based on mean temperature difference, $g\beta\Delta T_m L^3/\nu\alpha$
S = stratification parameter $aL/\Delta T_m$
T = temperature
ΔT = temperature difference between wall and free stream, $T_w - T_\infty$
u, v = x and y velocity components
x, y = vertical and horizontal coordinates
α = thermal diffusivity
β = coefficient of thermal expansion
η = dimensionless horizontal distance, equation (5)
ν = kinematic viscosity
Ψ = stream function
ϕ = auxiliary function, $\partial\theta/\partial\xi$
θ = dimensionless temperature, equation (5)
ξ = dimensionless vertical distance, equation (5)

Subscripts

iso = isothermal
0, m, t = leading edge, midheight and top of the plate, respectively
w, ∞ = wall and ambient, respectively

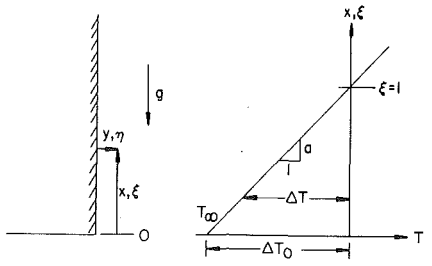

Fig. 1 Coordinate system and scheme of boundary conditions

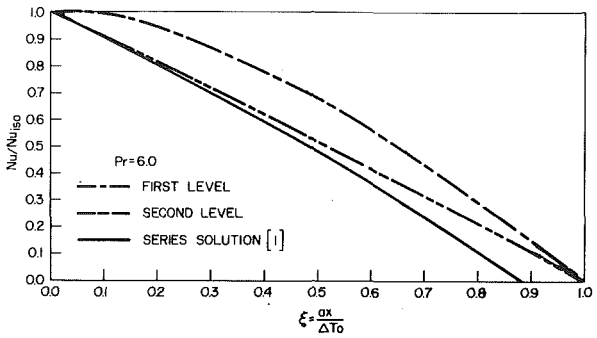

Fig. 2 Theoretical local heat transfer rate for Pr = 6.0

obtain the needed information. We found it necessary to place "infinity" very near $\eta = 0$ to start the solutions. "Infinity" was increased automatically as more and more refined estimates of the missing initial values were found. The computations were stopped when ($F'^2 + F''^2 + \theta^2 + \theta'^2$) at infinity was of the order 10^{-10}. With this criterion, infinity varied from $\eta = 10$–16.

Calculations were performed for Pr = 0.7 and Pr = 6.0 (the mean value of the experimental range) for each of the sets of equations (4) and (6). The heat transfer results for Pr = 6.0 are shown in Fig. 2 which also includes the series solution [1]. The form used illustrates directly the effect of stratification by comparing the actual local heat transfer rate with the rate for a plate at T_w in a uniform temperature environment at $T_{\infty 0}$.

A set of velocity and temperature profiles for Pr = 6.0 determined from equation (6) (second level of truncation) is shown in Fig. 3. They can be compared with Fig. 3 of reference [1] which shows the same case as determined by the series solution. The most noticeable difference

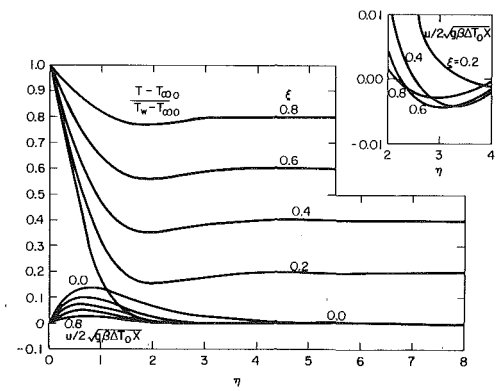

Fig. 3 Theoretical velocity and temperature profiles for Pr = 6.0

Table 1 Local heat transfer and friction coefficients for Pr = 0.7 and 6.0

ξ	Pr = 6.0		Pr = 0.7	
	$-\theta'(\xi, 0)$	$F''(\xi, 0)$	$-\theta'(\xi, 0)$	$F''(\xi, 0)$
0.0	1.0074	0.4648	0.4995	0.6789
0.1	0.9180	0.4094	0.4587	0.6249
0.2	0.8266	0.3560	0.4177	0.5705
0.3	0.7313	0.3076	0.3769	0.5152
0.4	0.6330	0.2616	0.3374	0.4587
0.5	0.5323	0.2169	0.3004	0.3994
0.6	0.4296	0.1731	0.2677	0.3331
0.7	0.3250	0.1296	0.2337	0.2513
0.8	0.2187	0.0864	0.1778	0.1606
0.9	0.1104	0.0432	0.0975	0.0764

is in the prominence of negative vertical velocities and temperature differences ($T - T_\infty$) exhibited by the series solution.

Numerical values of $\theta'(\xi, 0)$ and $F''(\xi, 0)$ for both Prandtl numbers for the second level of truncation are given in Table 1. The numerical solutions were carried only to $\xi = 0.9$. All previous cases which have been calculated have shown the third level to differ negligibly from the second. For the present case, calculations for the third level were carried out for Pr = 6.0 at $\xi = 0.4$ where the agreement between the absolute values of the first and second level is worst. The result was $F''(0.4, 0) = 0.2641$ and $\theta'(0.4, 0) = -0.6282$, each of which are within one percent of the second level values given in Table 1.

In applying the local nonsimilarity method, most authors have also deleted the underlined terms in equation (6). In the work of Chen and Mucoglu [10] the terms were retained without comment. The problem was discussed by Rogers [12], who concluded the additional terms led to a mathematical instability in the equations. Our experience with both forms of the equations does not agree with Rogers' conclusion. When the dimensionless temperature was formed with reference to the local temperature difference, a solution for the resulting equations could be found around $\xi = 0.7$, only if the additional terms were kept in the equations. In addition, retention of the terms gives closer agreement between the second and third level calculations than if the terms are dropped in the second level. By way of example, at $\xi = 0.4$ for Pr = 6.0, the second level calculation without the underlined terms gave $\theta'(0.4, 0) = -0.6533$ and $F''(0.4, 0) = 0.2543$. These values are about four percent from the third level solutions.

To compare the experimental results with theory requires average values for the heat transfer rate. These have been obtained by integration of polynomial expressions fitted by least squares to the local heat transfer results

$$\frac{\mathrm{Nu}}{\mathrm{Nu_{iso}}} = \frac{\theta'(\xi, 0)}{\theta'(0, 0)} = 1 + C_1\xi + C_2\xi^2 + C_3\xi^3 + C_4\xi^4 \qquad (7)$$

where the C's are given in Table 2. The local Nusselt number can be represented by the expression

$$\mathrm{Nu} = \frac{qx}{k\Delta T_0} = \left[-\frac{\theta'(0, 0)}{\sqrt{2}}\right](\mathrm{Gr}_x)^{1/4}(1 + C_1\xi + C_2\xi^2 + C_3\xi^3 + C_4\xi^4) \qquad (8)$$

where $\mathrm{Gr}_x = g\beta\Delta T_0 x^3/\nu^2$.

The overall heat transfer, obtained by integrating equation (8) over x is

$$\frac{Q}{k\Delta T_0} = \left[-\frac{4}{3\sqrt{2}}\theta'(0, 0)\right](\mathrm{Gr}_x)^{1/4} H(\xi) \qquad (9)$$

where Q is the heat transfer rate per unit width of the plate and

$$H(\xi) = 1 + \frac{3}{7}C_1\xi + \frac{3}{11}C_2\xi^2 + \frac{3}{15}C_3\xi^3 + \frac{3}{19}C_4\xi^4$$

Alternatively, the heat transfer rate can be expressed in terms of Nusselt and Grashof numbers based on a mean temperature difference over the length x:

$$\overline{\mathrm{Nu}} = \frac{Q}{k\Delta T_0} = \left[\frac{-4}{3\sqrt{2}}\theta'(0,0)\right](\mathrm{Gr})^{1/4}\left[\frac{H(\xi)}{(1-0.5\xi)^{5/4}}\right] \quad (10)$$

where $\mathrm{Gr} = g\beta\Delta T_m x^3/\nu^2$. For the unstratified case, the Nusselt number, $\overline{\mathrm{Nu}}_{\mathrm{iso}}$ is obtained simply by setting $\xi = 0$ in equation (10).

These results are appropriate for $S \leq 2$. For $S > 2$, a portion of the plate extends above the value of x at which the plate temperature equals the ambient temperature ($\xi = 1$). For $S = \infty$, if the properties are uniform, the *net* heat transfer from the plate will be zero, with the upper half absorbing as much heat as is rejected by the lower half. To find an expression for the heat transfer when $2 < S < \infty$, we will assume that the heat transfer rate for the portions of the plate above and below $\xi = 1$ are each given by equation (9) with $\xi = 1$. The heat absorbed by the upper portion then depends only on $T_w - T_{\infty t}$ and $L - L'$, where L' is the value of x at which $T_w = T_\infty$. Similarly, the heat rejected by the lower portion depends on $T_w - T_{\infty 0}$ and L'. The net heat transfer rate from the plate is

$$\frac{Q}{k\Delta T_0} = A\left[\left(\frac{L'}{L}\right)^{3/4} - \left(\frac{T_{\infty t} - T_w}{T_w - T_{\infty 0}}\right)^{5/4}\left(1 - \frac{L'}{L}\right)^{3/4}\right] \quad (11)$$

where $A = -4/3\sqrt{2}\,\theta'(0,0)\,H(1)\,(g\beta\Delta T_0 L^3/\nu^2)^{1/4}$. Expressing the ratio of lengths and the ratio of temperature differences in terms of S, the average Nusselt number based on the mean temperature difference is then given by

$$\frac{\overline{\mathrm{Nu}}}{\overline{\mathrm{Nu}}_{\mathrm{iso}}} = B(\mathrm{Pr})S^{1/4} \quad (12)$$

where $B = 1.480$ for $\mathrm{Pr} = 0.7$ and $B = 1.179$ for $\mathrm{Pr} = 6.0$ and $S = aL/\Delta T_m$.

We are not suggesting, in this simple analysis, that q is necessarily zero at $x = L'$. Except for the case $S = \infty$, the boundary layer from below will arrive in the vicinity of $x = L'$ with a higher momentum than the one from above. This will cause the point of separation from the surface to occur at some $x > L'$, and most likely, $q > 0$ at $x = L'$. It does appear, however, that very little heat transfer takes place near $x = L'$ so the point may be moot. In addition, near $x = L'$ the flow begins to turn so the boundary layer analysis is not appropriate anyway. The experimental results presented below seem to bear out the prediction very well indeed.

Experiment

The experimental apparatus is essentially the same as that described in [4]. A 25.5 cm cubical tank with plexiglas s side-walls contained stratified water. The top and bottom are isothermal copper plates, criss-crossed with tubing supplied with water from commercial constant-temperature water baths. The sides are insulated with 5 cm polyurethane foam, which can be slid apart on two opposing sides to permit observation.

The tank was heated on the top and cooled on the bottom to achieve a nearly linear vertical fluid temperature distribution. Two thin copper sheets were placed along two side walls to improve the linearity of the temperature distribution and to decrease the time required to achieve thermal equilibrium. The actual test object was a 1.9 cm dia by 7 cm long copper cylinder with a central heater suspended vertically in the center of the tank. Unheated plexiglas s extensions were fixed to the heated copper cylinder for 2.54 cm on the bottom and 3.81 cm on the top end. The extensions served to reduce heat loss from the ends of the cylinder. Calculations were made to assure that they had a negligible effect on the uniformity of the wall temperature. The test section was sufficiently small that, for the heat transfer coefficients we observed, its Biot number was considerably less than unity. Accordingly, it was essentially isothermal and its temperature was measured with a single thermocouple buried in the copper. As further assurance of the adequacy of the temperature data, a few initial measurements were made with three thermocouples spaced along the height of the cylinder. Differences were not detectable.

The thermocouples were 0.127 mm dia copper-constantan with an ungrounded junction sheathed in 0.5 mm OD stainless steel. To measure the fluid temperature distribution one thermocouple was traversed vertically through the fluid by a gear-motor, screw-Unislide mechanism at speeds up to 1.25 cm/min. The temperature profiles were plotted directly on an x-y recorder. Although the driving speed was very low, the time lag of the thermocouple could still be observed (<0.05°C). Therefore, the thermocouple was driven from the bottom to the top of the tank and then reversed in direction to the bottom. The actual temperature profile was taken as the average of the two profiles. The temperature difference between the cylinder and the ambient fluid at the midheight of the cylinder was measured directly with two thermocouples in series and read from a Leeds & Northrup 7554 type K-4 potentiometer. Power to the heater was calculated from the d-c voltage drops across the heater and across a precision series resistor. Both voltages were measured with a 0.5 percent accuracy digital voltmeter. The probable errors for the present data are: Nu: ±3.2 percent, Ra: ±4.3 percent, S: ±3.5 percent.

Visualization of the flow field was obtained by the thymol blue dye

Table 2 Coefficients of approximate polynomial for local Nusselt numbers for Pr = 0.7 and 6.0

Pr	C_1	C_2	C_3	C_4	RMS error
6.0	-0.8620	-0.1989	0.0865	-0.0256	0.0002
0.7	-0.7572	-0.7485	2.2715	-1.1770	0.0053

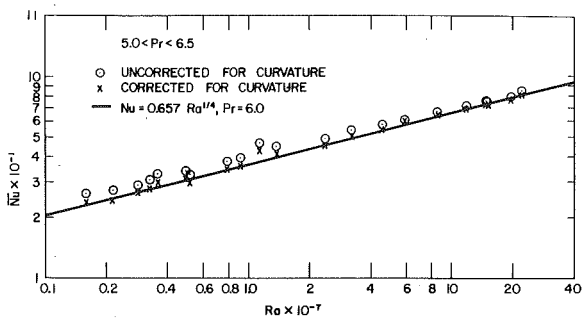

Fig. 4 Average heat transfer to vertical plate—unstratified case

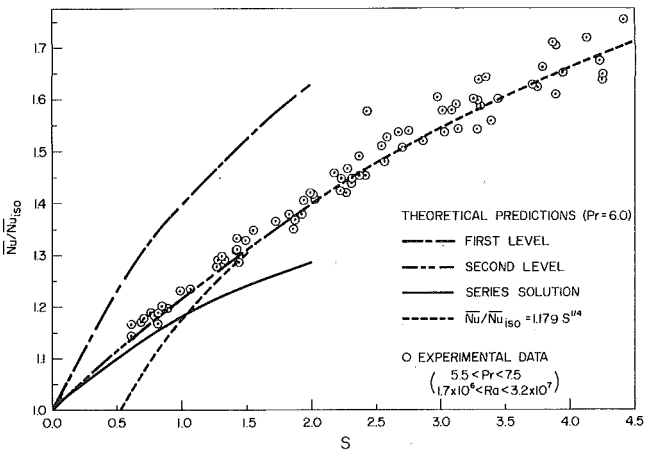

Fig. 5 Influence of the stratification on heat transfer

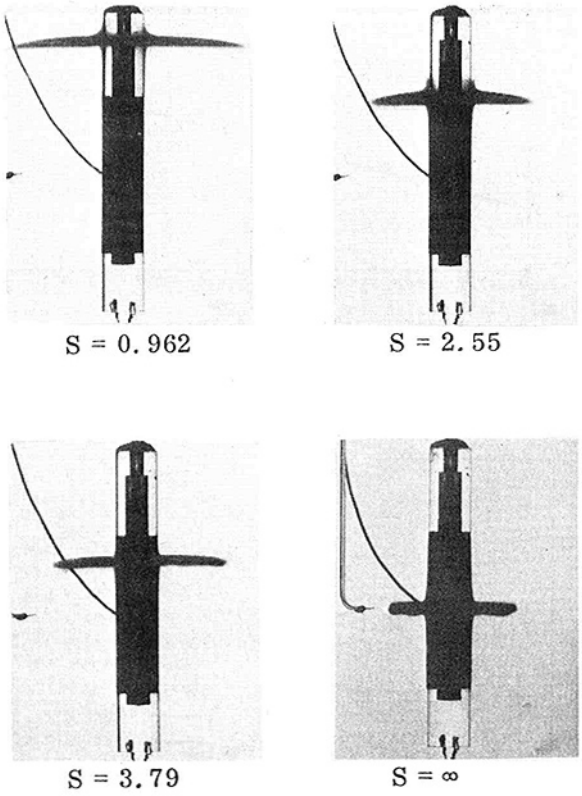

Fig. 6 Effect of the stratification on plumes

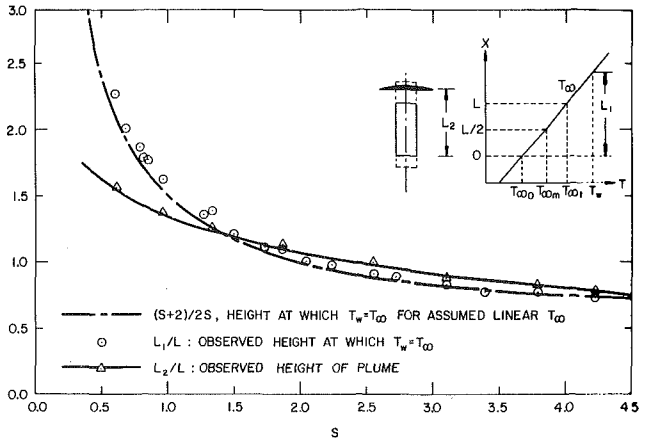

Fig. 7 Plume heights for vertical cylinder

method [13]. About one third of the data presented were taken with this fluid and the rest with distilled water. Since the stratification was not perfectly linear, a nominal value of the temperature gradient, a, was used to form S (see inset in Fig. 7). This value was defined as

$$S = \frac{L}{\Delta T_m}\left[\frac{T_w - T_{\infty 0}}{L_1}\right]$$

for plumes that rose above the top of the copper cylinder. For plumes leaving the sides of the cylinder (i.e., $S > 2$),

$$S = \frac{T_{\infty t} - T_{\infty 0}}{\Delta T_m}$$

In each case ΔT_m is the difference between the wall temperature and the ambient temperature at the midheight of the cylinder.

Overall heat transfer coefficients, $\bar{h}$, were obtained by dividing the observed heat input by the area of the heater and ΔT_m. These in turn were reduced to Nusselt numbers, $\overline{\mathrm{Nu}} = \bar{h}L/k$. Nusselt numbers were obtained for both an isothermal and a stratified fluid.

Experimental Results. Two sets of heat transfer data were obtained. The first set was for an unstratified fluid at about 25°C. They provided a test of the measurement methods against the results of other investigators. The second set was made with ambient temperature profiles and heat flows that gave a variation of S from 0.607 to 4.41. In order to compare with theoretical predictions for vertical flat plates, all the data from the vertical cylinder were corrected for a small curvature effect. These corrections were based on the work of Cebeci [14] and were less than 14 percent.

The unstratified data are shown in Fig. 4. All properties were evaluated at the film temperature. Both the uncorrected and the corrected data points are shown. The solid line is a least squares fit to the corrected data. Its formula, $\mathrm{Nu} = 0.657\ \mathrm{Ra}^{1/4}$ can be compared with (for $\mathrm{Pr} = 6.0$) $0.607\ \mathrm{Ra}^{1/4}$ from similarity solution calculations and $0.654\ \mathrm{Ra}^{1/4}$ from Squires' integral method. For $\mathrm{Pr} = 6.0$, we know of no published experimental data from vertical cylinders between $\mathrm{Ra} = 200$ and $\mathrm{Ra} = 2 \times 10^8$ with which to compare these data.

Fig. 5 shows experimental average heat transfer data for the stratified case. All properties were evaluated at the film temperature at the midheight of the cylinder. The heat transfer data were corrected for curvature in the same way as in the unstratified case and normalized with $\overline{\mathrm{Nu}}_{\mathrm{iso}} = 0.657\ \mathrm{Ra}^{1/4}$.

Several theoretical curves are also shown: For $S < 2$ the curves correspond to the first and the second level local nonsimilarity solutions and the series solution. For $S > 2$, we show the relation given by equation (16), which although approximate, contains no empirical constants. Agreement between experiment and theory is excellent for the second level of truncation and its extension (equation (12)) to values of $S > 2$. Except for one data point, the experimental results are within ±3.5 percent of the absolute value of the ordinate. In terms again of absolute values, the series solution (and its continuation in the manner of equation (12), if that were to be done) would lie at most 9 percent below the experimental data.

Observation of Plumes. Fig. 6 is a set of photographs of the plumes for various values of S. In measuring the plume height, two lengths, L_1 and L_2, measured above the leading edge, are defined:

L_1 = height at which $T_\infty = T_w$

L_2 = height at which the plume begins its horizontal spread.

The value of L_1 was obtained from the thermocouple traces, while L_2 was measured from 35 mm pictures of the plumes. Fig. 7 shows the results of these measurements as a function of S. Also shown is the formula, $(S + 2)/2S$, which would be identical to L_1/L if the temperature profiles were exactly linear.

For finite values of $S < 2$, the plume rises above the body to a distance determined by the maximum plume buoyancy and momentum. Above this distance, there is little fluid motion and the plume, upon reaching it, spreads horizontally and slightly downward. For $S = 2$, the ambient temperature on a horizontal even with the top of the body is equal to the body temperature and the final vertical excursion of the plume is near that plane. For $S > 2$, the ambient temperature adjacent to the upper edge of the body is higher than the body temperature. In this case, a nearly horizontal plume leaves the body near the point where the body temperature is equal to the local ambient temperature.

In performing the experiments, small values of S were achieved by combining a small ambient temperature gradient with a large temperature difference. Consequently the temperature distribution was more distorted for small S than for large S. This effect causes the difference between L_1/L and $(S + 2)/2S$ to increase as S decreases. For the same reason, reliable heat transfer data could not be obtained for S less than 0.6. The inconsistency between L_1 and L_2 is probably caused by (a) the boundary layers which meet to form the plume have unequal momenta by virtue of having developed over different lengths; (b) the plumes have time to cool down when they rise above the top of the cylinder; (c) the ambient temperature was not perfectly

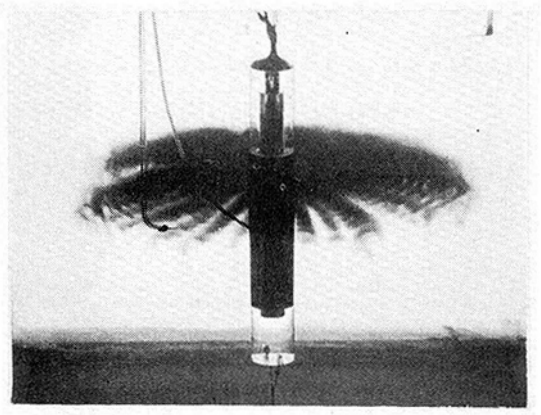

Fig. 8 View of plume from above

linearly stratified; and (*d*) the plexiglas s extension may have slightly affected the flow field.

Fig. 8 is a photograph of the plume taken at an angle of about 30 deg above the horizontal. The value of S was 3.12. The photograph clearly shows a radial striation of the plume. This effect is probably caused by the fact that the plume is initially colder on the top than on the bottom and is therefore unstable. This phenomenon, which was observed for all plumes for $S > 2$, is similar to that reported by Schetz and Eichhorn [15] for natural convection heat transfer with step changes in surface temperature. It leads to thicker plumes than would result if the instability was absent. Vertical mixing is probably also enhanced.

Conclusions

1 The local nonsimilarity method can be applied successfully to predict the effect of ambient temperature stratification on heat transfer to vertical surfaces, so long as the local temperature difference between the surface and the ambient remains of one sign. The local and average heat transfer rates for a linear stratification of the environment can be approximated by equations (8) and (10), together with Table 2.

2 If the thermal conditions are such that the temperature difference between the body and the ambient changes sign at some point on the body, the average heat transfer rate is simply determined by the difference in heat transfer between the two portions of the surface which are rejecting or absorbing heat. The result (for $S > 2$), which contains no empirical constants, is given in equation (12).

3 Observation of the plume from such bodies indicates that it rises to a point near where the ambient temperature is equal to the surface temperature and then flows horizontally away from the body.

4 For cases in which the temperature difference between surface and ambient changes sign, the horizontal plume has cold fluid on the top and warm fluid on the bottom and is, therefore, slightly unstable. An increase in vertical mixing results.

Acknowledgments

We are grateful to the National Science Foundation for their support of the work under NSF Grant GK-32938. The University of Kentucky contributed computer time. Many of the ideas expressed herein are those of Prof. J. H. Lienhard, who collaborated with us on earlier portions of this work.

References

1 Eichhorn, R., "Natural Convection in a Thermally Stratified Fluid," *Progress in Heat and Mass Transfer*, Vol. 2, Pergamon Press, 1969, pp. 41–53.

2 Fujii, T., Takeuchi, M., and Morioka, I., "Laminar Boundary Layer of Free Convection in a Temperature Stratified Environment," *Proceedings, Fifth International Heat Transfer Conference*, Tokyo, NC2.2, 1974, pp. 44–48.

3 Piau, J. M., "Influence Des Variations Des Properties Physiques Et De La Stratification En Convection Naturelle," "*International Journal of Heat Mass Transfer*, Vol. 17, 1974, pp. 465–476.

4 Eichhorn, R., Lienhard, J. H., and Chen, C. C., "Natural Convection From Isothermal Spheres and Cylinders Immersed in a Stratified Fluid," *Proceedings, Fifth International Heat Transfer Conference*, Tokyo, NC1.3, 1974, pp. 10–14.

5 Cheesewright, R., "Natural Convection from a Plane, Vertical Surface in Non-Isothermal Surroundings," *International Journal of Heat Mass Transfer*, Vol. 10, 1967, pp. 1847–1859.

6 Yang, K. T., Novotny, J. L., and Cheng, Y. S., "Laminar Free Convection from a Nonisothermal Plate Immersed in a Temperature Stratified Medium," *International Journal of Heat Mass Transfer*, Vol. 15, 1972, pp. 1097–1109.

7 Sparrow, E. M., Quack, H., and Boerner, C. J., "Local Nonsimilarity Boundary-Layer Solutions," *AIAA Journal*, Vol. 8, 1970, pp. 1936–1942.

8 Sparrow, E. M., and Yu, H. S., "Local Non-Similarity Thermal Boundary-Layer Solutions," JOURNAL OF HEAT TRANSFER, TRANS. ASME, Series C, Vol. 93, 1971, pp. 328–334.

9 Minkowycz, W. J., and Sparrow, E. M., "Local Nonsimilar Solutions for Natural Convection on a Vertical Cylinder," JOURNAL OF HEAT TRANSFER, TRANS. ASME, Series C, Vol. 96, 1974, pp. 178–183.

10 Chen, T. S., and Mucoglu, A., "Buoyancy Effects on Forced Convection Along a Vertical Cylinder," JOURNAL OF HEAT TRANSFER, TRANS. ASME, Series C, Vol. 97, 1975, pp. 198–203.

11 Nachtsheim, P. R., and Swigert, P., "Satisfaction of Asymptotic Boundary Conditions in the Numerical Solution of Boundary-Layer Equations," *Proceedings, Ninth Midwestern Mechanics Conference*, Madison, Vol. 3, Part 2, 1965, pp. 361–371.

12 Rogers, D. F., "Further Comments on Local Nonsimilarity Boundary-Layer Solutions," *AIAA Journal*, Vol. 12, No. 7, 1974, pp. 1007–1008.

13 Baker, D. J., "A Technique for the Precise Measurement of Small Fluid Velocities," *Journal of Fluid Mechanics*, Vol. 26, 1966, pp. 573–575.

14 Cebeci, T., "Laminar-Free-Convection-Heat Transfer From the Outer Surface of a Vertical Slender Circular Cylinder," *Proceedings, Fifth International Heat Transfer Conference*, Tokyo, NC1.4, 1974, pp. 15–19.

15 Schetz, J. A., and Eichhorn, R., "Natural Convection With Discontinuous Wall-Temperature Variations," *Journal of Fluid Mechanics*, Vol. 18, 1964, pp. 167–176.

G. D. Raithby
Thermal Engineering Group,
Department of Mechanical Engineering, University of Waterloo,
Waterloo, Ontario, Canada
Mem. ASME

A. Pollard
Department of Mechanical Engineering,
Imperial College of Science and Technology,
London, England

K. T. G. Hollands
Mem. ASME

M. M. Yovanovich
Mem. ASME

Thermal Engineering Group,
Department of Mechanical Engineering,
University of Waterloo,
Waterloo, Ontario, Canada

Free Convection Heat Transfer From Spheroids

Measurements of the heat transfer by free convection from isothermal spheroids to air are reported. The range of Rayleigh number, Ra, covered was sufficiently large that both thick boundary layer effects (at low Ra) and turbulence (at high Ra) affect the heat transfer. Data are reported for one prolate spheroid and two oblate spheroids. The results of an approximate method of analysis, which accounts for both thick boundary layers and turbulence, are also given. These are compared to the present measurements, and to earlier measurements for spheres. Excellent agreement with experiment is found. Correlation equations, from which average heat transfer rates can be calculated, are also given. These are thought to be valid at all Rayleigh numbers over a large range of eccentricity.

1 Introduction

Recent years have seen a rapid intensification of research related to the measurement, prediction, and understanding of heat transfer by free convection. For external free convection, measurements and predictions have focussed on problems where the flow is two-dimensional (e.g., vertical plates and cylinders, tilted plates, horizontal circular cylinders) or axisymmetric (e.g., spheres). References [1–10][1] list some of the important contributions to these problems from the analysis side.

The solutions in references [1–10] are obtained from simplified equations of motion which contain the boundary-layer approximations and which ignore curvature effects (the equations are written in local Cartesian coordinates). Also, no account has been taken of turbulent heat transfer from part or all of the surface.

Langmuir [11] recognized the importance of accounting for curvature effects and a few solutions, including at least some of these effects, have been obtained [12–16]. Reference [16] also makes allowance for turbulent heat transfer. It was shown in [16] that, for two-dimensional bodies, there is often *no* range in Rayleigh number for which solutions, ignoring curvature effects and turbulence, are in agreement with experiment. In this paper we extend this study to some axisymmetric bodies (spheroids). The organization of the presentation is as follows.

First, measurements are reported for isothermal spheroids of various eccentricities immersed in quiescent air. Previous measurements have been apparently restricted to spheres [17–21(*a*)].

Second, these measurements are compared with three analyses; the first of these neglects curvature and turbulence effects, the second corrects for curvature effects but neglects turbulence, the third accounts for both. The method of prediction is that proposed by Raithby and Hollands [16, 22]. By comparing experiment and these results of analyses it is possible: (*a*) to make a statement about the range of Rayleigh number over which adequate predictions of an *average* Nusselt number can be expected from analyses based on local Cartesian coordinates, and (*b*) to evaluate the success of the Raithby-Hollands method for accounting for turbulence and curvature effects.

Third, based on the analytical results, correlation equations are then obtained from which the average heat transfer from spheroids of moderate eccentricity can be calculated.

A separate note in this issue of the journal [22(*a*)] extends the analysis to the case of prolate spheroids with high eccentricity; these resemble vertical needles, tapered from the center toward both ends.

2 Experiment

Measurements of heat transfer by free convection from oblate and prolate spheroids of moderate eccentricity ($C/B = 0.5$), and from one

[1] Numbers in brackets designate References at end of paper.

Contributed by the Heat Transfer Division for publication in the JOURNAL OF HEAT TRANSFER. Manuscript received by the Heat Transfer Division March 3, 1976. Paper No. 76-HT-BBB.

Table 1 Constants f_1 and f_2

C/B	Prolate Spheroid f_1	Prolate Spheroid f_2	Prolate Spheroid $2^{\frac{1}{4}} f_2^{\frac{3}{4}}/f_1$	Oblate Spheroid f_1	Oblate Spheroid f_2	Oblate Spheroid $2^{\frac{1}{4}} f_2^{\frac{3}{4}}/f_1$
1.000	2.000	1.683	0.878	2.000	1.683	0.878
0.900	1.935	1.653	0.896	1.868	1.601	0.906
0.800	1.873	1.624	0.913	1.739	1.518	0.935
0.700	1.814	1.596	0.931	1.615	1.435	0.966
0.600	1.759	1.570	0.948	1.494	1.352	0.997
0.500	1.709	1.545	0.964	1.380	1.269	1.030
0.400	1.665	1.524	0.980	1.274	1.187	1.062
0.300	1.627	1.506	0.993	1.177	1.108	1.091
0.200	1.598	1.491	1.005	1.094	1.033	1.114
0.100	1.578	1.481	1.012	1.030	0.969	1.128
0.050	1.573	1.479	1.014	1.009	0.945	1.129
0.010	1.571	1.478	1.015	1.001	--	--
0.005	1.571	1.478	1.015	1.000	--	--
0.001	$\approx \pi/2$	1.478	1.015	1.000	--	--

Table 2 Values of f_3 (equation (5)) and n (equation (6))

(C/B)	f_3 Oblate Spheroid	f_3 Prolate Spheroid	n Oblate Spheroid	n Prolate Spheroid
1.00	0.73	0.73	6	6
0.80	0.79	0.73	5	6
0.60	0.87	0.72	5	6
0.50	0.93	0.71	4	6
0.40	0.99	0.71	3	6
0.20	1.20	0.71	2.5	6
0.10	1.44	0.71	2.5	-
0.05	1.73	0.71	-	-
0.01	-	0.71	-	-

oblate spheroid of large eccentricity ($C/B = 0.1$) to air are reported. Notation, cross-sectional drawings, and pertinent data on these spheroids are presented in Fig. 1.

The objective of the experiments was to measure *average* Nusselt numbers over a large Rayleigh-number range. This range was achieved by locating the spheroids in a pressure vessel (a cylinder 38.5 cm in diameter and 150 cm long) and performing the measurements at various pressure levels (as, for example, in [23, 24]) between 0.028 and 2.35 bar. The wall of the pressure vessel was maintained at a uniform temperature by water cooling. Its temperature, required for radiation corrections, and the air temperature far removed from the spheroid-location, were both measured using shielded thermocouples. The air pressure was measured using a U-tube manometer to an overall accuracy of ±0.0005 bar. Measurements showed that there was no appreciable thermal stratification of the air during the experiments.

Large spheroids were desired in order to obtain a significant turbulent heat transfer, but their size was limited by the additional requirement that enclosure effects [25] be unimportant; the compromise dimensions appear in Fig. 1. Isothermal-surface boundary conditions were achieved by manufacturing the spheroids from a high thermal conductivity material (Aluminum 6061-T6) and by keeping a low internal resistance to heat flow. The contours of the spheroids were accurately machined and their surfaces finely polished.

Two thermocouple junctions were imbedded at different locations in each spheroid and the leads buried in shallow grooves in the surface which conducted the wires to the rear stagnation region. A small heater (5 mm in diameter for the $C/B \approx 0.5$ spheroids and 3 mm for the $C/B = 0.1$ spheroid) was also imbedded through the rear stagnation region. A high thermal conductivity cement was used to fill the grooves and the space around the heater. Current was fed to the heater through two very fine bare wires (as small as 0.25 mm dia); some of the experiments were repeated using lead wires of different diameter and material. The mass of each spheroid was accurately determined by weighing; the mass of the heater, thermocouple wires, and cement amounted, in the worst case, to 0.4 percent of the total spheroid mass. Prior to testing, the appropriate spheroid was suspended in the center of the pressure cylinder from 0.3 mm nylon leads, and its axis of symmetry precisely aligned with the vertical direction. The cold junctions of the spheroid thermocouples were radiation shielded and located on the center line of the pressure vessel, one on each side of, and 50 cm removed from, the spheroid; the voltage output of these was a direct measure of the spheroid-to-air temperature difference.

The heat transfer from the spheroid was determined by measuring its transient temperature decay from an initially heated state. Nor-

Nomenclature[2]

A_s = surface area of spheroid, equation (B.6)
B = dimension of spheroid along its major axis
C = dimension of spheroid along its minor axis
C_ℓ = "universal" function of Pr for laminar flow $C_\ell = 0.50/[1 + (0.49/\mathrm{Pr})^{9/16}]^{4/9}$
$\bar{C}_\ell = 4C_\ell/3$
C_t = "universal" function of Pr for turbulent flow. $C_t = [0.14\ \mathrm{Pr}^{0.084}, 0.15]^*$, where $[A, B]^* =$ minimum of A and B
f_1, f_2 = definite integrals defined in Appendix B. Numerical values are given in Table 1
f_3: defined by equation (5)
k: thermal conductivity
ℓ: see Table B.1
m: see Table B.1
n: exponent in correlation equation, numerical values appear in Table 2
$\overline{\mathrm{Nu}}_B$ = average Nusselt number for spheroid based on the length B (measured, or predicted from analysis which includes thick-layer and turbulence effects)
$(\overline{\mathrm{Nu}}_B)_{\ell t}$ = predicted average Nusselt number based on laminar, thin-layer analysis (Appendix B)
$(\overline{\mathrm{Nu}}_B)_\ell$ = predicted average Nusselt number based on laminar analysis, where corrections for thick-layer effects have been made (Appendix B)
$(\overline{\mathrm{Nu}}_B)_{\mathrm{cond}}$ = Nusselt number in the conduction limit (equation (3))
$(\overline{\mathrm{Nu}}_B)_t$ = average Nusselt number from analysis in which turbulent heat transfer is presumed everywhere on the surface, and Ra_B is very large
Pr = Prandtl number calculated at temperature $(T_s + T_\infty)/2$
Ra_B = Rayleigh number based on ΔT and B
S = one-half the perimeter of body in flow direction
T_s = temperature of spheroid
T_∞ = temperature of ambient air far from spheroid
$\Delta T = T_s - T_\infty$
(η, θ, Ψ) = spheroidal coordinates (see Appendix B)

[2] Where symbols have been used only once, they are defined immediately after their appearance in the text, and are not repeated here.

mally, the surface temperature was elevated to 44°C above ambient and it was allowed to cool to 36°C before measurements were recorded. The rate of change of its temperature with time was determined by accurately measuring the time for the temperature difference to decrease by 0.6°C. The voltage output of the thermocouple determining the temperature difference was measured using a Leads and Northrup K-5 potentiometer (±0.005 percent of reading or ±0.1 μV, i.e., ±0.006°C). After making this measurement, the pressure, air temperature and wall temperature in the cylinder were noted. The Rayleigh number was calculated using the mean temperature difference over the measurement period, and evaluating all air properties at the average film temperature; all properties were calculated from equations by Hilsenrath [26]. The total rate of heat loss was determined from the measurements and a knowledge of the spheroid mass and specific heat. To calculate the heat transfer by free convection, upon which the Nusselt number is based, required corrections for radiation and conduction via the lead wires.

The heat transfer by radiation was determined using the measured temperatures, the surface area of the spheroid, and its emissivity. The total normal emissivity of a sample of the aluminum, with a similar surface finish, was measured on a Gier-Dunkle DB100 Reflectometer and this was converted to the hemispherical emissivity shown in Fig. 1 (see Eckert and Drake [27]). The heat loss by conduction along the nylon support wires, the thermocouple lead wires, and the heater lead wires was calculated by the method outlined in Appendix A. All of the lead losses were normally small, but at low pressures the heat transfer along the heater leads climbed to 16 percent of the heat loss by free convection. The calculated total heat loss via the leads and by radiation were subtracted from the total heat loss, and the Nusselt number calculated.

Five such measurements were repeated in rapid succession and an average Nusselt number and Rayleigh number were formed. A total of 78 of 85 recorded sets of data are reported. The unreported sets are those in which experimental conditions varied during the course of taking the measurements, or the total heat loss via the leads exceed 13 percent of the heat loss by free convection.

Experimental Results. For all the test conditions used, the Prandtl number was about 0.71 (actually $0.709 < \mathrm{Pr} < 0.711$). For the prolate spheroid with $C/B = 0.5$, the $\bar{\mathrm{Nu}}_B$ versus Ra_B results are plotted in the lower part of Fig. 2. The data show very little scatter and measurements for different heater-lead wires are entirely consistent. The solid curve drawn through the data is an analytical result which will be described later.

The upper part of Fig. 2 shows some experimental results by Elenbaas [18] and Mathers, et al. [19] for spheres ($C/B = 1.0$) and correlation equations based on the experimental results of Kyte, et al. [17], Tsubouchi and Sato [20], Yuge [21], and Amato and Tien [21a].

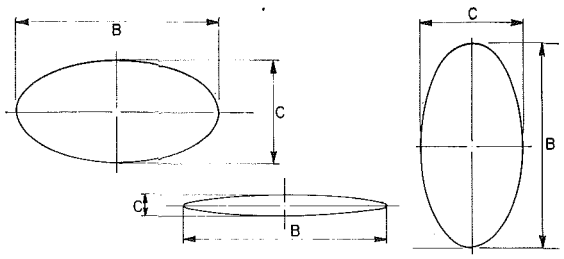

	C/B ≈ 0·5 OBLATE SPHEROID (SIDE VIEW)	C/B ≈ 0·1 OBLATE SPHEROID (SIDE VIEW)	C/B ≈ 0·5 PROLATE SPHEROID (SIDE VIEW)
C (mm)	39·2	8·00	40·0
B (mm)	78·6	80·0	77·1
MASS (kg)	0·341	0·0734	0·174
EMISSIVITY	0·056	0·056	0·056
SPECIFIC HEAT (kJ/kg C)	0·96	0·96	0·96

Fig. 1 Top and side views of spheroids, showing dimensions and other data

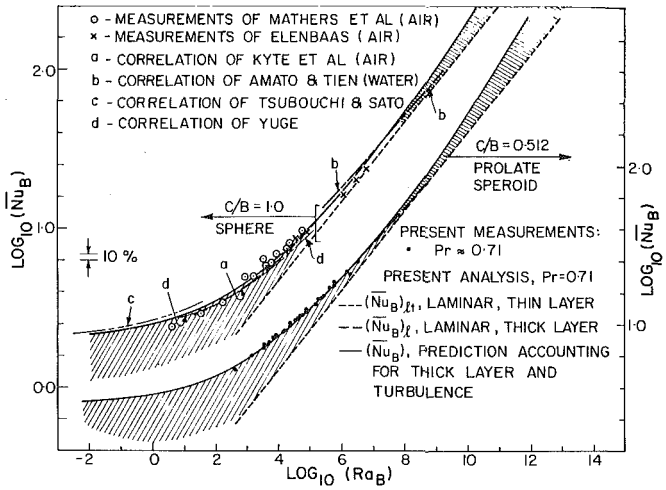

Fig. 2 Data, results of analysis, and correlation equations for prolate spheroid (lower) and sphere (upper)

Other curves are the result of the present analysis.

The data for the two oblate spheroids are plotted in Fig. 3. There is again little scatter in the measurements and no systematic differences between results obtained using different heater leads. The solid curves are the results of the analysis, which is now described.

3 Analysis

The foregoing measurements are now compared with analysis, keeping in mind the concerns expressed in the Introduction over the effects of curvature and turbulence on the average heat transfer. The first section in the following presents a simple analysis which neglects curvature and turbulence effects; the second corrects this result for curvature effects, and the third accounts for both curvature *and*

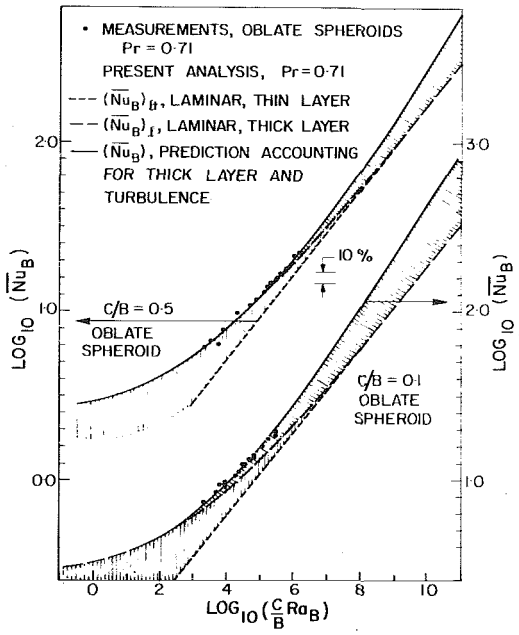

Fig. 3 Present data for two oblate spheroids, and the results of analysis

turbulence. Building up the analysis in this step-by-step way permits a direct insight into the relative importance of these effects.

Laminar, Thin-Layer Results. The term "thin-layer" [16] is associated with laminar boundary-layer analyses in which local Cartesian coordinates are used in expressing the conservation constraints. Thus, the general solutions for bodies of arbitrary contour [9, 10], and many of the other solutions to free convection problems, fall into this category. The results presented here are obtained by a direct application of the thin-layer solution of Raithby and Hollands [22]. Although this solution is approximate, it has been shown to be in good agreement with other thin-layer analyses for vertical plates and horizontal elliptic cylinders [16] and spheres [22] with uniform temperature boundary conditions. The form of the solution is correct, it is accurate to about 1 percent for isothermal surfaces for $\mathrm{Pr} \gtrsim 0.5$, and the evaluation of the solution is very easy.

An abbreviated account of the application of this solution to the spheroid problem is given in Appendix B. The final result for the average Nusselt number is

$$(\overline{\mathrm{Nu}}_B)_{\ell t} = \frac{\bar{h}B}{k} = \frac{2^{1/4} f_2^{3/4}}{f_1} \bar{C}_\ell \left(\frac{m}{B}\mathrm{Ra}_B\right)^{1/4} \tag{1}$$

where f_1 and f_2 are definite integrals whose values are given in Table 1, where $\bar{C}_\ell$ is a "universal" function of Prandtl number (see Nomenclature), and $m = B$ for prolate spheroids and $m = C$ for oblate spheroids. The subscript ℓt on the Nusselt number is a reminder that this is the laminar, thin-layer prediction.

Equation (1) is plotted in Figs. 2 and 3. The agreement is closest for spheres, followed by the prolate spheroid, the $C/B = 0.5$ and $C/B = 0.1$ oblate spheroids, respectively. For the $C/B = 0.1$ oblate spheroid, the data point nearest to the thin-layer prediction is about 32 percent high, with discrepancies at other Rayleigh numbers becoming (rapidly) larger. It is quite clear that the thin-layer analysis is considerably in error for all the geometries tested.

Correction for Thick-Layer Effects. As already suggested, writing the underlying equations in local Cartesian coordinates neglects important curvature or "thick-layer" effects when the boundary layers are not "thin." A detailed discussion of this, and a method of making a first-order correction to the thin-layer results to account for it, has been given previously [16]. Briefly described, the method consists of dividing the spheroid surface into a large number of segments and using the thin-layer solution to *estimate* the conduction thickness at each location. From the local surface shape (curvature), the local resistance to heat transfer from each segment can be estimated, and therefore one can correct the heat flux. The local heat flux is estimated in this way for each segment of the surface and the results numerically integrated to yield the total heat transfer (and, therefore, the average Nusselt number). The curves labeled $(\overline{\mathrm{Nu}}_B)_\ell$ in Figs. 2 and 3 have been obtained in this way, and the region between this curve and the thin-layer result has been cross-hatched to emphasize the magnitude of the correction. The correction is very significant over a large Rayleigh number range, diminishing only at high Rayleigh numbers where the boundary layers are thin.

It should be kept clearly in mind that:

(*a*) no account has yet been made for turbulence; and

(*b*) the Nusselt numbers, corrected for thick-layer effects, have been obtained by numerical integration so that these can no longer be *directly* evaluated from a closed-form solution.

Comparing measurements and these $(\overline{\mathrm{Nu}}_B)_\ell$ predictions, one finds excellent agreement for spheres and the prolate spheroid in Fig. 2, at least over the Rayleigh number range for which data are available. In Fig. 3, there is good agreement between these predictions and the data at lower Rayleigh numbers for the $C/B = 0.5$ oblate spheroid, but this gradually worsens at higher Ra_B. For the $C/B = 0.1$ oblate spheroid, the correction has improved the agreement but the data lie consistently above the prediction.

The main reason for the disagreement which remains is postulated to be the existence of turbulent heat transfer. This seems consistent with the above observations, for the areas first affected by turbulence (for an increasing Rayleigh number) would be the rear portions of the oblate spheroids. This is particularly true of the $C/B = 0.1$ spheroid where the rear surface is very nearly horizontal.

Allowance for Turbulent Heat Transfer. The procedure for accounting for turbulent heat transfer is described *very* briefly in Appendix B. The details are recorded elsewhere [16, 22].

The predictions, accounting for both turbulence and thick-layer effects, are depicted by the solid lines in Figs. 2 and 3. The curves are labeled $\overline{\mathrm{Nu}}_B$. The area between the $(\overline{\mathrm{Nu}}_B)_\ell$ results and these final predictions is cross-hatched to permit an immediate appreciation of the Rayleigh number range where turbulence is important, and the magnitude of this effect on the total heat transfer.

A comparison with the present data in these two figures indicates that these "final" predictions of the Nusselt number are in excellent agreement with the data. Most agree to within 5 percent (68 out of a total of 78 data points); the maximum difference is about 15 percent.

While the agreement between analysis and measurement is highly satisfactory, it is necessary to point out that the validation of the analysis at high Rayleigh numbers is incomplete. Measurements at higher Rayleigh numbers would be needed to complete the comparison. Also the reader is reminded that the analysis for heat transfer from the lower surface of the oblate spheroid is invalid in the limit as $C/B \to 0$, but this may not be a serious deficiency for predictions of $\overline{\mathrm{Nu}}_B$ since the heat transfer is dominated by turbulence on the top surface.

Data are available for spheres over a large range of Rayleigh number. Fig. 2 shows that the predictions for this geometry are also in excellent agreement with the measurements and correlations of Kyte, et al. [17], Elenbass [18], Mathers, et al. [19], Tsubouchi, et al. [20], and Yuge [21] (all for air), and in somewhat poorer agreement with the Amato-Tien [21(*a*)] correlation for water (partly because the Prandtl number is different, and partly because their equation does not fit their data well at the highest Rayleigh numbers). The agreement of the analysis with the present and earlier measurements for such a wide range of geometries lends strong support to the present method of analysis, and, therefore, to the other predictions for which experimental data are not yet available.

Graphs of $\overline{\mathrm{Nu}}_B$ for spheroids of other eccentricities are given in Figs. 4 (prolate) and 5 (oblate). From Fig. 4 it is seen that almost the same asymptotic relation between $\overline{\mathrm{Nu}}_B$ and Ra_B is approached for *all* eccentricities at high Rayleigh numbers. At the other extreme, the conduction limit, the $\overline{\mathrm{Nu}}_B$ value is sensitive to C/B, particularly for the larger eccentricities. If the curves were replotted with $(C/B)\,\mathrm{Ra}_B$ as the independent variable [22(*a*)], all the curves for small C/B would be brought together at small Rayleigh numbers.

For oblate spheroids (Fig. 5), using $(C/B)\,\mathrm{Ra}_B$ as the independent variable brings the high eccentricity curves together at low Rayleigh

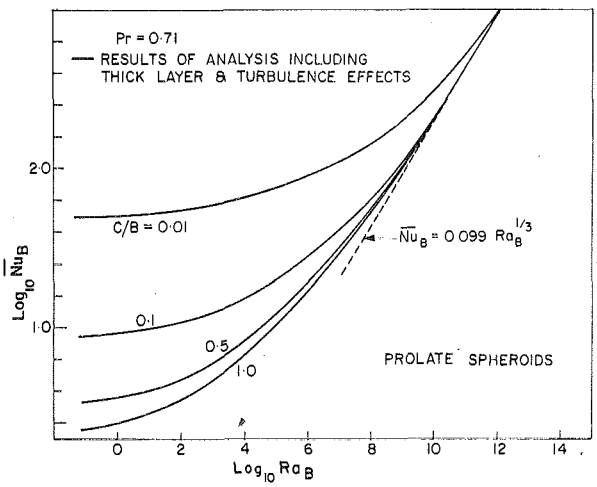

Fig. 4 Predictions for prolate spheroids

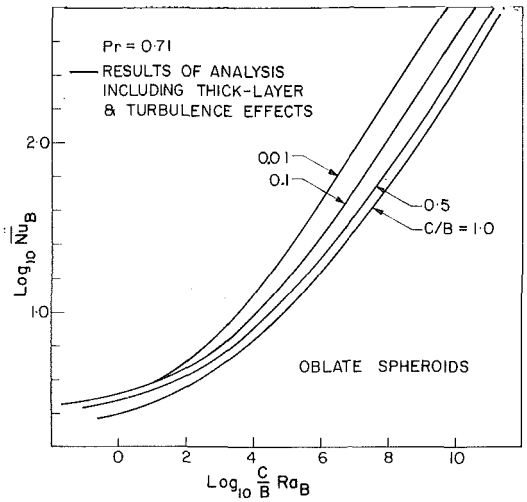

Fig. 5 Predictions for oblate spheroids

numbers, but distinctly different asymptotes are obtained for high Rayleigh numbers. If the independent variable were changed to Ra_B, the turbulent-heat transfer asymptotes would not be greatly different for different eccentricities; however, the curves would cross one another at intermediate Rayleigh numbers and a confusing graph would emerge.

4 Correlation Equations for Moderate Eccentricities

The "final" results of the analysis, plotted in the figures, have been obtained by carrying out the numerical integrations indicated in Appendix B. While this is neither a laborious task (the nonoptimized computer program in Fortran had about 120 statements), nor an expensive one (in terms of computing time), it would be more convenient if the results could be expressed in the form of equations. Equations have been obtained which are accurate for a wide range of eccentricities for both oblate and prolate spheroids; these are described in this section. It should be kept clearly in mind that the equations represent an *empirical fit* to the results of the analysis.

The equation should be constructed such that it has the correct asymptotes for small and large Ra_B, yet also fits the analytical results accurately at intermediate values. Since it is not immediately obvious what form this equation should take, the complexity of the problem was reduced by seeking first asymptotic equations which would be valid for laminar and turbulent heat transfer, respectively. These equations were then combined to give the desired result.

Evaluation of $(\overline{Nu}_B)_\ell$. First, for the laminar problem, the evaluation of the equations in Appendix B was carried out with the turbulent heat transfer "turned off" (i.e., laminar heat transfer at all locations on the surface). The output was values of laminar Nusselt number, $(\overline{Nu}_B)_\ell$, for various C/B and Ra_B; some of these Nusselt numbers have already been plotted in Figs. 2 and 3. For all eccentricities for oblate spheroids and for prolate spheroids for $C/B \gtrsim 0.2$, it was found that these results were very closely fit by an equation of the form

$$(\overline{Nu}_B)_\ell = (\overline{Nu}_B)_{cond} + (\overline{Nu}_B)_{\ell t} \tag{2}$$

where $(\overline{Nu}_B)_{cond}$ is the value of $\overline{Nu}_B$ in the conduction limit and $(\overline{Nu}_B)_{\ell t}$ is the Nusselt number from the laminar, thin-layer analysis, [equation (1)]. The error in approximating $(\overline{Nu}_B)_\ell$ by this equation is normally less than 1 percent. A maximum error of 2 percent occurs for the prolate spheroid for $C/B = 0.2$ (and 10 percent if the equation were to be used for $C/B = 0.1$).

Equations for $(\overline{Nu}_B)_{cond}$ can be obtained directly from the analysis in Appendix B (equation (B-12)). For the prolate and oblate spheroids, respectively, one finds

$$(\overline{Nu}_B)_{cond} = \frac{4\sqrt{1-(C/B)^2}}{f_1} \cdot \frac{-1}{(C/B)\ln\tanh(\eta_i/2)} \quad \text{(for prolate)} \tag{3a}$$

$$(\overline{Nu}_B)_{cond} = \frac{4\sqrt{1-(C/B)^2}}{f_1} \cdot \frac{1}{(\pi/2) - \tan^{-1}(\sinh\eta_i)} \quad \text{(for oblate)} \tag{3b}$$

where f_1 is given in Table 1 and, by definition,

$$\eta_i = 0.5 \ln\{[1+(C/B)]/[1-(C/B)]\} \tag{4}$$

Evaluation of $(\overline{Nu}_B)_t$. Now an equation is sought which is valid at asymptotically high Ra_B when the heat transfer is turbulent at (essentially) all locations on the surface. The corresponding Nusselt number is designated $(\overline{Nu}_B)_t$. The analysis suggests that this is proportional to $Ra_B^{1/3}$ for any C/B value. To keep the same independent variables as in the laminar equations, the following equation was used

$$(\overline{Nu}_B)_t = f_3 C_t \left(\frac{m}{B} Ra_B\right)^{1/3} \tag{5}$$

Values of f_3, obtained by rerunning the analysis at a high Ra_B with the laminar heat transfer "turned off," are tabulated in Table 2.

Final Correlation Equations. The foregoing equations for laminar and turbulent heat transfer respectively were combined according to the Churchill-Usagi [28] formula to give the following equation for $\overline{Nu}_B$

$$(\overline{Nu}_B)^n = (\overline{Nu}_B)_\ell{}^n + (\overline{Nu}_B)_t{}^n \tag{6a}$$

where n is a constant chosen to give best agreement between equation (6) and direct calculations of $\overline{Nu}_B$. The final equation, therefore, becomes

$$(\overline{Nu}_B)^n = \left[(\overline{Nu}_B)_{cond} + \left(\frac{2^{1/4} f_2^{3/4}}{f_1}\right) \bar{C}_\ell \left(\frac{m}{B} Ra_B\right)^{1/4}\right]^n + \left[C_t f_3 \left(\frac{m}{B} Ra_B\right)^{1/3}\right]^n \tag{6b}$$

where n and f_3 are given in Table 2, f_1 and f_2 in Table 1, $m = B$ and C for prolate and oblate spheroids, respectively, $(\overline{Nu}_B)_{cond}$ is given by equations (3), and $\bar{C}_\ell$ and C_t are Prandtl-number-dependent coefficients listed in the Nomenclature. Equation (6*b*) has been found to fit the results of the analysis to within about 5 percent.

5 Summary

1 Measurements of the average Nusselt number for free convection heat transfer from one prolate, and two oblate, isothermal, spheroids to quiescent, air at uniform temperature have been reported.

2 The results of an anysis, accounting for both thick-layer (or curvature) effects and turbulent heat transfer has been presented. Excellent agreement with experiment was found; but of perhaps greater significance than the agreement itself, an appreciation of the importance of curvature and turbulence effects was gained.

3 Correlation equations were presented which are valid for a wide range of eccentricity and for all Rayleigh numbers.

Acknowledgments

The work was supported through Operating Grants from the National Research Council of Canada.

We gratefully acknowledge the assistance of Mr. V. A. Wehrle at the Communications Research Centre, Department of Communications, Ottawa, for performing the reported emissivity measurements for aluminum on their Gier-Dunkle Reflectometer. Our thanks also to Prof. D. French and Mr. J. Minnema for their assistance in machining the prolate spheroid.

References

1 Schmidt, E., and Beckmann, W., "Das Temperatur—und Geschwindijkeitsfeld vor einer Warme algebenden senkrechten Platte bei naturlicher Konvection," *Techn. Mechan. und Thermodynamik*, Vol. 11, 1930, pp. 391–406.

2 Ostrach, S., see Bird, R., Stewart, W. E., Lightfoot, E. N., *Transport*

Phenomena, Wiley, New York, 1960.

3 Sparrow, E. M., and J. L. Gregg, "Laminar Free Convection From a Vertical Plate With Uniform Heat Flux," TRANS. ASME, Vol. 78, 1956, pp. 435–440.

4 Braun, W. H., Ostrach, S., and Heighway, J. E., "Free-Convection Similarity Flows About Two-Dimensional and Axisymmetric Bodies With Closed Lower Ends," *International Journal of Heat and Mass Transfer,* Vol. 2, 1961, pp. 121–135.

5 Chiang, T., and Kaye, J., "On Laminar Free Convection From a Horizontal Cylinder," *Proceedings of 4th National Congress of Applied Mechanics,* 1962, pp. 1213–1219.

6 Chiang, T., Ossin, A., and Tien, C. L., "Laminar Heat Transfer From a Sphere," JOURNAL OF HEAT TRANSFER, TRANS., ASME, Series C, Vol. 96, 1964, pp. 537–542.

7 Koh, J. C., "Laminar Free Convection From a Horizontal Cylinder With Prescribed Surface Heat Flux," *International Journal of Heat and Mass Transfer,* Vol. 7, 1969, pp. 811–823.

8 Koh, J. C. Y., and Price, J. F., "Laminar Free Convection From a Nonisothermal Cylinder," JOURNAL OF HEAT TRANSFER, TRANS., ASME, Series C, Vol. 78, 1956, pp. 237–242.

9 Saville, D. A., and Churchill, S. W., "Laminar Free Convection in Boundary Layers Near Horizontal Cylinders and Vertical Axisymmetric Bodies," *Journal of Fluid Mechanics,* Vol. 29, 1967, pp. 391–399.

10 Lin, F. N., and Chao, B. T., "Laminar Free Convection over Two-Dimensional and Axisymmetric Bodies of Arbitrary Contour," JOURNAL OF HEAT TRANSFER, TRANS., ASME, Series C, Vol. 96, 1974, pp. 435–442.

11 Langmuir, I., "Convection and Conduction of Heat in Gases," *Physical Review* Vol. 34, 1912, pp. 401–422.

12 Sparrow, E. M., and Gregg, J. L., "Laminar-Free-Convection Heat Transfer from the Outer Surface of a Vertical Circular Cylinder," TRANS. ASME, 1956, pp. 1823–1829.

13 Minkowycz, W. J., and Sparrow, E. M., "Local Non-similar Solutions for Natural Convection on a Vertical Cylinder," JOURNAL OF HEAT TRANSFER, TRANS., ASME, Series C, Vol. 96, 1974, pp. 178–183.

14 Peterka, J. A., Richardson, P. D., "Natural Convection From a Horizontal Cylinder at Moderate Grashof Numbers," *International Journal of Heat and Mass Transfer,* Vol. 12, 1969, pp. 749–752.

15 Hieber, C. A., "Natural Convection Around Semi-Infinite Vertical Plate: Higher Order Effects," *International Journal of Heat and Mass Transfer* Vol. 17, 1974, pp. 785–791.

16 Raithby, G. D., and Hollands, K. G. T., "Laminar ahd Turbulent Free Convection from Elliptic Cylinders, with a Vertical Plate and Horizontal Circular Cylinder as Special Cases," JOURNAL OF HEAT TRANSFER, TRANS. ASME, Series C, Vol. 98, 1976, pp. 72–80.

17 Kyte, J. R., Madden, A. J., Piret, E. L., "Natural Convection Heat Transfer at Reduced Pressure," *Chemical Engineering Progress* Vol. 49, 1953, pp. 653–662.

18 Elenbaas, W., "The Dissipation of Heat by Free Convection of Spheres and Horizontal Cylinders," *Physica,* Vol. 9, No. 3, 1942, pp. 285–296.

19 Mathers, W. G., Madden, A. J., and Piret, E. L., "Simultaneous Heat and Mass Transfer in Free Convection," *Fluid Mechanics in Chemical Engineering* Vol. 49, 1957, pp. 961–968.

20 Tsubouchi, T., Sato, S., "Heat Transfer From Fine Wires and Particles by Natural Convection," *Chemical Engineering Progress Symposium Series 30,* Vol. 56, pp. 269–284.

21 Yuge, T., "Experiments on Heat Transfer From Spheres Including Combined Natural and Forced Convection," JOURNAL OF HEAT TRANSFER TRANS., ASME, Vol. 82, 1960, pp. 214–220.

21(*a*) Amato, W. S., and Tien, C., "Free Convection Heat Transfer From Isothermal Spheres in Water," *International Journal of Heat and Mass Transfer,* Vol. 15, 1972, pp. 327–339.

22 Raithby, G. D., and Hollands, K. G. T., "A General Method of Obtaining Approximate Solutions to Laminar and Turbulent Free Convection Problems," *Advances in Heat Transfer,* Academic Press, 1974; see also *International Journal Heat Mass Transfer* Vol. 17, 1974, pp. 1620–1622.

22(*a*) Raithby, G. D., and Hollands, K. G. T., "Free Convection Heat Transfer From Vertical Needles," to be published in the JOURNAL OF HEAT TRANSFER, TRANS., ASME.

23 Saunders, O. A., "The Effect of Pressure on Natural Convection in Air," *Proc. Roy. Soc.,* London, Series A, Vol. 157, 1936, pp. 278–291.

24 Thompson, H. A., and Sogin, H. H., "Experiments on the Onset of Thermal Convection in Horizontal Layers of Gases," *Journal Fluid Mechanics* Vol. 24, 1966, pp. 451–479.

25 Powe, R. E., "Bounding Effects on the Heat Loss by Free Convection From Spheres and Cylinders," JOURNAL OF HEAT TRANSFER, TRANS., ASME, Series C, Vol. 96, 1974, pp. 558–560.

26 Hilsenrath, J., et al., "Tables of Thermal Properties of Gases," *U.S. Dept. of Commerce Circular* 564, 1955.

27 Eckert, E. R. G., Drake, R. M., *Heat and Mass Transfer,* McGraw-Hill, New York, 1959.

28 Churchill, S. W., and Usagi, R., "A General Expression for the Correlation of Rates of Transfer and Other Phenomena," *AIChE Journal,* Vol. 18, 1972, pp. 1121–1128.

29 Yovanovich, M. M., "A General Expression for Predicting Conduction Shape Factors, Progress in Astronautics and Aeronautics," *Thermophysics and Spacecraft Thermal Control,* Vol. 35, 1974, pp. 265–291.

30 Fujii, T., Takeuchi, M., Fujii, M., Suzaki, K., and Uehara, H., "Experiments on Natural Convection Heat Transfer From the Outer Surface of a Vertical Cylinder to Liquids," *International Journal of Heat and Mass Transfer,* Vol. 13, 1970, pp. 753–787.

31 Yovanovich, M. M., *Advanced Heat Conduction,* Hemisphere Publishing Corp., Washington, D. C., 1976.

APPENDIX A

Conduction Losses Along Lead Wires

Heat flows from the spheroids along the lead wires by conduction, transferring heat from its surface by radiation and either from or to its surface by convection. The local temperature of the air surrounding the wires changes along their length because they are immersed in the wake of the spheroid. This temperature distribution can be calculated fairly accurately using some reasonable equation based on the conduction thickness, Δ_t. (e.g., equation of Fujii, et al. [30]). A new free convection solution, accounting for both wall and surrounding temperature variations, was derived along the lines of reference [22] to obtain the convective component of the heat transfer from the wire surfaces. An expression for radiative exchange with the surroundings was also obtained. The total loss along the lead was calculated by subdividing the wire into a large number of segments and guessing a longitudinal distribution of temperature. From this guessed distribution the heat transfer by free convection and radiation was computed for each segment and an improved longitudinal distribution was obtained by a finite-difference solution of the heat conduction equation for the wire. The process was repeated until a converged solution was obtained.

APPENDIX B

Details of Heat Transfer Analysis

The Coordinate System and Nomenclature. The application of the general solution of Raithby and Hollands [22] is briefly outlined in this section. This requires converting to, and working in, spheroidal coordinate systems. These coordinates are depicted in Fig. B.1. To avoid giving a separate treatment for each spheroid, several new symbols are introduced and their definitions given in Table B.1.

The spheroids shown in Fig. B.1 are generated by choosing a value of $\eta = \eta_i$ in the coordinate transformation

$$x = a\, g(\eta) \sin\theta \cos\psi,\ y = a\, g(\eta) \sin\theta \sin\psi,\ z = a\, h(\eta) \cos\theta \quad \text{(B.1)}$$

and where θ runs from 0 to π, and ψ from 0 to 2π. a is just a scaling factor with dimensions of length. Curves of constant θ and constant η are, respectively, hyperboloids and ellipsoids. The differential distance in the η, θ, and ψ directions are, respectively, $\sqrt{g_\eta}d_\eta$, $\sqrt{g_\theta}d_\theta$, and $\sqrt{g_\psi}d_\psi$, where the metric coefficients g_η, g_θ and g_ψ have been given

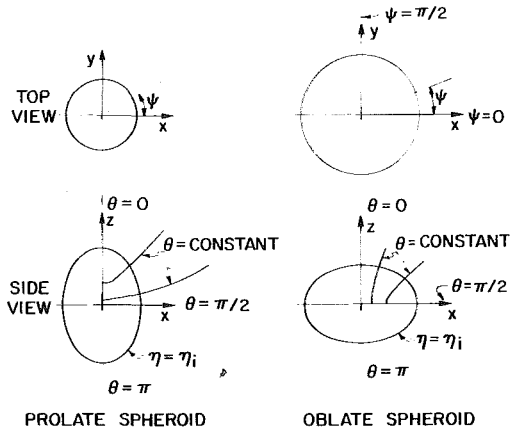

Fig. B.1 Schematic of spheroids showing spheroid coordinate systems

Table B.1 Definition of variables used in Appendix B

Symbol	Prolate spheroid	Oblate spheroid
ℓ	C	B
m	B	C
R	$\ln[\tanh(\eta_0/2)/\tanh(\eta_i/2)]$	$\tan^{-1}(\sinh\eta_0) - \tan^{-1}(\sinh\eta_i)$
S^*	$(\sinh^2\eta + \sin^2\theta)^{1/2}$	$(\cosh^2\eta - \sin^2\theta)^{1/2}$
$g(\eta)$	$\sinh\eta$	$\cosh\eta$
$h(\eta)$	$\cosh\eta$	$\sinh\eta$

by Yovanovich [31] as

$$g_\eta = g_\theta = a^2 S^{*2}; \quad g_\psi = a^2 \sinh^2\eta \sin^2\theta \tag{B.2}$$

Focussing attention on the η_i spheroid in Fig. B.1, from equation (B.1)

$$B = 2a\cosh\eta_i; \; C = 2a\sinh\eta_i; \; r = \sqrt{x^2+y^2} = (\ell/2)\sin\theta \tag{B.3}$$

Fixing the dimensions B and C fixes the scaling factor a and the value of η_i since, by equation (B.3)

$$a = \sqrt{(B/2)^2 - (C/2)^2}; \quad \eta_i = 0.5\ln[(B+C)/(B-C)] \tag{B.4}$$

The differential length, ds_θ, along the surface in the direction of increasing θ on the spheroid is

$$ds = (\sqrt{g_\theta})_{\eta=\eta_i} d\theta = (B/2)[(m/B)^2\sin^2\theta + (\ell/B)^2\cos^2\theta]^{1/2} d\theta = (B/2)\chi(\theta, C/B)d\theta \tag{B.5}$$

Equation (B.5) serves also as a definition for the function χ.

The surface area of the surface, A_s, is given by

$$A_s = \int_0^{2\pi}\int_0^{\pi} (\sqrt{g_\theta g_\psi})_{\eta=\eta_i} d\theta d\psi = (B\ell/4) \cdot \int_0^{\pi} \sin\theta\, \chi(\theta, C/B)d\theta = (\pi B\ell/2) f_1 \tag{B.6}$$

The integration can be carried out analytically and the resulting equation for f_1 evaluated. Numerical values of f_1 are given in Table 1 in the text.

These equations are now used in evaluating the free-convection heat transfer from the spheroids.

Thin-Layer Analysis. The general solution for the average Nusselt number is given by [22]

$$(\bar{\mathrm{N}}\mathrm{u}_S)_{\ell t} = \bar{C}_\ell \mathrm{Ra}_S^{1/4} \left[\frac{1}{S}\int_0^S \left(r^4 \frac{g_s}{g}\right)^{1/3} ds\right]^{3/4} \Big/ \left[\frac{1}{S}\int_0^S r ds\right] \tag{B.7}$$

where g_s is the component of g acting along the surface.

Converting from the local Cartesian coordinate s to the spheroid coordinate θ results in equation (1) in which

$$f_2 = \int_0^{\pi} \sin^{5/3}\theta\, \chi^{2/3}\, d\theta \tag{B.8}$$

Numerical values of f_2 are tabulated in Table 1.

Thick-Layer Correction. The local conduction-layer thickness at location s on the surface is [22]

$$\Delta_\ell = s\left[\frac{1}{s}\int_0^s \left(r^4\frac{g_s}{g}\right)^{1/3} ds\right]^{1/4} \Big/ \left[C_\ell \mathrm{Ra}_s^{1/4}\left(r\frac{g_s}{g}\right)^{1/3}\right] \tag{B.9}$$

Converting from s to the spheroid coordinate θ

$$\Delta_\ell = \frac{B}{2^{1/4} C_\ell ((m/B)\mathrm{Ra}_B)^{1/4}} \cdot \frac{\chi^{1/3}}{\sin^{2/3}\theta} \cdot \left[\int_0^\theta \sin^{5/3}\theta\, \chi^{2/3} d\theta\right]^{1/4} \tag{B.10}$$

The local value of η_0 a distance Δ_ℓ away from the η_i surface along a curve of constant θ (i.e., normal to the surface) is given by

$$\Delta_\ell(\theta) = a\int_{\eta_i}^{\eta_0} S^*(\eta, \theta) d\eta \tag{B.11}$$

where S^* is defined in Table B.1. The one-dimensional local resistance to heat transfer by conduction between the two spheroids η_i and η_0 at this location θ has been given by Yovanovich [29]. This is used to estimate the local heat transfer. These local values are integrated over the surface to yield the total heat transfer. Converted to an average Nusselt number, one finds

$$(\bar{\mathrm{N}}\mathrm{u}_B)_\ell = \frac{2\sqrt{1-(C/B)^2}}{(\ell/B) f_1}\int_0^{\pi} \frac{\sin\theta}{R(\eta_0(\theta), \eta_i)} d\theta \tag{B.12}$$

where R is given in Table B.1.

$(\bar{\mathrm{N}}\mathrm{u}_B)_\ell$ is the Nusselt number for laminar heat transfer, corrected to account for thick-layer effects. A numerical integration of (B.12) is required. This is easily done by dividing the surface into a large number of intervals of width $\Delta\theta$. The value of Δ_ℓ at the center of each interval is found from equation (B.10). With Δ_ℓ known, equation (B.11) is used to find η_0 at the corresponding locations; again, this must be done numerically. These values are substituted into the expression for R and the integration in (B.12) is performed to obtain the final result.

Accounting for Turbulence. According to the proposed equation for turbulent heat transfer [16], the local conduction-layer thickness is

$$\Delta_t = B/(C_t A(\phi)\mathrm{Ra}_B^{1/3}) \cdot \tag{B.13}$$

where C_t is a "universal" function of Prandtl number (see Nomenclature) and $A(\phi)$ depends on the local surface angle, ϕ, from the vertical. ϕ is related to the spheroid coordinate θ by

$$\phi = \sin^{-1}\{-(C/B)\cos\theta/\chi(C/B, \theta)\} \tag{B.14}$$

From these, the local Nusselt number can be found. The criterion for transition and the application of the analysis follows [16, 22].

S. W. Hong
Engineer,
General Electric Co.,
San Jose, Calif.
Assoc. Mem. ASME

A. E. Bergles
Professor and Chairman,
Department of Mechanical Engineering and
Engineering Research Institute,
Iowa State University,
Ames, Iowa
Mem. ASME

Theoretical Solutions for Combined Forced and Free Convection in Horizontal Tubes with Temperature-Dependent Viscosity

A boundary layer solution is presented for fully developed laminar flow in a horizontal circular tube, assuming large Prandtl number and temperature-dependent viscosity and density. The solution is given by $Nu = C_1\, Ra^{1/4}$, *where* C_1 *is a function of a nondimensional viscosity parameter and the heat flux boundary condition. The heat transfer predictions for large values of the viscosity parameter are 50 percent above the constant viscosity predictions. The present analysis is in good agreement with experimental data for water and ethylene glycol flowing in electrically heated tubes which approximate the boundary conditions assumed in the analysis.*

Introduction

It has been demonstrated experimentally that heat transfer coefficients for laminar internal flow are dependent on tube geometry, axial location, tube wall boundary conditions, flow rate, fluid thermophysical and transport properties, tube orientation, and temperature dependence of fluid properties. The analytical procedures to predict the effects of all variables except temperature-dependent properties (which in the case of variable density are coupled with tube orientation) are quite well established. In practice, however, the constant properties assumption is responsible for large deviations between analytical predictions and experimental data. Analytical efforts to date have concentrated on determining the effects of *either* variable density (e.g., [1–5])[1] or variable viscosity (e.g., [6–11]) which is the other most important temperature-dependent property. Pigford [12] and Lawrence and Chato [13] have analyzed the entrance region problem in vertical tubes, considering both density and viscosity as functions of temperature. This problem is relatively straightforward since the free convection generated by the buoyancy force is parallel to the axial flow so that the flow field remains two-dimensional. No similar analysis has been reported for horizontal tubes.

The present paper extends previous analyses to include variable viscosity effects on combined forced and free laminar convection in horizontal circular tubes, and compares the predictions with recently published data.

Problem Formulation

General Considerations. Consideration is given to the problem of the steady, fully developed, laminar flow of a Newtonian fluid in a horizontal circular tube. The fluid is assumed to have temperature-dependent density and viscosity. Both of the usual heat flux boundary conditions are considered: uniform axial average heat flux with uniform circumferential wall temperature (Case 1), and uniform heat flux axially and circumferentially (Case 2). The fully developed condition is considered where the tube is long, and the heat transfer coefficient changes only due to variation in the fluid temperature level. The secondary flow, which is caused by buoyancy forces, is essentially two-dimensional.

The equations of conservation of mass, momentum, and energy for this problem are still too complicated to solve analytically and would require an enormous expenditure of computer time. Accordingly, an alternate solution technique is utilized. The experimental results of Mori, et al. [1] and Siegwarth, et al. [2] indicate that a thermal boundary layer exists when the Rayleigh number is high. It can then be assumed that the secondary flow is composed of two regions: a thin boundary layer near the pipe wall and a core which is enclosed by the boundary layer. These investigators have been successful in using boundary layer integration techniques to solve the fully developed

[1] Numbers in brackets designate References at end of the paper.

Contributed by the Heat Transfer Division for publication in the JOURNAL OF HEAT TRANSFER. Manuscript received by the Heat Transfer Division March 12, 1976. Paper No. 76-HT-HHH.

combined forced and free convection problem for fluids of constant viscosity.

General Equations. The coordinate systems used in the analysis are shown in Fig. 1. A curvilinear orthogonal coordinate system (X, Y, Z) is applied to the boundary layer, and rectangular coordinates (X^+, Y^+, Z) are used in the core. The Z coordinate is coincident with, or parallel to, the tube axis for the core and boundary layer regions, respectively. Since the flow is assumed to be fully developed, the velocity components are invariant in the Z-direction.

Neglecting axial conduction and viscous dissipation, the two-dimensional conservation equations for the general flow field can be written as follows:

Continuity equation:

$$\frac{\partial U}{\partial X} + \frac{\partial V}{\partial Y} = 0 \tag{1}$$

Momentum equation in the X-direction:

$$\rho\left[U\frac{\partial U}{\partial X} + V\frac{\partial U}{\partial Y}\right] = -\frac{\partial P}{\partial X} + \frac{\partial}{\partial X}\left[2\mu\frac{\partial U}{\partial X}\right] + \frac{\partial}{\partial Y}\left[\mu\left(\frac{\partial U}{\partial Y} + \frac{\partial V}{\partial X}\right)\right] + \rho g_x \tag{2}$$

Momentum equation in the Y-direction:

$$\rho\left[U\frac{\partial V}{\partial X} + V\frac{\partial V}{\partial Y}\right] = -\frac{\partial P}{\partial Y} + \frac{\partial}{\partial X}\left[\mu\left(\frac{\partial U}{\partial Y} + \frac{\partial V}{\partial X}\right)\right] + \frac{\partial}{\partial Y}\left[2\mu\frac{\partial V}{\partial Y}\right] + \rho g_y \tag{3}$$

Momentum equation in the Z-direction:

$$\rho\left[U\frac{\partial W}{\partial X} + V\frac{\partial W}{\partial Y}\right] = -\frac{\partial P}{\partial Z} + \frac{\partial}{\partial X}\left[\mu\frac{\partial W}{\partial X}\right] + \frac{\partial}{\partial Y}\left[\mu\frac{\partial W}{\partial Y}\right] \tag{4}$$

Energy equation:

$$\rho C_p\left[U\frac{T}{\partial X} + V\frac{\partial T}{\partial Y} + W\frac{\partial T}{\partial Z}\right] = k\left[\frac{\partial^2 T}{\partial X^2} + \frac{\partial^2 T}{\partial Y^2}\right] \tag{5}$$

Boundary Layer Region Equations. The traditional boundary layer assumption is made that the pressure gradient in the X-direction is independent of Y so that the pressure in the boundary layer equals the pressure in the core evaluated near the wall. The pressure variation in the core is hydrostatic. Employing the thermal expansion coefficient, β, the pressure gradient and the gravitational force in equation (2) can be combined as follows:

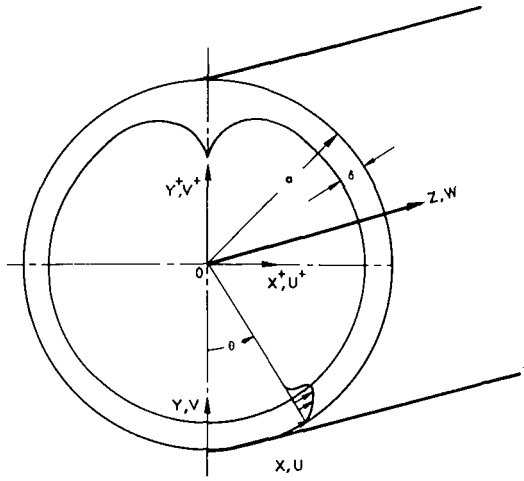

Fig. 1 Coordinate system for boundary layer and core region in horizontal tube

$$-\frac{\partial P}{\partial X} - \rho g\sin\frac{X}{a} = \rho g\beta(T - T_c)\sin\frac{X}{a} \tag{6}$$

Assuming viscosity is a function of temperature only and employing equations (1) and (6), equation (2) can be expressed as

$$U\frac{\partial U}{\partial X} + V\frac{\partial U}{\partial Y} = \nu\nabla^2 U - \gamma\nu\left[2\frac{\partial U}{\partial X}\frac{\partial T}{\partial X} + \left(\frac{\partial U}{\partial Y} + \frac{\partial V}{\partial X}\right)\frac{\partial T}{\partial Y}\right] + g\beta(T - T_c)\sin\frac{X}{a} \tag{7}$$

where

$$\gamma = \frac{-1}{\mu}\left(\frac{d\mu}{dT}\right) \tag{8}$$

a term analogous to the coefficient of thermal expansion, β. Equation (3) can be dropped according to the traditional boundary layer assumption.

To normalize the momentum and energy equations, the following dimensionless variables are introduced:

Nomenclature

a = tube radius
C_1 = coefficient, $\mathrm{Nu}/\mathrm{Ra}^{1/4}$; constant
C_p = constant pressure specific heat
g = gravitational acceleration
Gr = Grashof number, $g\beta\rho^2 a^3\Delta T/\mu^2$
$\bar{h}$ = circumferential average heat transfer coefficient, $\bar{q}''/(\bar{T}_w - T_b)$
k = fluid thermal conductivity
Nu = Nusselt number, $\bar{h}(2a)/k$
P = pressure
Pr = Prandtl number, $\mu C_p/k$
$\bar{q}''$ = circumferential average heat flux
Ra = Rayleigh number, Gr Pr
T = local fluid temperature
T_b = bulk temperature of entire flow field
T_c = core temperature evaluated at pipe wall
T_w = temperature at wall, circumferentially uniform for Case 1
ΔT = temperature difference, $T_w - T_b$
U, V, W = dimensional velocities in X-, Y-, Z-directions of boundary layer region
u, v, w = dimensionless velocities in x, y, z directions of boundary layer region, equation (9)
U^+, V^+, W^+ = dimensional velocities in X^+, Y^+, Z directions of core region
u^+, v^+, w^+ = dimensionless velocities in x^+-, y^+-, z-directions of core region, equation (15)
U_c, V_c = characteristic velocities given by equation (10)
$\bar{W}$ = bulk average velocity in axial direction
X, Y, Z = dimensional boundary layer coordinates: circumferential direction, perpendicular to wall, axial direction
x, y = dimensionless boundary layer coordinates, equation (9)
X^+, Y^+, Z = dimensional core region coordinates: horizontal direction, vertical direction, axial direction
x^+, y^+ = dimensionless core region coordinates, equation (15)
β = coefficient of thermal expansion, $-(1/\rho)(\partial\rho/\partial T)_P$
γ = coefficient of viscosity variation due to temperature change, equation (8)
δ = thickness of the thermal boundary layer
Δ = characteristic parameter for thermal boundary layer, equation (10)
μ = viscosity
ν = kinematic viscosity, μ/ρ
ρ = density
ϕ, ϕ^+ = dimensionless temperatures, equations (9) and (15)
$\phi_w{}^+$ = dimensionless temperature in core region evaluated at wall
Fluid properties are evaluated at the bulk temperature

$$x = \frac{X}{a}, \qquad y = \frac{Y}{\Delta}, \qquad \phi = \frac{T - T_b}{\Delta T}$$
$$u = \frac{U}{U_c}, \qquad v = \frac{V}{V_c}, \qquad w = \frac{W}{\bar{W}} \tag{9}$$

where the characteristic variables Δ, U_c, and V_c are chosen to be

$$\Delta = \frac{a}{(\mathrm{GrPr})^{1/4}}$$
$$U_c = \frac{\mu}{\rho a}\left(\frac{\mathrm{Gr}}{\mathrm{Pr}}\right)^{1/2} \tag{10}$$
$$V_c = \frac{\mu}{\rho a}\left(\frac{\mathrm{Gr}}{\mathrm{Pr}^3}\right)^{1/4}$$

When these variables are introduced into equation (7) and it is assumed that $(\Delta/a)^2$ is small and that GrPr is large, this equation can be expressed in dimensionless form as follows:

$$\frac{\partial^2 u}{\partial y^2} - \gamma \Delta T \frac{\partial u}{\partial y}\frac{\partial \phi}{\partial y} + (\phi - \phi_c)\sin x = \frac{1}{\mathrm{Pr}}\left[u\frac{\partial u}{\partial x} + v\frac{\partial u}{\partial y}\right] \tag{11}$$

Equation (11) is a general governing equation for most fluids.

For large Prandtl number fluids, the inertia terms comprising the right hand side of equation (11) can be ignored, and the equation can be simplified to

$$\frac{\partial^2 u}{\partial y^2} - \gamma \Delta T \frac{\partial u}{\partial y}\frac{\partial \phi}{\partial y} + (\phi - \phi_c)\sin x = 0 \tag{12}$$

In equation (12) ΔT is a reference temperature difference which is chosen to be $\bar{T}_w - T_b$.

The viscosity parameter $\gamma \Delta T$ appears always in the normalized momentum equation for fluids having temperature-dependent viscosity. As pointed out by Shannon and Depew [9], a constant γ implies a fluid with viscosity as an exponential function of temperature. Absolute values of $\gamma \Delta T$ may exceed unity when the viscosity is a strong function of temperature and temperature differences are large. For liquids, where viscosity decreases as temperature increases, $\gamma \Delta T$ is greater than zero for heating and less than zero for cooling. It is noted that zero $\gamma \Delta T$ corresponds to the traditional constant viscosity case.

Introducing the dimensionless variables, the energy equation in the boundary layer region, equation (5), can be simplified for uniform heat flux to

$$\frac{\partial^2 \phi}{\partial y^2} + \left(\frac{\Delta}{a}\right)^2 \frac{\partial^2 \phi}{\partial x^2} = u\frac{\partial \phi}{\partial x} + v\frac{\partial \phi}{\partial y} + w\frac{\mathrm{Nu}}{(\mathrm{Ra})^{1/2}} \tag{13}$$

For the very thin boundary layer assumption, the conduction in the X-direction and the convection due to the main flow become negligible for high Rayleigh numbers. The energy equation can then be reduced to

$$\frac{\partial^2 \phi}{\partial y^2} = u\frac{\partial \phi}{\partial x} + v\frac{\partial \phi}{\partial y} \tag{14}$$

Equation (14), which is the same equation as for free convection over a vertical plate, indicates that the heat transfer from the wall occurs by conduction perpendicular to the wall and by convection due to the secondary flow.

Core Region Equations. As shown in references [2, 14], the main flow will not be affected by the secondary flow for high Prandtl number fluid flow. Thus, the inertial force in equation (4) for the core region can be neglected.

The following dimensionless parameters are utilized for the core region:

$$x^+ = \frac{X^+}{a}, \qquad y^+ = \frac{Y^+}{a}, \qquad \phi^+ = \frac{T^+ - T_b}{\Delta T}$$
$$u^+ = \frac{U^+}{U_c}, \qquad v^+ = \frac{V^+}{V_c}, \qquad w^+ = \frac{W}{\bar{W}} \tag{15}$$

The axial momentum equation, equation (4), can be greatly simplified for the core region since the axial velocity is unaffected by the secondary flow for high Prandtl number fluids [2, 14]. The temperature variation in the core region is quite small compared to the temperature variation across the boundary layer; hence, the viscosity variation can be neglected. The simplified, dimensionless equation is then

$$\frac{a^2}{\mu \bar{W}}\frac{\partial P}{\partial Z} = \nabla_1^2 w^+ \tag{16}$$

With the usual assumption of a linear axial pressure gradient, the solution of equation (16) is the simple Poiseuille result:

$$w^+ = 2(1 - x^{+2} - y^{+2}) \tag{17}$$

With the assumptions that $\phi^+ = \phi(y^+)$, $v^+ = v(y^+)$, $u^+ = 0$, and large Rayleigh number, the nondimensionalized energy equation, equation (5), when nondimensionalized for the core region, can be reduced to

$$v^+\frac{\partial \phi^+}{\partial y^+} + \frac{\mathrm{Nu}}{(\mathrm{Ra})^{1/4}} w^+ = 0 \tag{18}$$

Nusselt Number. The Nusselt number can be obtained by considering the energy balance at the tube wall as follows:

$$\mathrm{Nu} = \frac{2ah}{k} = \frac{2a}{\pi \Delta}\int_0^\pi \left.\frac{\partial \phi}{\partial y}\right|_{y=0} dx$$
$$= \frac{2}{\pi}\int_0^\pi \left.\frac{\partial \phi}{\partial y}\right|_{y=0} dx\,(\mathrm{Ra})^{1/4} \tag{19}$$

Let

$$C_1 = \frac{2}{\pi}\int_0^\pi \left.\frac{\partial \phi}{\partial y}\right|_{y=0} dx \tag{20}$$

Then, the Nusselt number is obtained as

$$\mathrm{Nu} = C_1\,\mathrm{Ra}^{1/4} \tag{21}$$

Since only one parameter, $\gamma \Delta T$, appears in the governing equations, it is concluded that C_1 in equation (21) is a function of $\gamma \Delta T$. Thus, equation (21) can be rewritten as

$$\mathrm{Nu} = C_1(\gamma \Delta T)\mathrm{Ra}^{1/4} \tag{22}$$

Equation (18) can then be restated as

$$v^+\frac{\partial \phi^+}{\partial y^+} + C_1 w^+ = 0 \tag{23}$$

Analytical Solution Using Integral Method for Case 1

The first boundary condition considered is uniform axial average heat flux with uniform circumferential wall temperature at each axial location. The governing equations are given by equations (1), (12), (14), and (17)–(23), with the following boundary conditions:

$$\text{at } y = 0$$
$$v = 0, \qquad \phi = 1$$
$$\text{at } y = \delta$$
$$\frac{\partial u}{\partial y} = \frac{\partial \phi}{\partial y} = 0, \qquad \phi = \phi_w{}^+ \tag{24}$$

where $\phi_w{}^+$ is the dimensionless core region temperature evaluated at the wall (assuming the boundary layer to be very thin). It is noted that the boundary condition of the traditional free convection is $u = 0$ at $y = \delta$. However, it is apparent that the secondary flow velocity in the core is not zero. Therefore, it is more appropriate to set the velocity gradient equal to zero at $y = \delta$.

In the classical free convection problem for $\mathrm{Pr} > 1$, the hydrodynamic boundary layer thickness is greater than the thermal boundary layer thickness. In the present situation, however, when the downward return flow in the core is considered, it can be argued that the upward moving flow must be confined to the thermal boundary layer. The hydrodynamic and thermal boundary layer thicknesses are then ap-

proximately equal. In any event, an integral solution is utilized here and it has been shown that the integral solution for the classical problem, which assumes equal boundary layer thicknesses, produces a Nusselt number which is within 6 percent of the exact solution for large Prandtl numbers [16].

Following the usual boundary layer integration technique, it is assumed that the temperature variation through the boundary layer is a polynomial in y. The coefficients of this polynomial can be determined by utilizing the boundary conditions of equation (24) and by noting that at $y = 0$, $\partial^2\phi/\partial y^2 = 0$, with the following result:

$$\phi = 1 - \frac{3}{2}(1 - \phi_w{}^+)\frac{y}{\delta} + \frac{1}{2}(1 - \phi_w{}^+)\left(\frac{y}{\delta}\right)^3 \tag{25}$$

where the boundary layer thickness δ is a function of x.

Substituting ϕ and $\partial\phi/\partial y$ into equation (12) yields a differential equation for the modified variable u^*, with the subscript denoting a differentiation, as follows:

$$u_{\eta\eta}{}^* + A(1 - \eta^2)\, u_\eta{}^* + 1 - \frac{3}{2}\eta + \frac{1}{2}\eta^3 = 0 \tag{26}$$

where

$$u = u^*(\eta) \sin x \delta^2(1 - \phi_w{}^+)$$

$$\eta = \frac{y}{\delta}$$

$$A = \frac{3}{2}\gamma\Delta T(1 - \phi_w{}^+) \tag{27}$$

Equation (26) is a second-order ordinary differential equation with boundary conditions

$$\text{at } \eta = 0, \qquad u^* = 0$$

$$\eta = 1, \qquad u_\eta{}^* = 0 \tag{28}$$

Equation (26) can be easily solved by expanding u^* in terms of a finite series of η and determining the coefficients from the foregoing boundary conditions. Since $\phi_w{}^+$ is a very small value, the value of A in equation (27) can be approximated by $(3/2)(\gamma\Delta T)$.

Integrating equation (14) with respect to y from $y = 0$ to $y = \delta$, and eliminating v by means of equation (1), yields

$$\frac{\partial\phi}{\partial y}\bigg|_0^\delta = \frac{\partial}{\partial x}\int_0^\delta \phi u\, dy - \phi_w{}^+ \frac{\partial}{\partial x}\int_0^\delta u dy \tag{29}$$

Now, if u and ϕ as functions of y are substituted into equation (29), a first-order nonlinear ordinary differential equation in δ and $\phi_w{}^+$ is obtained. The boundary condition for this equation is obtained by assuming the symmetry of the boundary layer at $x = 0$, i.e.,

$$\frac{d\delta}{dx} = \frac{d\phi_w{}^+}{dx} = 0 \tag{30}$$

The parameter $\phi_w{}^+$ is obtained by integrating equation (23) with respect to x^+, from $x^+ = 0$ to $x^+ = \sqrt{1 - y^{+2}}$, with the following result:

$$\frac{d\phi_w{}^+}{dy^+}\int_0^{\sqrt{1-y^{+2}}} v^+ dx^+ = -C_1 \int_0^{\sqrt{1-y^{+2}}} w^+ dx^+ \tag{31}$$

A mass balance at any height in the pipe reveals that the flow rate downward in the core must equal the flow rate in the boundary layer at that value of x. Therefore, the temperature variation in the core is given by

$$B\frac{\partial\phi_w{}^+}{\partial y^+} = -C_1 \int_0^{\sqrt{1-y^{+2}}} w^+ dx^+ \tag{32}$$

where

$$B = -\int_0^{\sqrt{1-y^{+2}}} v^+ dx^+ = \int_0^1 u d\eta$$

By substitution of equations (27) and (17) for u and w^+, respectively, equation (32) can be solved for $d\phi_w{}^+/dy^+$. This derivative can be written in terms of the boundary layer coordinate x by recognizing that

$$y^+ = -\cos x \tag{33}$$

Once the core temperature distribution is determined, the bulk temperature can be obtained by integrating the product of the core temperature and the axial velocity profile as follows:

$$\phi_b{}^+ = \frac{4}{3}\int_0^\pi \phi_w{}^+ \sin^4 x\, dx = 0 \tag{34}$$

This equation is used as a constraint to determine the boundary values of $\phi_w{}^+$ at $x = 0$.

The coefficient C_1 is obtained by differentiating equation (25) and inserting the result in equation (20):

$$C_1 = \frac{1}{\pi}\int_0^\pi \frac{3(1 - \phi_w{}^+)}{\delta} dx \tag{35}$$

Equation (35) can be integrated, provided that $\phi_w{}^+$ and δ are given as functions of x.

Equations for $\phi_w{}^+$ [derived from equations (32) and (33)] and δ [derived from equation (29)] were integrated numerically by using the Fourth-Order Runge-Kutta method and assuming an initial arbitrary value of $\phi_w{}^+$ and the initial condition of equation (28) for δ at $x = 0$. With an initial value of C_1 assumed, the new value of C_1 was obtained by means of Simpson's rule. This new value of C_1 was carried on for the next calculation. In this manner, the procedure was repeated until the new calculated value of C_1 was equal to the previous C_1. Thus, δ and $\phi_w{}^+$ were determined when the iterative procedure was completed.

A computing time of 15 s was required for one value of $\gamma\Delta T$ with 100 divisions around the circumference, using the Iowa State IBM 360/65.

More details of the calculation procedure are given in reference [14].

Solution for Case 2

The second boundary condition considered in this analytical study is uniform heat flux axially and circumferentially (Case 2). The assumptions, governing equations, and solution procedure are the same for Case 2 as for Case 1. The boundary conditions for Case 2 are also the same as for Case 1, except that the heat transfer around the circumference is assumed to be

$$\frac{\partial\phi}{\partial y} = -C_1/2 \text{ at } y = 0 \tag{36}$$

Using the series solution for the dimensionless wall temperature, C_1 can be expressed as

$$C_1 = \frac{\pi - \int_0^\pi \phi_w{}^+ dx}{\frac{1}{4}\int_0^\pi \delta\, dx} \tag{37}$$

The detailed computational procedures for obtaining C_1, and thereby Nu, are given in reference [14].

Heat Transfer Results

Analytical Solutions. The heat transfer results for the present problem can be generally indicated as

$$\text{Nu} = C_1(\gamma\Delta T)\text{Ra}^{1/4} \tag{38}$$

The computed values of the coefficient C_1 are tabulated in Table 1 and plotted in Fig. 2 for various values of $\gamma\Delta T$. It is noted that $\gamma\Delta T = 0$ in the present analysis represents the constant viscosity solution. This solution for Case 1 has a numerical value of $C_1 = 0.8781$, which is lower than the value of $C_1 = 0.942$ given in reference [2]. The disagreement between these solutions is due to the utilization of different profiles for the secondary velocity, u, and the temperature in the boundary layer.

For $\gamma\Delta T > 0$, which corresponds to heating with liquids since vis-

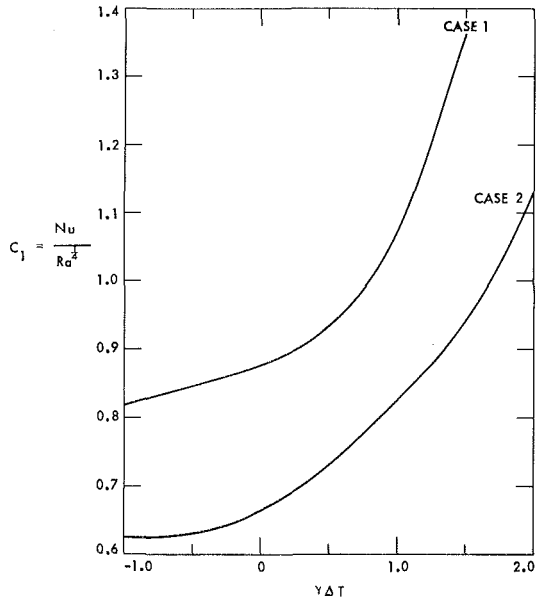

Fig. 2 Coefficient C_1 as function of viscosity parameter $\gamma\Delta T$

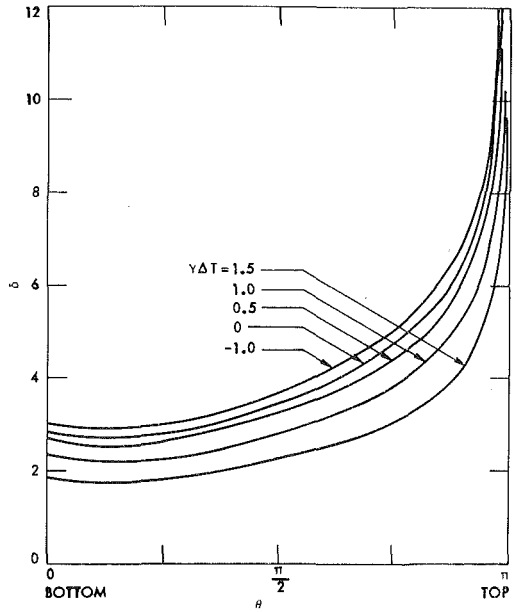

Fig. 3 Boundary layer thickness distribution along tube wall with $\gamma\Delta T$ as parameter

cosity generally decreases as temperature increases, C_1 increases with increasing $\gamma\Delta T$ for both boundary conditions. The parameter $\gamma\Delta T$ can usually be increased by increasing heat flux. In Case 1, for example, the coefficient C_1 for $\gamma\Delta T = 1.5$ is about 55 percent higher than that for the constant viscosity prediction. In Case 2, the constant C_1 for $\gamma\Delta T = 2.0$ is more than 70 percent above the constant viscosity value. Computational instability was observed when $\gamma\Delta T$ was greater than 1.5 in Case 1.

For $\gamma\Delta T < 0$, which corresponds to cooling with most liquids, C_1 decreases as the absolute value of $\gamma\Delta T$ increases. The variation of C_1 between $\gamma\Delta T = 0$ and -1.0 is about 7 percent in both cases.

The physical reason for the higher prediction of Nu with $\gamma\Delta T > 0$ is the thinner boundary layer associated with stronger secondary flow along the tube wall. Fig. 3 presents the boundary layer thickness around the tube circumference for Case 1. The boundary layer is thinner at the bottom of the tube; it gradually becomes thicker at $x = \pi/2$ and suddenly becomes very thick near the top of the tube wall. Fig. 3 also indicates that the boundary layer thickness decreases with increasing $\gamma\Delta T$. Since the Nusselt number is inversely proportional to the boundary layer thickness for constant Rayleigh number, the Nusselt number increases as $\gamma\Delta T$ increases. For most fluids, the viscosity gradient is large for higher $\gamma\Delta T$ due to larger ΔT. Thus, there is less resistance to motion along the tube wall. The increased velocity along the tube wall creates a stronger secondary flow which, in turn, increases the heat transfer coefficient.

The velocity and temperature profiles in the boundary layer for Case 1 are given by equations (27) and (25), respectively. These secondary velocity and temperature profiles are similar to those analytical profiles for the fully developed case (no viscosity variation) presented in previous investigations [1, 2, 5]. Fig. 4 indicates the temperature distribution in the core region at the vertical center line for Case 1. Since it is assumed that the isotherms in the core region are horizontal, Fig. 4 actually presents the temperature variation in the whole core region for various $\gamma\Delta T$.

Table 1 Computed values of the coefficient C_1

Case 1				Case 2			
$\gamma\Delta T \geq 0$		$\gamma\Delta T \leq 0$		$\gamma\Delta T \geq 0$		$\gamma\Delta T \leq 0$	
$\gamma\Delta T$	C_1	$\gamma\Delta T$	C_1	$\gamma\Delta T$	C_1	$\gamma\Delta T$	C_1
0.0	0.8781	0.0	0.8781	0.0	0.6643	0.0	0.6643
0.1	0.8854	-0.1	0.8713	0.1	0.6752	-0.1	0.6547
0.2	0.8942	-0.2	0.8653	0.2	0.6873	-0.2	0.6466
0.3	0.9047	-0.3	0.8596	0.3	0.7006	-0.3	0.6398
0.4	0.9175	-0.4	0.8542	0.4	0.7149	-0.4	0.6347
0.5	0.9330	-0.5	0.8487	0.5	0.7302	-0.5	0.6312
0.6	0.9519	-0.6	0.8433	0.6	0.7465	-0.6	0.6291
0.7	0.9748	-0.7	0.8378	0.7	0.7636	-0.7	0.6286
0.8	1.0023	-0.8	0.8322	0.8	0.7816	-0.8	0.6274
0.9	1.0351	-0.9	0.8265	0.9	0.8006	-0.9	0.6265
1.0	1.0740	-1.0	0.8208	1.0	0.8205	-1.0	0.6247
1.1	1.1209			1.1	0.8414		
1.2	1.1748			1.2	0.8635		
1.3	1.2359			1.3	0.8870		
1.4	1.2979			1.4	0.9120		
1.5	1.3368			1.5	0.9388		
				1.6	0.9680		
				1.7	1.0000		
				1.8	1.0356		
				1.9	1.0759		
				2.0	1.1227		

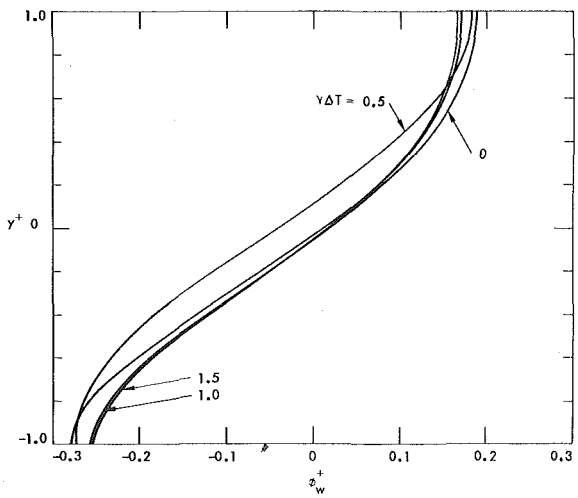

Fig. 4 Temperature distribution in the core region with $\gamma\Delta T$ as parameter

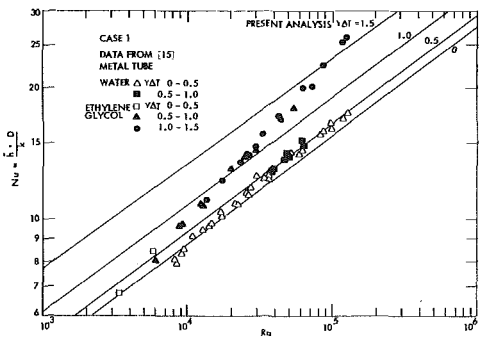

Fig. 5 Effect of $\gamma\Delta T$ on Nusselt number for Case 1, comparison with data for metal tube

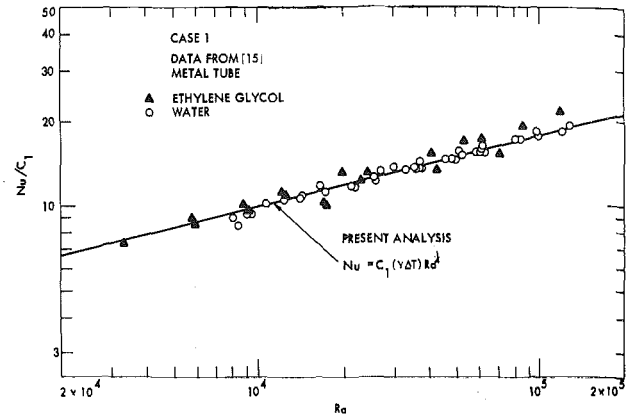

Fig. 7 Comparison of present analytical solution of Case 1 with experimental data for metal tube

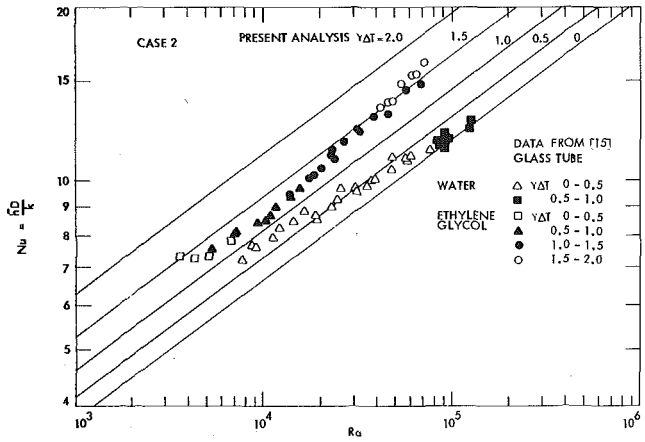

Fig. 6 Effect of $\gamma\Delta T$ on Nusselt number for Case 2, comparison with data for glass tube

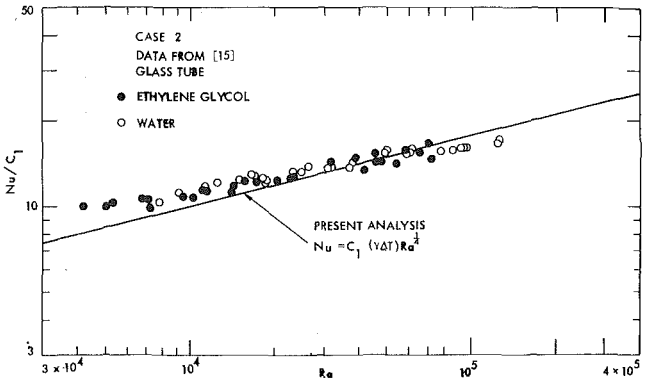

Fig. 8 Comparison of present analytical solution of Case 2 with experimental data for glass tube

The Nusselt number predictions are shown in Figs. 5 and 6. For practical application, these results can be accurately represented by the following equations:

Case 1

$$1.5 \geq \gamma\Delta T \geq 0 \qquad \mathrm{Nu} = [0.8823 + 0.0153\,\gamma\Delta T + 0.1481\,(\gamma\Delta T)^2 + 0.00334\,(\gamma\Delta T)^3]\mathrm{Ra}^{1/4} \quad (39)$$

$$0 > \gamma\Delta T \geq -1.0 \qquad \mathrm{Nu} = [0.877 + 0.0563\,\gamma\Delta T]\,\mathrm{Ra}^{1/4} \quad (40)$$

Case 2

$$2.0 \geq \gamma\Delta T \geq 0 \qquad \mathrm{Nu} = [0.661 + 0.140\,\gamma\Delta T - 0.0098\,(\gamma\Delta T)^2 + 0.027\,(\gamma\Delta T)^3]\,\mathrm{Ra}^{1/4} \quad (41)$$

$$0 > \gamma\Delta T \geq -1.0 \qquad \mathrm{Nu} = [0.663 + 0.0886\,\gamma\Delta T + 0.00526\,(\gamma\Delta T)^2]\,\mathrm{Ra}^{1/4} \quad (42)$$

It should be noted that these equations are not valid at very low Rayleigh numbers where both secondary flow and viscosity effects are negligible. Thus, no predictions less than Nu = 4.36 should be accepted.

Use of these equations for design requires iteration since ΔT is the dependent parameter of interest for tubes with a specified heat flux boundary condition. This inconvenience can be avoided by redefining the characteristic temperature difference in terms of heat flux. See, for example, reference [5]. This conversion and recorrelation were not carried out for the present analysis.

Comparison With Experimental Data. A number of experimental investigations have provided data which could be compared with the present analysis. However, since the data of Morcos and Bergles [15] are the most recent and fully documented, their data will be compared with the present analysis. This comparison is shown in Figs. 5–8.

Fig. 5 reveals the comparison of the present Case 1 solution and data for a metal tube using water and ethylene glycol as the working fluids. It is clear that the constant viscosity solution, $\gamma\Delta T = 0$, is valid only for $\gamma\Delta T < 0.5$ and that the experimental results depart from the constant viscosity prediction as the viscosity parameter increases. A similar comparison for water and ethylene glycol with the glass tube, which approximates the Case 2 boundary condition, is indicated in Fig. 6.

A more direct comparison of experimental results and analytical predictions is presented in Figs. 7 and 8 for the metal tube and the glass tube, respectively. The excellent agreement between the solutions of Case 1 and the experimental results for the metal tube is clearly shown in Fig. 7. The deviation of experimental data from the analytical solutions is seen to be within 10 percent.

A similar comparison of the present Case 2 solutions with glass tube experimental results is shown in Fig. 8. A larger discrepancy between prediction and experiment is observed, about 20 percent at low Rayleigh numbers and about 10 percent at high Rayleigh numbers. The disagreement of the present analysis and experimental results in the lower Rayleigh number region could be due to the high Rayleigh number assumption in this analysis and the small ΔT in the experimental work, which increases the uncertainty of the measurements. The larger deviation could also be caused by tube wall effects. The

metal tube data are closer to the boundary conditions of Case 1 than the glass tube data are to the boundary conditions of Case 2.

Concluding Remarks

A new viscosity parameter, $\gamma\Delta T = (-1/\mu)(d\mu/dT)\Delta T$, has been successfully employed in the present analysis to include temperature dependence of viscosity in the combined forced and free convection problem. This parameter is obtained directly from the governing equations by considering viscosity as temperature-dependent. Constant viscosity solutions reported to date are valid only when fluid viscosity is not a strong function of temperature.

The Nusselt number for laminar convection in horizontal tubes with large Prandtl number fluids is proportional to $Ra^{1/4}$ for both limiting boundary conditions, and the proportionality constant C_1 increases as $\gamma\Delta T$ increases. The heat transfer results for $\gamma\Delta T = 1.5$ in Case 1 and $\gamma\Delta T = 2.0$ in Case 2 are about 55 percent and 70 percent, respectively, above the constant viscosity predictions. The final correlations are given in equations (39)–(42). The present analysis and the experimental data for water and ethylene glycol generally agree to within 10 percent. The correlations are therefore acceptable for design purposes for fluids with Prandtl numbers greater than 3. These correlations are an alternative to the strictly empirical correlations given in reference [15].

In view of the success of the present analysis, the new dimensionless group $\gamma\Delta T$ should be useful in solving other convective heat transfer processes where temperature-dependent viscosity must be considered.

Acknowledgments

This study was supported by the National Science Foundation through Grant GK-36851 and by the Engineering Research Institute, Iowa State University.

References

1 Mori, Y., and Futagami, K., "Forced Convective Heat Transfer in Uniformly Heated Horizontal Tubes, 2nd Report—Theoretical Study," *International Journal of Heat and Mass Transfer* Vol., 10, 1967, pp. 1801–1813.

2 Siegwarth, D. P., Mikesell, R. P., Readal, T. C., and Hanratty, T. J., "Effect of Secondary Flow on the Temperature Field and Primary Flow in a Heated Horizontal Tube," *International Journal of Heat and Mass Transfer* Vol. 12, 1969, pp. 1535–1553.

3 Newell, P. H., Jr., and Bergles, A. E., "Analysis of Combined Free and Forced Convection for Fully Developed Laminar Flow in Horizontal Tubes," JOURNAL OF HEAT TRANSFER, TRANS. ASME, Series C, Vol. 92, 1970, pp. 83–89.

4 Cheng, K. C., and Ou, J. W., "Free Convection Effects on Graetz Problem for Large Prandtl Number Fluids in Horizontal Tubes With Uniform Wall Heat Flux," *Heat Transfer 1974*, Vol. III, Japan Soc. Mech. Eng., 1974, pp. 159–163.

5 Hong, S. W., Morcos, S. M., and Bergles, A. E., "Analytical and Experimental Results for Combined Forced and Free Laminar Convection in Horizontal Tubes," *Heat Transfer 1974*, Vol. III, Japan Soc. Mech. Eng., 1974, pp. 154–158.

6 Deissler, R. G., "Analytical Investigation of Fully Developed Laminar Flow in Tubes With Heat Transfer With Fluid Properties Variable Along the Radius," NACA TN 2410, 1951.

7 Rosenberg, D. E., and Hellums, T. D., "Flow Development and Heat Transfer in Variable Viscosity Fluids," *I. & E.C. Fundam.*, Vol. 4, 1965, pp. 417–422.

8 Test, F. L., "Laminar Flow Heat Transfer and Fluid Flow for Liquids With Temperature-Dependent Viscosity," JOURNAL OF HEAT TRANSFER, TRANS. ASME, Series C, Vol. 90, 1968, pp. 385–392.

9 Shannon, R. L., and Depew, C. A., "Forced Laminar Flow Convection in a Horizontal Tube With Variable Viscosity and Free Convection Effects," JOURNAL OF HEAT TRANSFER, TRANS. ASME, Series C, Vol. 91, 1969, pp. 251–258.

10 Hwang, S. T., and Hong, S. W., "Effect of Variable Viscosity on Laminar Heat Transfer in a Rectangular Duct," *Chem. Eng. Progr. Symp. Ser.*, Vol. 66, 102, 1970, pp. 100–208.

11 Martin, B. W., and Fargie, D., "Effect of Temperature-Dependent Viscosity on Laminar Forced Convection in the Entrance Region of a Circular Pipe," *Proc. Inst. Mech. Eng.*, Vol. 106, 1972, pp. 307–316.

12 Pigford, R. L., "Nonisothermal Flow and Heat Transfer Inside Vertical Tubes," *Chem. Eng. Progr. Symp. Ser.* 17, Vol. 51, 1955, pp. 79–92.

13 Lawrence, W. T., and Chato, J. C., "Heat Transfer Sheets on the Developing Laminar Flow Inside Vertical Tubes," JOURNAL OF HEAT TRANSFER, TRANS. ASME, Series C, Vol. 88, 1966, pp. 214–222.

14 Hong, S. W., and Bergles, A. E., "Analysis of Combined Forced and Free Laminar Convection in Horizontal Tubes," Heat Transfer Laboratory Report HTL-4, ISU-ERI-Ames-74155, Iowa State University, 1974.

15 Morcos, S. M., and Bergles, A. E., "Combined Forced and Free Laminar Convection in Horizontal Tubes," JOURNAL OF HEAT TRANSFER, TRANS. ASME, Series C, Vol. 97, 1975, pp. 212–219.

16 Rohsenow, W. M., and Choi, H., *Heat, Mass, and Momentum Transfer*, Prentice Hall, Englewood Cliffs, N.J., 1961, pp. 155–162.

A. A. Sfeir

Assoc. Professor,
School of Engineering and Architecture,
American University of Beirut,
Beirut, Lebanon

The Heat Balance Integral in Steady-State Conduction

The Heat Balance Integral Method is applied to solve for the heat flow and temperature distribution in extended surfaces of different shapes and boundary conditions. In most cases the analysis is found to be identical to the exact two-dimensional solutions at Biot numbers for which the one-dimensional analysis is almost 100 percent off. Other possible extensions of the method are briefly described.

1 Introduction

Approximate solutions to certain types of heat conduction problems can easily be obtained using the Heat Balance Integral Method (HBIM). This method which was first introduced by Goodman [1, 2][1] has, however, been restricted to solving one-dimensional unsteady heat diffusion. In such problems, the effect of the boundary condition is assumed to penetrate a certain distance $\delta(t)$ called the thermal boundary-layer. Inside this region, the temperature distribution is represented by a polynomial which satisfies a certain number of conditions on the surface and at δ. Integrating the partial differential equation with distance, reduces the problem to that of an ordinary differential equation.

This idea had previously been given by Pohlhausen and Von Karman [3] to solve for the viscous boundary-layer, and still is the most widely used method dealing with such problems.

Following the work of Goodman many extensions to the method have been presented but, to our knowledge, none dealt with applying this method to two-dimensional steady conduction. The reason is most certainly due to the fact that such problems are relatively easy to solve both numerically and analytically.

The analytical solutions are, however, quite cumbersome and there are cases where approximate simple analytical solutions are needed. This paper shows how the HBIM may be used to obtain such solutions. This method will be applicable mostly to problems where the conduction is almost one-dimensional but for which the one-dimensional theory becomes unreliable. The method is illustrated by few examples of heat transfer in extended surfaces where it is found that important improvements on the one-dimensional solution may be accomplished without complicating the analysis by any appreciable amount.

[1] Numbers in brackets designate References at end of paper.

Contributed by the Heat Transfer Division for publication in the JOURNAL OF HEAT TRANSFER. Manuscript received by the Heat Transfer Division March 19, 1975. Paper No. 76-HT-VV.

2 The Integral Method

The main steps of the method will now be outlined for the heat conduction problem in the region

$$0 < x < \ell$$

$$0 < y < b$$

with, say, convective heat transfer on the sides $y = 0, b$ and similar or other boundary conditions on $x = 0, \ell$.

The differential equation and boundary conditions are:

$$\frac{\partial^2 T}{\partial x^2} + \frac{\partial^2 T}{\partial y^2} = 0 \tag{1}$$

$$\left[\frac{\partial T}{\partial y}\right]_{y=0} = f_1\, T(x, 0)$$

$$\left[\frac{\partial T}{\partial y}\right]_{y=b} = f_2\, T(x, b) \tag{2}$$

$$\text{and at } x = 0, \ell \quad T \text{ or } \frac{\partial T}{\partial x} \quad \text{are given.} \tag{3}$$

If the boundary conditions are such that one would expect that the heat flux vector is almost parallel to x, it is usually assumed that T is independent of y and the problem is reduced to one-dimensional conduction. Instead we will approximate T using a polynomial in y:

$$T = \alpha + \beta y + \gamma y^2 \tag{4}$$

where α, β, and γ are functions of x. Applying the boundary conditions at $y = 0$ and $y = b$, two of the three coefficients can be determined in terms of the remaining one. Let α be the remaining unknown coefficient.

Integrating equation (1) we get:

$$\int_0^b \frac{\partial^2 T}{\partial x^2}\, dy + \left[\frac{\partial T}{\partial y}\right]_b - \left[\frac{\partial T}{\partial y}\right]_0 = 0$$

and defining $\theta = \int_0^b T dy$ we get:

$$\frac{d^2\theta}{dx^2} + \left[\frac{\partial T}{\partial y}\right]_b - \left[\frac{\partial T}{\partial y}\right]_0 = 0$$

Now using equation (4) we have $\theta = \theta(\alpha)$ also, the second and third terms of this equation can be written as function of α by using equations (2) and (4). The differential equation reduces to:

$$\frac{d^2\alpha}{dx^2} + F(\alpha) = 0 \tag{5}$$

The solution of this ordinary differential equation will yield α and, therefore, the coefficients of the approximate solution (4) are all defined.

Note that when solving equation (5) one needs a new form of the boundary conditions (3) which are consistent with the polynomial approximation (4). The conditions (3) are satisfied by the true solution while the approximate solution must satisfy the conditions:

$$\text{at } x = 0 \quad \theta(0) \quad \text{or} \quad \left\{\frac{d\theta}{dx}\right\}_0 \quad \text{are given}$$

and

$$\text{at } x = \ell \quad \theta(\ell) \quad \text{or} \quad \left[\frac{d\theta}{dx}\right]_\ell \quad \text{are given} \tag{6}$$

It can readily be seen that the one-dimensional heat conduction theory follows essentially the same steps as above except that the approximating polynomial for T is the much cruder form T = constant.

As will be seen later the method is not limited to simple geometries as above but may well be used for plates of nonuniform thicknesses, different boundary conditions, problems with axisymmetry etc. Also it can be extended to convert nonhomogeneous materials, variable conductivity, and it can be perfected by using higher order polynomials and writing more boundary conditions. This last point usually complicates the problem appreciably and does not guarantee an improvement in accuracy [4].

3 Sample Problems

(*a*) **The Straight Fin.** The method will now be used to solve for the temperature distribution in a straight fin as shown in Fig. 1. The one-dimensional analysis of this problem is straightforward but the results become unreliable for large Biot numbers or short fins [5]. The equation to be solved is

$$\frac{\partial^2 T}{\partial x^2} + \frac{\partial^2 T}{\partial y^2} = 0 \tag{7}$$

with boundary conditions:

$$\left[\frac{\partial T}{\partial y}\right]_{y=\pm\frac{b}{2}} = \mp \frac{h}{k}(T_s - T_f) \tag{8}$$

where h is the film coefficient, T_s the surface temperature and T_f the fluid temperature.

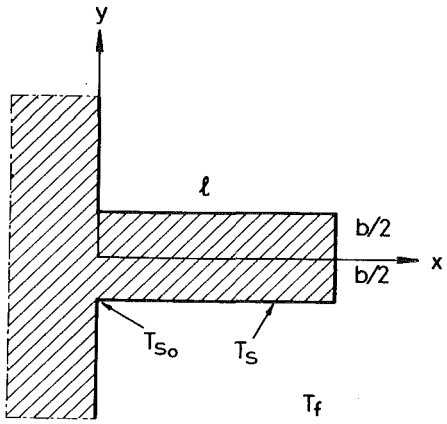

Fig. 1 The straight fin

The boundary conditions at $x = 0, \ell$ are, respectively,

$$\text{at} \quad x = 0 \quad T = T(0, y)$$

and

$$\text{at} \quad x = \ell \quad \left[\frac{\partial T}{\partial x}\right]_{x=\ell} = -\frac{h_e}{k}\left[T(\ell, y) - T_f\right] \tag{9}$$

where h_e is the film coefficient at the tip of the fin. These two boundary conditions will have to be expressed differently as explained in the foregoing.

Writing a polynomial approximation for T and using the boundary conditions (8) we get:

$$T = t_s + T_f + \frac{\mathrm{B}}{2} t_s - \frac{\mathrm{B}}{2} t_s \left(\frac{2y}{b}\right)^2 \tag{10}$$

where $t_s = T_s - T_f$ and B is the Biot number $\mathrm{B} = hb/2k$. From this we get $\theta = bt_s(1 + \mathrm{B}/3) + bT_f$. Integrating the partial differential equation and substituting from above we find:

$$\frac{d^2 t_s}{dx^2} - \frac{2h}{kb}\frac{1}{C} t_s = 0, \text{ where } C = 1 + \frac{\mathrm{B}}{3} \tag{11}$$

the conditions (9) will be written as:

$$\theta(0) = \int_{\frac{-b}{2}}^{\frac{b}{2}} T(0, y)\, dy$$

and

$$\left[\frac{d\theta}{dx}\right]_{x=\ell} = -\frac{h_e}{k}\theta(\ell) \tag{12}$$

Equation (11) is similar to what is obtained in one-dimensional

Nomenclature

b = fin thickness
f = triangular fin geometry factor
h = film coefficient
k = thermal conductivity
ℓ = fin length
q = heat flow rate at the base of the fin
t = temperature difference with the surrounding fluid temperature
x, y, z = cartesian coordinates
B = Biot number
C = a nondimensional constant involving B
D = parameter occuring in the solution for q
H = parameter involving the convection at the tip of the fin
I_0, I_1 = Bessel function of first kind
K_0, K_1 = Bessel function of second kind
M = parameter occuring in the solution for q
R_1 = inner radius of circular fin
R_2 = outer radius of circular fin
T = temperature
W = triangular fin base width
α = nondimensional distance along the circular fin
β = dimensionless film coefficient
δ = thermal boundary-layer thickness
θ = temperature integral
λ = dimensionless variable
φ = angular coordinate
η = nondimensional length of circular fin

Subscripts and Superscripts

$( )_e$ = conduction at the tip of the fin
$( )_f$ = conditions in the fluid surrounding the fin
$( )_s$ = surface conditions
$( )_0$ = condition at the root of the fin
$( )_1$ = upper surface
$( )_2$ = lower surface
$( )^*$ = value corresponding to the one-dimensional analysis

theory except for the constant C. Solving for the temperature distribution as in [5] we get:

$$\frac{t_s}{t_0} = \frac{\cosh M(\ell - x) / H \sinh M(\ell - x)}{\cosh M + H \sinh M} \tag{13}$$

where t_0 is the surface temperature at the root of the fin obtained from equation (12), and $M = \sqrt{B/C}\ 2/b$, $H = h_e/kM$

The rate of heat flow from the fin can be obtained from equations (10) and (13), and we get that, per unit width of the fin:

$$\frac{q}{kt_0} = Mb \frac{\sinh M\ell + H \cosh M\ell}{\cosh M\ell + H \sinh M\ell} \tag{14}$$

The foregoing results (13) and (14) are identical in form to those of the one-dimensional problem. Using starred symbols to denote one-dimensional theory, we have the following values for the parameters occuring in equations (13) and (14)

$$M^* = \sqrt{B\frac{2}{b}}$$

$$H^* = \frac{h_e}{kM^*}$$

$$t_0^* = Ct_0$$

This shows that as long as C is near one (i.e., B is small) our solution becomes identical to the one-dimensional case. This is easily interpreted by the fact that when h is small the curvature of the temperature profile near the surface becomes very small and the parabolic shape (10) becomes a straight line. On the other hand, for large B, the one-dimensional solution differs appreciably from equations (13) and (14).

The heat flow is shown on Fig. 2 for different values of B and $2\ell/b$ along with some values obtained by a numerical solution of the Laplace equation using a standard finite difference scheme. The HBIM results are very close to the numerical solution at all values of the Biot number while, as explained previously, the one-dimensional solution differs substantially with increasing B. The results shown in Fig. 2 are for $h_e = h$.

(*b*) **The Straight Fin With Different Film Coefficients on Each Face.** The same method may also be applied if, instead of equation (8), we are given different film coefficients on the upper and lower surfaces:

$$\left[\frac{\partial T}{\partial y}\right]_{y=-\frac{b}{2}} = \frac{h_1}{k}(T_{s1} - T_f)$$

$$\left[\frac{\partial T}{\partial y}\right]_{y=\frac{b}{2}} = -\frac{h_2}{k}(T_{s2} - T_f) \tag{15}$$

Following the same approach as before, we get an ordinary differential equation:

$$\frac{d^2 t_{s1}}{dx^2} - D^2 t_{s1} = 0 \tag{16}$$

where

$$D = \frac{2}{b}\left\{\frac{6(B_1 + B_2 + B_1^2 + B_2^2)}{9B_1 + 7B_2 + 4B_1B_2 + 12}\right\}^{1/2} \tag{17}$$

B_1 and B_2 being the Biot numbers on the lower and upper surfaces, respectively.

The solution of equation (16) is carried out as before and we get expressions that have the same form, namely:

$$\frac{t_{s1}}{t_{01}} = \frac{\cosh D(\ell - x) + H \sinh D(\ell - x)}{\cosh D\ell + H \sinh D\ell} \tag{18}$$

and

$$\frac{q}{kt_{01}} = Db\left(\frac{\sinh D\ell + H \cosh D\ell}{\cosh D\ell + H \sinh D\ell}\right) \tag{19}$$

where t_{01} is the lower surface temperature at the root of the fin determined from the boundary conditions in the form (12) and

$$H = \frac{h_e}{h_1}\frac{B_1}{D} = \frac{h_e}{h_2}\frac{B_2}{D}$$

Note that although the expression for D is not symmetric with respect to B_1 and B_2, the solution itself is actually symmetric.

Fig. 3 shows the rate of heat flow as function of B_1, B_2 and $2\ell/b$ assuming that h_e has an average value between h_1 and h_2. It can be seen that as long as B_1 and B_2 are close to each other, the heat flow rate is almost equal to the value computed on the basis of an average value of the Biot numbers. As B_1 and B_2 are made different from each other while their average is kept constant, the heat flow rate increases appreciably over the value based on the average Biot number. For low average Biot numbers, the effect of B_1/B_2 becomes negligible.

(*c*) **The Annular Fin.** Consider an annular fin of thickness b

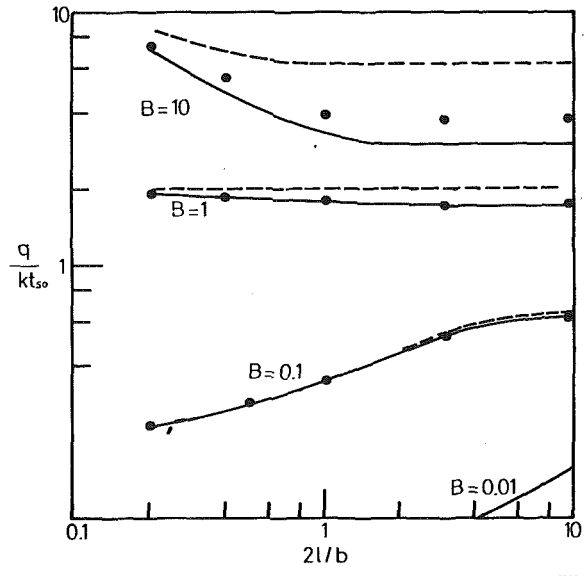

Fig. 2 Heat flow rates in straight fins of different aspect ratios and at different Biot numbers: - - - - one-dimensional analysis; — HBIM; O Numerical solution of the two-dimensional problem

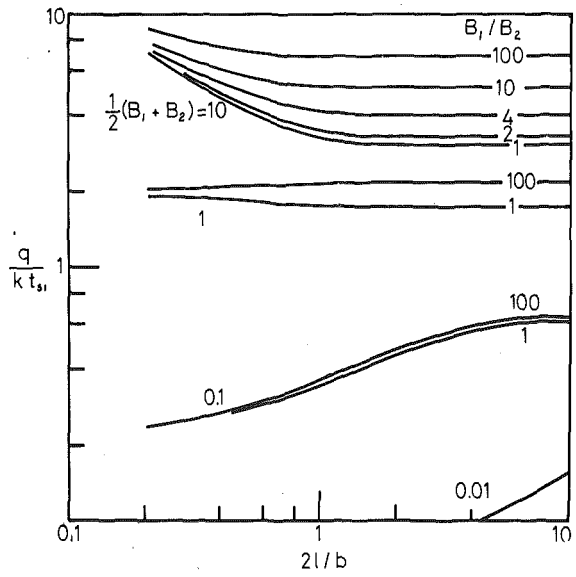

Fig. 3 The influence of different Biot numbers on the upper and lower surfaces of the fin

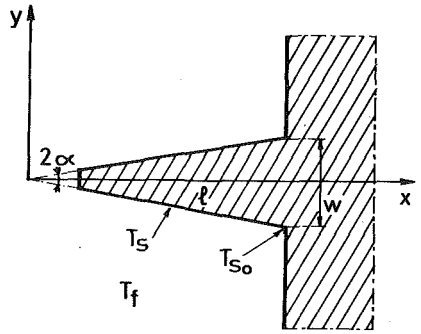

Fig. 4 The triangular fin

having an inner radius R_1 and outer radius R_2. The equation to be solved is:

$$\frac{1}{r}\frac{\partial}{\partial r}\left(r\frac{\partial T}{\partial r}\right)+\frac{\partial^2 T}{\partial x^2}=0 \tag{20}$$

with boundary conditions:

$$\left[\frac{\partial T}{\partial x}\right]_0=\frac{h}{k}(T_s-T_f)$$

$$\left[\frac{\partial T}{\partial x}\right]_b=-\frac{h}{k}(T_s-T_f) \tag{21}$$

and two boundary conditions similar to equation (9) on $r = R_1$ and r = R_2.

Integrating equation (20) with x from 0 to b and introducing $\theta = \int_0^b T dx$, we get:

$$\frac{d^2\theta}{dr^2}+\frac{1}{r}\frac{d\theta}{dr}-\frac{2ht_s}{k}=0 \tag{22}$$

The polynomial for T satisfying the boundary conditions (21) is found to be:

$$T=t_s+T_f+\left(\frac{h}{k}\right)t_s x-\left(\frac{h}{kb}\right)t_s x^2 \tag{23}$$

which gives

$$\theta=T_f b+t_s b\left(1+\frac{hb}{6k}\right) \tag{24}$$

Substituting in equation (22) we get:

$$\frac{d^2 t_s}{dr^2}+\frac{1}{r}\frac{dt_s}{dr}-\frac{2h}{2b}\frac{1}{C}t_s=0 \tag{25}$$

where

$$C=1+\frac{hb}{6k}=1+\frac{\mathrm{B}}{3}$$

Apart from C, equation (25) is a Bessel equation similar to that which occurs in the one-dimensional analysis. Its solution may be put in the dimensionless form [6]:

$$\frac{t_s}{t_{s0}}=\frac{I_0(\beta\eta)K_1(\beta)+K_0(\beta\eta)I_1(\beta)}{I_0(\beta\alpha)K_1(\beta)+K_0(\beta\alpha)I_1(\beta)} \tag{26}$$

where t_{s0} is the surface temperature at the root of the fin determined from equation (12), I and K are, respectively, the modified Bessel functions of the first and second kind, and

$\beta=\sqrt{\dfrac{2hR_2^2}{kbC}}$ a dimensionless film coefficient,

$$\alpha=\frac{R_1}{R_2};\quad \text{and } \eta=\frac{r}{R_2}$$

The heat flow rate is found to be:

$$\frac{q}{(1-\alpha^2)kbt_{s0}}=\frac{2\alpha\beta}{(1-\alpha^2)}\left[\frac{K_1(\beta\alpha)I_1(\beta)-I_1(\beta\alpha)K_1(\beta)}{K_1(\beta)I_0(\beta\alpha)+I_1(\beta)K_0(\beta\alpha)}\right] \tag{27}$$

The same relations also hold for one-dimensional conduction but β must be substituted by $\beta^* = \sqrt{2hR_2^2/kb}$ from which we can get a relation between β and β^*:

$$\beta=\frac{\beta^*}{\sqrt{1+\dfrac{\beta^*}{12}\left(\dfrac{b}{R_2}\right)^2}} \tag{28}$$

We can, therefore, use the results of the one-dimensional analysis which are available in chart form, provided the previous substitution is made for β^*. It is clear from equation (28) that the correction increases with β^* and b/R_2 which is quite natural.

(*d*) **The Triangular Fin.** Consider the triangular fin shown in Fig. 4. The equation to be solved is:

$$\frac{1}{r}\frac{\partial}{\partial r}\left(r\frac{\partial T}{\partial r}\right)+\frac{1}{r^2}\frac{\partial^2 \mathrm{T}}{\partial\varphi^2}=0 \tag{29}$$

with the boundary conditions

$$\left[\frac{1}{r}\frac{\partial T}{\partial\varphi}\right]_{\varphi=\pm\alpha}=\mp\frac{h}{k}(T_s-T_f) \tag{30}$$

and two other boundary conditions similar to equation (9) at the root and the tip of the fin.

Writing a polynomial of the form (4) for T and defining

$$\theta=\int_{-\alpha}^{\alpha} T\,d\varphi$$

we get after transforming to cartesian coordinates:

$$\theta=T_f\frac{W}{\ell}+t_s\frac{W}{\ell}\left(1+\frac{2}{3}\mathrm{B}f\frac{x}{\ell}\right)$$

where B = $hW/2k$ is the Biot modulus based on the thickness of the fin's root,

and $f=\sqrt{1+\left(\dfrac{W}{2\ell}\right)^2}$

Integrating (29) from $-\alpha$ to $+\alpha$, we get after substituting for the boundary conditions and for t_s in terms of θ:

$$\frac{d^2\theta}{dX^2}+\frac{1}{X}\frac{d\theta}{dX}-\frac{2fh^2}{kWX}\left(1+\frac{2}{3}\mathrm{B}fX\right)^{-1}\theta \tag{31}$$

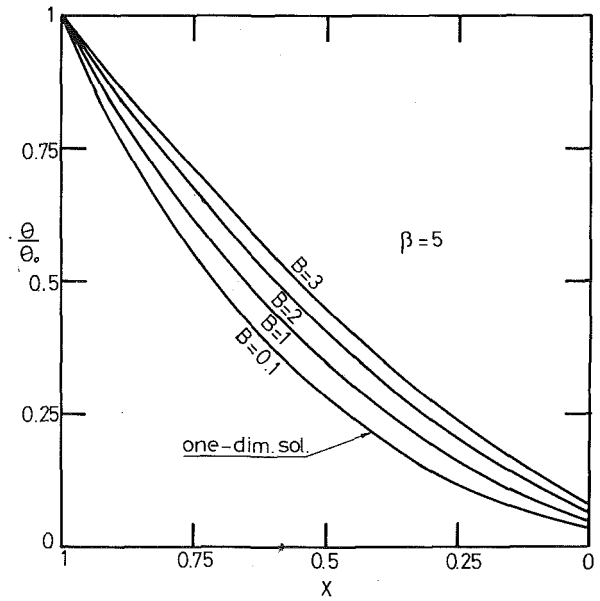

Fig. 5 Temperature distribution in the triangular fin

Table 1 Heat transfer from fin $q\ell/t_{s0}KW$

	ONE-DIMENSIONAL ANALYSIS $-\frac{\beta^*}{2}\frac{I_1(\beta^*)}{I_0(\beta^*)}$	H.B.I.M. (Numerical Solution)	H.B.I.M. (Approximate Solution) $-\frac{\beta}{2}\frac{I_1(\beta)}{I_0(\beta)}$
$\beta^* = 5$, B = 0.1	2.233	2.182	2.192
$\beta^* = 5$, B = 1	2.233	1.781	1.889
$\beta^* = 5$, B = 2	2.233	1.468	1.598
$\beta^* = 5$, B = 3	2.233	1.258	1.379

where X is the dimensionless distance x/ℓ.

Numerical solutions of equation (31) are shown in Fig. 5, along with the analytical solution of the one-dimensional analysis. The latter is independent of B as the one-dimensional analysis yields an equation similar to equation (31) but without the quantity in brackets in the third term.

If equation (31) must be solved numerically, the advantage of using the heat balance integral method will no more be justified. However, it is found that if one substitutes the term $\frac{2}{3}$ BfX by its average constant value along the fin, namely $\frac{1}{3}$ Bf, equation (31) will become identical to the one-dimensional analysis with

$$\beta = \frac{\beta^*}{\sqrt{1 + \frac{Bf}{3}}} \tag{32}$$

$$\beta^* = \sqrt{\frac{8fh^2}{kW}} \tag{33}$$

This approximation introduces only a small error on the heat flow from the fin as may be seen from Table 1.

Therefore, one may be able to use the analytical results of the one-dimensional analysis which are presented in most textbooks provided the proper corrected value of β is used.

4 Discussion and Conclusions

The few simple examples outlined in the foregoing show how the HBIM can be applied to solve for the heat transfer in extended surfaces. The analysis is extremely simple and in many instances the one-dimensional results can be used directly by changing the values of some of the nondimensional parameters appearing in the solution. We have not attempted in this study to evaluate the accuracy of the method but the results of Fig. 2 show a tremendous improvement over the one-dimensional analysis and an excellent agreement with the numerical solution of the two-dimensional problem.

In fact, a common feature of the integral methods, be it in viscous flow theory or in unsteady conduction, is that it is quite difficult to predict their accuracy in any general way. Although it is conceivable that higher order approximating polynomials may be used, it is not at all certain that these will improve the accuracy [2, 4]. A best polynomial has to be found for each type of problem and maybe even for the different types of boundary conditions. Many investigations on this point have been carried out in conjunction with the viscous boundary layer, and it is hoped that the same could take place for heat conduction.

The application of the method is by no means limited to the examples in the foregoing, a large number of other problems have been solved or are currently under study. Among those the temperature field in other types of extended surfaces, in moving slabs or rods and in three-dimensional bodies. The heat conduction field in some three-dimensional bodies can be reduced to that of the two-dimensional field by integrating the partial differential equation along one direction and thus make use of the large wealth of analytical solution which are available. The example of the rectangular parallelepiped is a straight forward case where, if one assumes some temperature polynomial function of z, writing the two boundary conditions on the surfaces of equal z and integrating we get a Laplace's equation in θ. This can be reduced into the Laplacian of the surface temperature which is then solved with the given boundary conditions giving a series solution as in [6].

Other areas of interest to which this method is being presently extended are nonhomogeneous bodies as well as bodies with variable thermal properties.

Acknowledgment

The author wishes to thank the Department of Mechanical Engineering of the Faculty of Engineering and Architecture, American University of Beirut, for supporting this study.

References

1 Goodman, T. R., "The Heat Balance Integral and Its Application to Problems Involving a Change of Phase," 1957 Heat Transfer and Fluid Mechanics Institute, Stanford University Press.

2 Goodman, T. R., "The Heat Balance Integral, Further Considerations and Refinements," JOURNAL OF HEAT TRANSFER, TRANS. ASME, Series C, Vol. 83, 1961, pp. 83–86.

3 Schlichting, H., *Boundary Layer Theory*, Sixth ed., McGraw Hill, New York, 1968, p. 144.

4 Langford, D., "The Heat Balance Integral Method," *International Journal of Heat and Mass Transfer*, Vol. 16, 1973, pp. 2424–2428.

5 Eckert, E. R. G., and Drake, R. M., *Heat and Mass Transfer*, Second ed., McGraw Hill, 1959, p. 44.

6 Chapman, A. J., *Heat Transfer*, Second ed., Macmillan, 1969, p. 79.

7 Lieblein, S., "Analysis of Temperature Distribution and Radiant Heat Transfer Among a Rectangular Fin of Uniform Thickness," N.A.S.A. TN D-196, 1959.

F. W. Schmidt
J. Szego

Mechanical Engineering Department,
The Pennsylvania State University,
University Park, Pa.

Transient Response of Solid Sensible Heat Thermal Storage Units—Single Fluid

The transient response of a solid sensible heat storage unit which receives or supplies heat to a single flowing fluid is presented. The storage unit is composed of a number of rectangular cross-sectional channels for the flowing fluid, connected in parallel and separated by the heat storage material. The energy equation for the fluid and the transient conduction equation for the storage material are solved using finite difference techniques. The parameters which characterize the transient behavior of these units are identified. Results suitable for the prediction of the rate of heat storage and the outlet temperature of the fluid leaving the storage unit are presented as functions of the identified nondimensional parameters.

1 Introduction

Energy management systems are being used by industrial and commercial establishments to reduce their overall energy consumption. Quite often many different sources and demands for energy exist and the overall energy consumption of the system can be reduced by the utilization of the waste heat from one or more processes as an energy source for others. Since the availability and the demand for the thermal energy may not coincide timewise, the flexibility of the energy utilization system can be greatly increased by the development of an efficient method for storing thermal energy.

There are many methods available for the storage of thermal energy. Some methods require the transformation of the thermal energy into other energy forms for storage purposes while others store the thermal energy directly. Examples of the first class of storage units include chemical systems, flywheels, batteries, compressed air, superconducting magnets, and underground pumped hydro systems. In direct thermal energy storage units the sensible heat of a liquid or a solid, the latent heat of fusion or evaporation, reversible chemical heat absorption, heat of hydration or heat of chemical change are used.

In order to predict the economic feasibility of energy systems containing thermal energy storage units the transient behavior of the units must be known. The performance and transient response of rotary periodic flow heat exchangers used for thermal energy storage have been the subject of several publications [1–5].[1] Willmott [6] utilized a finite difference technique for the determination of the thermal response of stationary regenerators where hot and cool gases were alternately passed through the unit in a periodic manner.

The need for efficient, low cost, and reliable energy storage systems for solar energy applications has been emphasized in the proceedings of the Workshop on Solar Energy Storage Subsystems for the Heating and Cooling of Buildings, held in 1975 [7]. The mathematical modeling of space and water heating storage systems was presented by Klein and is published in the proceedings. The transient response of a rock bed storage unit has been presented in the report of the Analytical Modeling Group of the Workshop by B. T. Rogers.

An analysis to determine the transient response of several different types of storage units was performed by Yang and Lee [8]. The exchange of energy between the heat storage material and the working fluid due to variations in the inlet temperature of the working fluid was studied. Griggs, et al. [9] reported on the transient response of a storage unit involving a change of phase material. The difficulty in rating the response of storage units has been of considerable concern and a method for testing and rating storage units has been presented by Kelly and Hill [10]. There are certain difficulties involved with the test procedures proposed and additional work will be required before a standardized rating system can be developed.

Although the aforementioned references deal to a degree with the prediction of the transient responses of heat storage units some rather severe assumptions have often been employed which greatly limit the usefulness of the results. In order to eliminate some of these ambiguities the transient response of a specific heat storage configuration composed of a number of rectangular cross-sectional channels for the flowing fluid connected in parallel and separated by the solid storage material has been determined. A sketch of the unit is shown in Fig. 1.

2 Analysis of the Response of the Storage Unit

For the purposes of this analysis, lines of symmetry are considered to exist at the midpoints of the storage material and flow channel.

[1] Numbers in brackets designate References at end of paper.

Contributed by the Heat Transfer Division for publication in the JOURNAL OF HEAT TRANSFER. Manuscript received by the Heat Transfer Division February 2, 1976. Paper No. 76-HT-XX.

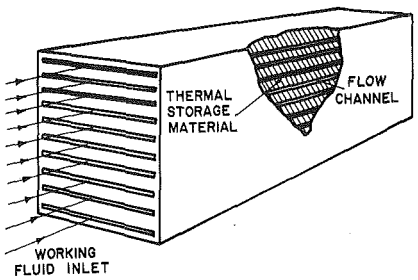

Fig. 1 Thermal storage unit

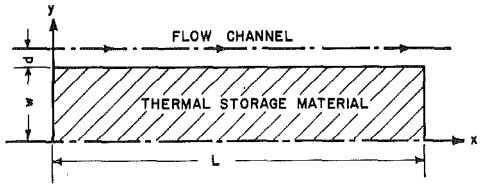

Fig. 2 Cross section of storage unit

These conditions would be present if the fluids were flowing at the same mass flow rate in parallel through the channels and if the unit was perfectly insulated from the surroundings. If the channels were used selectively, i.e., fluid flowing at different flow rates in adjacent channels or if different size channels were used, the analysis would apply if the midplanes of the storage material were perfectly insulated. The section to be analyzed is shown in Fig. 2. The following assumptions have been made:

(*a*) constant fluid and material properties;
(*b*) uniform heat transfer coefficient;
(*c*) step change in inlet fluid temperature;
(*d*) initial temperature distribution in the material is uniform;
(*e*) two-dimensional heat transfer in the storage material;
(*f*) constant fluid mean velocity.

The equations which govern the transient response of the storage unit are the one-dimensional conservation of energy equation for the moving fluid and the transient two-dimensional heat conduction equation for the storage material. The governing differential equations are:

$$\text{moving fluid:} \quad \rho CA\left[\frac{\partial t_f}{\partial \theta} + v\frac{\partial t_f}{\partial x}\right] = hP(t_w - t_f) \tag{1}$$

$$\text{and storage material:} \quad \frac{1}{\alpha}\frac{\partial t_m}{\partial \theta} = \frac{\partial^2 t_m}{\partial x^2} + \frac{\partial^2 t_m}{\partial y^2} \tag{2}$$

The initial and boundary conditions are:

$\theta = 0 \qquad t_f = t_m = t_0$

$\theta > 0 \quad x = 0 \quad t_f = t_{fi} \qquad \dfrac{\partial t_m}{\partial x} = 0 \quad \text{for} \quad 0 < y < w$

$x = L \qquad \dfrac{\partial t_m}{\partial x} = 0 \quad \text{for} \quad 0 < y < w$

$y = 0 \qquad \dfrac{\partial t_m}{\partial y} = 0 \quad \text{for} \quad 0 \le x \le L$

$y = w \qquad k\dfrac{\partial t_m}{\partial y} = -h(t_m - t_f) \quad \text{for} \quad 0 \le x \le L$

The following nondimensional groups are introduced:

$$X \equiv \frac{x}{w} \qquad Y \equiv \frac{y}{w}$$

$$V^+ \equiv \frac{w}{L} \qquad \text{Fo} \equiv \frac{\alpha\theta}{w^2}$$

$$\text{Bi} \equiv \frac{hw}{k} \qquad T \equiv \frac{t - t_0}{t_{fi} - t_0}$$

$$G^+ = \frac{Pk}{E} \text{ where } E = \dot{m}C = \rho_f v A C_f$$

The equation for the moving fluid becomes

$$\frac{\alpha}{wv}\frac{\partial T_f}{\partial \text{Fo}} + \frac{\partial T_f}{\partial X} + (G^+)(\text{Bi})(T_f - T_w) = 0 \tag{3}$$

The coefficient for $\partial T_f/\partial \text{Fo}$ can be expressed as

$$\frac{\alpha}{wv} = \left(\frac{\rho_f C_f}{\rho_m C_m}\right)\left(\frac{d}{L}\right)\left(\frac{G^+}{V^+}\right)$$

and may be used to determine if the heat capacity of the fluid may be neglected. This requires that the fluid and storage materials, channel width, length, fluid flow rate, and thickness of the storage unit be specified. Some general conclusions can be made using either water or air as the fluid, Feolite as the storage material and practical design dimensions and flow rates. The maximum practical values for the parameters are:

$\alpha = 0.0058$ cm^2/s for Feolite
$w_{\min} = 0.5$ cm
$v_{\min} = 30$ cm/s for water
$v_{\min} = 500$ cm/s for air

$$\frac{\alpha}{vw} = 4. \times 10^{-4} \quad \text{for water}$$

$$\frac{\alpha}{vw} = 2. \times 10^{-5} \quad \text{for air}$$

It can be concluded that the coefficient for $\partial T_f/\partial \text{Fo}$ is sufficiently small so that a negligible error is introduced in the analysis if the heat capacity of the fluid is neglected. This quantity α/wv can always be calculated for a given storage unit and an estimation of the error in-

Nomenclature

A = flow cross-sectional area
B = time transformed constant
C = specific heat at constant pressure
d = semichannel width
E = fluid heat capacity
h = convective film coefficient
k = thermal conductivity
L = length of heat storage unit
$\dot{m}$ = mass rate of flow
P = heated perimeter of flow channel
Q = total heat storage
t = temperature
$\bar{t}$ = mean temperature
V = volume of the storage material
v = fluid velocity
w = semithickness of the storage material
x = axial coordinate
y = transverse coordinate
α = thermal diffusivity of storage material
θ = time
θ_d = dwell time, L/v
λ = transformed time
ρ = density

Subscripts

f = moving fluid
fo = fluid outlet
fi = fluid inlet
o = initial condition
m = thermal storage material
w = wall in contact with fluid

troduced by neglecting the heat capacity of the fluid made.

The complete set of nondimensional equations neglecting the heat capacity of the fluid becomes:

$$\text{moving fluid:} \quad \frac{dT_f}{dX} + (G^+)(\text{Bi})(T_f - T_w) = 0 \tag{4}$$

$$\text{storage material:} \quad \frac{\partial^2 T_m}{\partial X^2} + \frac{\partial^2 T_m}{\partial Y^2} = \frac{\partial T_m}{\partial \text{Fo}} \tag{5}$$

with the initial condition:

$$\text{Fo} = 0 \qquad T_m = T_f = T_0$$

and the boundary conditions:

$$X = 0 \qquad T_f = 1 \qquad \frac{\partial T_m}{\partial X} = 0 \quad \text{for} \quad 0 < Y < 1$$

$$X = \frac{1}{V^+} \qquad \frac{\partial T_m}{\partial X} = 0 \quad \text{for} \quad 0 < Y < 1$$

$$Y = 1 \qquad \frac{\partial T_m}{\partial Y} = \text{Bi}(T_f - T_m) \quad \text{for} \quad 0 \le X \le \frac{1}{V^+} Y =$$

$$\text{Y} = 0 \qquad \frac{\partial T_m}{\partial Y} = 0 \quad \text{for} \quad 0 \le X \le \frac{1}{V^+}$$

These two equations (4) and (5) are solved simultaneously for the two dependent variables T_f and T_m. This is accomplished by the use of a numerical scheme described in the Appendix.

The rate of storage or removal of heat is determined in two different ways and comparison of the results obtained represents a check on the accuracy of the solution technique. The rate of heat storage can be evaluated using an overall energy balance for the system:

$$\frac{dQ}{d\theta} = E(t_{fi} - t_{fo}) \tag{6}$$

This equation placed in nondimensional form becomes:

$$\frac{dQ^*}{d\text{Fo}} = 1 - T_{fo} \tag{7}$$

where the nondimensional heat storage is defined as:

$$Q^* = \frac{\alpha Q}{Ew^2(t_{fi} - t_0)}$$

The heat storage can also be determined directly from the temperature distribution in the storage material, thus,

$Q = \rho CV(\bar{t} - t_0)$ and $\bar{t}$ is the mean temperature of the storage material. (8)

Using the previously defined definition of Q^*, equation (8) takes the following nondimensional form:

$$Q^* = \frac{G^+}{V^+} \bar{T} \tag{9}$$

The temperature distributions at times n and $n+1$, $\text{Fo}^{(n)}$ and $\text{Fo}^{(n-1)}$, can be calculated, thus allowing the average temperatures of the storage material and $Q^{*(n)}$ and $Q^{*(n-1)}$ to be determined using equation (9). A backward difference approximation can be used to determine $dQ^*/d\text{Fo}$,

$$\frac{dQ^*}{d\text{Fo}} = \frac{Q^{*(n)} - Q^{*(n-1)}}{\text{Fo}^{(n)} - \text{Fo}^{(n-1)}}$$

This value was compared with the value $dQ^*/d\text{Fo}$ obtained from equation (7) and a variation of less than 3 percent was found for the results presented in this paper. The largest differences were encountered during the latter stages of the heat storage when a relatively small amount of heat was being stored. The total energy balance of the unit was considered to be within acceptable accuracy.

3 Discussion of Results

In this study the fluid inlet temperature was held at a constant value, thus, the final or steady-state temperature distribution in the storage material was uniform having the value of the temperature of the entering fluid. The maximum amount of heat which can be stored by the unit can be easily determined.

If the flow rate of the fluid is very large, $G^+ \to 0$, the temperature of the fluid as it passes through the unit will remain constant and the heat transfer to the storage material is one-dimensional. Exact solutions for the total heat stored in the one-dimensional configuration have been presented in Gröber, et al. [11]. This solution is important since it represents a limiting case for the thermal storage units under consideration.

As the Bi number approaches zero, the temperature gradients within the material approach zero and a lumped parameter analysis can be used for the determination of the transient response of the fluid leaving the unit. The solution to this limiting case has been presented by London, et al. [12]. The nondimensional variables used are related to those used in this paper by the following expressions:

$$\text{NTU} = \left[\frac{\text{Bi}}{1 + \text{Bi}}\right]\frac{G^+}{V^+}, \quad C_w^* = \frac{G^+}{V^+}\frac{1}{\text{Fo}}\frac{\theta}{\theta_d}, \quad \epsilon_f^* = T_{fo}$$

$$\theta^* = \frac{\theta}{\theta_d} \quad \text{and} \quad \frac{\theta^* - 1}{C_w^*} = \frac{\text{Fo}\, V^+}{G^+}\left[1 - \frac{\theta_d}{\theta}\right]$$

where θ_d is the dwell time.

A comparison of these results with those presented in this paper indicates excellent agreement when the parameters are selected so that the internal temperature gradients in the y-direction are negligible, Bi <0.01 and at large values of θ/θ_d.

An analysis of the computer outputs indicated that the results for both the nondimensional fluid outlet temperature and the percentage of the maximum heat stored can be expressed in terms of Fo, Bi, and G^+/V^+ in the range of these variables studied. The grouping of G^+ and V^+ together in the presentation of the results is possible since the effect of axial conduction on the values of the dependent variables in the cases investigated is less than 3 percent. The errors are much less than 3 percent during the initial stages of storage when the potential for heat transfer by convection to the storage material is the greatest.

The nondimensional fluid outlet temperatures obtained in the study are presented in Figs. 3–9. The Biot number was varied from 0.03 and 30. As the Biot number increases, the transient response curves converge and, thus, the curves for a Biot number of 30 can be used for the calculation of the response of units with larger Biot numbers without introducing appreciable errors. It is felt that nearly all the practical flow conditions encountered in storage units using either a gas or liquid are covered in this range of Biot numbers. The ranges of the parameter G^+/V^+ covered depended on the Biot number. At the lower Biot number, 0.03, the value of G^+/V^+ varied from 2 to 200. For values of G^+/V^+ less than 2 the decrease in the nondimensional fluid outlet temperature was very small and approached the asymoptic value of one very quickly. At the higher Biot number, 30, the value of G^+/V^+ varied from 0.02 to 2.

The heat stored or removed from the unit may be determined using

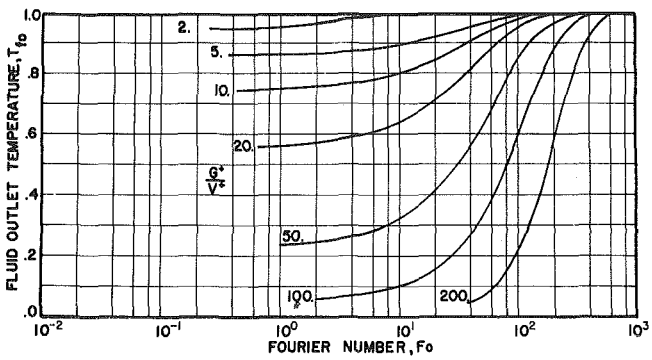

Fig. 3 Nondimensional fluid outlet temperature, Biot number = 0.03

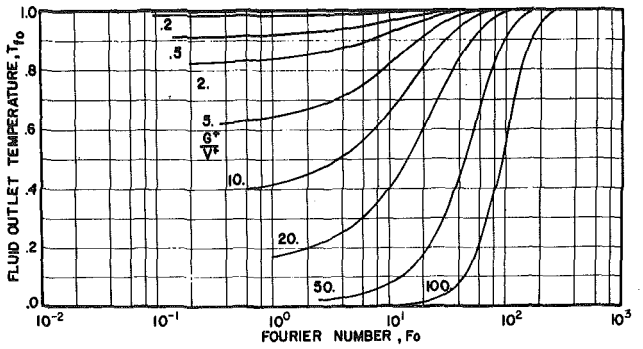

Fig. 4 Nondimensional fluid outlet temperature, Biot number = 0.1

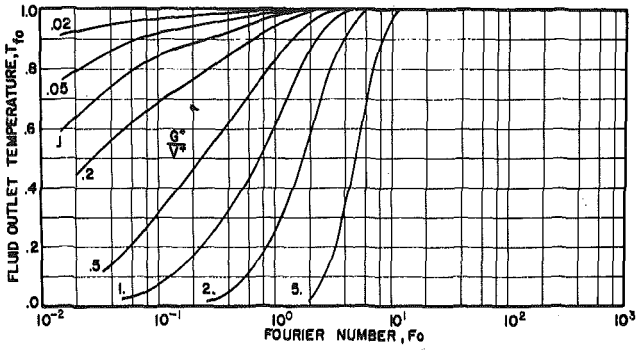

Fig. 8 Nondimensional fluid outlet temperature, Biot number = 10

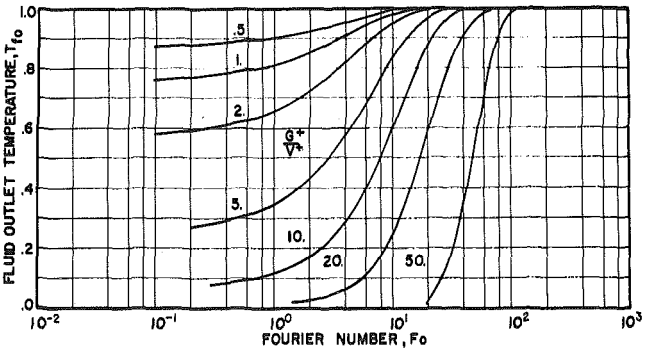

Fig. 5 Nondimensional fluid outlet temperature, Biot number = 0.3

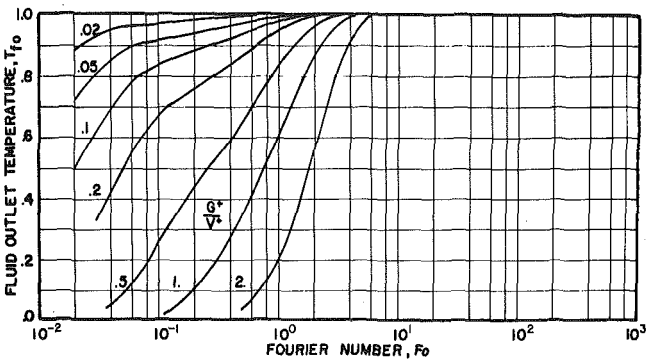

Fig. 9 Nondimensional fluid outlet temperature, Biot number = 30

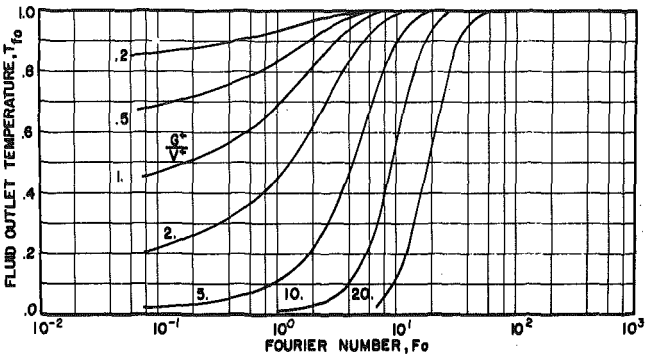

Fig. 6 Nondimensional fluid outlet temperature, Biot number = 1

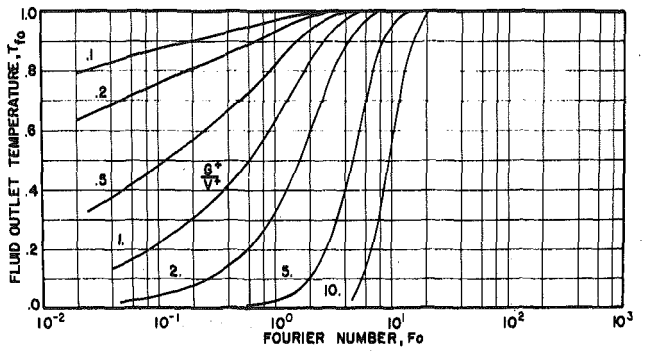

Fig. 7 Nondimensional fluid outlet temperature, Biot number = 3

the results presented in Figs. 10–14. These five curves indicate the values of the Fo number required to achieve 20, 40, 60, 80, and 95 percent of the maximum possible heat storage. The range of the Biot number investigated is from 10^{-3} to 10^{3} while G^+/V^+ varied from 0.0 to 100. If the product (G^+/V^+) Bi is less or equal to 0.05, the exact solution presented in Gröber [11] is a good approximation in the calculation of the heat storage. For large values of the Biot number the curves reach asymptotic values. This can be interpreted as the situation when conduction through the storage material becomes the limiting process. At the other extreme for small values of the Biot number, convection becomes the limiting process and as the fluid outlet temperature approaches that of the inlet, the exact solution, $G^+/V^+ = 0.0$, is approached.

The solutions presented in this paper do not account for the events that take place from the instant the fluid is allowed to flow in the unit to the moment the first particles of the fluid leave the unit. Typically this time interval is of an order of magnitude smaller than the characteristic time scale of the process, but care must be taken when results for small times are required.

The set of curves presented can be used to determine the transient response of a particular heat storage unit. In the determination of the amount of heat added or removed from storage, insignificant errors are introduced if in the use of Figs. 10–14 for a fixed Biot number, linear interpolation is used for G^+/V^+. When determining the fluid outlet temperature using Figs. 3–9 linear interpolation is initially used for G^+/V^+ and then for Bi. The results obtained using this procedure are quite accurate over the entire ranges of the independent variables presented. The response of the heat storage unit, with the characteristics and operating conditions listed in Table 1, has been calculated using these procedures and is presented in Fig. 15. The solid lines represent the solution obtained using the complete computer program. It is observed that excellent agreement was obtained using the described interpolation methods.

A computer program has been developed to perform the interpo-

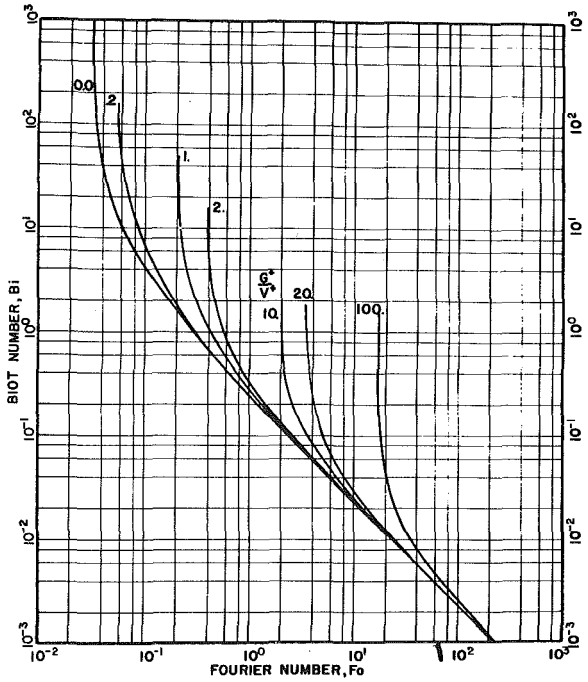

Fig. 10 Twenty percent heat storage

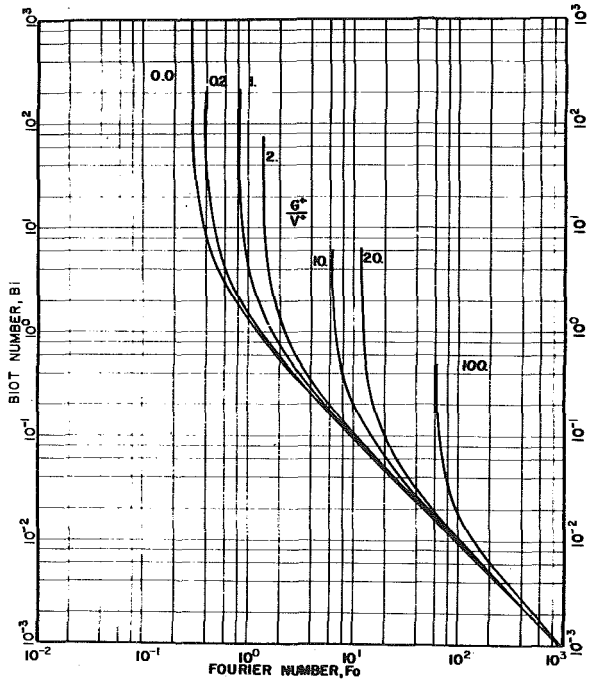

Fig. 12 Sixty percent heat storage

lation described in the previous paragraph. The program may be obtained from the Mechanical Engineering Department, The Pennsylvania State University, University Park, Pa. 16802 at a nominal cost to cover handling. The availability of the program will be guaranteed until December 31, 1978.

Acknowledgments

The authors wish to acknowledge that this work was performed under NSF-RANN Grant AER 75-16216.

References

1 Lambertson, T. J., "Performance Factors of a Periodic Flow Heat Exchanger," TRANS. ASME, Vol. 80, 1958, p. 586.

2 Bahnke, G. D., and Howard, C. P., "The Effect of Longitudinal Heat Conduction of Periodic Flow Heat Exchanger Performance," *Journal of Engineering for Power,* TRANS. ASME, Series A, Vol. 86, 1964, p. 105.

3 Mondt, J. R., Jr., "Vehicular Gas Turbine Periodic Flow Heat Exchanger Solid and Fluid Temperature Distributions," *Journal of Engineering for Power,* TRANS. ASME, Series A, Vol. 86, 1964, p. 121.

4 Paschkis, V., and Hlinka, J. W., "Electrical Analog Studies of the

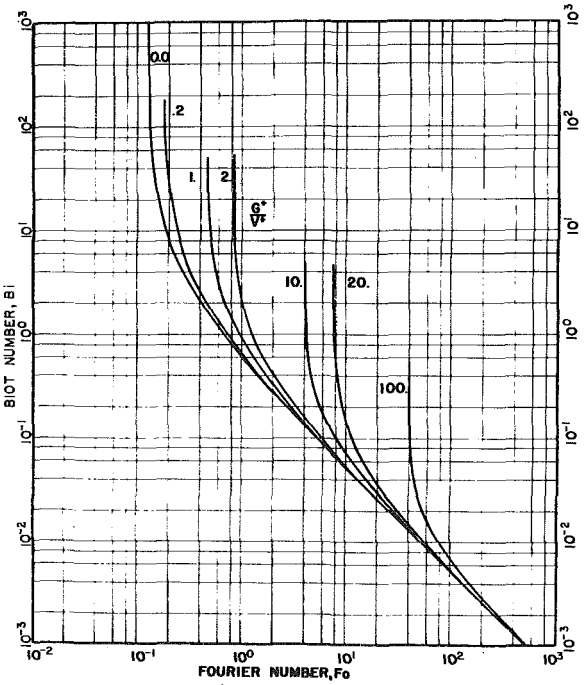

Fig. 11 Forty percent heat storage

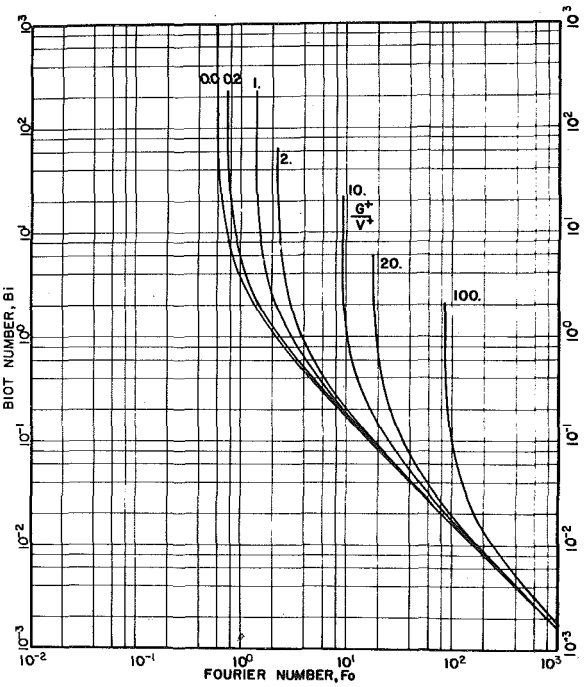

Fig. 13 Eighty percent heat storage

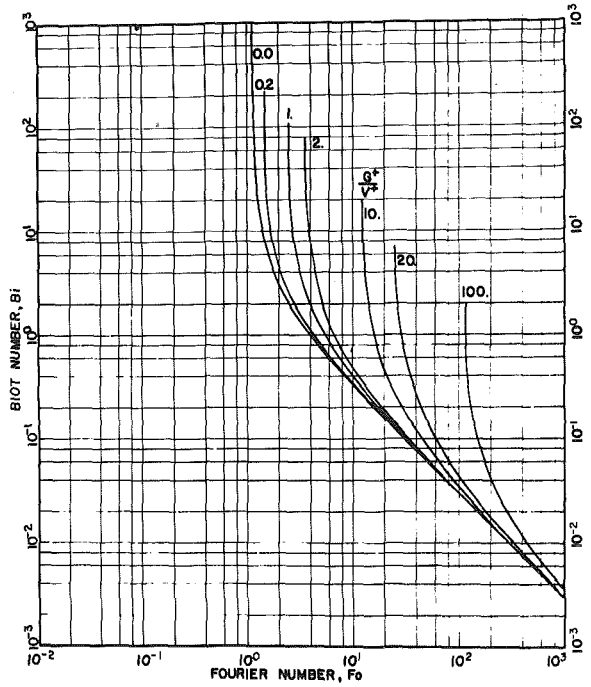

Fig. 14 Ninety-five percent heat storage

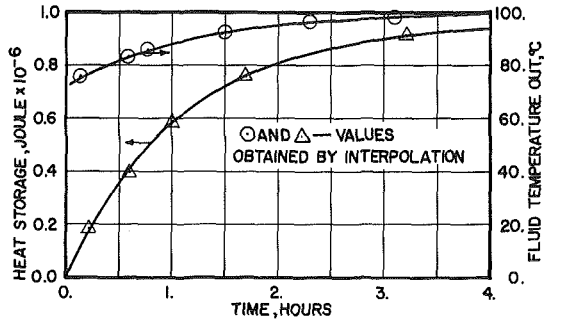

Fig. 15 Response of heat storage unit

Table 1 Example of calculations procedure

Dimensions	
Length (L)	195 cm
Semi-thickness (w)	4 cm
Channel width (d)	0.95 cm
Width	43 cm
Storage Material: Feolite	
Conductivity	0.021 W/cm-°C
Density	3.9 g/cm^3
Specific Heat	0.92 J/g-°C
Diffusivity	0.0058 cm^2/sec
Working Fluid: Air (at mean temperature of 60°C)	
Density	0.00106 g/cm^3
Specific Heat	1.01 J/g-°C
Conductivity	2.88 x 10^{-4} W/cm-°C
Kinematic Viscosity	0.1888 cm^2/sec
Operating Conditions	
Air Speed	2000 cm/sec
Air Inlet Temperature	100°C
Initial Temperature	20°C
Maximum Heat Storage	9.6 x 10^6 J

Heat Transfer Coefficient

$Re_D = 3.86 \times 10^4$ where D is the hydraulic diameter of the channel

$Nu_L = 0.029\, Re_L^{0.8} \left(\frac{L}{D}\right)^{0.08}$ (reference 13)

$h = 6.61 \times 10^{-3}$ W/cm^2-°C

Dimensionless Parameters

$V^+ = 0.0205$

$G^+ = 0.0107$

$G^+/V^+ = 0.525$

$Bi = 1.26$

Transient Behavior of Heat Exchangers," *Trans. N.Y. Acad. Sci.*, Series II, Vol. 19, 1957, p. 714.

5 London, A. L., Lampsell, D. F., and McGowan, J. G., "The Transient Response of Gas Turbine Plant Heat Exchangers—Additional Solutions for Regenerators of the Periodic Flow and Direct Transfer Types," *Journal of Engineering for Power*, TRANS. ASME, Series A, Vol. 86, 1964, p. 127.

6 Willmott, A. J., "Digital Computer Simulation of a Thermal Regenerator," *International Journal of Heat and Mass Transfer*, Vol. 7, 1964, p. 1291.

7 Lilleleht, L. U., Beard, J. T., and Iachetta, F. A., *Proceedings of the Workshop on Solar Energy Storage Subsystems for the Heating and Cooling of Buildings*, NSF-RA-N-75-041, American Society of Heating, Refrigeration and Air Conditioning Engineers, Inc., N. Y., 1975.

8 Yang, W. J., and Lee, C. P., "Dynamic Response of Solar Heat Storage Systems, ASME Paper No. 74-WA/HT-22, 1974.

9 Griggs, E. I., Pitts, D. R., and Humphries, W. R., "Transient Analysis of a Thermal Storage Unit Involving a Phase Change Material," ASME Paper No. 74-WA/HT-21, 1974.

10 Kelly, G. E., and Hill, J. E., "Method of Testing for Rating Thermal Storage Devices Based on Thermal Performance," NBS Report NBSIR 74-634, 1975.

11 Gröber, H., Erk, S., and Grigull, U., *Fundamentals of Heat Transfer*, McGraw Hill, New York, 1961, pp. 50–52.

12 London, A. L., Biancardi, F. R., and Mitchell, J. W., "The Transient Response of Gas Turbine-Plant Heat Exchangers-Regenerators, Intercoolers, Precoolers, and Ducting," *Journal of Engineering for Power*, TRANS. ASME, Series A, Vol. 81, 1959, p. 433.

13 Legkiy, V. M., and Makarov, A. S., "Heat Transfer in the Thermal Entry Region of Circular Pipes and Rectangular Ducts With Stabilized Turbulent Flow of Air," *Heat Transfer —Soviet Research*, Vol. 3, No. 6, 1971.

14 Forsythe, G. E., "Generation and Use of Orthogonal Polynomials for Data-Fitting With a Digital-Computer," *J. Soc. Indust. Appl. Math.*, Vol. 5, No. 2, 1957, p. 74.

APPENDIX

Outline of the Numerical Solution

The set of two equations, equations (4) and (5), were solved simultaneously for the dependent variables T_f and T_m. The dimensionless heat storage Q^* was computed from the temperature distribution in the storage material. The thermal storage material was subdivided into six columns of nodes in the axial direction and four rows of nodes in the transverse direction. Initially a larger number of nodes was used but it was verified that using a finer grid configuration did not change substantially the accuracy of the results. Equation (5) was then rewritten in finite difference form for each of the 24 nodes. Prior to forming the difference equations a transformed time domain, λ, was introduced:

$$\lambda \equiv 1 - e^{-B\mathrm{Fo}} \tag{A-1}$$

where B is a constant parameter. The differential equation for the storage material thus becomes:

$$\frac{\partial^2 T_m}{\partial X^2} + \frac{\partial^2 T_m}{\partial Y^2} = B(1-\lambda)\frac{\partial T_m}{\partial \lambda} \tag{A-2}$$

The rationale for the use of the transformation is that the complete transient range must be covered by the solution. In order to keep discretization errors within reasonable limits, small steps in real time are required at the beginning of the process while the step size can be increased as steady state is approached. With the time domain transformation, equal spacing in λ will yield the desired conditions. A constant value of 100 steps ($\Delta\lambda = 0.01$) was selected as the maximum number of steps in λ to reach steady state. Consequently the values of the parameter B were adjusted to obtain nearly steady-state conditions at the ninety-seventh step.

A backward difference method was used to approximate $\partial T_m/\partial\lambda$ while a central difference method was used for the approximation of the spatial derivatives.

Equations (4) and (5) are coupled, therefore, the computational

procedure involved an iterative scheme at each value of λ. At a particular value of λ corresponding to step n ($\lambda = n\Delta\lambda$), the temperature distribution in the moving fluid T_f is known and T_m at step $n + 1$ is initially approximated using that temperature distribution. An orthogonal polynomial of third order is fitted through the wall temperature T_w using the least squares method proposed by Forsythe [14]. Substitution of this polynomial in equation (4) yields a first order differential equation which is solved exactly and a new temperature distribution T_f is obtained. The finite difference solution is recalculated using this new fluid temperature distribution and the iterative process is repeated until convergence is obtained i.e., the maximum change in T_m is less than 10^{-7} and in T_f is less than 10^{-4}. The solution then proceeds to step $n + 2$. The foregoing convergence criteria was shown to give good results at reasonable computational times.

The reported curves summarize the results of over one hundred runs, hence, keeping computational times within reasonable limits was a major concern. Backward differences were used in order to avoid instabilities due to the uneven time-step sizes. They result in an implicit set of difference equations being formed where the number of equations is equal to the number of nodal points. Since an iterative solution is used because of the coupling of the temperatures of the fluid and storage material, no additional inconvenience is created in the computational procedure. The use of orthogonal polynomial fitting enables the differential equation for the fluid to be solved exactly with a few algebraic operations and thus serves to minimizing computational time. A more sophisticated function or a higher degree polynomial could have been used but it was judged to be an unnecessary refinement.

R. W. Lewis
B. R. Bass

Civil Engineering Department,
University College of Swansea,
Wales

The Determination of Stresses and Temperatures in Cooling Bodies by Finite Elements

This paper presents a finite element method for solving non-linear heat conduction and thermal stress problems. The nonlinearity is caused by the variation of thermo-physical and mechanical properties of the material with respect to temperature. The distribution of temperature and stress in a cooling body can be followed from the onset of solidification. The method is capable of handling complex geometries and initial non-linear boundary conditions.

Introduction

The application of the finite element method to heat conduction analysis has found particular relevance in both the linear and nonlinear regimes. In this paper we present a solution for the nonlinear heat conduction problem and for the thermal stresses and deformations resulting from a phase change.

Analytical formulations of such problems have been proposed by Kaump [1][1] and Weiner, et al. [2], but these find little application in real engineering situations due to the inherent complexity of geometry and boundary conditions. Also, as far as the authors are aware, no significant work has been published on stress development near the phase change. In this paper the finite element model of the temperature distribution and thermal stress development during solidification assumes that the thermo-physical and mechanical properties of the material are dependent on the level of temperature.

In the general formulation, latent heat effects are not included separately as these can be approximated to a very high degree of accuracy by rapid variations of heat capacity within a narrow temperature range. For certain substances the phase change occurs within a wide band of temperatures, and, thus, a physically realistic approximation can be easily dealt with computationally. For other materials the phase change takes place with almost no temperature variation, and a heat capacity (ρc) versus temperature (T) curve resembling a Dirac function must be used. In the latter case, it is convenient to define a new variable H (enthalpy), as an integral of the ρc-T curve and then estimate, for each element, average heat capacity values based on well-known enthalpy properties. This way a critical class of nonlinear problems can be dealt with as demonstrated by Comini, et al. [3]. Here, the temperature distribution analysis is also based on the formulation proposed by Comini, et al. [3] but incorporates the additional feature of isoparametric elements [4]. This enables us to solve problems with many fewer elements, therefore, reducing the quantity of input data required. A comparison is shown between a problem solved with linear triangular elements and also with parabolic isoparametric elements.

The nonlinearity in the thermal stress analysis is due to the dependency of both the constitutive matrix **D** and the coefficient of thermal expansion α on the temperature. This nonlinearity is handled in both the thermo-physical and mechanical properties by assuming a piece-wise linear relationship within a small temperature range ΔT_n. The thermo-physical or the mechanical property at any temperature can then be interpolated within this range.

Finite Element Formulation of the Heat Conduction Problem

Any heating or cooling process of a body in a planar domain Ω, is governed by the quasilinear parabolic equation

$$\rho c \frac{\partial T}{\partial \tau} = \frac{\partial}{\partial x}\left(k_x \frac{\partial T}{\partial x}\right) + \frac{\partial}{\partial y}\left(k_y \frac{\partial T}{\partial y}\right) + Q \tag{1}$$

The body may be subject to the following boundary conditions:

(a) Fixed boundary conditions

$$T = T_c(x,y) \text{ on } \Gamma_1 \tag{2a}$$

(b) Prescribed external heat flux q on Γ_2

(c) Heat flow across the boundary due to convection q_c, and radiation q_r, on Γ_3. The relationships are given as follows:

$$q_c = \alpha_c(T - T_{acb}), \quad q_r = \alpha_r(T - T_{ar}) \tag{2b,c}$$

[1] Number in brackets designate References at end of paper.

Contributed by the Heat Transfer Division for publication in the JOURNAL OF HEAT TRANSFER. Manuscript received by the Heat Transfer Division January 12, 1976. Paper No. 76-HT-YY.

where α_c is the convective heat transfer coefficient which is temperature-dependent if natural convection is considered, T_{ac} and T_{ar} are the equilibrium temperatures for which there is no convection or radiation, respectively, and α_r is defined as

$$\alpha_r = \epsilon\sigma(T^2 + T_{ar}{}^2)(T + T_{ar}) \tag{2d}$$

where ϵ is the emissivity and σ is the Stefan-Boltzmann constant.

Let the unknown temperature T at any point (x,y), and time τ be approximated by

$$\bar{T} = \sum_{i=1}^{n} N_i(x,y)T_i(\tau) = \mathbf{NT} \tag{3}$$

where N_i are the shape functions, and T_i are the nodal temperatures of an element. Using Galerkin weighting functions and Green's theorem, equation (1) becomes in matrix form

$$\mathbf{KT} + \mathbf{C}\dot{\mathbf{T}} + \mathbf{F} = \mathbf{0} \tag{4}$$

The elements of the matrix are

$$K_{ij} = \Sigma \int_{\Omega^e} \left(k_x \frac{\partial N_i}{\partial x}\frac{\partial N_j}{\partial x} + k_y \frac{\partial N_i}{\partial y}\frac{\partial N_j}{\partial y} \right) d\Omega + \Sigma \int_{\Gamma_3{}^e} (\alpha_c + \alpha_r) N_i N_j d\Gamma$$

$$C_{ij} = \Sigma \int_{\Omega^e} \rho c N_i N_j d\Omega \tag{5}$$

$$F_i = -\Sigma \int_{\Omega^e} N_i Q d\Omega + \Sigma \int_{\Gamma_2{}^e} N_i q d\Gamma - \Sigma \int_{\Gamma_3{}^e} N_i(\alpha_c T_{ac} + \alpha_r T_{ar}) d\Gamma$$

In the foregoing, the thermo-physical properties k, ρc, Q, and the coefficient α_r are temperature-dependent.

The set of ordinary differential equations (4) which defines the discretized problem can be solved using many different types of time integration schemes. As these equations are nonlinear, an unconditionally stable, three level scheme used by Comini, et al. [3] is employed here. This recurrence formula for integration is as follows:

$$\mathbf{T}_{\tau+\Delta\tau} = -\left(\mathbf{K}_\tau + \frac{3}{2\Delta\tau}\mathbf{C}_\tau\right)^{-1}\left(\mathbf{K}_\tau\mathbf{T}_\tau + \mathbf{K}_\tau\mathbf{T}_{\tau-\Delta\tau} - \frac{3}{2\Delta\tau}\mathbf{C}_\tau\mathbf{T}_{\tau-\Delta\tau} + 3\mathbf{F}_\tau\right) \tag{6}$$

The central values of the matrices **K, C,** and **F** are taken, and hence the time marching can be continued without recourse to iterative techniques. This algorithm has been shown [3] to be stable and convergent in the context of finite elements.

Some Special Features of the Numerical Model

The matrices **K, C,** and **F** are time-dependent because of the variation of coefficients with temperature, and a completely new solution has to be obtained at each stage. The evaluation of temperature-dependent quantities in the integrals [4, 5] requires special care, particularly if a rather coarse mesh is employed and spatial variation of the quantities is abrupt. Numerical integration has to be adopted and therefore heat capacity, thermal conductivity, and rate of internal heat generation must be estimated at integrating points in Ω^e. A direct evaluation will lead to satisfactory numerical integrations only if the ρc, k, and Q versus temperature curves do not present sharp peaks in the range of interest. If, instead, a "true" melting or freezing process is considered, difficulties are likely to arise.

In fact, when the temperature approaches the phase change temperature, the equivalent heat capacity tends to a Dirac δ function and cannot be satisfactorily represented across the peak by any smooth function. Such extreme problems can be successfully tackled by the technique proposed by Comini, et al. [3], where a more appropriate averaging process was employed.

The approach is a physical one and is based on the observation that the integral of heat capacity with respect to temperature (enthalpy)

$$H = \int_{To}^{T} \rho c dT \tag{7}$$

is a smooth function of temperature even in the phase change zone. Therefore, it is reasonable to interpolate the enthalpy, rather than the heat capacity directly, writing the relationship

$$\bar{H} = \sum_{i=1}^{n} N_i(x,y,z)H_i(\tau) = \mathbf{NH} \tag{8}$$

where again N_i are the shape functions and H_i are the enthalpy values at nodal points. Since by definition we have

$$\rho c = dH/dT \tag{9}$$

the values of heat capacity at the integrating points can be approximated by determining the gradient of enthalpy with respect to temperature, i.e.,

$$\langle \rho c \rangle_{x,y,z} \cong \frac{1}{3}\left(\frac{\partial H}{\partial x}\Big/\frac{\partial T}{\partial x} + \frac{\partial H}{\partial y}\Big/\frac{\partial T}{\partial y} + \frac{\partial H}{\partial z}\Big/\frac{\partial T}{\partial z}\right) \tag{10}$$

This averaging process gives representative values of heat capacity and preserves a correct heat balance by avoiding the possibility of missing peak values of the quantity ρc. Similar techniques are used in the program for the best determination of K and Q values.

A second special feature of the calculation involves an algorithm for a correct estimate of the radiation coefficient α_r. Since α_r is a cubic function of T and the temperature is assumed to vary linearly with time, it can be easily verified that the expression

$$\begin{aligned}\langle \alpha_r \rangle &= \frac{1}{2\Delta\tau}\int_{\tau-\Delta\tau}^{\tau+\Delta\tau} \epsilon\sigma(T^2 + T_{ar}{}^2)(T + T_{ar})d\tau \\ &\cong \epsilon\sigma\Big\{ [T(\tau)^2 + T_{ar}(\tau)^2][T(\tau) + T_{ar}(\tau)] \\ &+ \frac{1}{4}[T_{ar}(\tau+\Delta\tau) - T_{ar}(\tau-\Delta\tau)]^2[T_{ar}(\tau) + T(\tau) - \frac{2}{3}T(\tau-\Delta\tau)] \\ &+ \frac{1}{3}[T_{ar}(\tau+\Delta\tau) - T_{ar}(\tau-\Delta\tau)][T(\tau) - T(\tau-\Delta\tau)][T(\tau-\Delta\tau) \\ &+ T_{ar}(\tau-\Delta\tau)] + [T(\tau) - T(\tau-\Delta\tau)]^2 \\ &\times \left[T(\tau) + \frac{1}{2}T_{ar}(\tau+\Delta\tau) - \frac{1}{6}T_{ar}(\tau-\Delta\tau) \right] \Big\}\end{aligned} \tag{11}$$

which still involves only known values of temperatures, is a much better approximation to the time average value of α_r, in the interval from $\tau - \Delta\tau$ to $\tau + \Delta\tau$, than the direct calculation of α_r at time τ.

Finite Element Formulation for Thermal Stresses

The constitutive law for the stress-strain behavior is as defined by Duhamel-Newmann [5], which is valid for isotropic, elastic materials in a Cartesian coordinate system:

$$\sigma_{ij} = 2\mu\{\epsilon_{ij} + [\nu/(1-2\nu)]\epsilon_{kk}\delta_{ij} - [(1+\nu)/(1-2\nu)]\alpha T\delta_{ij}\} \tag{12}$$

where σ_{ij} is the stress tensor, ϵ_{ij} is the strain tensor, ν is the Poisson's ratio, μ is the shear modulus, α is the coefficient of thermal expansion, and δ_{ij} is the Kronecker delta. The strain tensor is defined as

$$\epsilon_{ij} = \frac{1}{2}(u_{i,j} + u_{j,i}), \quad i = 1,2, \quad j = 1,2 \tag{13}$$

The constitutive law can be expressed in matrix form as follows:

$$\boldsymbol{\sigma} = \mathbf{D}\boldsymbol{\epsilon} - \mathbf{D}\boldsymbol{\alpha}T \tag{14}$$

where **D** is the tangential mechanical property matrix, T is the temperature, α is the coefficient of linear expansion matrix defined by

$$\boldsymbol{\alpha} = \alpha\mathbf{e}, \quad \mathbf{e}^T = (1101) \tag{15a,b}$$

and ϵ is the strain matrix given by

$$\epsilon = \begin{bmatrix} \frac{\partial u}{\partial x} & 0 \\ 0 & \frac{\partial v}{\partial y} \\ \frac{\partial u}{\partial y} & \frac{\partial v}{\partial x} \end{bmatrix} \tag{15c}$$

If we consider a system in the domain Ω to be in equilibrium then

$$\sigma_{ji,j} + f_i - \rho\ddot{u}_i = 0 \tag{16}$$

where $\ddot{u}_i$ is the acceleration, ρ is the density, and f_i is the body force.

Using the principle of virtual work and ignoring inertia effects, we obtain the following:

$$\underbrace{\left[\int_\Omega (\mathbf{L}\delta\mathbf{u})^T \sigma d\Omega - \int_\Omega \delta\mathbf{u}^T \mathbf{f} d\Omega\right]}_{\text{Internal Virtual Work}} - \underbrace{\left[\int_\Gamma \delta\mathbf{u}^T \mathbf{t} d\Gamma\right]}_{\text{External Virtual Work}} = 0 \tag{17}$$

where Γ is the bounding surface of the domain Ω, $\delta\mathbf{u}$ is the virtual displacement, and virtual strains are defined as

$$\delta\epsilon = \mathbf{L}\delta\mathbf{u} \tag{18}$$

The linear operator $\mathbf{L}$ is as follows:

$$\mathbf{L} = \begin{bmatrix} \frac{\partial}{\partial x} & 0 \\ 0 & \frac{\partial}{\partial y} \\ \frac{\partial}{\partial y} & \frac{\partial}{\partial x} \end{bmatrix} \tag{19}$$

Let the unknown displacement $\mathbf{u}$ be approximated throughout the domain by the relationship

$$\hat{\mathbf{u}} = \mathbf{N}\mathbf{u} \tag{20a}$$

and in incremental form

$$\delta\hat{\mathbf{u}} = \mathbf{N}\delta\mathbf{u} \tag{20b}$$

On substituting equation (20b) into equation (17), we obtain

$$\int_\Omega (\mathbf{L}\mathbf{N}\delta\mathbf{u})^T \sigma d\Omega - \int_\Omega (\mathbf{N}\delta\mathbf{u})^T f - \int_{\Gamma_t} (\mathbf{N}\delta\mathbf{u})^T \mathbf{t} d\Gamma = 0 \tag{21}$$

Let

$$\mathbf{B} = \mathbf{L}\mathbf{N} \tag{22}$$

and substituting this expression into equation (21) we obtain the incremental form, i.e.,

$$\delta\mathbf{u}^T \left(\int_\Omega \mathbf{B}^T \sigma d\Omega - \int_\Omega \mathbf{N}^T \mathbf{f} d\Omega - \int_\Gamma \mathbf{N}^T \mathbf{t} d\Gamma\right) = 0 \tag{23}$$

This equation is, therefore, valid for any form of displacement.

Substituting equation (14) into (23),

$$\left(\int_\Omega \mathbf{B}^t \mathbf{D}\mathbf{B} d\Omega\right)\mathbf{u} - \left(\int_\Omega \mathbf{B}^T \mathbf{D}\alpha\mathbf{N} d\Omega\right)\mathbf{T} - \left(\int_\Omega \mathbf{N}^T \mathbf{f} d\Omega\right) - \left(\int_{\Gamma_t} \mathbf{N}^T \mathbf{t} d\Gamma\right) = 0 \tag{24}$$

On discretization, the above equation can be written as

$$\mathbf{K}\mathbf{u} + \mathbf{F} = \mathbf{0} \tag{25}$$

where the matrix elements are given by

$$\mathbf{K} = \Sigma \left(\int_{\Omega^e} \mathbf{B}^T \mathbf{D}\mathbf{B} d\Omega\right) \tag{26a}$$

$$\mathbf{F} = -\Sigma \left(\int_{\Omega^e} \mathbf{B}^T \mathbf{D}\alpha\mathbf{N} d\Omega\mathbf{T} + \int_{\Omega^e} \mathbf{N}^T \mathbf{f} d\Omega + \int_{\Gamma_t} \mathbf{N}^T \mathbf{t} d\Gamma\right) \tag{26b}$$

For the case of thermal loading only,

$$\mathbf{F} = -\Sigma \left(\int_{\Omega^e} \mathbf{B}^T \mathbf{D}\alpha\mathbf{N} d\Omega\right)\mathbf{T} \tag{26c}$$

At any time τ, the transient temperature T, the coefficient of linear expansion vector α, the strain vector ϵ, the tangential mechanical property matrix $\mathbf{D}$, and the stress vector σ are known and are defined as follows:

$$\mathrm{T} = \mathrm{T}(\tau),\ \alpha = \alpha(\tau),\ \mathbf{D} = \mathbf{D}(\tau),\ \epsilon = \epsilon(\tau),\ \sigma = \sigma(\tau) \tag{27}$$

Hence, the temperature-dependent constitutive law in thermal stress analysis involves a time variable.

Let us assume that at any time τ

$$\alpha(T) = \alpha(\tau),\ \mathbf{D}(T) = \mathbf{D}(\tau),\ \epsilon(T) = \epsilon(\tau),\ \sigma(T) = \sigma(\tau) \tag{28}$$

On substituting equation sets (27) into the constitutive equation (14), and differentiating with respect to time, we obtain the following:

$$\dot{\sigma}(\tau) = \dot{\mathbf{D}}(\tau)\epsilon(\tau) + \mathbf{D}\dot{\epsilon}(\tau) - \dot{\mathbf{R}}(\tau)T(\tau) - \mathbf{R}(\tau)\dot{T}(\tau) \tag{29}$$

where

$$\mathbf{R} = \mathbf{D}\alpha$$

If we neglect the rate of change of material properties with respect to time, i.e., the thermo-viscoelastic effects, then

$$\dot{\mathbf{D}}(\tau) = \dot{\mathbf{R}}(\tau) = 0 \tag{30}$$

and

$$\dot{\sigma}(\tau) = \mathbf{D}(\tau)\dot{\epsilon}(\tau) - \mathbf{R}(\tau)\dot{T}(\tau) \tag{31}$$

Thus, at any instant the stresses are given by

$$\sigma(\tau) = \int_{\tau_o}^{\tau} \mathbf{D}(\tau) \frac{d}{d\tau} [\epsilon(\tau) - \gamma(\tau)] d\tau \tag{32}$$

where the thermal strain rate vector is defined as

$$\dot{\gamma}(\tau) = \alpha(\tau)\dot{T}(\tau) \tag{33}$$

Integrating by parts we obtain

$$\sigma(\tau) = [\mathbf{D}(\tau)\{\epsilon(\tau) - \gamma(\tau)\}]_{\tau_o}^{\tau} - \int_{\tau_o}^{\tau} \dot{\mathbf{D}}(\tau)[\epsilon(\tau) - \gamma(\tau)] d\tau \tag{34}$$

Assuming that there are no initial strains at time τ_o, then

$$\epsilon(\tau_o) = \gamma(\tau_o) = 0 \tag{35}$$

Hence, the equation (34) becomes

$$\sigma(\tau) = \mathbf{D}(\tau)[\epsilon(\tau) - \gamma(\tau)] - \int_{\tau_o}^{\tau} \dot{\mathbf{D}}(\tau)[\epsilon(\tau) - \gamma(\tau)] d\tau \tag{36}$$

Integrating equation (33) by parts we obtain

$$\gamma(\tau) = \alpha(\tau)T(\tau) - \int_{\tau_o}^{\tau} \dot{\alpha}(\tau)T(\tau) d\tau \tag{37}$$

According to the assumptions made previously (equation 30), equation (36) becomes

$$\sigma(\tau) = \mathbf{D}(\tau)[\epsilon(\tau) - \alpha(\tau)T(\tau)] \tag{38}$$

It should be noted that this analysis has been restricted to the variation of thermo-physical and mechanical properties with respect to temperature. The effects of visco-elasticity, creep, and thermo-plasticity will be the subject of future research work in this field.

Illustrative Examples

Three examples have been solved to illustrate the applications of the finite element formulation given previously. In the analysis of

these problems, parabolic isoparametric elements have been used.

Example 1—Frost and Frost Heave of an Embankment. In areas that are susceptible to ground freezing, frost and frost heave are serious foundation engineering problems. It is necessary in this case to investigate the depth which is affected by frost and the effect of frost heave before any structure is erected or underground pipes are laid.

The thermo-physical and mechanical properties of soil are known to depend on the relative proportions of water, ice, air, and soil particles present per unit volume and also in the temperature variation. The following relationships have been used to calculate these values for the different types of soil conditions analyzed.

(*a*) *Thermal Capacity of Soil.*

(i) For frozen soil,

$$\rho c = \hat{\gamma}_d(c_s + c_i\omega) \tag{39}$$

(ii) For partially frozen soil,

$$\rho c = \hat{\gamma}_d[c_s + \{c_i + (c_w + c_i)W\}\omega] \tag{40}$$

(iii) For unfrozen soil,

$$\rho c = \hat{\gamma}_d(c_s + c_w\omega) \tag{41}$$

where

$\hat{\gamma}_d$ = dry density of soil
c_s = specific heat of soil
c_i = specific heat of ice
c_w = specific heat of water
ω = water content of soil

W = ratio of the weight of unfrozen water to the total weight of water (frozen plus unfrozen) in soil.

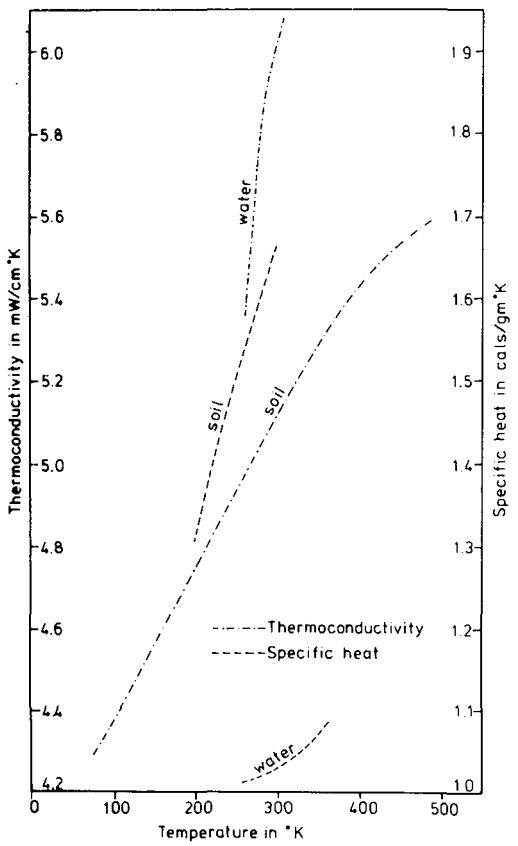

Fig. 1 Variation of thermoconductivity and specific heat with temperature

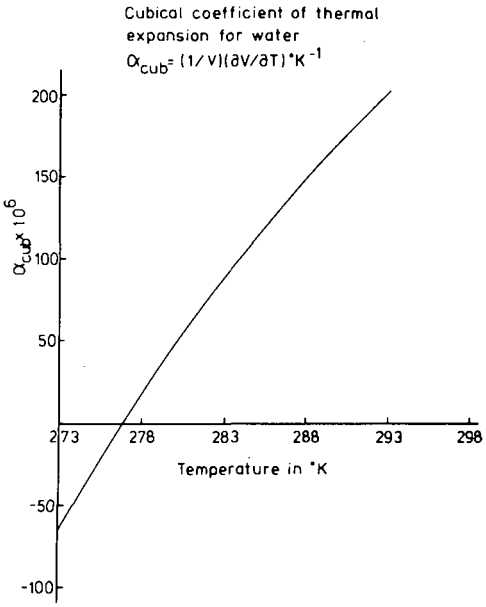

Fig. 2 Variation of coefficient of thermal expansion of water in the liquid phase with respect to temperature

(*b*) *The Volumetric Latent Heat of Fusion in Soil.* This is defined by the following relationship:

$$L = \hat{\gamma}_d\omega(1 - W)L_w \tag{42}$$

where L = volumetric latent heat of soil and L_w = latent heat of fusion of water.

(*c*) *Thermal Conductivity.*

(i) For frozen soil,

$$k = \hat{\gamma}_d(k_s + k_i\omega)/\hat{\gamma}_b = (k_s + k_i\omega)/(1 + \omega) \tag{43}$$

(ii) For partially frozen soil,

$$k = [k_s + \{k_i + (k_w - k_i)W\}\omega]/(1 + \omega) \tag{44}$$

(iii) For unfrozen soil,

$$k = (k_s + k_w)/(1 + \omega) \tag{45}$$

where

k_s = thermal conductivity of dry soil
k_i = thermal conductivity of ice
k_w = thermal conductivity of water
$\hat{\gamma}_b$ = bulk density of soil.

(*d*) *Coefficient of Thermal Expansion.* This is defined by the relation

$$\alpha = \omega\alpha_w \tag{46}$$

where α_w = coefficient of thermal expansion of water.

(*e*) *Modulus of Elasticity.* The modulus of elasticity is assumed to be a function of the coefficient of thermal expansion of water and of the temperature. The empirical formula by Cherepin, et al. [6] is used which results in the following expansion for the coefficient of elastic modulus:

$$\mathrm{E} = \frac{dE}{dT}\frac{1}{E}, \quad \mathrm{E} \cong 4 \times 10^{-4}\alpha$$

The variation of thermoconductivity and specific heat with temperature is shown in Fig. 1. The corresponding curve for the cubical thermal expansion of water in the liquid phase is given in Fig. 2, the cubical coefficient being approximately three times the linear coefficient. The linear thermal expansion coefficient for ice is approxi-

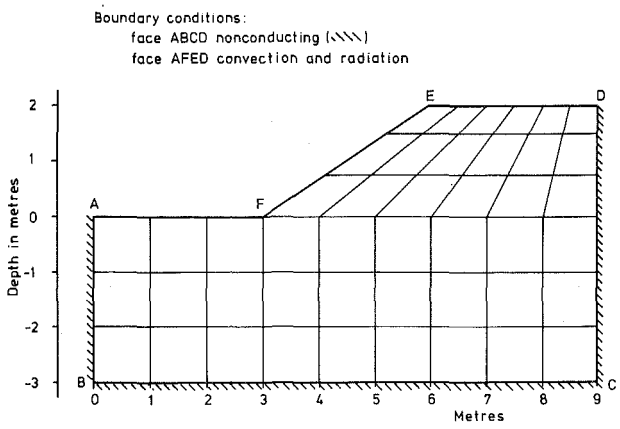

Fig. 3 Finite element mesh for embankment analysis

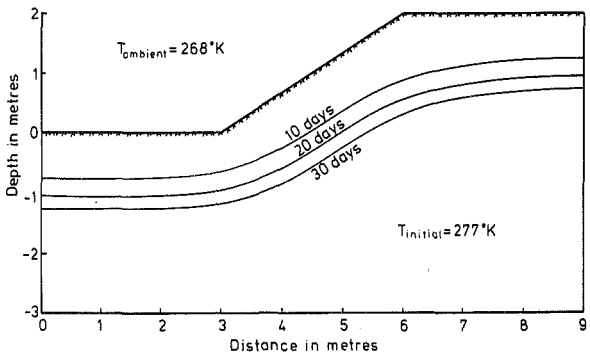

Fig. 4 Movement of the freezing front with time

mately 51 × 10^{-6} K^{-1} in the range 268–273 K. The volumetric expansion of water in transition from the liquid to the solid phase at 273 K is equivalent to a specific volume change of .0907.

An embankment of dimensions as shown in Fig. 3 was analyzed for movement of the freezing zone with time for the boundary conditions shown. The coefficient of heat transfer by convection is 1.728 × 10^6 J/m^2 day K, the emissivity is 0.08, and the Stefan-Boltzmann constant is 4.9051 × 10^{-3} J/m^2 day K. It was assumed that during freezing there was no water movement in the soil: therefore, the degree of water saturation remained constant and uniform.

As can be seen in Fig. 4, the rate of penetration of the front decreases with time. According to Schnitter and Zobrist [7], the frost penetration in soil is given by

$$x = 416\beta \sqrt{\frac{k_\chi FI}{L}} \tag{47}$$

where

FI = freezing index of air multiplied by the number of days
k = thermoconductivity of soil
L = latent heat of fusion of soil
χ = constant $0 < \chi < 1.0$
β = constant for a particular type of soil.

Let us assume that the freezing index is given by

$$FI = n\tau^m$$

where n is a constant and τ is the time in days. Thus, equation (47) can be written as

$$x = \theta\tau^n \tag{48}$$

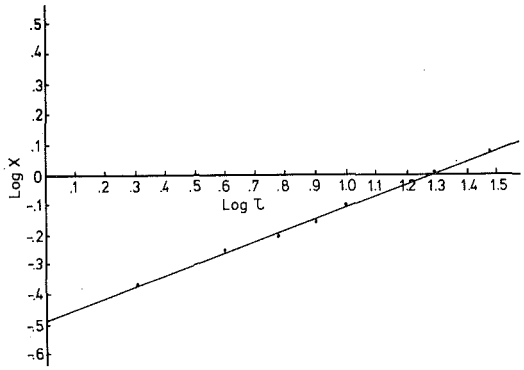

Fig. 5 The progress of the freezing front through the embanKment: logarithm of the depth versus logarithm of the time

where

$$\theta = 416\beta \sqrt{\frac{k\chi n}{L}} \text{ for a particular type of soil}$$

and

$$n = \frac{1}{2}m$$

The logarithm of the depth x, as shown in Fig. 5, against the logarithm of time τ, shows an approximate linear relation

$$\log x = \log \theta + n \log \tau$$

It was found that the value of n is approximately 0.48, and from the experimental work by Schnitter and Zobrist, n is approximately equal to 0.5.

In the determination of frost heave, the following assumptions were made in addition to those already stated;

(i) The soil is homogeneous and isotropic.

(ii) The coefficient of thermal expansion of the soil particles is negligible compared to that of water.

(iii) The change in specific volume of water from the liquid to the solid phase is assumed to take place over the finite temperature internal 273 K ± 0.20.

(iv) The embankment is weightless.

(v) The modulus of elasticity at 273 K is 31.5 N/m^2.

In Fig. 6, which depicts conditions at time τ equal to 30 days, it can be seen that the frost heave is uniform, relative to the original profile. This arises because the effect of lens growth, which will form ice zones in the embankment and cause unequal expansion, has been neglected.

Also illustrated in Fig. 6 are the contours of maximum shearing stress in the frost region. The frost heave and stress field depicted near the embankment surface at τ equal to 30 days are tending to steady-state conditions.

Example 2—Ground Freezing. This problem is of particular relevance in the Civil Engineering industry where a mass of unstable soil is to be excavated. When it is not possible to stabilize such a mass of soil by conventional drainage techniques, than resort has to be made to more sophisticated techniques such as ground freezing. In this instance, cooling pipes are inserted into the soil with the coolant being recirculated and maintained at a constant temperature. The growth of the freezing zone is allowed to develop until the complete volume to be excavated has been frozen.

The example demonstrated here was first solved by Comini, et al. [3] using triangular elements. These elements utilized linear shape functions and, hence, a large number were required for a satisfactory solution (Fig. 7(a)). The same problem was resolved using the higher order isoparametric elements available in the latest program (Fig. 7(b)). As may be seen, the number of elements required for the same degree of accuracy is of an order of magnitude lower. Thus, the saving in input data etc. is considerable. The results are shown in (Fig. 7(c))

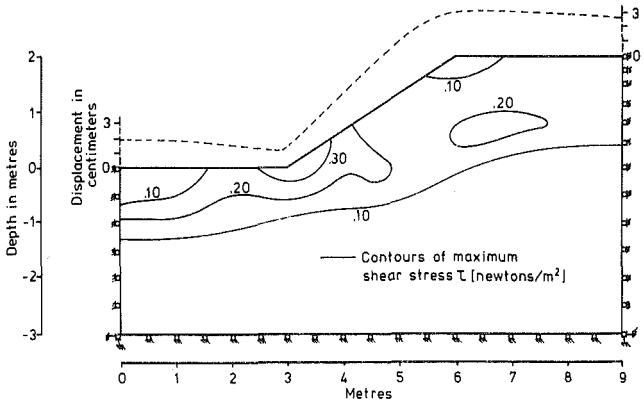

Fig. 6 Surface displacement and maximum shear stress contours in embankment

and demonstrate the progression of the freezing front with time. The thermo-physical properties used in this example are identical with the values used by Comini, et al. [3].

Example 3—Stress Distribution in a Solidifying Bar. This example has been solved using finite differences by Allen and Severn [8] for the time taken for the bar to solidify. Their result showed close agreement with Jones' [9] curve, given by the following equation:

$$\tau = \frac{\rho c}{k}\frac{(x-\ell)^2}{1.07} \tag{49}$$

where

τ = time taken by the cooling front to reach a point $(\ell - x)$
k = thermal conductivity
ρc = heat capacity
ℓ = length of the bar.

The thermo-physical and mechanical properties used are specified in dimensionless terms as follows:

$k = 1.0$, thermal conductivity
$\rho c = \sqrt{2}$, heat capacity
$L = 70.26\ \rho c$, volumetric latent heat of fusion
T_i = initial temperature
$T_c = 0°$ temperature causing solidification on surface AA in Fig. 8
$E = 1.0$, modulus of elasticity
$\mu = 0.38$, shear modulus
$\nu = 0.3$, Poisson's ratio
$\alpha = 1.0 \times 10^{-6}$, coefficient of linear thermal expansion.

The results obtained by Allen and Severn [8], using their finite difference relaxation technique, compared very favourably with the curve as given by Jones for the same problem. The finite element results given here (Fig. 8) also compare well with Jones' curve, but the rate of cooling is faster as the cooling front progresses along the bar.

The finite element program was also used for determining the influence of the cooling rate on the development of the stress level within the bar. The end AA of the bar is assumed to become solid at $\tau = 0$ and can therefore be taken as being rigidly fixed. The time variation of the stress along the bar, expressed with respect to the maximum stress $\sigma_{x_{max}}$ is also shown in Fig. 8(b) for three different values of time τ. This value of relative stress during solidification indicates the gradual increase in the value of residual stresses that could be expected as the cooling front progresses towards the other end of the bar. The authors are not aware of any other solutions against which their finite element model could be compared.

Conclusions

A finite element program has been presented which can deal with

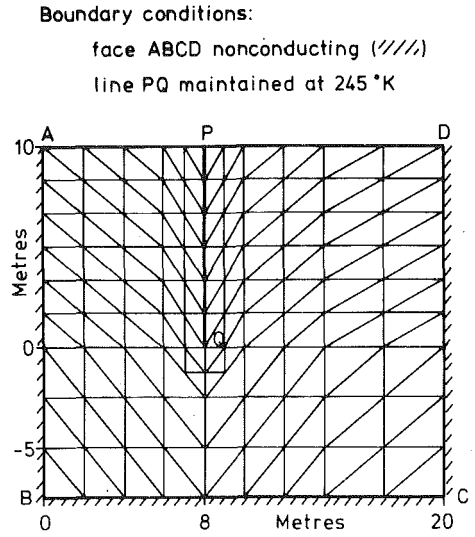

Fig. 7(a) Finite element mesh used by Comini, et al.

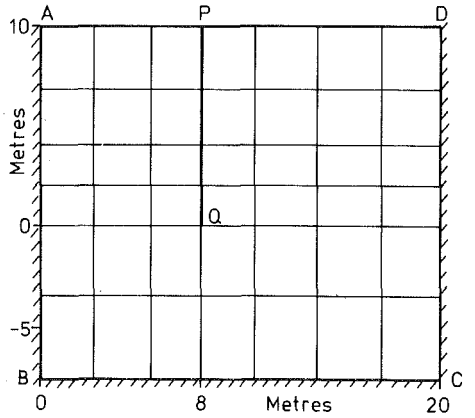

Fig. 7(b) Finite element mesh used in resolving the example

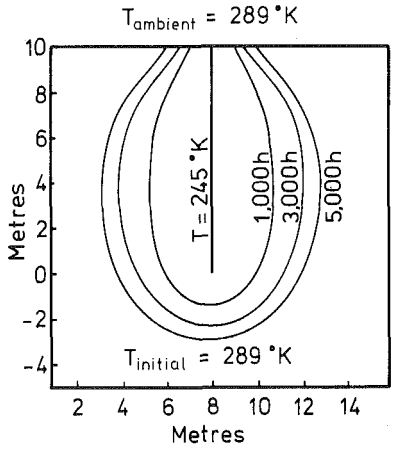

Fig. 7(c) Freezing front positions with respect to time. The freezing sheath PQ is maintained at 245 K. The ambient temperature is 289 K and the convective heat transfer $\alpha_c = 20$ W/m²K. The thermal conductivity and heat capacity for frozen soil, $k = 2.32$ W/mK, $\rho c = 2.04 \times 10^6$ J/m³K; for the unfrozen soil, $k = 1.65$ W/mK, $\rho c = 2.815 \times 10^6$ J/m³K; the volumetric latent heat of fusion, $L = 120 \times 10^6$ J/m³.

Fig. 7 Freezing of a moist soil (sand)

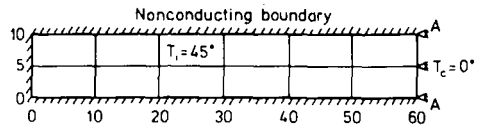

Fig. 8 8(*a*) Finite element mesh for solidification of a bar

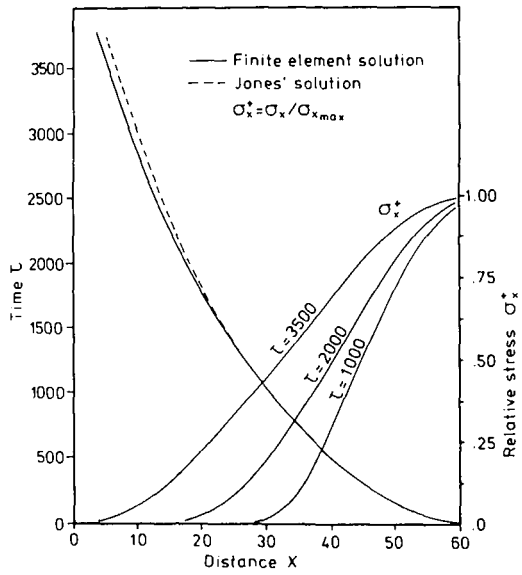

8(*b*) The progress of the freezing Front and thermal stress in the bar

nonlinear heat conduction both above and below the phase change. Also, an elastic stress routine has been linked with the heat conduction program to determine the residual stresses left in the body upon cooling. In the case of the temperature problems, comparisons were made with previously published results and were found to give favourable answers. In the case of the residual stress calculations, comparisons could not be made as the authors were unaware of any previous work.

The program utilizes isoparametric elements and can deal with irregularly-shaped boundaries and nonlinear boundary conditions.

References

1 Tien, R., and Kaump, V., "Thermal Stresses During Solidification on Basis of Elastic Model," TRANS. ASME, series E, Vol. 36 1969, pp. 763–767.

2 Weiner, J. H., and Boley, B. A., "Elasto-Plastic Thermal Stresses in a Solidifying Body," *J. Mech. & Physics of Solid.*, Vol. II, 1963, pp. 145–154.

3 Comini, C., Det Guidice, S., Lewis, R. W., and Zienkiewicz, O. C., "Finite Element Solution of Non-Linear Heat Conduction Problems With Special Reference to Phase Change," *International Journal for Num. Methods in Engineering.*, Vol. 8, 1974, pp. 613–624.

4 Zienkiewicz, O. C., *The Finite Element Method in Engineering Science*, Second ed., McGraw-Hill, London, 1971.

5 Fung, Y. C., *Foundation of Solid Mechanics*, Prentice-Hall, New York, 1969.

6 Cherepin, V. T., and Mellik, A. K., Experimental Techniques in Physical Metallurgy, *Asia Publishing House*, 1966.

7 Schnitter, G., and Zobrist, R., "Freezing Index and Frost Penetration in Switzerland," *Proc. 5th Int. Conf. Soil Mech. Found. Engng.* Vol. 2, 1961 pp. 315–320.

8 Allen, N. De G., and Severn, R. T., "The Application of Relaxation Methods to the Solution of Non-Elliptical Partial Differential Equation–II. The Solidification of Liquids," *Quart. J. Mech. and App. Maths.*, Vol. 5, 1952, pp. 447–454.

9 Jones, H., Unpublished, Ministry of Supply Report.

H. N. Fisher

Staff Member, Group Q-23,
Los Alamos Scientific Laboratory,
University of California,
Los Alamos, N. Mex.

Thermal Analysis of Some Subterrene Penetrators

Various types of rock melting drills have been designed at Los Alamos. These have included density consolidating penetrators up to 90 mm in diameter of varying configurations. A number of these consolidators have been tested in loams, alluvium, and tuff. Extruders up to 87 mm in diameter designed for an improved advance rate have been used in alluvium and basalt. The results of thermal analyses of some of these existing penetrators under conditions of constant advance rate in tuff, alluvium, and basalt are presented. The basic finite element heat conduction code (AYER) used in the calculations is briefly reviewed along with the methods of including radiation, temperature dependent material properties, and power generation. The internal temperature distribution, power requirements, and possible advance rates are determined for various consolidating and extruding penetrators. The effects of rock properties, penetrator configuration, and thermal limitations on the advance rate are considered. Heater designs and the use of heat pipes in specific designs are discussed. A comparison with experimental test data is made where possible.

Introduction

The factors affecting the performance of rock melting drills have been discussed in a number of publications [1–6].[1] In particular, the hydrodynamics of the molten layer of rock surrounding the hot penetrator is considered in detail in [7, 8]. The present paper is concerned with the detailed thermal analysis of four specific designs, two have been tested extensively and two are proposed designs. Of the two tested, one is a consolidator and one an extruder. A consolidator must form a glass liner that is denser than the unmelted rock and is of sufficient thickness to accommodate all material melted in the formation of the hole. An extruder is provided with a debris removal system and can operate in a rock with a density equal to or greater than that of its glass. The debris in the form of molten rock is extruded from the heated penetrator tip through a nozzle that is generally located on axis of the penetrator. All of the penetrators considered here are axially symmetric.

Fig. 1(*a*) is a schematic of a 51 mm dia consolidator. The outer surface of the molybdenum body is a parabola with a length of 125 mm. This penetrator has a cylindrical pyrolytic graphite heater that is electrically insulated from the body by a helium filled gap. A graphite radiation receptor fits tightly against the molybdenum. This penetrator has been extensively tested in tuff and various alluvia at velocities up to 0.25 mm/s. Fig. 2(*a*) is a schematic of the extruder considered here. This penetrator has been tested in basalt at velocities up to ~0.23 mm/s and in basaltic alluvium at velocities to 0.10 mm/s. Figs. 3(*a*) and 4(*a*) are proposed consolidators. The 90 mm dia conical penetrator with the pyrographite heater was originally designed for use in a basaltic alluvium. The heat pipe design was used to illustrate the configuration of a high velocity consolidator and to establish requirements on the heat pipe performance.

The thermal analysis has several uses. The most important of which is determination of a heater and body configuration that meet the following requirements:

1 The material temperatures do not exceed those permitted by stress or material compatibility limitation.

2 The axial distribution of power generation in the heater is such that the inside of the refractory metal body is at a nearly uniform temperature. These requirements must be met for the expected range of rock properties and velocities and do not rely on an accurate knowledge of the properties of any given rock sample or on a detailed treatment of the melt flow. The thermal analysis also provides temperature distribution for stress calculations and penetrator surface temperatures for the melt fluid dynamics codes. A priori predictions of velocities require accurate knowledge of the materials properties of the rock or soil in question and coupling with the melt fluid dynamics code which relates surface temperature and thrust to velocity. However, if the thermal analysis is correlated with test data, limited predictions of the performance of other similar penetrators in the same material can be made.

Method of Analysis

All of the calculations presented in this paper were done with the AYER [9] heat conduction code. AYER is a finite element computer

[1] Numbers in brackets designate References at end of paper.

Contributed by the Heat Transfer Division and presented at the Winter Annual Meeting, Houston, Texas, November 30–December 5, 1975, of THE AMERICAN SOCIETY OF MECHANICAL ENGINEERS. Revised manuscript received by the Heat Transfer Division, April 29, 1976. Paper No. 75-WA/HT-69.

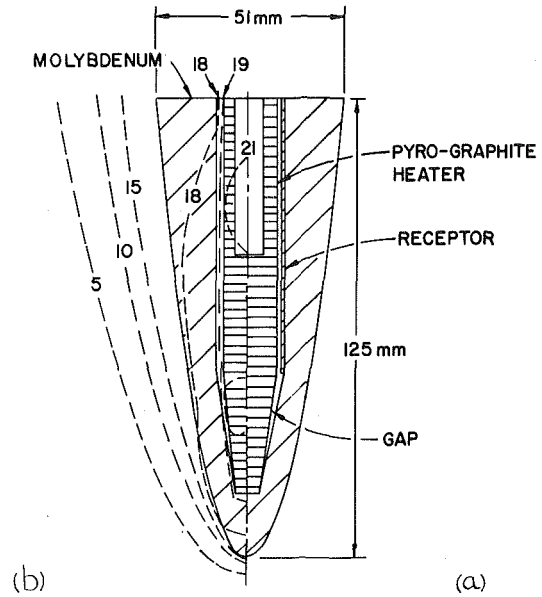

Fig. 1 (*a*) Parabolic consolidating penetrator; (*b*) temperature distribution in K × 10^{-2}

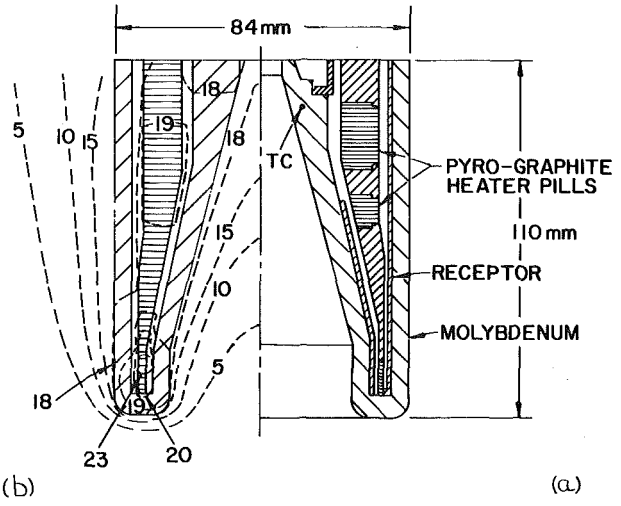

Fig. 2 (*a*) Extruding penetrator; (*b*) temperature distribution in K × 10^{-2}

program for solving the general two-dimensional equation of thermal conduction. Material properties can be time and temperature dependent, thermal conductivities can have two-dimensional anisotropy, and material velocity distributions are allowed. The integral form of the heat conduction equation

$$\int_S \left(-\lambda \frac{\partial T}{\partial \vec{n}}\right) dS = \int_V Q_g \, dV - \int_V \rho C \frac{\partial T}{\partial t} dV - \int_V \rho C \, \vec{v} \cdot \nabla T \, dV \quad (1)$$

is written for each finite volume element, boundary conditions are added and the resulting couple equations are solved iteratively for the temperatures. All other specifications of power generation, grid geometry, material properties and boundary conditions must be provided through subroutines programmed by the user. The axisymmetric penetrators, melt layer, and a sufficient amount of the surrounding rock were represented by a grid of between 700 and 1000 elements generated by a mesh generator appropriate to penetrator geometries.

The penetrator material densities, thermal conductivities, specific heats, and emissivities were either temperature dependent or appropriate constants. The gaps providing electrical insulations of the heaters from the penetrator body were filled with helium. In addition to the helium thermal conductivity, a temperature dependent radiation contribution was used as described in the following.

Power generation in the pyrolytic portions of the heater was calculated from the temperature dependent resistivity [10] of Fig. 5 and the specified current. In some problems the heater current was iterated automatically in the program to produce a power that gave a specified temperature (1450 K) along the rock-melt interface. The current was also adjusted for each problem to insure that the maximum material temperatures were not exceeded.

The exterior boundary of the grid was held at 300 K. Each grid was checked to insure that sufficient rock was included so that the position of the boundary did not effect the results. The boundary where the rock and melt leave the grid was adiabatic. The temperature gradients are generally perpendicular to this boundary and the conduction loss is negligible compared to the energy carried out of the grid by the moving rock. The steady-state velocity of the penetrator was accounted for by a constant velocity field in the solid rock. Because of the dependence of rock melt viscosity on temperature, the melt velocity is a function of radial position across the melt layer. In this analysis an average melt velocity was calculated from the melt layer geometry and the conservation of mass at each axial station of the grid. The position of the rock-melt interface (distinguished by a discontinuity in density and velocity) was adjusted in each problem to coincide with the isotherm in the center of the melting range.

The rock properties are those of basalt. The specific heat was constant except for a temperature dependent term that accounted for the latent heat of fusion.

$$C = C_0 + \left(\frac{H}{1.772\, T_R}\right) \exp\left(-\left(\frac{T - T_m}{T_R}\right)^2\right) \quad (2)$$

The integral over the second term is the latent heat of fusion L, and T_m and T_R define the center and half-width of the melting range.

The thermal conductivity of basalt was derived from the data of [11] by the removal of the radiation contribution. The melt layers are fairly thin ($\lesssim$1 mm) at the leading edge. The radiation contribution was replaced by an upper limit appropriate to thin transparent dielectrics. For a plane gap filled with a nonabsorbing dielectric bounded by a penetrator of emissivity ϵ_s and unmelted rock of emissivity ϵ_m the maximum flux of [12]

Nomenclature

C = specific heat
c = velocity of light
F = radiation flux
H = latent heat of fusion
K_R = equivalent of thermal conductivity for radiation
L = frequency average mean free path
n = index of refraction
Q_g = power generation per unit volume
S = finite element surface area
T = temperature
T_R = melting range of rock
V = finite element volume
$\vec{v}$ = rock or melt velocity
v^* = penetrator velocity
δ = melt layer thickness
ϵ = emissivity
λ = thermal conductivity
ρ = density
σ = Stefan-Boltzmann constant

Subscripts

i = unmelted rock
ℓ = liquid rock
m = at melt-rock interface
s = at surface of penetrator

$$F = E\, n^2 \sigma (T_s^4 - T_m^4) \tag{3}$$

where

$$E = \frac{\epsilon_s \epsilon_m}{\epsilon_s + \epsilon_m - \epsilon_s \epsilon_m}$$

the factor n^2 in equation (3) arises from the fact that the density of photon states in a dielectric is proportional to n^3 and the velocity is c/n; any flux then is proportional to n^2 [12]. Writing equation (3) in terms of radiation thermal conductivity gives

$$F = K_R \left(\frac{T_s - T_m}{\delta} \right) \tag{4}$$

where

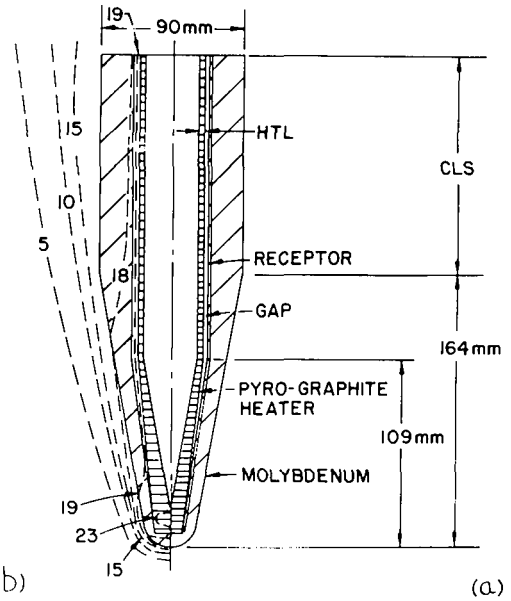

Fig. 3 (*a*) Conical consolidating penetrator; (*b*) temperature distribution in K × 10^{-2}

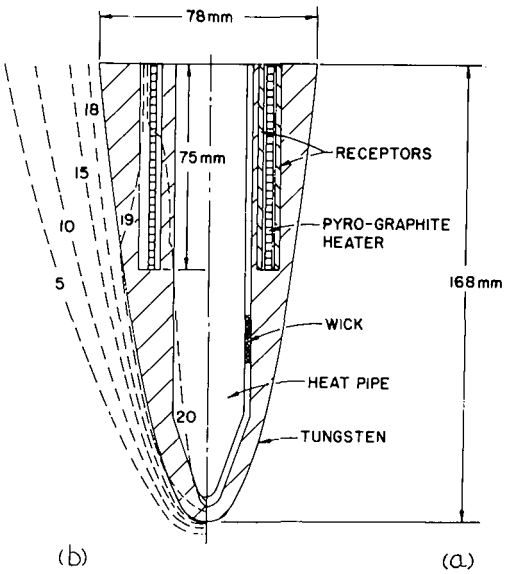

Fig. 4 (*a*) Parabolic consolidator utilizing a heat pipe; (*b*) temperature distribution in K × 10^{-2}

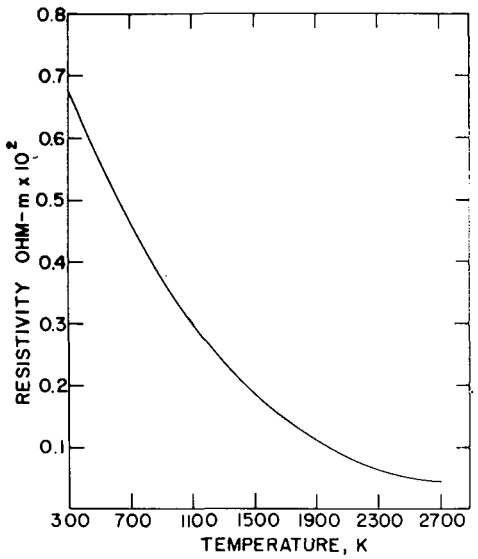

Fig. 5 Resistivity of pyrolytic graphite across the grain

$$K_R = En^2 \sigma \left(\frac{T_s^4 - T_m^4}{T_s - T_m} \right) \delta \tag{5}$$

Over a narrow range of operating temperatures, a convenient approximation to the flux can be written. Then

$$\frac{T_s^4 - T_m^4}{\delta} = \frac{dT^4}{dx} = 4T^3 \frac{dT}{dx} \tag{6}$$

in the gap and

$$F = K_R(T) \frac{dT}{dx} \tag{7}$$

where

$$K_R(\mathrm{T}) = 4En^2 \delta \sigma T^3 \tag{8}$$

For absorbing media the thermal conductivity is usually written [12]

$$K_R(T) = \frac{16}{3} n^2 L(T) \sigma T^3 \tag{9}$$

where $L(T)$ is a frequency averaged mean free path. For an exact treatment we need a $K_R(T)$ that limits to equation (9) for thick samples and to equation (5) or (9) for thin transparent samples. However, data on $L(T)$ is not always available for any given rock sample, and in the temperature range of 1450–2000 K, $L(T)$ is usually large compared to the thickness of melt layers. Equations (4) and (7) should be good approximations to the radiation contribution. Fig. 6 is a plot of these basalt thermal conductivities. Curve A is the conductive part. Curves B and C are K_R and $K_R(T)$ for a 1.0 mm gap width and D and E are for a 5 mm gap width. All are plotted for n = 1.5, ϵ_s = 0.20 and ϵ_m = 0.85.[2] K_R is for T_s = 1900 K and T_m = 1450 K. For small gap widths ($\delta \leq 1.0$ mm) as in the melt layer at the leading edge the heat flux due to the conductive part will be large compared to the radiative contribution. In the thicker portions of the melt layer ($\delta > 5.0$ mm) the conductive flux will diminish and the radiation contribution will dominate if $L(T)$ is large enough. Equations (4) and (7) are also applicable in the gaps that electrically isolate the heaters with n = 1.0 and the appropriate values of heater and receptor emissivities.

[2] The emissivities, ϵ_s and ϵ_m can be determined independently [2], as can the index of refraction, n. At the present time n is the most uncertain.

The 51 mm dia Parabolic Consolidator

The 51 mm dia parabolic penetrator of Fig. 1(*a*) was designed before a detailed thermal analysis was used to suggest modifications to the heater and to analyze its performance in tuff and basaltic alluvium. In a rock such as tuff, which resists compaction, the full consolidation condition must be met at the rear edge of the penetrator. That is, the outer radius of the melt layer is

$$r_m = r\left(\frac{1}{1-\rho_i/\rho_\ell}\right)^{1/2} \tag{10}$$

and it is derived from the conservation of mass [3]. Here r is the penetrator radius, and ρ_i and ρ_ℓ are the densities of the rock and melt. Tuff has a thermal conductivity somewhat higher than that of basalt, has a low density (1.5–1.6 Mg/m^3), and forms a glass of high density (2.7 Mg/m^3). Under these conditions the analysis indicates that the consolidation condition can be met at 0.2 mm/s with 3.0 kW of power and with molybdenum temperatures under 1950 K and heater temperatures under 2500 K. In numerous tests in tuff this penetrator has consistently achieved steady-state velocities between 0.15 and 0.20 mm/s for heater powers of 3.0 and 3.5 kW and thrust loads of 3–5 kN. A number of tests of this penetrator have been done in a basaltic alluvium with initial densities of 1.63 to 1.88 Mg/m^3 and which forms a glass with densities of $\gtrsim$2.4 Mg/m^3. With a thermal conductivity of basalt, the analysis indicates that the consolidation condition can be satisfied only at velocities below 0.05 mm/s in this density range. In the test, however, considerable compaction takes place and velocities up to 0.22 mm/s have been achieved with a consolidation fraction of $f = 0.32$. Where the f is the ratio of the thickness of the glass hole liner to that needed for full consolidation. Fig. 7 is a plot of steady-state penetrator velocity versus initial density for five tests and for calculations which predict the velocity only on the fraction of consolidation achieved. For tests and calculations with the similar values of f, agreement is fair.

The isotherm plot of Fig. 1(*b*) shows the temperature distribution calculated in basaltic alluvium at a density of 1.75 Mg/m^3 and at a velocity of 0.2 mm/s. The heater is heating the molybdenum body uniformly to between 1900 and 2000 K. The major internal temperature gradients are in the insulating gap and the maximum heater temperature is less than 2300 K. The largest impedance to heat flux to the unmelted rock is the melt layer. At this velocity the graphite heater with an insulating gap can still supply sufficient heat flux to the leading edge to keep the temperatures in the molybdenum near 1900 K.

The Heat Pipe Penetrator

The design of Fig. 4(*a*) was proposed as the consolidator having the highest potential velocity. The parabolic section would be followed by a heated cylindrical section of sufficient length to meet the consolidation condition at whatever velocity could be obtained by the leading edge. This cylindrical section would contain an extension of the heat pipe and supply part of the heat flux to the leading edge. The thermal analysis was used to compare this with other designs by examining the melt layer thickness at the leading edge as a function of velocity, leading edge temperatures, and rock properties. The isotherm plot of Fig. 4(*b*) was obtained for this design for the same conditions as that of Fig. 1(*a*). In a rock of this conductivity and with a maximum temperature of 2000 K in the molybdenum the heat pipe design shows no advantage, since the leading edge flux is determined by these two parameters. The calculated melt layer thickness is the same in both cases (0.2 mm). If the maximum body temperature is raised to 2100 K (for tungsten), the graphite heater design is limited by the maximum allowable heater temperature, taken to be 2500 K.

The 90 mm Conical Consolidator

The 90 mm conical consolidator of Fig. 3 was proposed for the production of stable glass lined holes in basaltic alluvium with densities up to 1.8 Mg/m^3. Designs with an overall length of 306 and 456 nm have been produced. The isotherm plot of Fig. 3(*b*) is for an initial

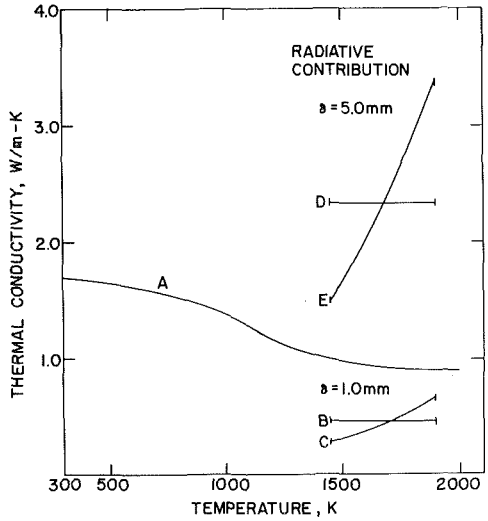

Fig. 6 Thermal conductivity of basalt

density of 1.75 Mg/m^3, a glass density of 2.4 Mg/m^3 and a velocity of 0.2 mm/s. Again the heater design provides uniform heating and the maximum heater temperature ($\lesssim$2400 K) occurs near the leading edge where the maximum fluxes are required.

The increased length-to-diameter ratio of these designs over the 51 mm dia design more than compensate for the need for thicker melt layer caused by the larger radius. The analysis shows that if sufficient compaction occurs to allow a consolidation fraction of 0.5 that the 306 mm long design can achieve a velocity of 0.2 mm/s and that the 456 mm long design can reach 0.4 mm/s. However, the calculated melt layer is becoming excessively thin (0.3 mm) at $v^* = 0.2$ mm/s and the leading edge flux may limit velocities to this value.

The Hare Extruder

The extruding configuration of Fig. 2(*a*) was designed to optimize the heat flux to the leading edge and to insure that the leading edge flux was the only limit to the velocity. The walls at the leading edge were reduced to 5.0 mm. The length was sufficient to insure complete melting at the extrudate nozzle at velocities up to 0.4 mm/s. The ex-

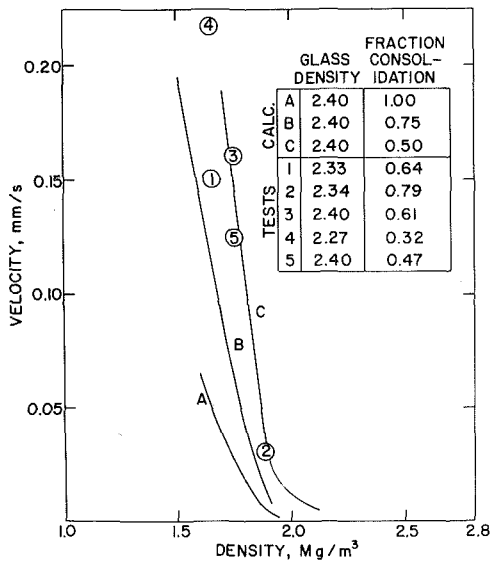

		GLASS DENSITY	FRACTION CONSOLIDATION
CALC.	A	2.40	1.00
	B	2.40	0.75
	C	2.40	0.50
TESTS	1	2.33	0.64
	2	2.34	0.79
	3	2.40	0.61
	4	2.27	0.32
	5	2.40	0.47

Fig. 7 Velocity versus density of alluvium for 51 mm dia penetrator

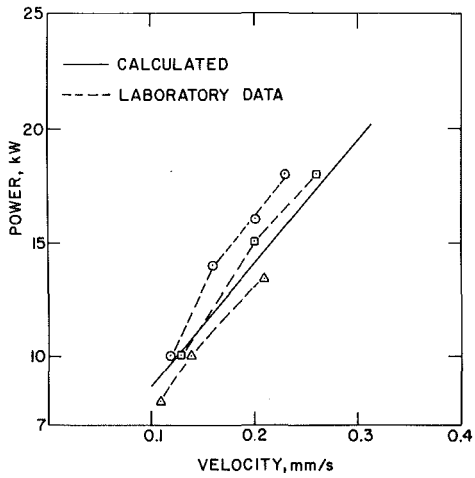

Fig. 8 Power versus velocity for extruding penetrator in basalt

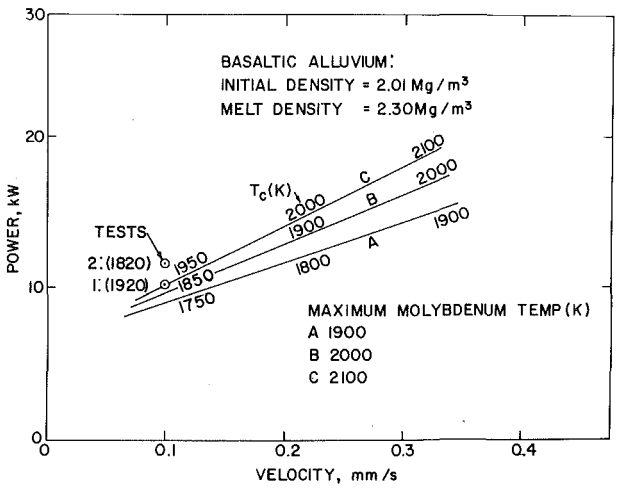

Fig. 9 Power versus velocity for extruding penetrator in basaltic alluvium

trudate temperatures are calculated to be $\gtrsim$1700 K at $v^* = 0.2$ mm/s. The cylindrical section of the heater was placed at the largest radius possible to increase the radiating area which helps prevent overheating of the heater. The cylindrical body section near the tip insures that the melt layer does not need to increase and that it will not be squeezed thin in this region, thereby allowing more heat flux to flow toward the leading edge.

This penetrator has been tested extensively in basalt ($\rho_i = 2.70$ and $\rho_\ell = 2.70$) and in densely packed basaltic alluvium ($\rho_i = 2.0$ and $\rho_\ell \simeq 2.3$). The velocity is insensitive to the thrust in the range 2–4 kN. The tests were run at ~4 kN thrust, which stress calculations indicate to be a safe maximum. Fig. 4(*b*) is the isotherm plot for this penetrator in basalt at $v^* = 0.2$ mm/s. The heater design results in uniform molybdenum temperatures with the maximum occurring near the leading edge. The maximum heater temperature is <2300 K and also occurs near the leading edge.

Power versus velocity for the test in basalt are shown in Fig. 8. The calculated curve was obtained by limiting the maximum molybdenum temperature to 1950 K. In the experimental runs the temperature was monitored by measuring the heater resistance (Fig. 5). The maximum steady state velocity limits at ~0.2 mm/s at thrust of 4 kN. The analysis indicates that the melt layer at the leading edge is becoming excessively thin (<0.4 mm) at this velocity. For the test in the basaltic alluvium, a thermocouple was placed in the molybdenum body at the point indicated by *TC* in Fig. 2(*a*). In these tests the steady-state velocity limited at 0.1 mm/s at a thrust of 4 kN. The test data are shown on Fig. 9 by the open circles at 1 and 2 with the measured thermocouple temperatures. The calculated curves were obtained by limiting the maximum molybdenum temperature to the values indicated. The calculated thermocouple temperatures (T_c) are annotated on the curves at the appropriate positions. These calculations also indicate the melt layer becoming excessively thin (<0.6 mm) at $v^* =$ 0.1 mm/s.

The glass walls produced thus far are of somewhat nonuniform thickness and contain some voids, but they are in the range of thicknesses calculated. Two of the runs in basalt with average velocities of 0.16 mm/s and average powers of 11.0 kW produced melt layers with thickness varying from 7.5 to 12.5 mm. The calculated thickness is 10 mm for $v^* = 0.2$ mm/s and 13.7 kW. For test 2 indicated in Fig. 9 the measured wall thickness was 12.5 to 14.5 mm. The calculated thickness for $v^* = 0.1$ and a penetrator body temperature of 1800 K, is 15 mm.

Subterrene Development

The analysis presented here has been restricted to basalt and basaltic alluvium for a number of reasons. The material properties of basalt were well known and a number of penetrators have been tested in basalt. The basalt rock, since it is uniform and fine grained, is best represented by the computer model which does not consider inhomogeneities. The basaltic alluvium was encountered in a field application. It consists of fine sand and gravel and was thought to have the same properties as the basalt rock, except for those effected by the porosity.

The relationship of the thrust to advance rate and power has not been considered here. It was first addressed in [7, 8]. However, calculated thrust were generally low compared to those encountered in the laboratory, specially for the low viscosity basalt. Work in progress indicates that further appropriate modifications of the thermal conductivity of the liquid melt, in addition to the limiting of the radiation flux described in the foregoing, bring the calculated and experimental thrust into good agreement.

This and related analyses are a small part of the development program of a penetrator capable of operating in the hot, high pressure environment encountered in drilling deep geothermal wells [13]. It is in this environment that conventional rotary methods become increasingly impractical. Included in the program have been tests in granite [14], the most common dense rock, in frozen alluvium [6], containing ~20 percent by weight water, and in various sandstones. At present the deepest hole produced in the field was 30 m deep in basalt and was drilled with an 87 mm dia extended area extruder [15, 16].

Another area of applicability of the rock melting is the production of unaltered cores encased in a thin glass liner. Such drills are possible in both the consolidating and extruding modes. A 114 mm dia coring consolidator which produced unmelted cores has been tested in tuff [17, 18].

Also of importance to the development program is the determination of penetrator lifetime under conditions of high temperature and stress. This includes the investigation of chemical reactions between interior components and the interaction of the refractory metal penetrator with the molten rock by corrosion and abrasion, [19–21]. The physical properties of rocks, rock melts, and rock glasses that are basic to this and the analytical program have also been the subject of continuing study, some results of which is contained in references [14, 22, 23].

Problems associated with potential applications, energy requirements, the environment, and general systems analysis are discussed in [24–26].

References

1 Armstrong, D. E., et al., "Rock Melting as a Drilling Technique," LA-3243, Los Alamos Scientific Laboratory, Los Alamos, N. Mex. Mar. 1965.

2 Gido, R. G., "Internal Temperature Distribution of a Subterrene Rock-Melting Penetrator," LA-5135-MS, Los Alamos Scientific Laboratory, Los Alamos, N. Mex., Jan. 1973.

3 Neudecker, J. W., "Design Description of Melting-Consolidating Prototype Subterrene Penetrators," LA-5212-MS, Feb. 1973, Los Alamos, N. Mex.

4 Gido, R. G., "Subterrene Penetration Rate: Melting Power Relationship," LA-5204-MS, Los Alamos Scientific Laboratory, Los Alamos, N. Mex., Mar. 1973.

5 Cort, G. E., "Rock Heat-Loss Shape Factors for Subterrene Penetrators," LA-5435-MS, Los Alamos Scientific Laboratory, Los Alamos, N. Mex., Oct. 1973.

6 Hanold, R. J., "Rapid Excavation by Rock MeltinLASL Subterrene Program," LA-5459-SR, Los Alamos Scientific Laboratory, Los Alamos, N. Mex. Nov. 1973.

7 McFarland, R. D., "Numerical Solution of Melt Flow and Thermal Energy Transfer for a Rock-Melting Penetrator," LA-5608-MS, Los Alamos Scientific Laboratory, Los Alamos, N. Mex., May 1974.

8 McFarland, R. D., and Hanold, R. J., "Viscous Melt Flow and Thermal Energy Transfer for a Rock-Melting Penetration," ASME Paper No. 74-WA/HT-38, presented at ASME Winter Annual Meeting, New York, N. Y., Nov. 1974.

9 Lawton, R. G., "The AYER Heat Conduction Computer Program," LA-5613-MS, Los Alamos Scientific Laboratory, Los Alamos, N. Mex., May 1974.

10 Giger, A. J., and Cort, G. E., "66 mm Universal Extruding Tests," S-63, Los Alamos Scientific Laboratory, Los Alamos, N. Mex., June 1973.

11 Murase, T., and McBirney, A. R., "Thermal Conductivity of Lunar and Terrestrial Igneous Rocks in Their Melting Range," *Science*, Vol. 170, 1970, pp 165–167.

12 Condon, E. U., and Odishaw, H., *Handbook of Physics*, McGraw-Hill, New York, 1958.

13 Altseimer, J. H., "Geothermal Well Technology and Potential Applications of Subterrene Devices—A Status Review," LA-5689-MS, Los Alamos ScientificLaboratory, Los Alamos, N. Mex., Aug. 1974.

14 Krupka, M. C., "Phenomena Associated with the Process of Rock Melting," LA-5208-MS, Los Alamos Scientific Laboratory, Los Alamos, N. Mex., Feb. 1973.

15 Giger, A. J., "Design, Development and Testing of 84 mm Diameter Subterrene Extruder Used to Produce 30 Metres in Jemez Basalt," Memo S-91, Los Alamos Scientific Laboratory, Los Alamos, N. Mex., Mar. 1975.

16 Williams, R. E., "The Field Operations for Melting a 30 m Deep Hole in Basalt With a Subterrene Penetrator," Memo S-89, Los Alamos Scientific Laboratory, Los Alamos, N. Mex., Apr. 1975.

17 Neudecker, J. W., "Conceptual Design of a Coring Subterrene Geoprospector," LA-5517-MS, Los Alamos Scientific Laboratory, Los Alamos, N. Mex., Feb. 1974.

18 Murphy, H. D. and Cort, G. E., "Results and Analysis of 114 mm Corer Calibration Test," Memo S-71, Los Alamos Scientific Laboratory, Los Alamos, N. Mex., Nov. 1973.

19 Stark, W. A., and Krupka, M. C., "Chemical Corrosion of Molybdenum and Tungsten in Liquid Basalt, Tuff, and Granite with Application to Subterrene Penetrators," LA-5857-MS, Los Alamos Scientific Laboratory, Los Alamos, N. Mex., Feb. 1975.

20 Krupka, M. C., "Thermodynamic Stability Considerations in the Mo-BN-C System. Application to Prototype Subterrene Penetrators," LA-4959-MS, Los Alamos Scientific Laboratory, Los Alamos, N. Mex., May 1972.

21 Stark, W. A., and Krupka, M. C., "Carbon Receptor Reactions in Subterrene Penetrators," LA-5423-MS, Los Alamos Scientific Laboratory, Los Alamos, N. Mex., Oct. 1973.

22 Ehrenberg, S. N., et al., "Petrography and Chemistry of Minerals and Glass in Rocks Partially Fused by Rock Melting Drills," LA-5838, Los Alamos Scientific Laboratory, Los Alamos, N. Mex., Sept. 1975.

23 Lundberg, L. B., "Characterization of Rock Melts and Glasses Formed by Earth-Melting Subterrenes," LA-5826-MS, Los Alamos Scientific Laboratory, Los Alamos, N. Mex., Jan. 1975.

24 Robinson, E. S., et al., "A Preliminary Study of the Nuclear Subterrene," LA-4547, Los Alamos Scientific Laboratory, Los Alamos, N. Mex., Apr. 1971.

25 Sims, D. L., "Identification of Potential Applications for Rock-Melting Subterrenes," LA-5206-MS, Los Alamos Scientific Laboratory, Los Alamos, N. Mex., Feb. 1973.

26 Altseimer, J. H., "Technical and Cost Analysis of Rock Melting Systems for Producing Geothermal Wells," (to be published), Los Alamos Scientific Laboratory, Los Alamos, N. Mex.

B. S. Singh
Assoc. Mem. ASME

A. Dybbs
Mem. ASME

Department of Fluid, Thermal and Aerospace Sciences, Case Western Reserve University, Cleveland, Ohio

Error in Temperature Measurements Due to Conduction Along the Sensor Leads

When a sensor is embedded in a solid body to measure its internal temperature, any conduction to, or from, its sensing element may cause the indicated temperature to be different from the true temperature. This paper describes an analysis of the error caused by conduction when there is an arbitrary temperature distribution in thebbody along the sensor. The sensor is modeled as a cylindrical fin and the appropriate conduction equation is solved. The solution gives a correction for the error which depends on such parameters as, depth of immersion, thermocouple wire and insulation properties, contact between the sensor and the body, and temperature distribution in the body. The latter may not be known, but the measured temperature distribution can be used as a first approximation. The corrected value can then be used to obtain a better estimate of the error. The results show good agreement with experimental observations.

Introduction

When a temperature sensor such as a thermocouple or a platinum resistance thermometer is used to measure the temperature of a solid, the measured temperature is only an approximation to the true value of the temperature at that location. The error or the deviation between the sensor output and the true temperature at the point in the absence of the sensor may be caused by a number of factors. First, the presence of the sensor itself may alter the temperature field at that location. Second, any heat transfer from (or to) the sensing element through the leads to (or from) either the body or ambient may cause the temperature of the sensing element to be different from the temperature of the body at that location. Since a sensor can only measure the temperature of its own sensing element, any temperature difference between the sensing element and body results in an error. Third, in transient processes the thermal inertia of the sensing element may introduce additional error.

The problems of the first class, i.e., the installation error, are significant for solid materials having low thermal conductivity. This problem has been studied by Beck [1, 2],[1] Turner [3] and others. Turner [4] has also studied the error for a porous material with fluid flowing through it.

The second effect, the heat conduction through the sensor, may be considered in two parts. In case of a body at a uniform temperature the sensor leads may exchange heat with the surrounding environment causing a temperature difference between the sensing element and the body. This problem has been studied by Moffat [5], Sparrow [6], and others. The error in this case can be minimized to a desired level by a proper choice of sensor and a sufficient depth of immersion. In case of a body having a temperature gradient along the length of the sensor embedded in the body the errors may become unavoidable in many situations. If the temperature distribution in the body is one-dimensional then one may be able to locate the sensors along the isothermal paths thus overcoming the problem. But if the temperature distribution in the body is multidimensional and several different boundary conditions are to be studied, then the foregoing approach becomes impractical. Thus, an estimate of error is required to interpret the measured temperatures. Little work seems to have been done in this area.

Thus, this paper presents an approximate analysis of the error introduced in the measurement of temperature when there is an arbitrary temperature gradient in the body along the sensor length. The body in which the sensor is embedded is considered to be much larger than the cavity and the thermal conductivity of the body is relatively high so the effect of cavity is negligible. The result of the analysis is compared with some experimental measurements.

Model of the System

Fig. 1 shows a sensor embedded in a solid. The sensor is inserted in the hole drilled in the body and some filler (a cement or an adhesive) is used to fill the gap. The leads are much longer than the embedded length ℓ. Upon emerging from the solid the leads pass through

[1] Numbers in brackets designate References at end of paper.

Contributed by the Heat Transfer Division and presented at the Winter Annual Meeting, Houston, Texas, November 30–December 5, 1975, of THE AMERICAN SOCIETY OF MECHANICAL ENGINEERS. Revised manuscript received by the Heat Transfer Division June 14, 1976. Paper No. 75-WA/HT-92.

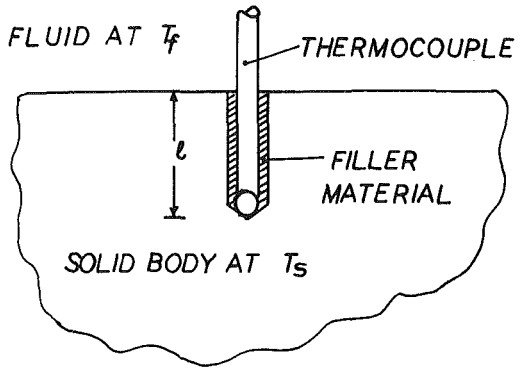

Fig. 1 Sketch of a thermocouple embedded in a solid body

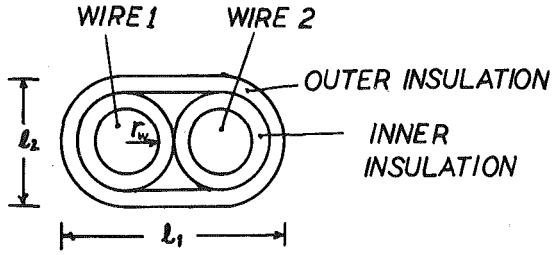

Fig. 2 Cross section of a double wire duplex insulated leads

a fluid whose temperature is T_f. The temperature of the solid is T_s (not uniform). The sensor leads are exchanging heat between the body and the ambient.

Fig. 2 shows a cross section of the insulated leads. This geometry is not easy to analyze. Thus, the sensor leads are modeled as a cylindrical fin as shown in Fig. 3. The fin has radius $\sqrt{2}r_w$ and a thermal conductivity $k = (k_1 + k_2)/2$ where k_1 and k_2 are the thermal conductivities of the individual lead wires. It is assumed that all the heat conduction along the leads takes place through the metal wires and the radial temperature variation in the wire is negligible. This is a reasonable assumption in view of the high thermal conductivity and large length to diameter ratio of the wire. This model is similar to the one used by Moffat [5] and Sparrow [6].

The part of the fin that is inside the solid is surrounded by insulation and filler material. The overall conductance between the solid and the lateral surface of the fin (in the embedded region) can be approximated to be

$$(UP)_1 = \frac{1}{\frac{1}{2\pi k_f}\ln\frac{r_h}{r_2} + \frac{1}{2\pi k_i}\ln\frac{r_2}{r}} \tag{1}$$

where

k_f = thermal conductivity of the filler material
k_i = thermal conductivity of the insulation
r_h = radius of the hole

$$r_2 = \frac{\ell_1 + \ell_2}{4}$$

$r = \sqrt{2}\, r_w$, the radius of the fin.

The contact between the sensing element (thermocouple junction or resistance thermometer) and the body is difficult to estimate. The bottom of the hole is generally conical and the sensing element may be cylindrical or spherical. The overall conductance for this is approximated by

$$(UA)_3 = h_e \pi r^2; \quad h_e = \frac{k_f}{\delta} \tag{2}$$

Where δ is an equivalent thickness of the filler layer between the sensing element and the bottom of the hole. Moffat [5] has shown that $\delta = 0.004$ in. gave a satisfactory comparison between his analytical and experimental results. For a porous medium with flow, h_e can be approximated as the heat transfer coefficient for a sphere of radius r in uniform flow.

The part of the fin that is exposed to the ambient may exchange heat through convection and radiation. Thus, the overall conductance between the fin lateral surface and the ambient fluid may be approximated by:

$$(UP)_2 = \frac{1}{\frac{1}{hP'} + \frac{1}{2\pi k_i}\ln\frac{r_2}{r}} \tag{3}$$

Moffat [7] has given correlations for determining h as a function of Reynolds number for two cases, namely flow perpendicular to the fin and parallel to the fin.

The temperature distribution in the solid body along the sensor is assumed to be a polynomial of nth degree.

$$T_s(x) - T_a = \sum_{i=1}^{n} a_i x^i \tag{4}$$

where

T_a = temperature of the body at $x = 0$, i.e., surface

Nomenclature

A = area of cross section of the fin
a_1 = temperature gradient in the solid body along the sensor
b = temperature gradient in the ambient fluid
d = thickness of the thermal boundary layer in the ambient fluid
h = heat transfer coefficient
k = thermal conductivity of the fin ($(k_1 + k_2)/2$)
k_1, k_2 = thermal conductivity of two lead wires
k_f = thermal conductivity of the filler material
k_i = thermal conductivity of the insulation
ℓ = embedded length of the sensor
ℓ_1 = major diameter of the insulated sensor leads
ℓ_2 = minor diameter of the insulated sensor leads
$m_1 = ((UP)_1/kA)^{1/2}$
$m_2 = ((UP)_2/kA)^{1/2}$
$m_3 = ((UA)_3/kA)$
n = degree of the polynomial used to approximate the temperature distribution in the body along the embedded sensor length
$N_1 = m_2/m_1$
$N_2 = m_3/m_1$
$N_3 = m_1\ell$
P = perimeter of the fin
P' = external perimeter of the insulated sensor leads
r = radius of the fin
r_h = radius of the hole
r_w = radius of the individual lead wires
r_2 = equivalent radius of the fin with insulation
T = temperature of the fin
T_f = temperature of the ambient fluid
T_s = temperature distribution in the solid body along the embedded sensor
T_a = temperature of the body surface at the sensor location
T_0 = temperature of fin at the body surface
U = overall conductance
x = distance along the lead wires
$\alpha = T - T_f$
$\theta = T - T_a$
δ = equivalent thickness of the filler material between the sensing element and the body
ϵ = error in the measured temperature

x = axial coordinate along the sensor

Analysis of the Model

The cylindrical fin is divided into two segments, shown in Fig. 3, the segment embedded in the solid and that in the ambient. The conduction equation is solved for both regions and the solutions are matched at the surface.

The Embedded Region. The heat balance for the fin [8] gives the following equation for the temperature distribution along the fin.

$$kA\frac{d^2T}{dx^2} - (UP)_1(T - T_s) = 0 \tag{5}$$

b.c. @ $x = 0$, $T = T_0$ (unknown at this point)

$$@\ x = \ell, \quad -kA\frac{dT}{dx} = (UA)_3(T(\ell) - T_s(\ell))$$

Equation (5) can be written as,

$$\frac{d^2\theta}{dx^2} - m_1{}^2\theta = -m_1{}^2\sum_{i=1}^{n} a_i x^i \tag{6}$$

where

$$\theta = T - T_a$$

and

$$m_1{}^2 = \frac{(UP)_1}{kA}$$

The solution of equation (6) with b.c. at $x = 0$, is

$$\theta = C_1(e^{m_1 x} - e^{-m_1 x}) + \theta_0 e^{-m_1 x} + \sum_{i=1}^{n}\beta_i x^i \tag{7}$$

where $\theta_0 = T_0 - T_a$, C_1 will be evaluated by using the b.c. at $x = \ell$;

$$\beta_i = a_i + \frac{1}{m_1{}^2}(i+1)(i+2)a_{i+2}, \quad a_i = 0, \quad i > n$$

Ambient Region. For the ambient region the equation describing the axial temperature distribution is,

$$kA\frac{d^2T}{dx^2} - (UP)_2(T - T_f) = 0 \tag{8}$$

b.c. at $x = 0$, $T = T_0$

at $x \to -\infty$, $T = T_f$

Equation (8) can be written as,

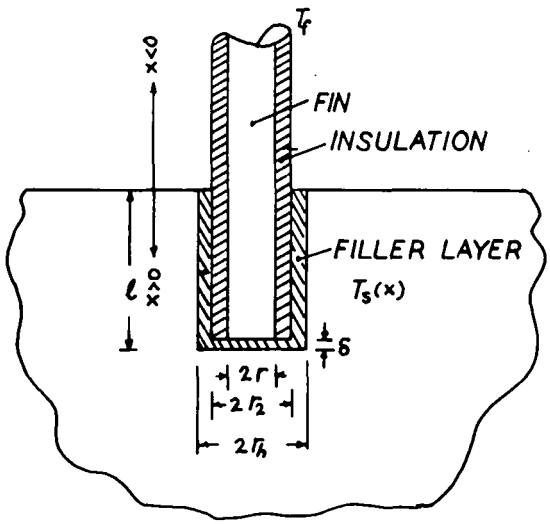

Fig. 3 Model of the system

$$\frac{d^2\alpha}{dx^2} - m_2{}^2\alpha = 0 \tag{9}$$

where

$$\alpha = T - T_f, \quad m_2{}^2 = \frac{(UP)_2}{kA}$$

The solution of equation (9) with the b.c. at $x = 0$ and $x = \infty$ is

$$\alpha = \alpha_0 e^{m_2 x} \tag{10}$$

where

$$\alpha_0 = T_0 - T_f$$

By matching the heat fluxes at $x = 0$ one obtains an expression for T_0,

$$\theta_0 = T_0 - T_a = \frac{2m_1C_1 + m_2(T_f - T_a) + \beta_1}{m_1 + m_2} \tag{11}$$

In this equation C_1 is yet to be determined. This can be achieved by using equations (7) and (11) and applying the b.c. at $x = \ell$. This gives

$$C_1 = \frac{\dfrac{m_2(T_f - T_a) + \beta_1}{m_1 + m_2}(m_1 - m_3)e^{-m_1\ell} + Bm_3 - D}{m_1(e^{m_1\ell} + e^{-m_1\ell}) + m_3(e^{m_1\ell} - e^{-m_1\ell}) - \dfrac{2m_1}{m_1 + m_2}(m_1 - m_3)e^{-m_1\ell}} \tag{12}$$

where

$$B = \sum_{i=1}^{n}(a_i\ell^i - \beta_i\ell^i) = -\frac{1}{m_1{}^2}\sum_{i=1}^{n-2}(i+1)(i+2)a_{i+2}\ell^i$$

$$D = \sum_{i=1}^{n} i\beta_i\ell^{i-1}$$

$$m_3 = (UA)_3/kA$$

Equation (7) gives the temperature distribution in the embedded region of the fin. The constants, θ_0, and C_1 are given from equations (11) and (12), respectively. The temperature of the sensing element can be obtained from equation (7) by substituting $x = \ell$. This is the temperature that the sensor will measure. The actual temperature of the body is $T_s(\ell)$. Thus, the error in the measurement is

$$\epsilon = T(\ell) - T_s(\ell)$$

$$= C_1(e^{m_1\ell} - e^{-m_1\ell}) + \theta_0 e^{-m_1\ell} + \sum_{i=1}^{n-2}\frac{(i+1)(i+2)}{m_1{}^2}a_{i+2}\ell^i \tag{13}$$

Where θ_0 and C_1 are given by equations (11) and (12), respectively.

Equation (13) gives the error for a general case which includes the effect of heat transfer to the ambient as well as the effect of an arbitrary temperature distribution in the body. In what follows the results are reduced for some special cases to facilitate application as well as comparison with some previous works.

Special Cases. (*a*) The solid body is at a uniform temperature T_s which is different from the temperature of the ambient fluid T_f. In this case the error is due to the so called "fin effect" i.e., conduction to the ambient. In nondimensional form:

$$\frac{T(\ell) - T_s}{T_f - T_s} = \frac{\dfrac{N_1(1-N_2)}{1+N_1}\left(1 - e^{-2N_3} + \dfrac{2}{1+N_1}e^{-2N_3}\right)}{e^{N_3} + e^{-N_3}) + N_2(e^{N_3} - e^{-N_3}) - 2\dfrac{1-N_2}{1+N_1}e^{-N_3} + \dfrac{N_1}{1+N_1}e^{-N_3}}$$

where

$$N_1 = \frac{m_2}{m_1}, \quad N_2 = \frac{m_3}{m_1}, \quad \text{and } N_3 = m_1\ell$$

$$\frac{T(\ell) - T_s}{T_f - T_s} \simeq \frac{1}{\cosh N_3[1 + N_2 + (N_1 + N_2)\tanh N_3]}, \quad \text{for } e^{N_3} \gg 1$$

which is exactly the result obtained by Moffat [5]. For this case the error may be reduced by increasing the depth of immersion or using heavily insulated low thermal conductivity and small diameter sensors.

(*b*) Linear temperature distribution in the body and surface temperature equal to the ambient fluid temperature. In this case the fin effect is absent. If a_1 is the temperature gradient in the body then in dimensionless form

$$\frac{T(\ell) - T_s(\ell)}{a_1/(m_1 + m_2)} = \frac{(1 - N_2)\left(1 - e^{-2N_3} + \dfrac{2}{1 + N_1}\right)}{(e^{N_3} + e^{-N_3}) + N_2(e^{N_3} - e^{-N_3}) - 2\dfrac{1^{-N_2}}{1 + N_1}e^{-N_3}}$$

$$+ e^{-N_3} \simeq \frac{1}{\cosh N_3\left[1 + \dfrac{N_2}{1 + N_1} + \dfrac{N_1 N_2}{1 + N_2}\tanh N_3\right]}, \quad \text{for } e^{N_3} \gg 1$$

(*c*) If the depth of immersion of the thermocouple in the solid body is sufficiently large, i.e., $m_1\ell \gg 1$. Then the fin effect becomes negligible.

$$\epsilon \simeq \frac{Bm_3 - D}{m_1 + m_3} + \sum_{i=1}^{n-2} \frac{(i+1)(1+2)}{m_1{}^2} a_{i+2}\ell^i$$

For this case the error cannot always be decreased by increasing the depth of immersion. A choice of a heavily insulated low thermal conductivity and small diameter sensor will reduce the error.

(*d*) Linear temperature variation in the solid as well as the fluid in the vicinity of the solid. The fluid away from the body is at a temperature T_f. (This would be an approximation to study the effect of the thermal boundary layer in the fluid near the body.) Thus we have,

$$T_s(x) = T_a + a_1 x, \quad 0 \le x \le \ell, \quad \text{(in the solid body)}$$

$$T_s(x) = T_a + bx, \quad -d \le x \le 0, \quad \text{(in the boundary layer)}$$

$$T_f(x) = T_f \quad x \le -d$$

For this case the analysis was carried out by dividing the fin into three regions and matching the solutions as in the previous case. The expression for error is given as

$$\epsilon = T(\ell) - T_s(\ell) = c_1\left(e^{m_1\ell} - e^{-m_1\ell} + 2\frac{m_1}{m_1 + m_2}e^{-m_1\ell}\right) + \left(a_1 - b + b\frac{1 - e^{2m_2 d}}{e^{-m_2 d} - e^{m_2 d}}\right)\frac{e^{-m_1\ell}}{m_1 + m_2}$$

where

$$c_1 = \frac{\dfrac{1}{m_1 + m_2}\left[(a_1 - b) + b\dfrac{1 - e^{2m_2 d}}{e^{-m_2 d} - e^{m_2 d}}\right](1 - N_2)e^{-N_3} - \dfrac{a_1}{m_1 + m_2}}{(e^{N_3} + e^{-N_3}) + N_2(e^{N_3} - e^{-N_3}) - 2\dfrac{1 - N_2}{1 + N_1}e^{-N_3}}$$

Results and Discussion

The error in the temperature measurement due to conduction along the sensor leads is given by equation (13). The analysis takes into account the heat conduction from the sensing element to the external environment as well as the effect of the temperature gradient in the body along the sensor. The previous investigators have considered only the former source in analyzing the error.

The expression for the error depends upon the parameters m_1, m_2, m_3, ℓ, T_f, and T_s the temperature distribution in the solid along the embedded length of the sensor. Of these parameters m_1, m_2, m_3 depend upon the sensor properties, the contact between the sensing element and the body, and the installation. The method for calculation of these was discussed earlier. The depth of immersion ℓ may be dictated by the nature of the experiment i.e., the positions where the temperatures are to be measured. T_f is the surrounding temperature which may be fixed. The calculation of error also requires an a priori knowledge of T_s, the temperature distribution in the body along the sensor which is the aim of the measurement and generally not known. For estimating the error, the measured temperature distribution, which has not been corrected for error, can be used as a first approximation for the temperature distribution in the body. From this the errors can be calculated and the measured values can be corrected. The corrected temperature distribution can be used to obtain a better approximation for the error. If the inherent error of the thermocouple is greater than the correction obtained from equation (13) then the correction is not necessary.

At first glance equations (11), (12), and (13) appear to be quite involved. But once the parameters m_1, m_2, m_3 have been calculated one finds that for most cases $e^{m_1\ell} \gg 1$ (also $e^{-m_1\ell} \ll 1$); thus, the expressions will be greatly simplified.

A problem of this nature was encountered in the measurement of the two dimensional temperature distribution in porous media with fluid flow [9]. The porous specimens were cylindrical having radial as well as axial temperature variations. Both the radial and the axial temperature variations were nonlinear and varied with the fluid flow rate. Thus, the location of the thermocouples along isothermal paths was not feasible. The thermocouples were radially located and the result of the present analysis was used to correct the measured temperatures. The corrected values produced a better agreement between the experimental and the theoretical temperature profiles.

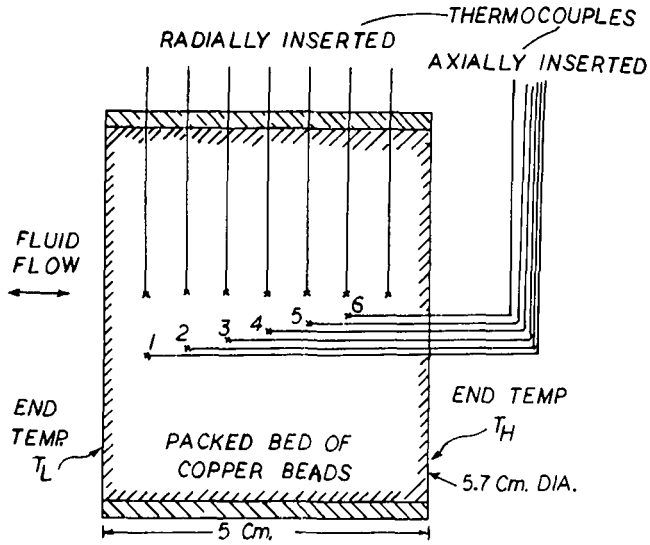

Fig. 4 Schematic diagram of the test section indicating the location of the thermocouples (numbers near the junctions of the axially located thermocouples represent station numbers)

Comparison with Experiments

To check the validity and the applicability of the analytical model some experiments were performed. A 5.7-cm (2.225 in.) ID 5-cm (2 in.) long plexiglass tube was packed with 0.0183-cm copper beads. A number of 30 gauge (AW30) enamel insulated copper-constantan thermocouples were inserted in the bed at various axial and radial locations. As shown schematically in Fig. 4 some of the thermocouples were inserted radially through the tube wall and the remaining were inserted axially. A one-dimensional (axial) temperature distribution was maintained in the packed bed. Thus, the thermocouples located axially had a temperature gradient along them whereas the thermocouples that were inserted radially were along isothermal paths. The depth of immersion of the radially inserted thermocouples was at least 1.9 cm (¾ in.) such that the effect of conduction along the leads was

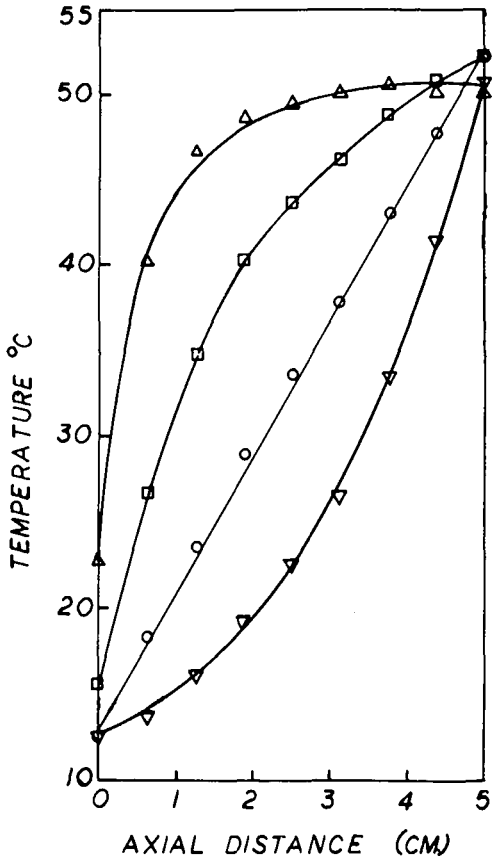

Fig. 5 Some representative axial temperature distributions in the cylindrical porous specimen 5 cm (2 in.) long and 5.7 cm (2.25 in.) dia

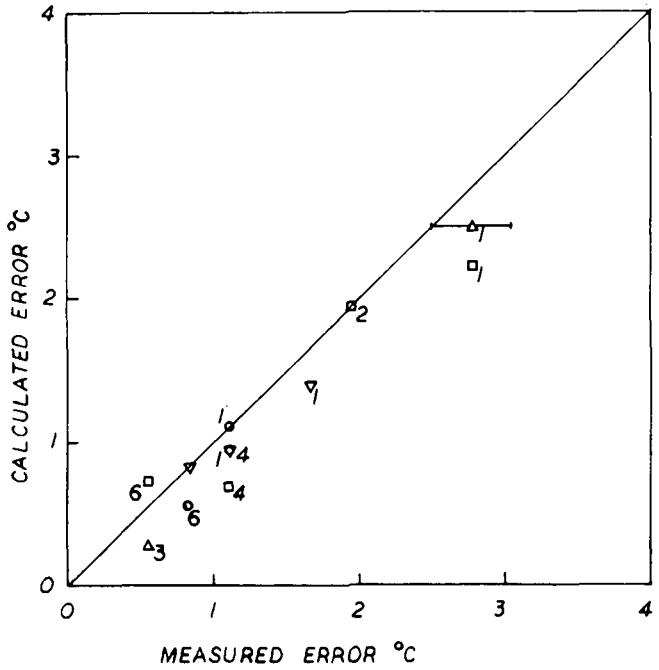

Fig. 6 Comparison of measured error with those calculated from the model (equation (13)) (the symbols correspond to the temperature distributions in Fig. 5 and the numbers indicate the location of the thermocouples as shown in Fig. 4

negligible. Linear as well as nonlinear axial temperature gradients were established in the packed bed and the output of all the thermocouples were measured in steady state using a digital temperature recorder. Some representative temperature profiles are shown in Fig. 5. The difference between the radially and axially inserted thermocouples along the same cross section indicates the error due to the temperature gradient along the thermocouple length.

Fig. 6 shows a comparison of the measured error and that obtained from the analytical model. The figure shows the error at various locations (station (1) to station (6) as shown in Fig. 4). The symbols used i.e., circles, triangles, squares, etc., correspond to the temperature distributions in the specimen shown in Fig. 5. For the cases where the temperature gradient was nonlinear a third order polynomial was used in equation (4). The results indicate that the model is satisfactory. The corrected values are within ±1.5 percent of the true temperature while the maximum error due to conduction is ±5.5 percent. Deviation between the analytical results and the measured values may be due to two reasons. First the analysis is approximate and second the measured values themselves may be in error due to uncertainties in the location of the thermocouples and error in their output. An estimate of this error is up to ±1.5°C. It can be seen that the deviations are within this range.

Conclusion

This paper presents an analysis for estimating the error in the measurement of temperature of a solid body or a porous material due to conduction along the sensor leads. It considers the effect of an arbitrary temperature gradient along the embedded length of the sensor and also the conduction to the external surroundings. The analytical results are compared with some experimental measurements. The agreement between the measured and the calculated error is reasonably good.

It is recommended that whenever possible the probes be located along isothermal paths. But if the situation does not permit this then the results of the present analysis can be used to satisfactorily correct the measured data.

Acknowledgment

Financial support for this work was provided by National Aeronautics and Space Administration through grant number NGL-36-003-064.

References

1 Beck, J. V., "Thermocouple Temperature Disturbances in Low Conductivity Materials," JOURNAL OF HEAT TRANSFER, TRANS. ASME, Series C, Vol. 89, May 1962, p. 126.

2 Beck, J. V., and Hurwieg, H., "Effects of Thermocouple Cavity on Heat Sink Temperature," JOURNAL OF HEAT TRANSFER, TRANS. ASME, Series C., Vol. 82, 1960, pp. 27–36.

3 Turner, A. B., "Heat Transfer Instrumentation," *High Temperature Turbines*, Paper No. 5, AGARD Conference Proceedings No. 73.

4 Turner, A. B., "The Heat Transfer Characteristics of Transpiration Cooled Gas Turbine Blades," D. Phil. thesis, University of Sussex, June 1968.

5 Moffat, R. J., "Temperature Measurements in Solids: Errors Due to the Thermal Resistance Between the Thermocouple and the Specimen," *Proceedings Symposium on Advances in Test Measurements*. Vol. 5, No. 68-54. Pittsburgh, Pa.

6 Sparrow, E. M., "Error Estimates in Temperature Measurements," AGARDograph No. 130. *Measurement Techniques in Heat Transfer*, E. R. G. Eckert and R. J. Goldstein, eds., 1970, pp. 13–32.

7 Moffat, R. G., "Gas Temperature Measurement," *Temperature its Measurement and Control in Science and Industry*, Reinhold, N. Y., 1962, p. 553.

8 Rohsenow, W. M., and Choi, H., *Heat, Mass, and Momentum Transfer*. Prentice Hall, Chapter 6, 1961, p. 106.

9 Singh, B. S., and Dybbs, A., "Study of Nonisothermal Flow and Heat Transfer in Porous Media," Case Western Reserve University, Cleveland, Ohio, FTAS/TR-75-106, 1975.

L. K. Brumfield
T. G. Theofanous[1]

School of Chemical Engineering,
Purdue University,
West Lafayette, Ind.

On the Prediction of Heat Transfer Across Turbulent Liquid Films

The film hydrodynamics determined by Dukler and coworkers, together with standard heat transfer considerations, provide a coherent description of heat transfer across turbulent liquid films. Predictions are found to be in agreement with overall heat transfer measurements for nonsheared (falling) films. Qualitative features are deduced for heat transfer across sheared films.

Introduction

More than a decade ago, Wilke [1] measured and correlated heat transfer coefficients for falling, turbulent, liquid films (without vaporization). He determined a Reynolds number dependence to the 0.4 power. The same trend was recently established by Chun and Seban [2] for evaporating (by wall heating) falling, turbulent, liquid films. The latter investigators found Dukler's model [3] inadequate for predicting their data. Specifically, a discrepancy by a factor of two in the Reynolds number dependence was noted, with Dukler's prediction giving the lower value. Further, Chun and Seban made the important observation that "no conventional friction factor relationship" would produce the experimental trend. While the usual relation, $f/2 \propto \mathrm{Re}^{-0.25}$, gives the correct behavior for the "mean" film thickness, its substitution into the Colburn analogy gives a Reynolds number dependence which is also low by a factor of two.

A couple of approaches have been taken to rectify this situation. Both have been based on the empirical eddy diffusivity concept, but they have sought to modify the profile, away from the solid wall, in order to reproduce the experimental trends. Limberg [4] was guided by the data of Wilke, and he found it necessary to reduce the van Driest profile by the factor of $\exp\{-1.66y/\delta\}$ and to maintain the profile uniform beyond a distance 0.6δ from the wall. Mills and Chung [5], who examined the data of Chun and Seban, also chose the van Driest profile for the wall region. However, based on Levich's eddy-damping concept, they imposed a heat transfer resistance in the vicinity of the gas-liquid interface. For this, they chose the eddy diffusivity determined by Lamourelle and Sandall [6] from gas absorption experiments in falling films. The complete eddy diffusivity profile was then obtained by extending one profile from the wall and the other from the gas-liquid interface until they intersected.

Both approaches produced the correct Reynolds number exponent with these quite different choices of diffusivity distributions. Certain differences must arise between the corresponding physical mechanisms that presumably dictate these distributions. There is a distant "similarity," however, in that both stipulate "some form of damping" within "some distance from the free interface."

Different interpretations also exist for the case of sheared liquid films. Ueda, et al. [7] recently measured heat transfer coefficients for the film condensation of steam in vertical tubes, where interfacial shear was provided by cocurrent, high-velocity steam flow. They attempted to predict their data using the analysis of Rohsenow, et al. [8], in which the eddy diffusivity profile was determined from the universal velocity profile and extended all the way to the free interface. They obtained a reasonable order-of-magnitude agreement, but predicted heat transfer coefficients were somewhat greater than measured ones, especially at lower liquid Reynolds numbers. In attempting to refine their predictions, they used a two-layer eddy diffusivity model to back-calculate the laminar sublayer thickness from their heat transfer data and concluded that the turbulence level in the near-wall region was lower than that corresponding to single-phase, full-tube flow.

The purpose of the present paper is to offer an alternative point of view as a means for rationalizing this interesting behavior. Both nonsheared (falling) and sheared films will be considered.

Analysis

The approach here is similar to that recently utilized to model mass transfer (gas absorption) in turbulent falling films [9]. It is based on the recent experimental information on the physical structure of turbulent films. The heat transfer considerations which complete the model are quite standard.

The classical work of Brauer [10] and the more recent work of Telles and Dukler [11, 12], among others, have shown that the film structure consists essentially of two portions: a base-film portion flowing next to the wall and turbulent waves. The latter carry a significant fraction of the total flow and move over the base film with no change in speed or shape. As a wave moves at a much higher velocity than the base film, it continuously overtakes the fluid in the base film found in front of it and mixes with it as the base film loses its identity beneath the wave. An equivalent amount of fluid is continuously left behind and undergoes relaminarization to make up the laminar base film in back of the wave. The turbulent waves have an extremely large base-to-

[1] Also with the School of Nuclear Engineering.

[2] Numbers in brackets designate References at end of paper.

Contributed by the Heat Transfer Division for publication in the JOURNAL OF HEAT TRANSFER. Manuscript received by the Heat Transfer Division February 23, 1976. Paper No. 76-HT-EEE.

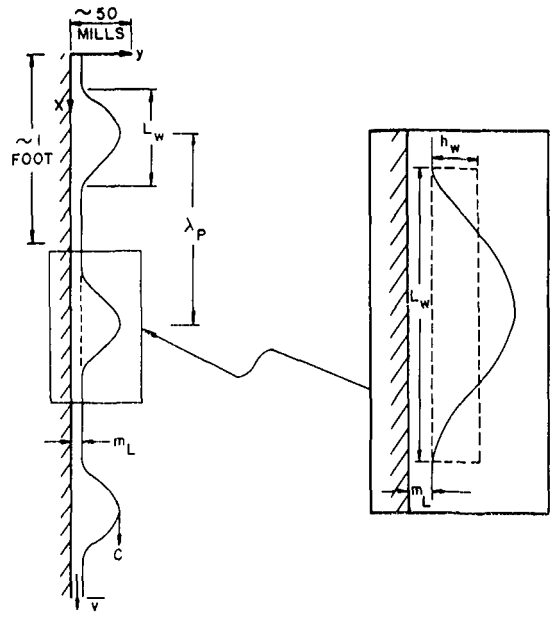

Fig. 1 Representation of thin film according to average wave analysis of Telles and Dukler [12]

height ratio, move independently of each other, and may better be envisioned as solitary segments of thicker turbulent films. Brauer was the first to illustrate this structure (by means of shadowgraphs), and he also provided the first quantitative information on the statistical characteristics of these waves. Telles and Dukler provided a useful characterization of the whole large-wave structure by means of a periodic average wave idealization, as illustrated in Fig. 1. They determined the parameters which characterize this structure for liquid Reynolds numbers up to about 6000 and for gas Reynolds numbers, from 0 to 57,600. Details of their analysis, which was based on representing the large-wave shape by a truncated Gram-Charlier series,

$$m(x) = m_L + \frac{1}{\sqrt{2\pi}} \exp\left[-\frac{1}{2}\left(\frac{x}{X}\right)^2\right]\left[m_0 - m_1\left(\frac{x}{X}\right)\right] \quad (1)$$

have been summarized in [12]. In a related study, Chu [13] also determined average-wave parameters, but only for nonsheared films.

It has been traditional to assess turbulence in falling films in an overall fashion. For a total-film Reynolds number in the turbulent range (Re $\gtrsim$ 1000), however, the dual structure discussed in the foregoing makes it possible to have a laminar base film and turbulent waves. In particular, this is the case for nonsheared films up to a total-film Reynolds number of at least 6000. For flow at very large total-film Reynolds numbers, it appears possible that both waves *and* base film can be in turbulent motion. In the absence of direct information on this subject, we have taken the transition point at a *local* (base-film or wave) Reynolds number of 2000. The base-film and wave Reynolds numbers may be easily calculated from a knowledge of the overall flow rate and the film-structure parameters (as specified by equations (A.7) and (A.8), and equation (9), respectively).

For the base film, when laminar, the heat transfer is determined by steady-state conduction, $q = k(\Delta T/m_L)$, giving

$$h_c = \frac{k}{m_L} \quad (2)$$

For the turbulent waves (or base film when applicable), heat transfer is controlled by the wall region. Any eddy-diffusivity profile accurate in the near-wall region will be adequate. So will an analogy between heat and momentum transfer for the high Reynolds-number range. Here the van Driest profile

$$\frac{\epsilon_M}{\nu} = \frac{1}{2}\{1 + 0.64y^{+2}[1 - \exp(-y^+/26)]^2\}^{1/2} - \frac{1}{2} \quad (3)$$

was chosen and extended all the way up to the free interface. The heat flux, which is approximately uniform across the wave, is given by

$$q = \rho C_p(\alpha + \epsilon_H)\frac{dT}{dy} = h_c \Delta T \quad (4)$$

Integration of this equation over the wave thickness, $H = m_L + h_w$, or the base film thickness, m_L, when applicable, gives the expression for the heat transfer coefficient

$$h_c = \frac{\rho C_p}{\displaystyle\int_0^H \frac{dy}{\alpha + \epsilon_H}} = \frac{\rho C_p V_*}{F(H^+)} \quad (5)$$

where

$$F(H^+) = \int_0^{H^+} \frac{dy^+}{\dfrac{1}{\mathrm{Pr}} + \dfrac{(\epsilon_M/\nu)}{\mathrm{Pr}_t}} \quad \text{and} \quad H^+ = \frac{HV_*}{\nu}$$

The turbulent Prandtl number, Pr_t, was taken to be 0.9, in accordance with recent boundary-layer practice. For a given H^+ and τ_i the shear velocity, V_*, is found from

$$V_*^3 - \frac{\tau_i}{\rho} V_* - g\nu H^+ = 0 \quad (6)$$

Figs. 2 and 3 show results calculated from equation (5) for water. These figures will be used in predicting heat-transfer coefficients for the experiments of Chun and Seban [2] and Ueda, et al. [7].

The overall, fully developed, heat transfer coefficient for the film

Nomenclature

C = wave celerity
C_p = specific heat capacity
g = gravitational acceleration
$\langle h \rangle$ = mean film thickness
$H = m_L + h_w$, mean height of wave above wall
$H^+ = HV_*/\nu$
h_c = heat transfer coefficient
$h_{\max}$ = height at the wave crest
h_w = mean height of wave above base film
k = thermal conductivity
L_w = base length of "average wave"
m = average wave profile, equation (1)
m_0, m_1 = parameters of average wave profile, equation (1)
m_L = base-film thickness in average wave representation
$\mathrm{Pr} = C_p\mu/k$, Prandtl number
Pr_t = turbulent Prandtl number
q = heat flux
Q = volumetric flow rate per unit width of wall
$\mathrm{Re} = 4Q/\nu$, Reynolds number
T = temperature
V_* = shear velocity, equation (6)
X = characteristic base dimension of average wave, equation (1)
x, y = cartesian coordinates, Fig. 1
$y^+ = yV_*/\nu$
$\alpha = k/\rho C_p$, thermal diffusivity
δ = mean film thickness
ϵ_H = eddy diffusivity for heat transfer
ϵ_M = eddy diffusivity for momentum transfer
λ_p = average wave separation distance
μ = molecular viscosity
$\nu = \mu/\rho$, kinematic viscosity
ρ = density
τ_i = interfacial shear stress
$\tau_i^* = \tau_i(g/\nu^2)^{1/3}/\rho g$

Subscripts

f = base film
w = wave

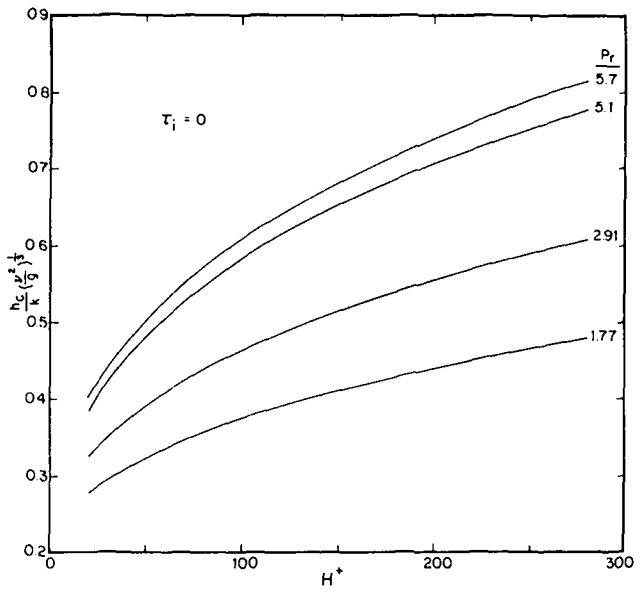

Fig. 2 Dimensionless heat transfer coefficient for turbulent wave with no interfacial shear. Results calculated from equation (5). Pr values correspond to experiments of Chun and Seban [2]

as illustrated in Fig. 1, then, is given by the following area average:

$$h_c = \left(1 - \frac{L_w}{\lambda_p}\right) h_{c,f} + \left(\frac{L_w}{\lambda_p}\right) \frac{\rho C_p V_*}{F(H^+)} \tag{7}$$

where the heat transfer coefficient for the base film, $h_{c,f}$, is given by equation (2) when the base film is laminar and by equation (5) (with $H = m_f$) when the base film is turbulent. Values of L_w, the wave base length, were obtained from plots of equation (1). Fig. 4 shows the Reynolds number dependence of L_w/λ_p, the fractional area occupied by the average wave.

The above heat transfer calculations for the wave and base film have neglected any transient processes. These, in principle, may be of two types: one occurring as the wave front overtakes the base film, and the other occurring as the base film is left behind at the rear of the wave. However, since the base length of the turbulent wave is large compared to its thickness, typically a ratio of 100, the turbulence structure over the major portion of the wave should be described well by the van Driest eddy diffusivity profile (i.e., the turbulent wave may be envisioned as a solitary segment of a thicker turbulent film). The length-to-height ratios for the base film are even greater. One would expect, then, that these "entrance" and "exit" transient effects would not be very important for the heat transfer cases considered here. For the case of a heated film (by constant wall temperature, for example), however, bulk temperatures of individual large waves and base-film segments will increase in the mean-flow direction. The overall heat transfer coefficient will then depend on the way in which local individual base-film and wave bulk temperatures are altered by the mixing between the base film and wave. This heat transfer case is somewhat analogous to that of gas absorption by films previously analyzed in [9], and a similar analysis could be used.

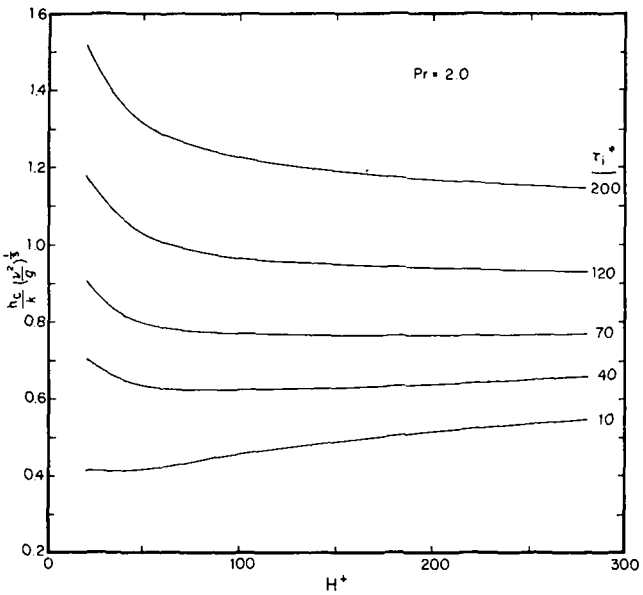

Fig. 3 Dimensionless heat transfer coefficient for turbulent wave (or turbulent base film) with interfacial shear. Results calculated from equation (5). Pr and τ_i^* values correspond to experiments of Ueda, et al. [7]

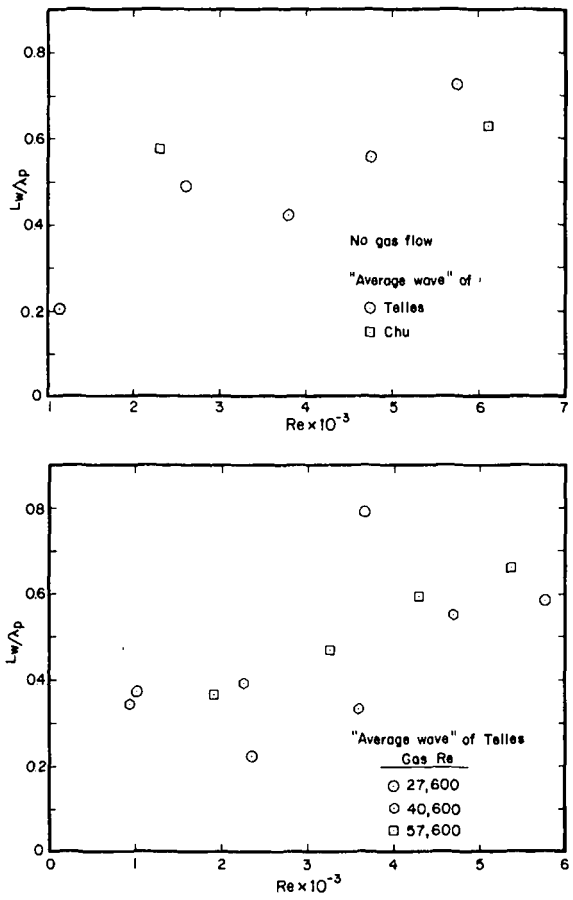

Fig. 4 Reynolds number dependence of L_w/λ_p, the fractional area occupied by the average wave

Results

Flow With no Interfacial Shear. Predicted overall heat transfer coefficients for falling films are shown in Fig. 5 for the Reynolds numbers (and temperature) for which Telles determined average wave parameters. Predictions based on Chu's average wave data are also shown. The Chun-Seban experimental data for these conditions (Pr ~ 5.7) are represented by the solid line, which is described by their empirical relation

$$\frac{h_c}{k}\left(\frac{\nu^2}{g}\right)^{1/3} = 3.8 \times 10^{-3}\,\mathrm{Pr}^{0.65}\,\mathrm{Re}^{0.4} \tag{8}$$

It may be seen that the fluid-mechanical structure of the film and its

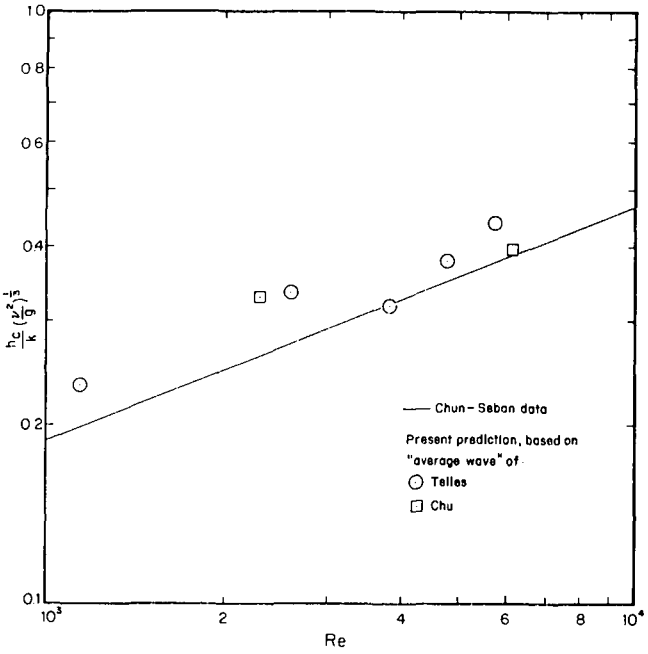

Fig. 5 Comparison between predicted (equation (7)) and measured overall heat transfer coefficients for falling films—Pr = 5.7

variation with the total-film Reynolds number can yield the experimentally observed sensitivity. Furthermore, a good absolute estimate (~15 percent, on the average, too high) of the heat transfer coefficient is also obtained.

For these calculations, the variation of the turbulent-wave thickness over the base length was ignored, and the wave was treated as having a constant thickness of $(m_L + h_w)$. To check the effect of this approximation, wave base widths were divided into ten equal segments, and local coefficients for each segment (based on the average film thickness over that segment) were averaged to give the overall coefficient for the wave. The difference between the results of the two methods was not significant. No data for the film-structure parameters are available for temperatures corresponding to the other Prandtl numbers considered by Chun and Seban. Heat transfer predictions were not carried out for these cases, due to the uncertainties involved in predicting the temperature dependence of the average wave parameters.

The basis of the heat transfer calculations is summarized and clarified in Table 1 for Telles' average wave representation. Here, wave Reynolds numbers were calculated from the knowledge of the base-film thickness (from which Re_f can be calculated) and the total-film Reynolds number:

$$\mathrm{Re}_w = \frac{\mathrm{Re} - (1 - L_w/\lambda_p)\mathrm{Re}_f}{L_w/\lambda_p} \tag{9}$$

A check on the internal consistency of the fluid mechanical representation is provided by an independent estimate of Re_w provided by $4HC/\nu$ (i.e., the waves move with celerity C). The agreement between the Re_w and $4HC/\nu$ values in Table 1 is felt to be very good.

Flow With Interfacial Shear. The shear-flow data of Ueda, et al. [7] were obtained for Pr ~ 2.0, but average wave parameters are available for only Pr ~ 5.7. As mentioned earlier, there is no firm basis for predicting the average wave parameters for temperatures corresponding to different Prandtl numbers. However, we would expect that the heat transfer results for sheared films would not be as sensitive to the details of the flow structure, especially if both the base film and waves were in turbulent motion. It is, therefore, felt worth the effort to attempt the prediction by grossly scaling Telles' data to the temperature conditions of Ueda, et al. With a change in temperature, the pertinent film-structure parameters (L_w/λ_p, H, and m_L) can be influenced only by changes in temperature-dependent fluid properties (density, viscosity, and surface tension). Dimensional analysis provides scaling relations. Details are given in Appendix A.

Interfacial shear stresses were calculated from the pressure-drop data of Telles and used in conjunction with the corresponding average wave parameters to predict heat transfer coefficients for the experimental conditions (Pr ~ 2.0) of Ueda, et al. The predictions are compared with the experimental results in Fig. 6. A direct comparison between the predictions and the data is not possible in all cases, since the τ_i^* values for Telles' experiments do not exactly correspond to those of Ueda, et al. However, the predictions for $\tau_i^* = 8$ and 11 in Fig. 6(*a*) and those for $\tau_i^* = 37$ and 43 in Fig. 6(*b*) are seen to be in reasonable agreement with the magnitude of the experimental data. For the conditions indicated in Fig. 6, calculated base-film Reynolds numbers were in the range 300–1800, and base-film heat transfer was calculated assuming laminar flow. Wave Reynolds numbers, calculated from equation (9), were in the range 2200–8700, indicating turbulent flow for this portion of the film. The pertinent calculations and results are summarized in Table 2.

Discussion

Flow With no Interfacial Shear. It should be pointed out that Chu's average wave profiles are somewhat different from those of Telles. While the results of both investigators show increasing maximum wave height, substrate thickness, and base length with increasing liquid Reynolds number, Chu's profiles are characterized by a pronounced minimum in the film thickness at the wave front. Telles' profiles are more symmetrical and show a negligible minimum at the wave front. These differences are probably due to geometry effects and/or different schemes for calculating the Gram-Charlier coefficients for the wave profile. Chu's data were obtained in a 2 in. OD tube, 13.7 ft from the inlet, while those of Telles were taken in a rectangular channel, 6 × 0.75 in., 12 and 13 ft from the inlet. In spite of these differences, however, Chu's experimental values of modal frequency, wave celerity, and mean film thickness are in good agreement with

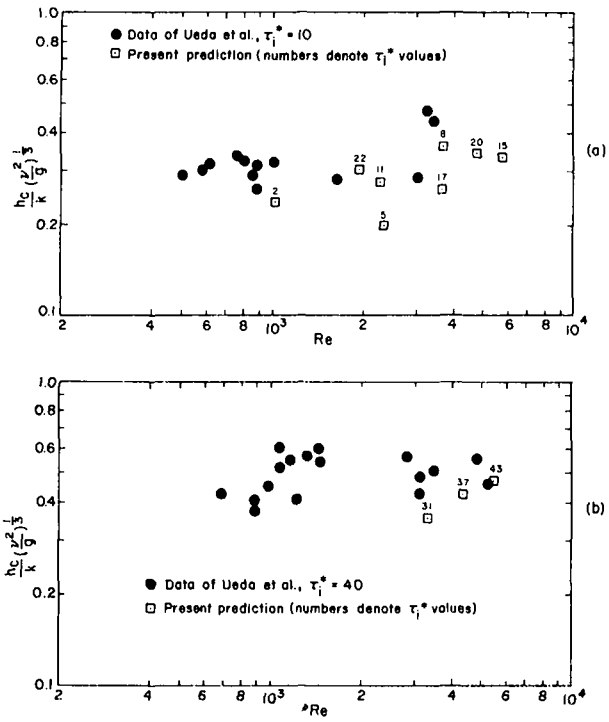

Fig. 6 Comparison between predicted (equation (7)) and measured overall heat transfer coefficients for films with interfacial shear. Predictions based on Telles' average wave—Pr = 2.0

Table 1 Heat transfer calculations for falling films using Telles' average wave representation [12]—Pr = 5.7

Re	m_L,cm	Re_f	$\frac{h_{c,f}}{k}\left(\frac{\nu^2}{g}\right)^{1/3}$	L_w,cm	λ_p,cm	H,cm	Re_w	$\frac{h_{c,w}}{k}\left(\frac{\nu^2}{g}\right)^{1/3}$	$\frac{h}{k}\left(\frac{\nu^2}{g}\right)^{1/3}$	C,cm/sec	$\frac{4HC}{\nu}$
1150	.0231	215	.179	8.99	44.2	.0420	4810	.447	.234	137	2760
2600	.0287	385	.144	24.6	50.3	.0632	4910	.529	.333	171	5180
3800	.0340	580	.122	22.6	53.6	.0803	8240	.582	.315	201	7750
4750	.0356	650	.116	32.3	57.9	.0800	8000	.581	.376	226	8660
5750	.0356	650	.116	44.2	61.0	.0787	7680	.558	.437	250	9430

m_L, λ_p, and C given in reference [12]

Re_f calculated from equations (A.7) and (A.8)

L_w obtained from graphical examination of equation (1)

$H = \int m(x)\,dx/L_w$, where integration limits extend over the wave base length

Re_w calculated from equation (9)

Local and overall heat transfer coefficients calculated as described in "Analysis" section

Table 2 Heat transfer calculations for sheared films using Telles' average wave representation [12] and analysis in Appendix A—Pr = 2.0

Gas Re	Re	m_L',cm	H',cm	L_w',cm	λ_p',cm	m_L,cm	Re_f	$\frac{h_{c,f}}{k}\left(\frac{\nu^2}{g}\right)^{1/3}$	L_w/λ_p	H,cm	Re_w	$\frac{h_{c,w}}{k}\left(\frac{\nu^2}{g}\right)^{1/3}$	$\frac{h_c}{k}\left(\frac{\nu^2}{g}\right)^{1/3}$,
27,600	1020	.0224	.0367	14.9	40.2	.0121	300	.185	.371	.0198	2240	.326	.238
	2350	.0290	.0638	9.45	42.7	.0157	690	.143	.221	.0345	8190	.403	.201
	3650	.0254	.0504	35.1	44.2	.0137	680	.163	.793	.0272	4430	.411	.360
	5750	.0345	.0683	26.5	45.4	.0187	1580	.120	.584	.0369	8720	.487	.334
40,600	935	.0229	.0350	14.6	42.1	.0124	475	.181	.348	.0189	1800	----*	----*
	2250	.0234	.0465	15.8	40.5	.0126	670	.177	.391	.0251	4710	.429	.276
	3600	.0279	.0585	13.1	39.3	.0151	1160	.148	.333	.0316	8480	.485	.260
	4700	.0279	.0542	21.3	38.7	.0151	1280	.148	.551	.0293	7480	.504	.344
57,600	1920	.0229	.0364	10.7	29.0	.0124	1020	.181	.368	.0197	3460	.515	.304
	3270	.0244	.0414	14.0	29.7	.0132	1360	.170	.472	.0224	5410	.572	.360
	4300	.0250	.0419	18.0	30.2	.0135	1620	.165	.596	.0227	6120	.611	.431
	5350	.0260	.0447	20.1	30.5	.0141	1830	.159	.660	.0242	7160	.639	.476

Primes denote values at Pr=5.7; otherwise, Pr=2.0

m_L' and λ_p' given in reference [12]

L_w' obtained from graphical examination of equation (1)

$H' = \int m'(x)\,dx/L_w'$, where integration limits extend over the wave base length

H, m_L, and L_w/λ_p calculated from equations (A.1), (A.2), and (A.3), respectively

Re_f calculated from equations (A.7) and (A.8)

Re_w calculated from equation (9)

Local and overall heat transfer coefficients calculated as described in "Analysis" section

*"Average wave" representation is not detailed enough for accurate calculation of $h_{c,w}$ for low total-film Reynolds numbers (i.e., where $Re_w \lesssim 2{,}000$) -- large-wave amplitude distribution information is required. See "Discussion" section.

those of Telles. Telles based his calculation of the Gram-Charlier coefficients for the wave shape on the second and third central moments of the film thickness, while Chu employed the autocorrelation. The effect of these differences in the average wave on the local heat transfer coefficients is small, as may be seen from Fig. 7. In addition, it is seen that at higher Reynolds numbers, the heat transfer coefficient for the turbulent-wave portion is about five times that for the substrate. Also, from Fig. 7 it may be seen that the Reynolds number dependence for each heat transfer coefficient is small for Re $\gtrsim$ 3000. As the total-film Reynolds number increases, the fractional area occupied by the wave (Fig. 4) increases, and the turbulent contribution to the overall heat transfer coefficient (second term of equation (7)) increases from about 40 percent of the total for Re $\sim$ 1000 to about 90 percent of the total for Re $\sim$ 6000. It is this interaction between the variables of Figs. 4 and 7 that results in the sensitivity for the overall heat transfer coefficient shown in Fig. 5. The reduction of the overall heat transfer coefficient due to the laminar heat transfer in the base film provides for the kind of additional resistance that was supplied as an interfacial resistance in the models of Mills and Chung [5] and Limberg [4].

A more detailed picture of the thin-film structure has recently been provided by Chu and Dukler [13–15], who extracted the statistics of the base film and the large waves from a time-series analysis of the film thickness. Their results suggest the existence of several discrete large-wave sizes for Re $\gtrsim$ 750. To assess the effect on the overall heat transfer prediction, calculations were carried out based on the experimental large-wave amplitude histograms of Chu [13]. (Some of the probability densities are shown in Fig. 8 of [15].) Contributions from large waves of *all* different sizes in the flow were thus included in the predicted overall heat transfer coefficient. The details are presented in Appendix B. Predicted results are shown in Fig. 8 for the Reynolds numbers for which Chu provided histogram information. The Chun-Seban experimental data are represented by the solid line, which is described by equation (8) for Re $\gtrsim$ 1000 and by their empirical relation

$$\frac{h_c}{k}\left(\frac{\nu^2}{g}\right)^{1/3} = 0.606(\mathrm{Re}/4)^{-0.22} \qquad (10)$$

for Re $\lesssim$ 1000. Agreement between predicted and measured values is good.

It is informative to compare film-structure parameters determined from the average wave representation with those obtained from the time-series analysis. Wave amplitudes determined by each method are in reasonable agreement. Values of base-film thickness determined from the average wave analyses of both Telles and Chu are somewhat greater than corresponding mean substrate-thickness values obtained from the time-series analysis. Also, modal frequencies, which characterize the average wave, are about one-half the mean large-wave frequencies reported by Chu and Dukler; and wave base-length values for the average wave are greater than the mean values determined from the time-series analysis. These apparent discrepancies, however, are easily resolved. In the time-series analysis, the large-wave criterion is based, somewhat arbitrarily, on $h_{max} > \langle h \rangle$. However, Chu [13] reports that time-series analyses based on a large-wave criterion of $h_{max} > 2\langle h \rangle$ give mean wave frequencies in reasonable agreement with the modal frequencies. In short, in the average wave analysis, smaller waves are lumped into the base film, while in the time-series analysis, they are considered to be part of the "large-wave" structure. For the present heat transfer calculations, the application of the *local* transition criterion (base-film or wave Reynolds number of 2000) has the effect of equalizing both film-structure representations. For example, examination of wave Reynolds numbers calculated from Chu's large-wave histogram data indicates that for $600 \lesssim Re \lesssim 3000$, some large waves are in turbulent flow while some are in laminar flow. For the purposes of heat transfer, then, these smaller large waves ($Re_w \lesssim 2000$) are relegated to the laminar portion of the film, and compatibility with the average wave representation is achieved. For $Re \gtrsim 3000$, Re_w calculations indicate that all large waves are in turbulent flow. Since the turbulent heat transfer coefficient is not extremely sensitive to wave height (Fig. 2) over the ranges encompassed by the histograms, heat transfer predictions based on the average wave structure are reasonably accurate. For low total-film Reynolds numbers, where the majority (or all) of the large waves are in laminar flow, the average wave representation cannot be expected to give as accurate an estimate of the heat transfer, due to the greater sensitivity to wave-height variations ($h_c \propto 1/H$).

Flow With Interfacial Shear. One interesting aspect of the calculations presented here for heat transfer across sheared films concerns the scaling of the film-structure parameters from Pr = 5.7, at which they were measured, to Pr = 2.0, at which the comparison is made with the data of Ueda, et al. [7]. For given Re and τ_i^* values, equations (A.4) and (A.5) indicate that both the base-film thickness and the mean height of the average wave are reduced by about 50 percent as Pr changes from 5.7 to 2.0. In addition, calculations show that the individual Reynolds numbers for the base-film and wave portions remain constant. No direct information is available concerning the effect of surface tension variations on the film-structure parameters. However, since surface tension decreases by only 15 percent as Pr changes from 5.7 to 2.0, its influence was neglected in the scaling procedure. This approximation would undoubtedly be more correct for sheared films than for nonsheared (falling) films. The calculations show that for Telles' shear-flow conditions the heat transfer coefficient for the turbulent-wave portion ranges from 2 to 4 times greater than that for the laminar base-film portion. The turbulent contribution to the overall heat transfer coefficient (second term of equation (7)) ranges from about 45–90 percent of the total.

The heat transfer results for this case are on a much less firm basis than those for the falling-film case, since speculations had to be made about the variation of film-structure parameters with temperature. This variation is undoubtedly complex, and the approach described in Appendix A can be expected to yield only qualitative trends. The important points of the analysis, however, are summarized in the next paragraph and follow readily from qualitative considerations.

It is to be expected that at large total-film Reynolds numbers and at greater τ_i^* values than considered here, both waves *and* base film will be in turbulent motion. (Observe the trend of Re_f with liquid- and gas-phase Re in Table 2.) For this case, the calculations (Fig. 3) show that the heat transfer coefficients for the wave and substrate will be essentially equal and, furthermore, independent of film thickness over a wide range. As a result, the overall heat transfer coefficient becomes insensitive to the finer features of the flow, allowing engineering estimates to be made without recourse to the dual-film structure. For this reason, Ueda's heat transfer prediction based on Rohsenow's eddy diffusivity analysis (applied over the "mean" film thickness) gives good agreement with the experimental data only at higher values of Re and τ_i^*. For lower values, where the base film is in laminar flow, the dual-film structure of the flow must be considered in calculating overall heat transfer rates.

Conclusions

An alternative way of describing heat transfer across turbulent films (with and without interfacial shear) has been presented. The proposed model, which couples standard heat transfer concepts with the essential hydrodynamic features of the film-flow structure, predicts overall heat transfer coefficients which are in reasonable agreement with both the order-of-magnitude and trend of the experimental data.

Acknowledgment

This work was supported by NSF Grant No. 7521700.

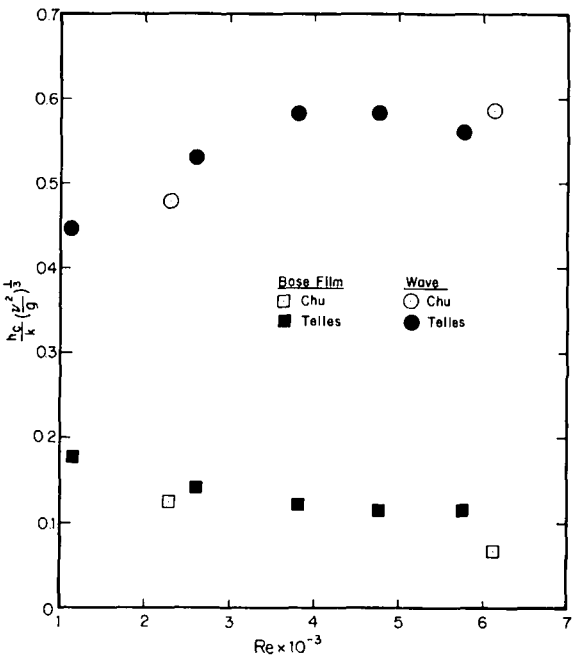

Fig. 7 Heat transfer coefficients for laminar base film and turbulent wave calculated from equations (2) and (6), respectively—τ_I = 0, Pr = 5.7

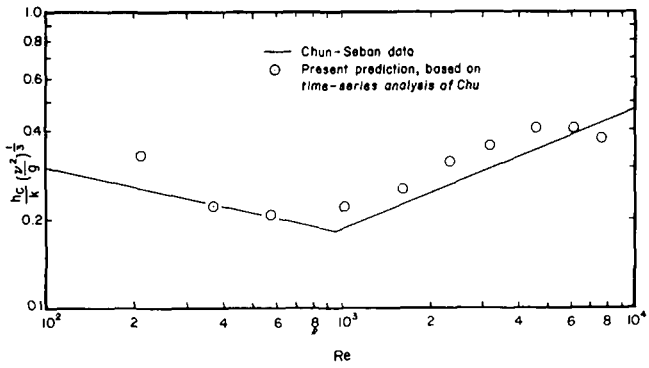

Fig. 8 Comparison between predicted (equation (B.1)) and measured overall heat transfer coefficients for falling films—Pr = 5.7

References

1 Wilke, W., "Warmeubergang an Rieselfilme," *ForschHft. Ver. Dt. Ing.*, Vol. 490, 1962.

2 Chun, K. R., and Seban, R. A., "Heat Transfer to Evaporating Liquid Films," JOURNAL OF HEAT TRANSFER, TRANS. ASME, Series C, Vol. 93, 1971, pp. 391–396.

3 Dukler, A. E., "Fluid Mechanics and Heat Transfer in Vertical Falling-Film Systems," *Chem. Engng. Prog. Symp. Ser.*, Vol. 56, 1960, pp. 1–10.

4 Limberg, H., "Warmeubergang an Turbulente und Laminare Rieselfilme," *International Journal of Heat and Mass Transfer*, Vol. 16, 1973, pp. 1691–1702.

5 Mills, A. F., and Chung, D. K., "Heat Transfer Across Turbulent Falling Films," *International Journal of Heat and Mass Transfer*, Vol. 16, 1973, pp. 694–696.

6 Lamourelle, A. P., and Sandall, O. C., "Gas Absorption Into a Turbulent Liquid," *Chem. Engng. Sci.*, Vol. 27, 1972, pp. 1035–1043.

7 Ueda, T., Kubo, T., and Inoue, M., "Heat Transfer for Steam Condensing Inside a Vertical Tube," *Proceedings of the Fifth International Heat Transfer Conference*, Tokyo, Vol. 3, 1974, pp. 304–308.

8 Rohsenow, W. M., Webber, J. H., and Ling, A. T., "Effect of Vapor Velocity on Laminar and Turbulent-Film Condensation," TRANS. ASME, Vol. 78, 1956, pp. 1637–1643.

9 Brumfield, L. K., Houze, R. N., and Theofanous, T. G., "Turbulent Mass Transfer at Free, Gas-Liquid Interfaces, With Applications to Film Flows," *International Journal of Heat and Mass Transfer*, Vol. 18, 1975, pp. 1077–1081.

10 Brauer, H., "Stromung und-Warmeubergang bei Rieselfilmen," *ForschHft. Ver. Dt. Ing.*, Vol. 457, 1956.

11 Telles, A. S., "Liquid Film Characteristics in Vertical Two-Phase Flow," PhD thesis, University of Houston, Texas, 1968.

12 Telles, A. S., and Dukler, A. E., "Statistical Characteristics of Thin, Vertical, Wavy, Liquid Films," *I/EC Fundamentals*, Vol. 9, 1970, pp. 412–421.

13 Chu, K. J., "Statistical Characterization and Modelling of Wavy Liquid Film in Vertical Two-Phase Flow," PhD thesis, University of Houston, Texas, 1973.

14 Chu, K. J., and Dukler, A. E., "Statistical Characteristics of Thin, Wavy Films: Part II. Studies of the Substrate and Its Wave Structure," *AIChE Journal*, Vol. 20, 1974, pp. 695–706.

15 Chu, K. J., and Dukler, A. E., "Statistical Characteristics of Thin, Wavy Films: Part III. Structure of the Large Waves and Their Resistance to Gas Flow," *AIChE Journal*, Vol. 21, 1975, pp. 583–593.

APPENDIX A

Variation of Film-Structure Parameters With Temperature. On assuming that the film-structure parameters depend on the operating variables Q and τ_i, the physical properties ρ, μ, and σ, and gravitational acceleration, g, dimensional analysis yeilds

$$H(g/\nu^2)^{1/3} = \Phi_1(\mathrm{Re}, \tau_i^*, Ka) \tag{A.1}$$

$$m_L(g/\nu^2)^{1/3} = \Phi_2(\mathrm{Re}, \tau_i^*, Ka) \tag{A.2}$$

$$L_w/\lambda_p = \Phi_3(\mathrm{Re}, \tau_i^*, Ka) \tag{A.3}$$

where the Φ's are unknown functions. Here σ is surface tension, and $Ka = \mu^4 g/\rho\sigma^3$, the Kapitza number. In the present calculations, the dependence on Ka (i.e., surface tension) will be neglected. If the temperature is changed from T' (where film-structure parameters are assumed known) to T while Re and τ_i^* are held constant, then

$$H \sim H'(\nu/\nu')^{2/3} \tag{A.4}$$

$$m_L \sim m_L'(\nu/\nu')^{2/3} \tag{A.5}$$

$$(L_w/\lambda_p) \sim (L_w/\lambda_p)' \tag{A.6}$$

where the prime denotes values at temperature T'. The film Reynolds number at temperature T, Re_f, may be determined from the knowledge of m_L. For large base-film Reynolds numbers ($\mathrm{Re}_f \gtrsim 2000$), the relation resulting from the definition of eddy diffusivity, $\tau = \rho(\nu + \epsilon_M)dU/dy$, is adequate:

$$\mathrm{Re}_f = \frac{4}{\nu}\int_0^{m_L} U(y)dy \tag{A.7}$$

where

$$U(y) = \int_0^y \frac{\tau_w - \rho g y}{\rho(\nu + \epsilon_M)}dy \tag{A.8}$$

where τ_w is the shear stress at the wall. For low Re_f values, results calculated from equation (A.7) were also in good agreement with results based on the laminar flow equation. Thus, equation (A.7) was applied for all values of m_L to determine Re_f. Depending on the value of Re_f, heat transfer across the base film at temperature T may be calculated using either the laminar or turbulent flow equations given in the paper.

APPENDIX B

Heat Transfer Calculations Based on Time-Series Analysis Data. Here, the heat transfer considerations discussed in the "Analysis" section are applied locally to each component wave in the large-wave amplitude histogram. On assuming, for a given Reynolds number, that all large waves are geometrically similar in shape (i.e., wave base length $\propto$ wave amplitude) and move with the same velocity, C, it follows that

$$h_c = F_s\frac{k}{\langle h_s\rangle} + (1 - F_s)\frac{\sum_{j=1}^{N} N_j A_j (h_{c,w})_j}{\sum_{j=1}^{N} N_j A_j} \tag{B.1}$$

where the local heat transfer coefficients for the waves are given by

$$(h_{c,w})_j = \begin{cases} \dfrac{k}{H_j} & \text{for } \mathrm{Re}_{w,j} \le 2000 \\ \dfrac{\rho C_p V_{*,j}}{F(H_j^+)} & \text{for } \mathrm{Re}_{w,j} > 2000 \end{cases} \tag{B.2}$$

Here, the subscript j refers to the large waves in the jth amplitude interval. N is the total number of amplitude intervals. N_j is the number of large waves in the jth amplitude interval. F_s is the fractional time of exposure of the substrate, and $\langle h_s\rangle$ is the mean substrate thickness (both terms defined as in [14]). A is the amplitude of the large waves (Fig. 3 of [15]). Examination of Chu's [13] average wave shapes showed that $h_w = 0.92\,A$, a relation independent of Re over the entire range ($200 \lesssim \mathrm{Re} \lesssim 6100$). This result was close to that calculated from Telles' [11] average wave shapes, $h_w = 0.78A$ for $1100 \lesssim \mathrm{Re} \lesssim 5800$. Thus, in equation (B.2), H_j was calculated as

$$H_j \simeq \langle h_{\max}\rangle - 2\langle A\rangle + h_{w,j} \tag{B.3}$$

where $h_{w,j} = 0.92A_j$ (refer to Fig. 3 of [15]). From this equation, the expected value of the mean large-wave height is $\langle H\rangle \simeq \langle h_{\max}\rangle - 1.08\langle A\rangle$. A plot of Re_w (calculated from equation (9)) versus $4\langle H\rangle C/\nu$ showed that for $\mathrm{Re}_w = 2000$, $4\langle H\rangle C/\nu \simeq 3500$. Thus, in carrying out the calculations indicated in equation (B.2), the transition criterion, $4H_jC/\nu = 3500$, was employed. The calculations show that the overall heat transfer predictions are relatively insensitive to the choice of the transition-criterion value.

S. Aiba
Asst. Professor.

Y. Yamazaki
Research Assistant.

Department of Mechanical Engineering,
Akita Technical College,
Akita, Japan

An Experimental Investigation of Heat Transfer Around A Tube in A Bank

An experimental investigation of heat transfer and flow around the second cylinder of three cylinders in cross flow of air was conducted. The cylinders were situated in tandem at equal distances between centers. Their in-line pitch ratio was in the range 1.3 ≦ c/d ≦ 5.0 (c = center-to-center distance; d = diameter); the Reynolds number was 40000.

Heat transfer results indicate a strong dependence on the difference between the maximum static pressure on the surface and the static pressure at the front stagnation point of the second cylinder. The maximum local heat transfer around the second cylinder occurs at the position where the free vortex layer (free shear layer) shed from the first cylinder attaches. However, the turbulence intensity near the wall at this same position is lower than that at other angular positions.

Introduction

Although a large number of studies on heat transfer and flow have been devoted to a single cylinder or tube banks placed traversely in a stream [1, 2],[1] there have been relatively few investigations of the detailed correlation between the flow and heat transfer around a tube in a horizontal bank.

Even for a single cylinder, a clear explanation of the mechanism of heat transfer in its wake region has not been provided. This is mainly due to the basic lack of understanding of the flow structure in the wake region (because of the unsteady and nonpotential character of the flow in it) and also due to discrepancies among the experimental data reported by a number of authors.

Van der Hegge Zijnen [3] reported that the turbulence intensity and the macroscale of turbulence of the mainstream have an important influence on the heat transfer for a single cylinder. It is also likely that the heat transfer around a tube in a bank will be influenced by these factors.

Recently, Igarashi and Hirata [4] proposed a new model for prediction of the heat transfer in the separated flow region behind bluff bodies. In their model, a flow component induced by the pressure gradient normal to the surface is assumed to exist and to be capable of transporting heat by convection. The centripetal force acting toward the center of Kármán vortices formed behind the object, which is equivalent to the magnitude of the pressure gradient, acts as a body force on infinitesimal fluid elements near the heating surface.

It is well known that the flow and heat transfer around a tube in the first row in a bank are similar to those around a single cylinder [2].

Kostić and Oka [5] have carried out interesting investigations of the flow and heat transfer in the case of two aligned cylinders in cross flow. However, in their experiments the distributions of the velocity and the turbulence intensity around cylinders have not been measured, so that the heat transfer mechanism or the detailed correlation between heat transfer and flow has not been sufficiently well organized.

The purpose of the present paper was to obtain basic data on heat transfer in a tube bank and to investigate the characteristics of heat transfer mechanism in the turbulent wake region. As a first step, the heat transfer and flow around the second cylinder of three cylinders placed at equal intervals in cross flow of air have been studied varying the distance between cylinders in the range of c/d from 1.3 to 5.0.

Experimental Apparatus and Procedures

Experiments were carried out in an open circuit wind tunnel whose test section is a rectangle 225 mm wide and 325 mm high. Most measurements were made at a Reynolds number (based on d) of 40000; the turbulence intensity of the main flow $\sqrt{\overline{u'^2}}/U_\infty$ was about 0.7

[1] Numbers in brackets designate References at end of paper.

Contributed by the Heat Transfer Division for publication in the JOURNAL OF HEAT TRANSFER. Manuscript received by the Heat Transfer Division January 26, 1976. Paper No. 76-HT-AAA.

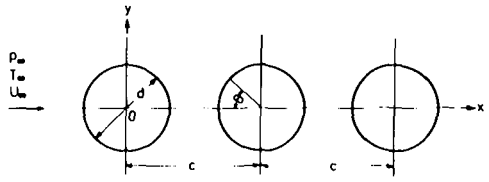

Fig. 1 Arrangement of cylinders and coordinate system

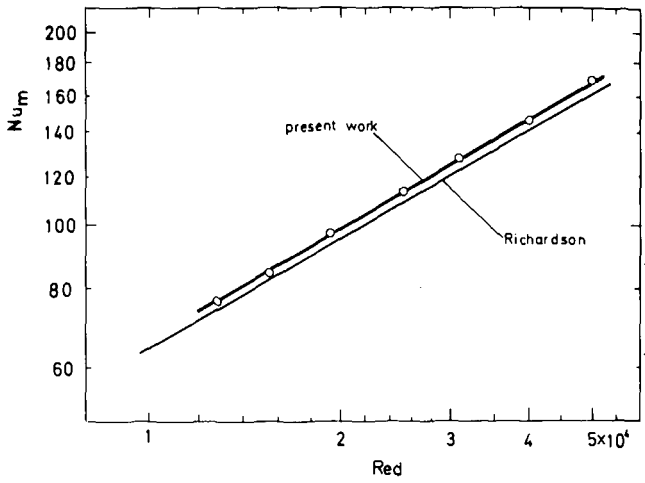

Fig. 2 Correlation of Nu_m with Reynolds number for single cylinder

percent throughout the experiments.

Three cylinders are placed at equal intervals at the center of the test section as shown in Fig. 1. The distributions of heat transfer, pressure, velocity, and turbulence intensity around the second cylinder (the test cylinder) were measured for various intervals.

For heat transfer measurements, a stainless steel ribbon wound helically around the center section of a hard vinyl chloride tube was electrically heated. A length of 600 mm of the stainless steel ribbon (20 × 0.05 mm in cross section) provides for seven full turns. The hard vinyl chloride tube is 26 mm dia and 225 mm long and its inside is filled with a rigid urethane foam to minimize heat loss. The temperature distributions were measured at intervals of 10 deg around the test cylinder with 0.065 mm dia copper-constantan thermocouples which are attached to the back of the stainless steel ribbon.

The local heat transfer coefficients were evaluated from the following equation described by Giedt [6]

$$h_\theta = \{c_1 VI + c_2 d^2 T/d\theta^2 - q_{cond}/S - q_{rad}/S\}/(T - T_\infty)$$

where c_1, c_2 are constants (in this work, $c_1 = 0.0846$, $c_2 = 15.4$), q_{cond}/S is the loss by conduction, and q_{rad}/S the loss by radiation. These corrections amount to less than 1 percent of the electric power inputs for all of the test conditions.

The experiments should, for practical purposes, be conducted under the condition that all three cylinders are heated. Under such a condition, when evaluating the heat transfer coefficient around the second cylinder, it is necessary to estimate a temperature of the oncoming flow to the second one, but that is not easy. However, it was found that whether the first cylinder is heated or unheated, the experimental result for the heat transfer coefficient around the second one is not affected, as is witnessed by the following preliminary experiment: The wall temperature of the second cylinder and the temperature distribution of the free shear layer shed from the first cylinder were measured under the condition that only the first cylinder was heated. The difference between the wall temperature of the second cylinder and the mean temperature of the layer was negligible, independent of the distance between cylinders in the whole range discussed in the present work. If such a mean temperature of the layer is chosen as the temperature of the oncoming flow to the second cylinder, the experimental result for the heat transfer coefficient around the second one is almost identical with that obtained under the following conditions: the first cylinder is unheated; the main flow temperature is chosen as that in the upstream region of the first cylinder.

Therefore, in the present work, the first and the third cylinder are unheated, and a main flow temperature T_∞ is chosen as that in the upstream region of the first cylinder, in order to avoid the complexity due to the superposition of the temperature field and the flow field.

For the measurements of the wall static pressure, another tube 26 mm in diameter was provided, which has a pressure tap 0.5 mm in diameter on the surface and is devised to be rotated on its axis.

For measuring the distributions of the velocity and turbulence intensity in the flow field, a constant temperature hot wire anemometer with a linearizer was used with a single wire of 0.005 mm dia tungsten, which is placed parallel to the cylinder axis, as the sensing element. The velocity and turbulence measurements were carried out under the unheated condition.

Experimental Results and Discussion

Heat Transfer. Before conducting the principal experiments, the accuracy of measurements on the main test cylinder was examined by measurements of the heat transfer for a single cylinder in cross flow.

As shown in Fig. 2, the results of the mean Nusselt number over the

Nomenclature

c = distance between the axes of the cylinders, m
c_1, c_2 = constants
C_p = static pressure coefficient, $(p - p_\infty)/(\frac{1}{2})\rho U_\infty^2$
C_{pmax} = maximum local static pressure coefficient
C_{pf} = static pressure coefficient of the front stagnation point
$\Delta C_p = C_{pmax} - C_{pf}$
C_D = pressure drag coefficient, $\int_0^\pi C_p \cos\theta \, d\theta$
d = cylinder diameter, m
h_θ = heat transfer coefficient, kW/(m²K)
I = electric current, A
Nu = Nusselt number
Nu_m = mean Nusselt number
Nu_{max} = maximum Nusselt number
p = static pressure, N/m²
Red = Reynolds number, $U_\infty d/\nu$
S = area of heating surface, m²
T = temperature, K
U_∞ = upstream velocity of the cylinders, m/s
$\bar{U}$ = time mean velocity, m/s
$\bar{U}_x$ = time mean velocity in the x-direction, m/s
$\sqrt{\overline{u'^2}}$ = r.m.s. velocity fluctuation, m/s
$\sqrt{\overline{u'^2}}/U_\infty = Tu$ = turbulence intensity
V = electric voltage, V
x = horizontal distance from the first cylinder axis, m
y = vertical distance normal to the axis of cylinder, m
δ = distance normal to the cylinder surface, mm
θ = angular distance from the front stagnation point, deg
λ = thermal conductivity, kW/(mK)
ν = kinematic viscosity, m²/s
ρ = density, kg/m³

Subscripts

a = attachment point
f = front stagnation point (θ = 0 deg)
r = rear stagnation point (θ = 180 deg)
∞ = main flow

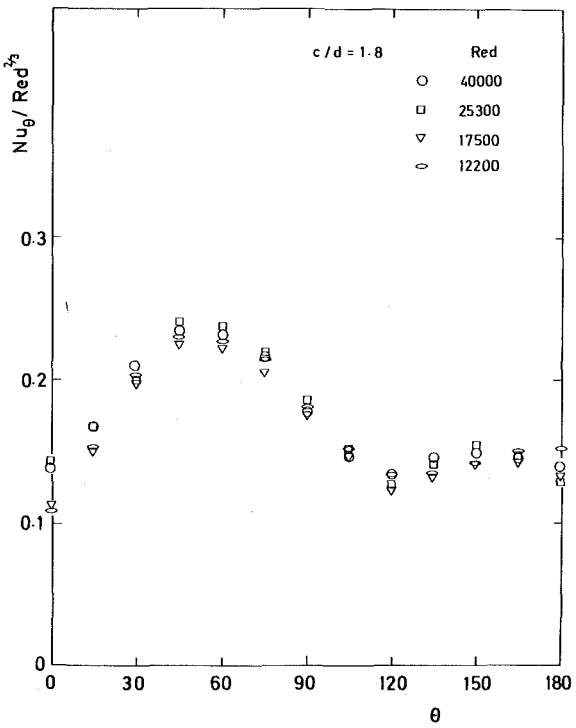

Fig. 3 Local Nusselt number distribution with Reynolds number

whole cylinder surface agree with the one by Richardson [7] to within a few percent. In the present work, no correction for the tunnel wall effects was made.

Fig. 3 shows an example (c/d = 1.8) of the variation of the Nusselt number with Reynolds number around the test cylinder when mounted in the center of three. From this figure it can be seen that the local Nusselt number at any angular position is approximately proportional to $Red^{2/3}$ except for the front stagnation part of the cylinder. That is, the heat transfer behaviors may be regarded as characteristics of a general turbulent vortex flow region. Such a trend is obtained in the range of $1.6 < c/d \leqq 3.8$ and $1.2 \times 10^4 \leqq Red \leqq 4.0 \times 10^4$; however for the smaller values of c/d scatter of the data occurs at the cylinder front portion.

It is also found that the local heat transfer coefficient has a maximum value around $\theta \approx 53$ deg independently of the Reynolds number. This is due to the effect of the free vortex layer (free shear layer) in which the vortices are shed from the first cylinder. The maximum Nusselt number point will be defined hereafter as the point of attachment. This was confirmed by observing the behavior of wool tufts attached to the wall and by hot wire anemometer measurements (as will be shown later, a turbulence intensity near the wall has a minimum value at this point).

Figs. 4 and 5 show, respectively, the local heat transfer and pressure distributions for various values of c/d at a Reynolds number of 40000. In the range $1.3 \leqq c/d \leqq 3.8$, the maximum local heat transfer coefficient occurs between 50 and 60 deg, while the maximum local static pressure coefficient occurs between 55 and 70 deg. That is, the maximum Nusselt number Nu_{max} on the second cylinder occurs at 5–10 deg upstream of the angular position of the maximum static pressure coefficient C_{pmax}. The result by Kostić and Oka [5] around the second cylinder in the case of two cylinders (a diameter of 100 mm, a blockage ratio of 0.2) is included for comparison in Fig. 4. The distribution of Nu found by Kostić and Oka for c/d = 1.8, Red = 38300 shows lesser variation than the one reported here. Such a trend is clearly seen for other values of c/d.

In the range of $c/d \geqq 4.0$, the variation of local Nusselt number and of static pressure coefficient are quite different from those in the preceding range. As the main flow is rolled up near the front part of the second cylinder, both distributions become similar to that of a single cylinder. However, the local Nusselt number at any angular position is larger than that for the single cylinder because of the effect

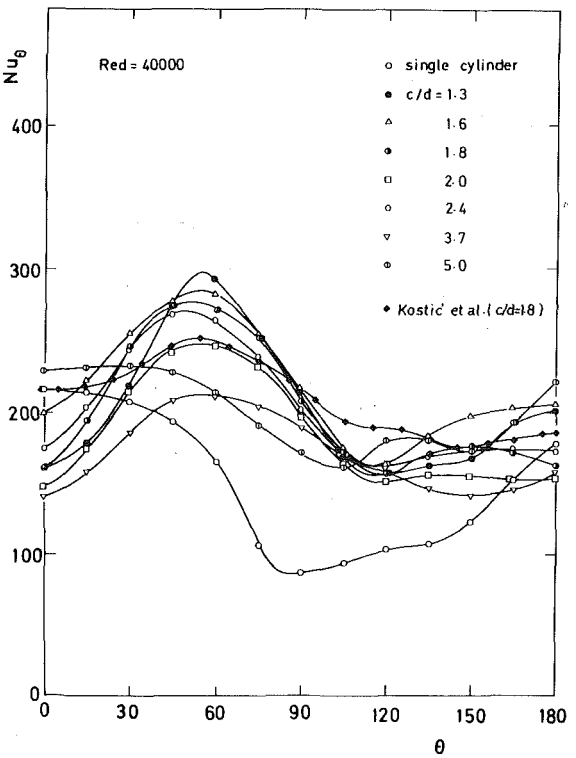

Fig. 4 Variation of local Nusselt number with *c/d*

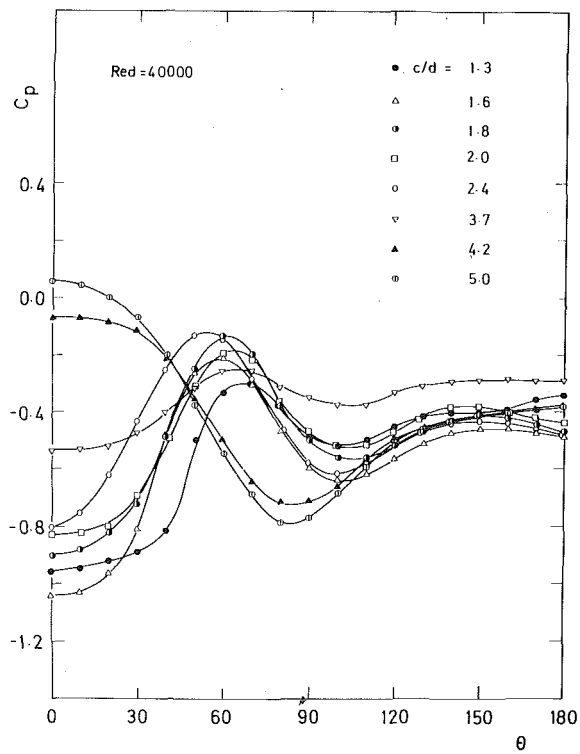

Fig. 5 Variation of local static pressure with *c/d*

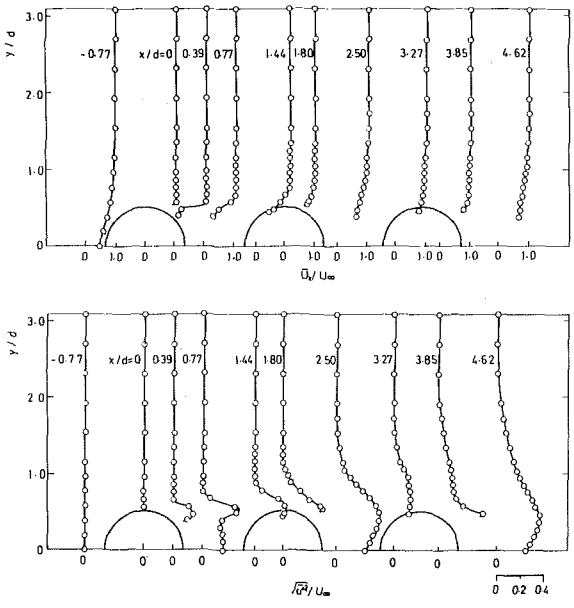

Fig. 6(*a*) Distribution of velocity and turbulence intensity over the test field for c/d = 1.8, Red = 40000

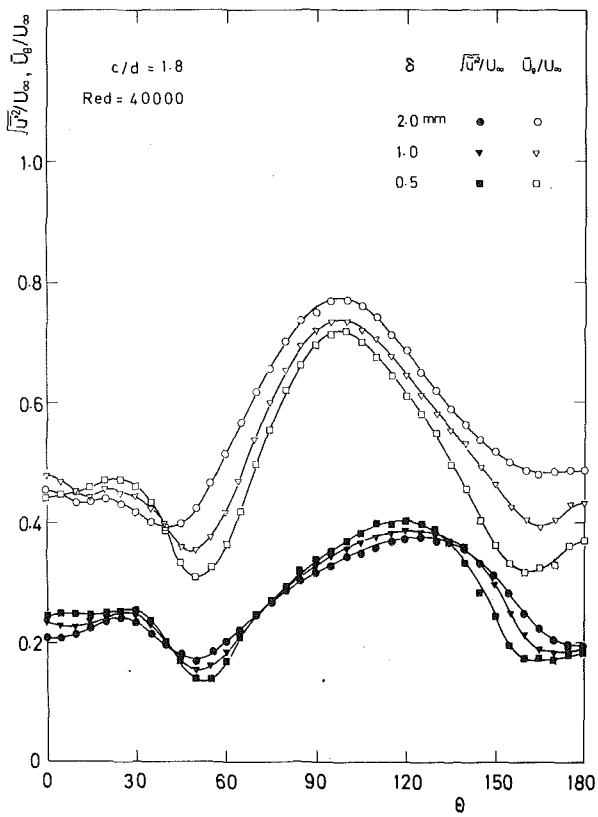

Fig. 6(*b*) Variation of velocity and turbulence intensity with angular position θ in the second cylinder for c/d = 1.8, Red = 40000

of turbulence generated by the first cylinder (which will be shown in Fig. 8), as has been suggested by Kostić and Oka [5].

Velocity and Turbulence Intensity. In general, various difficulties are encountered in any method for the measurement of velocity and turbulence intensity in a wake region with low velocity and high turbulence intensity. In spite of the problems of measurement in such flow fields, the hot wire anemometer is possibly the most adequate and useful one in order to examine qualitatively the relation between the heat transfer and the flow. The turbulence intensity were calculated from the mean and r.m.s. voltage readings from the hot wire anemometer with a linearizer. No corrections were made for flow direction.

Fig. 6(a) shows an example (c/d = 1.8, Red = 40000) of measurements of the time-mean velocity in the x-direction and the turbulence intensity over the test field. Only the upper half of the distributions is shown since they exhibited symmetry with respect to the horizontal axis. The wake width from the first cylinder increases downstream and develops over the second cylinder. Moreover, in the field between the first and second cylinders, the velocity gradient in the free shear layer (free vortex layer) perpendicular to the main flow decreases in the downstream direction as in the case of a free jet.

Regarding the turbulence intensity, it was found that it has a remarkably high value behind the first cylinder (the maximum is about 25 percent), and then decreases slightly near the attached region of the second cylinder, and again increases in the downstream direction, being influenced by the presence of the second cylinder itself. The same trend is also seen around the third cylinder.

It has been demonstrated by Spalding [8] and Mori and Daikoku [9] that in the turbulent separated flow field an increase of heat transfer at the attachment point is due to the effect of the turbulence which is generated in the remote high shear region of a separated flow and conveyed to the vicinity of the wall.

The variations of local mean velocity and turbulence intensity (at radial positions of 0.5, 1.0 and 2.0 mm from the surface) with angular position θ in the second cylinder (c/d = 1.8, Red = 40000) are shown in Fig. 6 (b). From this figure, in the range between the stagnation point and attachment point θ_f and θ_a, the following can be observed: as θ is approached θ_a, both the velocity and the turbulence intensity decrease with decreasing δ (distance normal to the cylinder surface). As has already been shown in Fig. 3, the maximum heat transfer occurs at this position. Similar trends are also observed for any spacing c/d in the range from 1.3 to 3.8.

Such results might suggest that the heat transfer at the point of attachment in a flow field such as is studied herein is not governed by the wall turbulence alone. Furthermore, the behavior of velocity distribution around θ_a also shows that a part of the kinetic energy of the free shear layer from the first cylinder is converted into a pressure rise. Both the velocity between 15 and 40 deg and the turbulence intensity between 0 and 40 deg increase with decreasing δ, contrary to these behavior around θ_a. From the foregoing, the existence of a large scale vortex can be postulated in this region between θ_f and θ_a. Such a vortex will be, at first, entrained by the vortex layer from the first cylinder, then impinge itself on the point of attachment (the behavior of such a vortex may be the most important factor influencing the heat transfer, as will be shown later), and then grow in size as it is conveyed along the wall toward the front stagnation point. Such behavior of the vortex was confirmed also with flow visualization experiments conducted in a water tunnel with floated aluminum powders.

In the region between θ_a and θ_r, the velocity has a maximum value around the angular position θ = 100 deg where it is further influenced by the main flow. The intensity of turbulence retained by the shear layer from the first cylinder is strengthened by the presence of the second cylinder itself and has a maximum value at about 120 deg, especially nearer the wall. Upon referring to the distributions of the local heat transfer or the static pressure coefficient, it may be inferred that the turbulent boundary layer separation occurs around this position (θ = 120 deg)—while Kostić and Oka [5] have proposed the existence of laminar boundary layer downstream of the reattachment point on the second cylinder, it seems, in the light of the present high turbulence intensity in that region, unjustifiable to accept their proposal. After the separation, the fluid particles merge into the outer layer near the main flow. Some of them entrained with the layer will reattach to the third cylinder and then flow toward the rear of the second cylinder.

Fig. 7 presents the variations of heat transfer, pressure difference (as defined in the Nomenclature) and form drag, all as a function of the spacing c/d. It can be seen that in the range $1.3 \leqq c/d \leqq 3.8$, the pressure coefficient difference ΔC_p, the local Nusselt numbers Nu_f at θ = 0 deg, and Nu_{150} at θ = 150 deg, and the mean Nusselt number

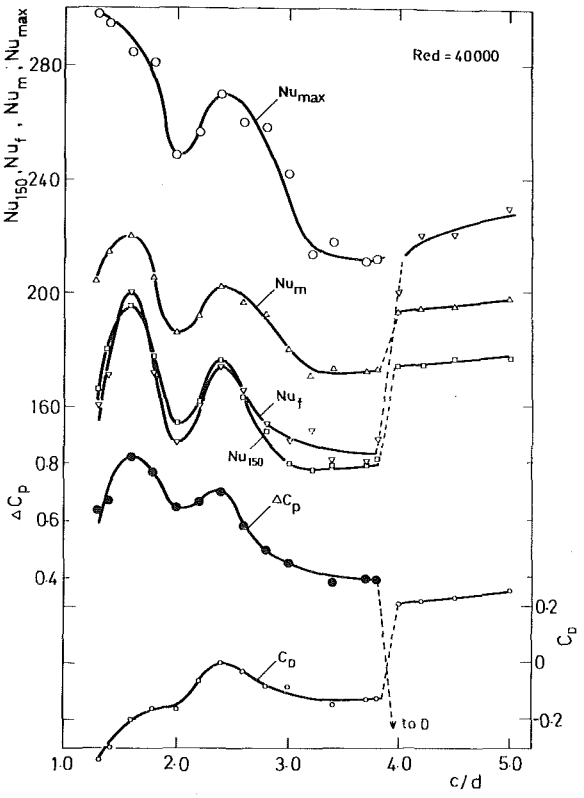

Fig. 7 Variation of Nu_{max}, Nu_m, Nu_f, Nu_{150}, ΔC_p and C_D with c/d

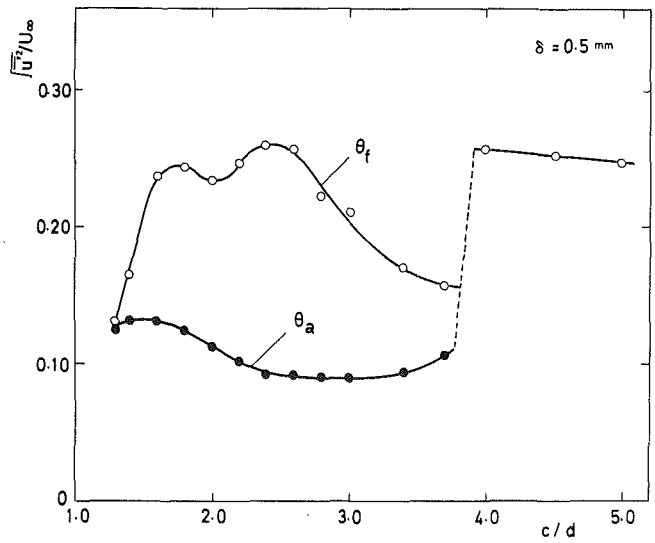

Fig. 8 Variation of turbulence intensity with c/d for Red = 40000

Nu_m, jointly show a maximum at 1.6, then fall to a minimum at 2.0 and then rise to another maximum at 2.4. It is of interest that in the range $1.6 \leqq c/d \leqq 3.8$, the variation of ΔC_p (in spite of the complexity of its variation due to the mutual interference of cylinders) is very similar to that of Nu_m, Nu_f, Nu_{150} and Nu_{max}. The variation of the turbulence intensity Tu with c/d at θ_a *and* θ_f is presented in Fig. 8.

By comparison of Nu and Tu versus c/d, it is seen that they do not agree with each other at θ_a and at θ_f. From the foregoing, it is difficult to say that there is a close correlation between heat transfer and turbulence intensity near the wall in such the flow field treated in the present study.

On the other hand, it appears that the pressure difference does correlate with the heat transfer in this field. If it is assumed that ΔC_p (the difference between C_{pmax} and C_{pf}, where C_{pf} can be regarded as the back pressure in a separated region between the first and the second cylinder) represents the strength of a vortex in the vortex layer from the first cylinder, it may be considered that the heat transfer (not only the overall heat transfer, but also the local heat transfer) around the second cylinder is strongly influenced by the strength of such a vortex. For instance, the fact that ΔC_p together with Nu_f, Nu_{150}, and Nu_m has a maximum value at $c/d = 1.6$ might suggest the most intensive and the best defined vortex is formed behind the first cylinder at this spacing.

In the range $1.3 \leqq c/d < 1.6$, only Nu_{max} increases with decreasing c/d. This may be due to the action of the more violent small eddies in the vortex layer from the first cylinder. However, as shown in Fig. 4, Nu_θ in the front part of the cylinder ($\theta < 40$ deg) decreases with decreasing c/d, because of the fact that a narrow space prevents the eddies growing in size and flowing towards the front stagnation point.

In the range of $c/d \geqq 4.0$, the following also can be seen in Fig. 7. Nu_{max} and Nu_f begin to agree with each other because the front part of the second cylinder, as well as that of single cylinder, is more exposed to the main flow. Nu_m abruptly changes at the distance of $c/d = 4.0$, and thereafter increases steadily with increasing c/d in the range $4.0 \leqq c/d \leqq 5.0$. ΔC_p falls to zero at $c/d = 4.0$.

The form drag coefficient C_D is almost negative in the range $1.3 \leqq c/d \leqq 3.8$, and increases drastically at $c/d = 4.0$. However, in the range $4.0 \leqq c/d \leqq 5.0$, C_D is considerably smaller than that for a single cylinder.

Finally, it may be noted that, in the whole range of c/d studied herein, the mean Nusselt number Nu_m is 17 to 50 percent larger than that for a single cylinder and has a maximum at $c/d = 1.6$.

Concluding Remarks

Heat transfer and static pressure measurements were carried out around the second cylinder of a horizontal row of three. Distributions of velocity and turbulence intensity were also measured in the flow field. It was found that the maximum heat transfer occurs at the position of flow attachment which is located at about 50–60 deg from the front stagnation point (in the range $1.3 \leqq c/d \leqq 3.8$), while the turbulence intensity near the wall at this position is lower than that at other angular positions. It is inferred from the test results that the strength of a vortex in the vortex layer from the first cylinder is the more important factor affecting the heat transfer in the range of $1.3 \leqq c/d \leqq 3.8$.

Acknowledgment

The authors are grateful to Professor N. Seki, of Hokkaido University and Assistant Professor T. Ota, of Akita University, Japan, for their valuable suggestions and to Mr. S. Hosaka for his assistance in the process of producing the experimental apparatus. Significant comments and suggestions of the referees of this paper are gratefully acknowledged.

References

1 McAdams, W. H., *Heat Transmission*, Third ed., McGraw-Hill, New York 1954.

2 Zúkauskas, A., *Advances in Heat Transfer*, Academic Press, New York, Vol. 8, 1972.

3 Van der Hegge Zijnen, B. G., "Heat Transfer From Horizontal Cylinder to a Turbulent Air Flow," *Applied Scientific Research*, Section A, Vol. 7, 1958, pp. 205–223.

4 Igarashi, T., and Hirata, M., "Heat Transfer in Separated Flows," *Proceedings of the Fifth International Heat Transfer Conference*, Vol. 2, 1974, pp. 300–304.

5 Kostić, Ž. G., and Oka, S. N., "Fluid Flow and Heat Transfer With Two

Cylinders in Cross Flow," *International Journal of Heat and Mass Transfer*, Vol. 15, 1972, pp. 279–299.

6 Giedt, W. H., "Investigation of Variation of Point Unit-Heat Transfer Coefficient Around a Cylinder Normal to an Airstream," TRANS. ASME, Vol. 71, 1949, pp. 375–381.

7 Richardson, P. D., "Heat and Mass Transfer in Turbulent Separated Flows," *Chemical Engineering Science*, Vol. 18, 1963, pp. 149–155.

8 Spalding, D. B., "Heat Transfer From Turbulent Separated Flows," *Journal of Fluid Mechanics*, Vol. 27, Part 1, 1967, pp. 97–109.

9 Mori, Y., and Daikoku, T., "Effect of Two-Dimensional Roughness on Forced Convective Heat Transfer," *Transactions of the Japan Society of Mechanical Engineers*, Vol. 38, 1972, pp. 832–841.

ERRATUM

Erratum: P. Carajilescov and N. E. Todreas, "Experimental and Analytical Study of Axial Turbulent Flows in an Interior Subchannel of a Bare Rod Bundle," published in the May 1976 issue of the JOURNAL OF HEAT TRANSFER, pp. 262–268.

Fig. 1, page 263: Mean Velocity Line should read Maximum Velocity Line.

Table 1, page 263: $-\frac{1}{\nu r}(rv_r'v_\theta')\left[\frac{\partial}{\partial r}\frac{1}{r}\frac{\partial}{\partial r}r-\frac{\partial^2}{r^2\partial\theta^2}\right]$ should be $-\frac{1}{\nu r}\left[\frac{\partial}{\partial r}\frac{1}{r}\frac{\partial}{\partial r}r-\frac{\partial^2}{r^2\partial\theta^2}\right](rv_r'v_\theta')$.

Equation (5), page 264: $\frac{\ell}{\hat{y}}=0.44+0.66\sin\left[\frac{\pi}{0.38}\left(\frac{y}{\hat{y}}-0.44\right)\right]$ should be $\frac{\ell}{\hat{y}}=0.44+0.066\sin\left[\frac{\pi}{0.38}\left(\frac{y}{\hat{y}}-0.44\right)\right]$

Equation (9), page 264: $\frac{p'}{\rho}\left(\frac{\partial v_\theta'}{r\partial\theta}\frac{\partial v_r'}{\partial r}\right)\simeq 0$ should read $\frac{p'}{\rho}\left(\frac{\partial v_\theta'}{r\partial\theta}-\frac{\partial v_r'}{\partial r}\right)\simeq 0$.

A. Steiner

Senior Engineer,
CADE-IDP, Ingenieriay
Desarrollo de Proyectos,
Santiago, Chile

Pipe Heating With Steam Tracers

Steam tracers are widely used in industry for heating pipes transporting fluid that cannot be pumped beneath a certain temperature. In most industrial operations the need for heating does not arise during flow from heated tanks, for the residence time of the pipe content is normally short enough to avoid excessive cooling. However, steam tracers must be added to the pipe to allow warming when pumping is stopped. In this paper a mathematical solution for the heat transfer problem is developed giving the mean temperature of the pipe content and the hottest point temperature as a function of time, under nonflow conditions. The analysis covers the cases of pipes with one or two tracers and with or without heat conducting cement. The equations are cumbersome, but their evaluation for steel pipes with diameters spanning from 38.1 to 355.6 mm and filled with heavy oil products shows that in this particular case they can be greatly simplified.

1 Introduction

Long pipes filled with hot products in oil refineries and similar plants are heat insulated to avoid excessive losses when liquids are pumped from heated tanks. When the pipe content becomes solid or too viscous to be pumped beneath a certain temperature, heaters must be considered to allow warming during intervals between pumping. Steam jackets, electrical tracing and steam tracing are normally used for this purpose, but steam tracing is by far the most commonly employed.

Steam tracers are small diameter pipes, usually some 6 mm OD attached and normally parallel to a main pipe to which they transmit heat and under a common insulation. Because of surface irregularities and thermal expansion the tracer cannot be assumed to be in continuous contact with the main pipe. The small pipes are fed from a header with steam that condenses on the inner walls, the condensate flowing by gravity to the end of the small pipe where it is expelled through a steam trap.

The technical literature on steam tracers is almost nonexistent. References [3, 4][1] give descriptions of practical systems and design hints for steam tracing pipes, valves and fittings. Reference [5] gives a nomograph based on data gathered over a number of weeks on existing installation, and may be used to determine the number and size of steam tracers, the product temperature, the heat loss from a traced product line, the heat transfer from tracer to product, and the outside temperature of insulation.

To our knowledge, no attempt has been made to analyze the heat transfer problem, and no information exists about the transient response of steam traced pipes.

The purpose of this paper is to develop a model for the heat conduction problem whose mathematical solution may lead to predictions of the steady-state value of the mean temperature as well as its evolutions in time.

A single initial temperature is assigned to the nonflowing content of the main pipe and four possible cases are studied: pipes with one or two tracers and the eventual use of heat conducting cement between tracers and main pipe. The ambient air and steam temperatures are considered constants.

2 Heat Conduction Model

Fig. 1 represents a cross section of a steam tracer attached without cement to a main pipe, showing the heat flux path assumed by the model. All arrows in the figure, except the one labeled r which stands for a position vector, are meant to indicate heat flow. The model as-

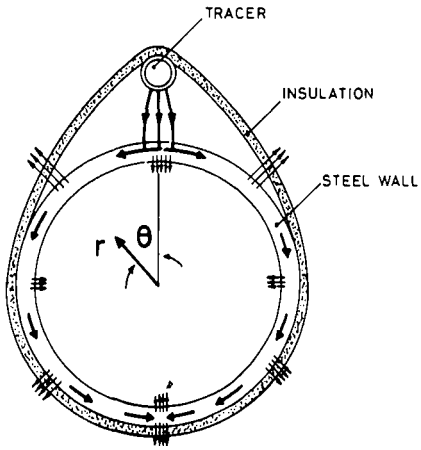

Fig. 1 Model showing assumed heat flux path

[1] Numbers in brackets designate References at end of paper.

Contributed by the Heat Transfer Division for publication in the JOURNAL OF HEAT TRANSFER. Manuscript received by the Heat Transfer Division November 11, 1975. Paper No. 76-H-T-ZZ.

sumes heat flowing from the condensing steam in the tracer to the main wall pipe through an air gap, whose dimension is out of proportion in the figure, and from this wall both to the outer air through the insulation and to the liquid content.

If the pipe is heated by two tracers, they are assumed to be in locations 180 deg apart. The temperature of the pipe wall under the tracer and the steam temperature are considered to be the same if heat conducting cement sticks the tracers to the pipe wall. If the tracers are not stuck but held against the pipe with bands or any other suitable means, a 1 mm mean distance between surfaces is assumed. In the latter case, the temperature of the pipe wall under the tracer is linked to the heat flux between tracer and pipe per unit length by $q = h(T_v - T_w)$, where h is given by equation (1). Equation (1) describes the heat transfer between infinite parallel cylinders with constant surface temperature submerged in an infinite medium.

The flux lines between pipe and tracer are clustered around the line joining the centers because their diameters are very different and thus it is reasonable to assume that the heat flux from the tracer enters the pipe at $\theta = 0$, if there is only one tracer, or $\theta = 0$ and $\theta = \pi$ if two tracers are present.

The radial and longitudinal gradients of tracer and pipe are neglected. The heat capacity of the pipe wall has been considered negligible though this may be, in some cases, an oversimplification.

3 The Differential Equations

The heat conduction coefficient per unit length between pipe and tracer [1] is given by

$$h = 2\pi k_a/\cosh^{-1}[1 + (R_1 + R_2)d/R_1R_2] \tag{1}$$

Let $T_w(\theta, t)$ denote the pipe wall temperature. A heat balance in a wall element, per unit length of pipe, gives

$$(k_s e/R)\partial^2 T_w/\partial\theta^2 = RH(T_w - T_0) + Rk_c(\partial T/\partial r')_{r'=R} \tag{2}$$

where $H = k_i/R_1 \operatorname{Ln}(1 + \Delta/R_1)$ [2].

In equation (2) the left side represents the balance in a wall element of the heat flowing circumferentially. The first term on the right is the heat loss to ambient through the insulation and the second the heat flowing to the pipe content.

A boundary condition for equation (2) is

$$(k_s e/R)\partial T_w/\partial\theta = -(h/2)(T_v - T_w) \quad \text{at } \theta = 0$$

where $-(h/2)(T_v - T_w)$ represents the heat flowing from the tracer to the left side pipe wall. By symmetry reasons another boundary condition is

$$\partial T_w/\partial\theta = 0 \quad \text{at } \theta = \pi \text{ if there is only one tracer}$$

or

$$\partial T_w/\partial\theta = 0 \quad \text{at } \theta = \pi/2 \text{ if two tracers are present.}$$

The heat equation for the pipe content is

$$\rho C(\partial T/\partial t) = k_c\left(\frac{1}{r'}\frac{\partial T}{\partial r'} + \frac{\partial^2 T}{\partial r'^2} + \frac{1}{r'^2}\frac{\partial^2 T}{\partial\theta^2}\right) \tag{3}$$

A boundary condition for this equation is

$$T = T_w \quad \text{at} \quad r' = R$$

The preceding equation being dependent on temperature differences only, the initial temperature T_i can be taken as zero level, and a last boundary condition is then

$$T = 0 \quad \text{at} \quad t = 0$$

Written in dimensionless terms, equations (2) and (3) and the boundary conditions are

$$\partial^2 T_w/\partial\theta^2 - \omega^2 T_w = -\omega^2 T_0 + \nu(\partial T/\partial r)_{r=1} \tag{4}$$

$$\frac{1}{K}\frac{\partial T}{\partial t} = \frac{1}{r}\frac{\partial T}{\partial r} + \frac{\partial^2 T}{\partial r^2} + \frac{1}{r^2}\frac{\partial^2 T}{\partial\theta^2} \tag{5}$$

$$T = 0 \quad \text{at} \quad t = 0 \tag{6}$$

$$T = T_w \quad \text{at} \quad r = 1 \tag{7}$$

$$B(\partial T_w/\partial\theta) = -(T_v - T_w) \quad \text{at} \quad \theta = \pi \quad \text{or} \quad \theta = \pi/2 \tag{8}$$

with

$$K = k_c/\rho CR^2, \quad \omega^2 = HR^2/k_s e$$

$$\nu = k_c R/k_s e, \quad B = 2k_s e/hR$$

The constants ω^2, ν, and B are dimensionless. Constant K has t^{-1} dimensions.

Using boundary conditions (8) and (9), an integration of equation (5) between 0 and π gives

$$\left(\frac{T_v - T_w}{B}\right)_{\theta=0} = -\pi\omega^2 T_0 + \int_0^\pi \left[\omega^2 T_w + \nu\left(\frac{\partial T}{\partial r}\right)_{r=1}\right] d\theta \tag{5a}$$

If two tracers are present, (5a) keeps its form unaltered but π must be replaced by $\pi/2$.

4 Solution of the Differential System

A solution in the form of separate variable function products is sought.

We take the time Laplace transforms of equations (4)–(9). In order to avoid burdening the nomenclature the same letters are used for the functions and their transforms, the latter being indicated by an overbar.

Nomenclature

a_n = coefficient in the Fourier expansion of the temperature
$B = 2k_s e/hR$
C = heat capacity of the pipe content
d = mean distance between pipe and tracer surfaces
e = wall thickness
H = heat conduction coefficient between pipe and ambient air through insulation, per unit area of pipe outer surface
h = heat conduction coefficient between pipe and tracer per unit length of pipe
I_n = modified Bessel function of order n
J_n = Bessel function of order n
$K = k_c/\rho CR^2$
k_a = heat conductivity of air
k_s = heat conductivity of steel wall
k_i = heat conductivity of insulation
k_c = heat conductivity of pipe content
n = natural integer
q = heat flux per unit length between tracer and pipe
R = pipe inner radius
R_1 = pipe outer radius
R_2 = tracer outer radius
r' = radial coordinate
$r = r'/R$
s = Laplace transform parameter
T = pipe content temperature
T_0 = ambient air temperature
T_i = initial temperature
T_w = wall temperature
T_m = pipe content mean temperature
T_v = steam temperature
T_c = wall temperature under the tracer
t = time
$\alpha = \sqrt{s/K}$
Δ = insulation thickness
ρ = specific mass of pipe content
$\nu = k_c R/k_s e$
θ = angular coordinate
$\omega^2 = HR^2/k_s e$

Superscripts

$\bar{T}$ = transformed variable

$$\frac{s\bar{T}}{K} = \frac{1}{r}\frac{\partial \bar{T}}{\partial r} + \frac{\partial^2 \bar{T}}{\partial r^2} + \frac{1}{r^2}\frac{\partial^2 \bar{T}}{\partial \theta^2} \tag{10}$$

$$\partial^2 \bar{T}_w/\partial\theta^2 - \omega^2 \bar{T}_w = -\omega^2 T_0/s + \nu(\partial \bar{T}/\partial r)_{r=1} \tag{11}$$

$$\bar{T} = \bar{T}_w \quad \text{at} \quad r = 1 \tag{12}$$

$$B(\partial \bar{T}_w/\partial\theta) = -(T_v/s - \bar{T}_w) \quad \text{at} \quad \theta = 0 \tag{13}$$

$$\partial \bar{T}_w/\partial\theta = 0 \quad \text{at} \quad \theta = \pi \quad \text{or} \quad \theta = \pi/2 \tag{14}$$

A solution of (10) that fits the boundary conditions is

$$\bar{T} = \sum_{n=0}^{\infty} I_n(\alpha r) a_n \cos n\theta \tag{15}$$

with $\alpha^2 = s/K$, for the pipe with only one tracer, or

$$\bar{T} = \sum_{n=0}^{\infty} I_{2n}(\alpha r) a_{2n} \cos 2n\theta$$

if two tracers are present.

Coefficients a_n and a_{2n} are functions of α, to be determined. And $I_n(\alpha r)$ is the modified Bessel function of order n, solution of the modified Bessel equation

$$\frac{1}{\alpha r}\frac{dI_n(\alpha r)}{d(\alpha r)} + \frac{d^2 I_n(\alpha r)}{d(\alpha r)^2} = I_n(\alpha r)\left[1 + \frac{n^2}{\alpha^2 r^2}\right]$$

$I_n(\alpha r)$ may be expanded as

$$I_n(\alpha r) = \sum_{k=0}^{\infty} \frac{(\alpha r/2)^{n+2k}}{k!(n+k)!}$$

The solution (15) satisfies equation (10) identically. Introducing equation (15) in equation (11), with boundary conditions (12)–(14), a solution for equation (11) is found to be

$$\bar{T}_w = A\left[\sum_{n=0}^{\infty} \frac{\nu I_n'(\alpha) a_n}{\omega^2 + n^2} + \frac{T_v - T_0}{s}\right] \cosh \omega(\pi - \theta) + \frac{T_0}{s} - \sum_{n=0}^{\infty} \frac{\nu\alpha I_n'(\alpha) a_n \cos n\theta}{\omega^2 + n^2} \tag{17}$$

with

$$1/A = \cosh \omega\pi + B\omega \operatorname{senh} \omega\pi.$$

Coefficients a are computed by equating (17) and (15) under condition (12), and equating coefficients of cosinus functions. The solution (15) takes then the form

$$\bar{T} = \frac{2[T_v F - \omega^2 T_0 I_0(\alpha)]}{s[I_0(\alpha) + F(2L + \pi B)]} \sum_{n=1}^{\infty} \frac{I_n(\alpha r)\cos n\theta}{(\omega^2 + n^2) I_n(\alpha) + \nu\alpha I_n'(\alpha)} + \left[\frac{T_v + \omega^2 T_0(2L + \pi B)}{s[I_0(\alpha) + F(2L + \pi B)]}\right] I_0(\alpha r) \tag{18}$$

with

$$F = \omega^2 I_0(\alpha) + \nu\alpha I_0'(\alpha)$$

and

$$L = \sum_{n=1}^{\infty} \frac{I_n(\alpha)}{(\omega^2 + n^2) I_n(\alpha) + \nu\alpha I_n'(\alpha)}$$

The solution for the two tracers heated pipe is formally the same, but the summations in (18) and L must include the even terms only and π must be replaced by $\pi/2$.

The solution (18) is a Fourier expansion and thus it cannot satisfy condition (13). The derivative in equation (13) is discontinuous at $\theta = 0$ and the value obtained for this derivative from equation (18) tends to zero, its mean value, at this point. Nevertheless, equation (18) is a solution of the transformed alternative system.

$$\frac{s\bar{T}}{K} = \frac{1}{r}\frac{\partial \bar{T}}{\partial r} + \frac{\partial^2 \bar{T}}{\partial r^2} + \frac{1}{r^2}\frac{\partial^2 \bar{T}}{\partial \theta^2}$$

$$\left(\frac{T_v/s - \bar{T}_w}{B}\right)_{\theta=0} = -\frac{\pi\omega^2 T_0}{s} + \int_0^{\pi}\left[\omega^2 \bar{T}_w + \nu\left(\frac{\partial \bar{T}}{\partial r}\right)_{r=1}\right] d\theta$$

$$\bar{T} = \bar{T}_w \quad \text{at} \quad r = 1 \tag{19}$$

If the tracer is fastened to the pipe with heat conducting cement $B = 0$, but $\bar{T}_w = T_v/s$ at $\theta = 0$, and (19) changes into

$$-(\partial \bar{T}_w/\partial\theta)_{\theta=0} = -\pi\omega^2 T_0/s + \int_0^{\pi} [\omega^2 \bar{T}_w + \nu\partial T/\partial r)_{r=1}] d\theta \tag{19a}$$

Equation (18), in which $B = 0$, satisfies equation (19a).

The transformed mean temperature is obtained from equation (18),

$$\bar{T}_m = \frac{2I_0'(\alpha)[T_v + T_0\omega^2(2L(\alpha) + \pi B)]}{s\alpha[I_0(\alpha) + F(\alpha)[2L(\alpha) + \pi B]]} \tag{20}$$

and so is the temperature of the point under the tracer, $\bar{T}_w(s, 0) = \bar{T}_c$,

$$\bar{T}_c = \frac{T_v[2F(\alpha)L(\alpha) + I_0(\alpha)] + \omega^2\pi B T_0 I_0(\alpha)}{s[I_0(\alpha) + F(\alpha)[2L(\alpha) + \pi B]]} \tag{21}$$

The primitives of the transformed temperatures are cumbersome equations that can be obtained by the use of the complex inversion theorem. They are given in the following, including in them the initial temperature. The argument of the Bessel functions in the following equations are the α_p values obtained from equation (26), corresponding to the term order in the summation.

$$T_m = T_0 + \frac{T_v - T_0}{\omega^2(2L(0) + \pi B) + 1} - \frac{4}{\nu}\sum_{p=1}^{\infty} \frac{[\omega^2 J_0 J_1(T_v - T_0) - \nu\alpha_p J_1^2(T_v - T_i)]e^{-K\alpha_p^2 t}}{\alpha_p^2[2(\omega^2 J_0 - \nu\alpha_p J_1)^2\sigma(\alpha_p) - \alpha_p(J_0^2 + J_1^2)]} \tag{22}$$

$$T_c = T_0 + \frac{(2\omega^2 L(0) + 1)(T_v - T_0)}{\omega^2(2L(0) + \pi B) + 1} - \frac{2\pi B}{\nu}\sum_{p=1}^{\infty} \times \frac{[(\omega^2 J_0 - \nu\alpha_p J_1)(T_v - T_i) - \omega^2 J_0(T_0 - T_i)](\omega^2 J_0 - \nu\alpha_p J_1)e^{-K\alpha_p^2 t}}{2(\omega^2 J_0 - \nu\alpha_p J_1)^2\sigma(\alpha_p) - \alpha_p(J_0^2 + J_1^2)} \tag{23}$$

with

$$L(0) = \sum_{n=1}^{\infty} (\omega^2 + n^2 + \nu n/2)^{-1} \tag{24}$$

and

$$\sigma(\alpha_p) = \sum_{n=1}^{\infty} \frac{(n/2)J_n(J_{n+1} + J_{n-1}) - \alpha_p(J_n^2 + (J_{n-1} - J_{n+1})^2/4)}{[(\omega^2 + n^2)J_n + \nu\alpha_p(J_{n-1} - J_{n+1})/2]^2} \tag{25}$$

where α_p are the roots of

$$(\omega^2 J_0 - \nu\alpha J_1)\left(2\sum_{n=1}^{\infty} \frac{J_n}{(\omega^2 + n^2)J_n + (J_{n-1} - J_{n+1})\nu\alpha/2} + \pi B\right) + J_0 = 0 \tag{26}$$

Equations (22)–(26) apply to all the cases considered. If the tracers are fastened with heat conducting cement, $B = 0$. If two tracers are present, the summations over n must include the even terms only and π must be replaced by $\pi/2$.

5 Applications and Simplifications

To evaluate the terms in the summation in equations (22)–(23), a computer program was run for pipes with diameters spanning from 38.1 to 355.6 mm, ϕ 12.7 mm tracers, heavy oil content and 25.4 mm insulation for diameters less than 101.6 and 3.81 mm for diameters greater than 152.4 mm.

It was found that in equations (22) and (23) the coefficient of the first exponential, even in the less favorable case, was greater than 94 percent of the value of the whole series for $t = 0$. For all other value of t, the weight of the first term is obviously greater. A good approximation of the summation can then be obtained by replacing it by the first exponential multiplied by the summation of the coefficients, which has a simpler expression than the first coefficient.

With this simplification T_m and T_c can be made to depend on a single exponential. In nondimensional form they read

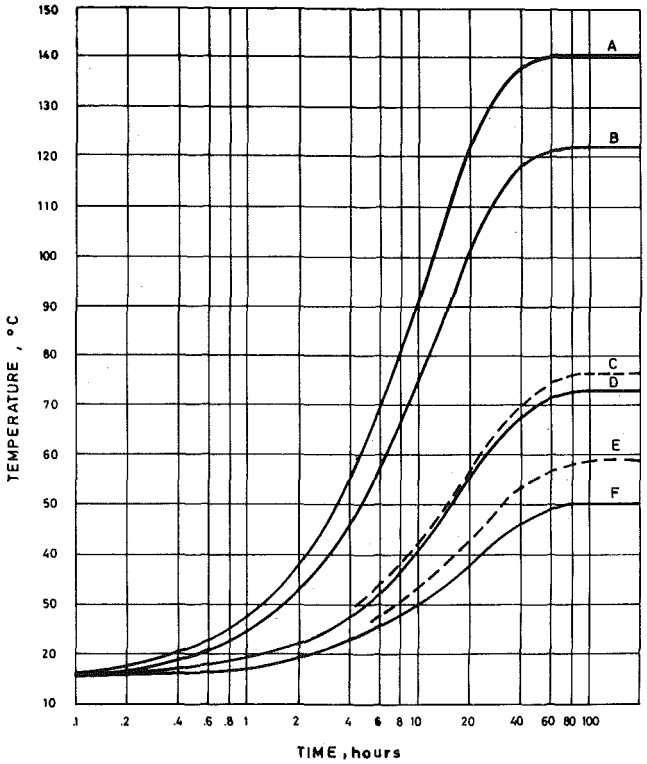

Fig. 2 Heating from ambient temperature with 147°C steam (50 psi) ϕ 8 in. Sch 20, Δ = 38.1 mm, ϕ 12.7 tracers: A = content mean temperature with two tracers, with cement; B = content mean temperature with one tracer, with cement; C = temperature of the wall under the tracers with two tracers, no cement; D = content mean temperature with two tracers, no cement; E = temperature of the wall under the tracer with one tracer, no cement; F = content mean temperature with 1 tracer, no cement

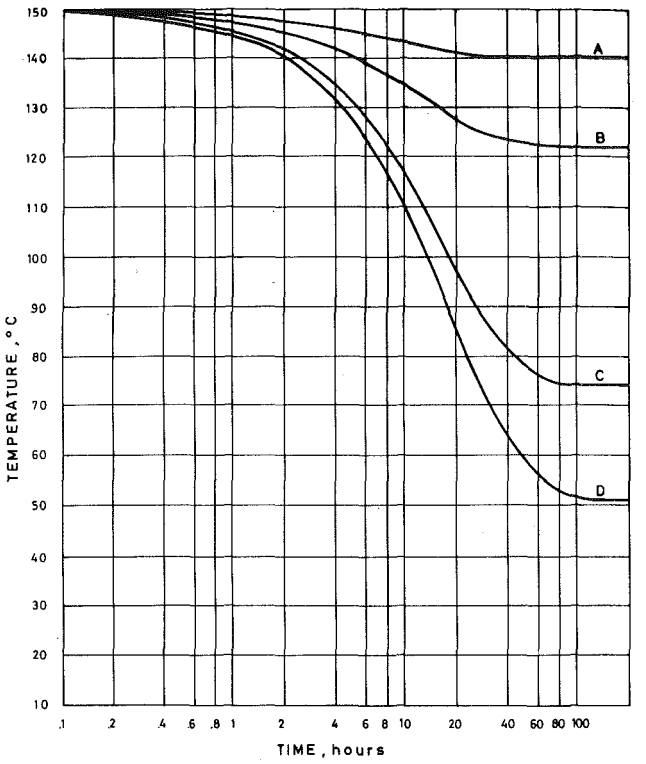

Fig. 3 Cooling from 148.9°C with 147°C steam (50 psi) ϕ 8 in. Sch 20, Δ = 38.1 mm, ϕ 12.7 tracers: A = content mean temperature with two tracers, with cement. B = content mean temperature with one tracer, with cement. C = content mean temperature with two tracers, no cement; D = content mean temperature with one tracer, no cement

$$T_m^+ = 1 + (T_i^+ - 1)e^{-K\alpha_1^2 t} \tag{27}$$

and

$$T_c^+ = 1/G - \omega^2\pi B + (T_i^+ - 1/G + 1)e^{-K\alpha_1^2 t} \tag{28}$$

where

$$T^+ = \frac{T - T_0}{G(T_v - T_0)} \quad \text{and} \quad 1/G = \omega^2(2L(0) + \pi B) + 1, \quad \text{and} \quad \alpha_1$$

is the first root in equation (26). In applying equation (28) B must be different from zero.

If two tracers are present, the summation in $L(0)$ must include the even terms only and π must be replaced by $\pi/2$. If there is heat conducting cement, $B = 0$ in equation (27).

For ω^2 and ν both ranging from 10^{-2} to 20×10^{-2}, the summations can be replaced by

$$\sum_{n=1}^{\infty} \frac{J_n(\alpha)}{\omega^2 + n^2 + \nu\alpha\left[\dfrac{J_{n-1}(\alpha) - J_{n+1}(\alpha)}{2}\right]} = 0.87226 + 0.334\nu + \frac{2.2090 - 0.7\nu}{\omega^2 + 1 + \nu(\alpha J_0(\alpha)/J_1(\alpha) - 1)} \tag{29}$$

and

$$L(0) = \sum_{n=1}^{\infty} (\omega^2 + n^2 + \nu n/2)^{-1} = 1.6376 - 0.89276\omega^2 - (0.53982 - 0.67441\omega^2)\nu \tag{30}$$

for one tracer, and

$$\sum_{n=2}^{\infty} \frac{J_n(\alpha)}{\omega^2 + n^2 + \nu\alpha\left[\dfrac{J_{n-1}(\alpha) - J_{n+1}(\alpha)}{2}\right]} = 0.22673 - 0.0202\nu + \frac{2.17151 - 0.0348\nu}{\omega^2 + 4 + \nu\left[\dfrac{\alpha^2}{2 - \alpha J_0/J_1} - 2\right]} \tag{31}$$

and

$$L(0) = \sum_{n=2}^{\infty} (\omega^2 + n^2 + \nu n/2)^{-1} = 0.41102 - 0.06424\omega^2 - (0.071437 - 0.02775\omega^2)\nu \tag{32}$$

for two tracers.

With equation (30) or (32) the steady-state temperatures in equations (27) and (28) can be easily computed.

With the help of a table of $J_1(\alpha)$ and $J_0(\alpha)$ and equation (29) or (32), the first root of equation (26), laying between 1 and 2.5 for the preceding range of ω^2 and ν, can be computed by iteration.

The transient part of equation (27) and (28) can then be calculated.

It may be of interest to show the variation of the steady-state mean temperature as a consequence of a change in the insulation thickness. Equations (27) and (30) or (32) give

$$\Delta\frac{\partial T_m^+}{\partial\Delta} = \frac{1}{1 - (T_m - T_0)/(T_v - T_m)} \times \frac{\Delta/R_1}{(1 + \Delta/R_1)\,Ln\,(1 + \Delta/R_1)} \tag{33}$$

As an example let's consider a ϕ 8 in. Sch 20 pipe, with ϕ 12.7 mm tracers, 38.2 mm insulation filled with heavy oil. The values of the parameters are $\omega^2 = 8.0530\ 10^{-2}$, $\nu = 4.5180\ 10^{-2}$, $\pi B = 3.1327\ 10^{1}$ and $K = 0.1789\ (\text{hr})^{-1}$.

If there is one tracer and no cement, equation (30) gives $G = 0.2701$. With 3.4 bar steam $T_v = 147.2°C$ and if $T_0 = 15.6°C$ the steady-state mean temperature is $T_m = T_0 + (T_v - T_0)G = 51°C$.

Equation (33) gives $\partial T_m/\partial \Delta = 78.7$ [°C/cm], which shows that the steady-state mean temperature is very sensitive to the insulation thickness. The transient term of the mean temperature needs the computation of α_1 from equations (26) and (29). This gives $\alpha_1 = 1.692$.

Figs. 2 and 3 show the complete set of curves displaying the results of the analysis considering the different alternatives, applied to the preceding pipe. It must be remembered that in this analysis the pipe content is not flowing, while the steam is passing through the tracers. It can be seen that the use of more powerful means of heating not only raises the steady-state temperature but also shortens the transient period.

References

1 Carslaw, H. S., and Jaeger, J. C., *Conduction of Heat in Solids*, Oxford University Press, Second ed., p. 451.

2 Ibid, p. 189.

3 Chapman, F. S., and Holland, F. A., "Keeping Piping Hot," *Chemical Engineering*, Jan. 17, 1966, p. 133.

4 Bower, J. N., and Peterson, H. R., "Guide to Steam Tracing Design," *Hydrocarbon Processing and Petroleum Refiner*, Vol. 42, No. 3, Mar. 1963, p. 149.

5 Horvath, L., "Size Steam Tracer Lines by Nomograph," *Hydrocarbon Processing and Petroleum Refiner*, Vol. 41, No. 2, Feb. 1962, p. 198.

ERRATUM

Erratum on: H. H.-S. Chu and S. W. Churchill, "The Effect of Heater Size, Location, Aspect Ratio, and Boundary Conditions on Two-Dimensional, Laminar, Natural Convection in Rectangular Channels," published in the May 1976 issue of the JOURNAL OF HEAT TRANSFER, pp. 194–201.

1 C. V. S. Patterson should be deleted as an author.
2 In the Nomenclature, Gr = $g\beta(T_h - T_c)h^3/\nu^2$ and the sub-bar under ℓ should be a superbar over Nu.
3 In equation (1) the + sign ahead of Gr should be replaced by an = sign.
4 An overbar should be added over Nu: page 195, first column, lines 9, 23, and 30; page 200, first column, lines 1 and 2.
5 The line designations under Fig. 10 should be repeated under Figs. 13, 14, 15, and 16.
6 The second line, second column, page 199 should read Fig. 14 and the first line, first column, page 200 should read Figs. 15 and 16.
7 Fig. 3: The code for $x = 0.250$ and $z = 0.250$ should be - - - not ----------.

B. Rubinsky
A. Shitzer

Faculty of Mechanical Engineering,
Technion-Israel Institute of Technology,
Haifa, Israel

Analysis of a Stefan-Like Problem in a Biological Tissue Around a Cryosurgical Probe

Analysis of a Stefan-like problem in the in vivo freezing of a biological tissue is presented in cartesian coordinates. The analysis allows the inclusion of blood perfusion, metabolic heat and tissue heat capacity. Solutions are obtained for the temperature distributions in the frozen and unfrozen regions at different times. A constant freezing rate, in accordance with the optimal tissue destruction rate, is assumed. Results indicate the importance of the blood perfusion factor in the problem and allow the prediction of probe temperature and heat flux variations for optimal results in tissue destruction.

Introduction

Cryosurgery deals with the controlled destruction of biological cells due to deep freezing and thawing. Freezing of cells involves the removal of pure water from both the intercellular and the extracellular solutions. The water freezes, as the temperature is dropped, into biologically inert foreign ice crystal. The rates of ice crystal nucleation and growth are both temperature and vapor pressure dependent. Evidence in the literature indicates that the rate of cooling at the frozen-unfrozen tissue interface is of prime importance in determining the percentage of surviving cells [1].[1] There is also evidence that the rate of thawing influences the destruction rate of the cells too, with.the least number of cells surviving a slow rate of thawing immediately following rapid freezing [1-4]. According to Farrant only a small number of cells are destroyed by low temperatures alone [1]. As discussed in the literature [2-4], at slow cooling rates formation of ice crystals in the extracellular solutions will occur first. These crystals will cause the shrinkage of the cell. At high cooling rates, however, the intercellular water will freeze before shrinkage will have occurred.

Two mechanisms are commonly assumed to be involved in the destruction of biological cells during the freezing and thawing processes. *"At a slow cooling rate it is presumed that damage is linked to the consequences of a raised concentration of extracellular solutes interacting on the shrunken cell. As damage is due to the uptake of extracellular solutes through a leaky membrane, then as the cooling rate becomes faster there will be less time for this (phenomenon) to take place and damage will be reduced at higher cooling rates"* [1]. At higher cooling rates, however, damage is correlated with the formation of intercellular ice before shrinkage occurs thus reducing the number of surviving cells [5, 6].

It should be noted that each cell type was found to possess a different survival curve, i.e., number of surviving cells versus cooling rate. Thus, a certain cooling rate may not cause formation of intercellular ice in one cell type whereas the opposite might hold for another cell type. An example of this phenomenon might be given by observing mouse embryos and red blood cells. Cooling rates larger than 2°C/min will cause intercellular ice to form in mouse embryos while only at 850°C/min will the same occur in red blood cells. Thus, a selective destruction of certain cell types in a tissue might be achieved should their particular survival curves be known.

Cryosurgery has been applied for a number of years to the destruction of malignant and other tissues. Cryosurgical devices come in various shapes and sizes as reviewed by Barron [7]. As the probe is introduced into the tissue and the flow of the cryofluid is initiated, a frozen front starts to form. A physician employing this technique is faced with two basic difficulties: one is the extent to which the frozen front has penetrated, and the second is the possible percentage of destroyed cells to be expected in the tissue [1].

Attempts in the literature were directed at obtaining the location of the frozen front by analytical methods. In 1968, Barron published a paper dealing with heat transfer problems in cryosurgery. Assuming a constant heat flux at the probe surface, he obtained solutions for the ice sphere radius and probe-tip temperature variations [8]. Barron did not consider the effects of either

[1] Numbers in brackets designate References at end of paper.

Contributed by the Heat Transfer Division for publication in the JOURNAL OF HEAT TRANSFER. Manuscript received by the Heat Transfer Division September 25, 1975. Paper No. 76-HT-PP.

blood perfusion or heat generation in the tissue. Assuming a constant probe-tip temperature Trezek and Cooper presented in spherical coordinates a numerical solution which was quite time consuming [9]. In a subsequent paper by the same authors an approximate analytical solution to the rate of growth of the frozen front for the same conditions was presented [10]. In this second work the authors assumed that the heat capacity of both the frozen and unfrozen regions are negligible compared to the latent heat of fusion. This assumption permits the determination of a quasi-steady temperature field. Recently, Warren and co-workers presented an approximate integral technique solution to this problem in cartesian coordinates [11]. They assumed the temperature of the cryofluid to be constant with the probe surface temperature varying until it reaches that of the cryofluid. The temperature distribution in the tissue was taken as a second-degree polynomial while neglecting the metabolic heat rate, and with the heat capacity also neglected relative to the latent heat of fusion.

The purpose of the present paper is to obtain an analytical solution to the problem of freezing of biological tissues taking into account heat capacity, blood perfusion, and metabolic heat rate so that a large enough cooling rate at the frozen-unfrozen tissue interface be produced. As noted previously, the achievement of this minimal cooling rate at the freezing front is of utmost importance where maximum destruction rate is desired. The analysis is presented in cartesian coordinates for simplicity and should, thus, be regarded as a first approximation to the solution of the problem.

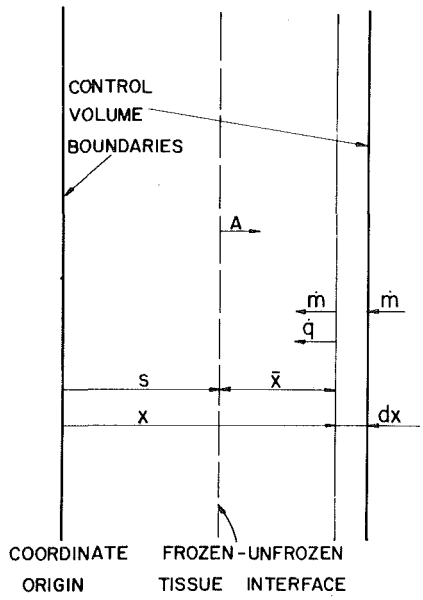

Fig. 1 Schematic drawing of control volume used in the analysis

Analysis

Heat transfer in the living tissue is assumed to be governed by the bio-heat equation [12]. In the frozen region diffusion of heat is described by the heat equation. For both regions the physical and thermophysical properties are assumed homogeneous and constant. The entire tissue is assumed at a constant temperature prior to the initiation of the flow of the cryofluid in the probe. This assumption was shown to be valid at the deeper layers of the tissue [13] and might further be assumed as a good approximation for small volumes of the tissue.

Difference between deep body temperature and blood stream temperature at steady state is assumed constant. The magnitude of this difference is directly proportional to the total metabolic rate and inversely proportional to the average blood perfusion rate [9].

As for blood perfusion and volumetric metabolic rates, two assumptions were tried. One was that both these quantities remain constant throughout the cooling period and then drop to zero when freezing commences. The constancy of blood perfusion rate prior to freezing was observed by Rothenberg [14]. He claims that due to the high rate of cooling applied during cryosurgery, the blood vessels do not have sufficient time to contract, thus, blood continues to flow until it freezes as a bulk. This assumption is also in accordance with Walder [15] and Chato [16]. The second assumption was identical for the blood perfusion rate while the volumetric metabolic rate was assumed to drop linearly to zero with tissue temperature. This linear variation of the metabolic rate could not be supported by the literature and was assumed for the purpose of studying its influence on tissue temperature. It turned out that this second assumption complicated the analysis slightly but did not change the results significantly. Therefore, the first assumption is used in the analysis.

The problem is divided into two time domains: $t < t_0$ and $t > t_0$ where t_0 denotes the time of formation of the first ice crystals. In the first time interval, lowering of tissue temperature to the freezing level takes place. In the second, freezing of the tissue adjacent to the probe occurs with the advancement of the frozen front. At the beginning of the second time interval, temperature distribution immediately preceding formation of the first ice crystals is assumed to be compatible with that obtained by the analysis of the freezing region. This could be obtained by varying the temperature of the probe in a certain manner which will be described later.

The analysis of the freezing region is performed according to the technique of solution of the ablation problem [17]. Temperature distributions in the frozen region are based on solutions to the inverse Stefan problem [18].

The control volume for which the analysis is performed is shown in Fig. 1. In this figure the location of the frozen front is indicated

Nomenclature

A = frozen-unfrozen interface velocity
B = imaginary temperature in equation (13); defined by equation (14)
c_b = specific heat of blood
c_p = specific heat of tissue
h = modified Peclet number, defined by equation (18)
H = frozen-unfrozen interface cooling rate
k = thermal conductivity of unfrozen tissue
k_f = thermal conductivity of frozen tissue
L = latent heat of fusion of water
$\dot{m}$ = imaginary mass flux through the moving control volume surface, defined by equation (7)
$\dot{q}_m$ = metabolic heat generation rate
s = frozen-unfrozen interface location
t = time
t_0 = time of formation of the first ice crystals
T = temperature
T_a = arterial systemic blood temperature
T_0 = initial temperature
T_{ph} = phase change temperature
$\dot{w}_b$ = blood perfusion rate
x = length
x_0 = characteristic length
$\bar{x}$ = length inside control volume, defined in Fig. 1
α = thermal diffusivity
$\beta = \dot{w}_b c_b x_0^2/k$, nondimensional blood perfusion flow rate
$\gamma = \dot{w}_b c_b/k$
ρ = density
ϵ = maximum initial temperature deviation, defined by equation (21)
τ = Fourier number, defined by equation (19)
$\xi = x/x_0$, nondimensional length

Subscripts

f = frozen tissue
b = blood

by the dashed line at a distance s from the coordinate origin (i.e., probe surface). Also shown are the heat flux vector, $\dot{q}$, and the imaginary mass flux, $\dot{m}$, which is discussed in the following.

Solution to the second time domain is obtained in stages. First a solution is sought for the unfrozen region adjacent to the frozen one, i.e., $t > t_0$ and $x > s$. Mathematically, the problem is stated as follows:

$$\frac{\partial T}{\partial t} = \alpha \frac{\partial^2 T}{\partial x^2} + \frac{\dot{w}_b c_b}{\rho \cdot c_p}(T_a - T) + \frac{\dot{q}_m}{\rho \cdot c_p} \tag{1}$$

with the boundary conditions:

$$T(s, t) = T_{ph} \tag{2}$$

$$T(\infty, t) = T_0 \tag{3}$$

and the initial condition

$$T(x, t_0) = T_0 + (T_{ph} - T_0) \exp\left[-\frac{\dot{m}c_p}{k} x\right] \tag{4}$$

where T_0 is defined by [9]

$$T_0 = T_a + \frac{\dot{q}_m}{\dot{w}_b c_b} \tag{5}$$

The control volume surface is assumed to move with the frozen-unfrozen tissue interface. A solution was sought so that the resulting cooling rate at the interface be constant and predictable, which is the physiological requirement for controlling tissue destruction rate.

The temperature profile inside the control volume is obtained by writing a quasi-steady heat balance and integrating twice over the region $\bar{x} = 0$ to infinity. At $\bar{x} \to \infty$ an additional adiabatic condition is imposed to yield

$$T = T_0 + (T_{ph} - T_0) \exp\left[-\frac{\dot{m}c_p}{k}(x - s)\right] \tag{6}$$

which satisfies conditions (2)–(4). Equation (1) is satisfied by equation (6) when $\dot{m}$ is given by[2]

$$\dot{m} = \frac{\{A + [A^2 + 4\gamma\alpha^2]^{1/2}\} \cdot \rho}{2} \tag{7}$$

and by imposing a constant velocity, A, of the freezing front

$$\frac{ds}{dt} = A \text{ with } s(t_0) = 0 \tag{8}$$

[2] $\dot{m}$ is an imaginary mass flux which includes the blood perfusion into and the amount of tissue mass passing through the moving control volume surface.

For a constant cooling rate, $\partial T/\partial t(s, t) = H$, the following expression is obtained

$$A = \left\{\frac{\alpha^2 \cdot H^2}{\gamma \cdot \alpha^2 (T_{ph} - T_0)^2 + \alpha \cdot H(T_{ph} - T_0)}\right\}^{1/2} \tag{9}$$

Next, the analysis is performed for the frozen region subject to the following equations [18]

$$\frac{\partial T_f}{\partial t} = \alpha_f \frac{\partial^2 T_f}{\partial x^2} \qquad t > t_0 \text{ and } x < s \tag{10}$$

$$T_f(s, t) = T_{ph} \text{ with } s = A(t - t_0) \tag{11}$$

$$k_f \frac{\partial T_f}{\partial x}(s, t) = k \frac{\partial T}{\partial x}(s, t) + \rho \cdot L \frac{ds}{dt} \tag{12}$$

Solution to equations (10)–(12) is given by

$$T_f = T_{ph} + B\left\{1 - \exp\left[\frac{A}{\alpha_f}\left(s - x\right)\right]\right\} \tag{13}$$

where

$$B = \left\{\frac{\rho \cdot c_p (T_0 - T_{ph})}{2} \cdot [A + [A^2 + 4\gamma\alpha^2]^{1/2}] + \rho \cdot L \cdot A\right\} \frac{1}{\rho_f c_{pf} A} \tag{14}$$

In the first time domain, $t < t_0$, an exact solution to the problem might be obtained by assuming a constant cooling rate at the probe-tissue interface, i.e.,

$$\frac{\partial T}{\partial t}(0, t) = H \tag{15}$$

The governing equation and the additional boundary condition are given by equations (1) and (3), respectively, and the initial condition is given by:

$$T(x, 0) = T_0 \tag{16}$$

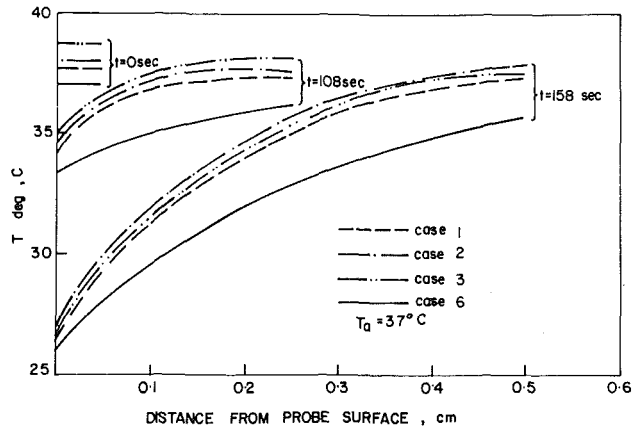

Fig. 2(*a*) Approximate temperature distributions in the unfrozen tissue as calculated from equation (6) for different cases

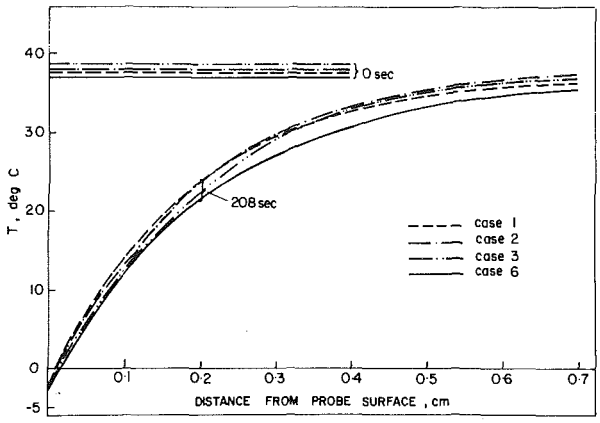

Fig. 2(*b*) Approximate temperature distributions at the onset of freezing for different cases

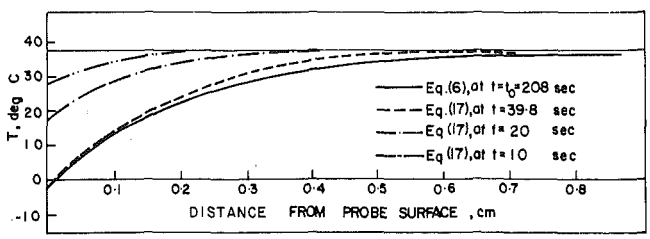

Fig. 2(*c*) Exact temperature distributions in the unfrozen tissue for case 2 and comparison with the required distribution at the onset of freezing

The solution is obtained by a Laplace transform and is given by

$$T = T_0 + \frac{(T_a - T_0)}{2} \cdot h\left\{\left(\tau - \frac{\xi}{2\sqrt{\beta}}\right) \exp(-\xi\sqrt{\beta}) \operatorname{erfc}\left(\frac{\xi}{2\sqrt{\tau}} - \sqrt{\beta \cdot \tau}\right) + \left(\tau + \frac{\xi}{2\sqrt{\beta}}\right) \exp(\xi\sqrt{\beta}) \operatorname{erfc}\left(\frac{\xi}{2\sqrt{\tau}} + \sqrt{\beta \cdot \tau}\right)\right\} \quad (17)$$

where

$$h = \frac{H \cdot \rho \cdot c_p \cdot x_0^2}{(T_a - T_0) \cdot k} \quad (18)$$

$$\tau = \frac{tk}{\rho c_p x_0^2} \quad (19)$$

and

$$\xi = \frac{x}{x_0} \quad (20)$$

It turned out that the required initial condition at $t = t_0$, i.e., equation (4), could not be satisfied exactly. A maximum deviation of about 7 percent between the desired equation (4), and obtained equation (17), was obtained (see Fig. 2(*c*)). Thus, a slightly different approach was adopted. Accordingly, it was assumed that the shape of the temperature distribution in the tissue at $t = t_0$ be identical to the one given by equation (4). This assumption dictates that the temperature profile at $t < t_0$ and $x > 0$ be given by equations (6)–(9). However, when equation (6) is examined, it is observed that t_0 should attain a very large value if the initial condition, equation (16), is to be satisfied. This result is due to the exponential nature of equation (6). Thus, an engineering compromise in the form of permitting a slight deviation in the initial condition was required. If ϵ denotes this maximum deviation

$$\epsilon \equiv \frac{T(0, 0) - T_0}{T_{ph} - T_0} \quad (21)$$

then t_0 is determined by

$$t_0 = -\frac{k}{\dot{m} c_p A} \ln\epsilon \quad (22)$$

For the set of physical parameters as given in Table 1, t_0 was calculated at about 39 s. On the other hand, taking $\epsilon = 0.005$, t_0 is obtained at 208 s which is considerably longer; for t_0 to be equal to 39 s the deviation is calculated at about 0.38 which is a prohibitively high value.

Discussion

First, the effects of the various parameters are examined. From equation (9), with T_0 replaced by equation (5), it is obtained that the velocity of the freezing front, A, decreases somewhat with increasing the volumetric metabolic rate, $\dot{q}_m$. Increasing blood perfusion rate, $\dot{w}_b$, also decreases A but more sharply indicating the importance of this factor in energy transport in the tissue. It follows from equations (4), (5), (7), and (9) that the temperature gradient at the freezing front becomes larger when both $\dot{q}_m$ and $\dot{w}_b$ increase. It is also evident, from equation (7), that the effect of $\dot{w}_b$ is much stronger than that of $\dot{q}_m$.

Analysis of the results is performed for the numerical values and 6 cases as given in Tables 1(*a*) and 1(*b*). In this table the corresponding values for T_0 as calculated by equation (5) are also shown. Case 6 in which both $\dot{q}_m$ and $\dot{w}_b$ vanish is included for completeness and is probably applicable to situations where in vitro freezing occurs. In all cases $t_0 = 208$ s, such that $\epsilon < 0.005$.

Temperature distributions in the unfrozen region, equation (6), when $t < t_0$, for cases 1–3 and 6, are shown in Figs. 2(*a*) and 2(*b*). It is seen that deviation from the initial temperature remains small for relatively long times and then increases exponentially with time. In Fig. 2(*c*) the exact solution, equation (17), is plotted for case 2. At $t = t_0$ both the exact solution and the required one, equation (4), are compared. The maximum deviation found for these two graphs is about 7 percent.

In Fig. 3, temperature distribution in both the frozen and unfrozen regions at $t = t_0 + 100$ s are shown for all six cases. It is seen that the higher $\dot{w}_b$ and $\dot{q}_m$ the closer the location of the frozen front, at $x = s$, to the tissue-probe interface. Also, the effects of $\dot{q}_m$ are seen to be smaller than those of $\dot{w}_b$. For the limiting case 6, i.e., $\dot{w}_b = \dot{q}_m = 0$, the tissue-probe interfacial temperature is the lowest at about −152°C, increasing to about −107°C for case 1.

Probe-tissue interfacial temperature and heat flux and location of the frozen front as functions of time are shown in Figs. 4 and 5. Fig. 4 gives the values for cases 1–3 and 6 whereas Fig. 5 is for cases 2–6 excluding 3. These figures again support the previous observations regarding the freezing front velocity and the probe-tissue interface temperature. It is observed in Fig. 5 that the effect of varying $\dot{q}_m$ on the temperature distribution in the tissue is very small and might be neglected without introducing large errors. It is also seen that the heat flux is larger for smaller values of $\dot{w}_b$ and $\dot{q}_m$. Another result is associated with a limited minimal probe temperature which might be due to the use of different cryofluids. When this limitation is considered coincidental with the desired constant cooling rate, it is obtained that the higher $\dot{w}_b$ and $\dot{q}_m$, the deeper the extent of destruction of the tissue.

Table 1 Physical and thermophysical properties

c_p, kj/kg°C	c_b, kj/kg°C	k, W/m°C	k_f, W/m°C	α, m²/s	α_f, m²/s	L, kj/kg	H, °C/s	T_{ph}, °C
3.72	3.64	0.46	1.4	11	33	285	−1	−2

(*a*)

Case	1	2	3	4	5	6
$\dot{q}_m$, kW/m³	251	251	251	167	84	0
$\dot{w}_b$, kg/m³s	10	7.0	4.0	7.0	7.0	0
T_0, °C	37.7	38	38.7	37.6	37.3	37

(*b*)

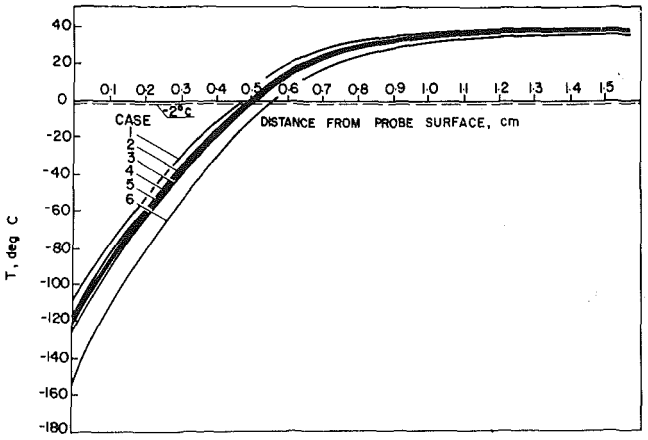

Fig. 3 Temperature distributions in both the frozen and unfrozen regions 100 s after freezing commenced for all six cases

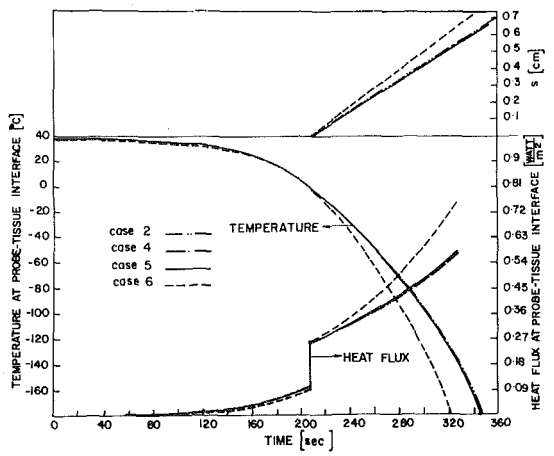

Fig. 5 Probe temperature and heat flux variations and location of the frozen front for various metabolic heat rates

Fig. 6 shows typical temperature distributions for case 2. For the assumed set of parameters and a minimum probe temperature of −180°C the depth of freezing is 6.4 mm reached 133 s after formation of the first ice crystals. This result is also easily obtained from Figs. 4 and 5.

Results of the present work were compared to those reported previously. It is found that Warren and co-workers obtained the same slowing effect of blood perfusion on the velocity of the freezing front [11]. When examining their cooling rates at the frozen front, they found a −7°C/s temperature drop for $s = 0$ decreasing to −1°C/s at a depth of 6 mm reached 120 s after initiation of freezing. These results were obtained for a minimum probe temperature of −160°C. These cooling rates could be inside the range where a considerable number of cells may survive freezing, depending on the tissue type [1]. In the present work, with heat capacity and heat generation considered, and for a constant cooling rate of −1°C/s, the frozen front is located at a depth of about 6.1 mm after 120 s (see Fig. 4). Trezek and Cooper obtained similar results for spherical coordinates [9].

Conclusions

An analysis of a Stefan-like problem in the freezing of a biological tissue in cartesian coordinates is presented. Blood perfusion and metabolic heat generation rates are included in the thermal energy balance of the tissue. Heat capacity of the tissue is also considered and the solution is obtained for a constant imposed cooling rate at the freezing front.

Based on this analysis, the following conclusions are drawn:

1 The effect of metabolic heat generation rate, $\dot{q}_m$, on the temperature distribution in the tissue is small and might, therefore, be neglected without causing significant errors in the results. On the other hand, blood perfusion effects are significant both in regard to the location of the freezing front and the temperature distribution in the tissue.

2 The occurrence of small values of blood perfusion and metabolic rate cause a high velocity of the freezing front with a small depth of the frozen region.

Results presented in this work facilitate the estimation of required probe temperature and heat flux variations such that a constant cooling rate at the freezing front is achieved. As indicated previously, the present cartesian model yields values close to those obtained by the spherical or cylindrical models. These results allow, therefore, the surgeon to employ a controlled cryoprocess for optimal results in tissue destruction.

References

1 Farrant, J., "Cryobiology—The Basis to Cryosurgery," in *Cryogenics in Surgery,* Medical Examination Publishing Co. Inc., June 1971.

2 Meryman, H. T., "Mechanics of Freezing in Living Cells and Tissues," *Science,* Vol. 124, Sept. 1956, pp. 515–521.

3 Leibo, S. P., and Mazur, P., "The Role of Cooling Rates in Low Temperature Preservation," *Cryobiology,* Vol. 8, 1971, pp. 447–452.

4 Ling, G. R., and Tien, C. L., "An Analysis of Cell Freezing and Dehydration," JOURNAL OF HEAT TRANSFER, TRANS. ASME, Series C,

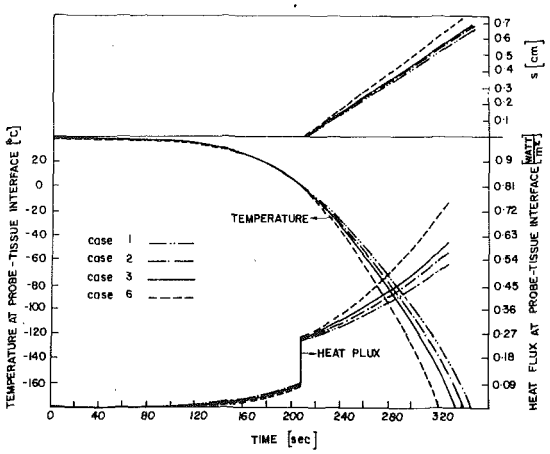

Fig. 4 Probe temperature and heat flux variations and location of the frozen front for various blood perfusion rates

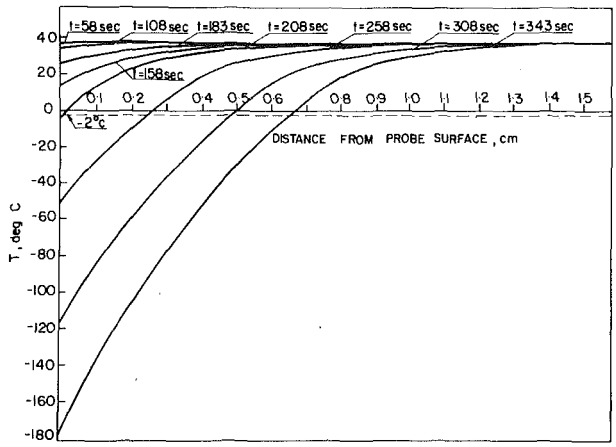

Fig. 6 Temperature distributions in both the frozen and unfrozen regions for case 2

Vol. 92, No. 3, 1970, pp. 393–397.

5 Diller, K. R., "Intracellular Freezing: Effect of Extracellular Supercooling," *Cryobiology*, Vol. 12, Oct. 1975, pp. 480 485.

6 Toscano, W. M., Cravalho, E. G., Silveras, O. M., and Huggins, C. E., "The Thermodynamics of Intracellular Ice Nucleation in the Freezing of Erythrocytes," JOURNAL OF HEAT TRANSFER, TRANS. ASME, Series C, Vol. 97, 1975, pp. 326–332.

7 Barron, R. F., "Cryoinstrumentation," in *Cryogenics in Surgery*, Medical Examination Publishing Co. Inc., June 1971.

8 Barron, R. F., "Heat Transfer Problems in Cryosurgery," *J. Cryosurgery*, Vol. 1, 1968, pp. 316 325.

9 Cooper, T. E., and Trezek, G. J., "Mathematical Predictions of Cryogenic Lession," in *Cryogenics in Surgery*, Mecical Examination Publishing Co. Inc., June 1971.

10 Cooper, T. E., and Trezek, G. J., "Rate of Lesion Growth Around Spherical and Cylindrical Cryoprobes," *Cryobiology*, Vol. 7, No. 4, 1971, p. 6.

11 Warren, R. P., Bingham, P. E., and Carpenter, J. D., "Heat Flow in Living Tissue During Cryosurgery," ASME Paper No. 74-WA/Bio-6, 1974.

12 Pennes, H. H., "Analysis of Tissue and Critical Blood Temperatures in the Resting Human Forearm," *J. Appl. Phys.*, Vol. 1, 1968, pp. 93–122.

13 Shitzer, A., and Kleiner, M. K., "Thermal Behaviour of Biological Tissues —A General Analysis," to apper in *Bulletin of Mathematical Biology*, 1976.

14 Rothenberg, H. W., "Cutaneous Circulation in Rabbits and Humans Before, During, and After Cryosurgical Procedures Measured by Xenn-133 Clearance," *Cryobiology*, Vol. 6, No. 6, 1970, pp. 507–511.

15 Walder, H. A. D., "Experimental Cryosurgery," in *Cryogenics in Surgery*, Medical Examination Publishing Co. Inc., June 1971.

16 Chato, J. C., "A Method for the Measurement of the Thermal Properties of Living Tissue," *Thermal Problems in Biotechnology*, ASME Symposium Series, 1968, pp. 16–25.

17 Freedman, S. J., *Ablation in Developments in Heat Transfer*, London, 1964.

18 Langford, D., "New Analytical Solutions of the One Dimensional Heat Equation for Temperature and Heat Flow Rate Both Prescribed at the Same Fixed Boundary (With Application to the Phase Change Problem)," *Quart. Appl. Math.*, Vol. XXIV, No. 4, 1967, pp. 316–322.

ERRATUM

Erratum on: H. Ozoe, K. Yamamoto, S. W. Churchill, and H. Sayama, "Three-Dimensional, Numerical Analysis of Laminar Natural Convection in a Confined Fluid Heated From Below," published in the May 1976 issue of the JOURNAL OF HEAT TRANSFER, pp. 202–207.

1 The first two lines of the Introduction should read, "Three-dimensional, numerical analysis of natural convection in a confined fluid has been rather neglected following the pioneering"

2 In the Nomenclature, D/Dv_τ should be D/D_τ

3 The first and third columns of Table 1 should read

2000	1.451
2600	.
3000	1.966
4000	. ..
6000	2.617
8000	—

4 In Fig. 7, the × at $Ra \times 10^{-3} = 5$ should be at $Ra \times 10^{-3} = 6$.

5 The caption of Fig. 4 should read $\Delta\tau = 5.0$ instead of 50.0, and the caption of Fig. 6 should read $\Delta\tau = 1.54$ instead of 15.4.

journal of heat transfer

technical notes

Experiments on a Three-Row Fin and Tube Heat Exchanger

F. E. M. Saboya[1] and E. M. Sparrow[1]

Introduction

This note is a brief addendum to a previously reported experimental study of air-side transfer characteristics of one- and two-row plate fin and tube heat exchanger configurations [1, 2].[2] The experiments were performed as mass transfer studies using the naphthalene sublimation technique, with corresponding heat transfer results being obtainable via the analogy between heat and mass transfer. Quantitative results were given for the local and average transfer coefficients. Various transfer mechanisms were identified, the most remarkable being the vortices which develop in front of the tubes and are swept around the sides.

An extension of the original research program to include configurations with three staggered rows of tubes has recently been carried out, and the results are reported herein. A schematic plan view of the fin surface, showing dimensions and other nomenclature, is presented in Fig. 1. Local mass transfer measurements were performed for the typical element of the third-row fin bounded by the dashed lines indicated in the diagram. The overall mass transfer from the entire three-row fin surface was determined with a precision balance.

Information about the experimental apparatus and procedure, the preparation of the naphthalene surfaces, the data reduction techniques, and the dimensionless parameters is available in [1, 2]. The dimensions D, S, L, and h (spacing between fins) were maintained as before to facilitate comparisons of results.

Results

The presentation of results will begin with the average transfer coefficients. All the results are for a Schmidt number Sc = 2.5 (Sc is analogous to Pr).

Average transfer coefficients for the fin surface as a whole were evaluated using the log-mean concentration difference and are presented in Fig. 2, where the average Sherwood number $\overline{Sh}$ (analogous to the average Nusselt number $\overline{Nu}$) is plotted against the Reynolds number. The figure contains results for the three-row coil, as well as results for one- and two-row coils, respectively, from [1, 2]. It is seen from the figure that at low Reynolds numbers, the fewer the rows, the higher the average transfer coefficients. However, with increasing values of Reynolds number, the transfer coefficients for the multirow coils tend to overtake that for the one-row coil, and the curves appear to cross. The relatively better performance of the multirow coils at higher Reynolds numbers is due to the strengthening of the vortices of the second and third rows which occurs as the Reynolds number increases.

The contributions of the various portions of the fin surface to the overall rate of mass transfer in a three-row coil will now be examined.

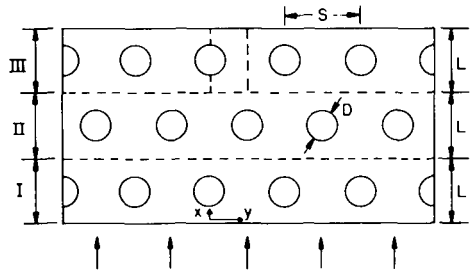

Fig. 1 Schematic plan view of fin surface

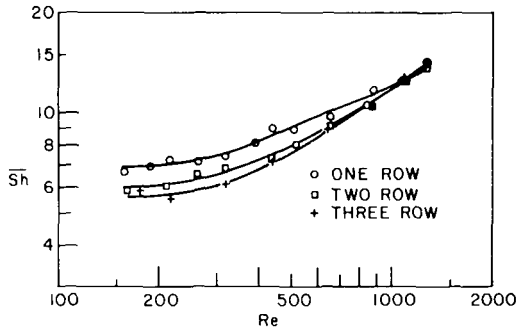

Fig. 2 Average Sherwood numbers for one-, two-, and three-row coils

[1] Department of Mechanical Engineering, University of Minnesota, Minneapolis, Minn.

[2] Numbers in brackets designate References at end of technical note.

Contributed by the Heat Transfer Division of THE AMERICAN SOCIETY OF MECHANICAL ENGINEERS. Manuscript received by the Heat Transfer Division March 23, 1976.

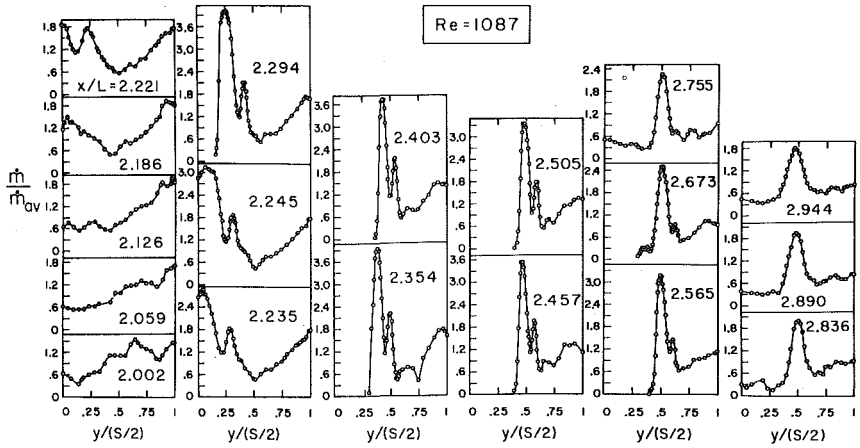

Fig. 3(*a*) Local mass transfer distributions for the third-row fin, Re = 1087

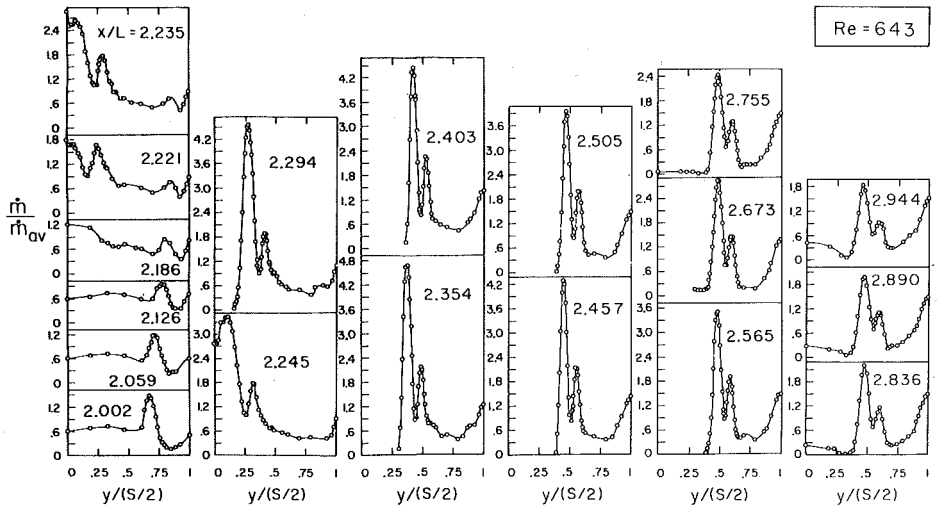

Fig. 3(*b*) Local mass transfer distributions for the third-row fin, Re = 643

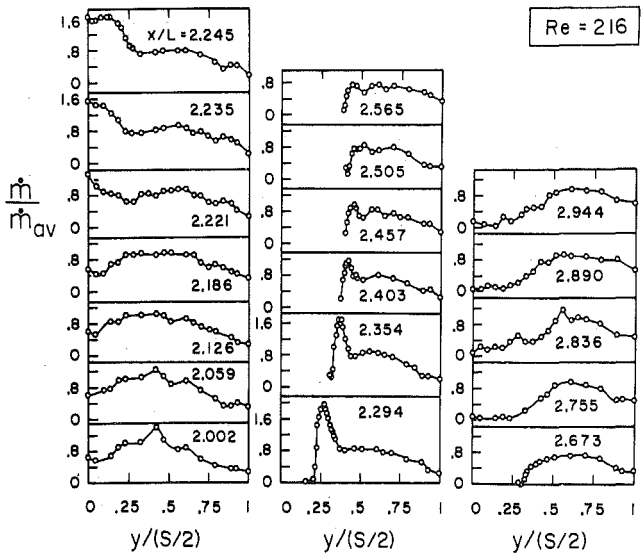

Fig. 3(*c*) Local mass transfer distributions for the third-row fin, Re = 216

Table 1 Relative transfer capabilities of regions I, II, and III

Re	$\dot{M}_I/\dot{M}_{total}$	$\dot{M}_{II}/\dot{M}_{total}$	$\dot{M}_{III}/\dot{M}_{total}$
216	0.497	0.286	0.217
643	0.422	0.316	0.262
1087	0.348	0.314	0.338

For this purpose, the parts of the fin respectively associated with the first, second, and third tube rows are designated as I, II, and III (see Fig. 1), with $\dot{M}_I$, $\dot{M}_{II}$, and $\dot{M}_{III}$ denoting the corresponding mass transfer rates and $\dot{M}_{total}$ the overall mass transfer rate. Table 1 lists results for these quantities in ratio form for three Reynolds numbers.

Table 1 shows that the relative contributions of the various rows to the overall mass transfer are strongly affected by the Reynolds number of the flow. At low Reynolds numbers, the first row is the greatest contributor by far. As the Reynolds number increases, the relative contributions of the second and third rows increase. At the highest Reynolds number of Table 1, the contribution of each of the

three rows is nearly equal. The relative increase in the mass transfer in the second and third rows is due to two causes. First, strong vortices are activated in these rows at higher Reynolds numbers. Second, the streamwise rise in bulk vapor concentration (analogous to bulk temperature) decreases as the Reynolds number increases, with the result that the wall-to-bulk concentration difference tends to be more uniform along the length of the passage. Table 1 indicates that the downstream rows of a multirow heat exchanger are used more efficiently at higher Reynolds numbers.

Local mass transfer results for the third-row fin are plotted in Figs. 3(*a*), 3(*b*), and 3(*c*), respectively, for Re = 1087, 643, and 216. Each figure contains a succession of graphs which correspond to streamwise positions between $x/L = 2$ and $x/L = 3$ (see Fig. 1 for nomenclature). At each streamwise position, the ratio $\dot{m}/\dot{m}_{av}$ is plotted as a function of the dimensionless spanwise coordinate $y/(S/2)$. The quantity $\dot{m}$ is the local rate of mass transfer at position (x,y), whereas $\dot{m}_{av}$ is the mass transfer rate averaged over the entire three-row fin.

Inspection of these figures indicates that except near the forward portion of the third-row fin, the spanwise mass transfer distributions for the higher Reynolds numbers are dominated by the effects of the vortices. At low Reynolds numbers, the vortices have a substantially lesser influence.

A detailed comparison of the results of Figs. 3(*a*)–3(*c*) with those for the second-row fin of a two-row coil [2, 3] reveals an overall similarity in the distribution curves, but with a number of differences in detail. The highest peak in evidence among the distribution curves for the third row is at the side of the tube, just downstream of the forward edge, whereas the highest peak in the second row (as well as in the first row) is in front of the tube. This shift in the position of the highest peak is, in all likelihood, due to the blockage imposed by the first row upon the third row. Furthermore, the pairs of peaks in the distributions for the higher Reynolds numbers are somewhat differently disposed one to the other in the second and in the third rows. Differences are also in evidence in the "filling in" of the distribution curves in the wakes behind the respective tubes. It may be concluded that row-to-row sameness in the fluid flow pattern has not yet been established.

References

1 Saboya, F. E. M., and Sparrow, E. M., "Local and Average Transfer Coefficients for One-Row Plate Fin and Tube Heat Exchangers," JOURNAL OF HEAT TRANSFER, TRANS., ASME, Series C, Vol. 96, 1974, pp. 265–272.

2 Saboya, F. E. M., and Sparrow, E. M., "Transfer Characteristics of Two-Row Plate Fin and Tube Heat Exchanger Configurations," *International Journal of Heat and Mass Transfer*, Vol. 19, 1976, pp. 41–49.

3 Saboya, F. E. M., "Local and Average Transfer Coefficients in Plate Fin and Tube Exchanger Configurations," PhD thesis, University of Minnesota, 1974.

Free Convection Heat Transfer From Vertical Needles

G. D. Raithby[1] and K. G. T. Hollands[1]

An analysis of the heat transfer by free convection from oblate and prolate spheroids, and a comparison of predictions with measurements, are reported elsewhere in this issue of the journal [32].[2] As the ratio of the minor to major axis of the prolate spheroid approaches zero, the prolate spheroid resembles a thin vertical needle tapered from the center toward both ends. Since the problems of heat transfer from thin vertical wires (of constant diameter) and from needles tapered toward only one end (projecting toward the incoming flow [33, 34]) have received a great deal of attention in the free convection literature, it is useful to extend the analysis of [32] to this closely related problem. The numbering of equations and references in this note carry on from that paper; figures and equations in [32] will be referred to, and nomenclature used, without any further explicit identification of the Reference.

The results of the analysis for this limiting case are included in Fig. 4 where $\bar{\mathrm{Nu}}_B$ is plotted against Ra_B. However, this figure reveals that, as $C/B \to 0$, the laminar heat transfer portion of the curves become very sensitive to the particular value of C/B. It would be preferable to choose an independent variable such that the Nusselt number changes little for small C/B.

To obtain this, an equation is sought which correlates the analytical results well for laminar flow. Equation (2) is one possible form that has the correct asymptotic limits, but it has already been stated that it is an unsatisfactory choice for $C/B \lesssim 0.2$ for prolate spheroids. Another equation with the correct limits can be obtained by applying Langmuir's idea [11], as follows

$$(\bar{\mathrm{Nu}}_B)_\ell = \frac{2\sqrt{1-(C/B)^2}}{f_1(C/B)} \int_0^\pi \frac{\sin\theta}{\ln\left[\tanh(\eta_0/2)/\tanh(\eta_i/2)\right]}\, d\theta \quad (7a)$$

$$\overset{?}{=} \frac{2\sqrt{1-(C/B)^2}}{f_1(C/B)} \frac{2}{\ln\left[\tanh(\eta_0/2)/\tanh(\eta_i/2)\right]} \quad (7b)$$

Equation (7*a*) is the result of the laminar heat transfer analysis (equation B.12), where η_0 depends on θ, Ra_B, and C/B. The "?" above the second equality indicates that the adequacy of equation (7*b*) in approximating the results from (7*a*) is not yet established.

Equation (7*b*) is the Nusselt number based on conduction alone between two confocal isothermal spheroids (see Yovanovich [29]), the inner one designated by η_i and the outer by η_0. The question is, can an expression for η_0 (involving Ra_B and C/B) be found such that equations (7*a*) and (7*b*) can be made approximately equal? The method used by Eckert [27] and Sparrow and Gregg [12] for finding this function is to demand that $\bar{\mathrm{Nu}}_B$ yield the thin-layer result at asymptotically high Ra_B. This results in

$$\eta_0 = \eta_i + 2^{7/4}/(\bar{C}_\ell f_2^{3/4} Ra_B^{1/4}) \quad (8)$$

Now it will also be noted that as $\mathrm{Ra}_B \to 0$, $\eta_0 \to \infty$, so that equation (7*b*) also yields the correct lower (conduction) limit. There is *no* guarantee from the analysis here that equations (7*b*) and (7*a*) are in *good agreement for intermediate* Ra_B. However, *calculations* show that the agreement is excellent for $C/B \lesssim 0.05$, and the Langmuir-type correction is justified. This is consistent with Sparrow and Gregg's [12] discovery that the Langmuir correction gave excellent agreement with their more exact analysis for vertical cylinders. An important result here is the establishment of an upper bound for C/B (or the aspect ratio of the needle) beyond which the Langmuir method of correction fails to give accurate answers.

Making several approximations in equation (7*b*) which are valid at small C/B, one obtains

$$(\bar{\mathrm{Nu}}_C)_\ell = \left(\frac{8}{\pi}\right) \Big/ \ln\left[1 + 2.51/\left(\bar{C}_\ell \left(\frac{C}{B}\mathrm{Ra}_C\right)^{1/4}\right)\right] \quad (9)$$

This equation: (*a*) approximates with high accuracy (to within about 1 percent) the results of the analysis for *laminar* heat transfer for $C/B \lesssim 0.05$; and (*b*) reveals the sought independent variable, $(C/B)\mathrm{Ra}_B$. This variable was introduced for vertical cylindrical wires by Sparrow and Gregg [12].

The final equation has the same form as the equation obtained by Sparrow and Gregg by applying the Langmuir correction for thin vertical cylinders, if one replaces the minor axis of the present needle by the (constant) diameter of their vertical wire. The numerical

[1] Thermal Engineering Group, Department of Mechanical Engineering, University of Waterloo, Waterloo, Ontario, Canada. Mems. ASME

[2] Numbers in brackets designate References at end of technical note.

Contributed by the Heat Transfer Division of THE AMERICAN SOCIETY OF MECHANICAL ENGINEERS. Manuscript received by the Heat Transfer Division March 3, 1976.

three rows is nearly equal. The relative increase in the mass transfer in the second and third rows is due to two causes. First, strong vortices are activated in these rows at higher Reynolds numbers. Second, the streamwise rise in bulk vapor concentration (analogous to bulk temperature) decreases as the Reynolds number increases, with the result that the wall-to-bulk concentration difference tends to be more uniform along the length of the passage. Table 1 indicates that the downstream rows of a multirow heat exchanger are used more efficiently at higher Reynolds numbers.

Local mass transfer results for the third-row fin are plotted in Figs. 3(*a*), 3(*b*), and 3(*c*), respectively, for Re = 1087, 643, and 216. Each figure contains a succession of graphs which correspond to streamwise positions between $x/L = 2$ and $x/L = 3$ (see Fig. 1 for nomenclature). At each streamwise position, the ratio $\dot{m}/\dot{m}_{av}$ is plotted as a function of the dimensionless spanwise coordinate $y/(S/2)$. The quantity $\dot{m}$ is the local rate of mass transfer at position (x,y), whereas $\dot{m}_{av}$ is the mass transfer rate averaged over the entire three-row fin.

Inspection of these figures indicates that except near the forward portion of the third-row fin, the spanwise mass transfer distributions for the higher Reynolds numbers are dominated by the effects of the vortices. At low Reynolds numbers, the vortices have a substantially lesser influence.

A detailed comparison of the results of Figs. 3(*a*)–3(*c*) with those for the second-row fin of a two-row coil [2, 3] reveals an overall similarity in the distribution curves, but with a number of differences in detail. The highest peak in evidence among the distribution curves for the third row is at the side of the tube, just downstream of the forward edge, whereas the highest peak in the second row (as well as in the first row) is in front of the tube. This shift in the position of the highest peak is, in all likelihood, due to the blockage imposed by the first row upon the third row. Furthermore, the pairs of peaks in the distributions for the higher Reynolds numbers are somewhat differently disposed one to the other in the second and in the third rows. Differences are also in evidence in the "filling in" of the distribution curves in the wakes behind the respective tubes. It may be concluded that row-to-row sameness in the fluid flow pattern has not yet been established.

References

1 Saboya, F. E. M., and Sparrow, E. M., "Local and Average Transfer Coefficients for One-Row Plate Fin and Tube Heat Exchangers," JOURNAL OF HEAT TRANSFER, TRANS., ASME, Series C, Vol. 96, 1974, pp. 265–272.

2 Saboya, F. E. M., and Sparrow, E. M., "Transfer Characteristics of Two-Row Plate Fin and Tube Heat Exchanger Configurations," *International Journal of Heat and Mass Transfer*, Vol. 19, 1976, pp. 41–49.

3 Saboya, F. E. M., "Local and Average Transfer Coefficients in Plate Fin and Tube Exchanger Configurations," PhD thesis, University of Minnesota, 1974.

Free Convection Heat Transfer From Vertical Needles

G. D. Raithby[1] and K. G. T. Hollands[1]

An analysis of the heat transfer by free convection from oblate and prolate spheroids, and a comparison of predictions with measurements, are reported elsewhere in this issue of the journal [32].[2] As the ratio of the minor to major axis of the prolate spheroid approaches zero, the prolate spheroid resembles a thin vertical needle tapered from the center toward both ends. Since the problems of heat transfer from thin vertical wires (of constant diameter) and from needles tapered toward only one end (projecting toward the incoming flow [33, 34]) have received a great deal of attention in the free convection literature, it is useful to extend the analysis of [32] to this closely related problem. The numbering of equations and references in this note carry on from that paper; figures and equations in [32] will be referred to, and nomenclature used, without any further explicit identification of the Reference.

The results of the analysis for this limiting case are included in Fig. 4 where $\bar{\mathrm{Nu}}_B$ is plotted against Ra_B. However, this figure reveals that, as $C/B \to 0$, the laminar heat transfer portion of the curves become very sensitive to the particular value of C/B. It would be preferable to choose an independent variable such that the Nusselt number changes little for small C/B.

To obtain this, an equation is sought which correlates the analytical results well for laminar flow. Equation (2) is one possible form that has the correct asymptotic limits, but it has already been stated that it is an unsatisfactory choice for $C/B \lesssim 0.2$ for prolate spheroids. Another equation with the correct limits can be obtained by applying Langmuir's idea [11], as follows

$$(\bar{\mathrm{Nu}}_B)_\ell = \frac{2\sqrt{1-(C/B)^2}}{f_1(C/B)} \int_0^\pi \frac{\sin\theta}{\ln\left[\tanh(\eta_0/2)/\tanh(\eta_i/2)\right]}\, d\theta \quad (7a)$$

$$\overset{?}{=} \frac{2\sqrt{1-(C/B)^2}}{f_1(C/B)} \frac{2}{\ln\left[\tanh(\eta_0/2)/\tanh(\eta_i/2)\right]} \quad (7b)$$

Equation (7*a*) is the result of the laminar heat transfer analysis (equation B.12), where η_0 depends on θ, Ra_B, and C/B. The "?" above the second equality indicates that the adequacy of equation (7*b*) in approximating the results from (7*a*) is not yet established.

Equation (7*b*) is the Nusselt number based on conduction alone between two confocal isothermal spheroids (see Yovanovich [29]), the inner one designated by η_i and the outer by η_0. The question is, can an expression for η_0 (involving Ra_B and C/B) be found such that equations (7*a*) and (7*b*) can be made approximately equal? The method used by Eckert [27] and Sparrow and Gregg [12] for finding this function is to demand that $\bar{\mathrm{Nu}}_B$ yield the thin-layer result at asymptotically high Ra_B. This results in

$$\eta_0 = \eta_i + 2^{7/4}/(\bar{C}_\ell f_2^{3/4} Ra_B^{1/4}) \quad (8)$$

Now it will also be noted that as $\mathrm{Ra}_B \to 0$, $\eta_0 \to \infty$, so that equation (7*b*) also yields the correct lower (conduction) limit. There is *no* guarantee from the analysis here that equations (7*b*) and (7*a*) are in *good agreement for intermediate* Ra_B. However, *calculations* show that the agreement is excellent for $C/B \lesssim 0.05$, and the Langmuir-type correction is justified. This is consistent with Sparrow and Gregg's [12] discovery that the Langmuir correction gave excellent agreement with their more exact analysis for vertical cylinders. An important result here is the establishment of an upper bound for C/B (or the aspect ratio of the needle) beyond which the Langmuir method of correction fails to give accurate answers.

Making several approximations in equation (7*b*) which are valid at small C/B, one obtains

$$(\bar{\mathrm{Nu}}_C)_\ell = \left(\frac{8}{\pi}\right) \Big/ \ln\left[1 + 2.51/\left(\bar{C}_\ell \left(\frac{C}{B}\mathrm{Ra}_C\right)^{1/4}\right)\right] \quad (9)$$

This equation: (*a*) approximates with high accuracy (to within about 1 percent) the results of the analysis for *laminar* heat transfer for $C/B \lesssim 0.05$; and (*b*) reveals the sought independent variable, $(C/B)\mathrm{Ra}_B$. This variable was introduced for vertical cylindrical wires by Sparrow and Gregg [12].

The final equation has the same form as the equation obtained by Sparrow and Gregg by applying the Langmuir correction for thin vertical cylinders, if one replaces the minor axis of the present needle by the (constant) diameter of their vertical wire. The numerical

[1] Thermal Engineering Group, Department of Mechanical Engineering, University of Waterloo, Waterloo, Ontario, Canada. Mems. ASME

[2] Numbers in brackets designate References at end of technical note.

Contributed by the Heat Transfer Division of THE AMERICAN SOCIETY OF MECHANICAL ENGINEERS. Manuscript received by the Heat Transfer Division March 3, 1976.

constants, however, are somewhat larger in the present equation resulting in slightly larger values of the Nusselt number. This seems reasonable since the average diameter of the tapered wire along its length is less than C; the thick-layer correction is therefore more important and the Nusselt number larger than if the wire had a constant diameter of C along its length.

Replacing the wire diameter and length in their analysis respectively by C and B, one finds that the present Nusselt numbers $(\bar{\mathrm{Nu}}_C)_\ell$ are larger by 4, 10, 18, and 22 percent, respectively, for $\bar{C}_\ell(C/B)\mathrm{Ra}_C$ values of 10, 1, 0.1, and 0.01.

References

32 Raithby, G. D., Pollard, A., Hollands, K. G. T., and Yovanovich, M. M., "Free Convection Heat Transfer From Spheroids," JOURNAL OF HEAT TRANSFER, TRANS, ASME, Series C, Vol. 98, 1976, pp. 452–458.

33 Cebeci, T., and Na, T. U., "Laminar Free-Convection Heat Transfer From a Needle," *The Physics of Fluids*, Vol. 12, No. 2, 1969, pp. 463–465

34 Narain, J. P., and Uberoi, M. S., "Laminar Free Convection From Vertical Thin Needles," *The Physics of Fluids*, Vol. 15, No. 5, 1972, pp. 928–929.

Buoyancy Effects on Forced Convection Along a Vertical Cylinder With Uniform Surface Heat Flux

A. Mucoglu[1] and T. S. Chen[1]

Nomenclature

C_f = local friction factor
F = reduced stream function, equation (2)
$G = \xi$ – derivative of F
g = gravitational acceleration
Gr_x^* = modified Grashof number, $g\beta|q_w|x^4/k\nu^2$
k = thermal conductivity
Nu_x = local Nusselt number, $q_w x/(T_w - T_\infty)k$
Pr = Prandtl number
q_w = local surface heat transfer rate per unit area
r = radial coordinate
r_0 = radius of cylinder
Re_x = Reynolds number, $u_\infty x/\nu$
T = fluid temperature
T_w = wall temperature
T_∞ = free stream temperature
u = axial velocity component
u_∞ = free stream velocity
v = radial velocity component
x = axial coordinate
β = volumetric coefficient of thermal expansion
η = pseudo-similarity variable, equation (1)
θ = dimensionless temperature, equation (2)
μ = dynamic viscosity
ν = kinematic viscosity
ξ = transformed axial coordinate, equation (1)
$\phi = \xi$ – derivative of θ
ψ = stream function
Ω^* = buoyancy parameter, $\mathrm{Gr}_x^*/\mathrm{Re}_x^{5/2}$

Introduction

In forced convection along an inclined or a vertical heated surface, the buoyancy force plays an important role in modifying the flow field and hence the rate of heat transfer from the surface. In a recent study [1],[2] the present authors determined analytically the effects of buoyancy force on laminar forced convective heat transfer along an isothermal vertical cylinder. The numerical results for assisting flow in that study showed that the buoyancy force increases considerably the wall shear stress and the surface heat transfer rate. The present note is an extension of the previous work by the authors and deals with the case when a uniform surface heat flux is prescribed on the cylindrical surface. The boundary layer problem encountered here is nonsimilar, the nonsimilarity arising both from the transverse curvature of the cylindrical surface and from the buoyancy forces.

Analysis

Consider a vertical cylinder of radius r_0 which is aligned in a direction parallel to a fluid flow with uniform free stream velocity u_∞ and temperature T_∞. Let x and r denote the streamwise and radial coordinates, respectively. The gravitational force is acting in the direction opposite to the x coordinate. A uniform heat flux q_w is maintained at the surface of the cylinder. The analysis parallels that given in reference [1] and, to conserve space, its details are omitted here. The governing conservation equations and the boundary conditions for the present problem are identical to those given by equations (1)–(4) of reference [1], except that the uniform surface temperature condition therein is now replaced by the uniform surface heat flux condition $\partial T/\partial r = -q_w/k$ at $r = r_0$.

By introducing the new variables

$$\xi = \frac{4}{r_0}\left(\frac{\nu x}{u_\infty}\right)^{1/2}, \qquad \eta = \frac{r^2 - r_0^2}{4r_0}\left(\frac{u_\infty}{\nu x}\right)^{1/2} \tag{1}$$

along with a reduced stream function $F(\xi, \eta)$ and a dimensionless temperature $\theta(\xi, \eta)$ in the form

$$F(\xi, \eta) = \frac{\psi(x, r)}{r_0(\nu u_\infty x)^{1/2}}, \qquad \theta(\xi, \eta) = \frac{(T - T_\infty)(u_\infty x/\nu)^{1/2}}{q_w x/k} \tag{2}$$

where the stream function ψ satisfies the mass conservation equation such that $ru = \partial\psi/\partial r$ and $rv = -\partial\psi/\partial x$, the conservation equations along with their boundary conditions can be transformed into

$$(1 + \xi\eta)F''' + (F + \xi)F'' \pm 8\Omega^*\theta = \xi(F'\partial F'/\partial\xi - F''\partial F/\partial\xi) \tag{3}$$

$$\frac{1}{\mathrm{Pr}}(1 + \xi\eta)\theta'' + \left(F + \frac{\xi}{\mathrm{Pr}}\right)\theta' - F'\theta = \xi(F'\partial\theta/\partial\xi - \theta'\partial F/\partial\xi) \tag{4}$$

$$F'(\xi, 0) = 0, \qquad F(\xi, 0) + \xi\partial F(\xi, 0)/\partial\xi = 0, \qquad \theta'(\xi, 0) = -2 \tag{5}$$

$$F'(\xi, \infty) = 2, \qquad \theta(\xi, \infty) = 0 \tag{6}$$

In the foregoing equations, the primes stand for partial differentiation with respect to η, and

$$\Omega^* = \frac{g\beta|q_w|\nu^{1/2}x^{3/2}}{ku_\infty^{5/2}} = \frac{\mathrm{Gr}_x^*}{\mathrm{Re}_x^{5/2}} \tag{7}$$

is the buoyancy parameter. The modified local Grashof number Gr_x^* and Reynolds number Re_x are defined, respectively, by

$$\mathrm{Gr}_x^* = \frac{g\beta|q_w|x^4}{k\nu^2}, \qquad \mathrm{Re}_x = \frac{u_\infty x}{\nu} \tag{8}$$

The plus and minus signs in front of the buoyancy term in equation (3) apply to assisting flow and opposing flow, respectively. The quantitative effects of buoyancy forces on the forced convective flow are governed by the magnitude of the buoyancy parameter Ω^*. It is noted here that the transformed axial coordinate ξ is a measure of the transverse curvature of the cylinder as well as a measure of the boundary layer thickness relative to the cylinder radius r_0.

The pair of coupled partial differential equations (3) and (4) subject to boundary conditions (5) and (6) were solved by the local nonsimilarity method. This method is well documented (see, for example, [1–4]) and involves deriving several sets of equations from equations

[1] Department of Mechanical and Aerospace Engineering, University of Missouri-Rolla, Rolla, Mo.

[2] Numbers in brackets designate References at end of technical note.

constants, however, are somewhat larger in the present equation resulting in slightly larger values of the Nusselt number. This seems reasonable since the average diameter of the tapered wire along its length is less than C; the thick-layer correction is therefore more important and the Nusselt number larger than if the wire had a constant diameter of C along its length.

Replacing the wire diameter and length in their analysis respectively by C and B, one finds that the present Nusselt numbers $(\bar{\mathrm{Nu}}_C)_\ell$ are larger by 4 , 10 , 18 , and 22 percent, respectively, for $\bar{C}_\ell(C/B)\mathrm{Ra}_C$ values of 10, 1, 0.1, and 0.01.

References

32 Raithby, G. D., Pollard, A., Hollands, K. G. T., and Yovanovich, M. M., "Free Convection Heat Transfer From Spheroids," JOURNAL OF HEAT TRANSFER, TRANS, ASME, Series C, Vol. 98, 1976, pp. 452–458.

33 Cebeci, T., and Na, T. U., "Laminar Free-Convection Heat Transfer From a Needle," *The Physics of Fluids*, Vol. 12, No. 2, 1969, pp. 463–465

34 Narain, J. P., and Uberoi, M. S., "Laminar Free Convection From Vertical Thin Needles," *The Physics of Fluids*, Vol. 15, No. 5, 1972, pp. 928–929.

Buoyancy Effects on Forced Convection Along a Vertical Cylinder With Uniform Surface Heat Flux

A. Mucoglu[1] and T. S. Chen[1]

Nomenclature

C_f = local friction factor
F = reduced stream function, equation (2)
$G = \xi$ – derivative of F
g = gravitational acceleration
Gr_x^* = modified Grashof number, $g\beta|q_w|x^4/k\nu^2$
k = thermal conductivity
Nu_x = local Nusselt number, $q_w x/(T_w - T_\infty)k$
Pr = Prandtl number
q_w = local surface heat transfer rate per unit area
r = radial coordinate
r_0 = radius of cylinder
Re_x = Reynolds number, $u_\infty x/\nu$
T = fluid temperature
T_w = wall temperature
T_∞ = free stream temperature
u = axial velocity component
u_∞ = free stream velocity
v = radial velocity component
x = axial coordinate
β = volumetric coefficient of thermal expansion
η = pseudo-similarity variable, equation (1)
θ = dimensionless temperature, equation (2)
μ = dynamic viscosity
ν = kinematic viscosity
ξ = transformed axial coordinate, equation (1)
$\phi = \xi$ – derivative of θ
ψ = stream function
Ω^* = buoyancy parameter, $\mathrm{Gr}_x^*/\mathrm{Re}_x^{5/2}$

Introduction

In forced convection along an inclined or a vertical heated surface, the buoyancy force plays an important role in modifying the flow field and hence the rate of heat transfer from the surface. In a recent study [1],[2] the present authors determined analytically the effects of buoyancy force on laminar forced convective heat transfer along an isothermal vertical cylinder. The numerical results for assisting flow in that study showed that the buoyancy force increases considerably the wall shear stress and the surface heat transfer rate. The present note is an extension of the previous work by the authors and deals with the case when a uniform surface heat flux is prescribed on the cylindrical surface. The boundary layer problem encountered here is nonsimilar, the nonsimilarity arising both from the transverse curvature of the cylindrical surface and from the buoyancy forces.

Analysis

Consider a vertical cylinder of radius r_0 which is aligned in a direction parallel to a fluid flow with uniform free stream velocity u_∞ and temperature T_∞. Let x and r denote the streamwise and radial coordinates, respectively. The gravitational force is acting in the direction opposite to the x coordinate. A uniform heat flux q_w is maintained at the surface of the cylinder. The analysis parallels that given in reference [1] and, to conserve space, its details are omitted here. The governing conservation equations and the boundary conditions for the present problem are identical to those given by equations (1)–(4) of reference [1], except that the uniform surface temperature condition therein is now replaced by the uniform surface heat flux condition $\partial T/\partial r = -q_w/k$ at $r = r_0$.

By introducing the new variables

$$\xi = \frac{4}{r_0}\left(\frac{\nu x}{u_\infty}\right)^{1/2}, \qquad \eta = \frac{r^2 - r_0^2}{4r_0}\left(\frac{u_\infty}{\nu x}\right)^{1/2} \tag{1}$$

along with a reduced stream function $F(\xi, \eta)$ and a dimensionless temperature $\theta(\xi, \eta)$ in the form

$$F(\xi, \eta) = \frac{\psi(x, r)}{r_0(\nu u_\infty x)^{1/2}}, \qquad \theta(\xi, \eta) = \frac{(T - T_\infty)(u_\infty x/\nu)^{1/2}}{q_w x/k} \tag{2}$$

where the stream function ψ satisfies the mass conservation equation such that $ru = \partial\psi/\partial r$ and $rv = -\partial\psi/\partial x$, the conservation equations along with their boundary conditions can be transformed into

$$(1 + \xi\eta)F''' + (F + \xi)F'' \pm 8\Omega^*\theta = \xi(F'\partial F'/\partial\xi - F''\partial F/\partial\xi) \tag{3}$$

$$\frac{1}{\mathrm{Pr}}(1 + \xi\eta)\theta'' + \left(F + \frac{\xi}{\mathrm{Pr}}\right)\theta' - F'\theta = \xi(F'\partial\theta/\partial\xi - \theta'\partial F/\partial\xi) \tag{4}$$

$$F'(\xi, 0) = 0, \qquad F(\xi, 0) + \xi\partial F(\xi, 0)/\partial\xi = 0, \qquad \theta'(\xi, 0) = -2 \tag{5}$$

$$F'(\xi, \infty) = 2, \qquad \theta(\xi, \infty) = 0 \tag{6}$$

In the foregoing equations, the primes stand for partial differentiation with respect to η, and

$$\Omega^* = \frac{g\beta|q_w|\nu^{1/2}x^{3/2}}{ku_\infty^{5/2}} = \frac{\mathrm{Gr}_x^*}{\mathrm{Re}_x^{5/2}} \tag{7}$$

is the buoyancy parameter. The modified local Grashof number Gr_x^* and Reynolds number Re_x are defined, respectively, by

$$\mathrm{Gr}_x^* = \frac{g\beta|q_w|x^4}{k\nu^2}, \qquad \mathrm{Re}_x = \frac{u_\infty x}{\nu} \tag{8}$$

The plus and minus signs in front of the buoyancy term in equation (3) apply to assisting flow and opposing flow, respectively. The quantitative effects of buoyancy forces on the forced convective flow are governed by the magnitude of the buoyancy parameter Ω^*. It is noted here that the transformed axial coordinate ξ is a measure of the transverse curvature of the cylinder as well as a measure of the boundary layer thickness relative to the cylinder radius r_0.

The pair of coupled partial differential equations (3) and (4) subject to boundary conditions (5) and (6) were solved by the local nonsimilarity method. This method is well documented (see, for example, [1–4]) and involves deriving several sets of equations from equations

[1] Department of Mechanical and Aerospace Engineering, University of Missouri-Rolla, Rolla, Mo.

[2] Numbers in brackets designate References at end of technical note.

Table 1 Representative results of $F''(\xi, 0)$ and $\theta(\xi, 0)$ for Pr = 0.7, assisting flow

$F''(\xi,0)$								
ξ	$\Omega^* = 0$	0.10	0.30	0.50	0.70	1.00	1.25	1.50
0	1.3282	2.1599	3.3863	4.3710	5.2284	6.3665	7.2221	8.0165
1	1.9113	2.4708	3.4435	4.2591	4.9789	5.9414	6.6684	7.3451
2	2.3847	2.8163	3.6423	4.3743	5.0353	5.9322	6.6160	7.2558
3	2.8070	3.1611	3.8778	4.5410	5.1524	5.9934	6.6404	7.2490
4	3.1977	3.4997	4.1324	4.7381	5.3068	6.0992	6.7141	7.2955
$\theta(\xi,0)$								
ξ	$\Omega^* = 0$	0.10	0.30	0.50	0.70	1.00	1.25	1.50
0	2.4637	2.2682	2.0733	1.9598	1.8798	1.7923	1.7367	1.6911
1	1.8543	1.7769	1.6627	1.5877	1.5325	1.4705	1.4303	1.3970
2	1.5343	1.4974	1.4321	1.3834	1.3453	1.3007	1.2710	1.2458
3	1.3271	1.3062	1.2651	1.2315	1.2039	1.1705	1.1477	1.1281
4	1.1787	1.1655	1.1378	1.1136	1.0929	1.0671	1.0491	1.0333

(3)–(6), with each set containing a different level of truncation. The formulation of the governing system of equations for each level of truncation and the solution method are similar to those given in [1] and are omitted here because of space limitation. It suffices to give the system of equations at the second level of truncation that were used in obtaining the numerical results, for it was found that this level of truncation provided sufficiently accurate results. If, in addition to F and θ, auxiliary dependent variables $G = \partial F/\partial\xi$ and $\phi = \partial\theta/\partial\xi$ are used, one can derive

$$(1 + \xi\eta)F''' + (F + \xi)F'' \pm 8\Omega^*\theta = \xi(F'G' - F''G) \tag{9}$$

$$(1 + \xi\eta)G''' + (F + \xi)G'' - F'G' + 2F''G \pm 8\Omega^*\phi + \eta F''' + F'' \pm 24(\Omega^*/\xi)\theta - \xi(G'G' - GG'') = 0 \tag{10}$$

$$\frac{1}{\mathrm{Pr}}(1 + \xi\eta)\theta'' + \left(F + \frac{\xi}{\mathrm{Pr}}\right)\theta' - F'\theta = \xi(F'\phi - G\theta') \tag{11}$$

$$\frac{1}{\mathrm{Pr}}(1 + \xi\eta)\phi'' + \left(F + \frac{\xi}{\mathrm{Pr}}\right)\phi' - 2F'\phi + \frac{1}{\mathrm{Pr}}\eta\theta'' + \left(2G + \frac{1}{\mathrm{Pr}}\right)\theta' - G'\theta - \xi(G'\phi - G\phi') = 0 \tag{12}$$

$$F'(\xi, 0) = F(\xi, 0) = 0, \qquad F'(\xi, \infty) = 2$$

$$G'(\xi, 0) = G(\xi, 0) = G'(\xi, \infty) = 0$$

$$\theta'(\xi, 0) = -2, \qquad \theta(\xi, \infty) = 0; \qquad \phi'(\xi, 0) = \phi(\xi, \infty) = 0 \tag{13}$$

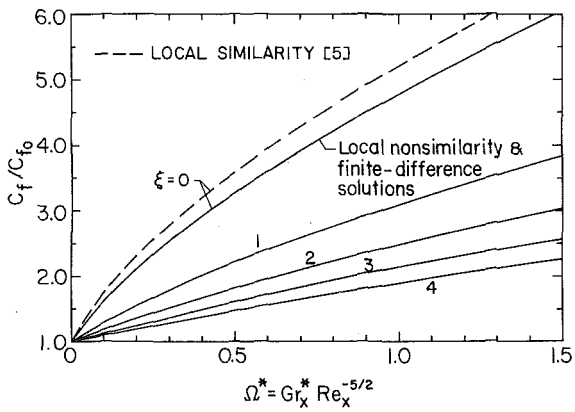

Fig. 1 The effect of buoyancy force on the local friction factor

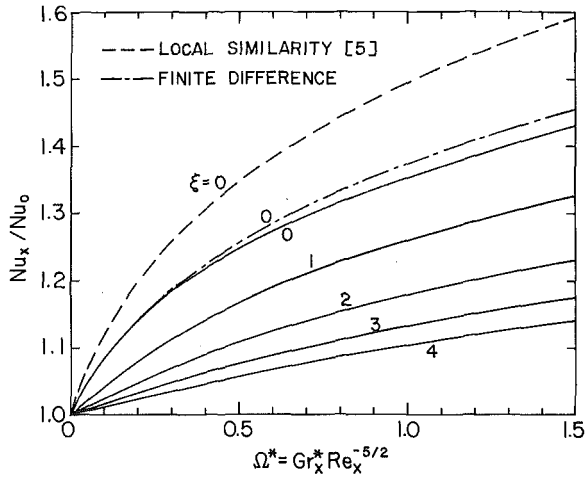

Fig. 2 The effect of buoyancy force on the local Nusselt number

The physical quantities of interest in the present study are the local friction factor C_f and local Nusselt number Nu_x defined, respectively, by

$$C_f = \frac{\mu(\partial u/\partial r)_{r_0}}{\rho u_\infty^2/2}, \qquad \mathrm{Nu}_x = \frac{q_w x}{(T_w - T_\infty)k} \tag{14}$$

With the aid of equations (1) and (2), it can be readily shown that

$$C_f \mathrm{Re}_x^{1/2} = \frac{1}{2}F''(\xi, 0), \qquad \mathrm{Nu}_x \mathrm{Re}_x^{-1/2} = \frac{1}{\theta(\xi, 0)} \tag{15}$$

As a note, it is pointed out that for the case of a flat plate with $\xi = 0$ (i.e., $r_0 \to \infty$), Ω^* is the only x-dependent variable. Thus, for this special case, (Ω^*, η) were used as the transformation variable in formulating the systems of equations for the various levels of truncation.

Results and Discussion

Numerical results for the case of assisting flow were obtained for gases having a Prandtl number of 0.7. They cover transverse curvature ξ ranging from 0 (i.e., a flat plate) to 4.0 and buoyancy parameter Ω^* ranging from 0 (i.e., pure forced convection) to 1.5. Representative results for $F''(\xi, 0)$ and $\theta(\xi, 0)$ are listed in Table 1.

To provide a better understanding of the effects of buoyancy force on the flow and heat transfer characteristics, Figs. 1 and 2 have been prepared to show, respectively, the relative increase in the local friction factor C_f/C_{f0} and local Nusselt number $\mathrm{Nu}_x/\mathrm{Nu}_0$, where C_{f0} and Nu_0 represent, respectively, the local friction factor and local Nusselt number without the buoyancy effect (i.e., $\Omega^* = 0$). It is evident from these figures that for a given curvature ξ, both C_f and Nu_x increase with increasing buoyancy force Ω^* and that the relative increase in the friction factor and Nusselt number decreases as ξ increases. The dotted lines corresponding to the case of a flat plate (i.e., $\xi = 0$) in the figures are the results from the local similarity solution [5]. To verify the accuracy of the local nonsimilarity solution method, solutions for a flat plate were also obtained from finite-difference method [6]. These results are listed in Table 1 and shown in the figure with solid-dotted lines. The excellent agreement between the two solution methods makes it difficult to distinguish the friction factor results in Fig. 1.

Acknowledgments

This work was partially supported by a grant from the National Science Foundation (NSF ENG 75—15033).

References

1 Chen, T. S., and Mucoglu, A., "Buoyancy Effects on Forced Convection Along a Vertical Cylinder," JOURNAL OF HEAT TRANSFER, TRANS. ASME, Series C, Vol. 97, 1975, pp. 198–203.

2 Sparrow, E. M., Quack, H., and Boerner, C. J., "Local Nonsimilarity Boundary-Layer Solutions," *AIAA Journal*, Vol. 8, 1970, pp. 1936–1942.
3 Sparrow, E. M., and Yu, H. S., "Local Non-Similarity Thermal Boundary-Layer Solutions," JOURNAL OF HEAT TRANSFER, TRANS. ASME, Series C, Vol. 93, 1971, pp. 328–334.
4 Minkowycz, W. J., and Sparrow, E. M., "Local Nonsimilar Solutions for Natural Convection on a Vertical Cylinder," JOURNAL OF HEAT TRANSFER, TRANS. ASME, Series C, Vol. 96, 1974, pp. 178–183.
5 Wilks, G., "Combined Forced and Free Convection Flow on Vertical Surfaces," *International Journal of Heat and Mass Transfer*, Vol. 16, 1973, pp. 1958–1964.
6 Keller, H. B., and Cebeci, T., "Accurate Numerical Methods for Boundary-Layer Flows. II: Two-Dimensional Turbulent Flows," *AIAA Journal*, Vol. 10, 1972, pp. 1193–1199.

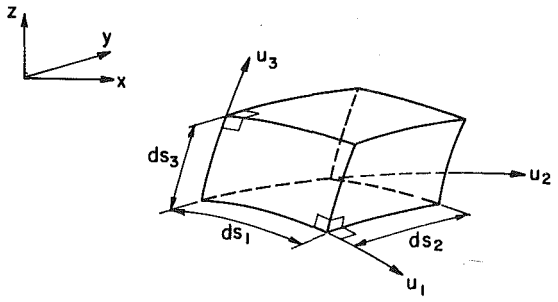

Fig. 1 General orthogonal curvilinear coordinate system

Finite Element Formulation of the Heat Conduction Equation in General Orthogonal Curvilinear Coordinates

G. E. Schneider[1]

Introduction

In the analytic solution of heat conduction and other potential field problems, the governing equation is conventionally formulated in one of the three coordinate systems: cartesian, circular cylinder, or spherical. Where the bounding surfaces of the solution domain lend themselves to one of these coordinate systems, many solutions are available [1].[2]

When this geometric compatibility is not present, it is sometimes possible to set up a "more natural" coordinate system in which the coordinate surfaces conform to the lines of flow and potential surfaces and, moreover, provides geometric compatibility with the bounding surfaces. In many instances these more natural coordinates, determined by the problem geometry and field behavior, allow a simple solution whereas use of the conventional ones leaves the solution unmanageable. While many problems cannot be so reduced, benefits similar to those gained in the analytic solutions referred to in the foregoing can be realized in the numerical solution of problems for which the heat flow is predominantly uni-directional in nature.

It is the intent of this note to introduce to the finite element method, as applied to conduction heat transfer, the use of general orthogonal curvilinear coordinates. By considering the governing functional equation and boundary conditions in a general orthogonal curvilinear frame, the solution can be readily effected using the finite element method. Where the bounding surfaces form part of an orthogonal net, substantial savings in both computational time and programing effort can be gained.

Preliminary Remarks

Considering a general orthogonal curvilinear coordinate system, illustrated in Fig. 1, u_1, u_2, and u_3 are used to denote the three principal coordinate directions. The cartesian coordinates of Fig. 1 can in general be related to the curvilinear ones through relations of the form [2]

$$x = x(u_1, u_2, u_3); \quad y = y(u_1, u_2, u_3); \quad z = z(u_1, u_2, u_3) \tag{1}$$

From these relations the metric coefficients of transformation are defined by [2]

$$g_i \equiv \left(\frac{\partial x}{\partial u_i}\right)^2 + \left(\frac{\partial y}{\partial u_i}\right)^2 + \left(\frac{\partial z}{\partial u_i}\right)^2, i = 1, 2, 3 \tag{2}$$

Applying the first law of thermodynamics to the differential curvilinear volume element of Fig. 1, the governing differential equation can be written as [2]

$$\frac{\partial}{\partial u_1}\left[\frac{k_1\sqrt{g}}{g_1}\frac{\partial T}{\partial u_1}\right] + \frac{\partial}{\partial u_2}\left[\frac{k_2\sqrt{g}}{g_2}\frac{\partial T}{\partial u_2}\right] + \frac{\partial}{\partial u_3}\left[\frac{k_3\sqrt{g}}{g_3}\frac{\partial T}{\partial u_3}\right] + P\sqrt{g} = \sqrt{g}\rho C_p\frac{\partial T}{\partial t} \tag{3}$$

where $g \equiv g_1 g_2 g_3$ and Fourier's law of heat conduction has been used to describe the local transfer of heat within the continuum. Boundary conditions (excepting nonlinearized radiative conditions) which the solution to equation (3) must satisfy, will be generally given over S_1 by

$$T = T_A(u_1, u_2, u_3, t) \tag{4a}$$

and by

$$k_n\frac{\partial T}{\partial n} + hT + C = 0 \tag{4b}$$

over the remaining surface S_2, where n is the outward normal to the surface. The initial condition is represented by

$$T(u_1, u_2, u_3, 0) = T_0(u_1, u_2, u_3) \tag{4c}$$

Variational Statement

If the concept of a variational principle is applied to the heat conduction problem, then the governing differential equation (3) must correspond to the Euler equation for the corresponding variational problem. In this treatment we shall follow the approach taken by Visser [3], Zienkiewicz and Parekh [4], and Zienkiewicz [5] where a particular instant of time is considered. This is in contrast to the use of convolution integrals in time put forward by Gurtin [6] in establishing a true variational principle. The approach adopted here leads to a quasi-variational statement and can readily be converted to a restricted variational statement as indicated by Finlayson and Scriven [7].

Invoking the requirement that (3) be the Euler equation of a variational principle, and proceeding to determine the extremum functional as presented in reference [8], leads to the functional equation

$$\delta\left[\int_{u_1}\int_{u_2}\int_{u_3}\left\{\frac{f_1}{2}\left(\frac{\partial T}{\partial u_1}\right)^2 + \frac{f_2}{2}\left(\frac{\partial T}{\partial u_2}\right)^2 + \frac{f_3}{2}\left(\frac{\partial T}{\partial u_3}\right)^2 - P\sqrt{g}T + \sqrt{g}\rho C_p\left(\frac{\partial T}{\partial t}\right)T\right\}du_1du_2du_3 + \int\int_{S_2}\left[\frac{hT^2}{2} + CT\right]dS_2\right] = 0 \tag{5}$$

---

[1] Project Engineer, Thermal Engineering Group, Department of Mechanical Engineering, University of Waterloo, Waterloo, Ontario, Canada.
[2] Numbers in brackets designate References at end of technical note.
Contributed by the Heat Transfer Division of THE AMERICAN SOCIETY OF MECHANICAL ENGINEERS. Manuscript received by the Heat Transfer Division December 1, 1975.

2 Sparrow, E. M., Quack, H., and Boerner, C. J., "Local Nonsimilarity Boundary-Layer Solutions," *AIAA Journal*, Vol. 8, 1970, pp. 1936–1942.
3 Sparrow, E. M., and Yu, H. S., "Local Non-Similarity Thermal Boundary-Layer Solutions," JOURNAL OF HEAT TRANSFER, TRANS. ASME, Series C, Vol. 93, 1971, pp. 328–334.
4 Minkowycz, W. J., and Sparrow, E. M., "Local Nonsimilar Solutions for Natural Convection on a Vertical Cylinder," JOURNAL OF HEAT TRANSFER, TRANS. ASME, Series C, Vol. 96, 1974, pp. 178–183.
5 Wilks, G., "Combined Forced and Free Convection Flow on Vertical Surfaces," *International Journal of Heat and Mass Transfer*, Vol. 16, 1973, pp. 1958–1964.
6 Keller, H. B., and Cebeci, T., "Accurate Numerical Methods for Boundary-Layer Flows. II: Two-Dimensional Turbulent Flows," *AIAA Journal*, Vol. 10, 1972, pp. 1193–1199.

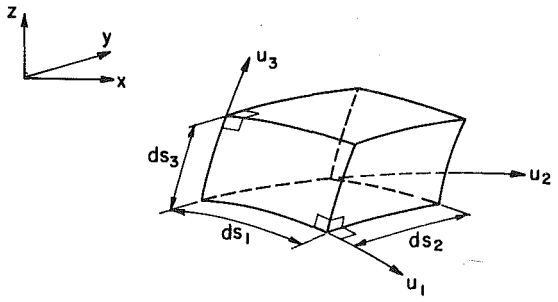

Fig. 1 General orthogonal curvilinear coordinate system

Finite Element Formulation of the Heat Conduction Equation in General Orthogonal Curvilinear Coordinates

G. E. Schneider[1]

Introduction

In the analytic solution of heat conduction and other potential field problems, the governing equation is conventionally formulated in one of the three coordinate systems: cartesian, circular cylinder, or spherical. Where the bounding surfaces of the solution domain lend themselves to one of these coordinate systems, many solutions are available [1].[2]

When this geometric compatibility is not present, it is sometimes possible to set up a "more natural" coordinate system in which the coordinate surfaces conform to the lines of flow and potential surfaces and, moreover, provides geometric compatibility with the bounding surfaces. In many instances these more natural coordinates, determined by the problem geometry and field behavior, allow a simple solution whereas use of the conventional ones leaves the solution unmanageable. While many problems cannot be so reduced, benefits similar to those gained in the analytic solutions referred to in the foregoing can be realized in the numerical solution of problems for which the heat flow is predominantly uni-directional in nature.

It is the intent of this note to introduce to the finite element method, as applied to conduction heat transfer, the use of general orthogonal curvilinear coordinates. By considering the governing functional equation and boundary conditions in a general orthogonal curvilinear frame, the solution can be readily effected using the finite element method. Where the bounding surfaces form part of an orthogonal net, substantial savings in both computational time and programing effort can be gained.

Preliminary Remarks

Considering a general orthogonal curvilinear coordinate system, illustrated in Fig. 1, u_1, u_2, and u_3 are used to denote the three principal coordinate directions. The cartesian coordinates of Fig. 1 can in general be related to the curvilinear ones through relations of the form [2]

$$x = x(u_1, u_2, u_3); \quad y = y(u_1, u_2, u_3); \quad z = z(u_1, u_2, u_3) \tag{1}$$

From these relations the metric coefficients of transformation are defined by [2]

$$g_i \equiv \left(\frac{\partial x}{\partial u_i}\right)^2 + \left(\frac{\partial y}{\partial u_i}\right)^2 + \left(\frac{\partial z}{\partial u_i}\right)^2, i = 1, 2, 3 \tag{2}$$

Applying the first law of thermodynamics to the differential curvilinear volume element of Fig. 1, the governing differential equation can be written as [2]

$$\frac{\partial}{\partial u_1}\left[\frac{k_1\sqrt{g}}{g_1}\frac{\partial T}{\partial u_1}\right] + \frac{\partial}{\partial u_2}\left[\frac{k_2\sqrt{g}}{g_2}\frac{\partial T}{\partial u_2}\right] + \frac{\partial}{\partial u_3}\left[\frac{k_3\sqrt{g}}{g_3}\frac{\partial T}{\partial u_3}\right] + P\sqrt{g} = \sqrt{g}\rho C_p\frac{\partial T}{\partial t} \tag{3}$$

where $g \equiv g_1 g_2 g_3$ and Fourier's law of heat conduction has been used to describe the local transfer of heat within the continuum. Boundary conditions (excepting nonlinearized radiative conditions) which the solution to equation (3) must satisfy, will be generally given over S_1 by

$$T = T_A(u_1, u_2, u_3, t) \tag{4a}$$

and by

$$k_n\frac{\partial T}{\partial n} + hT + C = 0 \tag{4b}$$

over the remaining surface S_2, where n is the outward normal to the surface. The initial condition is represented by

$$T(u_1, u_2, u_3, 0) = T_0(u_1, u_2, u_3) \tag{4c}$$

Variational Statement

If the concept of a variational principle is applied to the heat conduction problem, then the governing differential equation (3) must correspond to the Euler equation for the corresponding variational problem. In this treatment we shall follow the approach taken by Visser [3], Zienkiewicz and Parekh [4], and Zienkiewicz [5] where a particular instant of time is considered. This is in contrast to the use of convolution integrals in time put forward by Gurtin [6] in establishing a true variational principle. The approach adopted here leads to a quasi-variational statement and can readily be converted to a restricted variational statement as indicated by Finlayson and Scriven [7].

Invoking the requirement that (3) be the Euler equation of a variational principle, and proceeding to determine the extremum functional as presented in reference [8], leads to the functional equation

$$\delta\left[\int_{u_1}\int_{u_2}\int_{u_3}\left\{\frac{f_1}{2}\left(\frac{\partial T}{\partial u_1}\right)^2 + \frac{f_2}{2}\left(\frac{\partial T}{\partial u_2}\right)^2 + \frac{f_3}{2}\left(\frac{\partial T}{\partial u_3}\right)^2 - P\sqrt{g}T + \sqrt{g}\rho C_p\left(\frac{\partial T}{\partial t}\right)T\right\}du_1du_2du_3 + \int\int_{S_2}\left[\frac{hT^2}{2} + CT\right]dS_2\right] = 0 \tag{5}$$

[1] Project Engineer, Thermal Engineering Group, Department of Mechanical Engineering, University of Waterloo, Waterloo, Ontario, Canada.
[2] Numbers in brackets designate References at end of technical note.
Contributed by the Heat Transfer Division of THE AMERICAN SOCIETY OF MECHANICAL ENGINEERS. Manuscript received by the Heat Transfer Division December 1, 1975.

where δ is the variational operator. Alternatively, equation (5) can be derived by starting from the variational principle given in vector notation by Finlayson [9] and introducing the explicit use of general orthogonal curvilinear coordinates. Equation (5) is the quasi-variational principle referred to earlier, and its satisfaction, within the limits of the treatment of time dependent terms adopted here, is equivalent to satisfying the governing differential equation (2) subject to boundary conditions (4).

Spatial Discretization

In what follows, it will be useful to define the following vectors and matrices. The first, a vector very similar to the gradient field vector [10] for a cartesian frame, is defined by

$$\{G\}^T \equiv \{\partial T/\partial u_1,\ \partial T/\partial u_2,\ \partial T/\partial u_3\} \tag{6}$$

and will be henceforth referred to as the curvilinear field vector. The second, a matric analogous the property matrix of a cartesian system, is defined by

$$[R] \equiv \begin{bmatrix} f_1(u_1, u_2, u_3) & 0 & 0 \\ 0 & f_2(u_1, u_2, u_3) & 0 \\ 0 & 0 & f_3(u_1, u_2, u_3) \end{bmatrix} \tag{7}$$

and will be referred to as the effective curvilinear property matrix. The f_i are defined by $f_i \equiv k_i\sqrt{g}/g_i$. For completeness, the remaining vectors are defined: $\{T\} \equiv \{T(u_1, u_2, u_3)\}$, $\{P\} \equiv \{P(u_1, u_2, u_3)\}$, $\{C\} \equiv \{C(u_1, u_2, u_3)\}$, and $\{\dot{T}\} \equiv \{\partial T/\partial t\}$. The variational statement (5) can now be written in vector notation as

$$\delta\left[\int_{u_1}\int_{u_2}\int_{u_3}\left\{\frac{1}{2}\{G\}^T[R]\{G\} - \sqrt{g}\,\{T\}^T\{P\} + \rho C_p\sqrt{g}\{T\}^T\{\dot{T}\}\right.\right.$$
$$\left.\left. du_1du_2du_3 + \int\int_{S_2}\left\{\frac{h}{2}\{T\}^T\{T\} + \{T\}^T\{C\}\right\}dS_2\right] = 0 \tag{8}$$

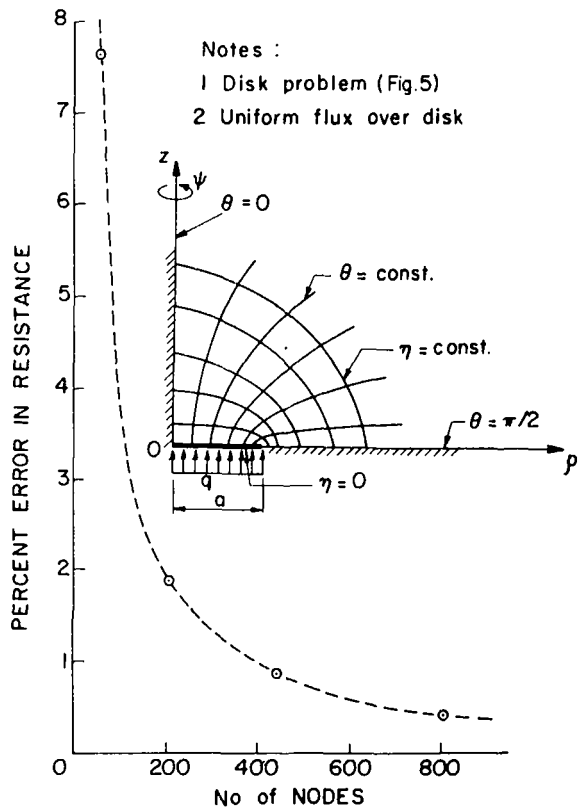

Fig. 2 Example problem geometry and convergence characteristics

Employing the concept of element level shape functions [5], the curvilinear field vector can immediately be written as

$$\{G\} = \begin{bmatrix} \partial N_1/\partial u_1 \partial N_2/\partial u_1 \ldots \\ \partial N_1/\partial u_2 \partial N_2/\partial u_2 \ldots \\ \partial N_1/\partial u_3 \partial N_2/\partial u_3 \ldots \end{bmatrix} \begin{Bmatrix} T_1 \\ T_2 \\ \vdots \end{Bmatrix} \equiv [B]\{T_i\} \tag{9}$$

In the foregoing, the N_1's are the shape functions [5] for the element under consideration, and their form and number will depend on the particular element selected for the application.

Determining the stationary value for the functional within the outermost parentheses of equation (5) by taking its first variation with respect to T is now equivalent to differentiating the approximate functional contained within the outermost parentheses of equation (8) with respect to each nodal temperature in turn, and setting the result equal to zero. This results in the matrix-differential equations

$$[K]\{T_i\} + [H]\{\dot{T}_i\} = \{F_i\} \tag{10}$$

where

$$[K] = \sum_{e=1}^{n}\left[\int\int\int_{V_e}[B]^T[R][B]\,du_1du_2du_3 + \int\int_{S_{2e}}h\{N_i\}\{N_i\}^T dS_2\right] \tag{11a}$$

$$[H] = \sum_{e=1}^{n}\left[\int\int\int_{V_e}\rho C_p\sqrt{g}\{N_i\}\{N_i\}^T\,du_1du_2du_3\right] \tag{11b}$$

and

$$\{F_i\} = \sum_{e=1}^{n}\left[\int\int\int_{V_e}\sqrt{g}\{N_i\}\{P\}du_1du_2du_3 + \int\int_{S_{2e}}\{N_i\}\{C\}dS_2\right] \tag{11c}$$

To complete the solution to equation (10), additional information is required to accommodate the time dependence. Following Zienkiewicz and Parekh [4], this time dependence is approximated by finite differences over the time interval from t to $t + \Delta t$. Using the first central difference quotient to approximate the time derivative, we obtain the algorithmic solution

$$([K] + 2[H]/\Delta t)\{T_i\}_{t+\Delta t/2} = \frac{2[H]}{\Delta t}\{T_i\}_t + \{F_i\}_{t+\Delta t/2} \tag{12}$$

with

$$\{T_i\}_{t+\Delta t} = 2\{T_i\}_{t+\Delta t,2} - \{T_i\}_t \tag{13}$$

The above equations, (12) and (13), complete the solution. It can easily be seen that these equations reduce to those for the cartesian case.

Application of the Results

The utility of the expressions derived in this work will be demonstrated here by example. Since the treatment of the heat generation and time-dependent terms is straightforward, attention will be restricted to steady-state heat conduction. Linear, isoparametric elements are used with the shape functions applied in the curvilinear frame.

The example considers the flow of heat from a thin circular disk to a semi-infinite solid. Over the disk a uniform flux is prescribed while outside the disk, the free surface is insulated. Deep within the half-space, the temperature tends toward a uniform value, $T_\infty = 0$. The problem geometry is illustrated in Fig. 2.

The oblate spheroidal coordinate system is appropriate for this problem and is defined by

$$x = a\cosh\eta\sin\theta\cos\psi;\ y = a\cosh\eta\sin\theta\sin\psi;$$
$$z = a\sinh\eta\cos\theta \tag{14}$$

where a is the disk radius. The metric coefficients are readily determined to be

$$g_\eta = g_\theta = a^2(\cosh^2 \eta - \sin^2 \theta); g_\psi = a^2 \cosh^2 \eta \sin^2 \theta \qquad (15)$$

where η, θ, and ψ are defined by the figure. It can be demonstrated that $\eta_\infty \approx 10$ will suffice for the location of the boundary far from the contact [2]. The effective curvilinear property matrix, considering axisymmetric heat transfer, can be found using equations (15) to be

$$[R] = \begin{bmatrix} ak \cosh \eta \sin \theta & 0 \\ 0 & ak \cosh \eta \sin \theta \end{bmatrix} \qquad (16)$$

The convergence characteristics for this problem are plotted in Fig. 2 versus the number of nodal points used to effect the solution. A rapid, monotone approach toward its limiting value is indicated. The value of 0.269 obtained using 800 nodes compares favorably with the exact solution for this problem of 0.27019 [2], yielding an error of 0.44 percent. Indeed, an error of less than 2 percent is obtained when only 200 nodes are used to represent the continuum. Both the ease of application and the accuracy of the results indicate the utility of this work in analyzing problems having a convenient "natural" coordinate system.

Discussion and Conclusions

Explicit consideration has been given in this work to the incorporation of general orthogonal curvilinear coordinate systems into finite element conduction heat transfer analysis. It was found that the incorporation can be effected by a direct extension of existing finite element codes by merely redefining the properties and heat generation rate as presented in this work. The effective curvilinear property matrix replaces the property matrix, $P\sqrt{g}$ replaces P for the heat generation rate, and $C_p\sqrt{g}$ replaces C_p for the energy storage terms. Once defined in this manner, the analysis is performed in the more uniform, thermally and geometrically, curvilinear space. This is of considerable utility since many problems have associated with them a natural or quasi-natural coordinate system.

An example has been presented which illustrates the ease of application of the results to other than the cartesian coordinate system. The solution converged rapidly and monotonically to its limiting value for the oblate spheroidal coordinate problem considered. Where only 800 nodes were used to represent a semi-infinite body and less than 0.5 percent error was incurred, the utility of formulating the problem in the appropriate coordinate frame becomes clear.

These results will find application to contact problems, problems involving semi-infinite or infinite domains, and generally to problems where a coordinate system more natural than the cartesian one exists to describe the problem geometry and field behavior. The result, where there exists a more appropriate coordinate system, will be a savings in both storage requirements and computational time to achieve a prescribed solution accuracy.

Acknowledgments

The author acknowledges the National Research Council and the Communications Research Centre, Department of Communications, Ottawa, Canada, for their financial support of this research. The author is grateful to Dr. M. M. Yovanovich of the University of Waterloo for suggesting the problem and to Dr. A. B. Strong and Dr. M. M. Yovanovich of this university for allowing time to be devoted to this work while working under their supervision. The author is grateful to Dr. G. M. McNeice and Dr. J. C. Thompson of this university for their assistance throughout the course of this work.

References

1 Carslaw, H. S., and Jaeger, J. C., *Conduction of Heat in Solids*, Oxford University Press, London, 1959.

2 Yovanovich, M. M., *Advanced Heat Conduction*, Hemisphere Publishing Corporation, Washington, D. C., 1976.

3 Visser, W., "A Finite Element Method for Determination of Non-Stationary Temperature Distribution and Thermal Deformations," *Proceedings of the Conference on Matrix Methods in Structural Mechanics*, held at the Air Force Institute of Technology, Wright-Patterson Air Force Base, Ohio, 1965, pp. 925–944.

4 Zienkiewicz, O. C., and Parekh, C. J., "Transient Field Problems: Two-Dimensional and Three-Dimensional Analysis by Isoparametric Finite Elements, *International Journal for Numerical Methods in Engineering*, Vol. 2, 1970, pp. 61–71.

5 Zienkiewicz, O. C., *Finite Elements in Engineering Science*, McGraw-Hill, London, 1971.

6 Gurtin, M. E., "Variational Principles for Initial-Value Problems, *Quarterly Journal of Applied Mathematics*, Vol. 22, 1964, pp. 253.

7 Finlayson, B. A., and Scriven, L. E., "On the Search for Variational Principles," *International Journal of Heat and Mass Transfer*, Vol. 10, 1967, pp. 799–821.

8 Schneider, G. E., "Finite Element Formulation of the Heat Conduction Equation in General Orthogonal Curvilinear Coordinates," presented at the ASME Winter Annual Meeting, Houston, Texas, Nov. 30–Dec. 4, ASME Paper No. 75-WA/HT-95, 1975.

9 Finlayson, B. A., *The Method of Weighted Residuals and Variational Principles*, Academic Press, 1972, p. 222.

10 Desai, C. S., and Abel, J. F., *Introduction to the Finite Element Method*, Van Nostrand, 1972.

A New Look at the Superposition of Boundary Conditions in the Evaluation of Temperature Distribution in a Finite Rectangular Plate With Adiabatic Faces at Steady State

A. Feingold[1]

The usual way to solve the governing Laplace equation for steady heat conduction

$$\frac{\partial^2 T}{\partial x^2} + \frac{\partial^2 T}{\partial y^2} = 0 \qquad (1)$$

is to assume that there exists a solution in the form of $T = XY$, where X is a function of x alone and Y is a function of y alone. After the substitution and the separation of variables, the equation becomes

$$\frac{1}{X}\frac{\partial^2 X}{\partial x^2} = -\frac{1}{Y}\frac{\partial^2 Y}{\partial y^2}$$

and the introduction of a separation constant μ leads to the two well-known total differential equations:

$$\frac{d^2X}{dx^2} - \mu X = 0, \qquad \frac{d^2Y}{dy^2} + \mu Y = 0 \qquad (2)$$

Given a rectangular plate, the temperature distribution throughout it is determined in terms of Fourier series using the method of superposition of boundary conditions. The correct given temperature distribution along one edge is coupled with a zero temperature along the other three edges, the Fourier series is obtained by putting $\mu > 0$ or $\mu < 0$, as the case may be, and the process is repeated for each edge in turn. The sum of the four solutions thus obtained represents the solution of the actual problem.

Of course if μ *could be* made equal zero, the general solution of equation (1) would simply be

$$T = (C_1 + C_2 x)(C_3 + C_4 y) \qquad (3)$$

The problem is that *working in the previously described manner,*

[1] Department of Mechanical Engineering, University of Ottawa, Ottawa, Ontario, Canada.

Contributed by the Heat Transfer Division of THE AMERICAN SOCIETY OF MECHANICAL ENGINEERS. Manuscript received by the Heat Transfer Division January 23, 1976.

where a is the disk radius. The metric coefficients are readily determined to be

$$g_\eta = g_\theta = a^2(\cosh^2 \eta - \sin^2 \theta); g_\psi = a^2 \cosh^2 \eta \sin^2 \theta \qquad (15)$$

where η, θ, and ψ are defined by the figure. It can be demonstrated that $\eta_\infty \approx 10$ will suffice for the location of the boundary far from the contact [2]. The effective curvilinear property matrix, considering axisymmetric heat transfer, can be found using equations (15) to be

$$[R] = \begin{bmatrix} ak \cosh \eta \sin \theta & 0 \\ 0 & ak \cosh \eta \sin \theta \end{bmatrix} \qquad (16)$$

The convergence characteristics for this problem are plotted in Fig. 2 versus the number of nodal points used to effect the solution. A rapid, monotone approach toward its limiting value is indicated. The value of 0.269 obtained using 800 nodes compares favorably with the exact solution for this problem of 0.27019 [2], yielding an error of 0.44 percent. Indeed, an error of less than 2 percent is obtained when only 200 nodes are used to represent the continuum. Both the ease of application and the accuracy of the results indicate the utility of this work in analyzing problems having a convenient "natural" coordinate system.

Discussion and Conclusions

Explicit consideration has been given in this work to the incorporation of general orthogonal curvilinear coordinate systems into finite element conduction heat transfer analysis. It was found that the incorporation can be effected by a direct extension of existing finite element codes by merely redefining the properties and heat generation rate as presented in this work. The effective curvilinear property matrix replaces the property matrix, $P\sqrt{g}$ replaces P for the heat generation rate, and $C_p\sqrt{g}$ replaces C_p for the energy storage terms. Once defined in this manner, the analysis is performed in the more uniform, thermally and geometrically, curvilinear space. This is of considerable utility since many problems have associated with them a natural or quasi-natural coordinate system.

An example has been presented which illustrates the ease of application of the results to other than the cartesian coordinate system. The solution converged rapidly and monotonically to its limiting value for the oblate spheroidal coordinate problem considered. Where only 800 nodes were used to represent a semi-infinite body and less than 0.5 percent error was incurred, the utility of formulating the problem in the appropriate coordinate frame becomes clear.

These results will find application to contact problems, problems involving semi-infinite or infinite domains, and generally to problems where a coordinate system more natural than the cartesian one exists to describe the problem geometry and field behavior. The result, where there exists a more appropriate coordinate system, will be a savings in both storage requirements and computational time to achieve a prescribed solution accuracy.

Acknowledgments

The author acknowledges the National Research Council and the Communications Research Centre, Department of Communications, Ottawa, Canada, for their financial support of this research. The author is grateful to Dr. M. M. Yovanovich of the University of Waterloo for suggesting the problem and to Dr. A. B. Strong and Dr. M. M. Yovanovich of this university for allowing time to be devoted to this work while working under their supervision. The author is grateful to Dr. G. M. McNeice and Dr. J. C. Thompson of this university for their assistance throughout the course of this work.

References

1 Carslaw, H. S., and Jaeger, J. C., *Conduction of Heat in Solids*, Oxford University Press, London, 1959.

2 Yovanovich, M. M., *Advanced Heat Conduction*, Hemisphere Publishing Corporation, Washington, D. C., 1976.

3 Visser, W., "A Finite Element Method for Determination of Non-Stationary Temperature Distribution and Thermal Deformations," *Proceedings of the Conference on Matrix Methods in Structural Mechanics*, held at the Air Force Institute of Technology, Wright-Patterson Air Force Base, Ohio, 1965, pp. 925–944.

4 Zienkiewicz, O. C., and Parekh, C. J., "Transient Field Problems: Two-Dimensional and Three-Dimensional Analysis by Isoparametric Finite Elements, *International Journal for Numerical Methods in Engineering*, Vol. 2, 1970, pp. 61–71.

5 Zienkiewicz, O. C., *Finite Elements in Engineering Science*, McGraw-Hill, London, 1971.

6 Gurtin, M. E., "Variational Principles for Initial-Value Problems, *Quarterly Journal of Applied Mathematics*, Vol. 22, 1964, pp. 253.

7 Finlayson, B. A., and Scriven, L. E., "On the Search for Variational Principles," *International Journal of Heat and Mass Transfer*, Vol. 10, 1967, pp. 799–821.

8 Schneider, G. E., "Finite Element Formulation of the Heat Conduction Equation in General Orthogonal Curvilinear Coordinates," presented at the ASME Winter Annual Meeting, Houston, Texas, Nov. 30–Dec. 4, ASME Paper No. 75-WA/HT-95, 1975.

9 Finlayson, B. A., *The Method of Weighted Residuals and Variational Principles*, Academic Press, 1972, p. 222.

10 Desai, C. S., and Abel, J. F., *Introduction to the Finite Element Method*, Van Nostrand, 1972.

A New Look at the Superposition of Boundary Conditions in the Evaluation of Temperature Distribution in a Finite Rectangular Plate With Adiabatic Faces at Steady State

A. Feingold[1]

The usual way to solve the governing Laplace equation for steady heat conduction

$$\frac{\partial^2 T}{\partial x^2} + \frac{\partial^2 T}{\partial y^2} = 0 \qquad (1)$$

is to assume that there exists a solution in the form of $T = XY$, where X is a function of x alone and Y is a function of y alone. After the substitution and the separation of variables, the equation becomes

$$\frac{1}{X}\frac{\partial^2 X}{\partial x^2} = -\frac{1}{Y}\frac{\partial^2 Y}{\partial y^2}$$

and the introduction of a separation constant μ leads to the two well-known total differential equations:

$$\frac{d^2X}{dx^2} - \mu X = 0, \qquad \frac{d^2Y}{dy^2} + \mu Y = 0 \qquad (2)$$

Given a rectangular plate, the temperature distribution throughout it is determined in terms of Fourier series using the method of superposition of boundary conditions. The correct given temperature distribution along one edge is coupled with a zero temperature along the other three edges, the Fourier series is obtained by putting $\mu > 0$ or $\mu < 0$, as the case may be, and the process is repeated for each edge in turn. The sum of the four solutions thus obtained represents the solution of the actual problem.

Of course if μ *could be* made equal zero, the general solution of equation (1) would simply be

$$T = (C_1 + C_2 x)(C_3 + C_4 y) \qquad (3)$$

The problem is that *working in the previously described manner,*

[1] Department of Mechanical Engineering, University of Ottawa, Ottawa, Ontario, Canada.

Contributed by the Heat Transfer Division of THE AMERICAN SOCIETY OF MECHANICAL ENGINEERS. Manuscript received by the Heat Transfer Division January 23, 1976.

no boundary conditions will lead to $\mu = 0$, and there is to the author's knowledge no example in the existing literature of an actual application of equation (3).

The primary object of this paper is to show that a particular temperature distribution along two adjoining edges of our rectangular plate considered jointly, rather than separately, does lead to $\mu = 0$. This has many interesting consequences, some of which are discussed further in the following.

Consider the following problem. A rectangular plate of width W and height H is limited by the lines $x = 0$, $x = W$, $y = 0$ and $y = H$. Determine the temperature distribution throughout the plate, given the boundary conditions:

(a) The sides $x = 0$ and $y = 0$ are maintained at temperature $T = 0$,

(b) the temperature along $x = W$ varies linearly according to the formula $T = T_{\max} y/H$,

(c) the temperature along $y = H$ varies linearly according to the formula $T = T_{\max} x/W$.

The application of conditions (a) reduces equation (3) to $T = C\,xy$, and both remaining conditions are satisfied by putting $C = T_{\max}/HW$.

The temperature distribution within the plate obeys, therefore, the law

$$T = \frac{T_{\max}}{HW} xy \tag{4}$$

All the isothermal lines are hyperbolas and the temperature in the center of the plate is $\frac{1}{4}T_{max}$.

The latter conclusion agrees with the result of an alternative reasoning. In the trivial case of the boundary conditions being $T_{\max}$ along all four edges of the plate, the temperature at the center would also be $T_{\max}$. But that case is a superposition of the two depicted in Figs. 1(a) and 1(b). Thus, in each of these the center temperature is $\frac{1}{2}T_{\max}$. On the other hand, the boundary condition shown in Fig. 1(c) is a superposition of the two illustrated in Figs. 1(d) and 1(e), and if the center temperature in Fig. 1(c) is T_2, then that in either case shown in Figs. 1(d) and 1(e) is $T_3 = \frac{1}{2}T_2$.

Similarly, from Figs. 1(f), 1(g), and 1(h) we conclude that $T_5 = \frac{1}{2}T_4$.

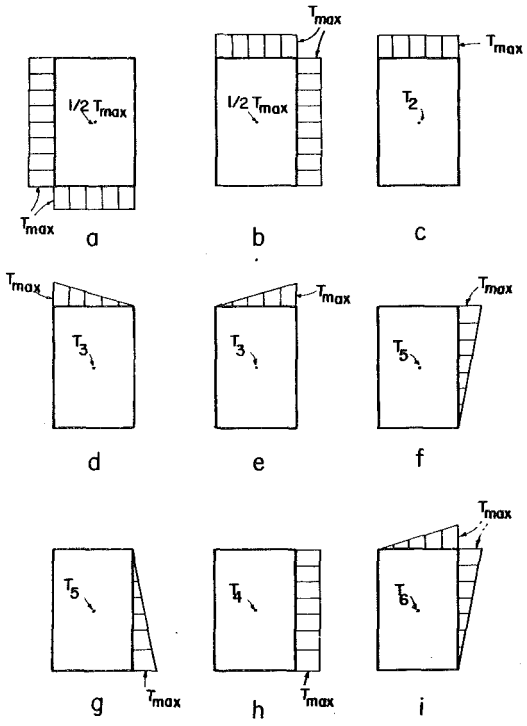

Fig. 1

Finally, since $T_2 + T_4 = \frac{1}{2}T_{\max}$, the boundary conditions of our problem, shown in Fig. 1(i), must produce the center temperature $T_6 = T_3 + T_5 = \frac{1}{4}T_{\max}$.

The temperature distribution throughout the plate obtained by the usual method of superposition of boundary conditions is

$$T = -\frac{2}{\pi} T_{\max} \sum_{n=1}^{\infty} \frac{(-1)^n}{n} \left[\frac{\sinh \frac{n\pi y}{W}}{\sinh \frac{n\pi H}{W}} \sin \frac{n\pi x}{W} + \frac{\sinh \frac{n\pi x}{H}}{\sinh \frac{n\pi W}{H}} \sin \frac{n\pi y}{H} \right] \tag{5}$$

Clearly, solutions (4) and (5) must be identical and, therefore,

$$\frac{xy}{HW} = -\frac{2}{\pi} \sum_{n=1}^{\infty} \frac{(-1)^n}{n} \left[\frac{\sinh \frac{n\pi y}{W}}{\sinh \frac{n\pi H}{W}} \sin \frac{n\pi x}{W} + \frac{\sinh \frac{n\pi x}{H}}{\sinh \frac{n\pi W}{H}} \sin \frac{n\pi y}{H} \right] \tag{6}$$

Putting $x = \frac{1}{2}W$, $y = \frac{1}{2}H$, and $R = H/W$, we obtain an interesting double series:

$$\frac{1}{\cosh \frac{\pi R}{2}} - \frac{1}{3 \cosh \frac{3\pi R}{2}} + \frac{1}{5 \cosh \frac{5\pi R}{2}} - \ldots + \frac{1}{\cosh \frac{\pi}{2R}} - \frac{1}{3 \cosh \frac{3\pi}{2R}} + \frac{1}{5 \cosh \frac{5\pi}{2R}} - \ldots + = \frac{\pi}{4} \tag{7}$$

The first of the two series in equation (7) is a function of R, which we shall call the "center function" and denote by $C(R)$. The second series is an identical function of $1/R$ and we, therefore, have

$$C(R) + C(1/R) = \frac{\pi}{4} \tag{8}$$

an interesting property of the center function.

The center function of unity is, of course,

$$\frac{1}{\cosh \frac{\pi}{2}} - \frac{1}{3 \cosh \frac{3\pi}{2}} + \frac{1}{5 \cosh \frac{5\pi}{2}} - \ldots = \frac{\pi}{8} \tag{9}$$

The author knows of no prior appearance of this unusual series in mathematical literature.

With the boundary conditions of Fig. 1(c), the center temperature previously denoted T_2 is $2C(R)T_{\max}/\pi$ which justifies our choice of the name center function. The values of $C(R)$ could be tabulated like the values of any other function, to be available for use in many problems not necessarily restricted to the field of heat transfer.

Let us now examine the plate in Fig. 2(a). The temperature at any point of that plate can again be obtained from equation (4). This may appear as a surprise only because we have been conditioned to a particular way of applying the principle of superposition of boundary conditions as described on the first page of this paper. The conditions in Fig. 2(a) are, however, equivalent to the superposition of conditions in Figs. 2(b) and 2(c), to each of which equation (4) is readily applicable with a suitable choice of axes.

It is now easily seen that the isotherms in Fig. 2(a) are a family of parallel horizontal lines and the temperature map is, thus, immediately obtainable. This would not at all be evident from the Fourier series solution, but is in agreement with the following observation.

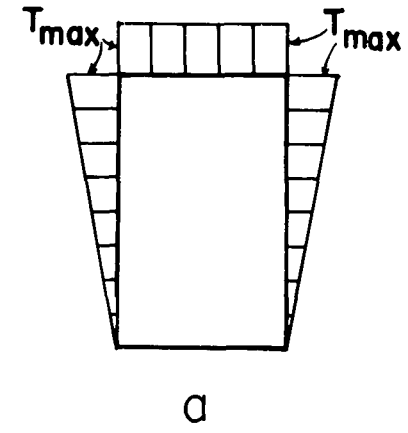

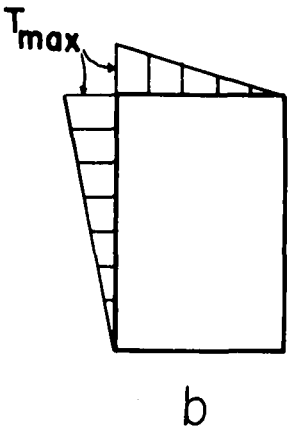

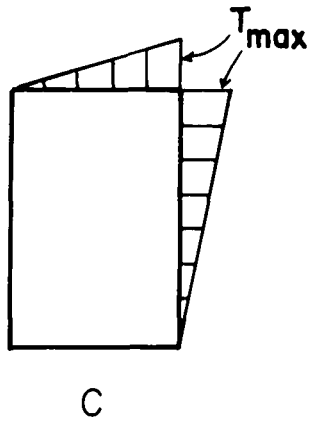

Fig. 2

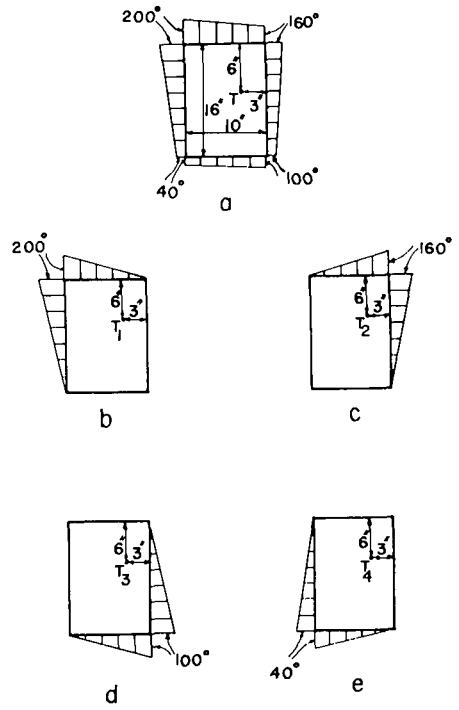

Fig. 3

If the boundary conditions of our plate were $T = T_{max}$ along the upper edge and $T = 0$ along the lower edge with the added condition that the vertical edges are perfectly insulated, the isotherms would be evenly spaced horizontal lines. This means that the temperature distribution at both vertical edges would be linear. Now, take off the insulation and simply impose this linear temperature distribution along the vertical edges and you have the conditions of Fig. 2(*a*) without affecting the temperature map throughout the plate.

Returning to equation (4), we now have a new tool, the use of which should become standard practice in all cases where there is a linear variation (or no variation) of temperature along all edges of a rectangular plate without jump discontinuity at the corners. The following numerical example illustrates the use of this tool.

Consider the plate in Fig. 3(*a*). Determine the temperature T at the point indicated in the figure.

Using our method, we see that the plate in Fig. 3(*a*) is a superposition of the four plates in Figs. 3(*b*), 3(*c*), 3(*d*), and 3(*e*).

$$T = T_1 + T_2 + T_3 + T_4$$

$$T_1 = 200\,\frac{10(3)}{16(10)} = 37.5$$

$$T_2 = 160\,\frac{10(7)}{16(10)} = 70$$

$$T_3 = 100\,\frac{6(7)}{16(10)} = 26.25$$

$$T_4 = 40\,\frac{6(3)}{16(10)} = 4.5$$

$$T = 138.25°$$

Not so easy by Fourier series.

It may finally be added that the previously mentioned restriction with respect to the absence of jump discontinuity at the corners merely reflects reality. Textbook examples, such as Fig. 1(*c*), do not have any real physical meaning, since the same point cannot have two different temperatures in a steady-state situation. Or, to put it differently, if two infinitely close points had a discrete temperature difference between them, there would exist in that neighborhood an infinite temperature gradient.

Minimization of Measurement Errors Involved in the Probe Method of Determining Soil Thermal Conductivity

J. G. Hartley[1] and W. Z. Black[2]

Nomenclature

a, b = inside and outside diameter, respectively, of thermal probe
c = volumetric heat capacity, cal cm^{-3} °C^{-1}
Bi = Biot number, = bh/k_2
Fo = Fourier number, = $\alpha_2 t/b^2$; subscripts i and f refer to initial and final states, respectively
h = unit thermal conductance at soil-probe interface
k, α = thermal conductivity and thermal diffusivity respectively; subscripts 1 and 2 refer to probe material and soil, respectively
Q = rate of heat input to probe per unit length of probe
S = porosity of soil; volume of voids per unit volume of soil
t = time
x_w = volumetric moisture content of soil, cm^3/cm^3
γ = Euler's constant, = 0.5772 . . .
δ = fractional measurement error defined in equation (8)
Δ = dimensionless parameter defined in equation (4)
ϕ = dimensionless parameter defined in equation (5)
θ = temperature rise of probe above ambient temperature of soil

Introduction

Ecological and aesthetic factors are forcing more and more heated pipelines and power cables to be buried rather than being located above the surface of the ground. Therefore, the problem of predicting the operating temperatures of buried pipelines and electrical cables has become more urgent. Accurate measurement of the thermal properties of the surrounding soil is a necessary prerequisite for the solution of the problem.

If one wishes to survey the soil along the entire route of a cable, rapid measurements are desirable and it is important that the soil conductivity not be altered by removal of the soil for laboratory testing. Therefore, some means of in situ determination of the thermal conductivity of the soil is preferred. At present the most widely used technique employs a thermal conductivity probe, and it is the purpose of this technical note to describe the optimum measurement time compatible with a specific probe design which minimizes measurement errors.

The usual probe configuration is that of a hollow cylinder consisting of a good thermal conductor which is supplied with a constant heat input Q per unit length of the probe. Thermocouples attached to the interior of the probe provide temperature measurements which are, in turn, related to the thermal conductivity of the medium being tested.

The simplest of the mathematical models involves an infinitely long wire, with vanishing diameter heated at a constant rate which is imbedded with zero contact resistance in an infinite medium. This "needle probe" theory [1][3] gives the temperature rise of the wire above the ambient soil temperature, θ, as a function of the time, t, in dimensionless form as

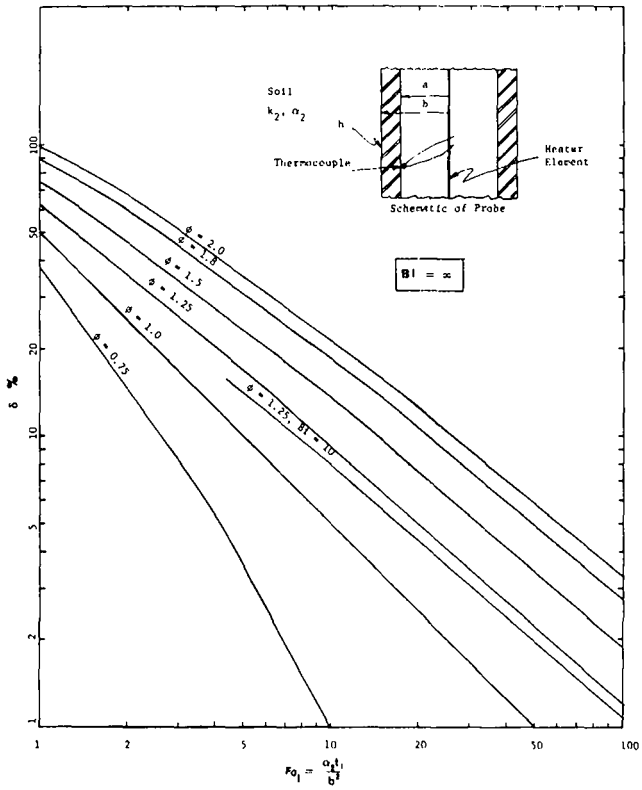

Fig. 1. Percent error in k_2 as a function of initial Fourier number for various values of the probe design parameter ϕ and schematic of probe

$$\frac{4\pi k_2 \theta}{Q} = \ln 4\text{Fo} - \gamma \tag{1}$$

for cases when Fo = $\alpha_2 t/b^2 \gg 1.0$. Due to the limitation of a Fourier number being much larger than unity, this solution is referred to as a long-time solution.

This equation is extremely simple but it often does not simulate the situation when a probe is actually inserted into a test medium. The actual probe can have (a) an imperfect thermal contact between the probe surface and the soil producing a temperature drop at the interface, (b) a finite diameter, (c) a finite thermal conductivity producing a radial temperature gradient in the probe wall, and (d) a finite heated length. Reference [2] discusses the effect of finite heated length and presents curves to aid in the selection of the required length of heated section. This error will therefore not be discussed here.

A detailed analysis of the probe method has been developed by Blackwell [3, 4] in which each of the above sources of error is considered.

Analysis

The following analysis presents a method of selecting the minimum acceptable initial measurement time which minimizes errors for a specific probe design. For a hollow probe with outside radius b and inside radius a with a unit thermal conductance h at the soil interface (see inset in Fig. 1), Blackwell has derived the following long-time solution for the temperature of the probe

$$\theta(t) = \frac{Q}{4\pi k_2}\left\{\ln 4\text{Fo} - \gamma + \frac{2}{\text{Bi}} + \frac{1}{2\text{Fo}} \times \left[\ln 4\text{Fo} - \gamma + 1 - \phi\left(\ln 4\text{Fo} - \gamma + \frac{2}{\text{Bi}}\right)\right] + 0\left(\frac{1}{\text{Fo}^2}\right)\right\} \tag{2}$$

If the effect of finite thermal conductivity of the probe is accounted for, a radial temperature gradient will exist within the probe material. Blackwell [3] has shown that, for this case, the long-time temperature

---

[1] Research Assistant, School of Mechanical Engineering, Georgia Institute of Technology, Atlanta, Ga.

[2] Professor, School of Mechanical Engineering, Georgia Institute of Technology, Atlanta, Ga.

[3] Numbers in brackets designate References at end of technical note.

Contributed by the Heat Transfer Division of THE AMERICAN SOCIETY OF MECHANICAL ENGINEERS. Manuscript received by the Heat Transfer Division January 16, 1976.

solution is (at $r = a$)

$$\theta(a, t) = \frac{Q}{4\pi k_2}\left\{\ln 4\mathrm{Fo} - \gamma + \frac{2}{\mathrm{Bi}} + \frac{1}{2\mathrm{Fo}} \times \left[\ln 4\mathrm{Fo} - \gamma + 1 - \phi\left(\ln 4\mathrm{Fo} - \gamma + \frac{2}{\mathrm{Bi}}\right) - \Delta\right] + 0\left(\frac{1}{\mathrm{Fo}^2}\right)\right\} \quad (3)$$

where

$$\Delta = \frac{1}{2}\left[\frac{\alpha_2}{\alpha_1}\right][1 - (a/b)^2 + (a/b)^2 \ln (a/b)^2] \quad (4)$$

and

$$\phi = [(k_1 \alpha_2/k_2 \alpha_1)][1 - (a/b)^2] \quad (5)$$

Equations (2) and (3) differ only by the factor $Q\Delta/(8\pi k_2\,\mathrm{Fo})$. For an extreme condition $\Delta_{max} = 0.08$ (wet soil, stainless steel thick-wall probe for which $\alpha_2/\alpha_1 = 0.003$ and $a/b = 0.5$), this factor is less than 5 percent of the contribution to the error in overall temperature measurement at Fo = 1, and is even less significant as the Fourier number increases.

In using the probe method for field determination of thermal conductivity, k_2 and Q are taken as constants and equation (1) is used in the form

$$\theta(t_f) - \theta(t_i) = \frac{Q}{4\pi k_2} \ln\left[\frac{\mathrm{Fo}_f}{\mathrm{Fo}_i}\right] \quad (6)$$

where Fo_f and Fo_i correspond to measurement times t_f and t_i. Thus, field measurements of $\theta(t_f)$ and $\theta(t_i)$ give the thermal conductivity as

$$k_2 = \frac{Q}{4\pi}\frac{\ln (\mathrm{Fo}_f/\mathrm{Fo}_i)}{\theta(t_f) - \theta(t_i)} = \frac{Q}{4\pi}\left[\frac{\ln (t_f/t_i)}{\theta(t_f) - \theta(t_i)}\right] \quad (7)$$

According to equation (7), any pair of temperature measurements could be used to calculate k_2 provided the heat input Q is known. Due to initial transients the needle theory does not give an accurate simulation of the process and the initial θ versus ln Fo curve is not linear as predicted by equation (1). In reality it is therefore necessary to wait until the θ versus ln Fo response of the probe becomes linear before equation (7) may be used to provide an accurate measure of the soil thermal conductivity. As a result, continuous monitoring of the data is necessary.

Information derived from equation (3) can eliminate the latter requirement and at the same time provide a means of reducing the extent of initial transients.

Taking the derivative of equation (3) one obtains

$$\frac{d}{d \ln \mathrm{Fo}}\left(\frac{4\pi k_2 \theta}{Q}\right) = 1 + \frac{1}{2\mathrm{Fo}}\left[(1 - \phi)(1 - \gamma - \ln 4\mathrm{Fo}) + 1 - \frac{2\phi}{\mathrm{Bi}}\right] = 1 + \delta \quad (8)$$

where δ represents the fractional measurement error in k_2. The error δ contains the effect of initial transients and surface conductance and is the difference between the slope of the curve of the extended theory (3) and that of the needle theory (1).

In Fig. 1, the error δ is plotted as a percent error in $4\pi k_2\theta/Q$ as a function of initial Fourier number for various values of ϕ and an infinite Biot number. (The curve of $\phi = 1.25$ and Bi = 10 shows that the smaller values of the Biot number do not have a significant influence.) The figure shows that for minimum initial measurement time and maximum accuracy, the parameter ϕ should be as small as possible. More important, however, for a given value of ϕ and a given acceptable level of accuracy, the curves of Fig. 1 provide an estimate of the time acceptable for the first measurement of temperature, $\theta(t_i)$, to be used in equation (7). Thereafter, any two measurements of temperature may be used to evaluate k_2 from equation (7).

In order to use Fig. 1, one must be able to estimate the values for the ratio k_2/α_2 and k_2 (or α_2) for the soil being tested. The first of these, k_2/α_2, is simply the volumetric heat capacity, c, of the soil which can be evaluated from the equation [5]

$$c = 0.46\,(1 - S) + x_w,\ \mathrm{cal\ cm^{-3}\ °C^{-1}}$$

which is valid for soils with negligible amounts of organic matter. (Values of c for most soils range from about 0.4 to 0.55 cal $\mathrm{cm^{-3}\ °C^{-1}}$). To determine the time which corresponds to a particular Fourier number from Fig. 1, one can make a reasonable estimate of the thermal conductivity of the soil and determine α_2 from k_2/c. Any uncertainties in the estimated values of k_2 may be overcome by using conservative values of the time t_i calculated from the Fourier number.

References

1 Carslaw, H. S., and Jaeger, J. C., *Conduction of Heat in Solids*, Oxford University Press, London, 1947, p. 283.

2 Christoffel, D. A., and Calhaem, I. M., "A Geothermal Heat Flow Probe for *in situ* Measurement of Both Temperature Gradient and Thermal Conductivity," *J. Sci. Instr.*, Series 2, Vol. 2, 1969, pp. 457–465.

3 Blackwell, J. H., "A Transient-Flow Method for Determination of Thermal Constants of Insulating Materials in Bulk," *J. Appl. Phys.*, Vol. 25, 1954, pp. 137–144.

4 Blackwell, J. H., "The Axial-Flow Error in the Thermal Conductivity Probe," *Can. J. Phys*, Vol. 34, 1956, pp. 412–417.

5 de Vries, D. A., "Thermal Properties of Soils," *Physics of Plant Environment*, North-Holland Publishing Co., Van Wijk, W. E., ed, Amsterdam, Chapter 7, 1963.

Melting Heat Transfer in Steady Laminar Flow Over a Flat Plate

M. Epstein[1] and D. H. Cho[1]

Nomenclature

B = melting parameter; equation (10)
c = heat capacity
F = dimensionless similarity variable
k = thermal conductivity
L = latent heat of fusion
Nu = Nusselt number; equation (11)
Nu_0 = Nusselt number in the absence of melting
Pr = Prandtl number; ν/α
Re = Reynolds number; $U_\infty x/\nu$
Sc = Schmidt number; ν/D (D = binary diffusivity)
T = temperature
u = velocity component in x-direction
U_∞ = free stream velocity of hot liquid
v = velocity component in y-direction
x = coordinate parallel to the melting surface
y = transverse coordinate measured from the melting surface
α = thermal diffusivity
η = dimensionless similarity coordinate; equation (1)
θ = dimensionless temperature; equation (6)
ν = kinematic viscosity
ρ = density

Subscripts

s = solid

[1] Argonne National Laboratory, Argonne, Ill.

Contributed by the Heat Transfer Division of THE AMERICAN SOCIETY OF MECHANICAL ENGINEERS. Manuscript received by the Heat Transfer Division April 2, 1976.

solution is (at $r = a$)

$$\theta(a, t) = \frac{Q}{4\pi k_2}\left\{\ln 4\mathrm{Fo} - \gamma + \frac{2}{\mathrm{Bi}} + \frac{1}{2\mathrm{Fo}} \times \left[\ln 4\mathrm{Fo} - \gamma + 1 - \phi\left(\ln 4\mathrm{Fo} - \gamma + \frac{2}{\mathrm{Bi}}\right) - \Delta\right] + 0\left(\frac{1}{\mathrm{Fo}^2}\right)\right\} \quad (3)$$

where

$$\Delta = \frac{1}{2}\left[\frac{\alpha_2}{\alpha_1}\right][1 - (a/b)^2 + (a/b)^2 \ln (a/b)^2] \quad (4)$$

and

$$\phi = [(k_1\,\alpha_2/k_2\,\alpha_1)][1 - (a/b)^2] \quad (5)$$

Equations (2) and (3) differ only by the factor $Q\Delta/(8\pi k_2\,\mathrm{Fo})$. For an extreme condition $\Delta_{max} = 0.08$ (wet soil, stainless steel thick-wall probe for which $\alpha_2/\alpha_1 = 0.003$ and $a/b = 0.5$), this factor is less than 5 percent of the contribution to the error in overall temperature measurement at Fo = 1, and is even less significant as the Fourier number increases.

In using the probe method for field determination of thermal conductivity, k_2 and Q are taken as constants and equation (1) is used in the form

$$\theta(t_f) - \theta(t_i) = \frac{Q}{4\pi k_2}\ln\left[\frac{\mathrm{Fo}_f}{\mathrm{Fo}_i}\right] \quad (6)$$

where Fo_f and Fo_i correspond to measurement times t_f and t_i. Thus, field measurements of $\theta(t_f)$ and $\theta(t_i)$ give the thermal conductivity as

$$k_2 = \frac{Q}{4\pi}\frac{\ln (\mathrm{Fo}_f/\mathrm{Fo}_i)}{\theta(t_f) - \theta(t_i)} = \frac{Q}{4\pi}\left[\frac{\ln (t_f/t_i)}{\theta(t_f) - \theta(t_i)}\right] \quad (7)$$

According to equation (7), any pair of temperature measurements could be used to calculate k_2 provided the heat input Q is known. Due to initial transients the needle theory does not give an accurate simulation of the process and the initial θ versus ln Fo curve is not linear as predicted by equation (1). In reality it is therefore necessary to wait until the θ versus ln Fo response of the probe becomes linear before equation (7) may be used to provide an accurate measure of the soil thermal conductivity. As a result, continuous monitoring of the data is necessary.

Information derived from equation (3) can eliminate the latter requirement and at the same time provide a means of reducing the extent of initial transients.

Taking the derivative of equation (3) one obtains

$$\frac{d}{d\ln \mathrm{Fo}}\left(\frac{4\pi k_2\theta}{Q}\right) = 1 + \frac{1}{2\mathrm{Fo}}\left[(1 - \phi)(1 - \gamma - \ln 4\mathrm{Fo}) + 1 - \frac{2\phi}{\mathrm{Bi}}\right] = 1 + \delta \quad (8)$$

where δ represents the fractional measurement error in k_2. The error δ contains the effect of initial transients and surface conductance and is the difference between the slope of the curve of the extended theory (3) and that of the needle theory (1).

In Fig. 1, the error δ is plotted as a percent error in $4\pi k_2\theta/Q$ as a function of initial Fourier number for various values of ϕ and an infinite Biot number. (The curve of $\phi = 1.25$ and Bi = 10 shows that the smaller values of the Biot number do not have a significant influence.) The figure shows that for minimum initial measurement time and maximum accuracy, the parameter ϕ should be as small as possible. More important, however, for a given value of ϕ and a given acceptable level of accuracy, the curves of Fig. 1 provide an estimate of the time acceptable for the first measurement of temperature, $\theta(t_i)$, to be used in equation (7). Thereafter, any two measurements of temperature may be used to evaluate k_2 from equation (7).

In order to use Fig. 1, one must be able to estimate the values for the ratio k_2/α_2 and k_2 (or α_2) for the soil being tested. The first of these, k_2/α_2, is simply the volumetric heat capacity, c, of the soil which can be evaluated from the equation [5]

$$c = 0.46\,(1 - S) + x_w,\ \mathrm{cal\ cm^{-3}\ °C^{-1}}$$

which is valid for soils with negligible amounts of organic matter. (Values of c for most soils range from about 0.4 to 0.55 cal $\mathrm{cm^{-3}\ °C^{-1}}$). To determine the time which corresponds to a particular Fourier number from Fig. 1, one can make a reasonable estimate of the thermal conductivity of the soil and determine α_2 from k_2/c. Any uncertainties in the estimated values of k_2 may be overcome by using conservative values of the time t_i calculated from the Fourier number.

References

1 Carslaw, H. S., and Jaeger, J. C., *Conduction of Heat in Solids*, Oxford University Press, London, 1947, p. 283.

2 Christoffel, D. A., and Calhaem, I. M., "A Geothermal Heat Flow Probe for *in situ* Measurement of Both Temperature Gradient and Thermal Conductivity," *J. Sci. Instr.*, Series 2, Vol. 2, 1969, pp. 457–465.

3 Blackwell, J. H., "A Transient-Flow Method for Determination of Thermal Constants of Insulating Materials in Bulk," *J. Appl. Phys.*, Vol. 25, 1954, pp. 137–144.

4 Blackwell, J. H., "The Axial-Flow Error in the Thermal Conductivity Probe," *Can. J. Phys*, Vol. 34, 1956, pp. 412–417.

5 de Vries, D. A., "Thermal Properties of Soils," *Physics of Plant Environment*, North-Holland Publishing Co., Van Wijk, W. E., ed, Amsterdam, Chapter 7, 1963.

Melting Heat Transfer in Steady Laminar Flow Over a Flat Plate

M. Epstein[1] and D. H. Cho[1]

Nomenclature

B = melting parameter; equation (10)
c = heat capacity
F = dimensionless similarity variable
k = thermal conductivity
L = latent heat of fusion
Nu = Nusselt number; equation (11)
Nu_0 = Nusselt number in the absence of melting
Pr = Prandtl number; ν/α
Re = Reynolds number; $U_\infty x/\nu$
Sc = Schmidt number; ν/D (D = binary diffusivity)
T = temperature
u = velocity component in x-direction
U_∞ = free stream velocity of hot liquid
v = velocity component in y-direction
x = coordinate parallel to the melting surface
y = transverse coordinate measured from the melting surface
α = thermal diffusivity
η = dimensionless similarity coordinate; equation (1)
θ = dimensionless temperature; equation (6)
ν = kinematic viscosity
ρ = density

Subscripts

s = solid

[1] Argonne National Laboratory, Argonne, Ill.

Contributed by the Heat Transfer Division of THE AMERICAN SOCIETY OF MECHANICAL ENGINEERS. Manuscript received by the Heat Transfer Division April 2, 1976.

mp = melting point
0 = conditions in the solid at large distances from the melting surface

Superscript

′ = differentiation with respect to η

Introduction

Approximate analyses of the heat transfer from a warm, laminar liquid flow to a melting flat surface are presented in references [1–3][2] for liquid Prandtl numbers >1.0. The similarity between melting problems and diffusional mass transfer or transpiration cooling problems was first noted in [1]. Based on this diffusion-melting analogy, a simple method for calculating melting rates in more complex flow situations was developed in [4]. In this paper, exact similarity solutions for melting heat transfer in steady laminar flow over a flat plate are collected from the diffusional mass transfer literature to provide solutions for Prandtl numbers from 0.001 to 100. An exact closed-form solution is introduced for the case of melting in porous media. The results are presented and discussed in such a way as to emphasize the similarity between melting and diffusional mass transfer.

Governing Equations

The physical model is identical to that in references [1–3], viz., we consider a flat plate melting at a steady rate into a constant property, warm liquid of the same material flowing at velocity U_∞. The temperature and velocity profiles in the liquid flow must obey the usual boundary layer equations which can be made one-dimensional by the following similarity transformations:

$$\eta = \left(\frac{U_\infty}{\nu x}\right)^{1/2} y \tag{1}$$

$$u = U_\infty F'(\eta) \tag{2}$$

$$v = \frac{1}{2}\left(\frac{\nu U_\infty}{x}\right)^{1/2} (\eta F' - F) \tag{3}$$

The velocity and temperature profiles are then determined by

$$F''' + \frac{1}{2} FF'' = 0 \tag{4}$$

$$\theta'' + \frac{1}{2} \Pr F\theta' = 0 \tag{5}$$

where θ is a dimensionless temperature defined by

$$\theta = \frac{T(\eta) - T_{mp}}{T_\infty - T_{mp}} \tag{6}$$

The free-stream conditions in the warm liquid flow, viz., $u = U_\infty$ and $T = T_\infty$ for $y \to \infty$; and the boundary conditions at the melting surface, viz., $u = 0$ and $T = T_{mp}$ at $y = 0$, become

$$F'(\infty) \to 1; \quad \theta(\infty) \to 1; \quad F'(0) = 0; \quad \theta(0) = 0 \tag{7}$$

Finally, we write the boundary condition at $y = 0$

$$k\left(\frac{\partial T}{\partial y}\right)_{y=0} = L\rho v(x,0) + c_s(T_{mp} - T_0)\rho v(x,0) \tag{8}$$

which states that the heat conducted to the melting surface is equal to the heat of melting plus the sensible heat required to raise the solid temperature T_0 to its melting temperature T_{mp}. It is important to note that equation (8) is consistent with a coordinate system fixed to the melting surface, so that the interior of the solid appears to move toward the (stationary) melting surface with constant velocity equal to the melting velocity $v(x,0)$. As long as the melting solid is large compared with its thermal boundary layer thickness $\delta_T = \alpha/v(x,0)$, transient effects in the solid are negligible (as discussed in references [5, 6]). Roberts [7] in his paper on the steady melting of a solid in a hot gas flow provides a detailed derivation of condition (8). In terms of the transformed variables, boundary condition (8) becomes

$$\Pr F(0) + 2B\theta'(0) = 0 \tag{9}$$

where B, the dimensionless melting parameter defined by

$$B \equiv \frac{c(T_\infty - T_{mp})}{L + c_s(T_{mp} - T_0)} \tag{10}$$

is a combination of the Stefan numbers $c(T_\infty - T_{mp})/L$ and $c_s(T_{mp} - T_0)/L$ for the liquid and solid phases, respectively. It is convenient to report the local heat transfer or melting rate in terms of a local heat-transfer coefficient or local Nusselt number defined as follows

$$\mathrm{Nu} = \frac{x k\left(\frac{\partial T}{\partial y}\right)_{y=0}}{k(T_\infty - T_{mp})} = \mathrm{Re}^{1/2}\theta'(0) \tag{11}$$

From equation (8), therefore, the melting velocity, $v(x,0)$, is obtained:

$$\frac{v(x,0)x}{\alpha} = B\mathrm{Nu} \tag{12}$$

Solution of the given equations is quite unnecessary as the functions F and θ satisfy the same boundary value problem already solved elsewhere in the context of diffusional mass transfer or transpiration cooling [10–15].

Results and Discussion

The melting rate is presented in Fig. 1 (in terms of the local Nusselt number Nu) as a function of the melting parameter B, with the Prandtl number as a parameter. The Nusselt number is normalized by the Nusselt number in the absence of melting, $\mathrm{Nu}_{B=0} = \mathrm{Nu}_0$. In the limit as $B \to 0$, the results become equivalent to solutions for heat transfer to an isothermal plate (see, e.g., references [8, 9]). The results for the range Pr = 0.001–100 were obtained from (tabulated) exact similarity solutions reported by Evans [15].

One interesting feature of the solutions is that the influence of the Pr number on the normalized Nusselt number disappears as Pr becomes large. The asymptotic relation between $\mathrm{Nu}/\mathrm{Nu}_0$ and B has been the subject of many investigations [1, 2, 10–14]. Most of this work exploits the "thinness" of the thermal (or diffusion) boundary layer in the high Pr (or Sc) number limit to arrive at a fairly complex, but mathematically exact *implicit* relationship between $\mathrm{Nu}/\mathrm{Nu}_0$ and B. A simple expression, namely,

$$\frac{\mathrm{Nu}}{\mathrm{Nu}_0} = \frac{\ln(1+B)}{B} \tag{13}$$

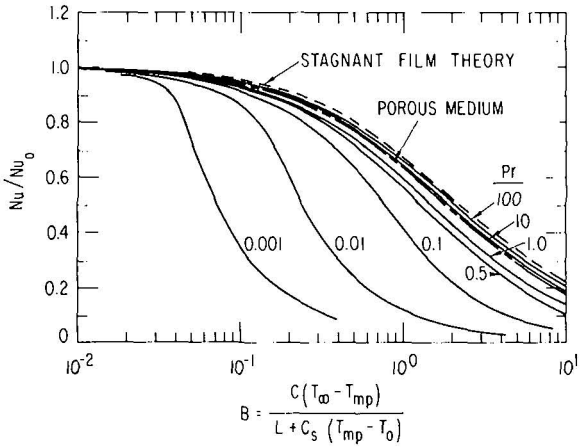

Fig. 1 Normalized Nusselt number as a function of melting driving force parameter B; dependence on liquid Prandtl number

[2] Numbers in brackets designate References at end of technical note.

based on the stagnant film model of a boundary layer [16], was first suggested by Spalding [10] to correct for the effect of interfacial mass transfer on diffusion in real boundary layers. This expression is also plotted in Fig. 1. While Nu/Nu_0 values from equation (13) do not coincide exactly with those indicated by the laminar-boundary-layer calculations, they are nevertheless comparable in form and magnitude for $Pr \gg 1$. Moreover, since it has been widely used with considerable success for mass transfer at complex surfaces submerged in laminar or turbulent flows (see, e.g., [17, 18]) equation (13) is expected to correctly account for the effects of melting in many complex flow systems [4].

Melting in Porous Media

Suppose that a flat plate is melting in a potential (inviscid) flow field. This case is approximately realized in practice when fluid flows through a porous medium (e.g., sand or soil; see [19, 20]) containing a frozen layer (e.g., ice or permafrost). Then, the momentum equation (4) reduces to $F'' = 0$, or, from boundary conditions (7) and (9),

$$F = \eta - \frac{2B}{\Pr}\theta'(0) \tag{14}$$

Introduction of this expression into equation (5) leads to

$$\theta = \frac{\operatorname{erf}\left[B/\Pr^{1/2}\theta'(0)\right] + \operatorname{erf}\left[\frac{1}{2}\Pr^{1/2}\eta - B/\Pr^{1/2}\theta'(0)\right]}{\operatorname{erf}\left[B/\Pr^{1/2}\theta'(0)\right] + 1} \tag{15}$$

Evaluating $d\theta/d\eta$ at $\eta = 0$, we obtain the following exact implicit relation for the normalized Nusselt number Nu/Nu_0:

$$Nu/Nu_0\left[1 + \operatorname{erf}\left(B\pi^{-1/2}\,Nu/Nu_0\right)\right] = \exp\left[-B^2\pi^{-1}(Nu/Nu_0)^2\right] \tag{16}$$

where

$$Nu_0 = \pi^{-1/2}\,(\mathrm{PrRe})^{1/2} \tag{17}$$

Recently, Reid [21] solved the problem of melting of permafrost by ground water movement using the approximate integral (profile) method. His analysis, however, is concerned with low melting rates ($B \ll 1$) so that $Nu \approx Nu_0$. Equation (16) is plotted in Fig. 1 (just below the curve for $Pr = 10$). One notes that equation (13) can be used to approximately correct for the effects of high melting rates in porous media.[3]

Acknowledgments

It is a pleasure to acknowledge the assistance of F. Pellett in carrying out the computations presented herein and in preparing the figures. This work was performed under the auspices of the U. S. Energy Research and Development Administration.

References

1 Yen, Y. C., and Tien, C., "Laminar Heat Transfer Over a Melting Plate, the Modified Leveque Problem," *J. Geophy. Res.*, Vol. 68, No. 12, 1963, pp. 3673–3678.

2 Pozvonkov, F. M., Shurgalskii, E. F., and Axselrod, L. S., "Heat Transfer at a Melting Flat Surface Under Conditions of Forced Convection and Laminar Boundary Layer," *International Journal of Heat and Mass Transfer*, Vol. 13, 1970, pp. 957–962.

3 Griffin, O. M., "Heat, Mass, and Momentum Transfer During the Melting of Glacial Ice in Sea Water," JOURNAL OF HEAT TRANSFER, TRANS. ASME, Series C, Vol. 95, 1973, pp. 317–323.

4 Epstein, M., "The Effect of Melting on Heat Transfer to Submerged Bodies," *Letters in Heat and Mass Transfer*, Vol. 2, 1975, pp. 97–104.

5 Epstein, M., and Cho, D. H., "Laminar Film Condensation on a Vertical Melting Surface," JOURNAL OF HEAT TRANSFER, TRANS. ASME, Series C, Vol. 98, 1976, pp. 108–113.

6 Landau, H. G., "Heat Conduction in a Melting Solid," *Quart. Appl. Math.*, Vol. 8, 1950, pp. 81–94.

7 Roberts, A. L., "On the Melting of a Semi-Infinite Body Placed in a Warm Stream of Air," *Journal of Fluid Mechanics*, Vol. 4, 1958, pp. 505–528.

8 Schlichting, H., *Boundary Layer Theory*, McGraw-Hill, New York, Chapter XIV, 1960.

9 Sparrow, E. M., and Gregg, J. L., "Summary of Low-Prandtl-Number Heat-Transfer Results for Forced Convection on a Flat Plate," *J. Aero. Sci.*, Vol. 24, 1957, pp. 852–853.

10 Spalding, D. B., "Mass Transfer in Laminar Flow," *Proc. Roy. Soc.*, Vol. A221, 1954, pp. 78–84.

11 Merk, H. J., "Mass Transfer in Laminar Boundary Layers Calculated by Means of a Perturbation Method," *Appl. Sci. Res.*, Vol. A8, 1959, pp. 237–260; see also pp. 261–277.

12 Mickley, H. S., Ross, R. C., Squyers, A. L., and Stewart, W. E., "Heat, Mass, and Momentum Transfer for Flow over a Flat Plate With Blowing or Suction," N.A.C.A. Technical Note 3208, 1954.

13 Acrivos, A., "The Asymptotic Form of the Laminar Boundary-Layer Mass-Transfer Rate for Large Interfacial Velocities," *Journal of Fluid Mechanics*, Vol. 12, 1962, pp. 337–357.

14 Stewart, W. E., and Prober, R., "Heat Transfer and Diffusion in Wedge Flows With Rapid Mass Transfer," *International Journal of Heat and Mass Transfer*, Vol. 5, 1962, pp. 1149–1163.

15 Evans, H. L., "Mass Transfer Through Laminar Boundary Layers—6. Methods of Evaluating the Wall Gradient for Similar Solutions; Some New Values for Zero Main-stream Pressure Gradient," *International Journal of Heat and Mass Transfer*, Vol. 3, 1961, pp. 321–339.

16 Bird, R. B., Stewart, W. E., and Lightfoot, E. N., *Transport Phenomena*, Wiley, New York, Chapter 21, 1960.

17 Ranz, W. E., and Dickson, P. F., "Mass and Heat Transfer Rates for Large Gradients of Concentration and Temperature," *Ind. Eng. Chem. Fundam.*, Vol. 4, 1965, pp. 345–353.

18 Humphrey, D. W., and Van Ness, H. C., "Mass Transfer in a Continuous Flow Mixing Vessel," *AIChE Journal*, Vol. 3, 1957, pp. 283–286.

19 Muskat, M., *Flow of Homogeneous Fluids Through Porous Media*, J. W. Edwards, Ann Arbor, 1946.

20 Harr, M. E., *Groundwater and Seepage*, McGraw-Hill, New York, 1962.

21 Reid, R. L., "Integral Methods for the Melting of Permafrost by Ground Water Flows," 15th National Heat Transfer Conference—San Francisco, Aug. 1975, Paper No. AIChE 32E10-G7.

[3] A practical upper limit for B for water is $B \leq 1.25$.

The Laminar Compressible Boundary Layer on a Rotating Sphere With Heat Transfer

M. Y. Hussaini[1] and M. S. Sastry[2]

Nomenclature

a = radius of the sphere
C_p = specific heat at constant pressure
g = acceleration due to gravity
Gr = Grashof number = $g\,\beta/C_p\,(h_w^* - h_\infty^*)(2a)^3/\nu_w^{*2}$
h = enthalpy
Nu = Nusselt number based on diameter = $2a/(h_w^* - h_\infty^*)(\partial h^*/\partial y^*)_{y^*=0}$
$\bar{\mathrm{Nu}}$ = average Nusselt number
Pr = Prandtl number
Re = Reynolds number based on diameter = $4a^2\Omega/\nu_w^*$
u = x-component of velocity (meridional)
v = y-component of velocity (radial)
w = z-component of velocity (azimuthal)
x = meridional coordinate measured from north pole

[1] Chief, Flow Fields, Aerodynamics Division, Space Science and Technology Centre, Trivandrum, India. Presently at NASA Ames Research Center, Calif.

[2] Scientist, Aerodynamics Division, Space Science and Technology Centre, Trivandrum, India.

Contributed by the Heat Transfer Division of THE AMERICAN SOCIETY OF MECHANICAL ENGINEERS. Manuscript received by the Heat Transfer Division September 5, 1976.

based on the stagnant film model of a boundary layer [16], was first suggested by Spalding [10] to correct for the effect of interfacial mass transfer on diffusion in real boundary layers. This expression is also plotted in Fig. 1. While Nu/Nu_0 values from equation (13) do not coincide exactly with those indicated by the laminar-boundary-layer calculations, they are nevertheless comparable in form and magnitude for $Pr \gg 1$. Moreover, since it has been widely used with considerable success for mass transfer at complex surfaces submerged in laminar or turbulent flows (see, e.g., [17, 18]) equation (13) is expected to correctly account for the effects of melting in many complex flow systems [4].

Melting in Porous Media

Suppose that a flat plate is melting in a potential (inviscid) flow field. This case is approximately realized in practice when fluid flows through a porous medium (e.g., sand or soil; see [19, 20]) containing a frozen layer (e.g., ice or permafrost). Then, the momentum equation (4) reduces to $F''' = 0$, or, from boundary conditions (7) and (9),

$$F = \eta - \frac{2B}{\Pr}\theta'(0) \tag{14}$$

Introduction of this expression into equation (5) leads to

$$\theta = \frac{\operatorname{erf}\left[B/\Pr^{1/2}\theta'(0)\right] + \operatorname{erf}\left[\frac{1}{2}\Pr^{1/2}\eta - B/\Pr^{1/2}\theta'(0)\right]}{\operatorname{erf}\left[B/\Pr^{1/2}\theta'(0)\right] + 1} \tag{15}$$

Evaluating $d\theta/d\eta$ at $\eta = 0$, we obtain the following exact implicit relation for the normalized Nusselt number Nu/Nu_0:

$$Nu/Nu_0\left[1 + \operatorname{erf}\left(B\pi^{-1/2}\,Nu/Nu_0\right)\right] = \exp\left[-B^2\pi^{-1}(Nu/Nu_0)^2\right] \tag{16}$$

where

$$Nu_0 = \pi^{-1/2}\,(\mathrm{PrRe})^{1/2} \tag{17}$$

Recently, Reid [21] solved the problem of melting of permafrost by ground water movement using the approximate integral (profile) method. His analysis, however, is concerned with low melting rates ($B \ll 1$) so that $Nu \approx Nu_0$. Equation (16) is plotted in Fig. 1 (just below the curve for $Pr = 10$). One notes that equation (13) can be used to approximately correct for the effects of high melting rates in porous media.[3]

Acknowledgments

It is a pleasure to acknowledge the assistance of F. Pellett in carrying out the computations presented herein and in preparing the figures. This work was performed under the auspices of the U. S. Energy Research and Development Administration.

References

1 Yen, Y. C., and Tien, C., "Laminar Heat Transfer Over a Melting Plate, the Modified Leveque Problem," *J. Geophy. Res.*, Vol. 68, No. 12, 1963, pp. 3673–3678.

2 Pozvonkov, F. M., Shurgalskii, E. F., and Axselrod, L. S., "Heat Transfer at a Melting Flat Surface Under Conditions of Forced Convection and Laminar Boundary Layer," *International Journal of Heat and Mass Transfer*, Vol. 13, 1970, pp. 957–962.

3 Griffin, O. M., "Heat, Mass, and Momentum Transfer During the Melting of Glacial Ice in Sea Water," JOURNAL OF HEAT TRANSFER, TRANS. ASME, Series C, Vol. 95, 1973, pp. 317–323.

4 Epstein, M., "The Effect of Melting on Heat Transfer to Submerged Bodies," *Letters in Heat and Mass Transfer*, Vol. 2, 1975, pp. 97–104.

5 Epstein, M., and Cho, D. H., "Laminar Film Condensation on a Vertical Melting Surface," JOURNAL OF HEAT TRANSFER, TRANS. ASME, Series C, Vol. 98, 1976, pp. 108–113.

6 Landau, H. G., "Heat Conduction in a Melting Solid," *Quart. Appl. Math.*, Vol. 8, 1950, pp. 81–94.

7 Roberts, A. L., "On the Melting of a Semi-Infinite Body Placed in a Warm Stream of Air," *Journal of Fluid Mechanics*, Vol. 4, 1958, pp. 505–528.

8 Schlichting, H., *Boundary Layer Theory*, McGraw-Hill, New York, Chapter XIV, 1960.

9 Sparrow, E. M., and Gregg, J. L., "Summary of Low-Prandtl-Number Heat-Transfer Results for Forced Convection on a Flat Plate," *J. Aero. Sci.*, Vol. 24, 1957, pp. 852–853.

10 Spalding, D. B., "Mass Transfer in Laminar Flow," *Proc. Roy. Soc.*, Vol. A221, 1954, pp. 78–84.

11 Merk, H. J., "Mass Transfer in Laminar Boundary Layers Calculated by Means of a Perturbation Method," *Appl. Sci. Res.*, Vol. A8, 1959, pp. 237–260; see also pp. 261–277.

12 Mickley, H. S., Ross, R. C., Squyers, A. L., and Stewart, W. E., "Heat, Mass, and Momentum Transfer for Flow over a Flat Plate With Blowing or Suction," N.A.C.A. Technical Note 3208, 1954.

13 Acrivos, A., "The Asymptotic Form of the Laminar Boundary-Layer Mass-Transfer Rate for Large Interfacial Velocities," *Journal of Fluid Mechanics*, Vol. 12, 1962, pp. 337–357.

14 Stewart, W. E., and Prober, R., "Heat Transfer and Diffusion in Wedge Flows With Rapid Mass Transfer," *International Journal of Heat and Mass Transfer*, Vol. 5, 1962, pp. 1149–1163.

15 Evans, H. L., "Mass Transfer Through Laminar Boundary Layers—6. Methods of Evaluating the Wall Gradient for Similar Solutions; Some New Values for Zero Main-stream Pressure Gradient," *International Journal of Heat and Mass Transfer*, Vol. 3, 1961, pp. 321–339.

16 Bird, R. B., Stewart, W. E., and Lightfoot, E. N., *Transport Phenomena*, Wiley, New York, Chapter 21, 1960.

17 Ranz, W. E., and Dickson, P. F., "Mass and Heat Transfer Rates for Large Gradients of Concentration and Temperature," *Ind. Eng. Chem. Fundam.*, Vol. 4, 1965, pp. 345–353.

18 Humphrey, D. W., and Van Ness, H. C., "Mass Transfer in a Continuous Flow Mixing Vessel," *AIChE Journal*, Vol. 3, 1957, pp. 283–286.

19 Muskat, M., *Flow of Homogeneous Fluids Through Porous Media*, J. W. Edwards, Ann Arbor, 1946.

20 Harr, M. E., *Groundwater and Seepage*, McGraw-Hill, New York, 1962.

21 Reid, R. I., "Integral Methods for the Melting of Permafrost by Ground Water Flows," 15th National Heat Transfer Conference—San Francisco, Aug. 1975, Paper No. AIChE 32E10-G7.

[3] A practical upper limit for B for water is $B \leq 1.25$.

The Laminar Compressible Boundary Layer on a Rotating Sphere With Heat Transfer

M. Y. Hussaini[1] and M. S. Sastry[2]

Nomenclature

a = radius of the sphere
C_p = specific heat at constant pressure
g = acceleration due to gravity
Gr = Grashof number = $g\,\beta/C_p\,(h_w^* - h_\infty^*)(2a)^3/\nu_w^{*2}$
h = enthalpy
Nu = Nusselt number based on diameter = $2a/(h_w^* - h_\infty^*)(\partial h^*/\partial y^*)_{y^*=0}$
$\bar{\mathrm{Nu}}$ = average Nusselt number
Pr = Prandtl number
Re = Reynolds number based on diameter = $4a^2\Omega/\nu_w^*$
u = x-component of velocity (meridional)
v = y-component of velocity (radial)
w = z-component of velocity (azimuthal)
x = meridional coordinate measured from north pole

[1] Chief, Flow Fields, Aerodynamics Division, Space Science and Technology Centre, Trivandrum, India. Presently at NASA Ames Research Center, Calif.

[2] Scientist, Aerodynamics Division, Space Science and Technology Centre, Trivandrum, India.

Contributed by the Heat Transfer Division of THE AMERICAN SOCIETY OF MECHANICAL ENGINEERS. Manuscript received by the Heat Transfer Division September 5, 1976.

y = radial coordinate measured normal to surface
β = coefficient of thermal expansion
μ = coefficient of viscosity
ν = kinematic viscosity
ρ = density
τ = torque
Ω = angular velocity about the vertical diameter

Superscript

* = dimensional quantity

Subscripts

∞ = value in the ambient fluid
w = value at the wall

Introduction

There are many theoretical investigations of the thermal boundary layer induced by an isothermal sphere rotating in an otherwise quiescent fluid [1–11].[3] The analyses of Kreith, et al. [1] and of Singh [2] are based on Nigam's solution [3], the applicability of which to the real situation is doubtful. It also has a further drawback—poor convergence for Prandtl numbers less than 3. The results of Banks [4] which are based on series solution (in powers of meridional angle) show notably poor agreement with experimental data. Similar criticism can be made about the approximate methods of Dorfman and Serazetdinov [5] and of Dorfman and Mironova [6]. None of these studies include the buoyancy effects. The present method seems to be devoid of such drawbacks and the analysis presented here considers the influence of buoyancy and viscous dissipation on torque, heat transfer, and the position of the ideal jet (the plane of impingement of the boundary layer from the northern and southern hemispheres).

Analysis

The equations of motion for the laminar compressible boundary layer on a sphere rotating in a fluid otherwise undisturbed are given in references [7–8] where the following nondimensional variables and transformations are introduced.

$$x = x^*/a, \quad y = y^*(\mathrm{Re})^{1/2}/2a, \quad u = u^*/a\Omega \sin x$$
$$\vartheta = \vartheta^*(\mathrm{Re})^{1/2}/2a\Omega \sin x,$$
$$w = w^*/a\Omega \sin x, \quad \rho = \rho^*/\rho_w^*; \quad \mu = \mu^*/\mu_w^*$$
$$h = (h^* - h_\infty^*)/(h_w^* - h_\infty^*) \text{ and } (\vartheta = \bar{\vartheta} + uy \cot X)$$
$$\bar{X} = \int \sin x\, dx, \quad \bar{Y} = \int \sin x\, dy, \quad \eta = \int \rho d\bar{y}, \quad \xi = 1 + \bar{X}, \quad \mu\rho = 1 \tag{1}$$

To apply the Galerkin-Kantrovich-Dorodnitsyn (GKD) method these transformed equations are multiplied by proper weight functions and are then integrated with respect to η across the boundary layer. It has been found expedient to replace η by w.

The integrands in the resultant integral relations are assumed to be polynomials in w. One-strip approximation in the GKD formulation yields a trivial solution. For the two-strip approximation the following polynomials are assumed which satisfy the pertinent boundary conditions.

$$\begin{aligned} u &= 4u_1 w(1 - w) \\ \theta &= (2\theta_0 - \theta_1) + (\theta_1 - \theta_0)/w \\ 1/\theta &= (4/\theta_1 - 1/\theta_0)w + (2/\theta_0 - 4/\theta_1)w^2 \\ h &= (4h_1 - 1)w + (2 - 4h_1)w^2 \end{aligned} \tag{2}$$

where

$$\theta = 1 \Big/ \frac{\partial w}{\partial \eta}, \left(\frac{\partial w}{\partial \eta}\right)_{\eta=0} = 1/\theta_0 \tag{3}$$

and u_1, θ_1, h_1 are the values of u, θ, and h at $w = \frac{1}{2}$. It may be observed that there is only one unknown for each u and h and hence only one equation each for u_1 and h_1 need be generated from the integral relations. Thus, the chosen weight functions in the GKD method are $f_2(u) = u^2$ and $H_2(h) = h^2$ so that all the terms in the integral relations could be retained. For the two unknowns in θ as is usually done in the GKD method $g_n(w)$ is chosen as $g_1(w) = w$ and $g_2(w) = w^2$. Substituting these weight functions and the polynominal expansions (2), the integral relations can be reduced to a set of four coupled ordinary differential equations to be solved as an initial value problem.

Appropriate initial conditions must be added to these equations for the complete specification of the problem. If the various terms in the foregoing equations are of the same magnitude to the lowest order in ξ near the pole, then it is found that u_1 = constant, $Z_0 = -A_0(\xi)^{1/2}$, $Z_1 = -A_1(\xi)^{1/2}$, h_1 = constant where $Z_0 = u_1\theta_0$, $Z_1 = u_1\theta_1$. These are referred to as starting solutions. The various constants in the starting solutions are obtained by solving the algebraic equations resulting from their substitution into the system of ordinary differential equations and letting ξ tend to zero. The starting solution implies that the flow at the pole for $\mathrm{Gr}/\mathrm{Re}^2 = 0$ is identical to that due to a rotating disk. The solution to the system of ordinary differential equations is then obtained by a Runge-Kutta method of integration.

Table 1 The coefficient of torque $\mathrm{Gr}/\mathrm{Re}^2 = 0$

	Methods	Coefficient of torque
Theoretical:	Dorfman and Serazetdinov [5]	4.1
	Dorfman and Mironova [6]	3.91
	Nigam [3]	3.98
	Manohar [9]	3.265
	Present method	3.279
Experimental:	Bowden and Lord [11]	3.5

Results and Discussions

(a) Velocity Boundary Layer. It is found that u_1 remains nonzero at the equator and its value is in agreement with Manohar's [9]. It is also found that the values of u_η and w_η at the surface as calculated by the present method for $\mathrm{Gr}/\mathrm{Re}^2 = 0$ agree very well with those of reference [9]. A comparison of the values of the torque coefficient as obtained in different studies is given in Table 1. More significantly, it is found that the kind of solution proposed by Nigam [3] does not exist. If we substitute $u_1 = 0$ at the equator, i.e., $\xi = 1$ in the resultant ordinary differential equations, we find after a little manipulation in two different ways that $du_1/d\xi$ at best vanishes at the equator, but in the case of Nigam's solution [3] it is negative.

(b) Heat Transfer. In the case of forced convection it is inferred from the analysis that the Prandtl number dependence of average Nusselt number can very well be approximated by $\bar{\mathrm{Nu}}/\mathrm{Re}^{1/2} = 0.318\,\mathrm{Pr}^{0.4}$. Fig. 1 gives a comparison of the present values of the local Nusselt number with those of Chao and Greif [10] for Pr = 10, and it

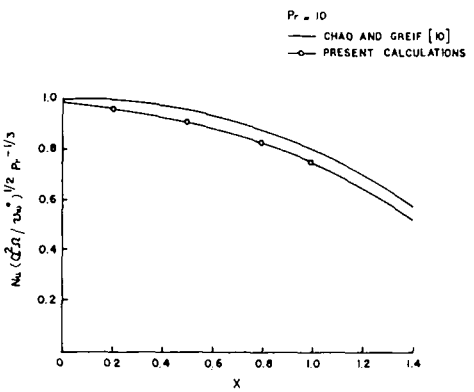

Fig. 1 Local Nusselt number versus X

[3] Numbers in brackets designate References at end of technical note.

Table 2 $\frac{\overline{Nu}}{Re^{1/2}}$ for $\frac{Gr}{Re^2} = 0$ and Pr = 0.7

Method	$\frac{\overline{Nu}}{Re^{1/2}}$	
Banks [4]	0.25	Theoretical
Dorfman and Mironova [6]	0.252	
Dorfman and Serazetdinov [5]	0.276	
Present method	0.291	
Kreith, et al. [1]	0.373	Experimental

can be seen that the results compare well for a two-strip approximation. Table 2 gives a comparison of the various theoretical predictions with experimental results of $\bar{N}u/Re^{1/2}$, and it is found that the present results are closer to, but still less than, the experimental values. The discrepancy may be explained by the neglect in the analysis of turbulent interaction at the equator.

In the absence of the buoyancy force the flow over the sphere possesses symmetry with respect to the equatorial plane, assuming of course that the equatorial jet is an infinitesimally thin sheet. The buoyancy effect destroys this symmetry. As the equations under consideration cannot describe the region of impingement of the boundary layers from the two poles, they are integrated from the north pole southward and from the south pole northward up to the latitude where the meridional velocity u_1 is equal in magnitude and opposite in sign. This fixes the position of the ideal jet. These are plotted for a series of values of Gr/Re^2 in Fig. 2. It is clear from that figure that the flow at the north pole is not identical to that at the south pole owing to the influence of buoyancy which opposes the meridional flow in the upper hemisphere and aids it in the lower hemisphere. However, buoyancy effect is suppressed at the poles, i.e., if the flow at the poles is taken to be that due to a Karman disk, the flow development in the meridional plane recovers more or less immediately from these forced initial conditions and the overall effect is negligible on the average Nusselt number, torque, and the locations of the ideal jet.

Fig. 2 also shows the shifting of the ideal jet toward the north pole as the buoyancy force is increased. It is observed that the local Nusselt number above the jet decreases, and that below the jet increases with the increase in Gr/Re^2. It is found that there is no meridional flow from the north pole toward the equator for $Gr/Re^2 = 0.22$, implying that the centrifugal force which causes such a flow is outbalanced by the buoyancy force, and hence, this may be taken as the limit beyond which free convection is predominant. For $Gr/Re^2 = 0.15$ it appears as if the boundary layer solution describes the flow over the whole sphere including a laminar jet whose extent is predicted to be roughly 50 deg $< X <$ 73 deg. For the values of Gr/Re^2 lying between 0.15 and 0.22 the meridional velocity in the boundary layers on the upper and lower hemisphere goes to zero before they could impinge upon each other, and thereafter the solution becomes unstable.

Although in practical situations transition occurs before dissipation becomes significant, the case of nonzero dissipation has also been

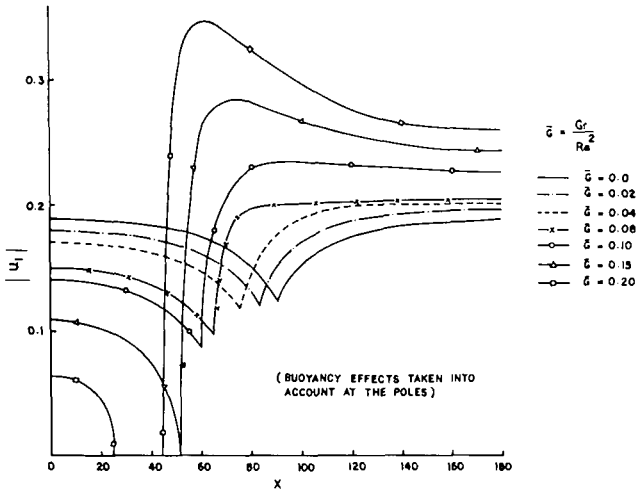

Fig. 2 The absolute value of U_1 versus X

considered in our study and it is found that increase in dissipation decreases the Nusselt number. The torque decreases for nonzero values of Gr/Re^2 as increasing dissipation pushes the ideal jet location upward. With an increase in Gr/Re^2 the torque decreases and the local Nusselt number above the jet decreases and increases below the jet.

References

1 Kreith, F., et al., "Convection Heat Transfer and Flow Phenomena of Rotating Spheres," *International Journal of Heat and Mass Transfer*, Vol. 6, 1963, pp. 881–895.

2 Singh, S. N., "Heat Transfer by Laminar Flow From a Rotating Sphere," *Applied Science Research*, Vol. A9, 1960, pp. 197–205.

3 Nigam, S. D., "Note on the Boundary Layer on a Rotating Sphere," *Z. Angew. Math. Phys.*, Vol. 5, 1954, pp. 151–155.

4 Banks, W. H. H., "The Thermal Laminar Boundary Layer on a Rotating Sphere," *Z. Angew., Math. Phys.*, Vol. 16, 1965, pp.780–788.

5 Dorman, L. A., and Serazetdinov, A. Z., "Laminar Flow and Heat Transfer Near Rotating Axisymmetric Surface," *International Journal of Heat and Mass Transfer*, Vol. 8, 1965, pp. 317–327.

6 Dorfman, L. A., and Mironova, V. A., "Solutions of Equations for the Thermal Boundary Layer on a Rotating Axisymmetric Surface," *International Journal of Heat and Mass Transfer*, Vol. 6, 1970, pp. 81–92.

7 Kreith, F., "Convection Heat Transfer in Rotating Systems" *Advances in Heat Transfer*, Vol. 5, Academic Press, 1968.

8 Hussaini, M. Y., and Sastry, M. S., "The Method of Integral Relations for Three Dimensional Boundary Layer Flow on an Axisymmetric Body," SSTC-ARD-TR-69-75, 1975.

9 Manohar, R., "The Boundary Layer on a Rotating Sphere," *Z. Angew, Math. Phys.*, Vol. 18, 1967, pp. 320–330.

10 Chao, B. T., and Greif, R., "Laminar Forced Convection Over Rotating Bodies," JOURNAL OF HEAT TRANSFER, TRANS. ASME, Series C, Vol. 96, 1974, pp. 463–466.

11 Bowden, F. P., and Lord, R. G., "Aerodynamic Resistance to a Sphere Rotating at High Speed," *Proc. Roy. Soc.*, A271 1963, pp. 143–153.